Transactions of the ASME®

Transactions of the ASME, Journal of Engineering for Gas Turbines and Power (ISSN 0742-4795) is published quarterly (Jan., Apr., July, Oct.) for $150.00 per year by The American Society of Mechanical Engineers, 345 East 47th Street, New York, NY 10017. Second class postage paid at New York, NY and additional mailing offices. POSTMASTER: Send address changes to Transactions of the ASME, Journal of Engineering for Gas Turbines and Power, c/o THE AMERICAN SOCIETY OF MECHANICAL ENGINEERS, 22 Law Drive, Box 2300, Fairfield, NJ 07007-2300.
CHANGES OF ADDRESS must be received at Society headquarters seven weeks before they are to be effective. Please send old label and new address.
PRICES: To members, $40.00, annually; to nonmembers, $150.00.
Add $30.00 for postage to countries outside the United States and Canada.

INDEXED by Applied Mechanics Reviews and Engineering Information, Inc.
Canadian Goods & Services Tax Registration #126148048

Journal of Engineering for Gas Turbines and Power

Published Quarterly by The American Society of Mechanical Engineers
VOLUME 117 • NUMBER 2 • APRIL 1995

TECHNICAL PAPERS

(Contents Continued on Page 244)

Contents (Continued)

ANNOUNCEMENTS

The Applicability of Electrically Driven Accessories for Turboshaft Engines

M. S. Jarvis

W. J. Ostergren

General Electric Aircraft Engines,
Lynn, MA 01910

B. Smith

Aviation Applied Technology Directorate,
U. S. Army Aviation and Troop Command,
Fort Eustis, VA 23604

Improved electrical power generation and actuation systems offer new design approaches for performing the engine control and accessory functions in helicopter propulsion systems. Present helicopter technology utilizes turboshaft engines with mechanically driven accessories. These accessories perform the functions of starting, fuel and lube pumping, variable stator actuation, and inlet particle separation. This paper discusses the applicability of replacing the mechanically driven accessories with their electrically driven counterparts. An electric accessory system is defined, which includes a switched reluctance starter/generator and its associated control unit; an electric pumping and actuation system; and the engine mounting for the starter/generator. A comparison between the mechanically and electrically driven accessory systems is performed on the basis of cost, weight, and reliability. Experience to date with switched reluctance machines and electrically driven turboshaft accessory systems is summarized. The benefits of electrically driven accessories are shown and recommendations for future activity for this important technology are discussed.

Introduction

Advances in electronic semiconductors and electric motors have now enabled traditional turboshaft engine controls and accessory designs to incorporate these technologies. The key developments that permit this are in the area of switched reluctance machines and the associated electronics. Given an efficient power source, more reliable, lighter, and less expensive motors are also in a position to compete with the traditional engine gearbox drives. This provides for simpler, more responsive fuel and the lube delivery systems. It also offers new challenges for the engine and cooling system design. This paper will give a brief description of the engine accessories that are considered for electric technologies, and an overview of the starter/generator system including a description of a switched reluctance machine and the associated electronics. This will be followed by a more detailed description of the electric accessories and the engine mounting, and electronics cooling considerations. Given the preliminary design of an electric system, a trade study was completed and the results are presented with a summary of the hardware experience.

Current Accessory Systems

Present gas turbine aircraft engines require control and accessory systems to provide stable control of the engine turbomachinery, lubrication, and starting. In order to ensure stable, efficient control of the engine, the control system provides metered fuel to the engine combustor, actuation for the compressor variable stators, and lubrication to the engine bearings. A typical turboshaft engine control system accomplishes these functions with accessories such as the fuel boost and high-pressure pumps, lube pump, alternator for electrical power, hydromechanical control unit, and electrical control unit. These accessories are driven by the engine gearbox. The gearbox is also utilized for starting the engine.

Electrical Accessory Systems

In addition to shaft power, typical turboshaft airframe applications also require large amounts of electrical power. Traditionally this electrical power is provided through generators that are mounted on the main rotor gearbox or transmission. By combining the starting and generating functions into one machine a turboshaft engine becomes capable of providing to the airframe both mechanical and electrical power. In addition the engine can benefit from the availability of this electric power by replacing the engine gearbox drive to the fuel and lube pumps and the hydraulic power for the variable stator actuator with electric motor drives. A conceptual electric accessory control system block diagram is shown in Fig. 1.

Engine Starter/Generator System

The engine starter is required for less than one minute for each start attempt and is not used after completion of engine starting. It is generally sized to produce adequate torque to start the engine. Figure 2 shows a typical starting and gener-

Contributed by the International Gas Turbine Institute and presented at the 38th International Gas Turbine and Aeroengine Congress and Exposition, Cincinnati, Ohio, May 24–27, 1993. Manuscript received at ASME Headquarters March 17, 1993. Paper No. 93-GT-313. Associate Technical Editor: H. Lukas.

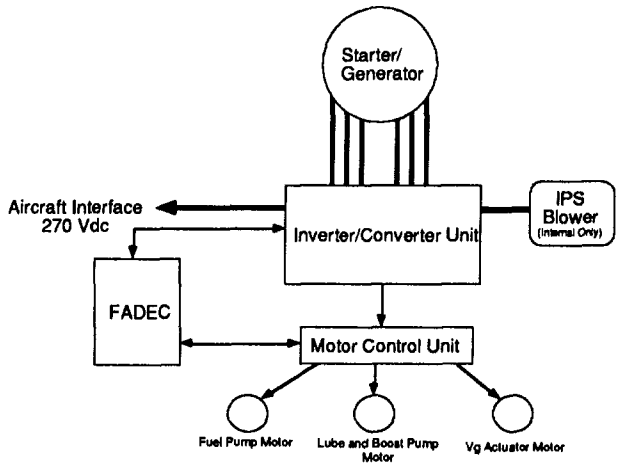

Fig. 1 Engine electric interfaces show a simple architecture

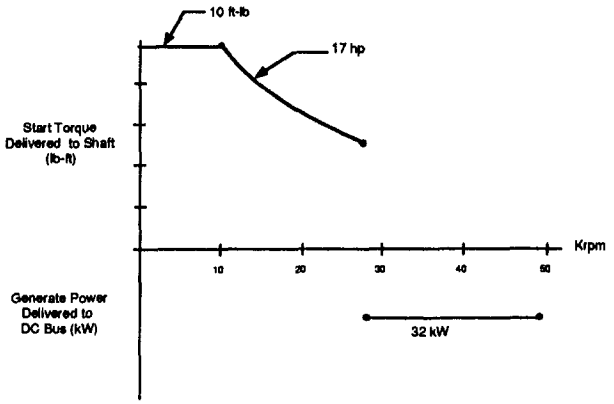

Fig. 2 Start and generating requirement

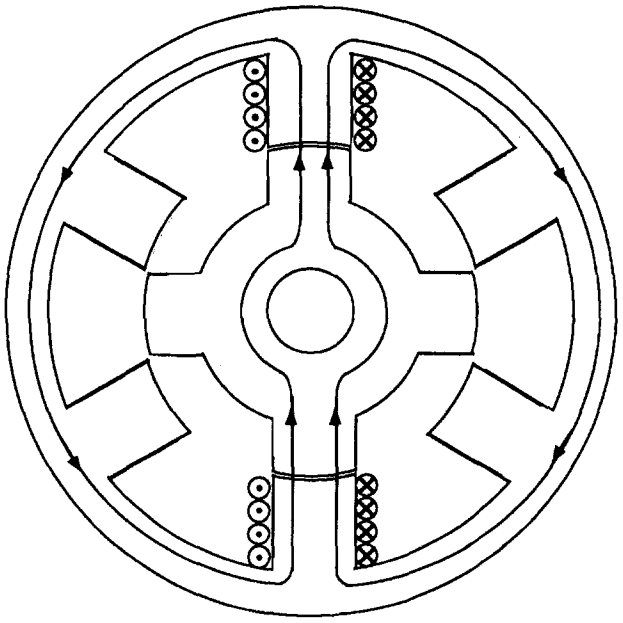

Fig. 3 Switched reluctance machine cross section shows a simple rotor and stator configuration

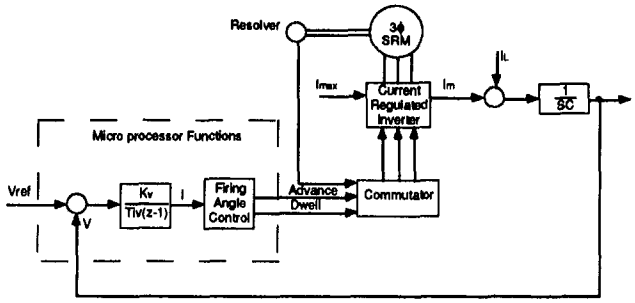

Fig. 4 Switched reluctance controller block diagram

ating requirement curve. Electric power generation is initiated after the starter has been turned off. This situation lends itself to a natural integration of the starting and generating functions into one electrical machine, the starter/generator. Since this machine acts as a starter for the engine, it is implied that it should be mounted to the engine compressor shaft. This enables extracting power, in the generation mode, directly from the compressor/gas generator shaft.

Several different machine technologies have been examined as candidates for implementing the starter/generator functions. The main issues for starter/generator machine selection are high rotational speed capability (in excess of 50,000 rpm for some directly coupled machines on small turboshaft engines), power density, reliability, and cost. Overall, it was concluded that the switched reluctance machine (SRM) offered the best compromise of these criteria for aircraft engine applications.

The switched reluctance machine is a brushless synchronous machine with salient rotor and stator poles, concentrated phase windings, and no permanent magnets or rotor windings. A diagram of the machine is shown in Fig. 3. The switched reluctance machine is inherently low in cost. Its rotor is constructed from a simple stack of laminations shrunk fit onto a shaft, making it a rugged and low-cost structure. This simple construction also gives the SRM rotor the capability of operating at very high engine speeds without the containment problems associated with rotor windings or permanent magnets.

Likewise the stator assembly process is simple and inexpensive. Each phase of the machine is made up of two coils wound around diametrically opposed stator poles and electrically connected in series. The concentrated stator winding can be externally form-wound and slipped over the salient stator poles, resulting in lower construction cost.

Switched reluctance machines also have the potential to run in very high temperature environments. Because it has no permanent magnets, the maximum operating temperature of the machine is limited primarily by the insulation system. Machine designs have been explored for operating temperatures up to 400°C.

Simplicity, ruggedness, and high temperature capability lead to high reliability in switched reluctance machines. Further discussion on the operation of the SRM can be found in the literature [4, 5].

Inverter/Converter Unit

The main function of the inverter/converter unit (ICU) is to supply unidirectional current to the machine during starting and accept unidirectional current from the machine during generation. The ICU is made up of a controller and a power bridge. The controller is a microprocessor-based digital control that is capable of high bandwidth control of the power switches in the power bridge. The controller block diagram is shown in Fig. 4 and the power bridge in Fig. 5. The power bridge contains the high power capacitors, diodes, and solid state switches necessary to perform the power switching to the machine windings. For the application being considered here, the power bridge requires parallel diodes and switching devices to handle the high currents.

It is the high currents that drive the size of the power

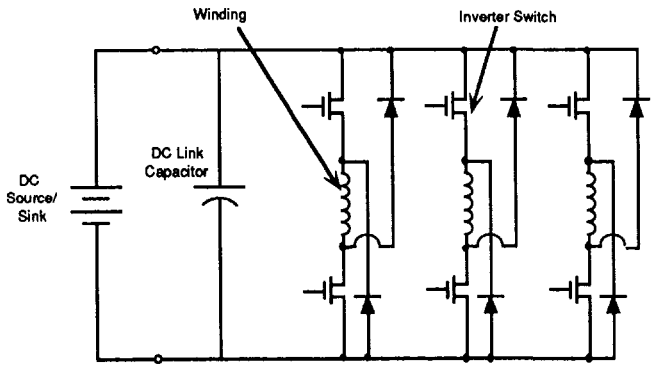

Fig. 5 High power solid state switches make the ICU power bridge practical

devices and thus the size and weight of the total ICU. In order to make this technology feasible for aircraft engines, reducing the size and weight is a major concern.

There are several types of device for each of these key components. Ceramic capacitors have offered the smallest volume for the DC link capacitor. Typically the power switches are either MOSFET's (metal oxide semiconductor (MOS) field effect transistors), or IGBT's (insulated gate bipolar transistors), with the emerging MCT's (MOS controlled thyristor) being the leading candidate for the next generation of ICU's. Although high current capability power devices have made possible compact brushless DC motors and generators, additional developments in high temperature power electronic devices and packaging techniques are needed to reduce the size and cost further and thereby enable the electric accessory drive technology to realize its full potential.

There is considerable flexibility in the topology of the power inverter/converter module used to drive the switched reluctance machine. The topology shown in Fig. 5 was chosen for the starter/generator because it offers the maximum control flexibility and has a high level of fault-tolerance.

Electric Accessories

Electric Fuel Pumping. In the traditional engine control system, the fuel pumps are driven from the engine gearbox. Because the gearbox is driven by the engine gas generator shaft, the fuel pump speed is confined to a ratio of the engine speed. This means that the pump is usually sized for a low speed and high fuel flow for engine starting. Due to this sizing condition, the pump becomes oversized at the higher engine speeds, thus causing large recirculating fuel flow. Electrically driven fuel systems offer more flexibility in the fuel system design. One of the electric systems being considered is a direct motor-driven fuel metering system.

The electric fuel metering system has the advantage of supplying the precise amount of fuel required by the engine and thereby eliminating the heating resulting from the recirculation. Major components of the fuel metering system are: the fuel pump rotor, the motor speed controller, and a gear pump directly coupled to the motor as shown in Fig. 6. Fuel flow is metered to the engine by varying pump speed. Engine fuel demand is determined by the engine FADEC that translates the desired fuel flow into a motor speed. The FADEC then sends a speed demand signal to the motor controller that turns the fuel pump motor at the required speed for correct engine fuel flow.

Other electric fuel pumping schemes are possible. One alternate fuel pumping scheme being considered is a constant speed electric motor drive as shown in Fig. 7. Fuel flow in excess of engine need is recirculated as the traditional system. However, the motor speed is chosen to minimize fuel

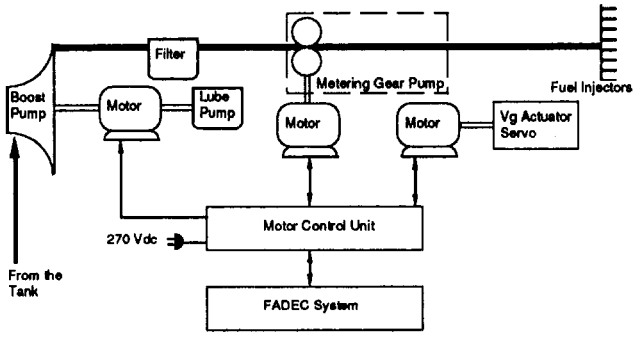

Fig. 6 Directly metered fuel flow simplifies fuel system design

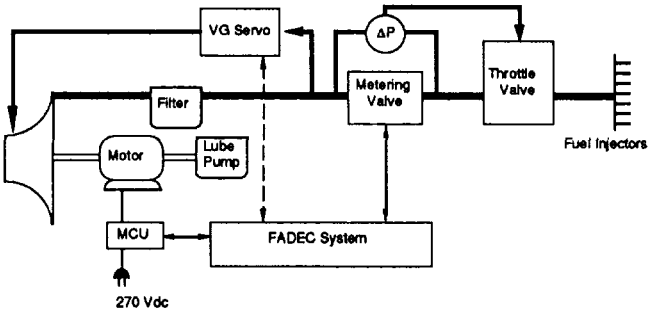

Fig. 7 Hybrid electrical / hydraulic fuel system eliminates two drive motors without compromising electric benefits

recirculation requirements and thereby reduces the resulting fuel heating. This constant speed fuel pumping scheme permits a variable geometry actuator to be fuel operated, which can be an advantage for small actuators.

Lube Oil Pumping Systems. The engine lube oil pumping system provides lubricating oil to the engine components as well as cooling oil for the starter/generator machine and ICU. The electrically driven lube oil system as presently designed uses a constant-speed brushless DC motor. For small engines, a motor rated between 2 and 5 hp is adequate. The motor is powered from the 270 VDC bus and runs at 9,000 rpm, although this speed is adjustable.

Variable Geometry Actuation System. The Variable Geometry (VG) actuation system is used to position the engine compressor variable stator vanes for optimum engine performance. For small engines this function requires very little power, on the order of 0.1 kW. There are several ways that VG actuation can be accomplished. The approach demonstrated to date applies a commercially available actuator that uses an induction motor powered from a DC source. The motor drives a ball screw through a high ratio gear train (1000:1) that positions the VG actuator within 0.5 deg of the desired position. The separate drive motor for VG actuation is used in conjunction with the electric motor driven fuel metering system. The motor is controlled by the engine FADEC in a closed-loop mode with position feedback.

Hydraulic power is another approach to VG actuation. This is used in conjunction with the constant-speed electric motor fuel pumping approach described earlier. In this approach VG actuation is achieved by fuel powered hydraulic actuators, similar to a traditional system.

Inlet Particle Separation Blower. The Inlet Particle Separator (IPS) performs the function of removing sand, dirt, and other debris from the engine inlet air stream. The IPS system for helicopter applications currently requires a large blower to help provide suction for the dirty air. For small engines, the inlet particle separation blower is approximately a 20 hp blower.

Complete elimination of the engine gearbox forces this blower to be driven electrically or requires a new design approach for inlet particle separation. A 20 hp electric motor is considerably larger than the other electric drives being considered and may be obstructively large for small engine applications. Other approaches have to be considered. One approach for near term or retrofit applications is to drive the blower and the starter/generator off a small engine gearbox. This mounting configuration is discussed below.

Engine Mounting Considerations

Starter/Generator Machine. Mounting designs were considered for starter/generators on front drive two-spool turboshaft engines. A two-spool front drive turboshaft engine was evaluated with the two shafts concentrically located with the output power turbine shaft running through the center of the compressor/gas generator shaft. In order to start this type of engine the starter must initiate turning of the gas generator shaft. This configuration requires a unique starter/generator mounting design. Two different designs were considered: internal and external mounting. The internal design mounts the starter/generator directly to the gas generator shaft concentrically located around the power turbine shaft. The external design utilizes the current gearbox power takeoff shaft and mounts the starter/generator and IPS blower on a small gearbox mounted to the external casing of the engine.

Internally Mounted Starter/Generator. Due to simplicity, fault-tolerance, and high speed capabilities, switched reluctance machine technology provides the potential of producing starter/generators that are reliable enough to be installed internally to the engine. Application of an internal starter/generator requires close coordination between the engine and the starter/generator at an early stage in the design process. Since the internal starter/generator can increase engine length and weight, careful consideration must be given to its impact on engine rotor dynamics. In-depth dynamic analyses should be performed to ensure that engine shaft bending modes do not occur at or near normal engine running speeds. Stress analyses must be conducted to ensure that the engine shaft passing through the starter/generator rotor bore does not force the rotor outer diameter to a dimension greater than the rotational stress handling capability of the rotor material at engine operating speeds.

Although the internally mounted starter/generator introduces increased complexity during the design stage and has less accessibility for maintenance, it allows the total elimination of the engine accessory gearbox (AGB). Figure 8 shows a conceptual engine with an internal starter/generator and electric accessory drives and controls. A conceptual cross-sectional sketch is shown in Fig. 9. Based on preliminary design efforts, it was concluded that retrofitting existing engines with an internally mounted starter/generator would be impractical.

Externally Mounted Starter/Generator. The externally mounted starter/generator does not permit the total elimination of the engine accessory gearbox, but it offers other attractive features, particularly for the initial applications of this new technology. It allows easy access for maintenance as can be seen from Fig. 10. Existing engines could be retrofitted with an externally mounted starter/generator for engine, flight testing and possible near-term applications. Since the other AGB functions would be performed electrically, the externally mounted starter/generator requires only a small gearbox that can be used to also drive the engine inlet particle separator (IPS) blower. Furthermore, the gearbox gear ratios can be chosen for speeds that optimize the starter/generator design.

Engine Accessories. The accessory placement was completed for both the internal and external starter/generator

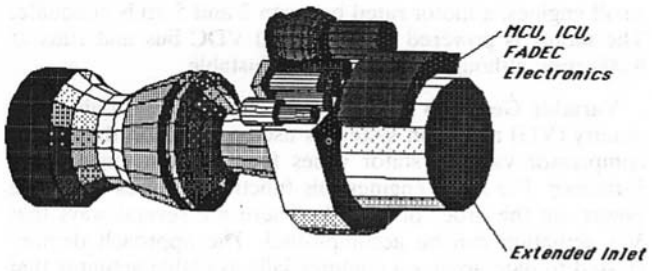

Fig. 8 Conceptual internal mounted S/G shows extended inlet and large IPS blower motor

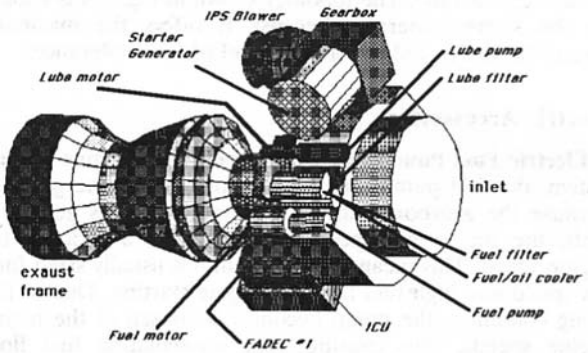

Fig. 10 Conceptual external configuration with reduced two-axis gearbox

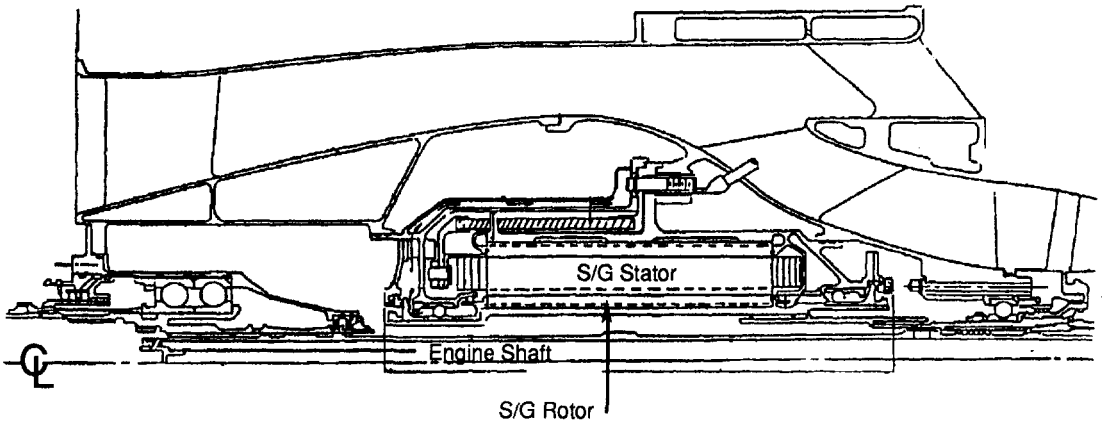

Fig. 9 Internal mounted S/G cross section

configurations. In visualizing the possible accessory arrangements, the following considerations were assumed as requirements: (1) maintaining the engine envelope and (2) turboshaft serviceability and maintainability. In the external configuration, as shown in Fig. 10, the electronic housings were shown in their isolated boxes and mounted around the engine compressor section. The IPS blower has been shown driven off the reduced two-axis gear box that is also driving the starter/generator. The third item of interest in the external configuration is the actuator placement that is flexibly located at the variable geometry roll bar, thus eliminating actuator linkages. The internal starter/generator configuration would also be able to take advantage of this actuator placement. On the internal configuration that is shown in Fig. 8, an integrated electronics package is shown mounted to the extended inlet front frame. This configuration also shows the elimination of the gearbox and a 20 hp IPS blower motor as the alternative drive. The IPS blower is no longer required to be mounted at its current location. However, because of the air piping and the sizable drive motor required, the IPS blower was kept at the same location. The other drive motors for the fuel and lube pumps have been placed for both configurations on the scroll frame of the engine. For the external configuration the motors and pumps have been stacked and have slightly less room than the internal configuration. However, there do not seem to be any restrictive problems in either configuration due to the highly flexible properties of the electric systems. This flexibility can also open the possibilities of off-engine mounting of the components to reduce the harsh engine temperature and vibration environment.

Cooling. A preliminary analysis of the cooling system for a turboshaft electric accessory engine was completed. The starter/generator and added electrical components for a system requiring 32 kW of electrical power adds, at worst case conditions, approximately 29,670 Btu/h to the engine cooling system. For this new design, the lube system was identified as the medium for removing the added heat. Even with the added components the oil temperature was found not to exceed temperature limits. However, with the calculated sizes of the ICU and an assumed worst case power dissipation, 120°C inlet oil will be pushing the maximum limits of the electrical component junction temperatures. Therefore, the new system is designed with an air/oil heat exchanger to remove the added heat. Figure 11 shows a proposed block diagram of a modified engine lube system. The heat exchanger was calculated to adequately handle removing the added heat and maintaining a lower inlet temperature. An air oil heat exchanger of approximately 500 in.^{3} accommodates removal of the added heat and maintains an oil inlet temperature yielding an approximate 20°C operating margin on the electronic junction temperatures. This shows that the given electrical system will add a more aggressive cooling/lube system, but the challenge is not insurmountable. This may lead to other design arrangements where the heat exchanger is mounted off the engine or put in a part of the engine air flow or piped from the inlet particle separation system.

System Comparison and Benefits of Electric Accessories

A trade study of traditional turboshaft engine controls accessory components versus the electric accessory control accessories was completed. The comparison included trade studies of engineering estimates based on 250th production shop costs and component weights, failure rates, and operational costs. The components or functions of the turboshaft engine that were considered were the starting and electrical

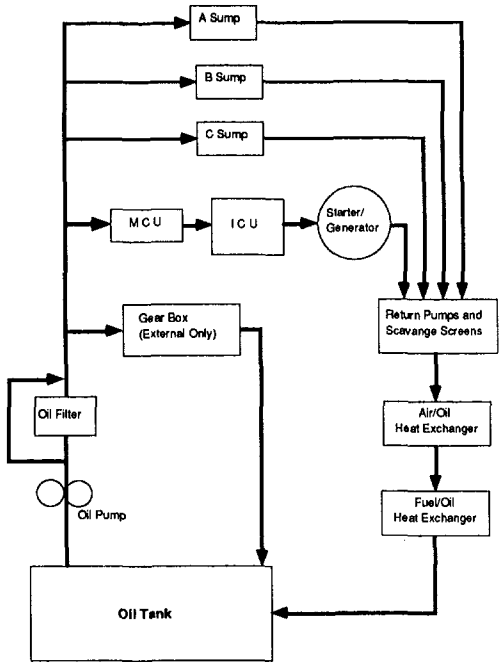

Fig. 11 Modified turboshaft lubrication / cooling system

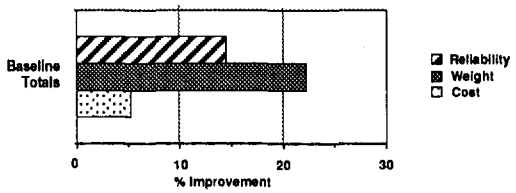

Fig. 12 Total electric accessory system shows improved cost, weight, and reliability

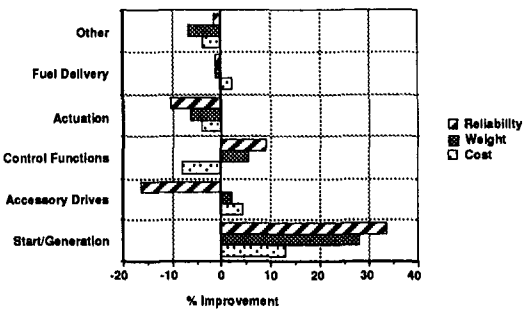

Fig. 13 Detailed functional areas indicate a hybrid electric hydraulic system design

generation, including the current airframe starter and generator, and the fuel, lube, actuation, control, and accessory drive systems.

The results of the system trade study are shown in Fig. 12 for the external starter/generator configuration. These graphs show the percent of improvement of the electric system over the traditional system in cost, weight, and reliability. The baseline traditional system is considered as 100 percent and the percent improvement is measured above that baseline system. Figure 12 shows that there is potential for overall benefits in all three areas in which comparisons are made. Figure 13 shows the comparisons in more detail for each of the categories evaluated. It can be seen that electric accessories are not beneficial in all categories. For example, the actuation system design shows benefits in none of the parameters compared. On the other hand, the starter/generator shows benefits in all areas of comparison. Functional categories such as the actuation system that show no benefits are

Table 1 Electric accessory engine and laboratory testing hours

Component	Rating	Operating Hours In Laboratory	Operating Hours On-Engine
Starter/Generator	32kW	200	250
Fuel Pump (Small Engine)	2 hp	320	150
VG Actuators	0.1 kW	50	150
VATN Actuators	0.1 kW	50	150
Lube Oil Pump	2 hp	50	150
Starter/Generator	90kW	8	-
Fuel Pump (Large Engine)	120 hp	43	-
Resolverless S/G Operation	-	30	-

VATN - Variable Area Turbine Nozzle

candidates for either redesign or basic technology developments or both. As can be expected design actions made to increase reliability, such as adding redundancy in motors and electronics, were drivers in increasing cost and weight. Components with inherent redundancy and fault-tolerance such as the SRM have good potential of reducing the penalty paid for redundancy.

Other engine benefits of electric accessory drives that are not quantifiable into the categories of weight, cost, and reliability include the following: increased flexibility of component location; increased modularity and line replaceable unit design for components; improved testability and diagnostics by operating accessories for checkout without having to run the engine; gas path and lube oil cooling by motoring the S/G after engine shutdown; and a more compact engine profile.

A system trade study for an internal configuration was also considered. The results from this trade study were not as promising as those for the external. This occurred because the study examined modifications required for an existing turboshaft engine. An internal configuration would increase the engine size and add a considerable amount of engine weight and cost to the existing engine design. However, in order to draw any firm conclusion about an internal starter/generator configuration, a trade study of a new engine design is required. This may indicate that the internal configuration is not a good candidate for retrofits but is more promising when there is an opportunity for an integral design effort between engine turbomachinery and the electric machinery.

Electric Accessory Hardware Experience

Since 1986, GE Aircraft Engines has been developing the electric accessory technologies for jet engines. Beginning in 1988, various electric accessory components have been used to run demonstration engines in test cells. Table 1 summarizes GEAE's experience with electric accessory technology for both laboratory and on-engine operation.

In addition to normal temperature range operation, the 17 hp starter/generator, lube oil pump, fuel pump, VG and VATN actuators were used to successfully start and operate an engine under cold temperature conditions down to $-15°C$.

Extended bench and on-engine testing have established electrically driven accessories to be reliable and capable of trouble-free operation. No inherent electric accessory technology shortcomings have been uncovered.

Conclusions

With emerging high-power-density electronic devices, smaller, more responsive lightweight electronic control offers excellent promise for turboshaft engines. Even in its infancy electronic control systems are showing improved cost, weight, and reliability over the matured mechanical systems. As well as the tangible benefits, it also offers improvements in modularity, flexibility, and LRU design. The switched reluctance starter/generator system provides an ideal way of combining two current engine/airframe functions into one for an overall system benefit. An electrically based system allows the fuel and lube systems to be designed without the dependence on the engine speed. By mounting the starter/generator internally on the engine gas generator shaft, the engine gear box can be eliminated, which is a major simplification to the accessories. For near-term applications an externally mounted starter/generator is easier to adapt. In either case, concurrent engineering of the airframe requirements, engine definition, and starter/generator system are required at an early stage of the design process. As with any new technology area, there are additional design challenges, such as the electronics cooling in the harsh engine environment, which must be addressed.

Recommended Future Directions

The More Electric Engine (MEE) is a critical technology and represents a crucial building block in the More Electric Aircraft (MEA)/More Electric Rotorcraft (MER) effort. It should be pointed out that to make MEA and MER work, a constant, reliable, and safe new source of electric power must be developed. A MEE system, integrated with a Starter/Generator, electric accessories, and magnetic bearings (for elimination of lube system) could provide airframe and engine power requirements. The experience to date with this new technology has shown great potential. There is much room for improvement, however. Further work is necessary to eliminate the resolver from the S/G. A next generation S/G needs development where air-cooling can be implemented without the weight/volume penalty. New, innovative cooling techniques will need to be developed for the ICU and related electronics. Further development is needed to reduce MCT size as well as improve current and temperature capacity. Capacitor development needs to be accelerated on the level of MCTs to reduce volume and weight. It is critical that industry go about this development with the intent to commercialize and mass produce.

It is important to develop further the magnetic bearing technology that will permit removal of the speed limitations caused by traditional mechanical bearings when used in conjunction with high power internally mounted starter/generators. Magnetic bearings are an important technology to develop concurrently with internally mounted starter/generators.

Acknowledgments

Development of the electric accessory technologies required support, encouragement, and contributions from many organizations and people. The authors would like to acknowledge and thank the US Army AATD, the US Army TACOM, GECRD, GEAE, W. D. Jones, A. R. Fletcher, J. Petrowicz, A. Radum, and all the other contributors to this technology.

References

1 Jarvis, M. S., Jones, W. D., Petrowicz, J., and Radun, A., "Electric Accessory Drive," Final Report for Contract DAAJ02-88-C-0007 US Army, Fort Eustis, VA, 1992.

2 Jones, T., "Development of High Temperature Acutation System for Advanced Aircraft Engines," presented at the AIAA/SAE/ASME/ASEE 26th Joint Propulsion Conference, Orlando, FL, July 16–18, 1990.

3 Jones, W. D., and Jarvis, M. S., "Electrically Driven Engines Controls and Accessories for Future Aircraft," American Helicopter Society, Rotary Wing Propulsion Specialists' Meeting, Williamsburg, VA, Nov. 13–15, 1990.

4 MacMinn, S. R., and Jones, W. D., "A Very High Speed Switched-Reluctance Starter-Generator for Aircraft Engine Applications," *Proceedings of NAECON 89*, Dayton, OH, May, 1989.

5 Radun, A. R., "High Power Density Switched Reluctance Motor Drive for Aerospace Applications," presented at the IEEE-IAS Annual Meeting, Oct. 1989.

6 Richter, E., "Application Consideration for Integral Gas Turbine Electric Starter/Generator Revisited," Aerospace Technology Conference and Exposition, Anaheim, CA, Sept. 25–28, 1989.

Condensation in Jet Engine Intake Ducts During Stationary Operation

J. B. Young
Whittle Laboratory,
University of Cambridge,
Cambridge, United Kingdom

The paper describes an analysis of the condensation of moist air in very long intake ducts of jet engines during stationary operation. Problems arising from such condensation include fan overspeed and increased stagnation pressure loss in the intake duct. The analysis demonstrates that, for moderate values of relative humidity, homogeneous condensation will occur in an outer annulus adjacent to the intake cowling if the local flow Mach number attains values of about 1.0. In the central region of the intake duct, where design Mach numbers of 0.8 may be attained, homogeneous condensation is unlikely to occur except, possibly, when the relative humidity is close to 100 percent and the ambient temperature very high. However, if the intake duct is very long, significant heterogeneous condensation on foreign particles present in the atmosphere is possible. The concentration of foreign nuclei required for this type of condensation is comparable to the likely levels of contamination at many industrial test sites. The effects of condensation on engine test results are twofold. First, condensation is a thermodynamically irreversible process and results in an increase of entropy and hence loss of total pressure in the intake duct. Uncorrected measurements using Pitot probes may not record this loss correctly. Second, the mass and energy transfer between the phases during the condensation process has a tendency to accelerate the flow approaching the engine, an effect that may be counteracted by a reduction in mass flow rate in order to maintain the static pressure constant. These conclusions are in agreement with experimental results obtained on-site during the testing of a jet engine fitted with a very long intake duct.

Introduction

It is well known that the condensation of humid air can cause serious limitations to the working range of transonic and supersonic wind tunnels (Wegener, 1966). Similar phenomena can also restrict the stationary operation of jet engines (Blake, 1975; Zerkle et al. 1982). The effects are particularly pronounced in configurations involving very long intake ducts such as those associated with tail-mounting, above the fuselage, on large three-engined civil airliners and purpose-built test cells for stationary engine testing. This paper presents a general theoretical analysis of the effects of homogeneous and heterogeneous nucleation of water vapor in the intake system. The conclusions are consistent with on-site measurements from a stationary jet-engine test conducted by Rolls-Royce. The analysis also provides guidelines for assessing the effects of unwanted condensation under any particular test condition.

It is important to appreciate that the results apply solely to the case of *stationary* operation on the ground. The same conclusions do not apply under normal flight conditions, even at low altitude where the humidity may be high, because of the change in the flow stagnation conditions relative to the aircraft.

Background

Figure 1 shows a typical long inlet duct feeding a high-bypass ratio jet engine. The duct is straight with diameter 2.4 m and length (from the inlet to the engine face plane) 8.5 m. The inlet cowling is specially designed to provide a smooth intake for the flow and the velocity in the long straight section is (with the exception of the boundary layer) near uniform across the duct for most of its length. On conventional designs, the Mach number in this section is usually about 0.6 but increased engine thrust can be obtained without increase of intake diameter if the Mach number is increased to about 0.8. It is at these high intake Mach numbers that problems associated with condensation are most marked.

Figure 1 also shows the *computed* Mach number contours for stationary operation with *dry air* and a Mach number of about 0.8 in the duct. Details of the flow field vary with the geometry of the inlet but the important characteristics are

Contributed by the International Gas Turbine Institute and presented at the 38th International Gas Turbine and Aeroengine Congress and Exposition, Cincinnati, Ohio, May 24–27, 1993. Manuscript received at ASME Headquarters February 12, 1993. Paper No. 93-GT-5. Associate Technical Editor: H. Lukas.

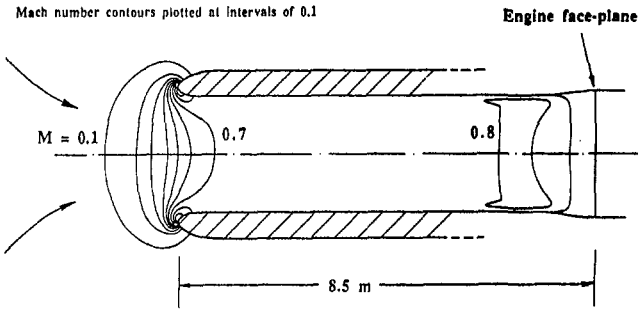

Fig. 1 Jet engine intake—contours of constant Mach number

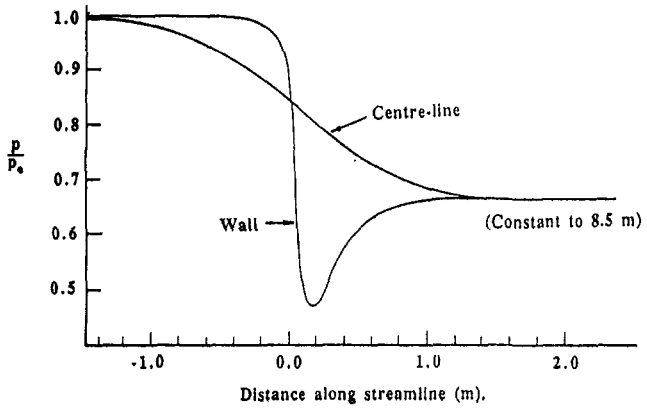

Fig. 2 Engine intake pressure distributions

common to most designs. Along the centerline of the duct the Mach number rises smoothly and monotonically to 0.8 and remains approximately constant to the engine face plane. Close to the lip of the cowling (but outside the boundary layer) the Mach number rises to about 1.1 (due to the high curvature of the streamlines) and then falls to the constant value of 0.8. Figure 2 shows typical pressure distributions along centerline and cowling wall streamlines, *plotted as functions of distance along the streamlines.*

It is important to appreciate that, because phase change proceeds at a certain rate, the effects of condensation are determined by absolute time scales and are therefore related, not only to the local Mach number, but also to its rate of change. Figure 2 shows that the rate of expansion near the cowling wall is much higher than along the centerline of the duct. It might therefore be expected that the characteristics of condensation close to the cowling are rather different from those near the centerline and this indeed proves to be the case. It should also be noted that the residence time of a

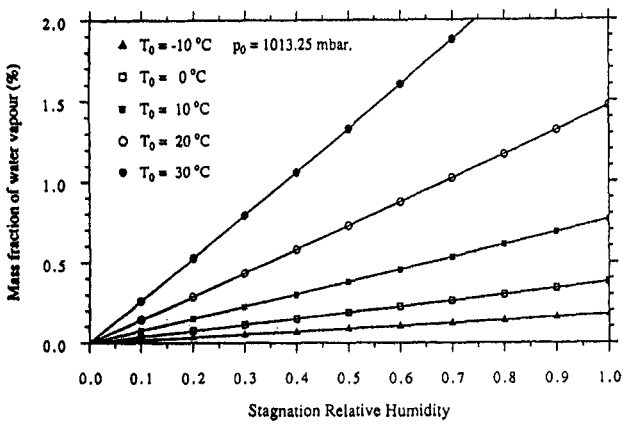

Fig. 3 Mass fraction of water vapor as a function of relative humidity

fluid particle in the long straight section of the intake (8 m at a Mach number of 0.8) is about 30 ms.

A full-scale configuration similar to the one shown in Fig. 1 was tested by Rolls-Royce at their experimental test facility at Hucknall in the United Kingdom. Hucknall is situated near Nottingham, a large industrial city with a rather damp climate. The following results were obtained at design conditions:

1 A fan overspeed of a few percent was recorded.
2 Pitot probes installed in the intake duct near the engine face plane and outside the wall boundary layer recorded stagnation pressure losses along the length of the duct of the order of 2–3 percent. (Outside the boundary layer, the expansion to the engine face plane was expected to be near isentropic.)
3 Condensed water was discovered in these same pitot tubes.

Similar experiments performed at a test site in the United States subject to a very dry climate showed none of these anomalies.

It was clear from the presence of water in the probes that condensation was occurring in the intake during the tests with humid air. Close to the intake cowling, the flow was transonic and it was suspected that homogeneous nucleation of water droplets might be occurring in this region. In the central core of the flow, where the Mach number was lower, the condensation was more probably heterogeneous in nature. Subsequent analysis confirmed these hypotheses and also demonstrated that condensation can give rise to effects that may seem disproportionate considering the very low mass fractions of water vapor actually present. To underline this point, Fig. 3 shows the mass fraction of water vapor in

Nomenclature

a = speed of sound
c_p = isobaric specific heat capacity
g = mass fraction of air
h = specific enthalpy
h_{fg} = specific enthalpy of evaporation
J = homogeneous nucleation rate per unit volume
k = Boltzmann's constant
M = Mach number
m = mass of a water molecule
p = pressure
R = specific gas constant
r_* = Kelvin–Helmholtz critical radius
S = supersaturation ratio
s = specific entropy
T = temperature
ΔT = vapor subcooling
t = time
V = velocity
y = wetness fraction (mass fraction of liquid H_2O)
γ = ratio of specific heat capacities
ρ = density
σ = surface tension
ϕ = relative humidity

Subscripts

e = equilibrium
f = frozen
g = gas (air)
m = mixture
s = saturated
v = water vapor
w = liquid water
0 = stagnation
1 = upstream of condensation zone
2 = downstream of condensation zone

Fig. 4 Control volume analysis of condensation in a parallel duct

air at 1 atm as a function of the relative humidity and temperature. Apart from very warm, damp days, the mass fraction of water vapor is less than 1.5 percent.

Condensation in a Parallel Duct

Before addressing the problem of predicting the likely occurrence and position of condensation under given operating conditions, it is instructive to assess the effects on the intake flow assuming such an event does occur. For demonstration purposes, a simple model is proposed, namely that the flow is steady, one dimensional, adiabatic, and inviscid in a duct of constant cross-sectional area (see Fig. 4). At inlet to the duct, the stagnation pressure p_0, the stagnation temperature T_0, and the relative humidity ϕ_0 are known. During the expansion to a given Mach number M_1 upstream of the condensation zone, the flow is assumed to be isentropic and, after crossing the saturation line, to remain in a dry (metastable) state. Downstream of the condensation zone thermodynamic equilibrium is assumed to be re-established. The analysis is rather similar to the Rankine–Hugoniot analysis of a normal shock wave in a parallel duct.

All conditions upstream of the condensation zone (station 1) can be calculated from the specified inlet stagnation state and the assumption that the air and water vapor behave as a mixture of perfect gases. Conditions downstream of the condensation zone (station 2) are computed by application of the conservation equations of mass, momentum, and energy.

Let the mass of air per unit mass of mixture be g. The mass of water vapor plus liquid per unit mass of mixture is therefore $(1 - g)$. Assuming zero velocity slip between gas and liquid droplets, g remains constant throughout the flow field. The local wetness fraction y is defined as the mass of liquid per unit mass of water vapor plus liquid (*not mixture*). y represents the local fraction by mass of H_2O, which is in the liquid phase. The mass of vapor per unit mass of mixture is $(1 - g)(1 - y)$ and the mass of liquid per unit mass of mixture is $(1 - g)y$. Obviously,

$$g + (1 - g)(1 - y) + (1 - g)y = 1. \tag{1}$$

If the partial densities of the air and water vapor components are ρ_g and ρ_v, respectively, then the density of the gas phase is $\rho = \rho_g + \rho_v$ and the mixture density ρ_m is (neglecting the volume occupied by the liquid droplets)

$$\rho_m = \frac{\rho}{g + (1 - g)(1 - y)}. \tag{2}$$

If h_g, h_v, and h_w represent the specific enthalpies of the air, water vapor, and liquid respectively, the specific enthalpy of the mixture h_m is given by

$$h_m = gh_g + (1 - g)h_v - (1 - g)y(h_v - h_w). \tag{3}$$

The air and water vapor components are assumed to behave as perfect gases with partial pressures p_g and p_v, respectively, and hence,

$$p_g = \rho_g R_g T,$$
$$p_v = \rho_v R_v T, \tag{4}$$

where T is the temperature of the gas phase and R_g and R_v are the specific gas constants of the air and water vapor. By Dalton's law, the mixture pressure is given by $p = p_g + p_v$, the partial pressure of the liquid droplets being neglected. (The term "total pressure" is avoided as this can be confused with the stagnation pressure.)

The conservation equations are identical in form to those for single-component, single-phase flow. Thus, for parallel duct flow,

$$\rho_{m1}V_1 = \rho_{m2}V_2,$$
$$p_1 + \rho_{m1}V_1^2 = p_2 + \rho_{m2}V_2^2,$$
$$h_{m1} + \frac{1}{2}V_1^2 = h_{m2} + \frac{1}{2}V_2^2. \tag{5}$$

At station 1 upstream of the condensation zone, the flow is dry and $y_1 = 0$. At station 2 thermodynamic equilibrium is assumed and

$$p_{v2} = p_s(T_2), \tag{6}$$

where $p_s(T_2)$ is the saturated vapor pressure at temperature T_2. It therefore follows that the term $(h_{v2} - h_{w2})$ in the expression for the mixture enthalpy is equal to $h_{fg}(T_2)$, the specific enthalpy of evaporation also evaluated at temperature T_2. Noting the relationships,

$$h_{g2} - h_{g1} = c_{pg}(T_2 - T_1),$$
$$h_{v2} - h_{v1} = c_{pv}(T_2 - T_1). \tag{7}$$

where c_{pg} and c_{pv} are the isobaric specific heat capacities of air and water vapor, respectively, the energy equation can be written,

$$\left[gc_{pg} + (1 - g)c_{pv}\right](T_2 - T_1) - (1 - g)y_2h_{fg}(T_2) + \frac{1}{2}\left(V_2^2 - V_1^2\right) = 0. \tag{8}$$

An empirical expression for the saturated vapor pressure of water (with range of validity from $-50°C$ to $+50°C$) is given by Lowe and Ficke and quoted on p. 625 on Pruppacher and Klett (1980). h_{fg} can be obtained in a thermodynamically consistent manner from this equation by application of the Clausius–Clapeyron equation.

Upstream of the condensation zone the mixture is in a nonequilibrium, metastable state. Departures from equilibrium are represented in terms either of the subcooling ΔT or the supersaturation ratio S. The subcooling is defined by

$$\Delta T = T_s(p_v) - T, \tag{9}$$

where $T_s(p_v)$ is the saturation temperature corresponding to the local vapor partial pressure p_v and T is the actual gas-phase temperature. (For superheated states $\Delta T < 0$ and for subcooled states $\Delta T > 0$.) The supersaturation ratio is defined by

$$S = \frac{p_v}{p_s(T)}. \tag{10}$$

(For superheated states $S < 1$ and for subcooled states $S > 1$.) The description of metastable states by either ΔT or S is equivalent and depends on personal preference. Downstream of the condensation zone where equilibrium is established, $\Delta T = 0$ and $S = 1$.

For a given inlet stagnation conditions (p_0, T_0, ϕ_0) and upstream Mach number M_1, the set of equations given above completely specifies the downstream state (p_2, T_2, y_2, M_2) following condensation. An analytical solution is not possible, however, and calculations must be performed by an iterative numerical method.

In general terms, the effect of condensation in a high-speed flow is similar to the effect of heat addition to a single-phase flow. Thus, in subsonic flow, condensation causes the flow to accelerate and the Mach number to increase. If the Mach number upstream of the condensation zone is high and appreciable phase change occurs, the flow may become ther-

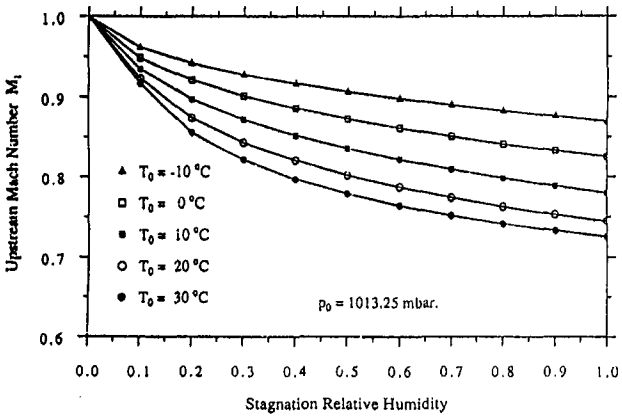

Fig. 5 Limiting Mach number for choking in a parallel duct

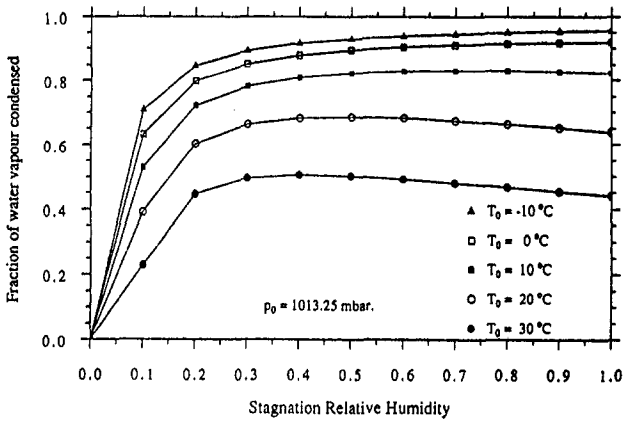

Fig. 6 Condensation in a parallel duct—fraction of water vapor condensed

mally choked. In this situation, there is no steady flow solution of the conservation equations. Practically, the mass flow rate and the upstream Mach number would both fall until the critical condition for choking was just attained at the very end of the duct.

Under the assumptions of the simple model, the condition for thermal choking corresponds to a Mach number of unity based on the equilibrium speed of sound a_e in the two-component, two-phase mixture. The derivation of an expression for this sound speed is algebraically rather complicated, but the result is (Smolders et al., 1990),

$$a_e^2 = \frac{ART}{B}, \tag{11}$$

where

$$A = 1 + \frac{gR_g}{(1-g)(1-y)R_v}\left(\frac{R_vT}{h_{fg}}\right)\left(\frac{c_pT}{h_{fg}}\right)$$

$$B = 1 - 2\left(\frac{R_vT}{h_{fg}}\right) + \frac{c_p - gR_g}{(1-g)(1-y)c_p}\left(\frac{R_vT}{h_{fg}}\right)\left(\frac{c_pT}{h_{fg}}\right),$$

$$R = gR_g + (1-g)(1-y)R_v,$$

$$c_p = gc_{pg} + (1-g)(1-y)c_{pv} + (1-g)yc_{pw},$$

and c_{pw} is the specific heat capacity of water. Note that a_e is always less than the frozen speed of sound a_f obtained by neglecting the response of the water content to small pressure disturbances. Typically, $a_e \cong 0.9a_f$.

At Mach numbers of about 0.8, the flow is very sensitive to condensation. This is easily demonstrated by calculating, for a range of inlet stagnation conditions (p_0, T_0, ϕ_0), the upstream Mach number M_1 such that the downstream flow is just thermally choked, $M_{e2} = V_2/a_{e2} = 1$. The results are shown in Fig. 5. Evidently, unless the relative humidity and ambient temperature are very low, the effect of condensation in accelerating the flow can be dramatic. For example, for most of the year in the United Kingdom, the temperature is above 10°C and the relative humidity above 50 percent. Figure 5 then shows that condensation to an equilibrium state in a parallel duct will thermally choke any flow at a Mach number exceeding about 0.83. The corresponding increase in flow velocity is of the order of 50 m/s. At relative humidities of 80–90 percent and ambient temperatures greater than 20°C, the effects are even more pronounced.

Not all the water vapor condenses during the process as some of the H_2O must remain in the form of vapor to satisfy the downstream thermodynamic equilibrium requirement, Eq. (6). The curves of Fig. 6 correspond to those of Fig. 5 and show the fraction of vapor condensed during the acceleration from the limiting Mach number M_1 to the thermally choked condition. By reference to Fig. 3 in conjunction with Fig. 6, it can be seen that a comparatively small precipitation of liquid water (usually constituting less than 1 percent of the total mixture flow rate) can have a very considerable effect on the flow velocity. This result is attributable to the very high latent heat of H_2O and the low specific heat capacity of air.

The calculations presented in Figs. 5 and 6 are highly idealized and it is as well to examine critically the assumptions under which they were obtained.

Firstly, it is assumed that the downstream two-phase flow is in thermodynamic equilibrium at $M_{e2} = 1.0$. Consideration of the nonequilibrium processes occurring in the condensation zone, however, shows that this cannot be the case (Young, 1984). Without presenting details, a study of the flow equations demonstrates that condensation occurring in a parallel duct at Mach numbers less than unity but greater than some critical value (usually about 0.92) displays an unusual instability whereby the heat release, instead of promoting a reversion to equilibrium, causes precisely the opposite effect. (The phenomenon is related to the well-known behavior of Rayleigh flow where, for Mach numbers in the range $1/\gamma < M < 1.0$, external heat addition to the flow causes a *decrease* in static temperature.) The upshot is that thermal choking occurs very rapidly but always under nonequilibrium conditions. In the context of the present problem, this would have the effect of *reducing* the limiting upstream Mach number below the values shown in Fig. 5 (see Young, 1984, for more details).

A second point that must be considered is that condensation may take place at an insufficient rate to cause complete reversion to equilibrium by the end of the duct. Later, it will be shown that, in general, foreign nuclei are most likely responsible for most of the phase change and should these not be present in sufficient concentrations, then the rate of condensation will be reduced. Partial condensation will, of course, still result in an increase in flow velocity but not to the extent suggested by the curves of Fig. 5.

Despite these provisos, the simple model of condensation presented above is very instructive in providing a general quantitative understanding of the flow behavior.

In the engine test performed with humid air, it was found that condensation occurring in the intake was associated with an increase in fan rotational speed. This result is compatible with the analysis above. Assuming the fan to be operating at, or near, the unique incidence condition, an increase in axial velocity of the flow would need to be accompanied by a corresponding increase in fan blade speed.

In a real engine test, however, it is unlikely that the mass flow rate through the engine would remain the same as when water vapor was completely absent (the assumption implicit in the analysis above). In the presence of condensation, the

tendency for the flow to accelerate and its pressure to fall would probably be counteracted by a reduction in mass flow rate entering the engine in order to maintain the static pressure at the engine face plane approximately constant. Obviously a more complete analysis involving the interaction of the intake system with the whole engine is required in order to predict the precise changes in operating conditions associated with the presence of condensation. This also raises the interesting question of the effect on the fan performance of droplet evaporation due to the static pressure increase within the blading. Evaporation is unlikely to be complete at fan exit because of the small flow transit time, but even partial evaporation would result in interphase heat and mass transfer between the droplets and the gas and may have a significant effect on fan performance by redistributing the flow and changing the position of shock waves.

Stagnation Pressure Loss Due to Condensation

Because of the interphase transfer of heat and mass, condensation is a thermodynamically irreversible process and results in an increase in entropy. When vapor molecules condense on a liquid droplet, "latent heat" is initially released at the droplet surface. This heat is then conducted back to the gas phase where it increases the gas temperature, thus reducing the vapor subcooling and promoting the reversion to equilibrium. For this process to occur, the droplet temperature must be higher than that of the gas phase and the resulting heat transfer across a finite temperature difference is responsible for the creation of entropy.

For the case of condensation in a parallel duct, the details of the droplet formation and growth processes are of no relevance if the sole objective is to calculate the entropy increase during the reversion from a dry metastable condition to a wet equilibrium state. (In this respect, the analysis is similar to that for a normal shock wave where it is also unnecessary to consider the details of the dissipation processes due to viscosity and heat conduction occurring within the wave itself.) Once conditions upstream and downstream of the condensation zone have been established, the increase in mixture specific entropy Δs follows from the expression

$$\Delta s = \left[g s_{g2} + (1-g)(1-y_2) s_{v2} + (1-g) y_2 s_{w2} \right] - \left[g s_{g1} + (1-g) s_{v1} \right], \quad (12)$$

where s_g, s_v, and s_w are the specific entropies of air, water vapor, and liquid water, respectively. Noting that the air and water vapor behave as perfect gases, this may conveniently be written

$$\Delta s = \left[g c_{pg} + (1-g) c_{pv} \right] \ln \frac{T_2}{T_1} - g R_g \ln \frac{p_{g2}}{p_{g1}} - (1-g) R_v \ln \frac{p_{v2}}{p_{v1}} - \frac{(1-g) y_2 h_{fg}(T_2)}{T_2}. \quad (13)$$

Having calculated the entropy increase across the condensation zone, the question now arises as to what is the corresponding stagnation pressure loss and whether or not conventional Pitot probes will record this loss correctly.

There is no difficulty in answering the first part of this question unambiguously. The stagnation pressure is defined as the pressure obtained if the flow is brought to rest adiabatically and reversibly. Downstream of the condensation zone, the two-phase flow is assumed to be in thermodynamic equilibrium. (Difficulties arise if this is not the case and the definition of stagnation pressure must then be re-examined.) A process can be conceived that decelerates the flow (including the droplets) to zero velocity while maintaining negligible interphase velocity slip and, simultaneously, allowing droplet evaporation to occur at such a rate that the temperature difference between the phase is also negligible. The pressure rise associated with this isentropic process is well defined and easily calculated from the energy and momentum conservation equations. In this way, it is possible to compute a well-defined stagnation pressure loss $\Delta p_0 = p_{01} - p_{02}$ across the condensation zone.

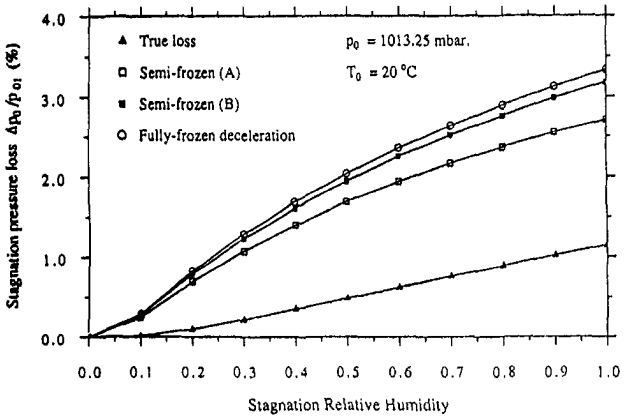

Fig. 7 Stagnation pressure loss in a parallel duct—constant T_0 = 20°C

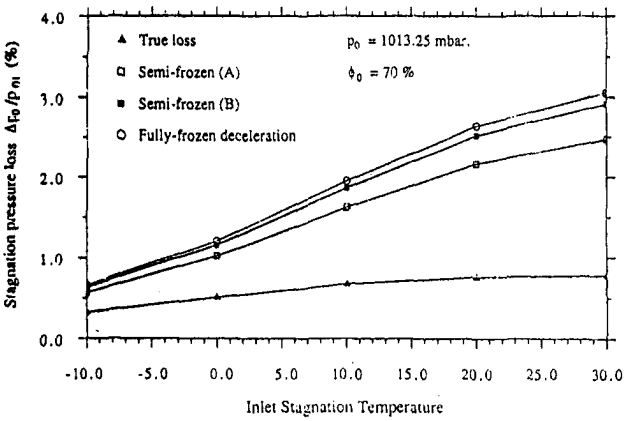

Fig. 8 Stagnation pressure loss in a parallel duct—constant ϕ_0 = 70 percent.

Figures 7 and 8 show curves of $\Delta p_0/p_{01}$ for parallel duct flows, which, after reversion to equilibrium, are thermally choked. Figure 7 shows the variation of $\Delta p_0/p_{01}$ with inlet stagnation relative humidity at a constant inlet stagnation temperature of 20°C. Figure 8 shows the variation with inlet stagnation temperature for a constant relative humidity of 70 percent. In both figures, the curves are labeled "true loss" because they represent the actual stagnation pressure loss. The loss increases with both relative humidity and temperature but is surprisingly small, hardly rising above 1 percent even under extreme conditions.

When a Pitot tube is inserted into a gas-droplet flow, the deceleration of the fluid approaching the tube is rapid and it is unlikely that the equilibrium conditions required for measuring the true stagnation pressure are achieved in practice. The conditions that do exist in the vicinity of the probe depend, among other things, on the droplet size but, apart from a recent analysis of Pitot measurements in pure steam by White (1992), there are few references in the literature to provide guidance for this difficult problem. It is possible, however, to define a limiting case whereby the droplets effectively take no part in the flow deceleration because they are deflected by the Pitot tube without change in mass, momentum and energy. This "fully frozen" deceleration of the gas stream would result in the measurement of a much

lower stagnation pressure and a considerable overestimate of the loss as is evident from the relevant curves in Figs. 7 and 8.

Other simple assumptions can also be made. Thus, the curves labelled "semi-frozen (A)" in Figs. 7 and 8 assume that full thermal and velocity equilibrium of the droplets occur during deceleration but that there is insufficient time for phase change so that the liquid mass fraction remains constant. These assumptions may well be quite realistic in practice because the relaxation time associated with phase change is an order of magnitude greater than the relaxation times associated with droplet temperature and velocity slip. The curves labeled "semi-frozen (B)" provide yet another possibility. Here it is assumed that the droplet temperature relaxes instantaneously to its steady-state value but that mass and momentum transfers are frozen.

The analysis of White showed that the pressure recorded by a Pitot tube in a gas-droplet two-phase flow is strongly influenced by the size of the droplets. However, assuming that the droplet diameters are comparatively large (i.e., of the order of 1 μm), White's analysis would suggest that Pitot tube measurements are likely to be in closer correspondence with the curves labeled "semi-frozen (A)" than those labeled "true loss." This conclusion is, indeed, in accord with the on-site measurements from the Rolls-Royce engine test referred to above, where the recorded loss was of the order of 2–3 percent. Evidently, caution must be exercised in interpreting Pitot measurements in condensing flows because the true stagnation pressure loss may not be as serious as is indicated by the uncorrected measurements.

Homogeneous Nucleation

In the previous sections, an analysis of condensation was presented, the assumption being that this would occur somewhere in the parallel intake duct. Further progress in this direction would require much more complex two-dimensional, nonequilibrium calculations. Instead, attention is shifted to predicting the inlet conditions under which phase change may be expected and the approximate position in the duct at which this occurs. Initially, only the possibility of homogeneous nucleation is considered.

Homogeneous (or spontaneous) nucleation occurs in supersaturated pure vapors or mixtures of vapors and inert gases when foreign particles (dust, salt molecules, ions, etc.) are absent. Under these circumstances, the formation and growth of a liquid nucleus is essentially a random event, the probability of which increases with increasing departure from equilibrium as measured by the subcooling ΔT or the supersaturation ratio S [see Eqs. (9) and (10)]. The theory of homogeneous nucleation is well developed but agreement with experimental measurement is by no means precise even for a substance like water, which has formed the basis for a very large number of experimental investigations. A critical discussion of homogeneous nucleation in nozzle expansions of pure steam can be found in Young (1982) and information on nucleation in moist air can be found in Wegener (1966).

The classical theory of homogeneous nucleation is very clearly described by McDonald (1962/63). There, it is shown that the rate of nucleation of liquid droplets per unit volume in a supersaturated vapor is given by

$$J = \sqrt{\frac{2\sigma}{\pi m^3}}\ \frac{\rho_v^2}{\rho_w} \exp\left(-\frac{4\pi\sigma r_*^2}{kT}\right), \tag{14}$$

where σ is the liquid surface tension, m is the mass of a water molecule, and k is Boltzmann's constant. The Kelvin–Helmholtz critical radius r_* is given by,

$$r_* = \frac{2\sigma}{\rho_w R_v T \ln(S)} \tag{15}$$

Obviously J is a very strong function of the supersaturation ratio and the nucleation rate changes by several orders of magnitude for quite modest changes in S.

Over the years, a number of corrections and amendments to the classical theory have been proposed. Experiments indicate, however, that, in the present context where the water vapor content is low, Eq. (14) is probably a fairly accurate representation of reality. Difficulties in application arise because the temperature in the engine intake upstream of condensation falls below 0°C, but in this situation the relevant saturated vapor pressure is that of subcooled liquid water rather than solid ice. (Although the equilibrium condensed phase at temperatures below the triple point is ice, Ostwald's law of stages and experimental evidence suggests that it is the liquid rather than the solid phase that is first nucleated.)

When first nucleated, droplets are assumed to be at the critical radius r_*. At high supersaturation ratios such as occur during rapid expansions, r_* is very small indeed and may represent a liquid cluster containing less than 50 molecules. Following nucleation, however, the clusters immediately start to grow to macroscopic size by the condensation of vapor from the gas phase. Equations describing the rate of growth are therefore required because it is the conduction to the gas phase of the latent heat liberated by condensation at the droplet surface that causes the reduction in subcooling and the corresponding decrease in the nucleation rate as the flow reverts to equilibrium. The droplet growth equations have been the focus of many theoretical studies and the subject is too complex to discuss here. Suffice it to say that the equations used for the present calculations are those derived by Young (1992a), which provide an accurate representation of droplet growth rates for a wide range of water vapor concentrations and droplet radii.

In order to predict the onset of homogeneous condensation in a rapid expansion, it is necessary to integrate the nucleation and droplet growth equations in conjunction with differential forms of the gas dynamic conservation equations. Calculations of this type in one-dimensional nozzles have been the subject of many studies and the requisite numerical techniques are well developed. As shown in Fig. 1, however, the flow entering the intake system is strongly two-dimensional (although axisymmetric). Two-dimensional calculation schemes for condensing flow have been reported in the literature [e.g., Schnerr and Dohrmann (1988) for moist air and Young (1992b) for pure steam] but they are a major undertaking and are not commonplace. However, instead of computing the actual two-dimensional pressure field for the true condensing flow, much useful information can be obtained by basing the calculations of wetness formation on the computed *dry* intake pressure distribution as shown in Figs. 1 and 2. This requires a much simpler, essentially one-dimensional, calculation and, although exact quantitative results cannot be expected, experience has shown that the technique is very useful in indicating the correct trends.

The input data for the calculations are therefore the pressure distributions of Fig. 2 rather than the geometric coordinates of the engine intake. The mass continuity equation is discarded and the differential forms of the momentum and energy Eqs. (5) combined to give the thermodynamic form,

$$\frac{Dh_m}{Dt} - \frac{1}{\rho_m}\frac{Dp}{Dt} = 0. \tag{16}$$

It is interesting to note that (in the absence of velocity slip), Eq. (16) is valid for two-phase as well as for single-phase flows. In single-phase flow, Eq. (16) implies that the entropy

of a fluid particle remains constant. This is not the case, however, when two phases in thermal disequilibrium are present. (It is a standard result that, for nonequilibrium two-phase flow the left-hand side of Eq. (16) cannot be equated to D_{sm}/Dt). Equation (16) is therefore not incompatible with the production of entropy due to irreversible condensation as described previously.

If the pressure variation is specified, the thermodynamics of the problem are effectively uncoupled from the fluid dynamic influences (in the sense that the flow velocity does not enter the equations) and Eq. (16) in conjunction with Eq. (14) and the droplet growth equations can be integrated in stepwise fashion in the flow direction. A detailed description of how this can be achieved for nucleation in expansions of pure steam can be found in Guha and Young (1991) and Young (1992b). Calculations for moist air are similar and the details will not be presented here.

For given inlet stagnation conditions (p_0, T_0, ϕ_0) and specified pressure distribution, the calculations predict the variation along the flow path of the subcooling ΔT, the wetness fraction y, and the droplet size distribution. The position of maximum subcooling (which coincides almost exactly with the maximum homogeneous nucleation rate J) is called the "Wilson Point." Immediately after the Wilson Point, the subcooling and nucleation rate fall rapidly as the condensational growth of existing droplets and release of "latent heat" promote the reversion to equilibrium. Theory and experiment show that the mean droplet diameter *downstream of the main condensation zone* (i.e., after reversion to equilibrium) is related to the maximum subcooling (at the Wilson Point) and both are a strong function of the rate of expansion in the nucleation zone just upstream of the Wilson Point. Most experiments reported in the literature have been performed in fairly small nozzles (10–50 cm in length) with correspondingly high rates of expansion. Under these circumstances, for high inlet stagnation relative humidities, an expansion to slightly supersonic Mach numbers is required before significant quantities of water are produced by homogeneous nucleation. Decreasing the inlet relative humidity has the effect of increasing the Mach number at the Wilson Point to higher values and displacing the condensation zone well into the supersonic part of the flow. The corresponding mean droplet diameters are very small, usually of the order of 0.1 μm or even less.

As shown in Fig. 2, the rate of expansion along the streamline adjacent to the cowling of the full-scale intake is comparatively high. In this region, homogeneous nucleation is therefore expected to occur at much the same Mach numbers as in smaller laboratory nozzles. The results of the numerical calculations confirm this expectation. Figure 9 shows the position of the Wilson Point on the cowling wall streamline in terms of the inlet stagnation temperature and relative humidity. [The abscissa scale of Fig. 9 has the same (arbitrary) origin as Fig. 2 but is greatly expanded because nucleation only occurs in a very narrow region close to the position of minimum pressure.] Taking, as an example, the calculations for an inlet stagnation temperature of 30°C, it can be seen that, for a relative humidity of 100 percent, the Wilson Point occurs at a streamwise distance of 46 mm, which corresponds to a Mach number of 0.96. (The Mach number corresponding to each streamwise position can be read from the scale at the top of the graph.) Decreasing the relative humidity displaces the Wilson Point to higher Mach numbers until, at $\phi_0 = 38$ percent (for $T_0 = 30$°C), it is situated at a streamwise position of 140 mm, which corresponds to the point of minimum pressure in Fig. 2. (The Mach number at this point is about 1.1.) At lower values of ϕ_0, homogeneous nucleation is inhibited because the maximum nucleation rate (which occurs at the minimum pressure point) falls rapidly with decrease in inlet relative humidity.

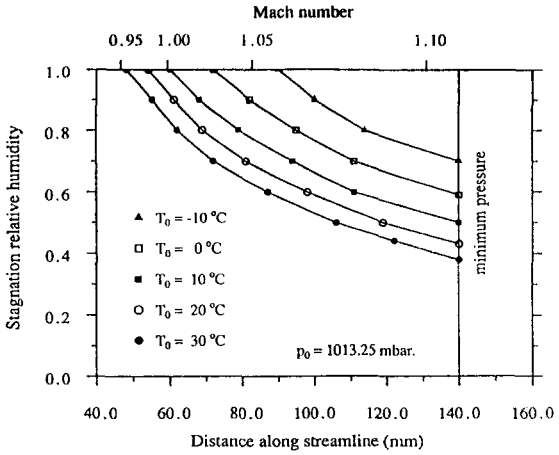

Fig. 9 Homogeneous nucleation at the wall streamline—position of Wilson Point as a function of inlet stagnation temperature and relative humidity

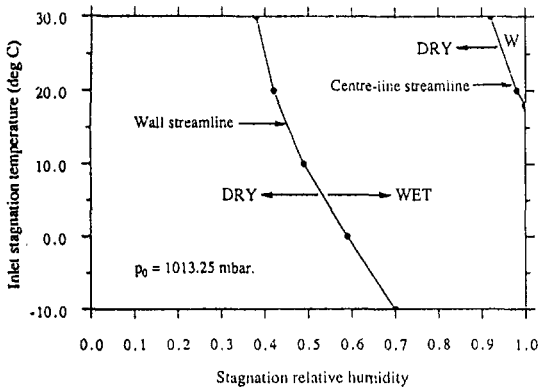

Fig. 10 Range of inlet conditions for homogeneous nucleation to occur along the wall and centerline streamlines

The boundary between wet and dry operation (in respect of homogeneous nucleation) therefore corresponds (at least approximately) to those inlet conditions such that the Wilson Point coincides with the point of minimum pressure on the streamline. Figure 10 shows this boundary (in terms of the inlet stagnation temperature and relative humidity) for the wall pressure distribution of Fig. 2. Other intake geometries would, of course, result in a different boundary between wet and dry operation. In particular, homogeneous nucleation may be inhibited completely if the design is such that the peak Mach number is restricted to subsonic values less than about 0.9.

The numerical calculations provide a complete analysis of the reversion to equilibrium but the details will not be presented here. However, it is of interest to note that, for all the cases shown in Fig. 9, the Wilson Point subcooling was in the range 33–39°C and the mean droplet diameter far downstream of the condensation zone was in the range 0.1–0.3 μm. (Decreasing the inlet relative humidity at constant stagnation temperature results in a *slight* decrease in Wilson subcooling and a *slight* increase in droplet diameter. Decreasing the stagnation temperature at constant relative humidity has the reverse effect.)

Turning now to the pressure distribution along the centerline of the intake, it can be seen from Fig. 2 that the Mach number is monotonically increasing and never exceeds a value of 0.8. At this Mach number, the subcooling does not exceed 27°C (for the range of inlet temperatures considered) and the corresponding homogeneous nucleation rates are low, suggesting that condensation by this method is negligible. It is important to recall, however, that the rate of

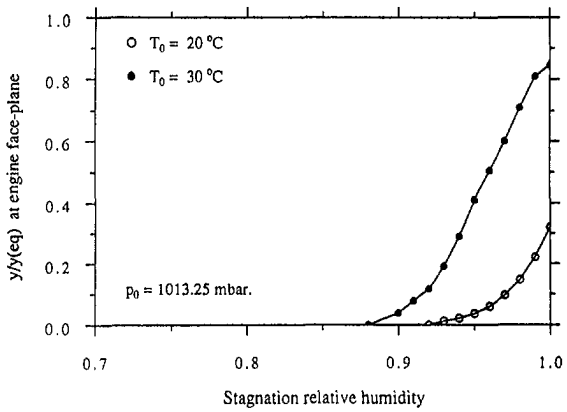

Fig. 11 Homogeneous nucleation on the centerline streamline—fraction of the equilibrium wetness condensed at the engine face plane

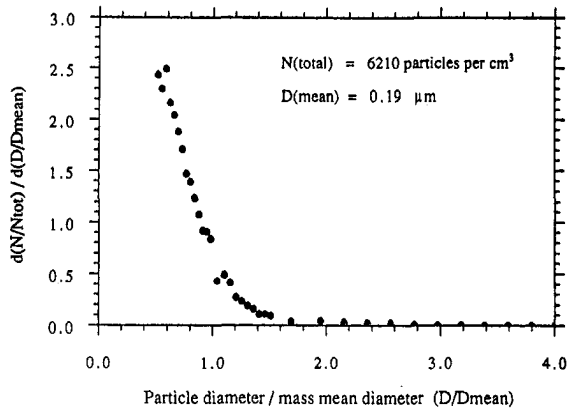

Fig. 12 On-site measurement of atmospheric particle size distribution

expansion along the centerline is much lower than along the wall streamline and also there is a very long time available for droplet growth in the straight section of the duct.

Nevertheless, the numerical calculations show that significant condensation by homogeneous nucleation is unlikely except for inlet stagnation temperatures approaching 30°C and relative humidities near 100 percent. Figure 11 shows the wetness fraction at the engine face plane normalized by the local equilibrium value corresponding to complete reversion. For inlet temperatures below 20°C, the water content of the flow is effectively zero for all values of ϕ_0. Even for an inlet temperature of 30°C, it is only when the relative humidity exceeds 90 percent that significant (although incomplete) condensation occurs. In these circumstances, it is the very long intake duct that makes homogeneous nucleation possible because, although the nucleation rate is low, the residence time of 30 ms provides an extended opportunity for droplet growth. Indeed, droplets formed under these conditions have diameters of the order of 3 μm (compared with 0.1–0.3 μm for droplets nucleated near the wall). Figure 10 shows the boundary between wet and dry operation for the centerline streamline and visually underlines the conclusion that homogeneous nucleation is unlikely to be responsible for significant water precipitation in the core of the flow, except under extreme conditions.

In summary, it has been shown that condensation due to homogeneous nucleation can be expected to occur in a narrow annulus adjacent to the cowling wall near the lip of the intake unless the relative humidity is less than about 50 percent (dependent on the inlet temperature). Homogeneous nucleation in the main core of the flow is unlikely except for a combination of very high temperature, relative humidity, and Mach number.

Heterogeneous Nucleation

If the concentration of foreign particles in the atmosphere is high, heterogeneous nucleation and droplet growth may be responsible for condensation in sufficient quantities to affect the flow behavior. There now exists a considerable bank of data concerning atmospheric particle concentration and size distribution (Pruppacher and Klett, 1980) and it is evident that particle concentrations are very much higher in the vicinity of large industrial conurbations than in isolated rural areas. Foreign particles act as condensation nuclei (just as in cloud formation) and, if the concentration is sufficiently large, the resulting precipitation of water can have a significant effect on the flow. Cloud condensation nuclei (CCN) lie in the size range 0.1–5.0 μm and can be "activated" (i.e., start to grow by vapor condensation) at subcoolings very much lower than those required for homogeneous nucleation. (However, although it is unusual to encounter subcoolings greater than 1°C in the atmosphere, it should be remembered that the cooling rates associated with cloud formation are orders of magnitude lower than those found in nozzle-type flows.)

Figure 12 shows the size distribution of "large" atmospheric particles actually measured by Rolls-Royce at Hucknall (the site of the jet engine test involving humid air). ("Large particles" is a well-defined category and refers to a range of diameters from 0.2–2.0 μm.) The distribution and overall concentration are typical of measurements made near industrial cities. In all, six measurements were made, the total recorded particle concentration ranging from 4000 to 8000 particles per cm^3. Figure 12 shows a typical distribution with a total concentration of 6210 particles per cm^3 and a mass mean diameter of 0.19 μm. It is important to note, however, that the particle counter was unable to record particles with diameters smaller than 0.1 μm and that these unrecorded "Aitken" nuclei are likely to be present in large concentrations at ground level (Pruppacher and Klett, 1980, p. 204). Although Aitken particles are too small to act as nuclei in normal cloud formation, they can be activated by the expansion to high subcoolings in a jet engine intake. Calculations based on measured concentrations of "large particles" therefore tend to underestimate the quantities of water condensed, possibly by quite a large factor.

The process of heterogeneous nucleation, unlike that of homogeneous nucleation, is not well understood and, at present, no satisfactory theory exists. Atmospheric particles are not spherical and their composition varies, some being water soluble and others not. In order to make progress, therefore, a very simple mechanism for nucleation is postulated, which, it must be admitted, is unlikely to model the real physical processes with any great accuracy. Thus, it is assumed that all particles are spherical and insoluble in water, and start to grow as spherical water droplets with a solid core when the Kelvin–Helmholtz critical radius r_* [defined by Eq. (15)] becomes marginally smaller than the actual particle radius. For an inlet stagnation temperature of 20°C and various relative humidities, Fig. 13 shows the Mach number required to activate atmospheric particles of different diameters. It is evident that, for the measured size distribution of Fig. 12, all the particles present (and many more Aitken nuclei) will be activated in an expansion to a Mach number of 0.8 unless the stagnation relative humidity is very low indeed.

Equation (15) implies that particles of diameter 0.1 μm are activated at very low subcoolings of about 0.2°C. As an approximate "rule of thumb," it can therefore be assumed that all the larger atmospheric particles become activated if the water vapor becomes dry saturated during an expansion.

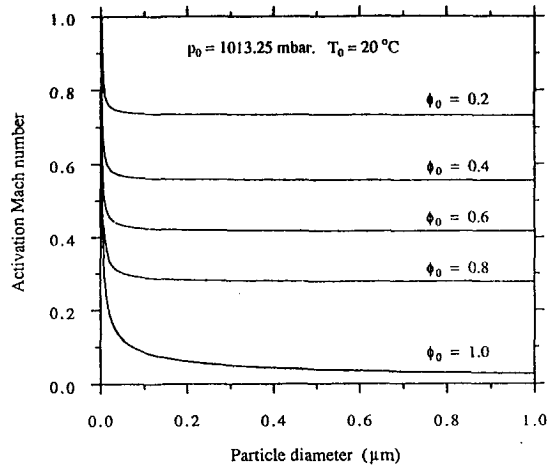

Fig. 13 Mach number required to 'activate' atmospheric particles of different diameters

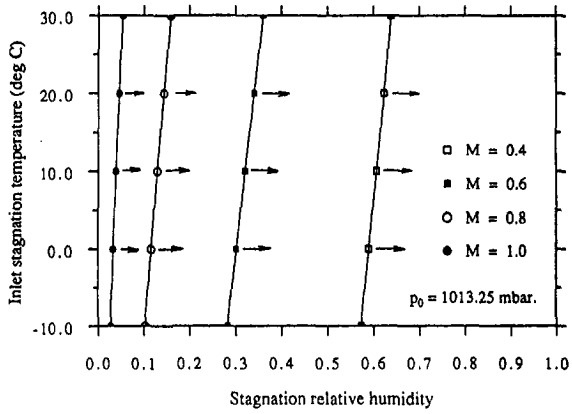

Fig. 14 Range of inlet conditions and Mach numbers for the activation of atmospheric particles larger than 0.1μm diameter

Figure 14 shows the range of inlet conditions and Mach numbers required to activate these particles under this assumption. Obviously, unless the relative humidity is very low, most atmospheric particles will be capable of acting as nuclei for vapor condensation during expansion in an engine intake.

However, even if all the foreign particles present become activated, this does not necessarily imply that sufficient water vapor will have condensed by the engine face plane to affect the flow behavior appreciably. The precise quantity condensed will also depend on the total concentration of particles and the rate of condensation as specified by the droplet growth equations.

In order to investigate these factors, calculations were performed adopting the model of heterogeneous nucleation described above. For simplicity, it was assumed that the particles were monodispersed with a diameter of 0.2 μm, the mass mean diameter of the measured distribution. (In fact, the results are almost independent of the size distribution so long as most of the particles are larger than about 0.01 μm diameter.) Calculations were performed for a range of particle concentrations and inlet stagnation conditions. Figure 15 shows the wetness fraction at the engine face plane (normalized by the equilibrium value corresponding to complete reversion) for an inlet stagnation temperature of 20°C and atmospheric particle concentrations in the range 5×10^3–1×10^5 per cm^3.

The results of Fig. 15 confirm that, below a relative humidity of about 15 percent, the flow at the engine face plane has no water content. This is simply because, in an expansion to a Mach number of 0.8, the water vapor remains unsaturated ($S < 1$). For relative humidities exceeding this threshold

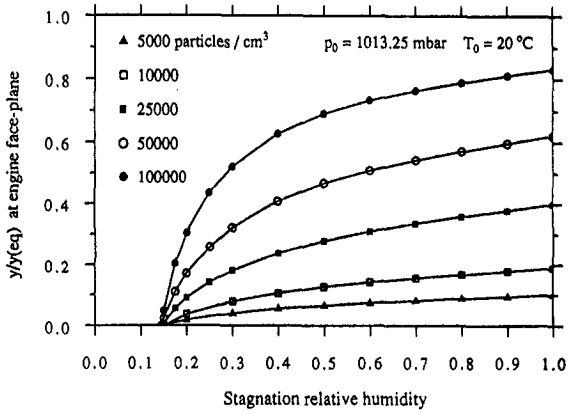

Fig. 15 Heterogeneous nucleation on the centerline streamline—fraction of the equilibrium wetness condensed at the engine face plane

value, the fraction of water vapor condensed depends strongly on the concentration of foreign particles present. The on-site measured concentration of Fig. 12 corresponds approximately to the curve labeled 5000 particles per cm^3 in Fig. 15. At this concentration the calculations indicate that only about 10 percent of the equilibrium wetness fraction will have condensed by the end of the intake duct. However, as noted above, the concentration of Aitken nuclei is very much higher than the concentration of CCN (perhaps by a factor of 10 or more) and the curves labeled 5×10^4 or 1×10^5 are probably more representative of the actual concentration of particles that become activated during the expansion. Assuming this to be the case, then very significant quantities of water will be present at the engine face plane for relative humidities exceeding, say, 25 percent (at $T_0 = 20$°C) and marked changes in the flow behavior should therefore be expected.

As plotted in terms of (y/y_{eq}), the curves of Fig. 15 are largely independent of the inlet stagnation temperature. However, for a given relative humidity, the vapor content of the atmosphere falls with temperature (see Fig. 3) and hence the actual mass fraction of condensed water at the engine face plane also decreases with temperature. The effect on the flow behavior is therefore not so pronounced at lower temperatures.

Because atmospheric particle concentrations are comparatively low (in comparison with droplet number densities resulting from homogeneous condensation), heterogeneous nucleation usually results in droplet sizes larger than those associated with homogeneous nucleation. For the calculations shown in Fig. 15, the droplet diameters at the engine face-plane ranged from 1 to 7 μm.

Figure 16 shows the growth of the liquid phase due to heterogeneous condensation as a function of distance along the centerline streamline for an arbitrary inlet condition of $T_0 = 20$°C, $\phi_0 = 70$ percent. The importance of duct length is now very evident. For short inlets associated with wing-mounted engines, the time available for droplet growth is insufficient for significant condensation to occur and the flow is unlikely to be seriously affected by the presence of foreign nuclei. It is only with the very long intake ducts associated with tail-mounting or purpose-built engine test cells that serious problems are likely to occur during stationary operation.

Conclusions

A theoretical and computational investigation of condensation in jet engine intake ducts has led to the following conclusions concerning *stationary* operation:

1 Homogeneous nucleation of water vapor is unlikely to occur in the core flow of the intake (at Mach numbers of 0.8)

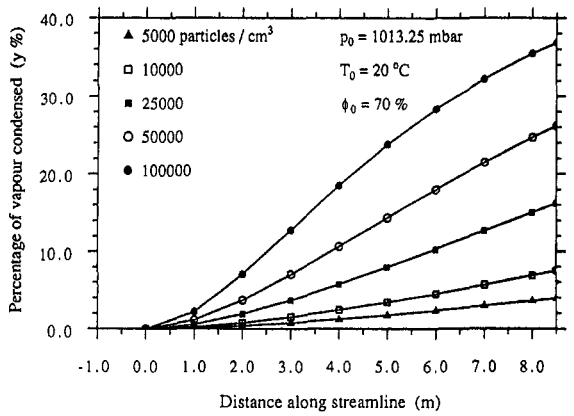

Fig. 16 Heterogeneous nucleation on the centerline streamline—fraction of vapor condensed as a function of distance

except for extreme conditions of very high inlet temperature and relative humidity. The converse is true, however, in a narrow annulus adjacent to the intake cowling where the high curvature of the streamlines results in an overexpansion to Mach numbers of about 1.0–1.1. Homogeneous nucleation will occur here for relative humidities exceeding 40–70 percent, the threshold value depending on the inlet stagnation temperature. Nucleation in this region is independent of the length (but not the geometry) of the intake duct and may, therefore, occur in short intakes designed for wing-mounted engines as well as in long ducts designed for tail-mounting. These conclusions have been substantiated by visual observation during stationary engine tests where condensation is often observed to occur in the region described above.

2 Heterogeneous condensation on atmospheric particles will occur whenever the inlet stagnation conditions are such that the water vapor becomes slightly supersaturated during the expansion to the engine face plane. Particles exceeding 0.1 μm diameter (cloud condensation nuclei, CCN) become activated at subcoolings of 0.2°C or less. Smaller Aitken nuclei require higher subcoolings but, unless the relative humidity is very low, it is expected that most atmospheric particles will be capable of acting as centers of condensation in an expansion to a high subsonic Mach number. The fraction of water condensed (and hence the effect on the flow) depends strongly on the total particle concentration and the time available for droplet growth (i.e., the duct length). For tail-mounted engines with very long intake ducts, heterogeneous condensation can be substantial for particle concentrations of the order of those found near industrialized areas. For wing-mounted engines, the intake is short and heterogeneous condensation is less important.

3 The actual mass fraction of vapor condensed in an expansion (and hence the effect on the flow) depends on the water vapor content of the ambient air. This increases substantially with temperature and relative humidity.

4 The effect of condensation at subsonic Mach numbers is to accelerate the flow. The effect can be dramatic at dry air Mach numbers of 0.8, when reversion to equilibrium in a parallel duct may be sufficient to choke the flow thermally (assuming the mass flow rate to remain constant). In practice, the mass flow rate through the engine may not remain constant but a more complete analysis involving the flow through the fan and bypass duct (where evaporation will occur) is required to predict the exact changes in engine operating conditions. However, an increased flow velocity approaching the engine is consistent with experimental on-site measurements, which detected an increase in fan rotational speed (required to maintain the unique incidence condition at blade inlet) when condensation occurred.

5 Because of the interphase temperature difference, condensation is a thermodynamically irreversible process and is associated with an increase in entropy and decrease in stagnation pressure. Calculations show that the loss in stagnation pressure is small, seldom exceeding 1 percent. Conventional Pitot probe measurements may not record this loss correctly because the rapidly decelerating two-phase flow in the vicinity of the probe can deviate markedly from equilibrium. The flow behavior in this region is complex and difficult to predict, but a simplified analysis showed that stagnation pressure losses computed from uncorrected Pitot measurements in the usual way could overestimate the true values by factors of 2 or 3. On-site measurements obtained during engine testing were in agreement with this prediction.

The analysis presented in this paper has demonstrated the importance of various aspects of condensation theory as applied to the stationary operation of jet engines, especially those fitted with very long intake ducts. The only way to avoid these complications during engine testing is either to locate the test site in a hot, dry region where the relative humidity is always low or to confine the test program to the winter months when ambient temperatures are low. Alternatively, the analysis may be viewed as providing the inspiration for the further investigation of some most unusual and interesting phenomena, which have a not insignificant effect on engine performance under certain operating conditions.

Acknowledgments

The author is grateful to Mr. C. Freeman of Rolls-Royce plc for introducing him to the problem of condensation in jet engine intake ducts and to Mr. P. Butler, also of Rolls-Royce, who performed the measurements of atmospheric particle concentration.

References

Blake, J. C., 1975, "Effects of Condensation in the JT9D Turbofan Engine Bellmouth Inlet," AIAA Paper No. 75-1325.

Guha, A., and Young, J. B., 1991, "Time-Marching Prediction of Unsteady Condensation Phenomena Due to Supercritical Heat Addition," Proc. Instn. Mech. Engnrs., Euro. Conf. on *Turbomachinery: Latest developments in a changing scene*, Paper C423/057, pp. 167–177.

McDonald, J. E., 1962/63, "Homogeneous Nucleation of Vapour Condensation, Part I: Thermodynamic Aspects, Part II: Kinetic Aspects," *Am. J. Physics*, Part I: Vol. 30, 1962, pp. 870–877, Part II: Vol. 31, 1963, pp. 31–41.

Pruppacher, H. R., and Klett, J. D., 1980, *Microphysics of Clouds and Precipitation*, D. Reidel Pub. Co.

Schnerr, G., and Dohrmann, U., 1988, "Theoretical and Experimental Investigation of 2-D Diabatic Transonic and Supersonic Flowfields," IUTAM, *Symp. Transonicum III*, Göttingen 1988, Springer-Verlag, 1989, pp. 132–40.

Smolders, H. J., Niessen, E. M. J., and van Dongen, 1990, "On the Similarity Character of an Unsteady Rarefaction Wave in a Gas–Vapour Mixture With Condensation," *Adiabatic Waves in Liquid Vapour Systems*, G. E. A. Meier and P. Thompson, eds., Springer-Verlag, pp. 197–205.

Wegener, P. P., 1966, "Gas Dynamics of Expansion Flows With Condensation and Homogeneous Nucleation of Water Vapour," in: *Nonequilibrium Flows, Part I*, P. P. Wegener, ed., Marcel Dekker Pub.

White, A. J., 1992, "Condensation in Steam Turbine Cascades," Ph.D. Thesis, Cambridge University Engineering Department.

Young, J. B., 1982, "The Spontaneous Condensation of Steam in Supersonic Nozzles," *Physico-Chemical-Hydrodynamics*, Vol. 3, pp. 57–82.

Young, J. B., 1984, "Critical Conditions and the Choking Mass Flowrate in Non-equilibrium Wet-Stream Flows," ASME *Journal of Fluids Engineering*, Vol. 106, pp. 452–458.

Young, J. B., 1992a, "The Condensation and Evaporation of Liquid Droplets at Arbitrary Knudsen Number in the Presence of an Inert Gas," to be published in *Int. J. Heat Mass Transfer*.

Young, J. B., 1992b, "Two-Dimensional Non-equilibrium Wet-Stream Calculations for Nozzles and Turbine Cascades," ASME *Journal of Turbomachinery*, Vol. 114, pp. 569–579.

Zerkle, R. D., Colley, W. C., and Doel, D. L., 1982, "Analysis of Moisture Condensation in Engine Inlet Ducts," *Particulate Laden Flows in Turbomachinery*, W. Tabakoff, C. T. Crowe, and D. B. Cale, eds., ASME, pp. 101–112.

Fan Noise Reduction From a Supersonic Inlet During Simulated Aircraft Approach

W. E. Nuckolls

W. F. Ng

Department of Mechanical Engineering,
Virginia Polytechnic Institute
and State University,
Blacksburg, VA 24061

A series of experiments was conducted to investigate the radiation of fan noise from a supersonic inlet during a simulated aircraft approach. A scaled-down model of an axisymmetric, mixed-compression, supersonic inlet (P-inlet) was used in conjunction with a 10.4 cm (4.1 in) diameter turbofan engine simulator as the noise source. The tests were conducted at an outdoor facility under static conditions. The main goal of the experiment was to reduce the forward radiating fan noise by modifying the auxiliary inlet doors. The modified doors are designed to reduce the inlet distortion to the fan face. In addition, the new door design also uses a converging flow passage in order to take advantage of the noise attenuation due to the choking effect at the auxiliary door. The simulator was tested at 60 percent design speed in an attempt to match the simulator noise source to that of a real aircraft engine on approach. Both aerodynamic and acoustic measurements were taken in the experiments. The results show that when compared to the original design, the modified auxiliary inlet doors reduced the circumferential inlet distortion to the fan face by a factor of two. The key result is that the blade passing frequency tone has been decreased by an average of 6 dB in the forward sector for the modified door design. Results from the closed auxiliary inlet door case are also presented to provide additional comparisons.

1 Introduction

Recently, there is a renewed research interest in pursuing a commercial supersonic transport. In order for a high-speed civil transport to be successful, its environmental impact must be minimized. The environmental issues involved are upper atmosphere emissions, airport community noise, and the sonic boom.

An experimental test program has been conducted to understand better the impact of a supersonic transport on airport community noise. The program focuses on the fan noise radiation from a supersonic inlet. Even though jet noise is the predominant noise source, previous analyses by Trefny and Wasserbauer (1986) "indicate that forward-propagated fan noise is a significant component during take off and approach." Supersonic inlets are complex and include many variable geometry features for aerodynamic reasons. The acoustic effect of these variable features on the noise-generating mechanisms involved is not completely understood.

The specific objective of this research is to reduce forward propagating fan noise by modifying the auxiliary door geometry. Previous research by Woodward et al. (1984) has shown a significant increase in the noise caused by the opening of the auxiliary inlet doors. Supersonic inlets are designed with a small inlet capture area for optimum cruise performance. However, the inlet capture area for cruise conditions is too small for low-speed flight. The auxiliary doors are therefore needed to provide additional air to the engine during takeoff and landing. This paper focuses on the problem of fan noise radiation during the aircraft landing approach, when the engine is throttled back to a lower speed, and when the predominant fan noise is the blade passing frequency and its harmonics. In order to match this condition, the simulator was tested at 60 percent design speed.

The modified auxiliary inlet door is designed to include two noise-attenuating features. The first goal is to decrease the distortion at the fan face. This goal is accomplished by modifying the auxiliary door to provide a more uniform air distribution to the engine. It will be shown that this modification decreases circumferential distortion, thereby decreasing unsteady blade loading and reducing fan noise. Decreasing inlet distortion is also important for aerodynamic reasons, since it allows the engine to operate with a greater stall margin. Second, the doors have been modified to employ the "choking effect" at the auxiliary doors. The overall objective is to reduce noise caused by the auxiliary doors.

Another motivation of the test program is to demonstrate that the small-scale 10.4 cm (4.1 in.) diameter simulator is a viable tool for preliminary acoustic testing. To this end, results from a closed-door case tested with the 10.4 cm (4.1 in.) diameter simulator will be compared to previous results obtained at NASA Lewis Research Center, from a test pro-

Contributed by the International Gas Turbine Institute and presented at the 38th International Gas Turbine and Aeroengine Congress and Exposition, Cincinnati, Ohio, May 24–27, 1993. Manuscript received at ASME Headquarters, March 10, 1993. Paper No. 93-GT-279. Associate Technical Editor: H. Lukas.

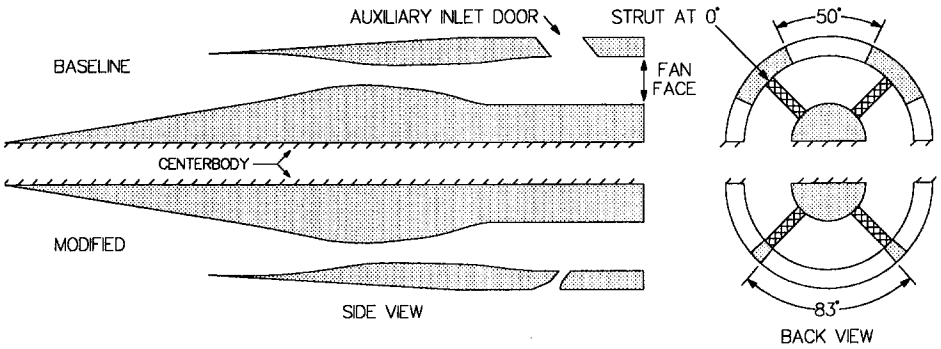

Fig. 1 Baseline versus modified door geometry

gram using a larger 50.8 cm (20 in.) diameter simulator (Woodward et al., 1984). The small-scale simulator can be used as an initial source of experimentation to test multiple concepts before a larger-scale test program is undertaken.

Most of the previous research with supersonic inlets has taken place under the Supersonic Cruise Aircraft Research program. Most of the previous work is related to the aerodynamic performance of the inlet (Koncsek, 1972; Smeltzer and Sorensen, 1973; Sorensen and Bencze, 1973; Syberg and Turner, 1981; Trefny and Wasserbauer, 1986; Wasserbauer et al., 1983). Research by Woodwood et al. (1984) and Ball and Pickup (1984), though, pertain to acoustic test programs. Woodward et al. (1984) is the only known work to present the acoustic effects of open versus closed auxiliary inlet doors. Also, Bangert et al. (1980, 1981) report full-scale inlet acoustic testing conducted on the YF-12 aircraft.

Under the Supersonic Cruise Aircraft Research program, NASA Lewis initiated an experimental program to determine the aerodynamic and acoustic performance of a representative supersonic cruise inlet. A 1/3-scale model of an axisymmetric mixed-compression supersonic inlet, named the "P-inlet," was chosen as the testbed for the experiments. The P-inlet was designed for Mach 2.65 cruise. The NASA Lewis research was primarily conducted in their 9 × 15 foot anechoic wind tunnel.

The previous acoustic research program concentrated on the far-field noise radiation level of both the fan fundamental Blade Passing Frequency (BPF) tone and broadband noise. The research focused on changing the centerbody position, bleed system, and auxiliary door configuration to determine their influence on the noise. One of the main findings was that opening the auxiliary doors significantly increases the fundamental BPF tone. The increase in tone was suspected to be caused by the auxiliary doors increasing the flow distortion to the fan. The previous research has also pointed out other noise mechanisms. The current need is to understand these noise mechanisms better and to develop better methods to decrease the noise.

Most of the variable features of the P-inlet, with the exception of the boundary layer bleed system, have been used in the present small-scale inlet. In previous testing, the bleed system itself was a noise source. In addition, to construct a bleed system for the present small-scale inlet would be complicated. For these reasons, a bleed system was not incorporated into the present test inlet.

2 The Experiment

The turbofan engine simulator features a single-stage air turbine that drives a single-stage fan. The model is similar to the one used by Pratt and Whitney to perform acoustic research (Topol, 1990). The design speed of the simulator is 80,000 rpm. The turbofan simulator has a 10.4 cm (4.1 in.) diameter fan with 18 blades and 26 stators. As discussed by Feiler and Conrad (1973), the Tyler–Sofrin theory predicts that the fundamental BPF tone caused by rotor–stator interaction will not propagate if the number of stator vanes is over twice the number of fan blades. Since the small-scale simulator has less than twice the number of stator vanes as compared to fan blades, the Tyler–Sofrin theory predicts that the fundamental BPF tone caused by rotor–stator interaction will propagate. Therefore the fundamental BPF tone from rotor–stator interaction is "cut-on" and will propagate.

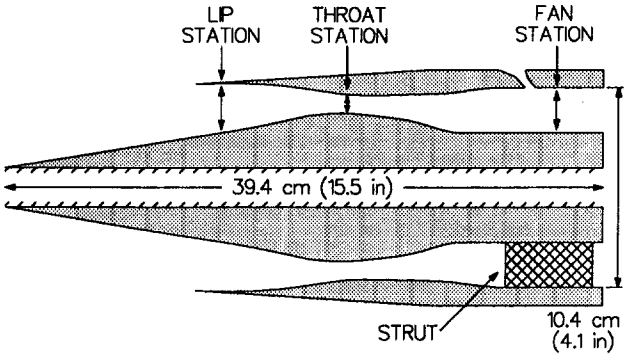

Fig. 2 Strut and pitot-static probe locations

As mentioned above, the simulator was tested at 60 percent design speed, which is about 50,000 rpm. The blade tip Mach number is 0.77, with the BPF at 15,000 Hz. The tests were conducted with the centerbody extended 0 percent. The 0 percent extension was chosen in order to produce the highest possible Mach number in the inlet throat and auxiliary doors.

2.1 Supersonic Test Inlets. In this paper, the small-scale model of the P-inlet is referred to as the baseline inlet. Figure 1 shows a side and back view of the baseline inlet versus the modified inlet. The fan face location is shown on the right of the side view. The main feature to note is the geometry of the auxiliary inlet doors. Each inlet has four doors equally spaced around the circumference. There are four struts supporting the centerbody, located between the auxiliary doors as indicated. The struts have an aerodynamic shape in order to minimize the wake that enters the fan. The axial location of a strut is shown in the bottom half of Fig. 2.

The most important design aspect of the modified door is shown in the back view of Fig. 1. It demonstrates that the modified design spans a greater percentage of the circumference. Each modified auxiliary inlet door spans 83 deg in an attempt to have the auxiliary door provide a more uniform air distribution to the fan face, as compared to each baseline door, which spans only 50 deg. Another important aspect of the modified door is the converging flow area, shown in the

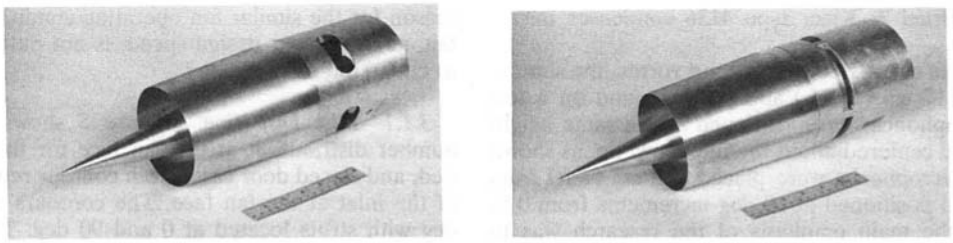

Baseline Modified

Fig. 3 Baseline versus modified inlet

Table 1 Kiel probe coordinates

R_1 = 5.43 cm (2.138 in)	Fan Entrance x/R_1 = 7.103	Fan Exit x/R_1 = 8.259
Outside r/R_1	0.869	0.906
Middle r/R_1	0.690	0.794
Inside r/R_1	0.511	0.683

Table 2 Pitot-static probe coordinates

R_1 5.43 cm (2.138 in)	Lip Station x/R_1 = 2.630	Throat Station x/R_1 = 4.150	Fan Station x/R_1 = 6.708
Outside r/R_1	0.853	0.817	0.869
Middle r/R_1	0.712	0.760	0.690
Inside r/R_1	0.561	0.703	0.511

side view of Fig. 1. This modification is an attempt to employ the choking effect at the auxiliary door. The baseline and modified doors both have the same "wetted" (exposed) area on the outside of the inlet. Figure 3 shows a picture of the baseline and modified inlet.

2.2 Aerodynamic Measurements. Aerodynamic measurements are needed for two reasons. First, they are used to make sure that the fan's operating conditions in the baseline and modified case are matched. This comparison insures that a difference in noise cannot be attributed to a difference in fan pressure ratio or mass flow rate. The fan pressure ratio was chosen to determine the fan's operating condition. Second, the aerodynamic measurements are used to determine the effect of the auxiliary doors on the flow entering the fan and the inlet performance. These measurements are used to help understand the influence of the aerodynamics on the acoustics. More detail on the experimental setup is available in Nuckolls (1992).

2.2.1 Fan Pressure Ratio. A 1.6 mm (1/16 in.) Kiel probe was chosen to measure the fan pressure ratio because it is insensitive to flow angularity. The Kiel probe, which measures total pressure, was placed both in front of and behind the fan. At the fan exit, the probe was placed in five different circumferential locations (0, 22.5, 45, 67.5, 90 deg). At the fan exit symmetry is achieved every 90 deg because as air is processed through the fan stage it is shifted in the circumferential direction. In the front of the fan, due to symmetry, it is only necessary to place the probe at three different circumferential locations (0, 22.5, 45 deg). In addition, three radial measurements were taken at every circumferential location. Table 1 lists the Kiel probe coordinates. The coordinates are normalized with respect to the inlet radius (R_1), which is the distance between the inlet centerline and the cowl lip. The axial location at the tip of the centerbody (x/R_1) is designated as zero. The individual results are then averaged by area weighting to determine the overall fan pressure ratio.

2.2.2 Inlet Aerodynamics. A 1.6 mm (1/16 in.) pitot-static probe was used to determine the inflow distortion and inlet performance. It was placed in the inlet at three axial stations, as shown in the top half of Fig. 2. Additional measurements were taken at the fan station with three circumferential angles (0, 22.5, 45 deg) to establish the effect of the different auxiliary doors on the flow field entering the fan. To facilitate the aerodynamic measurements at 0 deg, a strut had to be removed at that location. For all of the other measurements (both aerodynamic and acoustic) there were four struts present in the inlet. In addition, three radial measurements were taken at each circumferential location. Table 2 lists the pitot-static probe locations. Different circumferential measurements were taken at the lip and throat station. The results verified that there were no circumferential variations at those locations. Although other measurements showed that there was a small flow separation at the inlet lip, the flow was reattached by the time it reached the inlet throat station. This observation is consistent with what has been seen in previous research.

2.3 Acoustic Measurements. The acoustic measurements were conducted at an outdoor facility. The tests were "static," meaning air was pulled into the inlet from the surrounding atmosphere. Static testing can introduce various instabilities into the measurements. For instance, a ground vortex can be formed and pulled into the inlet. Also, the effect of atmospheric turbulence can be intensified when conducting static tests. These factors tend to increase the unsteadiness in acoustic measurements. To minimize these factors and to help simulate actual flight conditions, inlet control devices have been used to cover subsonic inlets in previous research. An inlet control device has not been included on the supersonic inlet in this study because an inlet control device will not cover the auxiliary inlet doors. In order to minimize the effect of the various instabilities, ten measurements were taken at each microphone position.

The instrumentation used for the acoustic test was a Bruel & Kjaer type 2034 spectrum analyzer. The Bruel & Kjaer analyzer was configured to measure a narrow band spectrum using a Hanning window with 50 percent overlap. The analyzer was configured to make three averages with each measurement at a frequency range of 25.6 kHz. More averages would have been preferred, but the air supply limited the duration of the run time to under 10 seconds. Also used were

6 mm (1/4 in) Bruel & Kjaer type 4136 condenser microphones.

To minimize the effect due to a ground vortex, the simulator was placed 117 cm (46 in.) above the ground on a test stand. The microphones were positioned at the same height above ground and centered about the inlet cowl lip, as shown in Fig. 4. The microphones were placed 122 cm (4 ft) from the inlet face and positioned at 10 deg increments from 0 to 110 deg. Since the main emphasis of the research was to investigate the forward propagating fan noise, acoustic measurements were not taken beyond 110 deg.

3 Results

3.1 Aerodynamic Results. Before any acoustic comparisons can be made between the different door designs, the fan pressure ratio must be determined to verify the fan's operating conditions. Two measurements were taken at each probe location for repeatability. In the worst case, the measurements differed by no more than 0.3 kPa (0.05 psi). The results show that the area-averaged fan pressure ratio is almost identical between the baseline and modified door case ($P_{t,\text{exit}}/P_{t,\text{in}} = 1.18$). In addition, the fan pressure ratio from the closed-door case is similar to the results from the baseline and modified door configurations. Since the fan rpm and pressure ratio are the same for all three cases, the three inlet configurations must have the same overall fan mass flow rate. The significance is that all of the following acoustic comparisons are made under similar fan operating conditions. (The fact that the fan operating point is the same for all three cases should not be a surprise, since the fan nozzle exit area and rpm were not changed during the experiment. The reason for the similar fan operating condition is because the fan, at 60 percent design speed, is not pulling in enough air to choke the inlet throat.)

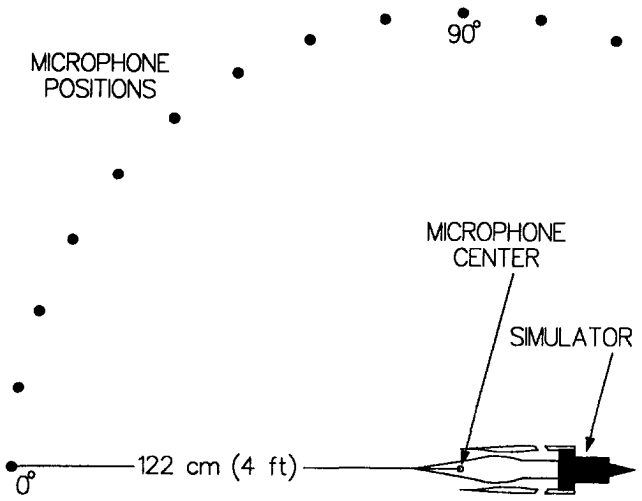

Fig. 4 Microphone layout

3.1.1 Inlet Distortion. Figure 5 shows the inlet Mach number distribution at the fan face for the baseline, modified, and closed door case. Each contour represents a quarter of the inlet at the fan face. The contours represent 0 to 90 deg with struts located at 0 and 90 deg. The contours only represent the area inside the probe measurement locations and therefore do not include the segment of area between the blade tip and the outside probe location or the area between the inside probe location and the hub. Shown on the outside of the baseline and modified door designs are the locations of the different auxiliary inlet doors. Figure 5 shows by comparing the baseline and modified case, that the modified case has a more uniform Mach number distribution. In the modified case most of the area is in the 0.33 to 0.36 Mach number range. This uniform region produces steady blade loading, which in turn reduces the noise generation. In contrast, the baseline case shows no uniform regions, and there are large gradients in the circumferential direction.

As a fan blade is rotating through circumferential distortion, it is exposed to a spatial varying Mach number, which produces an unsteady blade loading. The unsteady blade loading increases the noise generation (Mugridge, 1975). In the baseline case, the regions suspected of generating the most sound are near the blade tip in the 0 to 20 deg range and in the 70 to 90 deg range. When the blade tip traverses from 0 to 20 deg the Mach number changes from 0.30 to 0.40. The 0 to 20 deg region and the 70 to 90 deg region near the blade tip both have large gradients in the circumferential direction, and are therefore suspected of being predominant noise sources. Also, at the blade tip, the blade speed is higher, which causes any disturbance to produce more noise (Moore, 1975). Other disturbances like secondary flow and tip leakage also increase the aerodynamic complexity and noise at the blade tip.

Results from the Mach number distribution for the closed-door case in Fig. 5 show only radial gradients. Radial gradients produce a steady blade loading, and hence should not increase the noise generation as is the case for circumferential distortion. The small changes in the circumferential direction at 0 and 90 deg can be attributed to the strut removal, which is necessary in order to take the aerodynamic measurements at 0 deg. The removal of the strut decreases the flow blockage, which can lead to a slightly lower Mach number. The lower Mach numbers at the hub and tip are attributed to the buildup of the boundary layer in the inlet. Based on the circumferential distortion results in Fig. 5, the closed-door case will generate minimal noise.

When comparing the Mach number distribution from all three cases, the baseline door configuration is shown to have the greatest circumferential distortion. Table 3 quantifies this

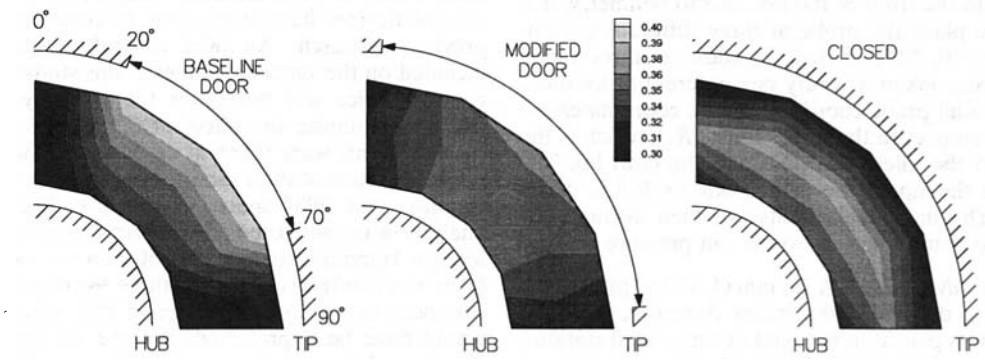

Fig. 5 Inlet Mach number distribution at fan face

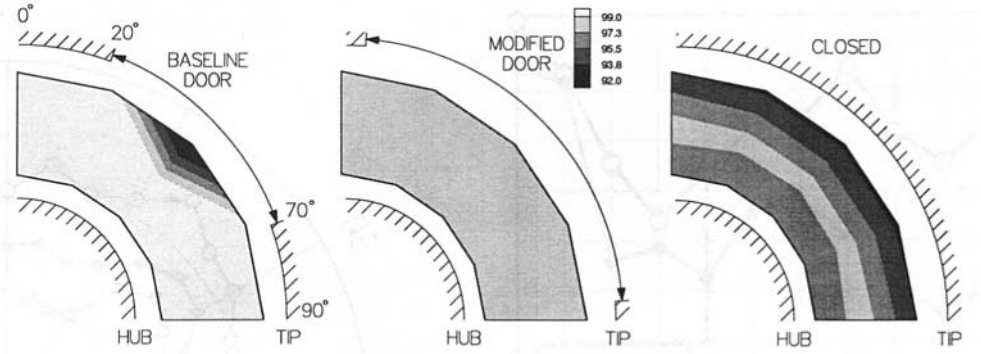

Fig. 6 Inlet fan face total pressure recovery (percent)

Table 3 Mach number distortion

Auxiliary Door	Circumferential Distortion
Baseline	0.22
Modified	0.11 (factor of 2 reduction)
Closed	0.06 (factor of 4 reduction)

distortion, that was shown graphically in Fig. 5, by calculating the Mach number distortion in the circumferential direction. To calculate the circumferential distortion, the formula $(M_{MAX} - M_{MIN})/M_{AVG}$ is used to calculate a distortion value for the measurements taken at one radius. This formula is then repeated on the measurements taken at the other radii. To calculate the overall circumferential distortion, the values from the different radii are then area averaged. The results here show that the baseline door configuration is suspected of generating the most noise. The closed-door case is expected to produce the least amount of sound. These hypotheses are confirmed by the acoustic results to be presented later.

Other aerodynamic results also substantiate similar trends. For instance, the inlet total pressure recovery at the fan face in Fig. 6 shows that the baseline configuration again has the highest distortion in the circumferential direction. The figure presents the inlet total pressure as a percentage of the ambient surrounding total pressure. The closed-door case has high losses at the inside and outside radius, which are caused by the buildup of the boundary layer. The modified case has a uniform total pressure contour. The baseline case has a loss of 10 percent at the 45 deg measurement location at the outside radius. This high loss, which is most likely caused by the airflow through the baseline door, increases the circumferential distortion, therefore producing an unsteady blade loading and increasing noise. Although not shown, the inlet mass flow and fan pressure ratio results have similar circumferential distortion trends (Nuckolls, 1992).

3.1.2 Inlet Aerodynamic Performance. Opening the auxiliary doors has a large effect on the throat station Mach number. The Mach number drops from 0.83 for the closed case to 0.32 and 0.50 for the baseline and modified cases, respectively. Previous research by Woodward et al. (1984) indicates that Mach numbers up to 0.5 are not expected to exhibit the choking effect. Since the throat Mach number for the closed case is above 0.5, there will be a choking effect at the throat station, thereby reducing the noise radiation.

The average Mach number in the auxiliary doors was estimated from the aerodynamic data. The door mass flow rate was approximated as being equal to the mass flow through the fan minus the mass flow through the inlet throat.

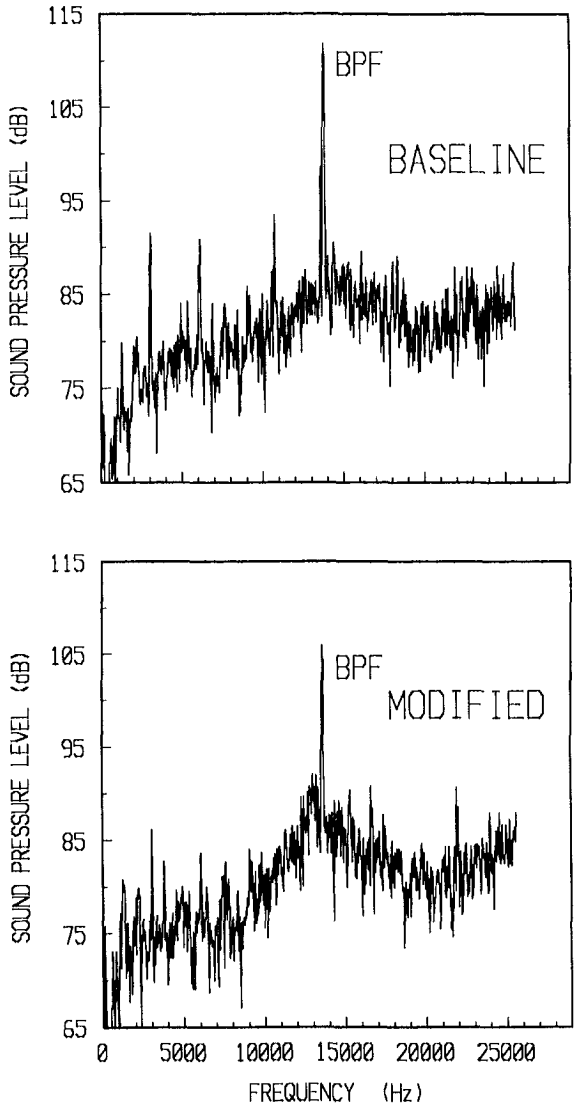

Fig. 7 Sample data

Then, an average Mach number in the auxiliary inlet doors was calculated using isentropic relations. The results indicate that the average Mach number in the auxiliary door is 0.23 for the baseline case, and 0.27 for the modified case. This result shows that one of the design objectives, to employ the choking effect in the modified auxiliary door itself, has not been achieved. This low Mach number in the auxiliary door is attributed to the fan not pulling a large enough mass flow at 60 percent design speed.

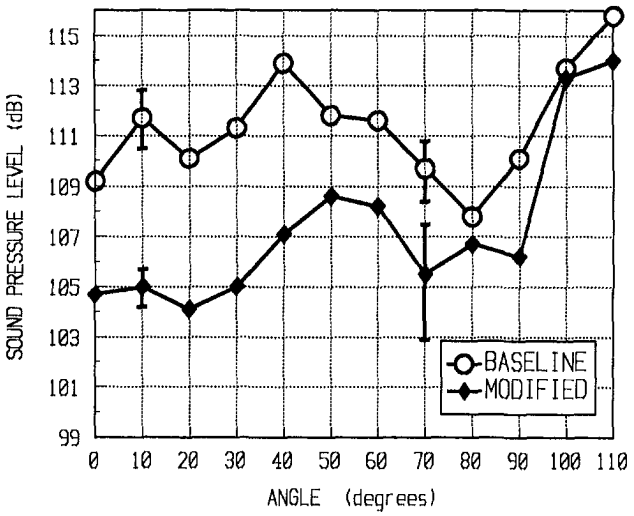

Fig. 8 BPF tone versus angle

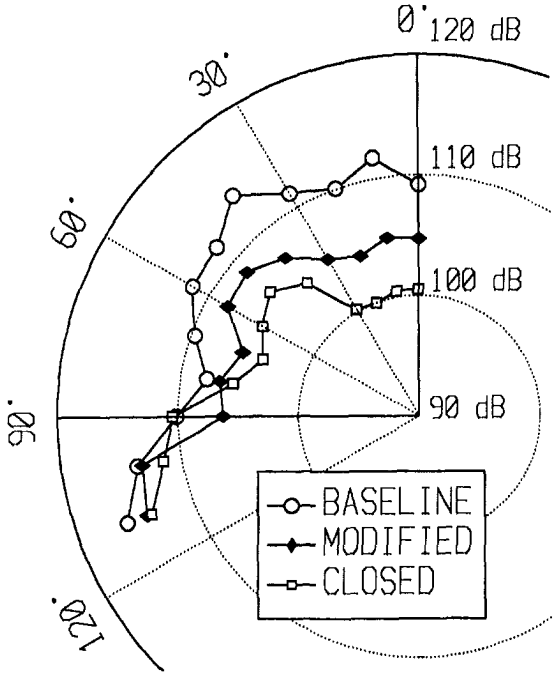

Fig. 9 Polar plot of BPF tone

3.2 Acoustic Results. Figure 7 compares the spectrum from the baseline and modified case measured with the microphone at 10 deg. This sample data, taken at about 50,000 rpm, shows the narrow band spectrum analysis of the sound pressure level versus frequency. The BPF tone is distinct and at least 10 dB above the broadband noise. The three tones shown in the baseline case from 3 to 11 kHz are attributed to the opening of the baseline door. These extra tones are observed at all angles. The extra tones vary in number and in their frequency location from run to run, for the baseline door case. Not enough data has been taken on the broadband noise to determine the effects of the different door configurations.

3.2.1 BPF Tone Versus Angle. Figure 8 shows the key result that compares the baseline and modified auxiliary inlet doors. The plot shows the sound pressure level of the BPF tone versus angle. The greatest reduction in the tone is observed in the forward sector. The tone is reduced by an average of over 6 dB in the 0 to 40 deg range. The primary reason for this reduction in noise is attributed to the reduction in the circumferential distortion from the modified door design. This illustrates that the modified auxiliary door configuration is successful in reducing the BPF tone. At the higher angles the two results tend to merge. The two BPF tone levels also tend to increase in the 90 to 110 deg range. Uncertainty bands are included in the figure at two angles. The uncertainty bands show a calculation of one standard deviation, from the mean, of the ten measurements taken at each angle. The uncertainty is acceptable, but it may be reduced by improving the test facility.

Figure 9 shows a polar plot of the BPF tone for all three inlet configurations. For the closed door case, there is an average 10 dB reduction in the 0 to 40 deg range, when compared to the baseline case. Comparing the closed and modified door case in Fig. 9, shows that there is an average reduction of 4 dB in the 0 to 40 deg range for the closed-door case. The reduction in the tone level for the closed-door case can be attributed to three factors: the reduced circumferential distortion at the fan face, the choking effect at the throat station, and the fact that there is no direct radiation path through an auxiliary door.

The effect of choking at the inlet throat on the fan noise radiation was also investigated for the closed-door case (Nuckolls, 1992). The centerbody was extended forward from the 0 percent position. This increases the inlet throat area and therefore causes the throat Mach number to drop from 0.83 to 0.44. Both the BPF and broadband noise were increased at the lower angles due to the reduction in the throat Mach number, as expected. At the 10 deg microphone location the increase in the BPF tone was about 4 dB.

Figure 9 can be further explained by the modal content of the noise generated in the inlet. As discussed by Tyler and Sofrin (1962) modes of circumferential order $(m) = n^*B + k^*V$ can be generated in the duct, where (n) is the harmonic of the BPF, (B) number of fan blades, (k) is the spatial distortion harmonic number taking on all positive and negative integers, (V) is the number of stator blades or inflow distortions per revolution. Based on the inlet diameter, simulator speed, number of fan blades, number of stator blades, it can be determined which modes can propagate due to rotor–stator interaction for the fundamental BPF tone. Based on this analysis, a mode of circumferential order $m = -8$ can propagate in the duct; the minus sign implies that the mode is spinning in the opposite direction from the rotor. The next step is to determine the predominant lobe location in the far-field due to this mode. From Homicz and Lordi (1975) it is predicted that a mode with $m = 8$ radiates into the far-field with a principle lobe at about 44 deg. Figure 9 shows an increase in the directivity pattern at 50 deg, especially for the modified and closed door case, which can be attributed to an eighth-order circumferential mode.

Opening the baseline doors increases the BPF tone in the 0 to 70 deg range. The increase in noise is attributed to additional modes generated by the interaction of the inflow distortion with the rotor. An analysis similar to rotor–stator interaction can be performed for the rotor–inflow interaction. Instead of using (V) as the number of stator blades the number four is entered because there are four inflow distortions caused by the four baseline doors. This analysis reveals that modes of order $m = -10, -6, -2, 2, 6$, and 10 can propagate in the inlet. These additional modes are attributed to the increase in the BPF for the baseline case, in particular the lower order modes because they have principle lobes at lower angles. A detailed analysis of the rotor–inflow interaction is not included because not enough measurements were taken of the inflow distortion to perform an analysis to determine which modes are most likely to be generated. In addition, a supersonic inlet is more complicated than a

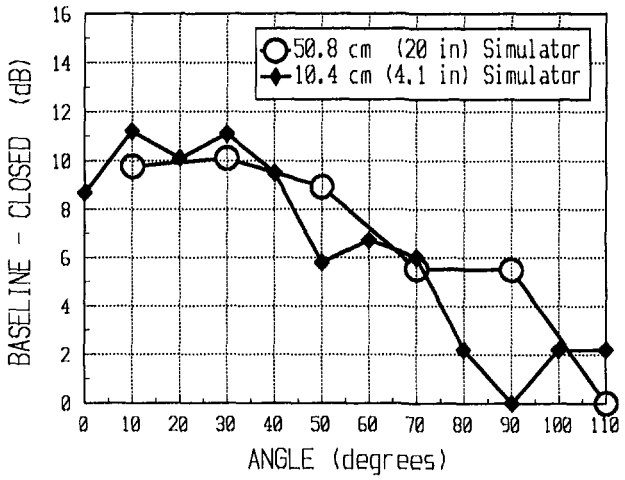

Fig. 10 Comparison of BPF tone

conventional subsonic inlet. Modes that are generated in a supersonic inlet must first propagate through the struts, then through the auxiliary doors and the converging diverging inlet passage. All of these factors increase the complexity of the far-field radiation associated with a supersonic inlet. Also, the previous analysis has not included the effect of the possible higher order radial modes.

3.2.2 Comparison With Previous Research. Figure 10 compares some of the present research with a previous test conducted at NASA Lewis (taken from Fig. 7, Woodward et al., 1984). Figure 10 in this report shows the difference in the BPF tone (baseline minus closed) versus the angle. The two different test programs show good agreement from 0 to 70 deg. This close agreement is particularly encouraging, given the fact that the Reynolds numbers were different in the two models, and that the two tests were not performed under identical conditions. At NASA Lewis, the research was performed in an anechoic wind tunnel operating at Mach 0.2, while at Virginia Tech the tests were conducted in an outdoor facility. In addition, the two test cases were not performed with matched inlet configurations; at NASA Lewis the centerbody was extended forward. However, since the throat station Mach numbers are similar, the tests should be acceptable for comparison. Despite the above-mentioned differences, Fig. 10 demonstrates that the small-scale simulator can produce results with similar trends when compared to a larger-scale experiment.

3.2.3 Reynolds Number Consideration. The Reynolds number is an important consideration in the experiment. A potential problem is that small-scale model results might not correctly predict the noise when compared to an actual full-size engine with a larger Reynolds number. This potential problem is not a great concern here, since the main emphasis of this research is on the trends and noise mechanisms, instead of results that can be directly used to predict full scale noise. Table 4 compares the Reynolds number (based on blade tip speed and fan diameter) between the 10.4 cm (4.1 in.) simulator, P-inlet tested at NASA Lewis, and an actual proposed flight engine. Even though the supersonic inlet tested was 1/5 the size of the previously tested P-inlet, the results were shown to compare favorably.

4 Conclusions

The main objective of this research was to reduce the fan noise radiating from a supersonic inlet during simulated aircraft landing by modifying the geometry of the auxiliary inlet door. A series of outdoor experiments was performed with a small-scale model of an axisymmetric, mixed-compression, supersonic inlet connected to a 10.4 cm (4.1 in.) diameter turbofan engine simulator. The simulator was tested at 60 percent design speed in an attempt to match the simulator noise source to that of an aircraft engine on approach. The modified auxiliary inlet door was successful in reducing the forward propagating fan BPF tone noise by an average of 6 dB in the 0 to 40 deg sector, when compared to the original baseline design of the auxiliary door. The modified door was designed to reduce the inlet distortion to the fan face. Results from the aerodynamic measurements show that the modified door was successful in reducing the Mach number distortion in the circumferential direction by a factor of two, when compared to the baseline configuration. The reduced BPF tone noise, from the modified door design, is attributed to the decrease in the circumferential distortion at the fan face.

A comparison of the baseline and closed-door case shows that the BPF tone is an average of 10 dB higher in the 0 to 40 deg range for the baseline case. This result is consistent with the previous research conducted by Woodward et al. (1984) at NASA Lewis, using a 50.8 cm (20 in.) diameter simulator. The decrease in BPF tone level, for the closed-door case, is attributed to three factors: the reduced inlet distortion at the fan face, the choking effect at the throat station, and the fact that there is no direct noise radiation path through an auxiliary inlet door.

Table 4 Reynolds number comparison

ReynoldsNumber (based on tip speed)	Fan diameter	Scale
1.7×10^6	10.4 cm (4.1 in) Virginia Tech	1/14
7.6×10^6	50.8 cm (20 in) P-inlet, NASA Lewis	1/3
22.7×10^6	152 cm (60 in) Actual Flight Engine	1

References

Ball, W. H., and Pickup, N., 1984, "Low Speed Performance and Acoustic Tests of an Axisymmetric Supersonic Inlet—Phase One Tests With Auxiliary Doors Closed," NASA CR-172390.

Bangert, L. H., Burcham, F. W., and Mackall, K. G., 1980, "YF-12 Inlet Suppression of Compressor Noise: First Results," AIAA Paper No. 80-0099.

Bangert, L. H., Feltz, E. P., Godby, L. A., and Miller, L. D., 1981, "Aerodynamic and Acoustic Behavior of a YF-12 Inlet at Static Conditions," NASA CR-163106.

Feiler, C. E., and Conrad, W. E., 1973, "Noise From Turbomachinery," AIAA Paper No. 73-815.

Homicz, G. F., and Lordi, J. A., 1975, "A Note on the Radiative Directivity Patterns of Duct Acoustic Modes," *Journal of Sound and Vibration*, Vol. 41(3), pp. 283–290.

Koncsek, J. L., 1972, "Transonic and Supersonic Test of a Mach 2.65 Mixed-Compression Axisymmetric Intake," NASA CR 1977.

Moore, C. J., 1975, "Reduction of Fan Noise by Annulus Boundary Layer Removal," *Journal of Sound and Vibration*, Vol. 43(4), pp. 671–681.

Mugridge, B. D., 1975, "Axial Flow Fan Noise Caused by Inlet Flow Distortion," *Journal of Sound and Vibration*, Vol. 40(4), pp. 497–512.

Nuckolls, W. E., 1992, "Fan Noise Reduction From a Supersonic Inlet," M.S. Thesis, Department of Mechanical Engineering, VPI SU, Blacksburg, VA.

Smeltzer, D. B., and Sorensen, N. E., 1973, "Analytic and Experimental Performance of Two Isentropic Mixed Compression Axisymmetric Inlets at Mach Numbers 0.8 to 2.65," NASA TN D-7320.

Sorensen, N. E., and Bencze, D. P., 1973, "Possibilities for Improved Supersonic Inlet Performance," AIAA Paper No. 73-1271.

Syberg, J., and Turner, L., 1981, "Supersonic Test of a Mixed-Compression Axisymmetric Inlet at Angles of Incidence," NASA CR-165686.

Topol, D. A., 1990, "Rotor Wake/Stator Interaction Noise-Predictions Versus Data," AIAA Paper No. 90-3951.

Trefny, C. J., and Wasserbauer, J. W., 1986, "Low-Speed Performance of an Axisymmetric, Mixed-Compression, Supersonic Inlet With Auxiliary Inlets," NASA TP-2557.

Tyler, J. M., and Sofrin, T. G., 1962, "Axial Flow Compressor Noise Studies," *Society of Automotive Engineers Transactions*, Vol. 70, pp. 309–332.

Wasserbauer, J. F., Cubbison, R. W., and Trefny, C. J., 1983, "Low Speed Performance of a Supersonic Axisymmetric Mixed Compression Inlet With Auxiliary Inlets," AIAA Paper No. 83-1414.

Woodward, R. P., Glaser, F. W., and Lucas, J. G., 1984, "Low Flight Speed Fan Noise From a Supersonic Inlet," *AIAA Journal of Aircraft*, Vol. 21, No. 9, pp. 665–672.

K. Nakakado[1]

T. Machida

Hitachi, Ltd.,
Tsuchiura, Japan

H. Miyata
Hitachi, Ltd.,
Hitachi, Japan

T. Hisamatsu

N. Mori

I. Yuri

Central Research Institute
of Electric Power Industry,
Yokosuka, Japan

Strength Design and Reliability Evaluation of a Hybrid Ceramic Stator Vane for Industrial Gas Turbines

Employing ceramic materials for the critical components of industrial gas turbines is anticipated to improve the thermal efficiency of power plants. We developed a first-stage stator vane for a 1300°C class, 20-MW industrial gas turbine. This stator vane has a hybrid ceramic/metal structure, to increase the strength reliability of brittle ceramic parts, and to reduce the amount of cooling air needed for metal parts as well. The strength design results of a ceramic main part are described. Strength reliability evaluation results are also provided based on a cascade test using combustion gas under actual gas turbine running conditions.

Introduction

In recent years, considerable effort has been expended in Japan to apply a combined gas/steam turbine cycle and increase the gas turbine inlet temperature (TIT) in order to raise the efficiency of thermal power generation. Structural ceramic materials offer excellent characteristics, compared with superalloys, in terms of heat, corrosion, and wear resistance at high temperatures. By employing ceramics for some of the key components of gas turbines—i.e., combustors, stator vanes, and rotor blades—gas turbines can be operated at higher temperatures and require less cooling air, which, in turn, can substantially enhance thermal efficiency. Ceramics, however, are brittle, and thus lack sufficiently reliable strength on their own as a structural material. Rather than a simple substitution of ceramics for metal parts, innovative structural design technologies are required for applications that exploit the advantages of ceramics while at the same time compensating for their deficiencies.

The authors are seeking to establish such design technologies through their studies on ceramic stator vanes, as part of a broader effort to develop a ceramic industrial gas turbine (Miyata et al., 1989). This effort culminated in the development of a hybrid ceramic/metal stator vane structure. This structure's strength reliability (Nakakado et al., 1990), and cooling characteristics (Mori et al., 1991), were investigated. Other types of hybrid ceramic stator vane have been previously developed by Ohkoshi et al. (1987), and by Krüger and Hüther (1989).

In this report, the structural and strength design results of prototype first-stage hybrid ceramic stator vanes for 1300°C class, 20-MW gas turbines are described. Strength reliability evaluation results are also provided based on thermal load cascade testing using combustion gas under actual gas turbine running conditions.

Construction of Hybrid Ceramic Stator Vane

A cross-sectional schematic drawing of the designed hybrid ceramic/metal stator vane for application to the first-stage nozzle of a 1300°C class, 20-MW gas turbine is shown in Fig. 1. The specifications of the gas turbine and the hybrid ceramic stator vane are shown in Table 1. The airfoil (the ceramic shell) that comes in direct contact with high-temperature combustion gas and the inner/outer shrouds (ceramic side walls) are formed from ceramics—a material having superior heat resistance properties and requiring no cooling. These ceramic parts are held by compressive force applied to the inner and outer metal supporting plates via the metal core and heat-insulating plates. The metal core, penetrating the ceramic parts and heat-insulating plates, holds these ceramic parts against horizontal external load through the heat-insulating layer in the turbine; it also holds heat-insulating plates directly. Both the heat-insulating layer and heat-insulating plates are double-layered, as shown in Fig. 1. Heat-insulating materials, i.e., an oxide ceramic composite for

[1]Now with Hitachi Construction Machinery Co., Ltd., Tsuchiura, Japan.

Contributed by the International Gas Turbine Institute for publication in the JOURNAL OF ENGINEERING FOR GAS TURBINES AND POWER. Manuscript received at ASME Headquarters February 1994. Associate Technical Editor: H. Lukas.

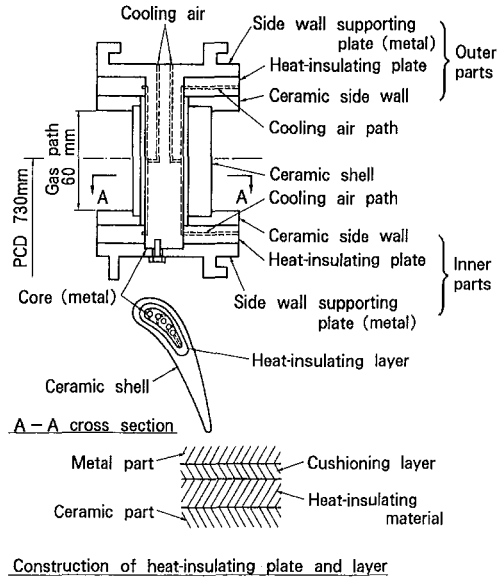

Fig. 1 Cross-sectional schematic drawing of a hybrid ceramic stator vane for a 1300°C class, 20-MW gas turbine

Table 1 Specifications of the gas turbine and the hybrid ceramic stator vane

Gas Turbine		
Output	20	MW
Turbine Inlet Temperature(TIT)	1300	℃(Mean)
Turbine Inlet Pressure	1.5	MPa
First-stage Hybrid Ceramic Stator Vane		
Configuration		
Pitch Circle Diameter(PCD)	730	mm
Height	60	mm
Cooling Air Temperature	400	℃

heat-insulating plates and porous castable oxide ceramics for the heat-insulating layer, are used for the layer facing the ceramic parts, while heat-resistant and flexible material, i.e., ceramic fiber, is used for the layer facing the metal parts, forming a cushioning layer.

The key features of this new hybrid ceramic stator vane can be summarized as:

1 Metal parts are used to provide reinforcement against external forces stemming from pressure differentials, so that ceramic parts are subjected to very slight mechanical loads.

2 Since the ceramic parts are not rigidly connected to the metal parts, no ceramic parts come under internal stress caused by differences in coefficients of the thermal expansion between the ceramic and metal parts. Therefore, most stress applied to the ceramic parts is thermal stress caused by temperature distribution characteristics of each individual part.

3 Since the ceramic component is divided into parts having simple shapes, manufacturing is relatively easy, compared to that of a mono block ceramic component. Moreover, by designing the ceramic parts in simple shapes, excessive local stress caused by stress concentration can be avoided.

4 The amount of heat penetrating to the metal parts is greatly suppressed by the ceramic parts and insulating material. As a result, the amount of cooling air required can be substantially reduced, compared with conventional air-cooled metal vanes.

Strength Design of Ceramic Components

Material Properties of Ceramics for Stator Vanes. As reported in EPRI-AP-4380 (1986), sintered structural ceramics are considered to be advantageous for reducing the fabricating cost of ceramic gas turbine components. Although they have one weak point in common, that is, a low fracture toughness, ceramic components with rather complicated shapes can be manufactured at a relatively low cost if dimensional deviation of approx. 0.2 to 0.3 mm is allowed, because they can be directly applied to practical use as fired. Since cost performance, along with reliability, is required for industrial ceramic gas turbines, application of sintered structural ceramics is an interesting subject for study. Therefore, sintered SiC, Si_3N_4, and Sialon were chosen as candidate materials for hybrid ceramic stator vanes.

Table 2 Material properties of typical sintered structural ceramics (at RT)

Ceramics	Young's Modulus GPa	Bending Strength MPa	Fracture Toughness $MPa\sqrt{m}$	Thermal Expansion Coef. 10^{-6}/℃	Thermal Conductivity W/(m·K)	Specific Heat kJ/(kg·K)
SiC	406	579	4.6	4.0 (~700℃)	126	0.67
Si_3N_4	309	696	6.8	3.2 (~800℃)	67	0.66
Sialon	283	666	7.5	2.2 (~700℃)	16	0.6

Table 3 Weibull modulus *m* of three kinds of sintered structural ceramics at RT and at 1250°C

Temp. (℃)	SiC	Si_3N_4	Sialon
RT	10.8	17.8	10.8
1250	11.7	21.9	22.6

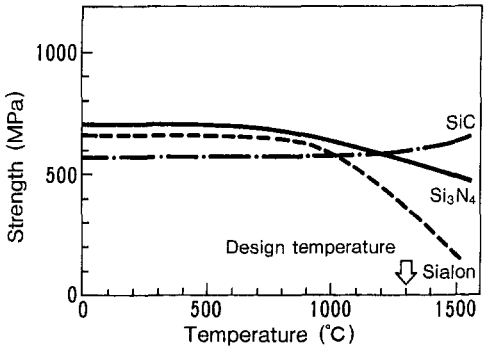

Fig. 2 High-temperature strength characteristics of three kinds of sintered structural ceramics for high-temperature gas turbines

Their material properties (at room temperature) are shown in Table 2. Compared to SiC, Si_3N_4 and Sialon have lower values for Young's modulus, thermal expansion coefficient, and thermal conductivity values, as well as higher values in terms of fracture toughness. Their high-temperature strength characteristics are shown in Fig. 2. Reported are the average values of results from the four-point bending test using a rectangular-section bar-type specimen (3 mm × 4 mm × 40 mm). SiC and Si_3N_4 were found to have almost the same strength, from room temperature through the design temperature (1300°C). However, Sialon showed lower strength than the others at the design temperature. The values of the Weibull modulus *m* at room temperature and at 1250°C are shown in Table 3. The values of Si_3N_4 and Sialon are about two times higher than that of SiC.

Thus, Si_3N_4 and SiC were chosen as candidate materials for detailed stress analysis, based mainly on their strength properties.

Thermal Stress Analysis. As noted in the previous section, the fundamental stress on ceramic parts is the thermal stress generated by combustion gas. Therefore, thermal stress on the ceramic parts was analyzed by FEM while the gas

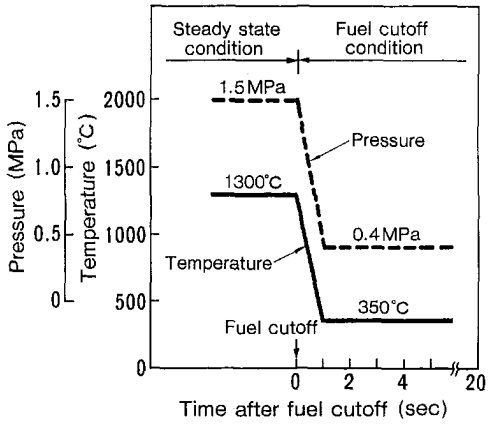

Fig. 3 Thermal stress analysis conditions in combustion gas

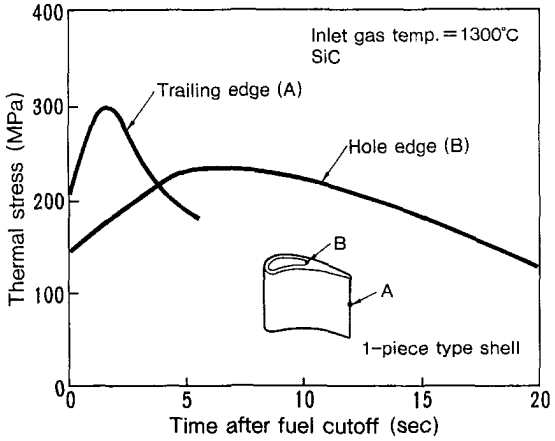

Fig. 4 Changes in principal thermal stress at two typical points on a one-piece type ceramic shell made of SiC with time after fuel cutoff

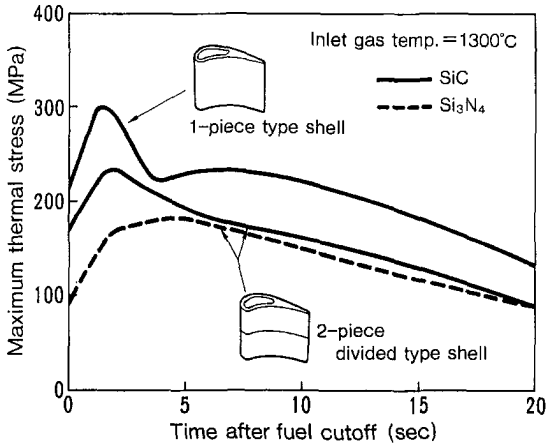

Fig. 5 Changes in the maximum principal thermal stress on two types of ceramic shell made of two kinds of ceramic material, with time after fuel cutoff

turbine was running. Following are the major conditions analyzed:

1 Construction: As shown in the cross-sectional schematic drawing of Fig. 1, a three-dimensional multilayered construction, consisting of ceramic parts (shell and side wall) and heat-insulating parts (plate and layer), was employed. In addition, we considered only the outer half of the vane, since the inner half is symmetric with the outer one. Two types of shell configuration, a one-piece type and a two-piece divided type, were considered.

2 Temperature analysis: (*a*) Boundary conditions: Thermal transfer coefficients between combustion gas and the surfaces of the ceramics parts were calculated by numerical analysis used for conventional metal stator vanes. The thermal transfer coefficient between cooling air and heat-insulating parts was decided by parameter survey, taking high-temperature strength of the metal parts into consideration. However, thermal resistance on contact surfaces between the parts was disregarded. (*b*) Temperature conditions: Two typical gas turbine running conditions were considered. One was a steady-state condition at rated running speed, and the other was a fuel cutoff condition for emergency stop. Figure 3 shows the thermal stress analysis conditions of combustion gas. For the fuel cutoff condition, a combustion gas temperature falloff of 950°C per 1-second interval was assumed, and considered to be the most severe case in conventional gas turbines. The cooling air temperature was a constant 350°C.

3 Stress analysis: (*a*) Boundary conditions: For each ceramic part, thermal stress analysis was performed, taking only temperature distribution into consideration. (*b*) Load conditions: The results of temperature analysis were employed.

4 Material: Two typical kinds of ceramic materials, sintered SiC and Si_3N_4, were considered. Their material characteristics were given as functions of temperature.

The calculations of thermal stress on a one-piece type ceramic shell made of SiC are shown in Fig. 4. This figure shows changes in principal thermal stresses at two typical points of the shell corresponding to time lapsed after fuel cutoff, t, where the steady thermal stresses are plotted at $t = 0$. At steady state and in the early period after fuel cutoff, the maximum stress on the shell always appears at the midheight of the trailing edge (point A). Its peak appears approximately 2 seconds after fuel cutoff. Later on, the stress at the trailing edge decreases sharply and the maximum stress appears at the hole edge (point B). The second peak appears approximately 6 seconds after fuel cutoff.

Since the peak thermal stress at point A is rather high, compared to the strength of SiC ceramic material, we sought to alleviate the excess thermal stress by dividing the ceramic shell into two pieces—an inner shell and an outer shell. The changes in the maximum principal thermal stress of the SiC two-piece divided type shell with time are shown in Fig. 5, and is compared with that of the original one-piece type shell. Thus, both the steady and peak thermal stresses of two-piece divided type shell are reduced to about 80 percent of those of the one-piece type shell. In Fig. 5, the maximum thermal stress changes in the Si_3N_4 two-piece divided type shell are also plotted. Here it should be noted that the thermal stress in the ceramic shell (inner/outer shell) was found to respond differently depending on whether it was made of SiC or Si_3N_4. Compared to SiC, the Si_3N_4 peak stress is about 30 percent lower and it appears later.

Strength Design of Ceramic Shell. In the first approximate strength design of the ceramic shell, the peak thermal stress is compared with the high-temperature strength of the ceramic material. Strength values at 1300°C (design temperature), expressed in terms of a margin of safety at the peak thermal stress on the two-piece divided type ceramic shell, were approximately 2.6 for SiC, and 3.4 for Si_3N_4.

A particularly important factor to ensure reliable fitting support between the ceramic shell and the ceramic side wall is fracture toughness. Taking the margin of safety, the fracture toughness, and the Weibull modulus m into account, Si_3N_4 was selected as the best candidate ceramic material.

Prototype Hybrid Ceramic Stator Vane and Thermal Load Cascade Test

Prototype Hybrid Ceramic Stator Vane. Based on the results reviewed above, a prototype hybrid ceramic stator

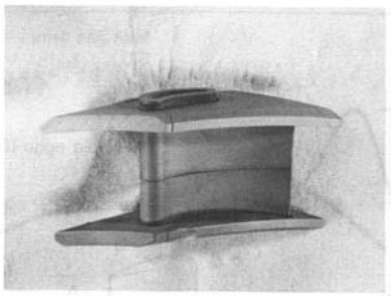

Fig. 6 Subassembly of the main ceramic parts made of sintered Si_3N_4

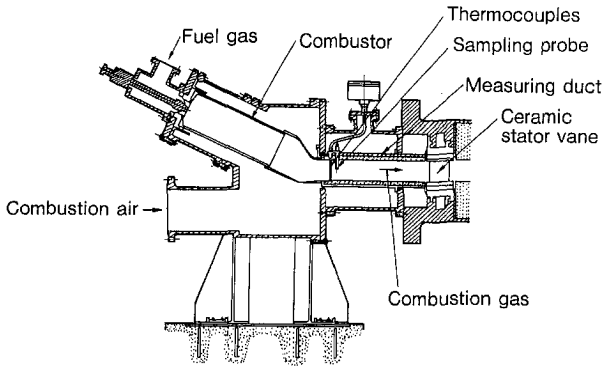

Fig. 7 Cascade test equipment used at high-temperature and high-pressure combustion gas for hybrid ceramic stator vane evaluation

vane was constructed. The ceramic parts were made of sintered Si_3N_4. They were formed using isostatic pressing combined with the green-machining method by a ceramic manufacturer. These ceramic parts were used as fired, except for a few modifications by machining. The subassembly of the main ceramic parts is shown in Fig. 6. The ceramic shell was 60 mm in height, and divided into two pieces (inner and outer shells) at the middle of the height. These shells were tightly fitted together, to prevent combustion gas from flowing into the inside of the stator vane. To make manufacturing easy, they had a blunt head, and in principle, the wall was 3 mm in thickness. The inner and outer side walls were of cylindrical shapes and had slits to release thermal stress. Then, they were supported by fitting their grooves over the ceramic shell.

The heat-insulating material for plates was an alumina fiber composite with high heat resistance, and the one for the layer surrounding the core was a castable mullite. The cushioning layer was made of an alumina fiber. Metal parts (core and supporting plates) were made of a heat-resistant alloy.

Five hybrid ceramic stator vanes were assembled and subjected to cascade testing.

Thermal Load Cascade Test. To evaluate the strength reliability of the prototype hybrid ceramic stator vane, a thermal load cascade test was conducted using combustion gas. A longitudinal cross section of the test equipment is shown in Fig. 7. The channel cross-sectional temperature distribution and pressure of the combustion gas were measured using a measuring duct. Subsequently the gas was successively introduced to the hybrid ceramic stator vanes. High-pressure air was supplied to the outer side of the hybrid ceramic stator vanes for cooling and sealing, and to their inner side for sealing. Given that the amount of sealing air to each side was equal, cooling air quantity could be calculated by measuring the air quantity supplied to each side.

The various test conditions, including quantity, pressure and temperature of combustion gas, and air for cooling/sealing were measured and controlled. At the same time, the temperatures of the ceramic shell, metal core, and other constituent parts of center hybrid ceramic stator vane in the assembly were measured in order to evaluate the cooling characteristics of the vane. As shown in Fig. 10, the temperature measuring point for the ceramic shell was located near the back side of the metal core, which was the thickest part of the ceramic shell, at a point approximately 7 mm toward the outside from the shell dividing line. The two temperature measuring points for the metal core were located near the head and suction sides radially at the middle of the gas path section.

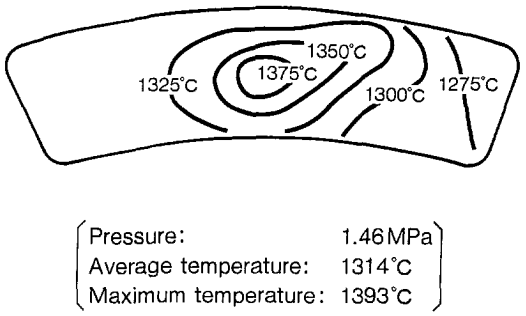

Pressure: 1.46 MPa
Average temperature: 1314°C
Maximum temperature: 1393°C

Fig. 8 Example of cross-sectional gas temperature distribution in the cascade test under the rated running conditions

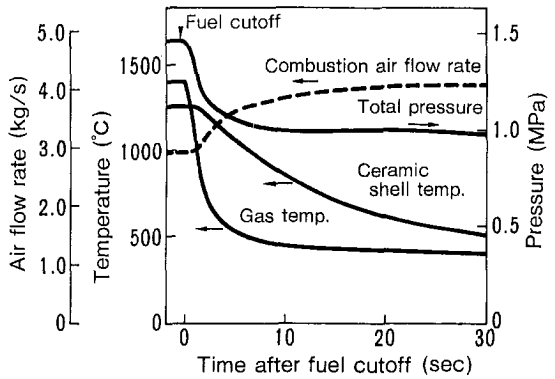

Fig. 9 Transient behavior of gas in the cascade test with time after fuel cutoff. The ceramic shell temperature of the center stator vane in cascade is also shown.

Test Conditions. First, for evaluating a cooling characteristics of the hybrid ceramic stator vane, a steady-state thermal load test was conducted twice, for a total of approximately 11 hours, during which temperature and pressure of the rated combustion gas were maintained at 1300°C (mean) and 1.5 MPa for a total of approximately 4 hours. An example of the cross-sectional gas temperature disribution under the rated running conditions is shown in Fig. 8. The maximum temperature was about 1400°C at the center of the cross section.

Next, for evaluating thermal shock resistance of the hybrid ceramic stator vane, a fuel cutoff test, starting from the rated combustion gas conditions, was conducted once at the end of the steady thermal load test. The transient behavior of the combustion gas and the ceramic shell temperature are shown in Fig. 9. The behavior, slower drop of combustion gas pressure and increase in combustion air flow rate, is different from that under the design gas turbine conditions.

Test Results and Discussion

Cooling Characteristics. Among all the turbine components, the metal core is exposed to the highest temperatures.

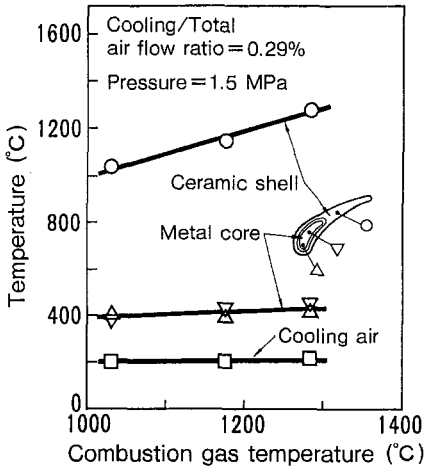

Fig. 10 Relationship between core and shell temperatures of the hybrid ceramic stator vane, cooling air temperature, and combustion gas temperature

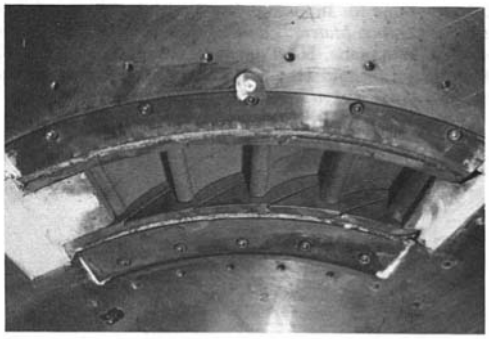

Fig. 11 Hybrid ceramic stator vanes after the cascade test using combustion gas at 1300°C and 1.5 MPa

Figure 10 shows the correlations between combustion gas temperature (mean), and the test results, including cooling air temperature, core temperature at a ratio of 0.29 percent cooling air to total air flow rate (corresponding to about 1/20th the amount for conventional air-cooled first-stage metal vanes) when the combustion gas pressure is held constant at 1.5 MPa, and ceramic shell temperature. As combustion gas temperature increases, the shell temperature increases linearly. However, the core temperature remains almost constant at approximately 450°C, even when the combustion gas is 1300°C, due to the good heat cutoff and cooling effects obtained. The core temperature is estimated to be 650°C when the cooling air is 400°C (designed value), and this level is acceptable in terms of the heat resistance of metal materials.

According to an EPRI report (1986), employment of ceramic in first-stage stator vanes has only little benefit. However, these findings show that the cooling air required for this new hybrid ceramic stator vane is drastically reduced, indicating that this material is very effective for enhancing the thermal efficiency of gas turbine engines. It also offers the prospects of gas turbine operation at even higher gas temperatures in the future.

Reliability of Ceramic Components. Figure 11 is a photograph of the stator vanes after the fuel cutoff test. All the ceramic parts were confirmed to be in sound condition after the test by fluorescent penetrant inspection.

The thermal stress analysis results of the ceramic parts under the cascade test conditions were different from those under design gas turbine conditions, as shown in Figs. 9 and 10, due to differences in test conditions. The calculation

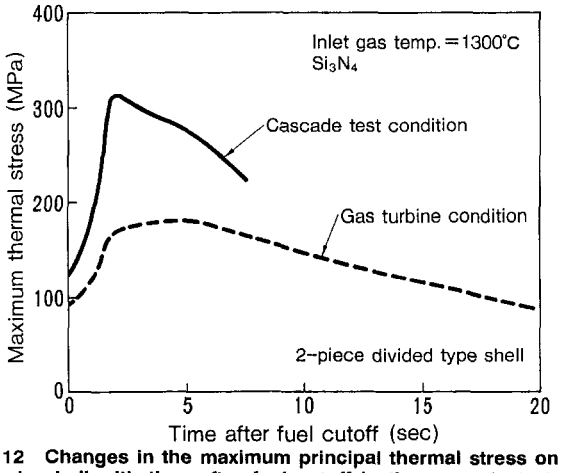

Fig. 12 Changes in the maximum principal thermal stress on the ceramic shell with time after fuel cutoff in the cascade test and under gas turbine conditions using a two-piece divided type shell made of sintered Si_3N_4

values of the maximum principal thermal stress on the ceramic shell (two-piece divided type, made of Si_3N_4) with time after fuel cutoff are shown in Fig. 12. The results shown in Fig. 5 for the gas turbine conditions are also presented here for reference purposes. The peak stress under the cascade test conditions is about 1.7 times higher than that under the gas turbine conditions. Therefore, the cascade fuel cutoff test is considered to be a 170 percent overload test of the ceramic shell.

In order to increase the strength reliability required for the hybrid ceramic stator vane, we have undertaken to decrease stresses applied to ceramic parts. First, as described above, we used a hybrid structure so as to decrease external force applied to the ceramic parts. We also employed a blunt head and specified the minimum thickness for the stator vane to make the manufacturing of ceramic stator vane easy. Next, in order to decrease thermal shock stress, we adopted an airfoil configuration and a design that were optimum for the stator vane, i.e., uniform in thickness and two-piece divided shell. We then selected the most appropriate ceramic materials to meet these requirements. Finally, in order to evaluate thermal shock resistance, we calculated the maximum transient thermal stress under the fuel cutoff test condition by thermal stress analysis; we compared the results to bending strength, and obtained the results mentioned above. Since the evaluation results match the test results, the appropriateness of the evaluation was proved. Although its accuracy is not confirmed yet, because the ceramic parts were not tested here to the point of fracture, this evaluation method is reported to be applicable to the evaluation of fracture strength of SiC test pieces for a thermal shock test conducted in combustion gas (Miyata et al., 1989).

Incidentally, the fuel cutoff condition during gas turbine operating life is considered to occur only a few times. On the other hand, usual gas turbine operation is made at a rated steady-state condition. Therefore, the steady-state thermal stress is compared with the static fatigue strength of Si_3N_4, used for the material of the prototype ceramic stator vane. Using the static fatigue strength value at 1300°C and thermal stress on the ceramic shell at steady state, the margin of safety was calculated to be approximately 4.4. This value is higher than the 3.4 obtained for the fuel cutoff thermal stress.

In the thermal load cascade test, considering the temperature distribution of the combustion gas, the vanes at the center of the cascade were exposed to the highest-temperature gases, 1460°C, at a pressure of 1.5 MPa. The pressure-side surface of the ceramic shell became slightly rough after

the cascade test. Examining the cross section of the ceramic shell through a SEM microscope, an oxide layer on the surface and a thermally affected layer just beneath the oxide layer were observed. However, they were very thin—about 10μm. Long-term oxidation behaviors of ceramic materials in combustion gas are a problem to be investigated in the future.

The strength reliability and imperviousness to environmental degradation (at least for short periods) of the hybrid ceramic stator vane made of Si_3N_4 was thus demonstrated.

Conclusions

The strength reliability and cooling characteristics of a hybrid ceramic stator vane with a ceramic/metal hybrid structure were investigated and the following results were obtained:

1 Based on an initial approximate evaluation of the thermal stress and strength reliability of a two-piece divided type ceramic shell made of sintered Si_3N_4, a prototype first-stage hybrid ceramic stator vane was developed for 1300°C class, 20-MW gas turbines.

2 Thermal load cascade testing using actual combustion gas conditions (mean temperature of 1300°C and pressure of 1.5 MPa) showed that the ceramic parts held up well under those conditions, thus demonstrating strength reliability and imperviousness to environmental degradation, at least for short periods. In addition, the prospect of substantially reducing the amount of cooling air required to about 1/20th that needed by conventional air-cooled metal stator vanes was shown.

References

Abe, T., Hisamatsu, T., Miyata, H., Iijima, S., and Nakakado, K., 1989, "R & D of Ceramic Stator Vane for High-Temperature Gas Turbine (II, Experimental Study on Heat Resistance and Cooling Characteristics)," *Proc. 17th Gas Turbine Congress*, GTSJ, p. 39 [in Japanese].

EPRI report, 1986, "Ceramic for Electric Power-Generating Systems," EPRI AP-4380, final report.

Krüger, W., and Hüther, W., 1989, "Metal Ceramic Guide Vanes: New Design Concept," ASME Paper No. 89-GT-334.

Miyata, H., Iijima, S., Ohshima, R., Abe, T., Hisamatsu, T., and Hamamatsu, T., 1989, "Application Technology on Ceramics for Structural Components of High-Temperature Machines," *JSME Int. J. Series I*, Vol. 32, No. 4, p. 596.

Mori, N., Hisamatsu, T., Yuri, I., Miyata, H., Nakakado, K., and Machida, T., 1991, "Development of Ceramic Stator Vanes for Power Plant Gas Turbines," *Proc. 1991 Yokohama International Gas Turbine Congress*, Japan, p. I-143.

Nakakado, K., Machida, T., Miyata, H., Hisamatsu, T., Mori, N., and Yuri, I., 1990, "Development and Strength Reliability Evaluation of a Ceramic Stator Vane for Industrial Gas Turbines," *Proc. 4th International Symposium on Ceramic Materials and Components for Engines*, in press.

Ohkoshi, A., Watanabe, N., Tsuji, I., Tsukagoshi, K., and Kawai, H., 1987, "Manufacturing and Hot Rig Testing of Ceramic Vanes for Gas Turbines," *Proc. 1987 Tokyo International Gas Turbine Congress*, GTSJ, p. I-169.

K. Stachel
Technical University of Vienna,
Vienna, Austria

H. U. Frutschi
Asea Brown Boveri,
Baden, Switzerland

H. Haselbacher
Technical University of Vienna,
Vienna, Austria

Thermodynamic Heating With Various Types of Cogeneration Plants and Heat Pumps

The thermodynamic heating method combines cogeneration power plants and heat pumps in order to maximize the heating energy that can be derived from a given amount of fuel. In doing this, unnecessary waste of primary energy and environmental damage can be prevented. In this paper, four cogeneration systems—combined cycle plants, steam and gas turbine power plants, and gas engines—and heat pump systems are investigated and compared with respect to fuel utilization for realistic site conditions. It is shown that the combined cycle cogeneration power plant is superior to the other three types of power plant.

Introduction: The Principle of Thermodynamic Heating

Conventional heating methods waste most of the exergy contained in the fuel. An improvement in this respect is the combined production or cogeneration, as it is most frequently called, of heat and power because a portion of the fuel is transformed into mechanical or electrical energy.

If this mechanical or electrical energy is used to drive heat pumps, ambient heat can be upgraded so that it can be used for space heating. The heating energy derived from a given amount of fuel can then be maximized. As a matter of fact, the quantity of heating energy can be several times the fuel energy input. Current conventional heating methods therefore constitute an avoidable waste of energy and, with respect to the production of carbon dioxide, unnecessarily high environmental damage.

The combination of cogeneration plants and heat pumps has been called the thermodynamic heating method and the amount of heating energy the thermodynamic heating potential of fossil fuel (Frutschi, 1990).

The quantitative result depends on the electrical efficiency η and the fuel utilization ν of the cogeneration plant as well as on the performance coefficient ϵ_H of the heat pump. These parameters are functions of the type and quality of the thermodynamic process, the temperature of the heating water, and the temperature of the ambient heat source.

A typical Sankey diagram (energy flow diagram) illustrating the thermodynamic heating principle is shown in Fig. 1. As an overview, a schematic showing the various cogeneration power plants that will be compared is displayed in Fig. 2. Although all four will be considered here, the emphasis will be on the combined cycle power plant. It is well known that steam and gas turbine as well as combined cycle power plants are usually of relatively large capacity, while gas engine cogeneration plants are relatively small and used therefore in decentralized applications; see Fig. 3. This means that, in general, these two classes of power plant would not be alternatives in a specific project. Nevertheless, all power plants indicated in Fig. 2 will be treated further below.

2 Representative Design Point Performance Data

Table 1 contains representative design point performance data of the cogeneration plants used in conjunction with heat pumps. These systems will be compared with conventional boilers, so boilers are included here as well. In real cases, the

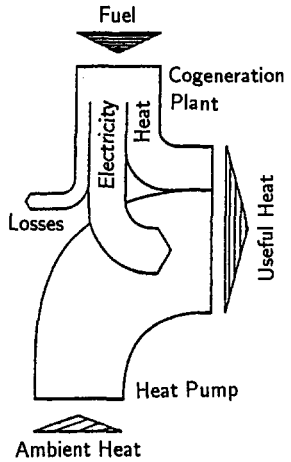

Fig. 1 Principle of thermodynamic heating, energy flow diagram

Contributed by the International Gas Turbine Institute and presented at the International Cogen-turbo Symposium and Exhibition, Bournemouth, United Kingdom, September 21–23, 1993. Manuscript received at ASME Headquarters June 1993. Associate Technical Editor: H. Lukas.

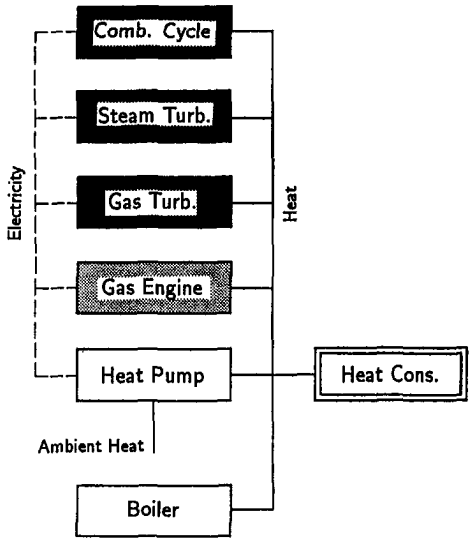

Fig. 2 Thermodynamic heating, overview of systems participating

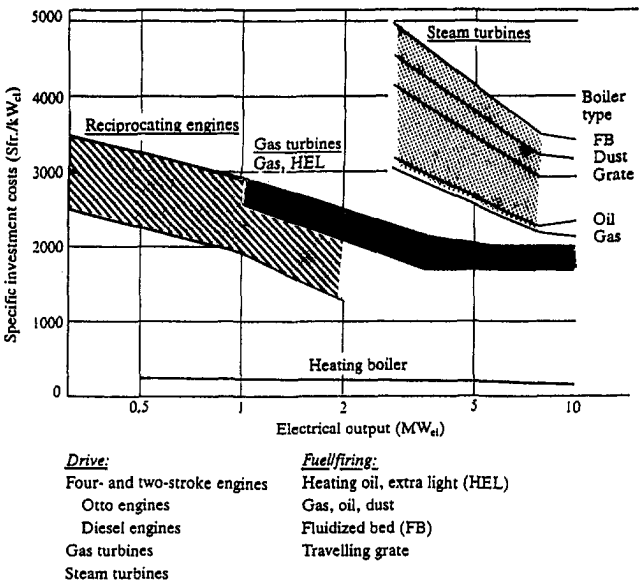

Fig. 3 Range of application and specific investment costs (1987) of small cogeneration plants (Hess, 1990)

performance data depend on various design criteria and site-specific requirements, which are not treated here in detail. Nevertheless, it is seen that the combined cycle plant performs very well as a cogeneration system, and it can be expected to be superior also when working together with heat pumps. Therefore, the combined cycle plant selected for the calculations below is elaborated on in the following section.

Table 1 Design point of cogeneration plants

System	Electr. Eff. η [%]	Fuel util. ν [%]
Combined cycle p. p.	46	88
Steam turbine p. p.	26	85
Gas turbine p. p.	35	88
Gas engine	32	86
Boiler	–	90

Table 2 Design point of gas turbine

Item	Unit	Value
Compressor inlet temperature	°C	15
Compressor inlet pressure	bar	1.013
Relative humidity	–	0.60
Compressor pressure ratio	–	13.9
Turbine outlet temperature	°C	516
Turbine oulet mass flow	kg/s	500
Output at generator terminals	MW	147.4
Thermal efficiency at generator terminal	%	34.9

3 Combined Cycle Plant

3.1 Gas Turbine. A modern, relatively large 50 cycle gas turbine was chosen. Its output is in the 150 MW range as can be seen from Table 2.

In the case of the combined cycle plant, the additional exhaust gas pressure loss in the steam generator needs to be taken into account. Figures 4 and 5 show the calculated values of the important parameters, including those for the layout of the steam cycle, as a function of ambient temperature. These calculations were based on the simplifying assumption that the gas side pressure drop in the steam generator is constant.

3.2 Steam Cycle, Condensing Operation. A complete cycle diagram of the pure condensing mode is depicted in Fig. 6. It is seen that a dual pressure steam cycle was selected. Since (sulfur-free) natural gas was chosen as fuel, a low-pressure economizer could be installed, taking care, however, that the exhaust gas temperature does not drop below the water dew point.

Design Point: The layout of the steam cycle was made for an ambient temperature of 10°C. The selection of the steam pressures of the high and low-pressure loops is the result of a parametric analysis. The high pressure was chosen relatively

Nomenclature

E = electrical energy
H = heat
K = ratio of coefficients of performance
$\dot{m}$ = mass flow
P = power
p = pressure
Q = fuel energy input
T = temperature
U = ambient heat
ϵ = coefficient of performance
η = thermal efficiency
ν = fuel utilization rate
Π = pressure ratio

Subscripts

a = ambient
A = ambient heat source
c = Carnot
C = combined cycle plant
Cd = condensation
D = delivery
E = exhaust gas
GT = gas turbine
H = heat pump
m = mean value
R = return
S = steam process
T = turbine
0 = design point
$2T$ = turbine outlet

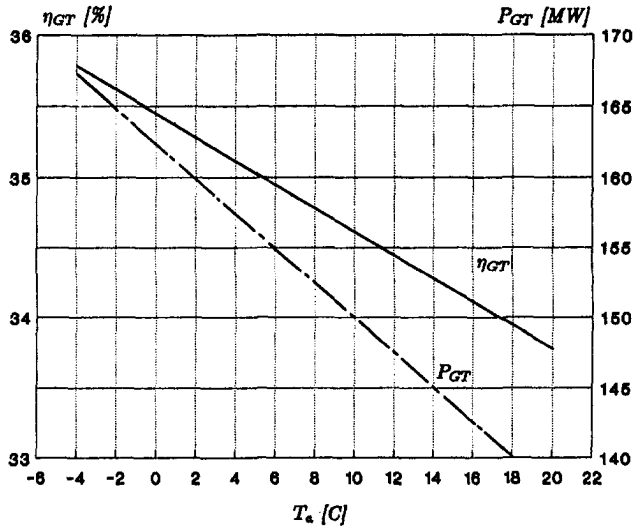

Fig. 4 Gas turbine output and efficiency versus ambient temperature

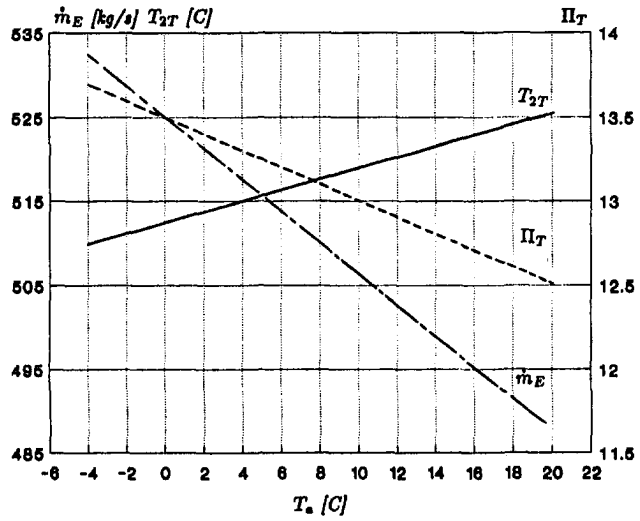

Fig. 5 Turbine operating parameters

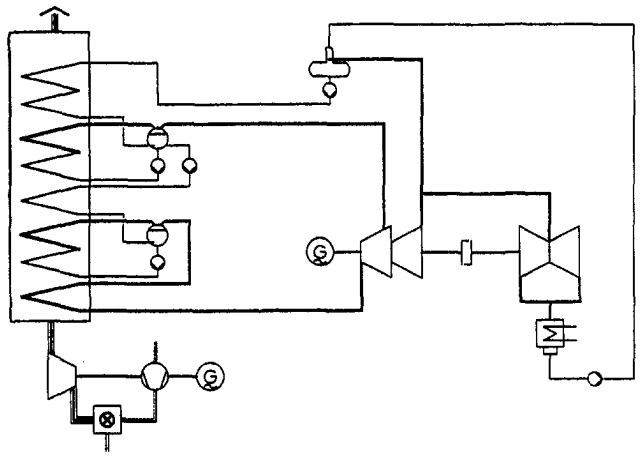

Fig. 6 Diagram of the combined cycle plant for the condensing mode

high and the low pressure relatively low in order to produce high-quality high-pressure steam and to make maximum use of the exhaust gas energy in the low-pressure steam generator. The high pressure is limited by the resulting end wetness

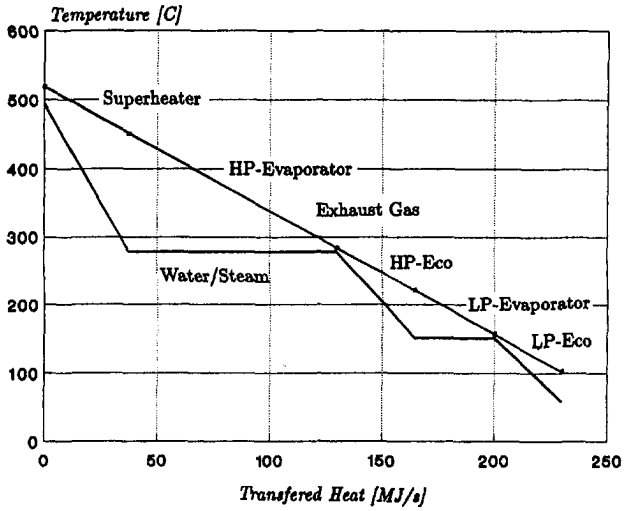

Fig. 7 Diagram of temperature versus transferred heat of the combined cycle steam generator

Table 3 Steam cycle

Item	Unit	Value
Feed water temperature	°C	60
Feed water pressure	bar	0.20
HP pressure	bar	63
Superheater temperature	°C	495
LP pressure	bar	5
End wetness	–	0.867
Output at generator terminals	MW	75.1
Thermal efficiency at generator terminal	%	32.5

and the low pressure by the large volumetric flow rates. A low-pressure superheater was not used because the thermodynamic benefits are rather modest. On the other hand, the end wetness and the risk of blade erosion would be reduced with the superheater. The feedwater is preheated in the feedwater tank by steam extracted from the low-pressure turbine to prevent the exhaust gas temperature from falling below the dew point. The condenser is supplied with cooling water from a wet cooling tower. A selection of data is given in Table 3. The relationship between thermal power transferred and temperatures is shown in Fig. 7.

Off Design: The results of the off-design calculations are summarized in Fig. 8. It is observed that the thermal efficiency of the combined cycle plant η_c is almost constant while the output P_{GT} increases sharply as the ambient temperature T_a is reduced.

3.3 Combined Cycle Cogeneration. The cogeneration plant derived from the combined-cycle condensing power plant discussed above can be seen in Fig. 9. In addition to condensing operation as before, the system allows back-pressure and mixed operation (by setting crossover valve 4). In the back-pressure mode, clutch 7 is disengaged and the low-pressure turbine shut down, thus avoiding the consumption of steam for cooling this turbine and reducing the mechanical losses. The installation of the crossover valve is justified if the power plant is run in back-pressure mode for longer periods of time. The water is heated in heating con-

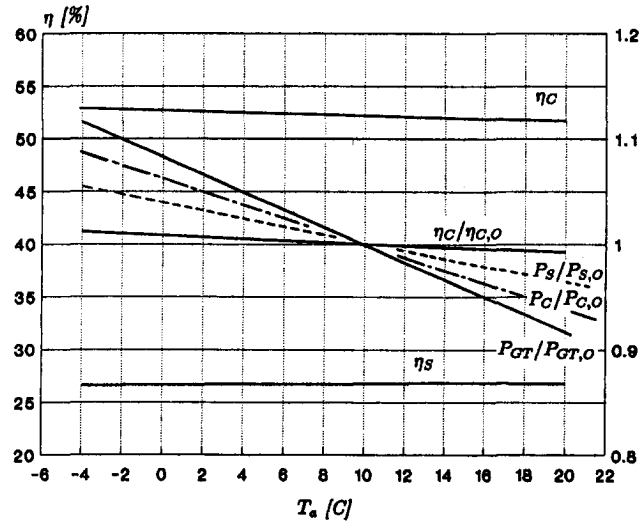

Fig. 8 Combined cycle plant output and efficiencies versus ambient temperature

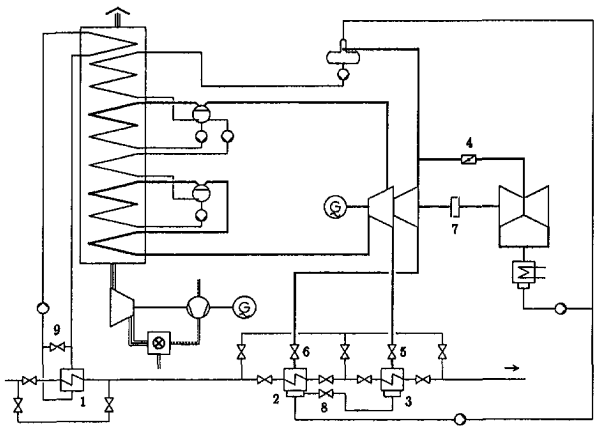

Fig. 9 Diagram of the combined cycle cogeneration plant

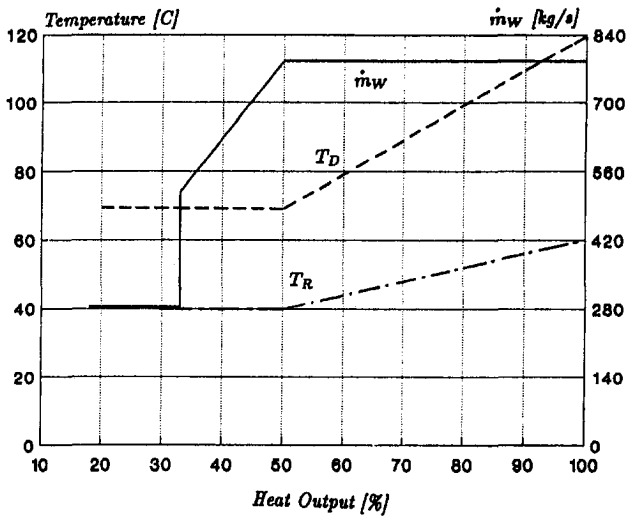

Fig. 10 District heating parameters

densers 2 and 3. The heating water mass flow ($\dot{m}_W$) and the delivery and return flow temperatures (T_D, T_R) versus heat output are shown in Fig. 10. The pressure and temperature in the feedwater tank are determined by the condensing steam properties in heater 2, which, in turn, are influenced by the position of the crossover valve 4. During back-pressure

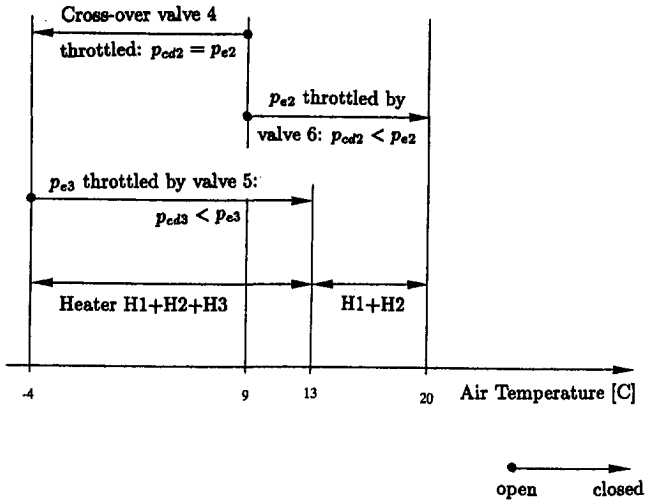

Fig. 11 Operating ranges of the heaters and valves

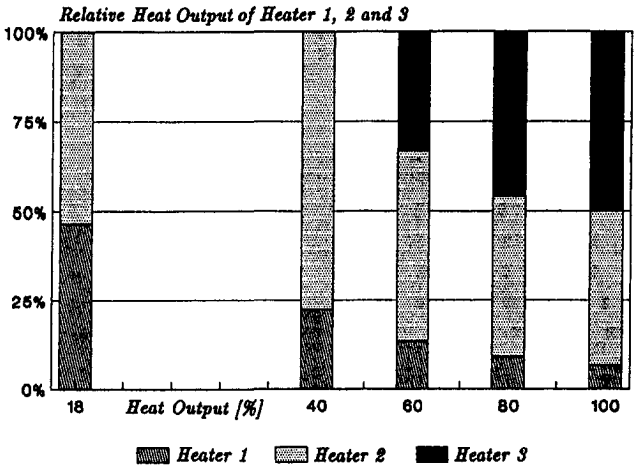

Fig. 12 Relative output of Heaters 1, 2, and 3 versus total heat output

operation (crossover valve 4 completely closed), the exhaust gas temperature would increase and the fuel utilization would drop. Such a situation would exist in particular during high heat demand. To avoid it, an additional heating loop with heater 1 is installed. All three heaters have bypass and isolation valves for control and maintenance purposes. Figure 11 indicates how valves 4, 5, and 6 are set to control the heat as a function of the ambient temperature T_a. This means that, at low heat demand (e.g., 40 percent), heater 3 is shut down (bypassed). At high heat demand (say 80 percent), the loads on heaters 2 and 3 are approximately equal; see Fig. 12.

4 Heat Pumps

Since electrical (mechanical) energy shall be used to raise the temperature of ambient heat to a level useful for space heating, this paper is limited to compression heat pumps. The coefficient of performance expresses the ratio of heat delivered to work put in:

$$\epsilon_H = \frac{H}{E} \tag{1}$$

The maximum coefficient of performance would result from the ideal Carnot process. With T and T_a as the absolute temperatures of the heat sink and source, respectively, the Carnot coefficient of performance is

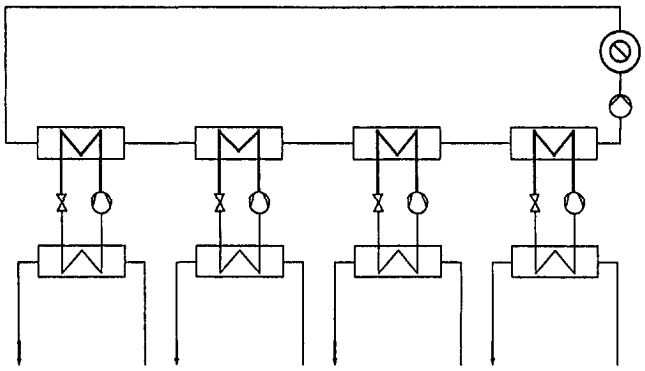

Fig. 13 Diagram of four heat pumps arranged in parallel

$$\epsilon_c = \frac{T}{T - T_a} = \frac{1}{\eta_c} \tag{2}$$

The quality of the heat pump is expressed by

$$K = \frac{\epsilon_H}{\epsilon_c} \tag{3}$$

If combustion engines are used to drive the heat pumps, the reject heat of the engines is usually also recovered.

The same process media are used as in refrigeration equipment; their properties are therefore well known. Criteria for their selection are discussed in Sulzer (1983). Issues of special concern are toxicity, environmental, and climatic effects (Favrat and Grivel, 1991). Ammonia was considered in the present calculations. The main reasons are:

- high coefficient of performance
- high volumetric heating coefficient resulting in low mass flow rates and small compressors
- considered as environmentally safe (ozone depletion, greenhouse effect)

A recent example of such an application is the heating system of the Swiss Federal Institute of Technology at Lausanne (Tastavi et al., 1991).

As heat sources, various types of water can be used such as

- lakes and oceans
- rivers
- ground water
- water from sewage treatment plants

The advantages of the last source are its availability and proximity to the heat consumers. Its high corrosion potential, however, is a disadvantage.

Air is also a potential heat source. Although its availability is practically unlimited, it is not very desirable because of its usually low temperature level when the heat demand is high. Therefore, monovalent heating would not be possible with air.

The part-load behavior of a heat pump heating system depends on the control behavior of the prime mover, the compressor, and the auxiliaries.

A distinction needs to be made between large heat pumps, which are used in central station type installations, and small heat pumps for individual buildings or smaller housing developments. Larger heat pumps can be arranged in several stages. See for example Fig. 13, which shows four heat pumps in parallel heating the water in steps from the return flow to the delivery flow temperature. Only the last heat pump heats the water to the delivery flow temperature. The other ones work according to their respective condensing temperature T_{Cd} with higher coefficients of performance ϵ_H. The coefficient of performance of such a layout $\epsilon_{H,m}$ is therefore better than that of a single heat pump ϵ_H for the same

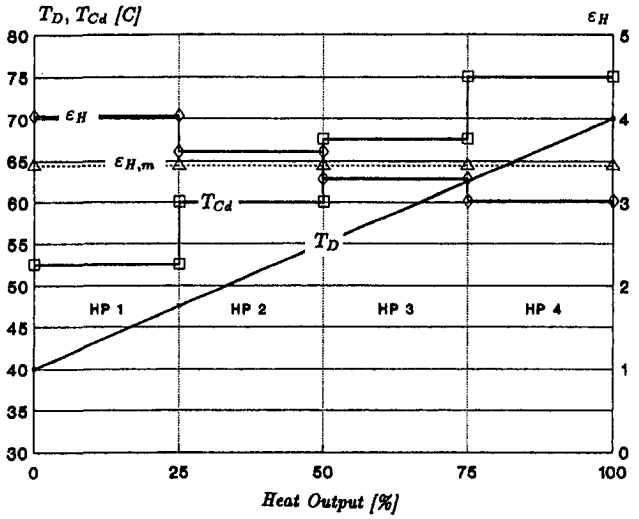

Fig. 14 Operating parameters of the individual heat pumps

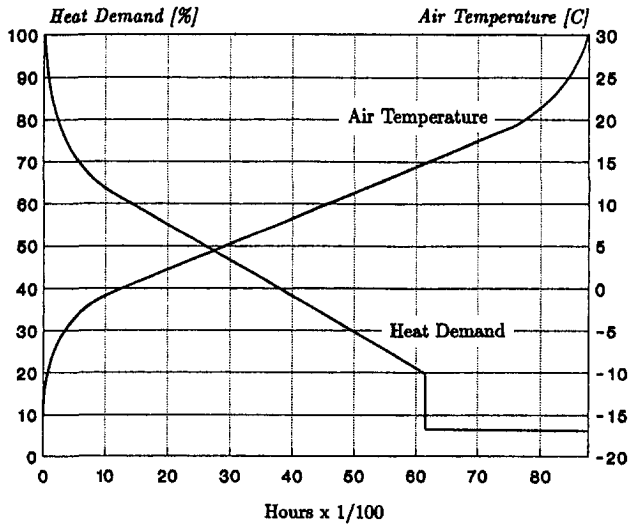

Fig. 15 Duration curves of the heat demand and air temperature for Vienna

temperature rise. Figure 14 shows the delivery flow temperature T_D, the condensing temperature T_{Cd}, and the coefficients of performance for four identical heat pumps arranged in parallel. At reduced heat demand, units are shut down beginning from the hot end, which reduces the delivery flow temperature and improves the coefficient of performance $\epsilon_{H,m}$. Also, such an arrangement is inherently more reliable than a single-stage heat pump heating system. No additional unit needs to be installed as a reserve, which leads to a cost advantage of the multi-unit plant.

Small heat pumps should be used decentralized in large public buildings and small housing developments. Such heat pumps are frequently driven by combustion engines, making speed control of the compressor possible. The lower quality expressed by K is usually compensated by the lower flow temperature and the lower distribution loss.

5 Main Assumptions

The ambient air temperature and the heat demand (space heating plus hot water) of the community to be served by the above-mentioned plants are represented by the two duration curves in Fig. 15. They correspond to conditions existing in Vienna.

Table 4 Cogeneration / heat pump characteristic

CG/HP System	CC	ST	GT	GE
Number of units	1	1	2	–
Max. heating output at max. load (%)	60	60	100	60
Difference supplied by peaking boiler	+	+	–	+

Table 5 Energy losses in percent

CP/HP System	CC		ST	GT	GE
HP centralization	c	dc	c	c	dc
Electricity	10	10	10	10	–
Heat:					
CG plant	10	10	10	10	–
HP	2	0	2	2	0
Peaking boiler	5	5	5	–	0
Peaking boiler efficiency	90	90	90	–	90

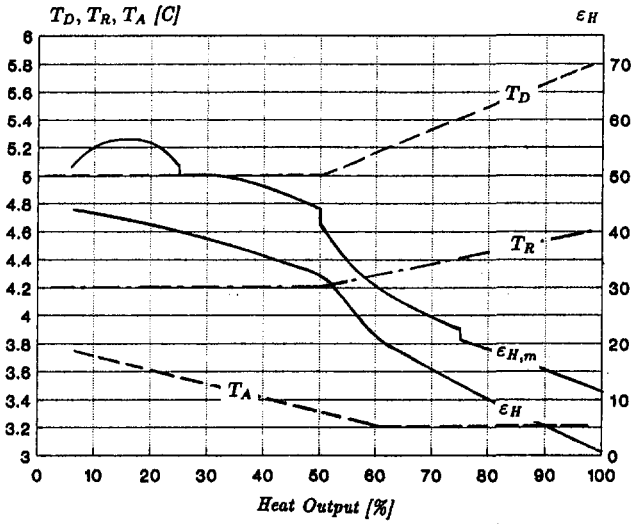

Fig. 16 Operating parameters for four parallel heat pumps

Tables 4 and 5 summarize important features of the cogeneration/heat pump systems that have been evaluated. Their plant diagrams are shown below.

6 Thermodynamic Heating Analysis

In this section, the cogeneration/heat pump systems will be discussed in more detail.

As a meaningful measure of their performance the annual mean value of the fuel utilization ν_m, weighted with the heating energy produced, was calculated. This requires first the determination of the fuel utilization as a function of the heat output relative to the maximum heat output. If, in the case of the combined cycle, steam, and gas turbine power plants, there was an excess of electricity produced, it was assumed to be used elsewhere by other consumers. If there was a shortage of heating power produced by the cogeneration/heat pump systems, the peaking boilers were put in operation or, in the case of the gas turbine power plant, the auxiliary firing of the exhaust gas boiler was started. See also Tables 4 and 5.

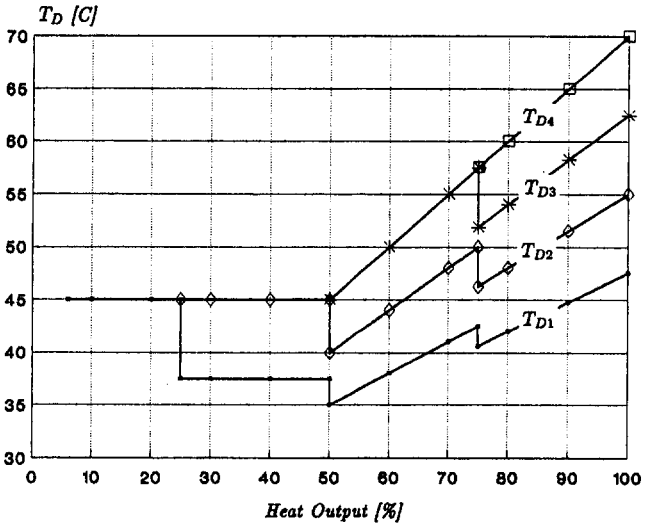

Fig. 17 Delivery flow temperatures of the individual heat pumps

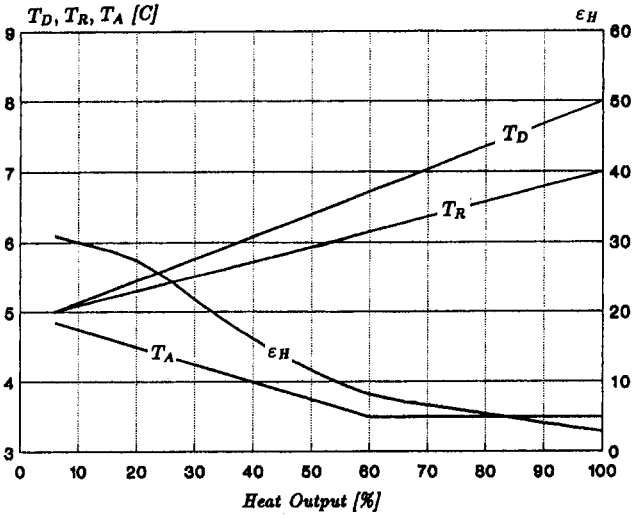

Fig. 18 Operating parameters for small heat pumps

6.1 Combined Cycle Plant. In case of the large heat pump heating system, the complete plant schematic diagram consists of the combination of the diagrams shown in Figs. 9 and 13, except for the peaking boiler, which is not shown.

The heat pump heating system was assumed to feed into a separate low-temperature district heating grid. Its relevant temperatures and the coefficients of performance $\epsilon_{H,m}$ are shown in Fig. 16. The delivery flow temperatures of the individual heat pumps can be read from Fig. 17.

The small heat pumps are driven by electric motors. Their corresponding temperatures and coefficients of performance are found in Fig. 18. It reflects installation directly at the heat consumer.

6.2 Steam Turbine Plant. The Hamburg Hafen plant was used as reference design (Fig. 19). The heat pump heating system is identical with that shown in Fig. 13.

6.3 Gas Turbine Plant. The plant consists of two identical gas turbines (Fig. 20). The reference design corresponds with the gas turbine discussed in subsection 3.1.

For part-load operation, two control methods can be employed: One is the widely practiced turbine inlet temperature

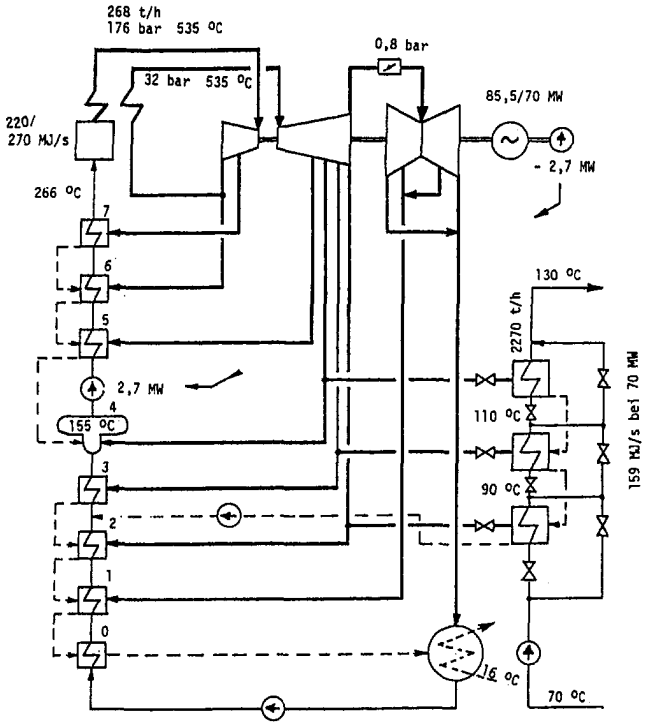

Fig. 19 Diagram of the Hamburg Hafen cogeneration plant

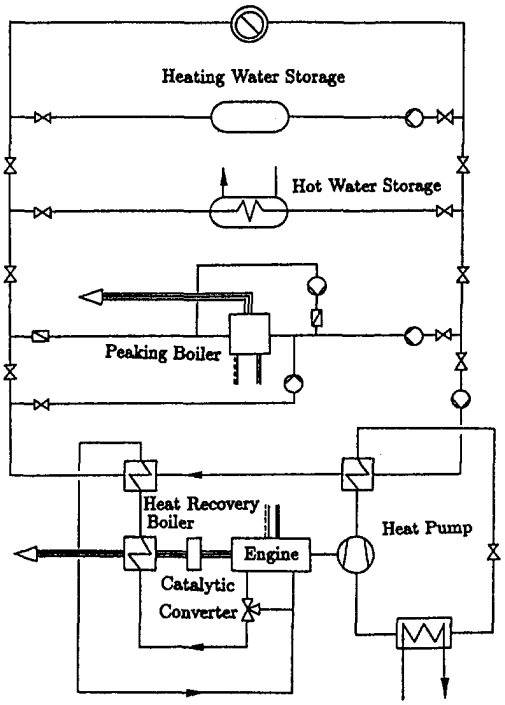

Fig. 21 Plant diagram of the gas engine and directly driven heat pump

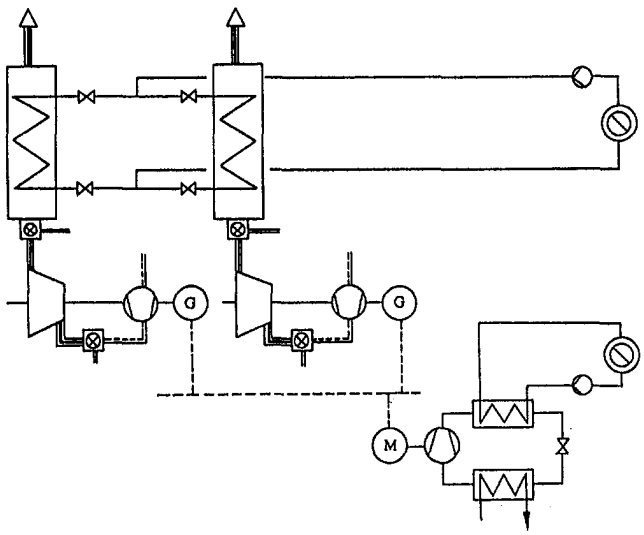

Fig. 20 Diagram of the gas turbine cogeneration plant

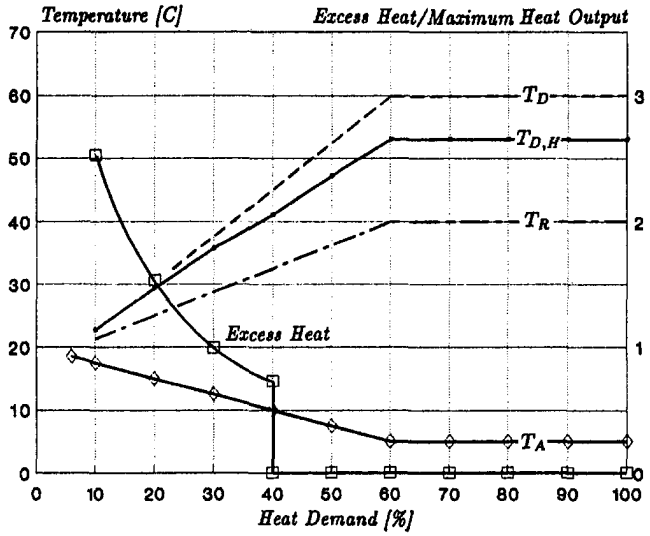

Fig. 22 Operating parameters of the gas engine and directly driven heat pump plant

control, the other the compressor back flow control (Frutschi, 1982). As this terminology implies, a portion of the compressed air is returned to the compressor inlet. The consequences are an increase of the compressor inlet temperature and, if the turbine inlet temperature is left constant, also an increase of the turbine outlet temperature. The limits of this control method are set by the allowable maximum material temperatures.

Here, the best overall result is obtained if combined temperature and compressor back flow control is applied at heat outputs above 20 percent. Below that, temperature control alone is used.

6.4 Gas Engine and Directly Driven Heat Pump. A schematic plant diagram is shown in Fig. 21.

It has been mentioned in section 4 that direct coupling of engine and heat pump permits speed control. This is practiced down to 40 percent heat output. Below 40 percent heat output, phased operation (on/off) is used. To improve the flexibility of the plant, storage tanks are employed, which are charged with excess heat. See also Fig. 22.

The operating data of the gas engine were taken from Jensch and Piller (1979).

7 Results

The main results of the calculations are summarized in Fig. 23. It contains the annual mean fuel utilization ν_m and the fuel utilization ν at maximum heating power. The combined cycle data are for the central heat pump heating system. (The values for the decentralized heat pumps are almost the same.)

It is noticed that, in terms of ν_m, the combined cycle plant

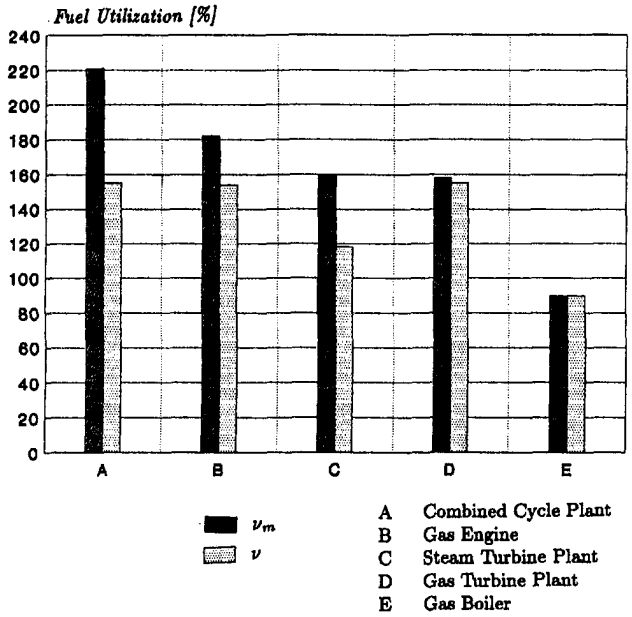

Fig. 23 Fuel utilization for the various types of heating system

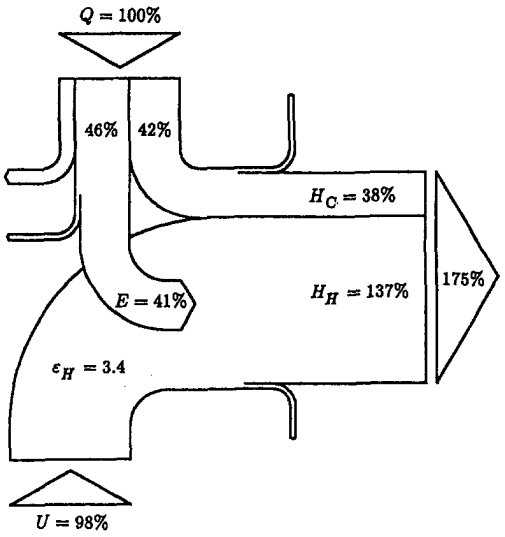

Fig. 24 Energy flow diagram for maximum heat output

is considerably better than the other plants. The steam and gas turbine plants are practically the same.

The differences between ν and ν_m are smaller for the gas turbine and the gas engine than for the combined cycle and the steam turbine plants. The explanation is that with heat extraction the thermal efficiencies of the combined cycle and the steam turbine plants go down, while for the other two power plants they remain constant.

For the combined cycle plant Figs. 24 and 25 have been

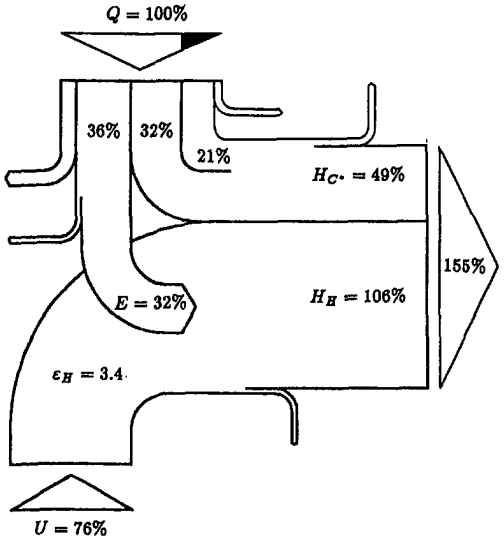

Fig. 25 Energy flow diagram for maximum heat output including the peaking boiler

included, showing energy flow diagrams at maximum heat output. The first one is for the combined cycle plant (with the heat pump system incorporated), while the second one includes also the peaking boiler, which is needed to satisfy the heat demand. Obviously, this ν value must be smaller than that for the combined cycle plant alone.

Conclusions

The detailed analysis and comparison of thermodynamic heating systems under realistic operating conditions have shown that, in terms of the mean annual fuel utilization ν_m, the combined cycle cogeneration power plant is significantly better than the other three cogeneration power plants. Since also the specific installation costs of combined cycle cogeneration power plants are relatively low (Frutschi, 1990), they should be very well suited for thermodynamic heating.

References

Favrat, D., and Grivel, T., 1991, "District Heating and Cooling With Heat Pumps and Refrigerant Networks," ICODISH 1991, Lausanne, Switzerland.

Frutschi, H. U., 1982, "Combined Power and Heat Production With Gas Turbines and Their Control Methods," ASME Paper No. 82-GT-111.

Frutschi, H. U., 1990, "Erhöhtes Heizpotential von Gas und Öl beim Einsatz Thermodynamischer Heizmethoden," *Bulletin SEV/VSE*, Vol. 81, Switzerland.

Hess, H., 1990, *Sulzer Technical Review*, Vol. 72, No. 2, pp. 28–31.

Jensch, K., and Piller, W., 1970, "Die Blockheizkraftwerks-technik und ihr Beitrag zur Rationellen Energienutzung," *BWK*, Vol. 31, No. 11, pp. 424–429.

Sulzer Escher Wyss, 1983, "Wärmepumpeneinsatz in Industrie und Gewerbe," Lindau, Germany.

Tastavi, A., Schmid, J., and Vögeli, A., 1991, "The Heating Network of EPFL With Cogeneration and Heat Pump Facilities," ICODISH 1991, Lausanne, Switzerland.

Sound Power and Pressure Level Measurements in the Inlet and Outlet of an HRSG Duct

D. E. Jungbauer

J. F. Unruh

Southwest Research Institute,
San Antonio, TX 78228

S. Rose
Enron Power Corp.,
Houston, TX 77002

P. J. Pantermuehl
Southwest Research Institute,
San Antonio, TX 78228

The ever-increasing size of cogeneration facilities has mandated the need for noise abatement in the design stage. Many noise projection models are available to the industry for predicting noise levels in and adjacent to new installations. However, the models all require accurate source noise information if valid noise predictions are to be expected. As a consequence of designing one of the world's largest cogeneration installations involving eight Model W-701 turbine units and their Heat Recovery Steam Generators (HRSGs), it became apparent that the attention between the exhaust of the turbine and the outlet of the HRSGs was not well known. Not having this information posed potentially expensive noise abatement modifications during the design and construction phases. In order to verify the adequacy of scaling studies from a W-501 turbine and HRSG to the W-701 system, a comprehensive field test of an existing W-501 installation was conducted. This paper describes the design of an acoustic intensity and sound pressure probe to operate inside the high-temperature ductwork, the access engineering required, data acquisition, and final results concerning noise attenuation across the HRSG.

Introduction

While in the process of constructing the world's largest cogeneration plant in the northeast of England, concerns were raised about the noise levels that might be radiated to the local communities.

The facility was to consist of eight Model W-701 gas turbines exhausting into HRSG systems. Since these were to be the first W-701 gas turbines placed into service, no measured noise information was available. All exhaust noise data were predicted on scaling information obtained from the W-501 series of gas turbines. Similarly, the acoustic performance characteristics of both the W-501 and W-701 HRSGs were based upon theoretical calculations, and empirical modeling of existing W-501 systems.

Numerous predictive noise analyses had been conducted in order to determine the expected noise levels, adjacent to the new cogeneration facility. Based upon design and community annoyance criteria, the noise from the new facility could not exceed the existing background by more than 1 dBA. All calculations indicated that the combined noise levels from the plant could result in a level of 48 dBA, a 1 dBA violation of the 47 dBA criterion.

Reviews of predicted calculations, supplied by other parties, suggested that the 48 dBA level was a worst-case scenario. There were several contingencies that could actually reduce existent levels. For example:

- The gas turbine exhaust noise level used was the criterion level supplied by the turbine manufacturer, and was probably 3 dBA high, based on test data and analyses for the W-501 provided by the manufacturer and an independent consultant.
- Shell radiation predictions were made by the consultant, and did not consider an exterior shroud, which was planned for the transition duct.
- A barrier wall could be added to provide additional noise reduction if start-up tests dictated.
- Inlet silencers and barriers could also be added to reduce cooling tower inlet noise, if required.

Similarly, there were other uncertainties that could increase or reduce noise levels:

- Calculation accuracy (i.e., field propagation calculations) was about 2 or 3 dBA depending on ground effects, shielding, and environmental conditions.
- Attenuation loss provided by the untreated HRSG was predicted by a consultant to be about 22 kBA. There was no way independently to confirm the prediction techniques, short of full-scale testing of a W-501 unit at an existing installation.
- Other plant noise sources might influence total plant noise unless they were well treated (gas turbine enclosure, inlet noise, generators, etc.).

Therefore, based upon the results of previous analyses, the conclusion was reached that as far as HRSG acoustic performance was concerned, the most realistic approach for resolv-

Contributed by the International Gas Turbine Institute and presented at ASME Cogen Turbo Power '93, Bournemouth, United Kingdom, September 20–23, 1993. Manuscript received at ASME Headquarters June 1993. Associate Technical Editor: H. Lukas.

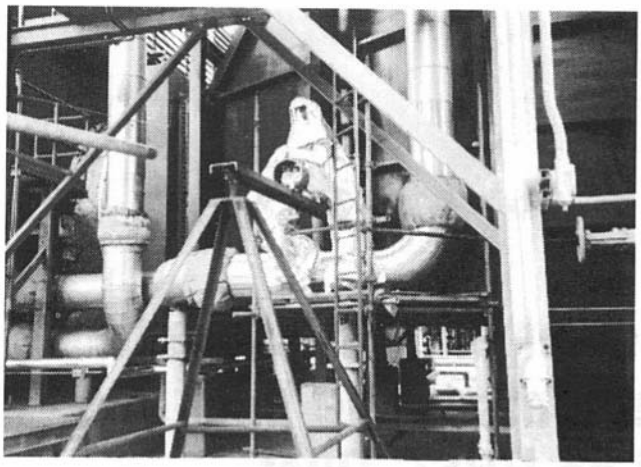

Fig. 1 Location of horizontal access port—transition duct

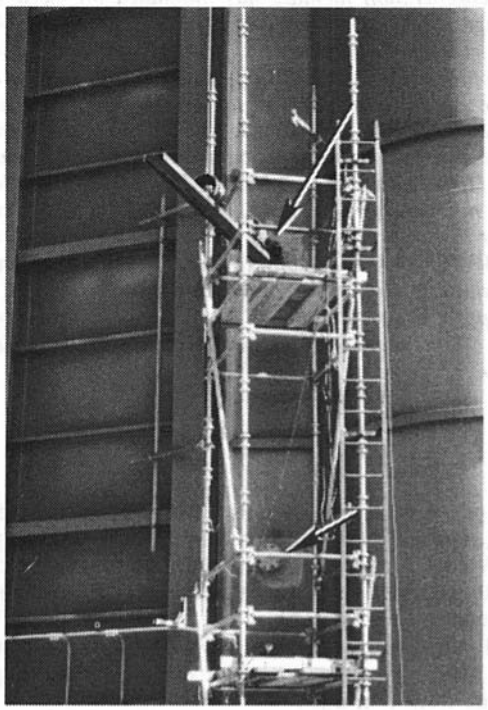

Fig. 2 Location of horizontal access ports—downstream of HRSG

ing actual HRSG acoustic performance would be field measurements.

Based upon the economic ramifications of additional noise reduction and the impact on community annoyance, it was decided to conduct a field test at an existing Westinghouse cogeneration facility to determine HRSG acoustic performance. The specific objectives were to:

1 Design an insertion probe for measurement of noise intensity and sound pressure levels that would function in an environment approaching 540°C.
2 Develop necessary calibration methods and software for quick and efficient data collection and analysis.
3 Assist in access engineering so that the probe could be inserted in the exhaust transition duct between the turbine and HRSG and in the outlet of the HRSG at the transition to the exhaust stack.
4 Obtain data at maximum, typical operating conditions at each of the test sections selected.
5 Reduce the data obtained and analyze results.

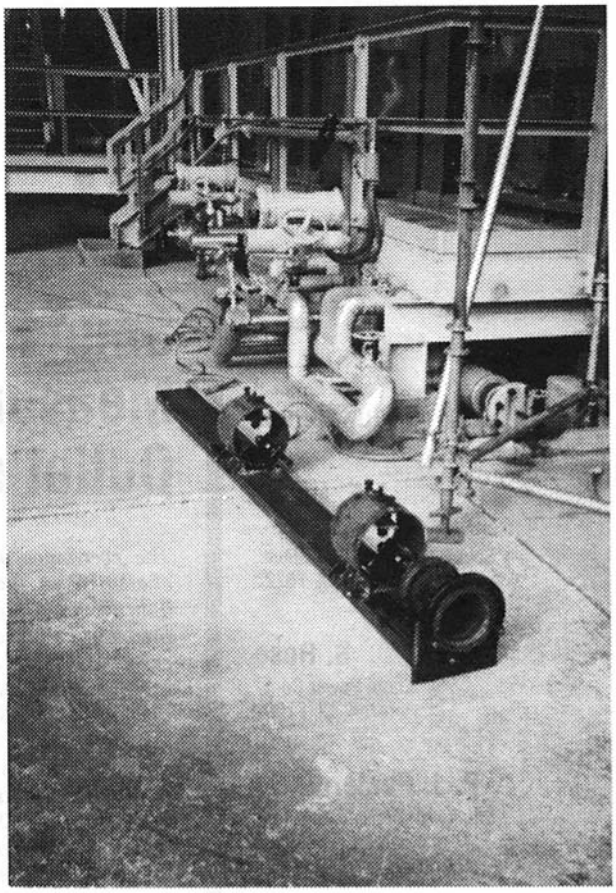

Fig. 3 Noise probe insertion fixture

6 Provide the user company with HRSG acoustic performance data either in sound pressure levels or sound power terms.

Results

Access Engineering. Preliminary access engineering and test planning were formulated by Enron and SwRI. A total of four access points was selected for insertion of the noise measurement probe. Two were located in the transition duct between the turbine and the HRSG; one was located vertically in the roof, and the other horizontally. The remaining two were located horizontally in the duct downstream of the HRSG in the pant-leg transition of the exhaust stack. Figure 1 presents a photograph of the transition duct between the turbine and HRSG. Similarly, Fig. 2 gives the locations of the two test points for horizontal traverses in the downstream section of the duct.

In order to facilitate alignment, insertion, and removal of the probe, the fixture shown in Fig. 3 was used. The fixture was bolted to the flange of the access port, and the three ball-bearing alignment assemblies in each of the two collars were adjusted to maintain probe alignment during insertion.

After the probe was positioned into the fixture and inserted 0.3–0.6 m into the duct, air and water flows were checked and adjusted. The probe was then inserted to the 1/4, 1/2, and 3/4 points of the duct width or height, and data recorded at these fixed positions.

Noise Measurement Probe Design and Calibration. The design of the noise measurement insertion probe was done concurrently with access engineering. The final design of the probe consisted of a pair of water-cooled PCB Model 10613 microphones installed in 316 S.S. head assembly as shown in

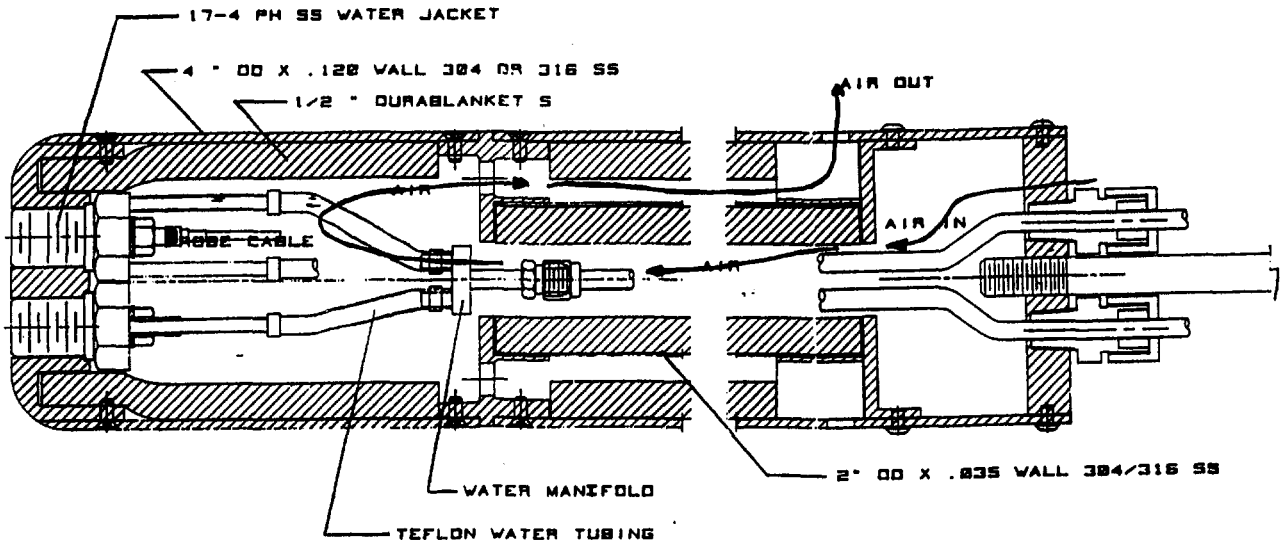

Fig. 4 Noise probe head assembly drawing

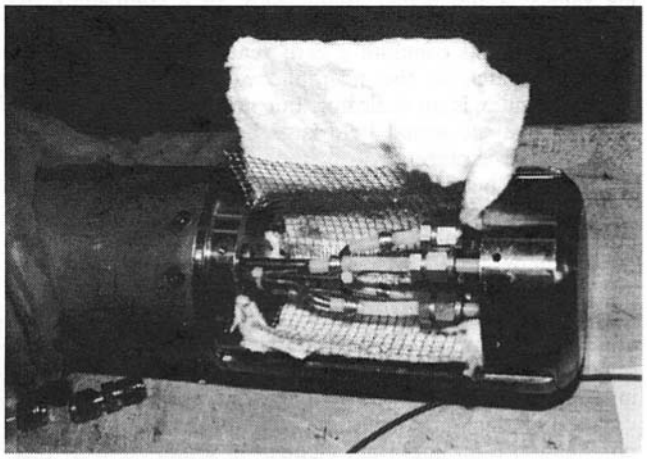

Fig. 5 Noise probe head assembly

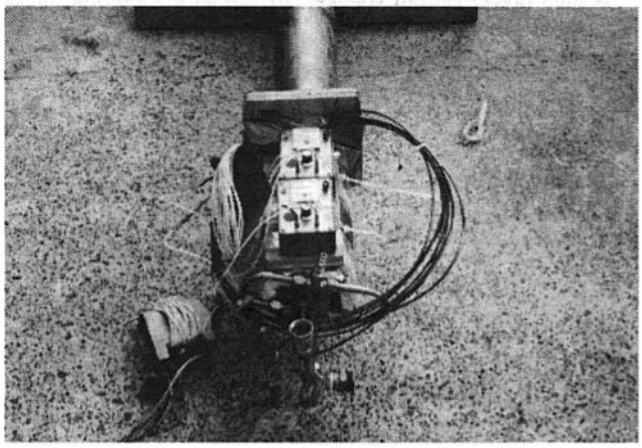

Fig. 7 Outboard end of noise probe

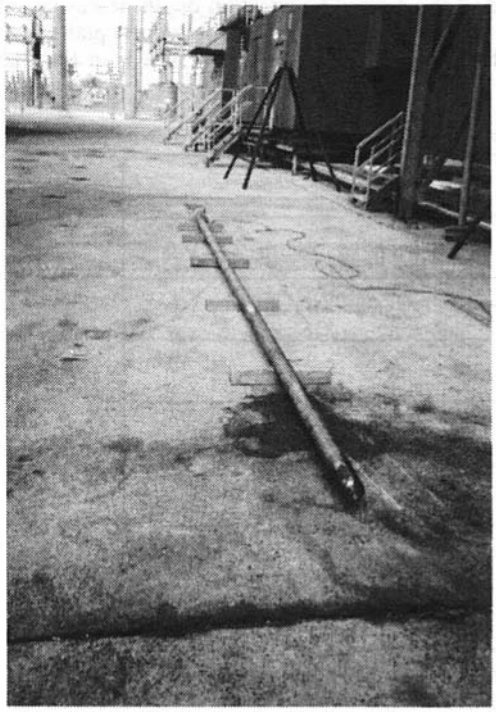

Fig. 6 Complete insertion noise probe assembly

Figs. 4 and 5. The head was lined with an inner annulus of Durablanket insulation having low volatility characteristics at high temperatures. Attached to the head was a 8.5 m section of 101 mm O.D., thin wall, AISI 301 stainless steel tubing. Figure 6 presents a photograph of the completed probe assembly lying on the ground adjacent to the field test unit.

The 8.5 m section was provided with a central core of 50.8 mm O.D. stainless steel tube, which housed the cooling water tubing and instrument electrical wiring. In addition, forced ambient air cooling was provided down the central core via tubing for additional thermal protection of the cooling water lines and instrumentation wiring. Return of the hot air was provided for by a path external to the central core. The outboard end of the field-ready probe is shown in Fig. 7, with cooling air and water inlet and return fittings, and microphone amplifiers. Thermocouples were installed to monitor microphone head temperatures.

The instrumentation package employed a pair of PCB 106B voltage-mode, vibration-compensated, sound pressure microphones with built-in amplifiers. The microphone signals were amplified using PCB 480 power units with selective gains of 1, 10, 100. The gain settings of 10 and 100 were employed for measurements in the HRSG inlet and exhaust ducts, respectively. Calibration of the individual microphones was performed using a B & K Type 4220 piston phone with an output of 124 dB at 250 Hz and a B & K Type 4230 sound level calibrator with an output of 94 dB at 1000 Hz.

Calibration of the sound intensity unit was conducted by

using a point intensity comparison to an in-laboratory quality B & K Type 3519 acoustic intensity probe equipped with B & K Type 4183 1/2-in. microphones. The microphone spacing of the field-ready unit was fixed at 30.48 mm, which was the minimum spacing that would accommodate adjacent placement of the microphones in their water cooling jackets. For calibration purposes, a 31.0 mm spacer was used with the B & K equipment in the laboratory environment. The expected upper frequency limit for 1 dB accuracy was computed to be 1600 Hz in the 1/3 octave band. Resolution of higher frequencies would require a decrease in the spacing of the microphones, which was physically impossible for the actual field unit. For the high frequencies, the wavelength of the sound expected to be measured should be six times the microphone spacer distance. The low end frequency resolution is mainly governed by the phase mismatch of the probe and analyzer system. The B & K system with the Rockland 9040 digital FFT signal analyzer used during this investigation maintains a phase mismatch of 0.20 deg. If the PCB system maintained a 0.30 deg phase mismatch, or less, the lower 1/3 octave band of resolution would be 50 Hz for 1 dB accuracy.

A high power output speaker, driven with a random noise signal in the frequency range from 25 to 4000 Hz, was used as a power source for calibration of the intensity probe. Acoustic intensity data and sound pressure level data were acquired at identical locations adjacent to the face of the speaker. These data were then analyzed and compared, as given in Table 1 and Fig. 8. As can be clearly seen, the performance of the field unit tracked the B & K intensity and pressure levels very closely within the prescribed frequency limits.

Table 1 Calibration summary: PCB microphone comparison to B & K intensity probe; point intensity measurement

1/3 Octave Center Frequency	Intensity Level (dBA)		Pressure Level (dBA)		Reactivity Index (dBA)	
	B&K	PCB	B&K	PCB	B&K	PCB
50	67.7	66.3	51.8	52.1	15.9	14.2
63	75.3	73.8	59.9	59.4	15.4	14.4
80	81.0	79.2	67.2	65.4	13.8	13.8
100	79.3	77.7	66.6	65.6	12.7	12.1
125	77.2	76.1	66.7	66.4	10.5	9.7
160	81.6	81.1	70.6	70.3	11.0	10.8
200	83.4	83.2	73.6	73.7	9.8	9.5
250	87.5	87.3	78.8	78.6	8.7	8.7
315	88.1	85.9	80.7	79.3	7.4	6.6
400	87.4	86.1	81.1	79.6	6.3	6.5
500	88.5	87.6	83.1	82.3	5.4	5.3
630	89.7	88.3	85.2	83.9	4.5	4.4
800	87.9	87.3	84.7	84.2	3.2	3.1
1000	87.5	87.4	85.6	85.3	1.9	2.1
1250	91.9	92.1	91.4	91.3	0.5	0.8
1600	90.3	92.0	91.7	92.3	-1.4	-0.3
2000	86.6	92.4	90.5	94.7	-3.9	-2.3
2500	85.0	93.1	92.3	99.2	-7.3	-6.1

In noise measurements it is also appropriate to compute the so-called reactivity index, which is the numerical difference between the measured intensity level and the sound pressure level. This is the usual index used to indicate data quality during sound intensity measurements. As indicated by the data in Table 1, the reactivity index for the two probes was very similar. In an identical environment, the B & K probe was calibrated against a B & K Type 4204 reference sound power source with excellent results. Unfortunately, the PCB probe could not be calibrated using the reference sound power source due to insufficient output power by the source. The point to be made is that one should expect higher reactivity index values for the lower frequencies with decreasing values at the higher frequencies. In a completely free field, with the probe aligned directly with the sound propagation, one should compute a zero reactivity index, given no phase mismatch in the microphone/analyzer system. The reactivity index is an indicator, but not a direct measure, of how reactive the sound field is or how much diffuse background noise is present.

Induction heating of a steep pipe containing the PCB probe head, with one microphone replaced by a dummy microphone containing a thermocouple to monitor microphone temperature, was used to ensure system integrity prior to the field tests. While the air temperature adjacent to the microphones was maintained at 540°C, the expected temperature in the turbine exhaust at the inlet of the HRSG, a water cooling flow rate of 23 liters per hour maintained microphone temperatures well below the maximum of 121°C.

Since microphone alignment with the direction of sound propagation is an important element in sound intensity measurements, a clamp-on fixture equipped with a bubble level and compass was developed to align the intensity probe after it reached the desired penetration depth. It was assumed that sound propagation occurred in a horizontal plane and aligned with the duct centerline. The flow speeds in the ducts were

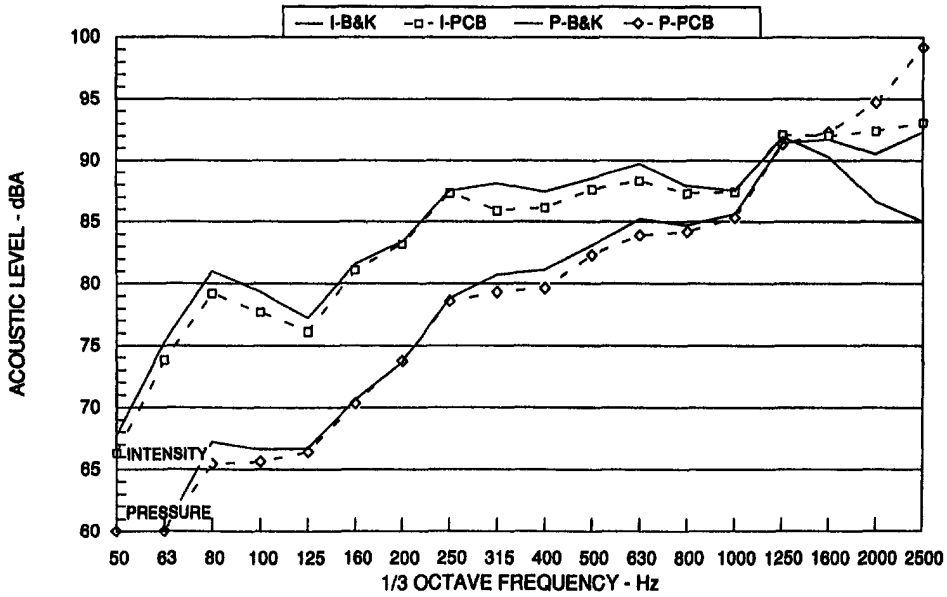

Fig. 8 PCB 106B microphone calibration comparison with B & K type 4183 (standard day)

much less than Mach 0.1 and, therefore, were not expected to influence the measurements.

Additional calculations were performed to predict the cantilevered resonant mechanical frequencies of the probe for expected insertion lengths. Vortex shedding frequencies based upon duct gas flow velocities were also calculated. No problems of severe flow-induced vibrations of the probe were anticipated that could not be quickly damped by reducing or increasing the insertion length.

Field Measurements. Data were first acquired in one leg of the HRSG exhaust duct where two horizontal penetrations had been installed. One was located approximately 3.2 m from the duct floor and the second at approximately 6.2 m from the duct floor. The duct cross section was estimated to be 47.5 square meters at the measurement location. It should be noted that in the data to be presented, the power transmitted is based on twice this area to account for sound power in the adjacent exhaust leg. The analyzer was set to capture 256 data averages in the frequency range up to 4000 Hz using a 1600 line spectral analysis. With maximum expected temperatures of 145°C, very little cooling was necessary to maintain microphone temperatures. The maximum internal probe surface temperature, adjacent to the microphones, was found to be 48°C.

In the HRSG inlet, a horizontal penetration was made at approximately 0.69 m from the duct floor, and again, data were recorded at the 1/4, 1/2, and 3/4 points. The duct area at this horizontal penetration location was 37.6 m^2. A second penetration in the inlet was made somewhat downstream from the horizontal penetration, in the vertical direction. Again, data were taken at the 1/4, 1/2, and 3/4 points along

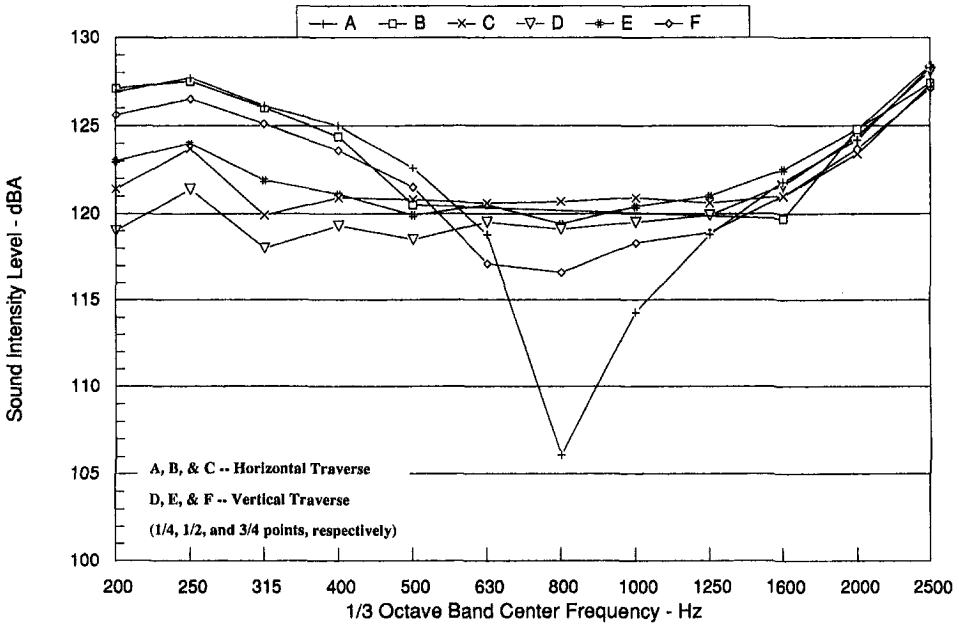

Fig. 9 HRSG inlet sound intensity variation

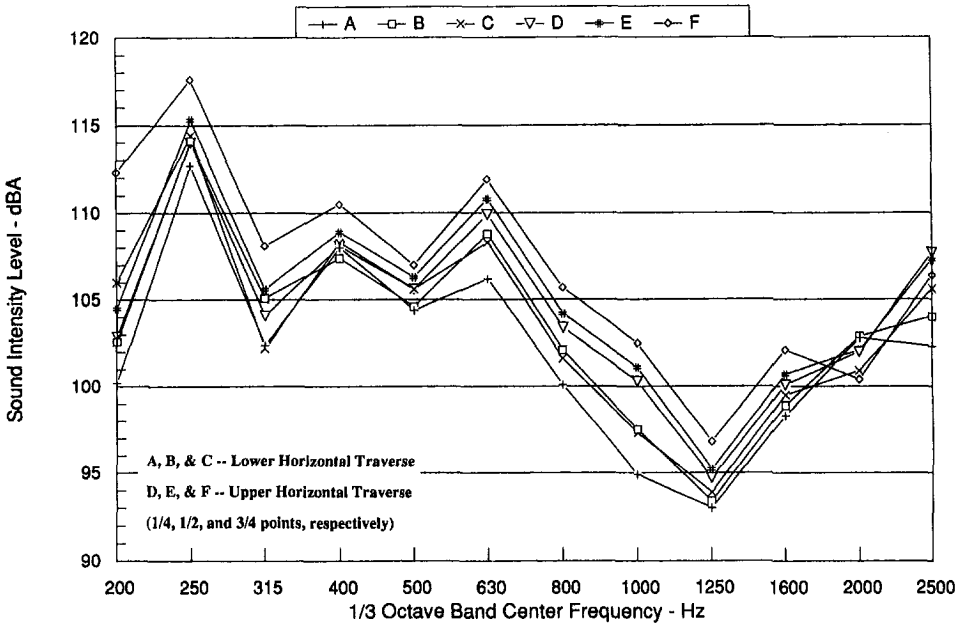

Fig. 10 HRSG outlet sound intensity variation

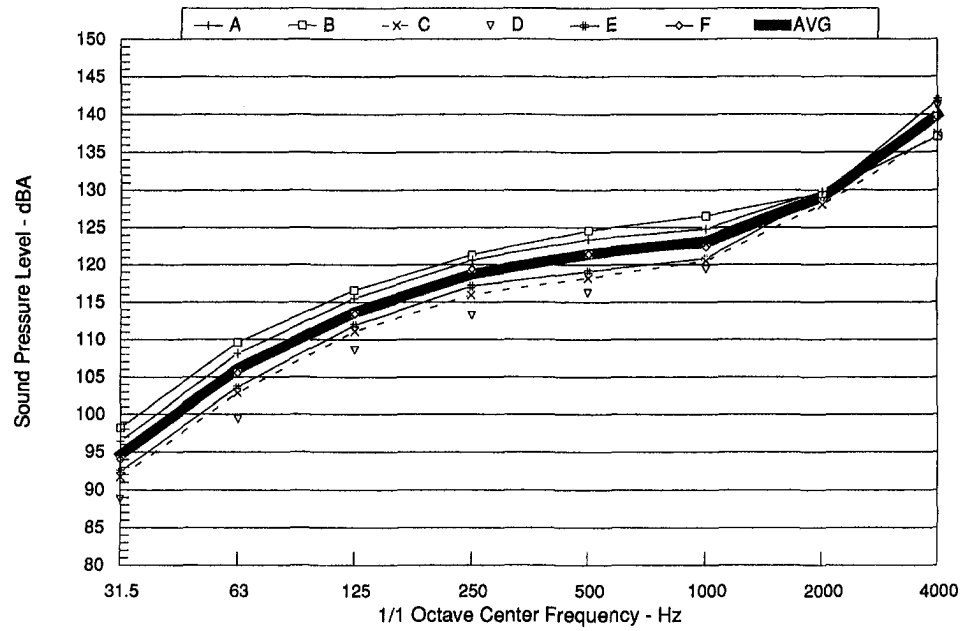

Fig. 11 HRSG inlet sound pressure level variation

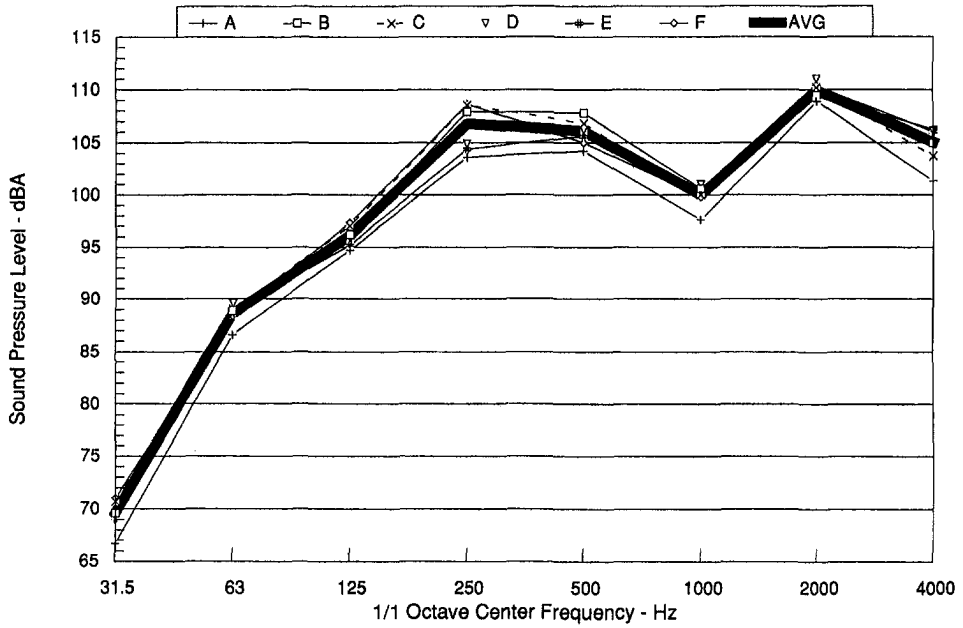

Fig. 12 HRSG outlet sound pressure level variation

the duct height. The cross-sectional area of the duct at the vertical penetration was 54.1 m^2. An average effective area of 45.85 m^2 was used for the HRSG inlet calculations. Due to the much higher expected temperatures in the inlet ducts, only 128 data samples were acquired at each measurement point to minimize probe exposure time. The maximum interior metal temperature reached 311°F; however, there was no indication of microphone malfunction during data acquisition.

A point-by-point sound intensity analysis for the 12 measurement points, 6 in each of the exhaust and inlet ducts of the HRSG, was performed. A summary of the HRSG inlet duct intensity and sound pressure level data is given in Fig. 9. Similar data are given for the HRSG exhaust duct in Fig. 10. In general, the spatial variation of intensity or sound pressure levels was small. For this reason, each of the intensity measurements for a given cross section was given equal weight (area) during the sound power estimations to be discussed below.

It should be noted that the general trend in the reactivity index in the HRSG outlet duct followed that of the probe calibration. The inlet to the HRSG did not show as extreme a trend; nevertheless, the trend of higher reactivity levels with lower frequency was still apparent.

The measured point pressures were used to make estimates of the HRSG noise reduction. This data analysis is given in Figs. 11 and 12 where power-averaged pressures were used at each of the cross sections. The data in Figs. 11 and 12 lists the 1/1 octave sound pressure level data from the individual point measurements. The six point measurements at a given cross section are listed as microphones *A* through *F*, the first three corresponding to the lower horizontal penetration data. Based on the pressure measurements, an overall *noise reduction* across the HRSG was computed to be

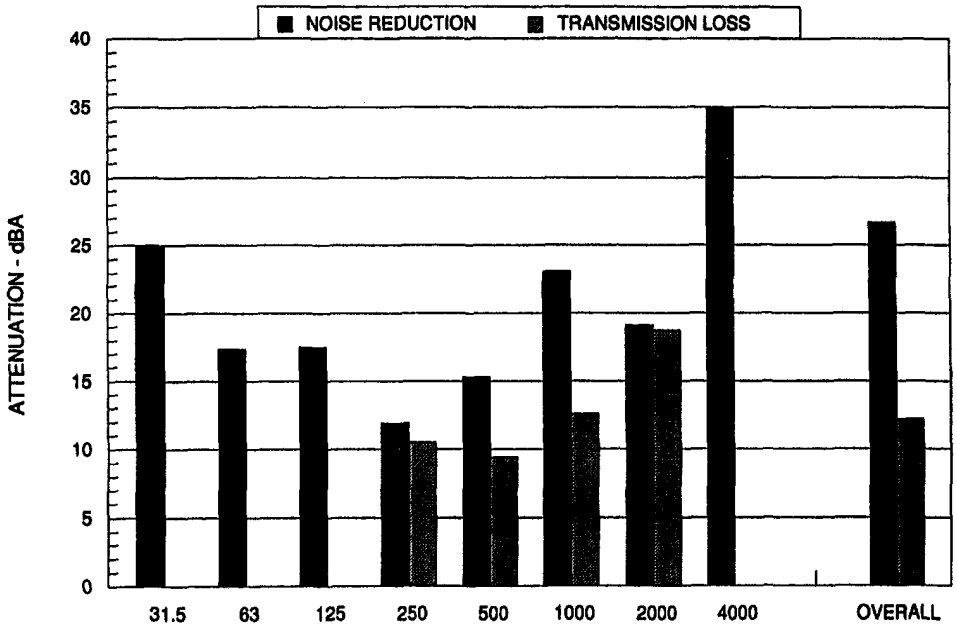

Fig. 13 Noise reduction summary

26.7 dBA, with the peak occurring in the 4000 Hz band at a value of 34.9 dBA, which was higher than expected.

An effective area of 7.64 m^2 each was assigned to the six HRSG inlet intensity measurements; likewise, an area of 15.84 m^2 each was assigned to the six HRSG outlet intensity measurements resulting in the sound power levels given in Fig. 13. The estimated power levels were then used to estimate the *sound power transmission loss* in the HRSG unit, also given in Fig. 13.

Conclusions

With the ever-increasing size of cogen systems, and density of equipment at one location, the need for effective noise abatement in the design stage is more important than at any time in the past. Even though many noise prediction models exist, these models are only as good as the input data for noise sources. This project and the results demonstrate the capability of obtaining acoustic data from existing high-temperature systems, which can then be applied to larger and more complex systems during the design stage.

The results of this program support the following conclusions:

1 Access engineering and fabrication of suitable ports for direct insertion of a noise measurement probe in high-temperature ducting can be accomplished.
2 A noise measurement probe can be designed, constructed, and calibrated, which will reliably operate in the hostile environment of a turbine exhaust.
3 The direct measurements taken across the HRSG reduced the uncertainty in transmission loss estimates when compared to modeling or external measurements. The reduced uncertainty in the source increased the reliability of noise prediction models in the design stage of the cogen facility, which had a favorable economic impact in the noise control measures need for the new facility, since no additional exhaust attenuation was required in the design stage.
4 A commitment to obtaining reliable data can pay large dividends to the industrial user, and the community at large.

A Design Procedure for Effervescent Atomizers

J. S. Chin
Visting Professor.

A. H. Lefebvre
Reilly Professor of Combustion Engineering.

Thermal Science and Propulsion Center, Purdue University, West Lafayette, In 47907

A methodology for the design of effervescent atomizers is described. The objective is to achieve sprays of minimum mean drop size for any stipulated values of liquid flow rate, air supply pressure, and air/liquid ratio. Application of the method leads to optimum values for all the key atomizer dimensions, including the number and size of the air injection holes, and the diameters of the mixing chamber and discharge orifice. It also enables optimum dimensions to be determined for a convergent–divergent nozzle should such a device be fitted to the nozzle exit to improve atomization performance. Examples are provided to demonstrate the application of the recommended design procedure and to illustrate the relative importance of various flow and geometric parameters in regard to their effects on atomization quality.

Introduction

A number of recent publications based on work carried out in the Atomization and Spray Laboratory at Purdue University by Lefebvre and co-workers (1988, 1989, 1992) have described a method of atomization commonly referred to as "effervescent atomization." In effervescent atomization, a gas (air in combustion applications) is introduced directly into a flowing liquid at some point upstream of the atomizer exit orifice in such a way as to create a bubbly two-phase flow. As the liquid flows through the discharge orifice it is squeezed by the gas bubbles into thin shreds and ligaments. If a sufficiently high pressure drop exists across the final discharge orifice, these shreds and ligaments are shattered into small droplets by the rapid expansion of the gas bubbles that occurs just downstream of the discharge orifice.

One of the main advantages of effervescent atomization is that it utilizes the available atomizing air in a highly efficient manner, so that good atomization can be achieved using very small flow rates of atomizing gas. This makes it a very attractive proposition for situations in which atomizing gas (referred to henceforth, for convenience, as air) is in short supply. Another attractive feature of effervescent atomizers is that they can achieve good atomization even when operating at low injection pressures. These performance advantages highlight the need for guidance to the designer on how best use can be made of the available atomizing air in terms of pressure and flow rate to achieve optimum atomization performance. Unfortunately, all previous work on effervescent atomization has focused almost entirely on the effects of liquid properties and operating conditions on drop-size distributions, and very little attention has been paid to atomizer design. Although Wang et al. (1989) showed that air injector geometry has little effect on mean drop size when the air injector is located well upstream of the final discharge orifice, this result is of limited value because in many practical applications, such as fuel injectors of aero engines, an important design objective, in addition to achieving fine atomization, is to minimize size and weight. Thus, the present situation is one in which the general dearth of information on how geometric features influence atomization performance is becoming a serious obstacle to successful atomizer design.

The design approaches and procedures outlined below are based mainly on analyses of the complex two-phase phenomena involved in effervescent atomization, and also on the considerable experience gained by the authors from their experimental and analytical studies on many widely different types of effervescent atomizers.

Due to its inherent simplicity the effervescent atomizer lends itself to a wide variety of design configurations. A comprehensive study embracing all potential design concepts is well beyond the scope of a single paper. The following discussion is confined to the design of what is regarded as the simplest form of effervescent atomizer. However, the recommended design procedures are considered to have broad application to all other types of effervescent atomizers.

Design Procedure

When designing an effervescent atomizer, certain key parameters are usually known at the outset. They include the liquid and gas (normally air) properties, the liquid flow rate, and the maximum available supply pressures of air and liquid. The air/liquid ratio may or may not be known. Sometimes the air/liquid ratio is specified and the design objective is then to achieve the minimum mean drop size in the spray. Commonly, the desired mean drop size may be specified, and the goal is then to achieve this level of atomization quality with the minimum amount of atomizing air.

The design procedure outlined below allows all the principal atomizer dimensions to be determined, including the diameters of the mixing chamber, discharge orifice, air injec-

Configuration by the International Gas Turbine Institute and presented at the 38th International Gas Turbine and Aeroengine Congress and Exposition, Cincinnati, Ohio, May 24–27, 1993. Manuscript received at ASME Headquarters March 17, 1993. Paper No. 93-GT-337. Associate Technical Editor: H. Lukas.

tion holes and, where appropriate, the exit diameter of the divergent-convergent nozzle. Consideration is also given to the number and spacing of the air injection holes, and the optimum length/diameter ratio of the final discharge orifice.

Discharge Coefficient. The effective flow area of an atomizer is usually described in terms of a flow number, which is expressed as the ratio of the liquid throughput to the square root of the injection pressure differential. The flow number in square meters is obtained as

$$FN = \frac{\text{flow rate, kg/s}}{(\text{pressure differential, Pa})^{0.5}(\text{liquid density, kg/m}^3)^{0.5}} \quad (1)$$

In essence, the flow number represents the product of a geometric flow area (usually the atomizer discharge orifice area) and a discharge coefficient, C_D. For most pressure atomizers the value of C_D depends only on internal geometric features and remains sensibly constant over the normal operating range. Only at very low Reynolds numbers does the discharge coefficient fall below its normal value. For internal-mixing, twin-fluid atomizers, the situation is more complex. At any given operating point, the liquid mass flow rate is governed by the following equation:

$$\dot{m}_L = C_{D_L} A^* (2\rho_L \Delta p_c)^{0.5} \quad (2)$$

where Δp_c is the pressure differential between the mixing chamber and the ambient air. Note that this pressure differential is less than the total liquid pressure drop across the nozzle due to the pressure loss incurred by the liquid as it exchanges momentum with the air jets and air bubbles downstream of the air injection holes.

The discharge coefficient of any internal-mixing, twin-fluid atomizer is inevitably low, owing to the presence of the air, which effectively blocks off a significant proportion of the discharge orifice. From tests carried out on many different nozzle designs, covering wide ranges of operating conditions, it was found that discharge coefficients depend not only on nozzle dimensions but also on nozzle operating conditions (Chin and Lefebvre, 1992). The most critical dimensions appear to be the length/diameter ratio of the final discharge orifice (or, for a convergent-divergent exit of the type shown in Fig. 1, the length/diameter ratio of the throat section) and the angle of the flow convergence downstream of the mixing chamber. This flow parameter of prime importance to discharge coefficient is air/liquid ratio, but the mixing chamber pressure also has a small effect.

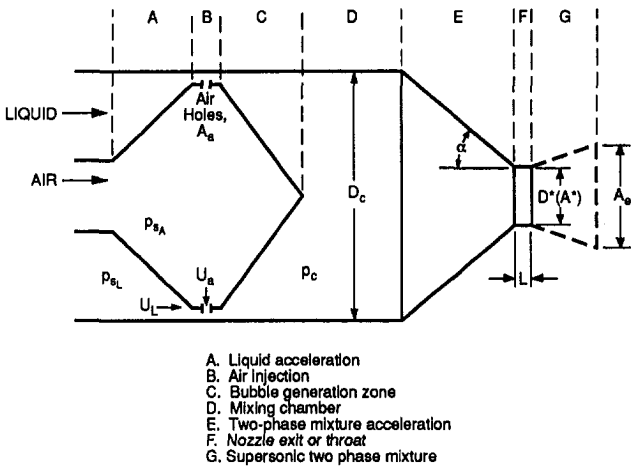

Fig. 1 Schematic diagram of effervescent atomizer

For water, the discharge coefficient may be expressed as

$$C_{D_w} = aX - b \quad (3)$$

where

$$X = \left[\left(\frac{L}{D^*}\right)(\sin 2\alpha)^{0.5}\right]^{-0.1}\left[\left(1 + \frac{1}{\text{ALR}}\right)^{0.25} - 1\right]\left[\frac{p_c}{239}\right]^{0.05} \quad (4)$$

Note that p_c, in this equation is expressed in kPa.

Nomenclature

A_a = air injection hole area (total), m^2
A_c = cross-sectioned area of mixing chamber, m^2
A_e = exit area of divergent duct, m^2
A^* = throat area, or final discharge orifice area, m^2
a, b = constants in Eq. (3)
ALR = air/liquid mass flow ratio
C_{D_L} = liquid discharge coefficient
C_{D_w} = discharge coefficient for water
D_b = bubble, diameter, m
D_c = mixing chamber diameter, m
D^* = diameter of throat or final discharge orifice, m
d_j = air jet initial diameter, m
FN = atomizer flow number, m^2
G = gas mass flow flux, kg/cm^2 h
L = length of throat or final discharge orifice, m
M_e = exit Mach number
$\dot{m}_A$ = air flow rate, kg/s
$\dot{m}_L$ = liquid flow rate, kg/s
n = number of air injection holes
p_{amb} = ambient air pressure, Pa
p_c = mixing chamber pressure, Pa [kPa in Eq. (4)]
p_e = pressure at exit of divergent duct, Pa
p^* = pressure in throat or final discharge orifice, Pa
p_{S_A} = air supply pressure, Pa
p_{S_L} = liquid supply pressure, Pa
Δp = pressure differential between p_{SA} and p_{amb}, Pa
Δp_a = pressure drop across air injection holes, Pa
Δp_c = pressure differential between p_c and p_{amb}, Pa
Q_{ah} = volumetric air flow rate per hole, m^3/s
Q_A = volumetric air flow rate, m^3/s
Q_L = volumetric liquid flow rate, m^3/s
U_A^* = air velocity in throat or final discharge orifice, m/s
U_a = air velocity through air injection holes, m/s
U_L = liquid velocity approaching air injection holes, m/s
α = half angle of convergent duct, deg
δ_0 = volumetric air/liquid ratio = Q_A/Q_L
θ = oblique shock wave angle, deg
$\lambda = (\rho'_G \rho'_L)^{0.5}$
μ'_L = ratio of liquid viscosity to water viscosity at standard conditions
ρ'_L = ratio of liquid density to water density at standard conditions
ρ'_G = ratio of gas density to air density at standard conditions
σ' = ratio of liquid surface tension to water surface tension at standard conditions
$\psi = (\sigma')^{-1}(\mu'_L)^{1.3}(\rho'_L)^{-2/3}$

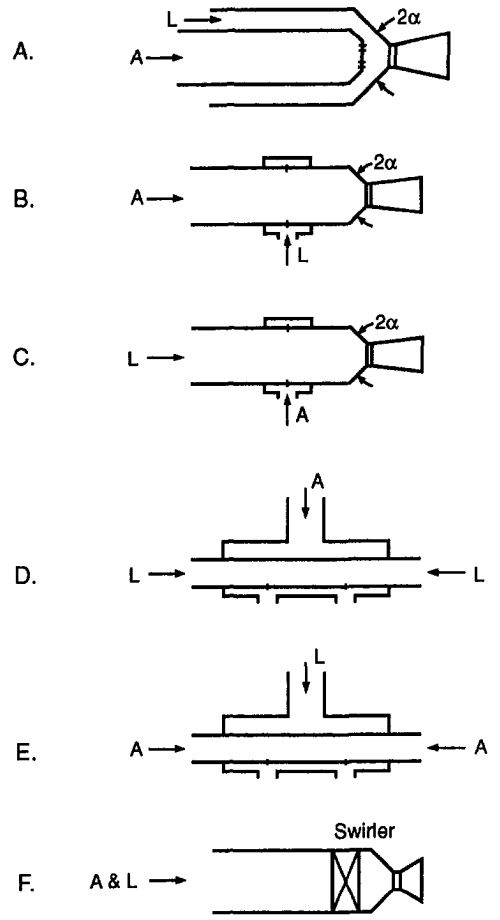

Fig. 2 Configurations of atomizers tested using air and water

Table 1 Experimentally determined values of *a* and *b*

Configuration	A		B		C		D		E		F	
	a	b	a	b	a	b	a	b	a	b	a	b
0.6 < X < 2	0.2783	0.067	0.2217	0.038	0.2287	0.04						
0.2 < X < 0.6	0.1714	0.0028	0.1657	0.0044	0.1686	0.004						
0.55 < X < 2							0.2316	0.033	0.2042	0.0022	0.20	0.02
0.2 < X < 0.55							0.1966	0.014	0.1866	0.0126		

Effervescent atomizers have been designed for a wide variety of applications. Some of the designs for which a considerable amount of flow data are available are shown schematically in Fig. 2. For these designs, appropriate values for a and b in Eq. (3) are given in Table 1.

For liquids other than water, the discharge coefficient may be obtained from the expression

$$C_{D_L} = C_{D_w} \cdot (\mu')^{0.04} (\sigma')^{0.02} \tag{5}$$

where μ' is the liquid/water viscosity ratio, and σ' is the liquid/water surface tension ratio.

When designing an atomizer for any given application, the air and liquid flow rates, and the maximum permissible air pressure differential Δp, are usually known at the outset. By proper design of the air injection holes (as discussed below) the pressure drop across the holes, Δp_a, can be calculated.

As the pressure difference between the mixing chamber and the ambient air is the same for both air and liquid, the value of Δp_c for substitution in Eq. (1) is readily obtained as

$$\Delta p_c = \Delta p - \Delta p_a \tag{6}$$

By a suitable choice of convergent angle, 2α, and L/D^* ratio, the design value of C_{D_L} may be calculated from Eqs. (3) and (5).

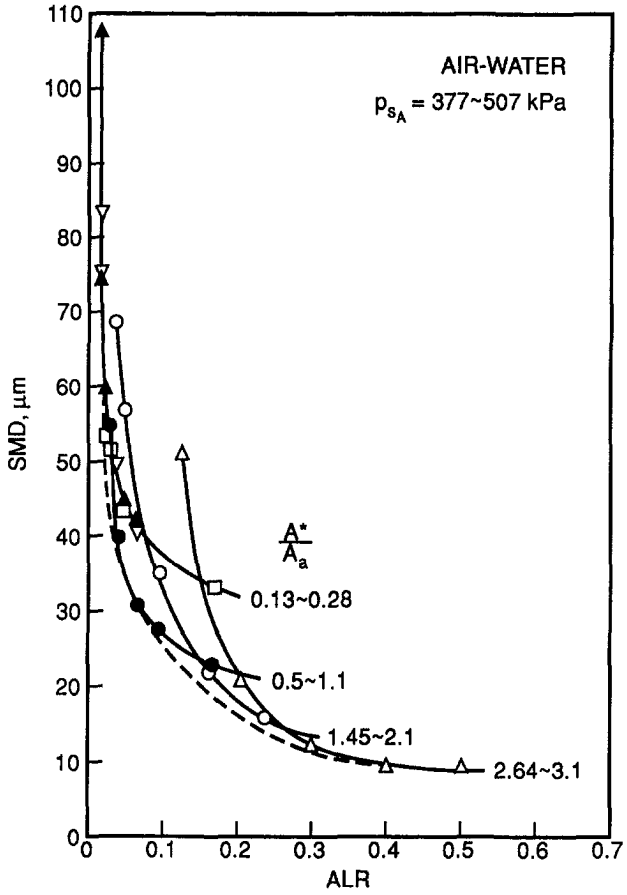

Fig. 3 Influence of ALR and A^*/A_a ratio on mean drop size

Air Injection. An important consideration in the design of effervescent atomizers is the determination of optimum values for the number, size, and spacing of the air injection holes. At this stage in the design process, the value of A^* required to give the desired liquid flow rate has been calculated from Eq. (1). Considerable experience with effervescent and other types of internal aerated-liquid atomizers has shown that one of the most important parameters affecting atomization performance is the ratio of the discharge-orifice (or throat) area to the area of the air injection holes. The ratio, A^*/A_a, governs the corresponding air velocity ratio, U_A^*/U_a (the ratio of the air velocity at the throat to the air velocity through the air injection holes), and also the pressure drop across the air injection holes, Δp_a. The manner and extent to which mean drop size is influenced by varations in A^*/A_a and air/liquid ratio (ALR) is illustrated in Fig. 3. From inspection of this figure, it is clear that from an atomization viewpoint it would be very desirable to arrange for the area ratio A^*/A_a to increase with increasing ALR. The dashed line in Fig. 3 represents an ideal situation, corresponding to an infinitely variable area ratio, whereby A^*/A_a is arranged to increase progressively with increase in ALR. The relationship between the optimum value of A^*/A_a for minimum mean drop size and air/liquid ratio is shown in Fig. 4. The straight line drawn through the origin in this figure corresponds to the equation.

$$A^*/A_a = 6.3\text{ALR} \tag{7}$$

Figure 4 suggests that for effervescent atomizers, which necessarily operate at low air/liquid ratios, the design value of A^*/A_a should be low, i.e., the total-air-injection hole area should be much larger than the atomizer exit area. This produces a low air velocity at exit from the air injection holes, which is an essential prerequisite for bubble genera-

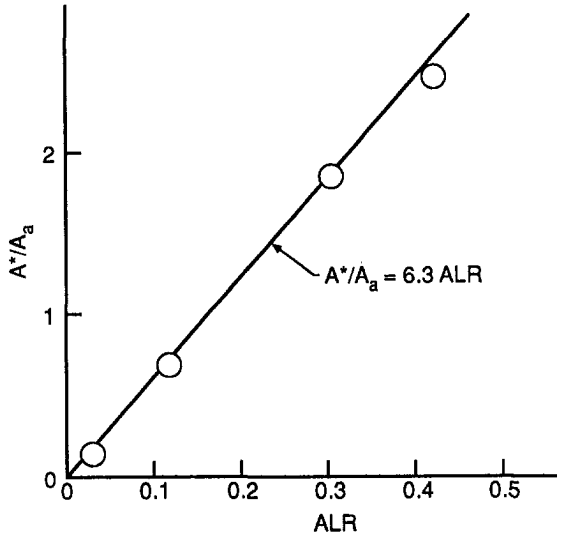

Fig. 4 Optimized A^*/A_a ratio versus design ALR

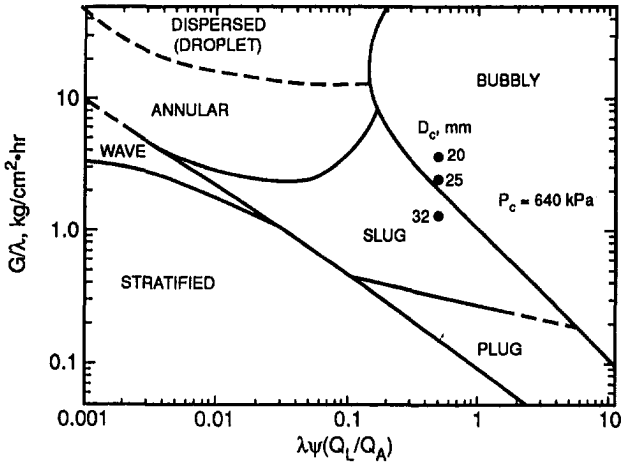

Fig. 5 Flow regimes for air–water mixtures in horizontal flow. Effect of mixing chamber diameter on flow pattern.

tion. Although this paper is concerned primarily with effervescent atomization, it is of interest to note in Figs. 3 and 4 that for the high air/liquid ratios at which conventional internal-mixing, twin-fluid normally operate, the atomizer should ideally be designed for a correspondingly high value of A^*/A_a. This ensures high velocity through the air injection holes. Such high velocities are essential for good atomization when the nozzle is operating in a conventional airblast mode.

For effervescent atomizers, the value of A^*/A_a corresponding to minimum mean drop size is read off Fig. 4 at the design ALR. As A^* is known, this fixes the value of A_a, which represents the total flow area of the air injection holes, i.e.,

$$A_a = n(\Pi/4)d_j^2 \tag{8}$$

strongly affects the pressure loss incurred by the liquid as it flows through the annular air-injection passage. A high liquid pressure loss is not necessarily disadvantageous because in many applications the main limitation is on available air pressure rather than liquid supply pressure. Furthermore, a high pressure loss in this region can effectively dampen the flow instabilities that sometimes occur when the atomizer is operating near its upper limt of ALR, which is usually between 0.05 and 0.2, depending on the air pressure. Experience has shown that a value of U_L of around 5 m/s represents a satisfactory compromise between the conflicting requirements of flow stability and low pressure loss.

Mixing Chamber.. The air-injection zone provides a region in which the air jets have ample time to disintegrate into bubbles, which then distribute themselves throughout the liquid to form a uniform and orderly flow within the mixing zone. Many different types of mixing chamber have been designed and operated successfully, including designs having circular, annular, and rectangular flow sections. The following discussion is confined to mixing chambers of circular cross section, but for all duct geometries the design objective is the same, namely to achieve the most desirable flow pattern in the two-phase flow at entry to the throat or discharge orifice. The various flow patterns that occur in a gas–liquid two-phase flow in a horizontal pipe have been studied by Baker (1954) and are illustrated in Fig. 5. Similar flow charts are available in the literature for two-phase flow in vertical pipes. The flow patterns shown in Fig. 5 include (1) stratified flow, whereby the liquid flows along the bottom of the pipe with gas flowing along the top, (2) wave flow, which is similar to stratified flow except that the interface has waves traveling in the direction of the flow, (3) slug flow, in which a wave is picked up periodically by the rapidly moving gas to form a frothy slug, which travels along the pipe at a higher velocity than the average liquid velocity, (4) bubbly flow, in which bubbles of gas are dispersed throughout the liquid, (5) annular flow, where the liquid forms a film along the pipe walls, and (6) dispersed flow, which comprises liquid droplets dispersed throughout a flowing gas stream. For effervescent atomization, a bubbly flow in the mixing chamber is essential. This requirement dictates the diameter of the mixing chamber, as illustrated in the following example for a two-phase mixture of air and water at the following flow conditions:

$\dot{m}_L$ = 128 g/s
$\dot{m}_A$ = 1.925 g/s
ALR = 0.015
p_c = 640 kPa

Figure 5 is essentially a reproduction of Baker's original chart except that the units have been changed. The flow parameters of importance in this figure are the following:

G = gas mass flow flux in kg/cm^2 h
Q_A = volumetric air flow rate, m^3/s
Q_L = volumetric liquid flow rate, m^3/s
$\lambda = (\rho'_G \rho'_L)^{1/2}$
$\psi = (\sigma')^{-1}(\mu'_L)^{1/3}(\rho_{l'})^{-2/3}$
ALR = air/liquid mass ratio
ρ'_G = ratio of gas density to air density at standard conditions
μ'_L = ratio of liquid viscosity to water viscosity at standard conditions
ρ'_L = ratio of liquid density to water density at standard conditions
σ' = ratio of liquid surface tension to water surface tension at standard conditions

The parameters above are calculated for the conditions listed above using values for D_c, the mixing-chamber diameter, of 20, 25, and 32 mm. The results of these calculations are indicated in Fig. 5. They show that a mixing-chamber diameter of 32 mm would be too large because it would result in slug flow. Values for D_c of 20 or 25 mm would both give the desired bubbly flow pattern. The smaller diameter often has the advantage of a more compact design at the expense of a slightly higher pressure loss. Thus an optimum value for D_c would depend on the relative importance of atomizer size and pressure loss and, for the example considered, would lie between 20 and 25 mm.

Convergence Angle and L/D^* Ratio. Convergence angle appears to have little effect on atomization performance

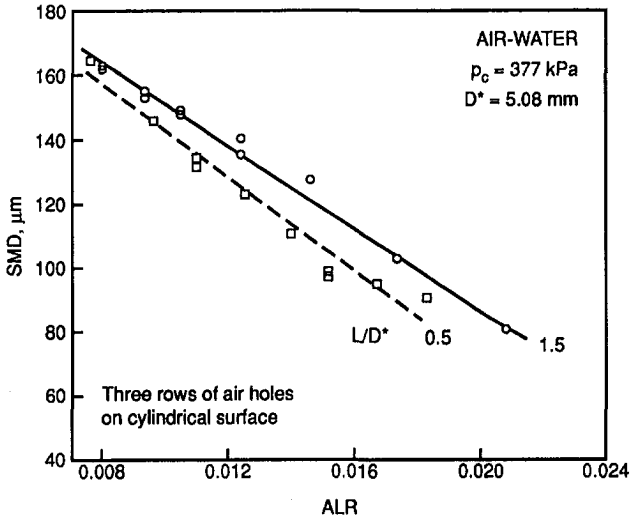

Fig. 6 Influence of ALR and L/D^* ratio on mean drop size

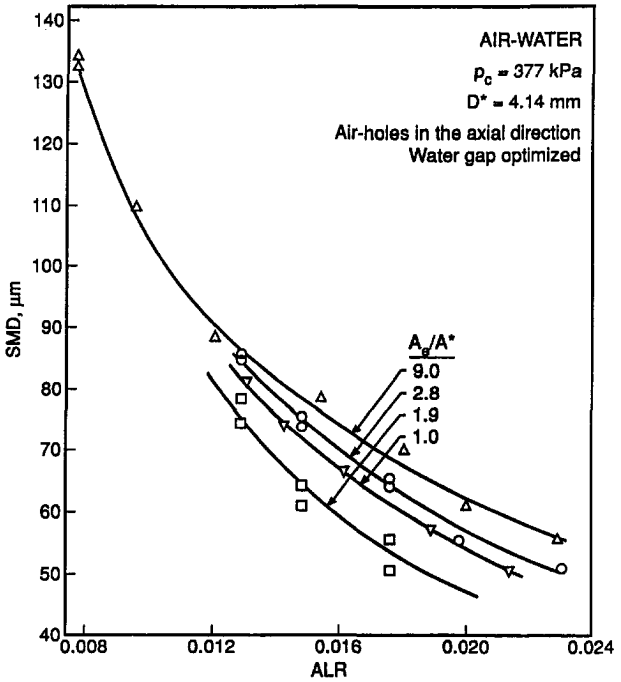

Fig. 7 Influence of ALR and divergent duct area ratio on mean drop size

provided it is less than around 120 deg. A value for 2α of 90 deg is recommended because it combines good flow characteristics with relatively short length. Of more importance to atomization is the length/diameter ratio of the final discharge orifice. This is illustrated in Fig. 6, which shows the effect on SMD of a reduction in L/D^* from 1.5 to 0.5. For a typical ALR of around 0.015 this reduction in L/D^* reduces the mean drop size by around 10 μm. Further reductions in L/D^* below 0.5 would undoubtedly yield additional improvements in atomization but are not recommended because atomizers having discharge orifices of very low L/D^* ratio are difficult to manufacture and are very susceptible to damage.

Divergent Section. For reasons of cost and simplicity, most effervescent atomizers employ a simple convergent nozzle through which the spray is discharged into the surrounding atmosphere. However, if a sufficient air supply pressure is available, better atomization can be achieved by providing a divergent section downstream of the throat, as illustrated in Fig. 1. Measurements of mean drop size carried out on effervescent atomizers featuring this type of convergent–divergent exit nozzle have shown that, for any given operating condition, there is an optimum value of A_e/A^*, the ratio of atomizer exit area to throat area, for minimum mean drop size. This point is well illustrated in Fig. 7 in which mean drop size is plotted against air/liquid ratio for an atomizer operating at a constant mixing chamber pressure of 337 kPa. This type of SMD data can only be obtained by varying both air and liquid flow ratio simultaneously in order to achieve a variation in air/liquid ratio while maintaining a constant chamber pressure. Inspection of Fig. 7 reveals that, for any given value of ALR, an increase in A_e/A^* from 1.0 to 1.9 leads to improved atomization; however, further increase in area ratio from 1.9 to 2.8 and then to 9.0 has an adverse effect on atomization performance.

When supplied with a bubbly two-phase flow, a convergent–divergent nozzle functions in much the same way as when it is supplied with pure air. For example, when the exit pressure is exactly the same as the ambient air pressure, i.e., $p_e = p_{amb}$, the flow exits the nozzle smoothly without forming either an expansion wave or a shock wave. When the nozzle is underexpanded, i.e., $p_e > p_{amb}$, an expansion wave is created at the nozzle exit, whereas for $p_e > p_{amb}$ the nozzle is over-expanded and oblique shock wave is formed when the two-phase flow leaves the nozzle. If p_e is then decreased continuously, eventually a normal shock wave will be established at the exit plane of the nozzle. At this condition, further decrease in p_e will result in the formation of a shock wave inside the divergent section.

It is of interest to note that the optimum value of A_e/A^*, corresponding to the minimum values of SMD in Fig. 7, is equivalent to the condition that if a homogeneous flow model is used the divergent section will be overexpanded to such an extent that an oblique shock wave will form at an angle of 45 deg to the nozzle unit. This suggests that a reasonable basis for nozzle design would be to use the homogeneous flow model to determine the value of A_e/A^* corresponding to the formation of a 45 deg angle oblique shock wave at the divergent section outlet (Wallis, 1969). This optimum value of A_e/A^* is obtained by first combining two different equations for M_e, the nozzle exit Mach number, to determine the expansion ratio p_e/p_c. This value of p_e/p_c is then substituted into another equation to obtain A_e/A^*.

We have

$$M_e = \frac{\frac{2}{\delta_o}\left[1 - \frac{p_e}{p_c} - \delta_o \ln\left(\frac{p_e}{p_c}\right)\right]}{\left[1 + \frac{p_e}{p_c}\cdot\frac{1}{\delta_0}\right]} \tag{11}$$

where δ_0, the volumetric air/liquid ratio in the mixing chamber, is given by

$$\delta_0 = \text{ALR}\,(\rho_L/\rho_G) \tag{12}$$

where ρ_L and ρ_G denote respectively the liquid and gas densities in the mixing section.

Also, for an oblique shock wave in homogeneous two-phase flow, we have (Wallis, 1969)

$$M_e^2 = \frac{p_{amb}}{p_e \sin^2\theta} \tag{13}$$

where θ is the oblique shock wave angle.

Combining Eqs. (11) and (13), and setting $\theta = 45$ deg, leads to

Table 2 Relationship between p^*/p_c and δ_0

δ_0	1	2	3	4	5	6	7	8
$\frac{p^*}{p_c}$	0.515	0.553	0.569	0.577	0.583	0.586	0.589	0.591

$$\left[\frac{p_{amb}}{p_c} + \delta_0\right] \cdot \left(\frac{p_e}{p_c}\right)^2 - \delta_0\left(1 - 2\,\frac{p_{amb}}{p_c}\right) + \delta_0^2 \cdot\left(\frac{p_e}{p_c}\right) \ln\left(\frac{p_e}{p_c}\right) + \frac{p_{amb}}{p_c} \cdot \delta_0 = 0 \quad (14)$$

Insertion of the appropriate known values of p_{amb}, p_c, and δ_0 into the equation above gives p_e/p_c. This value of p_e/p_c is then substituted into the following equation to obtain A_e/iA_0^*.

$$\frac{A_e}{A^*} = \frac{\left(\frac{p^*}{p_e}\right)\left(1 + \frac{p_e}{p_c} \cdot \frac{1}{\delta_0}\right)}{\left[\frac{2}{\delta_0}\left(1 - \frac{p_e}{p_c} - \delta \ln \frac{p_e}{p_c}\right)^{0.5}\right]} \quad (15)$$

In this equation, p^*/p_e is the critical pressure ratio for homogeneous two-phase flow. It is uniquely related to δ_0, the air/liquid volumetric ratio, by the relationship

$$\left(\frac{p^*}{p_c}\right)^2 = 4\delta_0\left(\frac{p^*}{p_c}\right) + 2\delta_0^2 \ln\left(\frac{p^*}{p_c}\right) + \delta_0^2 - 2\delta_0 = 0 \quad (16)$$

The manner and extent to which p^*/p_c varies with δ_0 for homogeneous two-phase flow is illustrated in Table 2.

Concluding Remarks

In this paper a procedure for effervescent atomizer design is outlined. The design objective is to achieve the finest possible atomization for any given values of air supply pressure and air/liquid mass ratio. The methods employed are based on a detailed analysis of the various two-phase flow and mixing process involved, supplemented where necessary by the results of experiments conducted on many different types of effervescent atomizers when operating over wide ranges of test conditions. Although it is anticipated that, as more experience is gained with effervescent atomizers, further improvements and refinements to the design methodology presented herein will emerge, it is considered that in its present form it provides a rational basis for effervescent atomizer design.

References

Baker, O., 1954, "Simultaneous Flow of Oil and Gas," *Oil Gas Journal*, Vol. 53, pp. 185–194.

Chin, J. S., and Lefebvre, A. H., 1992, "Studies on Internal-Mixing Air-Assist Atomizers," unpublished Purdue report.

Buckner, H. N., Sojka, P. E., and Lefebvre, A. H., 1989, "Aerated Atomization of High Viscosity Newtonian Liquids," *Proc. 3rd Annual Conference on Liquid Atomization and Spray Systems*, Irvine, CA, pp. 55–61.

Lefebvre, A. H., Wang, X. F., and Martin, C. A., 1988, "Spray Characteristics of Aerated-Liquid Pressure Atomizers," *AIAA Journal of Propulsion and Power*, Vol. 4, No. 4, pp. 293–298.

Lefebvre, A. H., 1988, "A Novel Method of Atomization With Potential Gas Turbine Applications," *Indian Defence Science Journal*, Vol. 38, No. 4, pp. 353–362.

Pilch, M., and Erdman, C. A., 1987, "Use of Breakup Time Data and Velocity History Data to Predict the Maximum Size of Stable Fragments for Acceleration-Induced Breakup of a Liquid Drop," *International Journal of Multiphase Flow*, Vol. 13, No. 6, pp. 741–757.

Roesler, T. C., and Lefebvre, A. H., 1989, "Studies on Aerated-Liquid Atomization," *International Journal of Turbo and Jet Engines*, Vol. 6, Nos. 3 and 4, pp. 221–230.

Wallis, G. B., 1969, *One Dimensional Two Phase Flow*, McGraw Hill, New York.

Wang, X. F., Chin, J. S., and Lefebvre, A. H., 1989, "Influence of Gas Injector Geometry on Atomization Performance of Aerated-Liquid Nozzles," *International Journal of Turbo and Jet Engines*, Vol. 6, No. 3 and 4, pp. 271–280.

Whitlow, J. D., and Lefebvre, A. H., 1992, "Effervescent Atomizer Operation and Spray Characteristics," to be published in *Atomization and Sprays*.

Numerical Investigation of Enhanced Dilution Zone Mixing in a Reverse Flow Gas Turbine Combustor

D. S. Crocker

C. E. Smith

CFD Research Corporation
Huntsville, AL 35805

An advanced method for dilution zone mixing in a reverse flow gas turbine combustor was numerically investigated. For long mixing lengths associated with reverse flow combustors (X/H > 2.0), pattern factor was found to be mainly driven by nozzle-to-nozzle fuel flow and/or circumferential airflow variations; conventional radially injected dilution jets could not effectively mix out circumferential nonuniformities. To enhance circumferential mixing, dilution jets were angled to produce a high circumferential (swirl) velocity component. The jets on the outer liner were angled in one direction while the jets on the inner liner were angled in the opposite direction, thus enhancing turbulent shear at the expense of jet penetration. Three-dimensional CFD calculations were performed on a three-nozzle (90 deg) sector, with different fuel flow from each nozzle (90, 100, and 110 percent of design fuel flow). The computations showed that the optimum configuration of angled jets reduced the pattern factor by 60 percent compared to an existing conventional dilution hole configuration. The radial average temperature profile was adequately controlled by the inner-to-outer liner dilution flow split.

Introduction

In conventional annular gas turbine combustors, hot combustion products exiting the intermediate zone are diluted by cooler air in the dilution zone. For reverse flow combustors typically utilized in turboshaft/turboprop engines, the dilution zone connects to a transition duct that turns the flow 180 deg into the turbine. Figure 1 shows a typical reverse flow combustor from the F109 engine of Allied Signal Aerospace Company/Garrett Engine Division (GED).

Current and advanced combustors inject dilution air into the dilution zone through a pattern of holes in the combustor liner. The dilution jets should effectively mix with the combustion gases, thereby establishing a temperature profile that is acceptable to the turbine. Two aspects of exit temperature profiles are important:

1 the average radial temperature profile that is critical in defining the life of first stage rotor blades; and
2 the maximum spatial temperature that controls the stress and erosion of the turbine inlet guide vanes.

The design radial temperature profile, with maximum temperature typically occurring at the 50 to 70 percent radial position, is usually obtained rather easily. On the other hand, the maximum spatial temperature is difficult to control in most cases. Reducing the maximum spatial temperature (for a given average combustor exit temperature) can result in significant improvement of turbine inlet guide vane life and/or engine efficiency. The maximum spatial temperature is normally presented in terms of pattern factor, defined by the equation:

$$PF = \frac{T_{max} - T_{exit}}{T_{exit} - T_{inlet}} \quad (1)$$

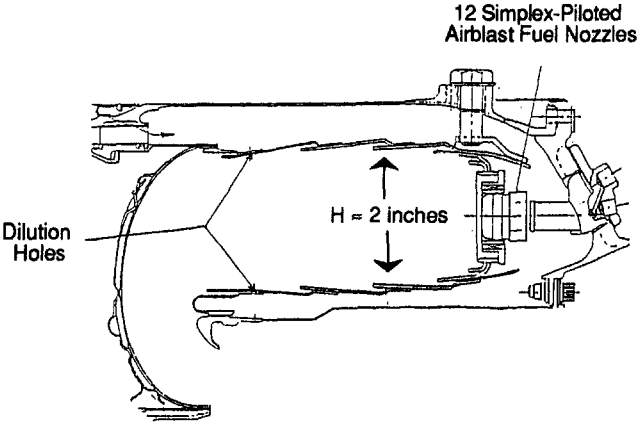

Fig. 1 Garrett F109 reverse flow annular combustor

Contributed by the International Gas Turbine Institute and presented at the 38th International Gas Turbine and Aeroengine Congress and Exposition, Cincinnati, Ohio, May 24–27, 1993. Manuscript received at ASME Headquarters March 1, 1993. Paper No. 93-GT-129. Associate Technical Editor: H. Lukas.

Engine pattern factor goals for small combustors ($\approx$ 10 lb/sec) of 0.15 to 0.20 are often difficult to achieve. The combustor designer must design dilution holes for a given liner pressure drop and airflow. Typical values of liner pressure drop ($\Delta p/p$) and dilution airflow are 3.0–4.0 percent and 20–30 percent of combustor airflow, respectively. Conventionally, two rows of dilution jets are designed, one on the inner liner and another on the outer liner. The holes are arranged to be opposed (in the same axial plane), and either circumferentially staggered (such that the jets can penetrate past each other) or in-line (such that the jets impinge upon each other).

A considerable amount of experimental and numerical work has been performed to understand and optimize conventional dilution zone mixing techniques. Experiments in rectangular ducts were performed for single-sided jets (Srinivasan et al., 1984); and double row and slotted jets (Srinivasan et al., 1985). In these investigations, algebraic correlations were developed to predict mixing performance as a function of design variables. Numerical modeling of jets in crossflow includes studies by Holdeman and Srinivasan (1986), and Smith (1990). Numerical modeling has generally been successful in predicting trends in mixing performance, but mixing rates are usually underpredicted when compared with experimentally measured mixing rates. The effects of curvature and convergence on dilution jet mixing have been studied by Reynolds and White (1986) and Holdeman et al. (1987a, 1988). Jet penetration and mixing for curved or converging ducts was observed to be similar to that of straight ducts. An exception is that both inner and outer jets remained closer to the inner liner because of the radial pressure gradient induced by the curvature.

Most of the recent work on jets in crossflow applicable to gas turbine combustors has been summarized by Holdeman (1991). It has been shown that the rate of mixing and penetration (for conventional dilution hole designs) of jets in crossflow is governed mainly by the hole spacing-to-duct height ratio (S/H) and the jet-to-mainstream momentum flux ratio given by

$$J = \left(\rho_j V_j^2\right)/\left(\rho_\infty V_\infty^2\right) \tag{2}$$

Practical design correlations have been developed for various types of dilution zone geometries. Optimum mixing for one-sided injection into a rectangular duct can be determined from

$$(S/H)\sqrt{J} = 2.5 \tag{3}$$

This correlation is also appropriate for in-line hole patterns if half the duct height is used in Eq. (3). Also, Holdeman (1991) suggests that this relation is appropriate for opposed rows of staggered holes if the constant of proportionality is 5.0 and the hole spacing is twice that for optimum single side injection; that is, alternate jets for optimum single side mixing are moved to the opposite wall.

Both cyclic and noncyclic circumferential temperature variations are experimentally measured. As an example, Fig. 2 shows measured temperature data at the F109 combustor exit. Cyclic temperature variations have a period that is a function of the fuel nozzle spacing. Cyclic variations are typically caused by uneven mixing of fuel and air in the primary zone and incomplete mixing of the dilution jets with hot combustion products in the dilution zone. Noncyclic temperature variations are typically caused by fuel flow and airflow circumferential nonuniformities. Noncyclic variations are typically very difficult to control.

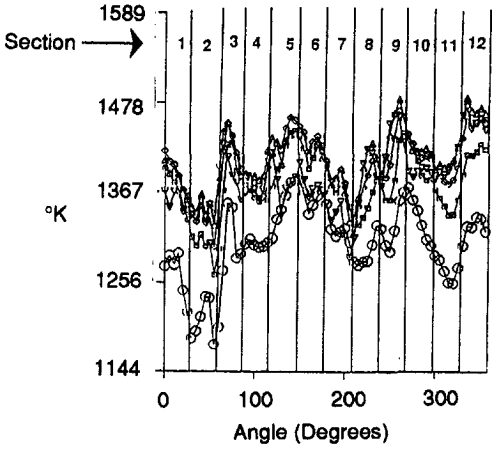

SECTION	PATTERN FACTOR
1	0.100
2	0.098
3	0.110
4	0.085
5	0.087
6	0.066
7	0.076
8	0.108
9	0.114
10	0.067
11	0.093
12	0.085
Avg	0.091

r/R
○ 0.08
□ 0.26
◇ 0.44
△ 0.62
▽ 0.80

Fig. 2 F109 experimental temperature at the inlet guide vane location

In reverse flow combustors, there is a relatively long mixing distance available, so cyclic temperature variations caused by incomplete dilution jet mixing are small if the dilution hole design is optimized. Pattern factors of 0.09 or less can be obtained if the dilution zone inlet temperature conditions are uniform. (Cooling of the transition duct liner limits the reduction of pattern factor in this case.) However, there is significant variation in dilution zone inlet temperature within each nozzle sector and between nozzles. This type of circumferential variation is clearly evident in the experimental data shown in Fig. 2. From Fig. 2, the overall pattern factor is 0.163, but the average pattern factor for the twelve 30 deg sectors is 0.091. These circumferential temperature variations with length scales larger than the dilution hole spacing (especially nozzle to nozzle variation) are the most difficult to

Nomenclature

D_h = hydraulic diameter
H = duct height
J = jet-to-mainstream momentum flux ratio
l_t = turbulent length scale
p = pressure
PF = pattern factor
S = spacing between dilution hole centers
T_{exit} = average combustor exit temperature
T_{inlet} = average combustor inlet temperature
T_{max} = maximum spatial combustor exit temperature
V = velocity
v = rms of velocity turbulent fluctuations
ρ = density

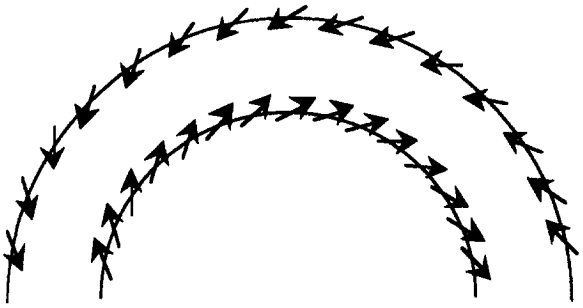

Fig. 3 Schematic of angled dilution jet concept

control. Such variations result in high combustor pattern factors.

Conventional dilution hole configurations, which inject dilution air radially with no circumferential component, are not designed for circumferential mixing over length scales greater than the hole spacing. There are no fundamental studies known to the authors that consider circumferential or transverse inlet temperature variations. Srinivasan et al. (1982) considered vertical inlet temperature variation (equivalent to radial variation) and found that the inlet temperature profile had a strong influence on the exit profile. The downstream flow could be modeled by superimposing the nonisothermal upstream profile on the downstream solution that would be obtained if the mainstream were isothermal.

In this numerical study, ways to reduce pattern factor in reverse flow combustors by increasing large-scale circumferential mixing were investigated. First, three-dimensional numerical analysis of the baseline F109 combustor configuration was performed. Then, parametric calculations were performed on advanced dilution hole designs. The most promising configuration turned out to be angled jets that produced a high circumferential velocity component. Figure 3 presents a schematic of the configuration. The jets on the outer liner are highly angled in one direction, while the jets on the inner liner are highly angled in the opposite direction. Numerical solutions of the flow fields for the baseline and advanced designs are discussed in the sections that follow.

Numerical Models

The test vehicle chosen for this study was the F109 combustor of GED. The F109 combustor geometry, shown in Fig. 1, is typical of small reverse flow combustors. The numerical analyses consisted of:

1 a primary zone model to determine dilution zone inlet conditions; and
2 three dilution zone/transition duct models that extended to the turbine inlet guide vanes.

The CFD code, numerical details, numerical grid, boundary conditions, and convergence/run times for the models are discussed below.

CFD Code. The code CFD-ACE (Owens, 1992) was used to perform the computations. The basic capabilities/methodologies in CFD-ACE include:

1 co-located, fully implicit, and strongly conservative finite volume formulation;
2 solution of two- and three-dimensional Navier–Stokes equations for incompressible and compressible flows;
3 Cartesian and nonorthogonal curvilinear coordinates;
4 single and multidomain grid topology;
5 upwind, central (with damping), second-order upwind, and Osher-Chakravarthy differencing schemes;
6 standard (Launder and Spalding, 1974) and extended (Chen and Kim, 1987) $k-\epsilon$ turbulence models, the two-scale turbulence model of Kim and Chen (1988), and the low-Reynolds-number $k-\epsilon$ model of Chien (1985);
7 instantaneous, one-step, and two-step combustion models;
8 modified form of Stone's strongly implicit solver and conjugate gradient solver; and
9 pressure-based solution algorithms including SIMPLE and a variant of SIMPLEC.

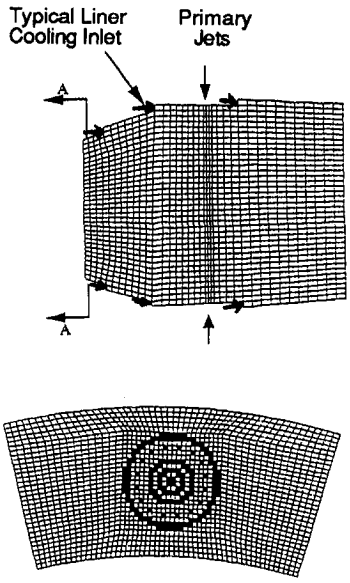

Fig. 4 Primary zone grid

CFD-ACE has undergone a considerable amount of systematic quantitative validation for both incompressible and compressible flows. Over 30 validation cases have been performed to date, and good-to-excellent agreement between benchmark data and predictions has been shown (Smith et al., 1989; Avva et al., 1990). Of particular interest to this study is the good agreement between numerical results and experimental data for jet mixing shown by Smith (1990).

Numerical Details. The numerical details of the calculations included:

1 whole field solution of u momentum, v momentum, w momentum, pressure correction, turbulent kinetic energy k, dissipation rate ϵ, total enthalpy, and mixture fraction;
2 upwind differencing for all variables;
3 variable fluid properties;
4 adiabatic walls;
5 standard $k-\epsilon$ model with wall functions;
6 turbulent Prandtl number of 0.9;
7 one-step reaction kinetics model (primary zone model only); and
8 premixed fuel and air (primary zone model only).

Grid and Boundary Conditions

Primary Zone Model. The primary zone grid consisted of 84,132 cells ($41 \times 38 \times 54$ in x, r, θ directions). The domain of interest, shown in Fig. 4, consisted of the first 37 cells in the axial direction. The additional four cells in the axial direction provided for variable pressure at the primary zone/dilution zone interface. Fuel nozzle and dome swirler airflow were introduced in the shaded cells shown in Fig. 4. A specified fuel flow was introduced in the center four cells and in the next shaded ring. Other airflow inlets were primary jets and liner cooling as shown in Fig. 4. The primary

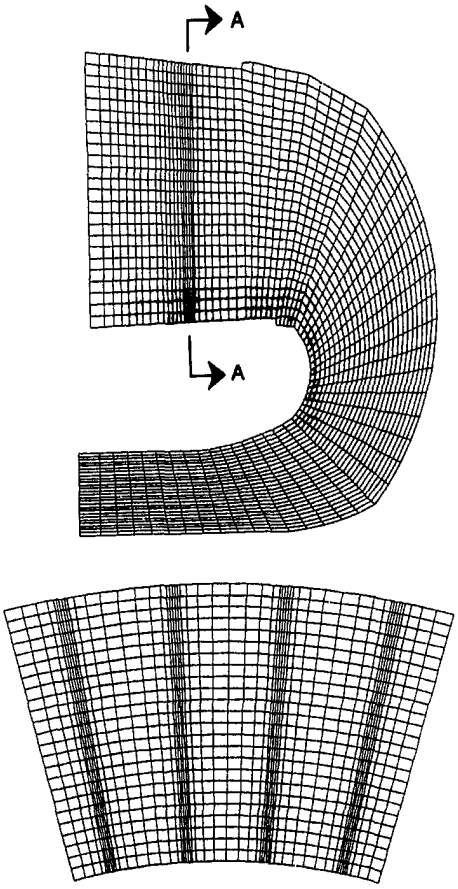

Fig. 5(a) Single nozzle sector dilution zone/transition duct grid

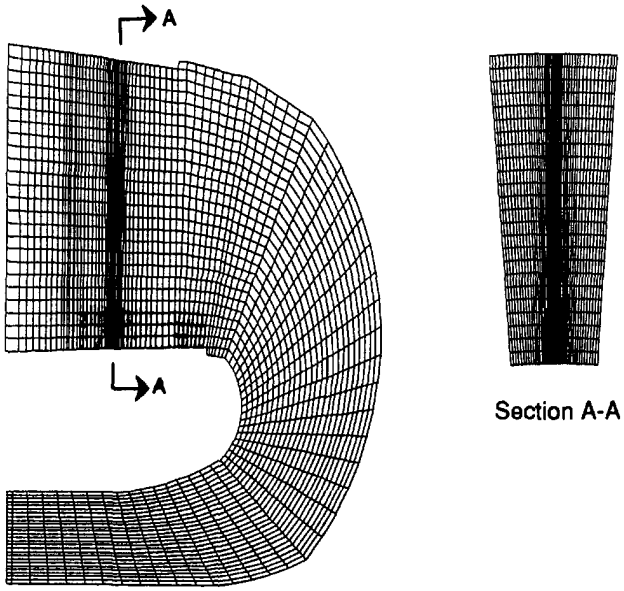

Fig. 5(b) Small sector dilution zone/transition duct grid

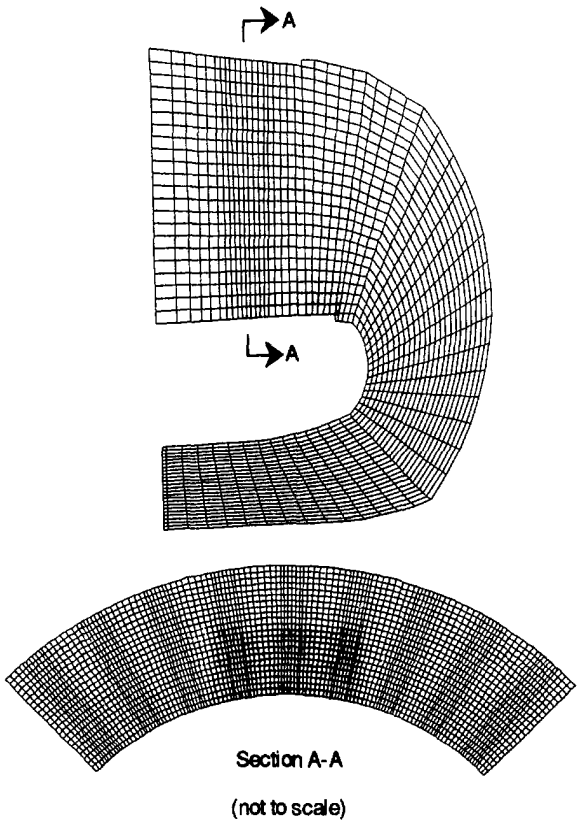

Fig. 5(c) Three nozzle sector dilution zone/transition duct grid

jets were modeled with a 3 × 3 square mesh. The transverse boundaries were assumed to be periodic and the exit boundary was assumed to be fixed pressure.

Dilution Zone/Transition Duct Models. Three models beginning upstream of the dilution jets and ending at the turbine inlet guide vanes were used in this study:

1 a 30 deg single nozzle sector model with 95,992 cells (71 × 26 × 52);
2 a small sector model that included just one dilution jet on the inner and outer liner with 128,700 cells (99 × 26 × 50); and
3 a 90 deg three nozzle sector model with 178,416 cells (59 × 24 × 126).

A typical grid for each of the dilution zone/transition duct models is shown in Fig. 5. The grid was changed slightly for each run to accommodate various dilution hole configurations; however, an approximately constant overall grid resolution was maintained for each model.

The mainstream inlet boundary conditions for each of these models were taken from the appropriate axial location of the primary zone model. All pertinent variables including the velocity components, turbulence parameters, enthalpy, density, and temperature were applied as a function of r and θ at the dilution zone inlet. Axial velocities at the primary zone exit were all positive, thus preventing feedback of information from the dilution zone to the primary zone. This justified the use of two separate models for the two regions of flow. As further demonstration, two coarse grid cases of the entire combustor were run with different dilution hole configurations and no variation in the primary zone region was found. Dividing the problem into separate zones provided large savings in computer time. The mainstream inlet composition was a mixture of air and combustion products and was assumed to be constant over the dilution zone inlet. The flow was assumed to be nonreacting, since the fuel was entirely consumed in the primary zone.

The dilution holes were modeled with a square mesh. Holdeman (1987b) has shown that square holes are a good approximation of circular holes with equivalent flow area. The holes were modeled with at least a 4 × 4 cell mesh. The

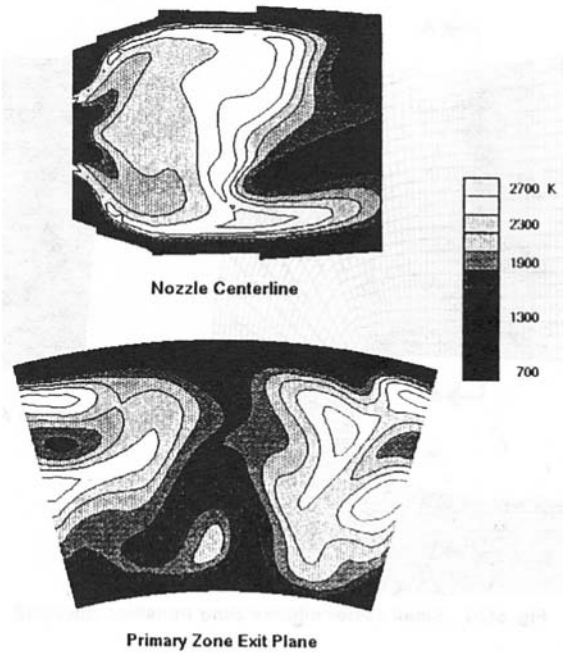

Fig. 6 Primary zone temperature contours

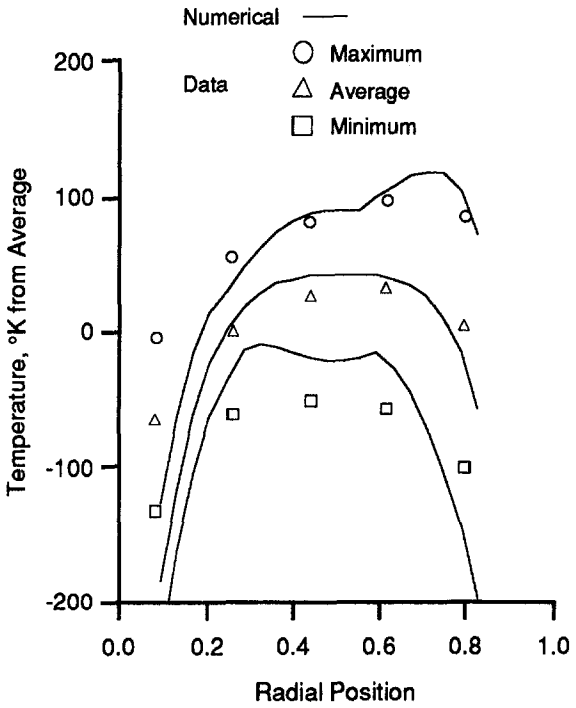

Fig. 7 Radial temperature profile at the turbine inlet plane baseline numerical result and experimental data

small sector model used a 16 × 16 cell mesh. Again, the grid resolution was maintained as constant as possible (the number of cells in the dilution holes was adjusted based on the hole size) for each model. The area of the holes was assumed to be the actual area times the discharge coefficient. The composition of the dilution jets was assumed to be that of air and the properties of the jets were assumed to be uniform across the jet inlet. The jet properties were:

temperature	= 717 K
density	= 7.72 kg/m^3
turbulent intensity (v/V)	= 3 percent
turbulent length scale (l_t/D_h)	= 0.03

The jet velocity was 101 m/s from the outer liner and 85 m/s from the inner liner. The difference in velocities was the result of pressure loss in the outer annulus. The corresponding momentum flux ratio was 191 and 136 for the outer and inner liner, respectively. The dilution air mass flow was 20 percent of the total combustor air flow.

The combustor cooling and transition liner cooling were included in the models. The transition liner cooling was particularly significant since it was approximately 13 percent of the total combustor airflow. The transverse boundaries were assumed to be periodic and the exit boundary was assumed to be fixed pressure.

Convergence/Run Times. The summation of error residuals for all variables was reduced at least four orders of magnitude. The cases were run on a dedicated Silicon Graphics Iris Workstation (4D/35TG) with 128 megabytes of ram memory. Typical run time for the largest model (178,416 cells) was 48 CPU hours.

Results/Discussion

Primary Zone Model. A solution for the primary zone was obtained for the purpose of providing mainstream inlet boundary conditions for the dilution zone models. Temperature contours on an axial plane through the nozzle centerline and at the primary zone exit plane (dilution zone inlet plane) are shown in Fig. 6. Although the fuel is entirely burned in the primary zone, the conditions at the primary zone exit are highly nonuniform. This nonuniformity plays an important role in the prediction and control of pattern factor.

Dilution Zone/Transition Duct Models. Three dilution zone/transition duct models were used in the analyses discussed in the following paragraphs. Insights gained from the results of the single nozzle sector and small sector models concerning large-scale circumferential temperature variations led to the three nozzle sector model. Parametric analyses of the angled jet configuration (Fig. 3) were performed using the three nozzle sector model.

Single Nozzle Sector Model. The baseline dilution hole configuration consisted of opposed in-line holes (4 holes/liner/nozzle). The diameter of the inner and outer holes was 0.12 and 0.17 in., respectively. An additional row of 0.10-in.-dia holes (12 holes/liner/nozzle) was located upstream of the dilution holes on the outer liner. The mass flow split was 80 percent outer liner/20 percent inner liner. The baseline configuration was developed through a series of experimental tests in the mid-1980s, and gave a pattern factor of approximately 0.16. Computations of the baseline configuration resulted in a pattern factor of 0.162. The close agreement with the experimental value was fortuitous, however, in that the experimental value was for the full 360 deg combustor while the numerical value is for a 30 deg sector. Comparison of the baseline experimental and computed radial temperature profiles at the turbine inlet plane are shown in Fig. 7.

After calculating the baseline case, parametric cases were run for

1 circumferentially inline and staggered hole arrangements;
2 outer/inner liner flow split; and
3 jet inlet turbulent intensity.

The single nozzle sector cases are listed in Table 1. The in-line arrangement was not an effective mixer for the hole spacings tested. The optimum hole spacing from Eq. (2) for inline holes would require 11 holes/nozzle on the inner liner and 19 holes/nozzle on the outer liner. Such a close hole spacing approaches a two-dimensional slot, which has been shown to be a poor mixer (Srinivasan et al., 1984). For the

Table 1 Single nozzle sector numerical test cases

CASE	NUMBER HOLES PER LINER PER NOZZLE	HOLE ORIENTATION	FLOW SPLIT (OUTER/INNER)	TURBULENT INTENSITY (v'/V)	PATTERN FACTOR
1	Baseline	Inline	80/20	0.03	0.162
2	2	Inline	50/50	0.03	0.235
3	3	Inline	50/50	0.03	0.227
4	4	Inline	50/50	0.03	0.211
5	8	Inline	50/50	0.03	0.222
6	2	Staggered	50/50	0.03	0.203
7	3	Staggered	50/50	0.03	0.133
8	4	Staggered	50/50	0.03	0.132
9	3	Staggered	40/60	0.03	0.137
10	3	Staggered	30/70	0.03	0.139
11	4	Staggered	40/60	0.03	0.128
12	4	Staggered	30/70	0.03	0.133
13	4	Inline	50/50	0.20	0.179
14	4	Staggered	50/50	0.20	0.131

staggered arrangement, the optimum hole spacing (based on Eq. (2)) requires 3 holes/nozzle on the inner liner and 4 holes/nozzle on the outer liner. The pattern factors of the 3 and 4 hole/liner/nozzle cases were 0.133 and 0.132, respectively. This compares with a pattern factor of 0.203 for the off-optimum staggered hole case of 2 holes/liner/nozzle.

The liner flow split and the jet inlet turbulent intensity were both varied for the staggered hole arrangement with very little effect on pattern factor. The increased jet inlet turbulence resulted in a substantial improvement in pattern factor for the poorly mixed in-line case, but had negligible effect on the relatively well-mixed staggered case. The implication is that the staggered cases were approaching a lower limit pattern factor of slightly less than 0.13 for conventional dilution hole configurations.

Small Sector Model. This model consisted of a periodic sector with one dilution hole on the outer liner and one dilution hole on the inner liner. The actual size of the sector depended on the hole spacing. The small sector size made finer grid resolution possible. The mainstream inlet boundary conditions were taken from the primary zone model as before, except that an appropriately smaller section was used. The results for the baseline dilution hole configuration and several cases repeated from the 30 deg sector model are shown in Table 2.

The pattern factor for the baseline configuration was 0.077 for the small sector model, which compares with 0.162 for the 30 deg sector model. The same result of 0.077 was obtained for the 4 staggered holes/liner/nozzle case. The poor mixing in-line case had a higher pattern factor of 0.102. A slightly higher pattern factor of 0.090 was obtained for the two 3 holes/liner/nozzle cases shown in Table 2. It appeared that the pattern factor was a strong function of the sector size. The 4 staggered holes/liner/nozzle (Case 17) was run with the small sector model, but with dilution hole configuration and grid resolution identical to Case 8, which was run with the 30 deg sector model. Comparison of Cases 8 and 17 confirmed that the pattern factor dependence was related to the sector size and not the grid resolution.

The reduction in pattern factor for the small sector model was apparently the result of decreased inlet circumferential temperature variation. Radial and small-scale circumferential variations were effectively mixed in the relatively long mixing length available in reverse flow combustors. The pattern factor for an optimized conventional dilution hole configuration approached a minimum as the sector size decreased. This minimum value of about 0.075 for the F109 combustor

Table 2 Small sector numerical test cases

CASE	NUMBER HOLES PER LINER PER NOZZLE	HOLE ORIENTATION	FLOW SPLIT (OUTER/INNER)	TURBULENT INSTENSITY (v'/V)	SECTOR SIZE (DEG.)	PATTERN FACTOR
15	Baseline	Inline	50/50	0.03	7.5	0.077
16	4	Staggered	50/50	0.03	7.5	0.077
17	4 (same grid resolution as Case 8)	Staggered	50/50	0.03	7.5	0.081
18	4	Inline	50/50	0.03	7.5	0.102
19	3	Staggered	50/50	0.03	10.0	0.090
20	3	45° slanted slot	50/50	0.03	10.0	0.090

was driven by the transition liner cooling. Recall that the transition liner cooling flow was 13 percent of the total combustor airflow. The models above consider only circumferential temperature variations within a single nozzle sector. Variations between nozzles, however, are probably equally important in determining pattern factor, if not more so, as illustrated by Fig. 2. It became obvious that large-scale circumferential mixing was needed, leading to the formulation of the three nozzle sector model.

Three Nozzle Sector Model. Analysis of mixing over large circumferential scales required a multinozzle sector model. A 90 deg three nozzle sector model was selected with the nozzles flowing at 90, 100, and 110 percent of design fuel flow, (100 percent design fuel flow had been assumed for the single nozzle sector model.) The mainstream inlet boundary conditions were taken from the primary zone model as before. Temperature contours of the inlet plane are shown in Fig. 8. Although these inlet boundary conditions were devised in a rather arbitrary manner, they provided a good basis for evaluating dilution hole configurations designed to enhance large-scale circumferential mixing.

The advanced dilution hole concept that was selected for analysis consisted of dilution jets injected with a high circumferential angle as shown in Fig. 3. Parametric cases run with the three nozzle sector model are shown in Table 3. The jet angle is defined such that 90 deg indicates jets normal to the injection wall (with only a radial component) and 0 deg indicates jets tangent to the liner in the circumferential direction. All of the angled jet parametric cases (Cases 24–40) were for in-line holes. However, the difference between in-line and staggered configurations is (probably) not significant for the low jet angle configurations modeled in Cases 24–40.

The baseline configuration (Case 21) had a pattern factor of 0.204 and the 3 staggered holes/liner/nozzle with 90 deg jets (Case 22) had a pattern factor of 0.201. Temperature contours for the baseline configuration are shown in Fig. 9. Cases 21 and 22 can be compared with Cases 1 and 7, respectively, in Table 1. The higher pattern factors in Cases 21 and 22 are apparently the result of increased inlet circumferential variation. Case 23, with a pattern factor of 0.142, was the same configuration as Case 22 except that design fuel flow was applied to all three nozzles. The lower pattern factor for Case 23 clearly demonstrated the effect of nozzle to nozzle variations. Case 7 and Case 23, each with 3 holes/liner/nozzle, had similar pattern factors of 0.133 and 0.142, respectively. This demonstrated consistency between the single nozzle sector model and the three nozzle sector model even though the three nozzle sector model had slightly lower grid resolution.

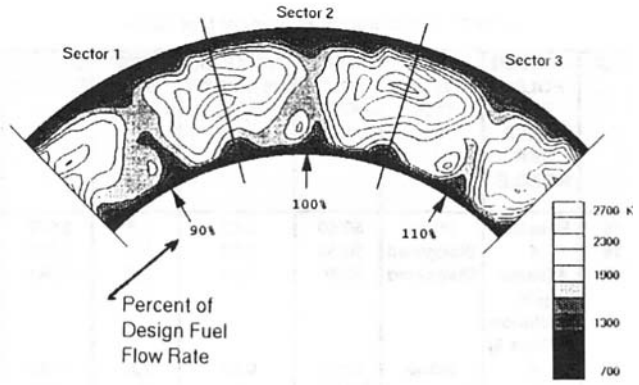

Fig. 8 Three nozzle sector model mainstream inlet temperatures

Table 3 Three nozzle sector numerical test cases

CASE	NUMBER HOLES PER LINER PER NOZZLE	HOLE ORIENTATION	JET ANGLE		FLOW SPLIT (OUTER/INNER)	PATTERN FACTOR
			OUTER	INNER		
21	Baseline	Inline	90	90	80/20	0.204
22	3	Staggered	90	90	50/50	0.201
23	Same as Case 22 with design fuel flow in all nozzles					0.142
24	1	Inline	30	30	50/50	0.230
25	2	Inline	30	30	50/50	0.219
26	3	Inline	30	30	50/50	0.120
27	3	Inline	15	15	50/50	0.090
28	4	Inline	30	30	50/50	0.149
29	6	Inline	30	30	50/50	0.143
30	2-D slots	Inline	30	30	50/50	0.161
31	3	Inline	15	30	50/50	0.083
32	3	Inline	22.5	30	50/50	0.092
33	3	Inline	45	30	50/50	0.163
34	3	Inline	15	22.5	50/50	0.086
35	3	Inline	15	37.5	50/50	0.095
36	3	Inline	15	45	50/50	0.120
37	3	Inline	15	30	30/70	0.143
38	3	Inline	15	30	40/60	0.100
39	3	Inline	15	30	60/40	0.074
40	3	Inline	15	30	70/30	0.075

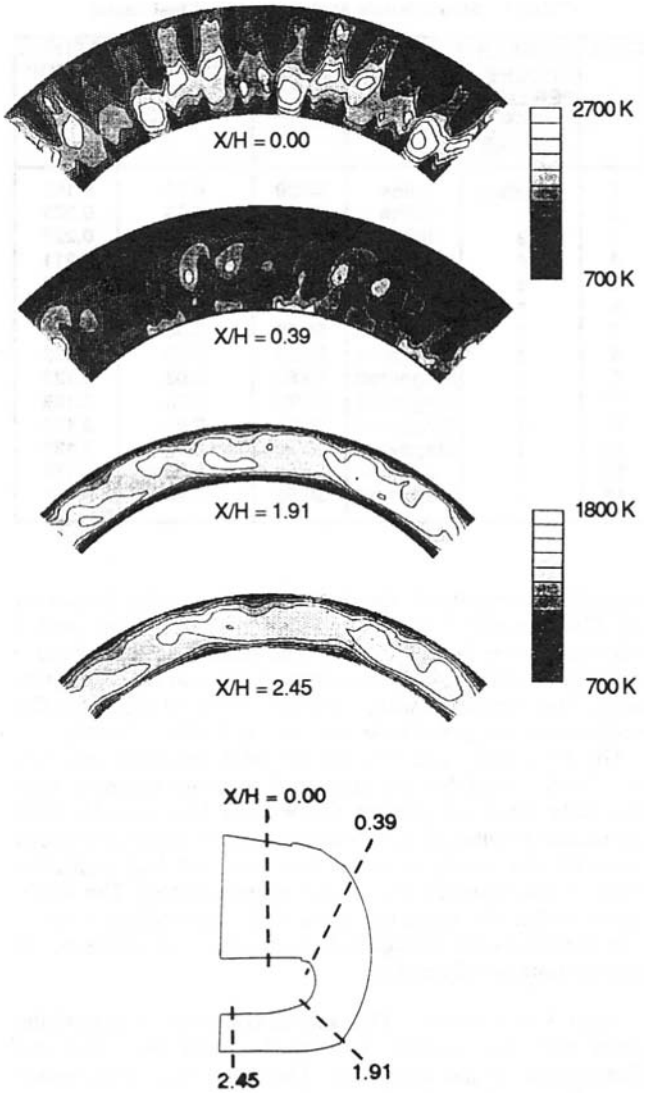

Fig. 9 Temperature contours for the baseline dilution hole configuration case 21

Parametric analyses of angled jet configurations were run for the following design variables:

1 number of holes/liner/nozzle;
2 outer liner jet angle;
3 inner liner jet angle; and
4 outer/inner liner mass flow split.

In the first parametric study, the jet angle was held constant at 30 deg for each liner and the flow split was 50/50. The pattern factor as a function of the number of holes/liner/nozzle is shown in Fig. 10 (Cases 24–26, 28–30). The best pattern factor of 0.120, which occurred for the 3 holes/liner/nozzle case (Case 26), was a substantial improvement compared to the baseline. Temperature contours for Case 26 are shown in Fig. 11. The 1 or 2 holes/liner/nozzle cases had a substantially higher pattern factor because an excessive amount of the mainstream could flow between the dilution jets, resulting in poor circumferential mixing.

In the second parametric study, the effect of outer liner jet angle was ascertained by maintaining the inner jet angle at 30 deg and a mass flow split of 50/50, while varying the outer liner jet angle. The pattern factor as a function of outer liner jet angle is shown in Fig. 12 (Cases 26, 31–33). The best case (Case 31) occurred for the minimum jet angle, with a pattern factor of 0.083. Temperature contours for Case 31 are shown in Fig. 13. Case 31 produced a significant reduction (60 percent) in the pattern factor compared to the baseline dilution hole configuration. Lower jet angles may result in even lower pattern factor, but angles less than 15 deg are probably not practical for fabrication in an actual combustor.

Figure 14 (Cases 27, 31, 34–36) shows the results of the third parametric study. In this figure, a plot of pattern factor is presented as a function of inner liner jet angle with the outer liner jet angle fixed at 15 deg and mass flow split held constant at 50/50. The optimum inner liner angle is 30 deg, although the influence of the inner liner jet angle was not as significant as the outer liner jet angle.

The final parametric study investigated the effect of liner mass flow split. The outer and inner liner jet angles were fixed at 15 and 30 deg, respectively. Pattern factor as a function of flow split is shown in Fig. 15 (Cases 31, 37–40). There was a slight improvement in pattern factor when the flow from the outer liner was increased above 50 percent. The most important influence of mass flow split, however, appeared to be on the radial profile as shown in Fig. 16. Increasing the outer liner mass flow had the effect of moving the peak radial average temperature to a larger radius.

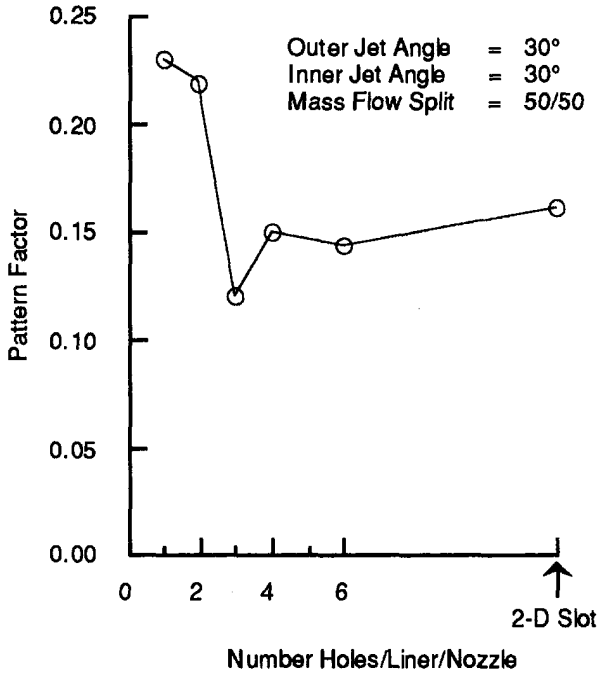

Fig. 10 Pattern factor as a function of number of holes / liner / nozzle

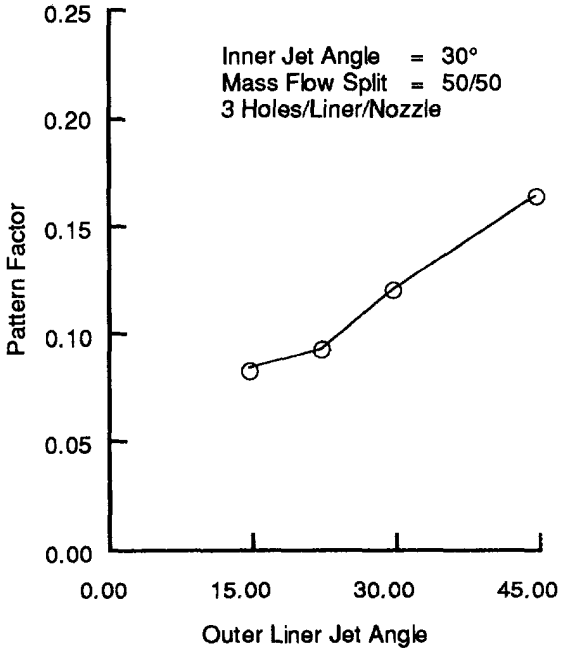

Fig. 12 Pattern factor as a function of outer liner jet angle

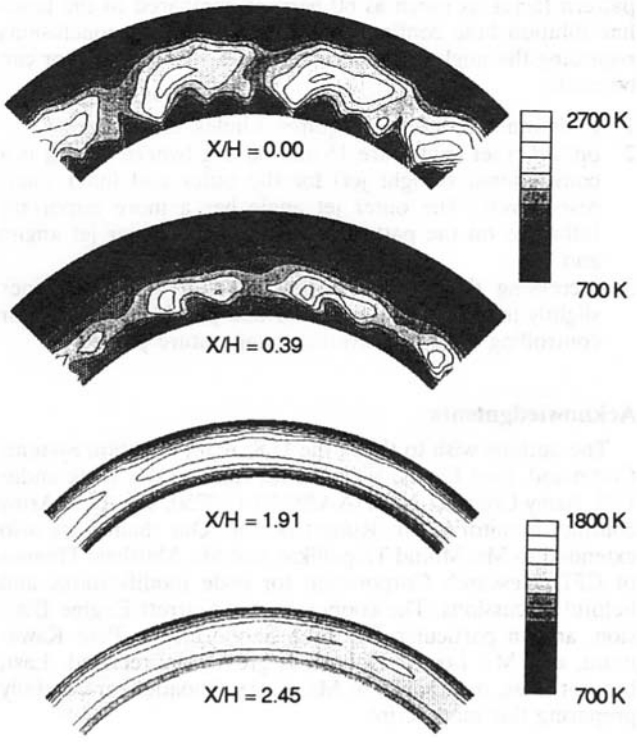

(See Figure 9 for X/H locations)

Fig. 11 Temperature contours for case 26

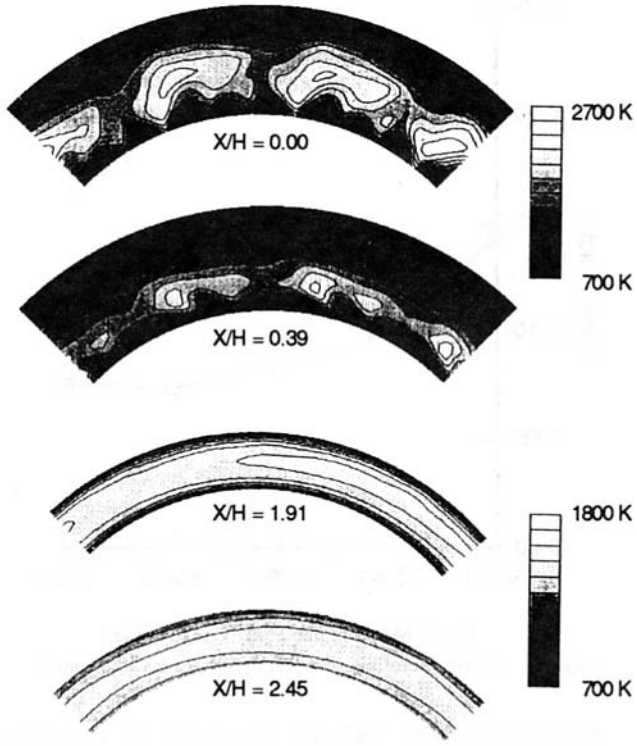

(See Figure 9 for X/H locations)

Fig. 13 Temperature contours for case 31

Numerical tests of the circumferentially angled dilution hole concept clearly indicated the potential for substantial pattern factor reduction. Some observations concerning the effects of angled jets in the F109 reverse flow combustor can now be made:

1 Radial momentum and radial mixing was sacrificed in favor of increased circumferential momentum and circumferential mixing.

2 Most of the circumferential momentum of the jets was converted to turbulent kinetic energy. In the absence of viscous forces, conservation of momentum requires that circumferential velocities approximately double through the transition duct because of the decrease of radius. However, the circumferential velocities actually decreased by a factor of more than two because of the high circumferential gradient from the inner to the outer liner. The

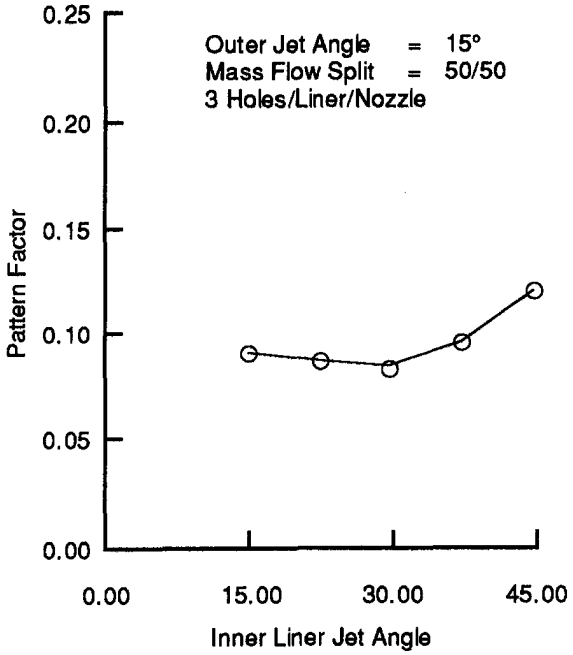

Fig. 14 Pattern factor as a function of inner liner jet angle

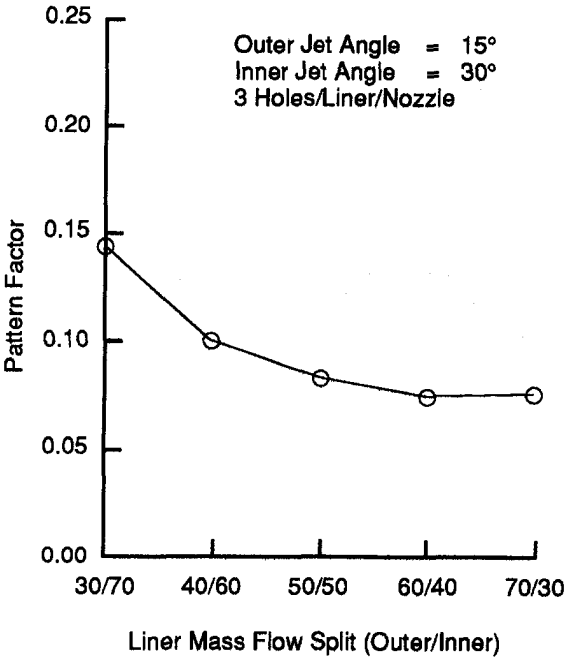

Fig. 15 Pattern factor as a function of liner mass flow split

turbulent viscosity levels for the angled jet case were almost an order of magnitude higher than for the baseline case.

3 Radial mixing was adequate because of the combined effect of the high turbulent viscosity and the long mixing length (X/H = 2.45).

Conclusions

Numerical tests using three-dimensional CFD models have been performed to analyze an advanced dilution hole concept for small reverse flow combustors. The specific geometry and flow conditions analyzed in this study were that of Garrett's F109 combustor. The advanced dilution hole concept consisted of injecting the dilution air jets with a high circumferential component. The results of the numerical

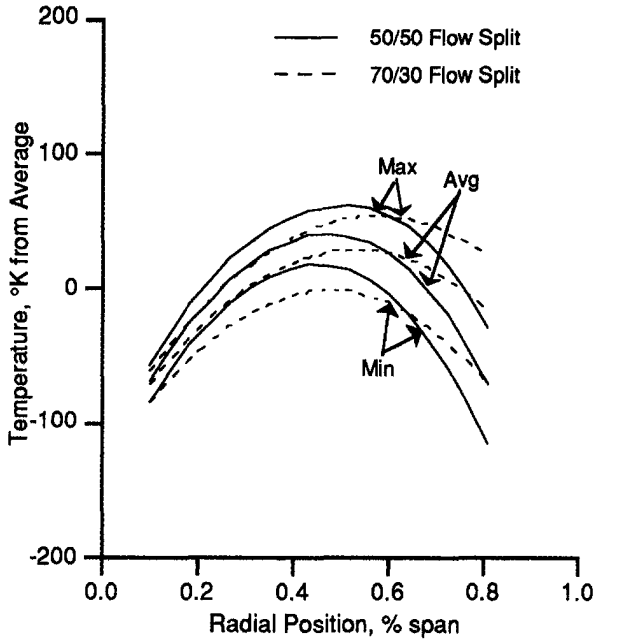

Fig. 16 Radial temperature profile at the turbine inlet plane for 50/50 and 70/30 mass flow

tests showed that this concept has the potential for reducing pattern factor as much as 60 percent compared to the baseline dilution hole configuration. Several specific conclusions regarding the angled jet concept for the F109 combustor can be made:

1 optimum hole spacing requires 3 holes/liner/nozzle;
2 optimum jet angles are 15 and 30 deg (where 90 deg is a conventional straight jet) for the outer and inner liner, respectively. The outer jet angle has a more important influence on the pattern factor than the inner jet angle; and
3 increasing the mass flow percent from the outer liner slightly improves pattern factor and provides a means for controlling the radial average temperature profile.

Acknowledgments

The authors wish to thank the U.S. Army Aviation Systems Command, Fort Eustis, Virginia, for funding this work under U.S. Army Contract No. DAAJ02-91-C-0050. The U.S. Army contract monitor is Mr. Robert Bolton. Our thanks are also extended to Mr. Milind Talpallikar and Mr. Matthew Thomas of CFD Research Corporation for code modifications and helpful discussions. The cooperation of Garrett Engine Division, and in particular Dr. John Sanborn, Mr. Pete Kawamura, and Mr. Lowell Hollars, is greatly appreciated. Last, but not least, our thanks to Ms. Kathy Rhoades for carefully preparing this manuscript.

References

Avva, R. K., Smith, C. E., and Singhal, A. K., 1990, "Comparative Study of High and Low Reynolds Number Versions of $k-\epsilon$ Models," Paper No. AIAA-90-0246.

Chen, Y. S., and Kim, S. W., 1987, "Computation of Turbulent Flows Using an Extended $k-\epsilon$ Turbulence Closure Model," NASA CR-179204.

Chien, K. Y., 1985, "Predictions of Channel and Boundary-Layer Flows With a Low-Reynolds-Number Turbulence Model," *AIAA Journal*, Vol. 23, No. 2.

Holdeman, J. D., and Srinivasan, R., 1986, "Modeling Dilution Jet Flowfields," *Journal of Propulsion and Power*, Vol. 2, No. 1, pp. 4–10.

Holdeman, J. D., Reynolds, R., and White, C., 1987a, "A Numerical Study of the Effects of Curvature and Convergence on Dilution Jet Mixing," Paper No. AIAA-87-1953.

Holdeman, J. D., Srinivasan, R., Coleman, E. B., Meyers, G. D., and White, C. D., 1987b, "Effects of Multiple Rows and Noncircular Orifices on Dilution Jet Mixing," *Journal of Propulsion and Power*, Vol. 3, No. 3, pp. 219–226.

Holdeman, J. D., Srinivasan, R., and White, C. D., 1988, "An Empirical Model of the Effects of Curvature and Convergence on Dilution Jet Mixing," Paper No. AIAA-88-3180.

Holdeman, J. D., 1991, "Mixing of Multiple Jets With a Confined Subsonic Crossflow—Summary of NASA Supported Experiments and Modeling," NASA TM-104412; Paper No. AIAA-91-2458.

Kim, S. W., and Chen, C. P., 1988, "A Multiple Time Scale Turbulence Model Based on Variable Partitioning of Turbulence Kinetic Energy Spectrum," Paper No. AIAA-88-1771.

Launder, B. E., and Spalding, D. B., 1974, "The Numerical Computation of Turbulent Flows," *Computer Methods in Applied Mechanics and Engineering*, Vol. 3, pp. 269–289.

Owens, S. F., 1992, "CFD-ACE: Command Language Reference Manual," CFD Research Corporation, Huntsville, AL, CFDRC Report GR-92-6.

Reynolds, R., and White, C., 1986, "Transition Mixing Study Final Report," NASA CR-175062.

Smith, C. E., Ratcliff, M. L., Przekwas, A. J., and Habchi, S. D., 1989, "Validation of an Advanced Turbulent Combustion Code: REFLEQS," presented at the 7th SSME CFD Workshop, NASA MSFC.

Smith, C. E., 1990, "Mixing Characteristics of Dilution Jets in Small Gas Turbine Combustors," Paper No. AIAA-90-2728.

Srinivasan, R., Berenfeld, A., and Mongia, H. C., 1982, "Dilution Jet Mixing Program—Phase I Report," NASA CR-168031.

Srinivasan, R., Coleman, E., and Johnson, K., 1984, "Dilution Jet Mixing Program—Phase II Report," NASA CR-174624.

Srinivasan, R., Myers, G., Coleman, E., and White, C., 1985, "Dilution Jet Mixing Program—Phase III Report, NASA CR-174884.

Influence of Hardware Design on the Flow Field Structures and the Patterns of Droplet Dispersion: Part I—Mean Quantities

H. Y. Wang

V. G. McDonell

S. Samuelsen

UCI Combustion Laboratory,
University of California,
Irvine, CA 92715-3550

In a gas turbine engine combustor, performance is likely tied to the spatial distribution of the fuel injected into the dome. The GE/SNECMA CFM56 combustor swirl cup is one example of a design established to provide a uniform presentation of droplets to the dome. The present study is part of a series to detail the dispersion of droplets in practical hardware, and to assess the effect of isolated parameters on the continuous- and dispersed-phase distributions. In this study, the influence of the swirling air outlet geometry is evaluated relative to the effect on the flow field structures and the patterns of droplet dispersion. This is accomplished by comparing the continuous-phase (air in the presence of a spray) and dispersed-phase (droplets) behavior downstream of the swirl cup assembly outfitted with two different conical expansions ("flares"). One features a narrow expansion angle, the other possesses a wide expansion angle. Two-component phase-Doppler interferometry was employed to provide the information of droplet size and velocity components as well as continuous-phase velocity components. Photographs of light scattered by droplets from a laser sheet were used for the study of flow field structures. This study reveals that (1) the air stream issued from the narrow flare remains close to the centerline and expands gradually downstream while the air stream issued from the wide flare expands immediately downstream of the swirl cup, and (2) the narrow flare provides weaker droplet dispersion, slower decay of droplet velocities, and finer droplet sizes compared to the wide flare. The results demonstrate that a relatively modest change in flare geometry can create a significant change in the structure of both the continuous and dispersed phases.

Introduction

Gas turbine engine combustors employ various types of swirl in order to provide reaction stability and high combustion efficiency over a whole range of operating conditions. One design approach is the GE/SNECMA CFM56 gas turbine engine.

A typical CFM56 gas turbine engine combustor swirl cup assembly is shown in Fig. 1. A simplex atomizer is mounted in the center of the swirl cup. Two air streams enter the swirl cup while rotating in opposite directions. Looking at the entry to the swirl cup from upstream, the primary air rotates clockwise while the secondary air rotates counterclockwise. The two air streams are separated by a venturi and a flare is used to provide expansion of the mixed air streams.

During operation of the spray, part of the droplets injected from the atomizer move directly downstream while the others first impinge onto the inner surface of the venturi, form a thin liquid film, and then re-atomize due to the shearing between the counterrotating air streams. Although complex in design, significantly more uniform droplet size and dispersion is achieved in contrast to using the atomizer alone (Wang et al., 1992a).

As specifications for improved performance, reduced emissions, and still lighter, more compact combustors become necessary, detailed understanding of the physics that govern fuel–air mixing is required in order to develop cost-effective designs in a timely fashion. To this end, a systematic study of the single- and two-phase flow fields downstream of the swirl cup is being conducted by the UCI Combustion Laboratory. For example, the characterization of the two-phase flow field downstream of both a production and a 3 × -scale model swirl cup has been completed (Wang et al., 1992b, 1992c). These two studies provide data that can be used for development of numerical models (e.g., Tolpadi et al., 1992) and reveal needed insight into the physics of the droplet dispersion. In another study, two geometrically scaled test articles have been used to examine the extent to which scaling of the

Contributed by the International Gas Turbine Institute and presented at the 38th International Gas Turbine and Aeroengine Congress and Exposition, Cincinnati, Ohio, May 24–27, 1993. Manuscript received at ASME Headquarters March 1, 1993. Paper No. 93-GT-199. Associate Technical Editor: H. Lukas.

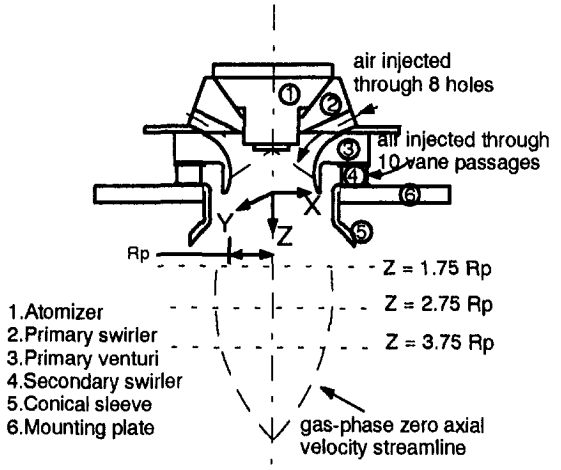

Fig. 1 Sketch of swirl cup assembly

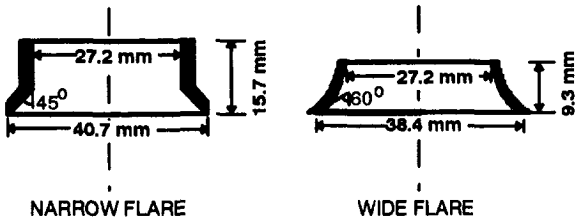

Fig. 2 Schematic of flares

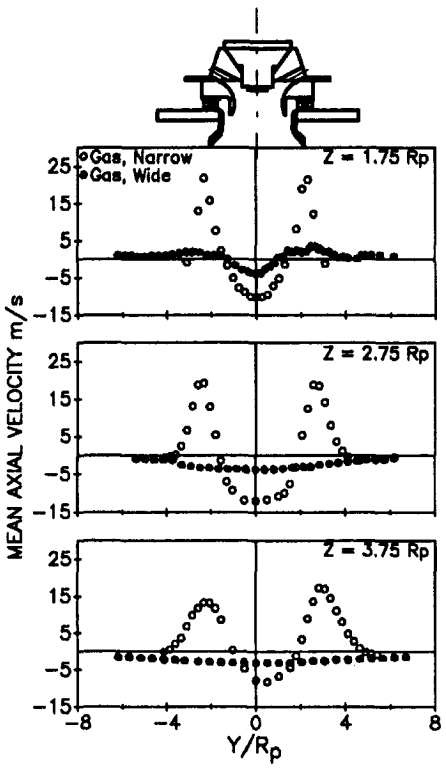

Fig. 3 Continuous phase mean axial velocity

continuous-phase and droplet dispersion can be carried out (Wang et al., 1992d). It was found that the continuous phase scaled reasonably well, but that scaling of the droplet dispersion was much more complicated due to the difficulty in accounting for the different time scales in the two flows.

The present study is the second in a series to focus on the impact of isolated parameters on the continuous and dispersed phase distributions. The first experiment examined the impact of atomizer spray angle (Wang et al., 1992a) and found that, for the particular operating condition considered, spray angle has little impact on the distribution of the droplets. The reason is that, for the condition considered, the continuous-phase dominates the droplet behavior.

The objectives of the present study were to evaluate the influence of flare sleeve geometry on (1) the continuous-phase flow field (i.e., large structures such as recirculation zone) and (2) the droplet dispersion pattern. Two different flares of expansion angles 90 deg (narrow) and 120 deg (wide), respectively, were employed. As shown in Fig. 2, the wide flare is shorter than the narrow flare. During the tests with these two different flares, the liquid and air flow rates were kept the same so that the change in the two-phase flow field could be attributed to the change in the hardware.

Experiment

Facility and Diagnostics. Details regarding the geometry of the swirl cup are shown in Figure 1. The radius of the exit of the primary venturi, *Rp*, is 9.7 mm. A 90 deg spray angle Hago simplex atomizer of flow number 0.65, which is based on ratio of flow rate (lb/hr) to square root of injection pressure differential (lb/in^2), was used in the tests with both flares.

A two-component PDPA (Aerometrics Model 3100-S) was used to measure continuous-phase velocities, droplet size, and droplet velocities. The PDPA used was calibrated by measuring monodispersed droplet streams. The repeatability of the measurement was examined several times during the testing to ensure that no significant change to the flow field occurred. As suggested by the manufacturer, the absolute errors in measurement of individual events are within ± 0.1 m/s for velocity and about the width of a bin for size (3–4 μm herein). The details of the swirl cup assembly, the characterization chamber, and PDPA setup, are provided by Wang et al. (1992b). A Spectra-Physics Ar^+ Model 2016 laser was run at about 3 W to provide illumination for laser sheet-lit photography.

A TSI six-jet atomizer Model No. 9306 was used to provide seeding for the measurement of the continuous-phase velocity (continuous-phase velocities were obtained using the statistics from the droplets with diameters smaller than 4.17 μm), and the continuous-phase and droplet velocities were measured separately.

Test Condition and Sample Points. During the tests with each flare, the air and liquid flow rates were kept constant. The air flow rate was 17 g/s (30.2 scfm) with a pressure drop across the swirl cup approximately 330 mm H_2O. Water was used to simulate the fuel at a flow rate of 0.86 g/s (0.82 gph). This gives a similar percentage of liquid in the dome region (about 6.5 percent) as a combustor firing kerosene types of fuel at nearly stoichiometric ratio. All tests were conducted at atmospheric pressure and temperatures in the absence of confinement.

The PDPA measurements were conducted along the centerline and at three axial locations, $Z = 1.75$, 2.75, and 3.75 *Rp*. The origin of the coordinates is at the center of the exit plane of the primary venturi.

The laser sheet-lit photos were taken in the planes perpendicular and parallel to the swirl cup exit plane.

Results and Discussion

In this paper, time-averaged quantities, such as droplet distribution length mean (D_{10}) and Sauter mean diameters (D_{32}), droplet mean velocities, and continuous-phase mean velocities, are presented and discussed. Three droplet size classes are selected to represent small, medium-sized, and large droplets in this study.

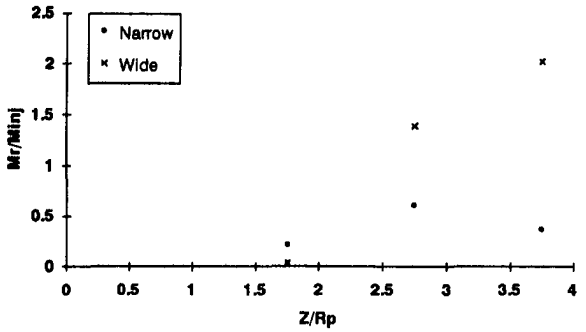

Fig. 4 Recirculation strength M_r / M_{inj}

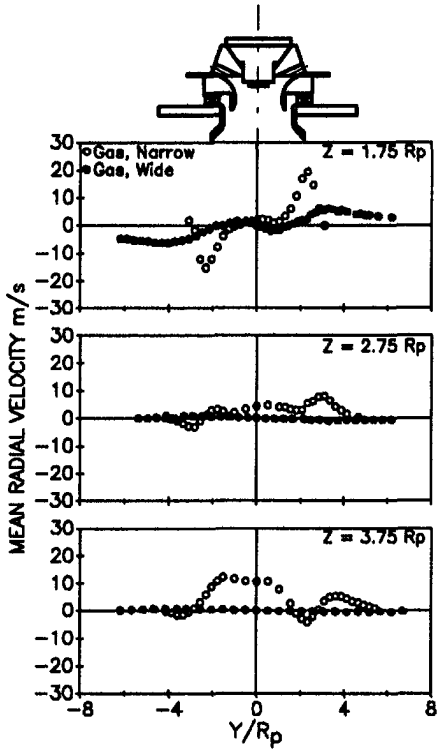

Fig. 5 Continuous phase mean radial velocities

- "Small" 11–20 μm
- "Medium-sized" 30–40 μm
- "Large" 74–88 μm

In the following, the results for the continuous phase are presented and discussed first, followed by the results for the droplets.

Continuous Phase

Mean Axial Velocity. Figure 3 compares the continuous-phase mean axial velocity. The continuous-phase mean axial velocity produced by the wide flare dissipates faster than that produced by the narrow flare. The wide flare produces a wide region of relatively low recirculating velocity, compared to a narrow region of high recirculating velocity produced by the narrow flare. The rapid expansion of the swirling air in the case of the wide flare causes the continuous-phase axial velocity dissipate rapidly in the axial direction. Eight *Rp* or farther away from the centerline, the positive axial velocity observed with the wide flare was moderate. Due to the low sample rate and hence the long sampling time required, detailed data were not acquired in this region.

In order to quantify the difference in recirculation strength, the radial profiles were integrated for each case. The results are presented in Fig. 4 as a function of distance from the swirl cup. Interestingly, the wide flare results in less mass recirculated near the exit of the swirl cup compared to the narrow flare. With increased distance from the swirl cup, however, the wide flare results in much greater mass recircu-

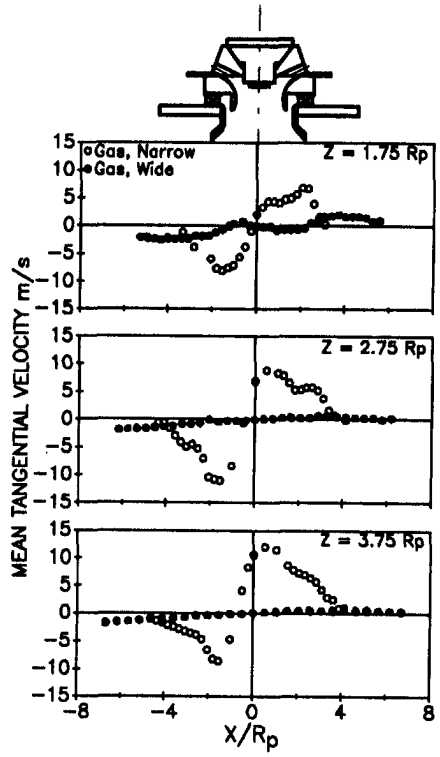

Fig. 6 Continuous phase mean tangential velocities

a) Narrow Flare

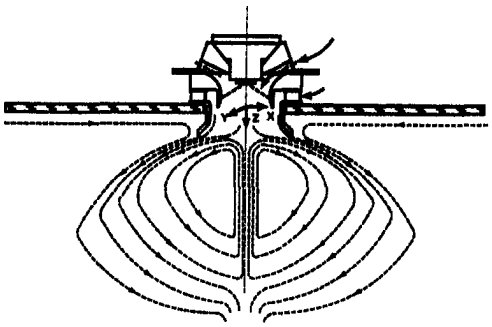

b) Wide Flare

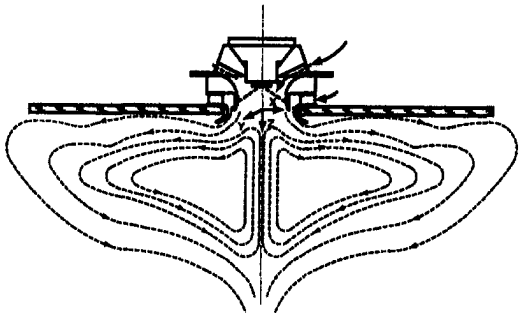

Fig. 7 Interpretation of the continuous-phase flow field structures

a) Narrow Flare

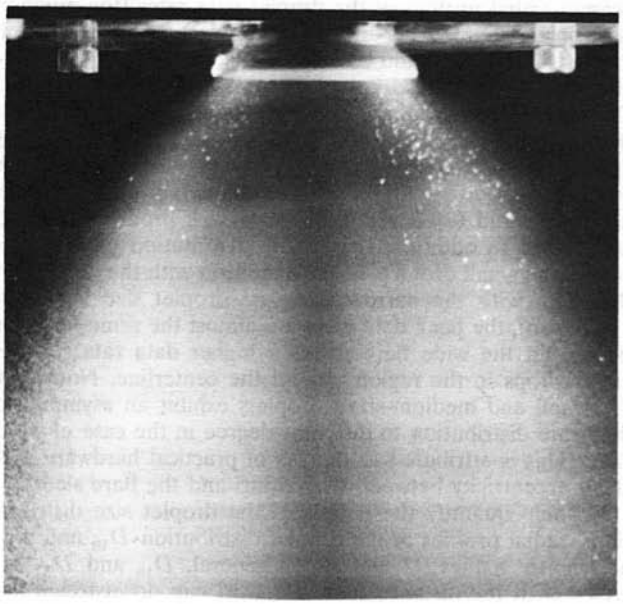

b) Wide Flare

Fig. 8 Laser sheet-lit photos in vertical plane

a) Narrow Flare

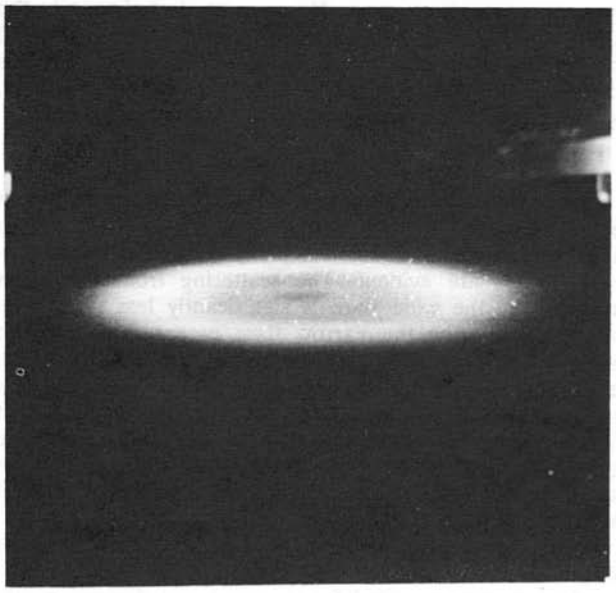

b) Wide Flare

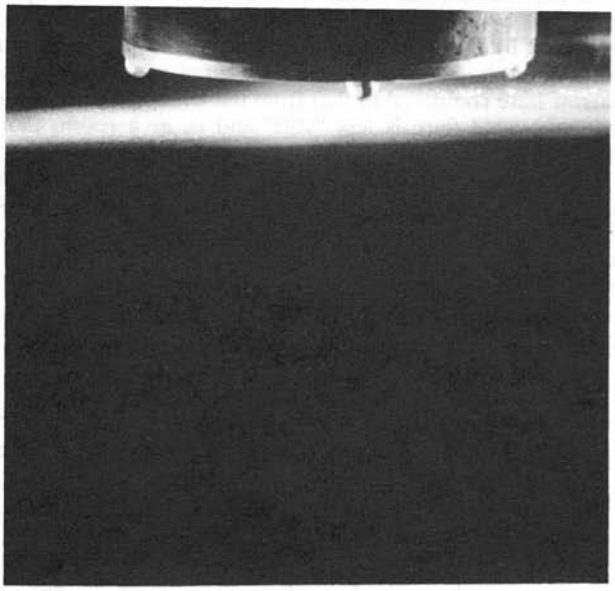

Fig. 9 Laser sheet-lit photos in the horizontal plane

lated and, in fact, shows that substantial air from the surroundings is swept into the recirculation zone (i.e., the recirculated mass exceeds that injected).

Mean Radial Velocity. Figure 5 presents the comparison of the mean radial velocities. The positive values on the $+Y$ side and the negative values on the $-Y$ side are defined as the velocity radially outward. The continuous-phase mean radial velocity of the wide flare, similar to the mean axial velocity, is smaller than that of the narrow flare. It dissipates rapidly downstream. At $Z = 1.75$ Rp, the wide flare produces flow away from the centerline except in regions close to the centerline in which the flow contracts slightly. From $Z = 2.75$ Rp downstream, the mean radial velocity of the wide flare is almost zero and shows slight contraction toward the centerline because the flow is dominated by recirculation.

Mean Tangential Velocity. Figure 6 presents the comparison of the mean tangential velocities. Clockwise rotation looking from the top of the swirl cup downstream is indicated by negative values on the $+X$ side and the positive values on the $-X$ side. The magnitude of the continuous-phase mean tangential velocity of the wide flare is smaller than that of the narrow flare as explained above as the faster expansion of the swirling air stream in the case of the wide flare, and the swirling air is counterclockwise-rotating dominated (secondary air dominated). At $Z = 1.75$ Rp and close to the centerline, the influence of the clockwise-swirling air stream is evident.

Combining the measurements of the three components of velocity, Fig. 7 presents an interpretation of the structure of the continuous-phase flow field. Instead of being bounded by a shear layer as observed with the narrow flare, the air

stream from the wide flare is restrained by the mounting plate of the swirl cup assembly. The on-axis recirculation zone remains in both cases. Hence, a modest change in the flare sleeve results in a remarkable change in the structure of the continuous phase. Given that the dispersed phase is strongly affected by the behavior of the continuous phase, significant differences for the droplets would be expected.

Dispersed Phase

Photographs. Figure 8 presents the photos that document the scattering by droplets from a sheet of laser light in the plane perpendicular to the exit plane of the swirl cup. Several features are evident. The scattering from the drops produced by the wide flare is significantly less than from those produced by the narrow flare except in the region immediately adjacent to the exit of the flare. This suggests that the wide flare provides a greater dispersion of droplets and possibly a large population of small droplets. It is evident that the flow field and the droplet dispersion from the narrow flare expands gradually downstream while those from the wide flare expand abruptly immediately downstream of the flare exit.

Figure 9 presents photographs taken with the laser sheet parallel to the exit of the swirl cup. In these photos, additional support is provided for the increased dispersion created by the wide flare. Note also a local void of scattering from the center of the spray produced by the narrow flare, which is not present in the spray produced by the wide flare. This implies that the "hollow-cone" structure of the spray produced by the narrow flare becomes "solid-cone" when produced by the wide flare. Finally, note the strong circular pattern of the scattering from the spray produced by the narrow flare compared to that from the wide flare. The spray from the wide flare is less "stiff" and is, as a result, more chaotic.

The photos reveal that, indeed, the spray is strongly affected by the flare geometry. The following sections discuss the PDPA measurements of droplet size and velocity, which add additional insight into the structure of the sprays produced by the two flares.

Droplet Data Rate and Size Comparison. In order to quantify better where droplets of a given size travel, Figs. 10(a–c) present radial profiles of the droplet data rates (the number of droplets counted per unit time interval), which represent the distribution of liquid volumetric flux qualitatively. Generally, the smaller the droplets, the greater their data rates. The narrow flare produces a higher data rate of small droplets than the wide flare (Fig. 10a). This can be attributed to two effects acting either independently or in concert with each other: (1) the dispersion of small droplets is greater with the wide flare and (2) fewer small drops are produced by the wide flare. In addition, the spatial distribution of the data rate of the small droplets is more uniform with the wide flare than that with the narrow flare. As droplet size increases (> 30 μm), the peak data rates are almost the same for both flares, but the wide flare shows a higher data rate for the larger drops in the region around the centerline. Note that the small and medium-sized droplets exhibit an asymmetric data rate distribution to different degree in the case of wide flare. This is attributed to the use of practical hardware and slight eccentricity between the venturi and the flare sleeve.

To help quantify the nature of the droplet size distributions, radial profiles of the droplet distribution D_{10} and D_{32} are shown in Figs. 11 and 12. In general, D_{10} and D_{32} increase with the distance from the swirl cup downstream for both flares. However, the wide flare produces larger and more widely dispersed droplets than the narrow flare, suggesting that the wide flare provides less efficient atomization of liquid than does the narrow flare. This also implies that the reduced data rate for the small drops for the wide flare (Fig. 10a) is due, at least in part, to a reduction in small drop production. Also note that the narrow flare produces a local maximum in size on each side of the centerline, whereas the wide flare presents a local maximum in both D_{10} and D_{32} at the centerline. This is consistent with the radial profiles of the data rate for the large drops (Fig. 10c), which reveal the same behavior.

Droplet Axial Velocity. Figure 13 presents radial profiles of the droplet mean axial velocity. As expected, the small

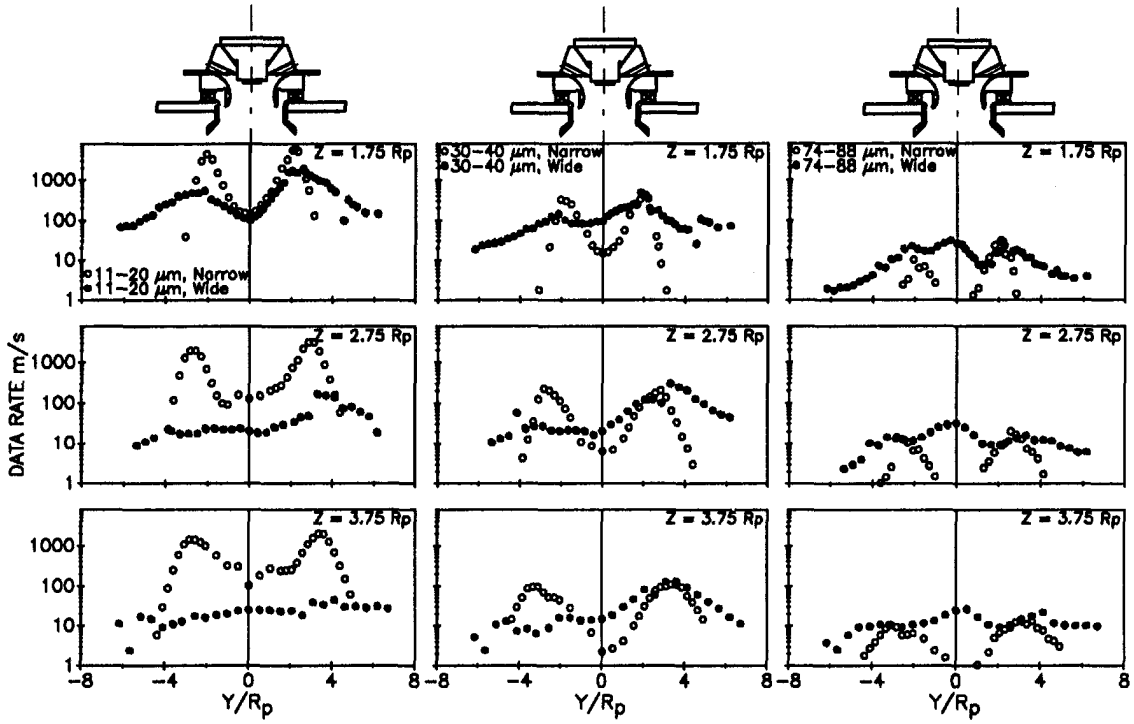

Fig. 10 Droplet data rates

droplets reflect the continuous-phase behavior more closely than do the medium-sized and large droplets with either flare (compare Figs. 3 and 13*a*). Generally, the maximum droplet velocities are greater and the velocity radial profiles are less uniform in the case of the narrow flare than those in the case of the wide flare. With the wide flare, the mean axial velocity of the medium-sized droplets, which is almost positive everywhere, is uniform in a wide region around the centerline (Fig. 13*b*). The mean axial velocity of the large droplets with the wide flare, on the other hand, shows a maximum at the centerline (Fig. 13*c*). This is attributed to (1) the rapid expansion of the swirling air streams, which cannot provide the shearing and entrainment strong enough to trap most of droplets in a narrower region, and (2) the inertia of the large droplets that permits them to overcome the reverse flow of the continuous phase.

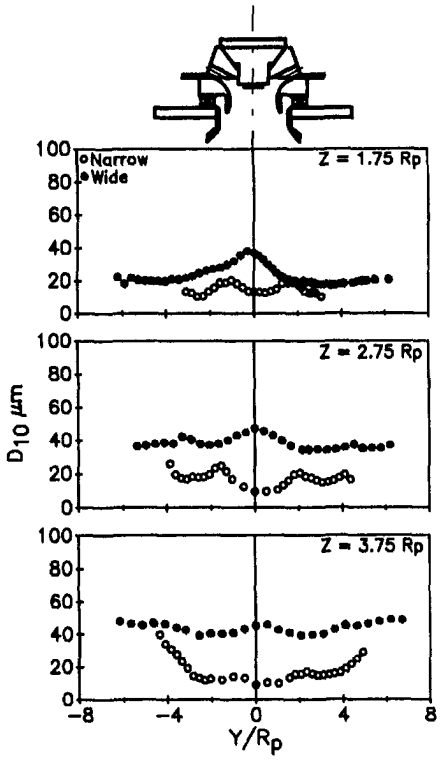

Fig. 11 Droplet D_{10} distributions

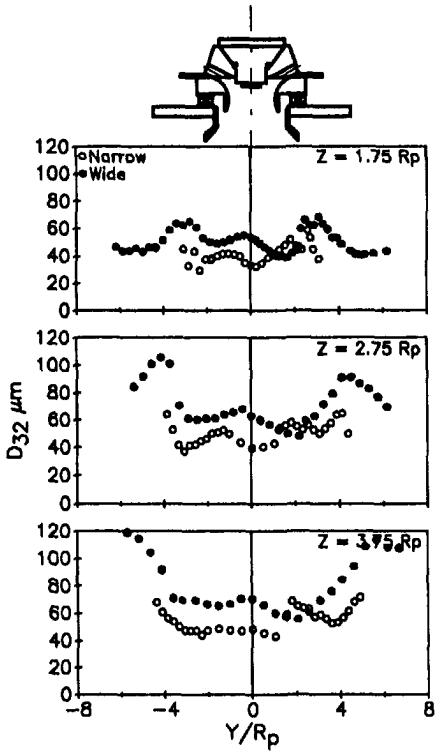

Fig. 12 Droplet D_{32} distributions

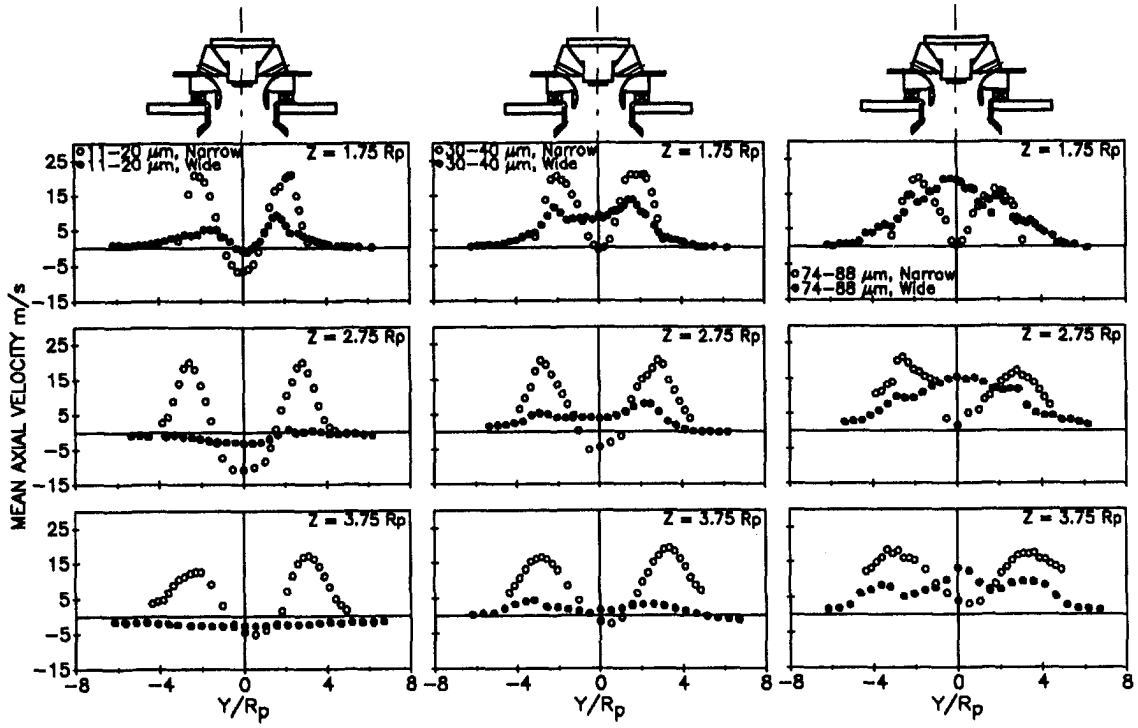

Fig. 13 Droplet mean axial velocities

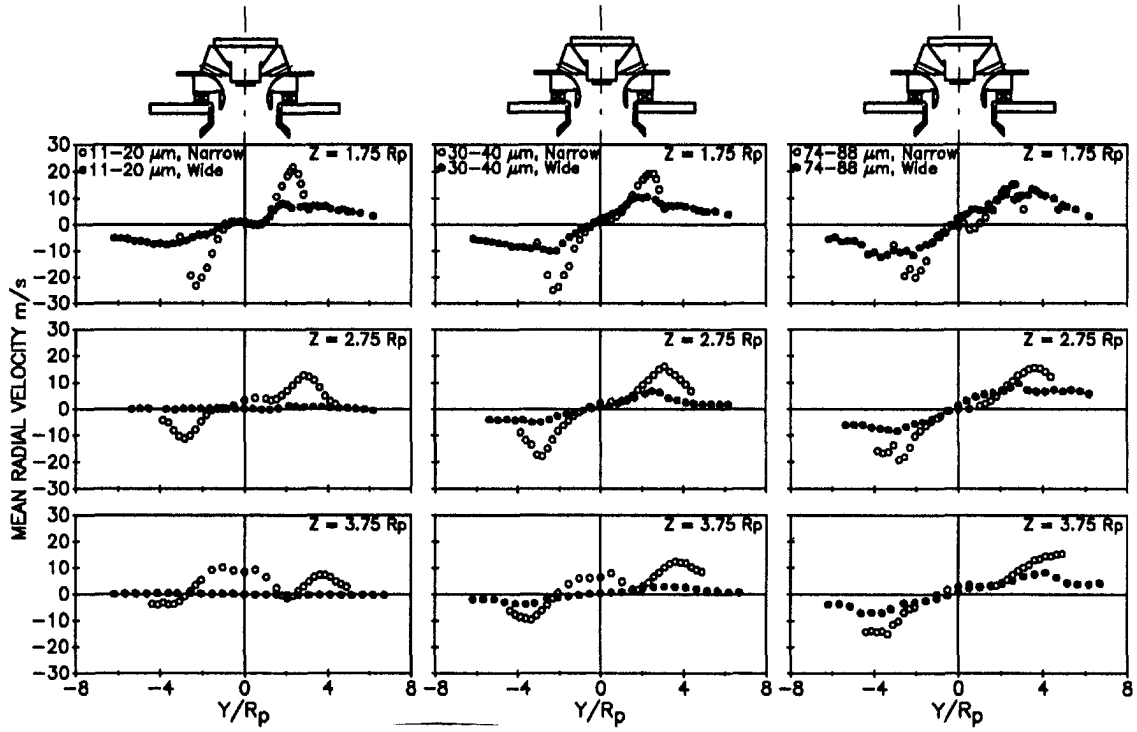

Fig. 14 Droplet mean radial velocities

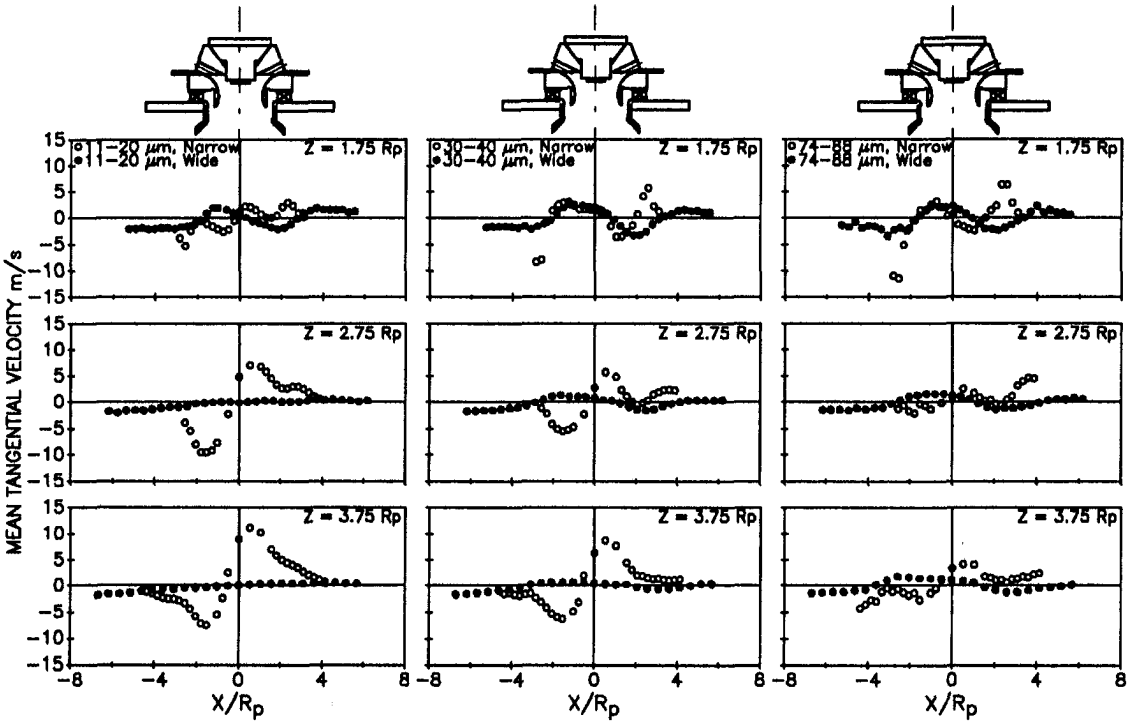

Fig. 15 Droplet mean tangential velocities

Droplet Radial Velocity. The comparison of the droplet radial velocities is shown in Figs. 14(*a–c*). The behavior of the small droplets is similar to that of the continuous phase (Fig. 14*a*). As droplet size increases, the maximum droplet mean radial velocities of the wide flare increase even though they are still smaller than the corresponding ones of the narrow flare (Figs. 14*b* and *c*). No contracting flow was observed for the droplets with diameter greater than 30 μm.

Droplet Tangential Velocity. Figures 15(*a–c*) present the comparison of the droplet mean tangential velocities. The droplets are influenced by the secondary air at locations away from the centerline. Close to the centerline, the droplets of the wide flare rotate clockwise (the same direction of the primary air rotation). This occurs because the droplets are first affected by the primary air right after injection from the atomizer. The droplets, due to their inertia, can retain this

influence downstream more prominently than the continuous phase, as evidenced in comparing Figs. 6 and 15(a–c). The greater the droplet diameter (therefore its inertia), the farther downstream this feature can be observed. The narrow flare also exhibits this feature but with less significance relative to that of the wide flare. More intense interaction between the counterrotating air streams occurs inside the swirl cup with the narrow flare than with the wide flare.

In summary, compared to the narrow flare, the wide flare results in (1) larger droplets, especially at the centerline, (2) wider dispersion of droplets, and (3) a more uniform spatial distribution of droplets. The large droplets at the centerline have higher velocities in the case of the wide flare suggesting that, although more mass is recirculated in that case, the ability to recirculate large drops is reduced. In general, the droplet radial and tangential velocities reveal increasing agreement for the two sprays with increasing drop size.

Conclusions

Time-averaged quantities measured within the two-phase flow fields downstream of two flare sleeves are evaluated and the differences due to the change in flare geometry are identified.

This study reveals that:

- A relatively modest change in flare design can cause a significant change in the two phase flow field. Therefore, the flare geometry represents one of the more important features of the swirl cup design that affects combustor performance.
- The recirculation zone produced by the wide flare is larger in size and features lower reverse flow velocities relative to that produced by the narrow flare. More mass is recirculated in the flow produced by the wide flare.
- The wide flare provides wider droplet dispersion and larger droplet size distribution than the narrow flare, and the droplet velocity decreases faster downstream of the wide flare than of the narrow flare.
- The larger droplets produced by the wide flare have a maximum velocity at the centerline.

To understand further the change in droplet dispersion pattern, the two-phase fluctuating velocities, and the detailed information of droplets, such as droplet velocity pdf based on droplet size, droplet size-velocity correlation, etc., should be considered. This part of the study is to be reported in a future companion paper.

Acknowledgments

The authors acknowledge the financial support from GE Aircraft Engines, and the assistance of Mr. S. W. Lee in preparing the plots for this paper.

References

Tolpadi, A. K., Burns, D. L., and Lawson, R., 1993, "Numerical Computation and Validation of Two-Phase Flow Downstream of a Gas Turbine Combustor Dome Swirl Cup," ASME Paper No. 93-GT-392.

Wang, H. Y., McDonell, V. G., and Samuelsen, G. S., 1992a, "The Influence of Spray Angle on the Continuous- and Discrete-Phase Flow Field Downstream of an Engine Combustor Swirl Cup," AIAA Paper No. AIAA 92-3231.

Wang, H. Y., McDonell, V. G., and Samuelsen, G. S., 1992b, "The Two-Phase Flow Downstream of a Production Engine Combustor Swirl Cup," *Twenty-Fourth Symposium (International) on Combustion*, the Combustion Institute, Pittsburgh, PA, pp. 1457–1463.

Wang, H. Y., McDonell, V. G., Sowa, W. A., and Samuelsen, G. S., 1992c, "Characterization of a Two-Phase Flow Field Downstream of a Gas Turbine Co-Axial, Counter-Swirling, Combustor Swirl Cup," AIAA Paper No. AIAA-92-0229.

Wang, H. Y., McDonell, V. G., Sowa, W. A., and Samuelsen, G. S., 1992d, "Scaling of the Two-Phase Flow Field Downstream of a Gas Turbine Combustor Swirl Cup: Mean Quantities," ASME JOURNAL OF ENGINEERING FOR GAS TURBINES AND POWER, Vol. 115, pp. 453–460.

A Semi-Analytical Emission Model for Diffusion Flame, Rich/Lean and Premixed Lean Combustors

N. K. Rizk

H. C. Mongia

Allison Gas Turbine Division,
General Motors Corporation,
P.O. Box 420,
Indianapolis, IN 46206-0420

To enhance gas turbine combustor performance and emissions characteristics, better design methods need to be developed. In the present investigation, an emission model that simulates a detailed chemical kinetic scheme has been developed to provide the rate of reactions of the parent fuel, an intermediate hydrocarbon compound, CO, and H_2. The intermediate fuel has variable carbon and hydrogen contents depending on operating conditions, that were selected in the development effort to simulate actual operation of rich/lean, diffusion flame, and lean combustor concepts. The developed reaction rate expressions address also the limited reaction rates that may occur in the near-wall regions of the combustor due to the admittance of radial air jets and cooling air in these regions. The validation effort included the application of the developed model to a combustor simulated by a multiple-reactor arrangement. The results indicate the accurate duplication of the calculations obtained from the detailed kinetic scheme using the developed model. This illustrates the great potential of using such a unified approach to guide the design of various types of combustor to meet the more stringent emissions and performance requirements of next-generation gas turbine engines.

I Introduction

The increasing demand for improved performance and reduced emission characteristics of the next-generation gas turbine combustor calls for better understanding of the coupled processes of fuel injection, evaporation, mixing, hydrocarbon combustion chemistry, and heat transfer. For example, current diffusion flame combustors operating on typical aviation fuels emit significant levels of oxides of nitrogen (NO_x) due to the high temperatures created in regions having sufficient concentration of fuel, atmospheric nitrogen, and oxygen. The reduction of the NO_x emission by operating at a lower reaction zone temperature could, however, have an adverse effect on the combustion stability, the emission of carbon monoxide (CO), and unburned hydrocarbons (UHC) especially under low power conditions.

To meet the often conflicting requirements of enhanced performance and minimized pollutant formation, improved design tools are needed to be utilized at different stages of the combustor development. Probably, the evaluation of the rate of the reaction of the hydrocarbons in the combustion zone is one of the key aspects to the success of the prediction capability of any design method. Lefebvre (1984, 1985) proposed a calculation approach that simulated the combustion process by global expressions to account for reaction temperature, system pressure, evaporation, and mixing. The mean gas residence time in the combustor recirculation zone was utilized by Mellor (1976) and Plee and Mellor (1978, 1979) to provide such important parameters as ignition, blowout, CO, and NO_x.

On the other hand, simplified reaction mechanisms have been used to yield information on burned gas composition and flame temperature. However, many of the simple kinetics models do not accurately reproduce experimental flame characteristics over a wide range of operation (Westbrook and Dryer, 1981). It is well recognized that to bring the reaction mechanism closer in simulating an actual combustion process, a detailed chemical kinetic model should be used in the calculation approach. The limitation of using such detailed mechanisms arises when the calculation domain is a multidimensional one because of the impractical computational time and cost involved. Thus, under such conditions, reaction mechanisms of significantly fewer steps are often used in the modeling of the gas turbine combustors. They involve the reaction of the parent fuel to intermediate species that, in turn, react to the final products. Although this approach has shown promising results, the omission of many elementary reactions from the calculation can still lead, in some instances, to significant deviation from the experimental results.

Contributed by the International Gas Turbine Institute and presented at the 38th International Gas Turbine and Aeroengine Congress and Exposition, Cincinnati, Ohio, May 24–27, 1993. Manuscript received at ASME Headquarters March 1, 1993. Paper No. 93-GT-128. Associate Technical Editor: H. Lukas.

It is therefore recognized that there is a great need to develop a reaction scheme that takes advantage of the available detailed chemical kinetic mechanisms and yet is relatively simple to use in the combustor analysis. In the last two years, an effort has been made by the authors to develop a reaction model that addresses these requirements. The first phase of this investigation involved the simulation of the reaction in the combustor by a number of reactors that represented different zones of the combustor. A number of expressions for CO, NO_x, and unburned hydrocarbons (UHC) were developed using a detailed kinetic scheme to provide the trends of formation and/or consumption of these species. Different sets of equations were used for each of the combustor categories of diffusion flame, rich-lean, and lean concepts (Rizk and Mongia, 1991, 1993a, 1995). It is the purpose of this paper to cover the effort to develop a unified reaction model that can be applied to various combustion concepts. In the next section, a review of reaction rate mechanisms used in the combustor analysis is described. The proposed model formulation and validation are given in the following sections of the paper.

II Reaction Rate Models

Several models have been reported in the literature to correlate the reacting species within the combustor. They vary in complexity from simple empirical expressions to highly sophisticated kinetic models. Each has its own advantages and limitations depending on the degree of accuracy required and the computation cost involved. In the empirical and semi-analytical models, the exhaust concentrations of the pollutants of importance are assumed to be governed by the residence time in the combustion zone, the chemical reaction rate, and the mixing rate. The calculations involve the estimation of such parameters as reaction temperature, fuel spray characteristics, and evaporation history. Overall emissions produced by the combustor are provided by these methods using some parameters related to operating conditions and combustor configuration.

More details of the reaction process within the combustor are provided by various reaction mechanisms. In a single-step scheme, the reaction of fuel into CO_2 and H_2O is represented by a global reaction. Although the use of this model is convenient, it does not account for the presence of other species such as CO and H_2, which results in overpredicting flame temperature. Multiple-step reaction mechanisms consider extra equations for the reaction of these species in addition to an intermediate fuel reaction in the four-step scheme. Review of some important reaction models proposed are given by Hautman et al. (1981), Jones and Lindstedt (1988), and Westbrook and Dryer (1981). The reaction rate equations offered in these investigations involve a number of constants that were evaluated from experimental results.

A comprehensive reaction mechanism for propane that incorporated 163 elementary reactions was proposed by Westbrook and Pitz (1984). By accounting for the 41 species in their model, they concluded that the mechanism accurately reproduced measurements over a wide range of operation. Thus, the proposed mechanisms are intended for application to a wide variety of combustion regimes. It should be noted that the experimental data used in the development of these reaction mechanisms were obtained using a special experimental setup.

When such models are applied to gas turbine combustors, the combustor is often divided into a number of reactors in series and/or in parallel to simulate various regions. In a review given by Mellor (1976), a model based on a number of perfectly stirred reactors is described (Hammond and Mellor, 1973). A global reaction mechanism was used, and no droplet calculations were considered in the approach. Volumes and flow splits were selected to yield best fits with detailed measurements of NO and CO. Fletcher and Heywood (1971) modeled the combustor primary zone as a partially stirred reactor burning fuel over a distribution about the primary zone equivalence ratio, a lateral mixing reactor, and a plug flow reactor. Two model-fitting parameters were used to give satisfactory correlation with NO_x measurements, except at low engine power. The discrepancy at low fuel/air ratio was attributed to ignoring the evaporation time of the fuel.

Rizk and Mongia (1991, 1993b, 1995) followed a similar approach to model the emissions produced by various types of combustor concepts. They divided the combustor into a number of reactors representing different zones in each combustor type. The details of this approach are given in the next section.

III Reaction Model Formation

The procedure used in the present investigation to develop a reaction model utilizes a detailed chemical kinetic model to provide the basis for reaction expressions, and defines the necessary reactors needed to simulate the combustor. Because the emissions calculations are based on a reaction rate concept, the model is applicable to various types of combustors. In the following subsections, the details of the model development effort are presented.

III.1 Combustor Flow Modeling. Because the emissions from gas turbine combustors are significantly affected by the details of the front end and the subsequent admittance of air into various zones, the combustor needs to be divided into a number of regions for modeling purposes. In an earlier effort, the rich zone of the rich-lean (RQL) combustor was simulated by two parallel reactors feeding into a plug flow reactor. Mixer air was admitted into the system to form plug flow reactors that represented quench and lean zones (Rizk and Mongia, 1991). A similar procedure was used to model emissions from conventional combustors. The selected reactors represented recirculation, primary, intermediate, and dilution zones, in addition to near-wall regions (Rizk and Mongia, 1993b). More recently, the premixed/prevaporized lean combustor was also modeled by defining main reaction and pilot reaction regions (Rizk and Mongia, 1995).

A reaction mechanism that combined the detailed kinetic scheme of Westbrook and Pitz (1984) with extended Zeldovich mechanisms for NO_x formation (Glassman, 1977) was used to provide the trends of pollutant formation in various simulated reactors. For each combustor concept, a practical range of operation was covered in a parametric study using the chemical reaction program. The critical issues addressed were the effects of the equivalence ratio, residence time, system pressure, and temperature on species concentrations.

Nomenclature

FAR = fuel/air ratio
P_3 = system pressure, kPa
T_3 = inlet temperature, K
T = reaction temperature, K
T_{eq} = equilibrium temperature, K
ϕ = equivalence ratio
τ = residence time, ms
τ_ℓ = critical residence time, ms
[ ] = specie mass concentration
( ) = emission index, g/kg fuel

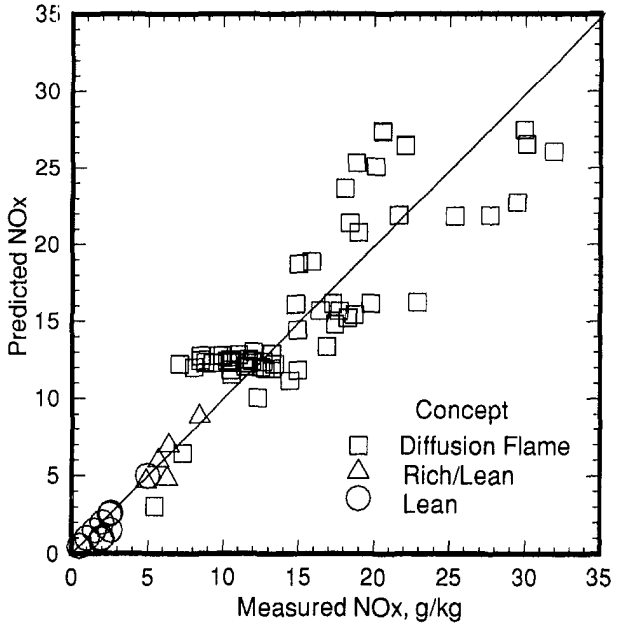

Fig. 1 Comparison between calculations and measurements for different combustors

Based on the results of this study, a number of expressions were developed to simulate the reaction mechanisms of various reactors for each combustor concept. Considering the effects of droplet evaporation and mixing process in the combustor, the developed model demonstrated the capability to match the emissions data of the three combustor types closely. Figure 1 shows a comparison between the calculations and measurements of NO_x emission. A different symbol is used for each combustor concept modeled.

III.2 Unified Calculation Approach. The calculation approach described in the previous subsection provides the overall concentrations of NO_x, CO, and UHC in each reaction within the combustor. The semianalytical expressions developed for each combustor concept are only applicable to that particular type. The parameters involved in these expressions are based on average properties of each reactor. These include fuel/air ratio, reaction temperature, and residence time. In the present effort, a unified calculation approach, based on the evaluation of the reaction rates of fuel and intermediate species, has been developed. The reaction rate expressions involve parameters related to operating conditions as well as the concentrations of the relevant species. The approach is therefore applicable to various combustion regimes. Because the reaction rate calculations provide the change in species concentrations with time, the details of the pollutant formulation and consumption within each model reactor are readily available.

Similar to the earlier emission model, the effort involved the establishment of wide data base using the detailed kinetic code described earlier. The reactor configurations selected for modeling are shown in Fig. 2. Reactor 1 is a well-stirred reactor, while Reactor 2 represents a plug flow reactor. The reactors illustrated in this figure represent various flow possibilities that may be encountered in an actual combustor. For instance, the first reactor simulates the reaction of fresh fuel and air in the combustor front end. The subsequent reactors receive more fresh fuel, due to continuous spray evaporation, additional air from radial injection holes, and cooling air, as well as the outcome of the combustion process in other reactors. The input data needed to run the chemical code were selected to simulate the actual operation of various types of combustors. The outcome of this effort was used to develop a multiple-step reaction rate mechanism, as described in the next section. By this means, a relatively simple calculation procedure could be used to simulate the reactions given by a 178 elementary reaction rate scheme. The obvious advantage offered is the potential to incorporate the developed reaction rate scheme into multidimensional combustor performance models for enhanced simulation of the combustion process.

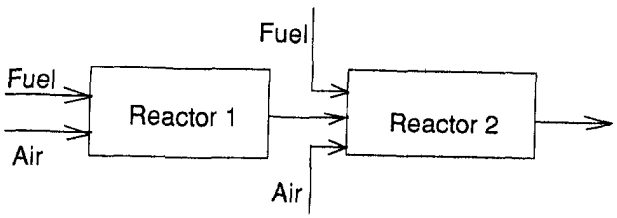

Fig. 2 Combustor flow model

IV Proposed Emission Model

The results of the chemical kinetic calculations include the concentrations of 46 different species. Twenty-nine of these species represent one form or another of intermediate hydrocarbon formations. In the present approach, all intermediate hydrocarbon concentrations are added together to yield the total concentration of an equivalent intermediate fuel. The structure of such intermediate fuel is evaluated from the carbon and hydrogen contents. The oxygen content in this intermediate compound is also determined in each case.

The reaction rate expressions were developed to simulate the detailed kinetic mechanism and assuming that the reaction proceeds through four main steps:

$$C_xH_y \rightarrow n_1C_IH_J + n_2H_2 \tag{1}$$

$$C_IH_J + \left(\frac{I}{2}\right)O_2 \rightarrow I\,CO + \left(\frac{J}{2}\right)H_2 \tag{2}$$

$$CO + \frac{1}{2}O_2 \rightarrow CO_2 \tag{3}$$

$$H_2 + \frac{1}{2}O_2 \rightarrow H_2O \tag{4}$$

where n_1 and n_2 are readily determined from the total mole balance of Eq. (1).

The details of the reaction rate expressions are given in the appendix. Only the main reaction equations are presented in the following subsection. The equation numbers that appear here are consistent with the numbers used in the appendix.

IV.1 Fuel Reaction Rate. The results of the detailed chemical kinetic code show different fuel reaction schemes depending on the conditions within the reactor. For example, in the first reactor shown in Fig. 2, the reaction follows an on/off behavior depending on the operating parameters and residence time in this reactor. But once the reaction starts almost all the fuel introduced into the rector is instantaneously reacted. In subsequent reactors, the freshly introduced fuel can either follow a gradual reaction rate or completely react within a very short time depending on the available residence time in the reactor. Thus, the reaction rate expressions developed for residence times below a critical value τ_ℓ are different from those obtained for larger residence times. Based on the results of the kinetic mechanism calculations, the proposed equation of the fuel reacted in g/kg fuel for reaction time τ larger than the critical residence time is given by:

$$-d(C_xH_y) = C_1 e^{-E/T}(P_3/345)^m(\tau/0.25)^{\ell} \tag{5}$$

The parameters C_1, E, m, and ℓ vary with equivalence ratio ϕ, pressure P_3, and inlet temperature T_3 according to Eqs. (6)–(17) given in the appendix. The equations needed to calculate the critical time, τ_ℓ are Eqs. (18)–(22).

For a time step less than τ_ℓ the fuel reaction proceeds gradually as given by:

$$-\frac{d(C_xH_y)}{dt} = C5\exp(-E_1/T)[C_xH_y]^b[O_2]^c [C_fH_f]^d\phi^{-1} \quad (23)$$

The terms within square brackets are mass concentration and the left-side term represents rate of fuel reaction in (g/kg fuel/s). The various constants in Eq. (23) are given by Eqs. (24)–(28) of the appendix.

IV.2 Intermediate Reaction Rate. Following the same concept of dividing the reaction rate into two regimes, above τ_ℓ and below τ_ℓ, it is found that once the intermediate fuel is formed from the breakup of the parent fuel, it reacts at a rapid rate (within the first time step in the reactor). The reaction proceeds at a significantly lower rate in the remaining residence time of the reactor. The proposed expression for the intermediate fuel reaction is given by:

$$-\frac{d(C_fH_f)}{dt} = C6\exp(-E2/T)[C_xH_y]^b [O_2]^e[C_fH_f]^d \cdot f(\phi)[CO]^e \quad (29)$$

Various parameters given in Eq. (29) are obtained using Eqs. (30)–(36) of the appendix. The set of constants is selected according to the reactor residence time, whether it is larger or smaller than the critical time, and a different set is used for the initial time step, as described in the appendix.

IV.3 CO Reaction Rate. The following equations are proposed for CO reaction rates. For a time step less than τ_ℓ, the rate of CO reaction is given by:

$$-\frac{d(CO)}{dt} = C7\exp(-14{,}500/T)\left([C_xH_y] + [CO]\right)^{-2} [O_2]^{7.4}(0.4/\phi)^{-4.0} \quad (37)$$

For reaction time above τ_ℓ, the CO reaction is given by:

$$-\frac{d(CO)}{dt} = C7\exp(-E3/T)[C_xH_y]^b[O_2]^c [C_fH_f]^d[CO]^e f1(\phi)[H_2O]^f - C8\exp(-E4/T)[O_2]^{cr}[C_fH_f]^{dr} [CO]^{er}[CO_2]^{fr} f2(\phi) \quad (39)$$

It is once again found that the rate of reaction of CO is high within the first time step of the reactor, followed by a much slower rate during the rest of the reactor residence time. The various parameters involved in Eq. (39) are calculated using Eqs. (40)–(46) of the appendix. The second term in Eq. (39) represents the backward reaction of CO_2 to CO, which becomes significant at higher values of equivalence ratio.

IV.4 Hydrogen Reaction Rate. The reaction of H_2 proceeds at different rates depending on the residence time criterion described earlier, and whether the calculation time step is the initial one in the reactor. The general form of the reaction rate expression is proposed as follows:

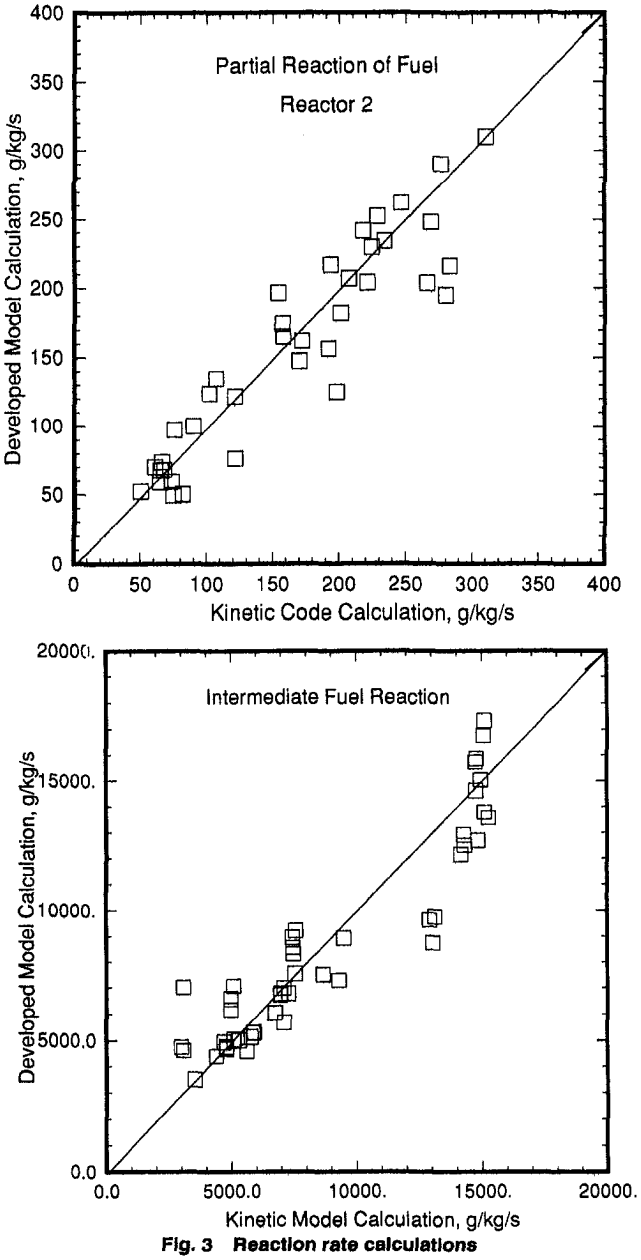

Fig. 3 Reaction rate calculations

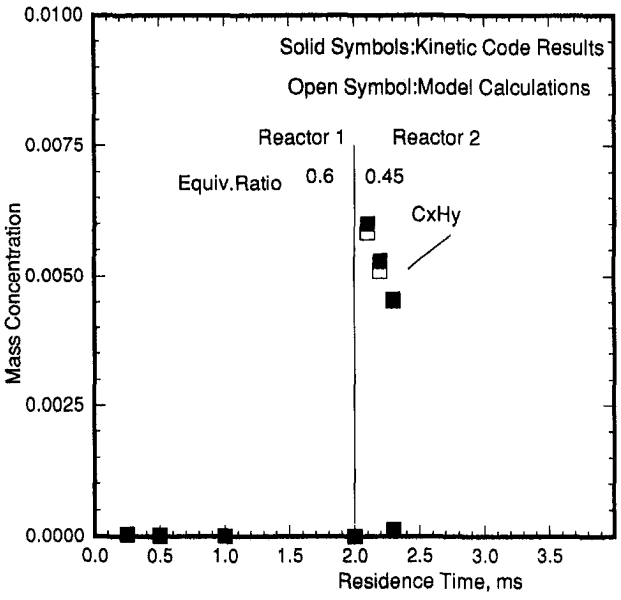

Fig. 4 Partial reaction of fuel

$$-\frac{d(\mathrm{H2})}{dt} = C9\exp(-E5/T)[\mathrm{C}_x\mathrm{H}_y]^b[\mathrm{O2}]^c$$
$$[\mathrm{C}_I\mathrm{H}_J]^d[\mathrm{H2}]^g f3(\phi) \quad (47)$$

The parameters of Eq. (47) vary with equivalence ratio and system pressure according to Eqs. (48)–(55) in the appendix.

By calculating the reaction rates of the fuel, intermediate fuel, CO, and H_2, their new concentrations could be calculated. The balance of the concentrations will give the concentrations of O_2, CO_2, and H_2O.

IV.5 NO_x Reaction Rate. Based on the concentrations of various species, the following NO_x reaction rate equation is proposed:

$$\frac{d(\mathrm{NO}_x)}{dt} = C11\exp(-29{,}000/T)[\mathrm{O}_2]^{0.9}$$
$$[\mathrm{CO}]^{0.8} f4(\phi) - C12\cdot\exp(-60{,}000/T)$$
$$[\mathrm{O}_2]^{0.8}[\mathrm{C}_I\mathrm{H}_J]^{0.7}[\mathrm{NO}]^{0.3}[\mathrm{CO}]^{2.5} f5(\phi) \quad (56)$$

The second term on the right-hand side of Eq. (56) represents the reduction in NO concentration at rich fuel mixtures.

IV.6 Intermediate Fuel Structure. As mentioned earlier, the intermediate fuel (C_IH_J) formed from the parent fuel is the addition of all hydrocarbon compounds, as given by the detailed chemical kinetic code, with an equivalent carbon/hydrogen ratio. It is observed from the results of the kinetic code that the intermediate fuel structure varies with the operating parameter in a consistent manner. To proceed with the reaction rate calculations, a method to calculate the equivalent carbon and hydrogen contents of the intermediate fuel needs to be devised. The expression developed for the two elements is as follows:

$$I \text{ or } J = C13\exp(E6/T)[\mathrm{C}_x\mathrm{H}_y]^b[\mathrm{O}_2]^c\left(\frac{0.4}{\phi}\right)^h[\mathrm{C}_I\mathrm{H}_J]^d \quad (60)$$

The parameters given in Eq. (60) are described by Eqs. (61)–(66) of the appendix. The expressions given in this subsection are adequate to evaluate the structure of the intermediate fuel under each condition.

IV.7 Fuel Oxygen. A number of the intermediate hydrocarbon compounds formed from the parent fuel contain oxygen. The oxygen content in the equivalent intermediate fuel was evaluated from the results given by the chemical kinetic code and a number of expressions were developed. Although the oxygen is assumed to separate from the intermediate fuel instantaneously, the calculation of its content is useful in determining the concentration of the intermediate fuel including oxygen. The expression for the oxygen given in (g/kg fuel) is as follows:

$$(f\mathrm{O}_2) = C14\exp(E7/T)[\mathrm{C}_x\mathrm{H}_y]^b[\mathrm{O}_2]^c$$
$$[\mathrm{C}_I\mathrm{H}_J]^d[\mathrm{CO}]^f f7(\phi) \quad (67)$$

The constants and parameters appearing in Eq. (67) are given in the relevant section of the appendix by Eqs. (68)–(75).

IV.8 Reaction Temperature. In order to calculate the reaction rate of various species and the structure of the intermediate fuel, a method to calculate the reaction temperature is needed. This step is readily provided when the reaction model is combined with multidimensional combustor models because of the iterative procedure used in the solution of the flow field and the fine grid network used in the calculation. The present model, however, when used to analyze the multiple reactor combustor configurations requires a means to estimate the reaction temperature. The developed expression, in terms of the equilibrium temperature T_{eq}, is given as follows:

$$T/T_{eq} = C15\exp(E8/T3)\exp\left(b[\mathrm{C}_x\mathrm{H}_y]\right)$$
$$\exp(c[\mathrm{O}_2])\cdot\exp(d[\mathrm{C}_I\mathrm{H}_J])$$
$$\exp(f[\mathrm{CO}])f8(\phi) \quad (76)$$

Various parameters of Eq. (76) are described by Eqs. (77)–(81) of the appendix.

The equations given in this subsection are sufficient to provide the expected value of the reaction temperature from the initial concentrations of various species at each time step.

The next section includes the description of the evaluation of the capability of the developed calculation procedure to duplicate the species concentrations given by the detailed chemical kinetic code.

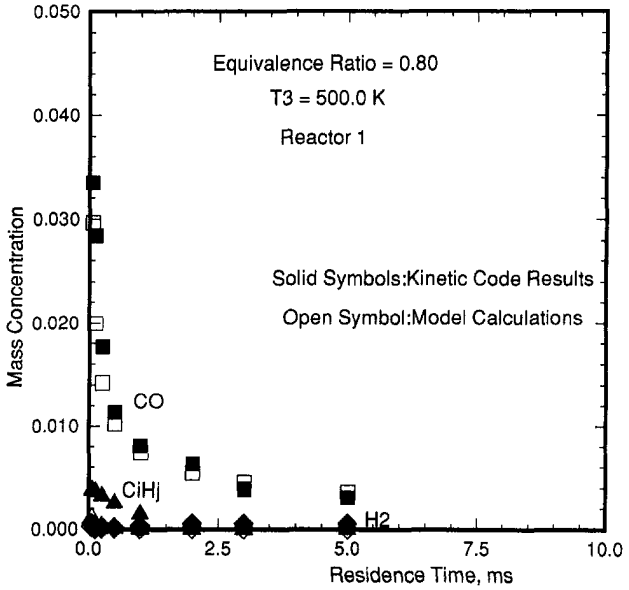

Fig. 5 Specie concentrations for Reactor 1 at equivalence ratio of 0.8

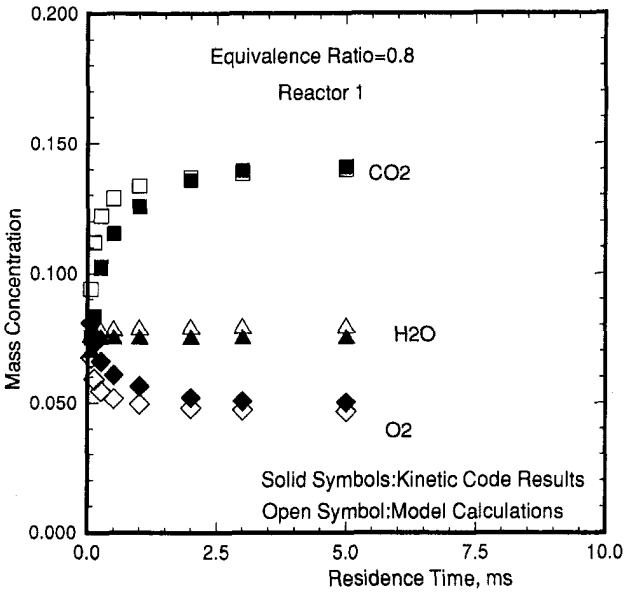

Fig. 6 CO_2, H_2O, and O_2 concentrations for Reactor 1 at equivalence ratio of 0.8

V Reaction Model Validation

It has been shown in the previous sections that in order to simulate the combustion process accurately, large numbers of finite rate reactions should be included in the chemical kinetic mechanisms. However, due to the lengthy computation involved, often mechanisms with a limited number of steps are employed in the combustion models. An earlier effort was made to simulate a detailed kinetic scheme with a number of semi-analytical expressions developed separately for each of the rich/quench, diffusion flame, and lean combustion concepts. The objective of the present investigation, therefore, was to develop a unified calculation approach that can closely duplicate the species concentrations offered by the detailed scheme and yet be applied equally well to the three combustor concepts. In this section, the results given by the developed model are compared with the chemical kinetic calculations.

The validation effort included a two-step procedure. The developed reaction rate equations were employed to separately compare the resulting rate of reactions of various species with the kinetic code results. Once this step was completed, the developed calculation approach was used to determine the species concentrations in the reactor arrangement shown in Fig. 2. In this figure, it is illustrated that the input to Reactor 1 includes fuel and air, while Reactor 2 receives, in addition to fresh fuel and air, the products of the combustion process of the upstream reactor. The two reactors represent different types of reaction in the combustor. To simulate the whole combustor flow field, additional reactors of either type may be included as required.

Figure 3 shows a comparison between the reaction rates as given by both the developed model and the detailed kinetic scheme. The first part of this figure illustrates the relatively low rate of reaction of the fresh fuel introduced into the already reacting stream leaving the first reactor when the conditions do not warrant full reaction. These conditions are typical of those occurring in the near-wall region of the combustor. In other words, if a fraction of the fuel spray manages to escape the front end recirculation zone, the

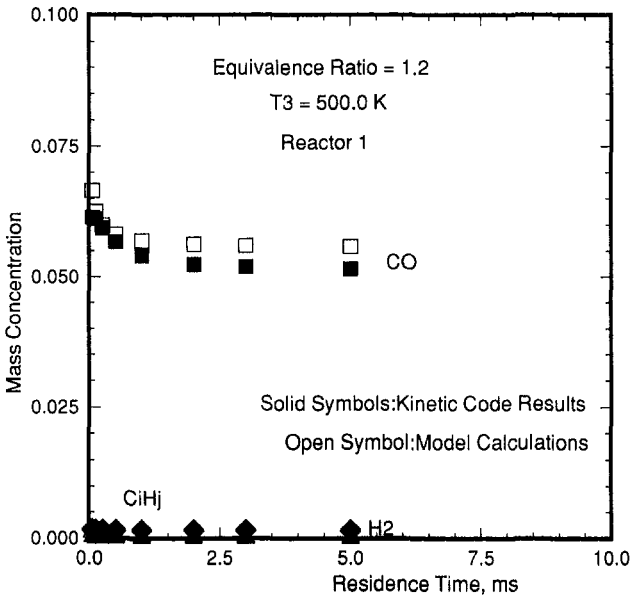

Fig. 7 Specie concentrations for Reactor 1 at equivalence ratio of 1.2

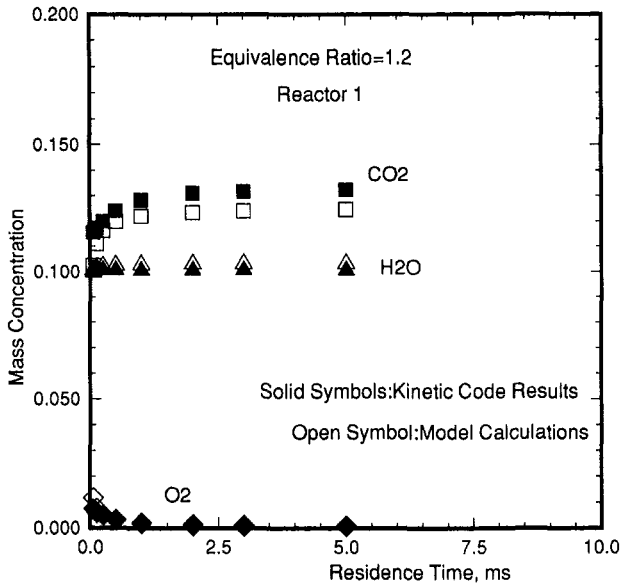

Fig. 8 CO_2, H_2O, and O_2 concentrations for Reactor 1 at equivalence ratio of 1.2

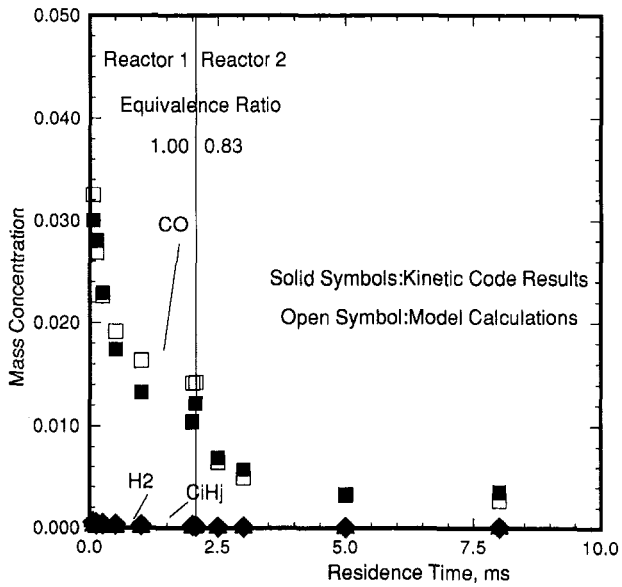

Fig. 9 Concentrations in multiple-reactor flow model

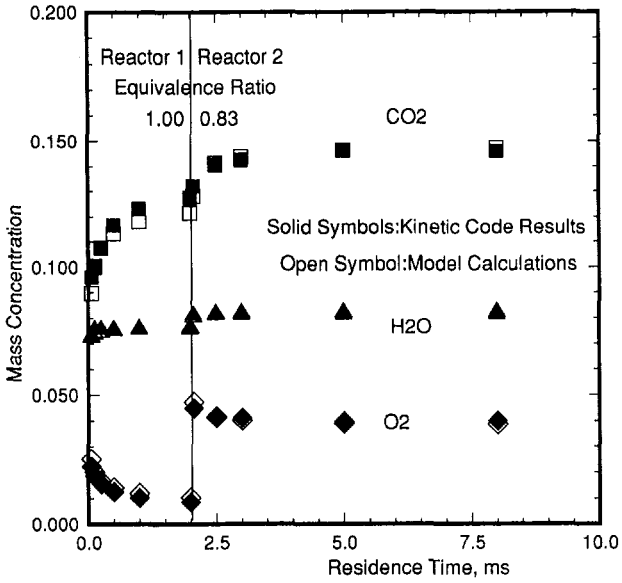

Fig. 10 CO_2, H_2O, and O_2 concentrations in multiple-reactor flow model

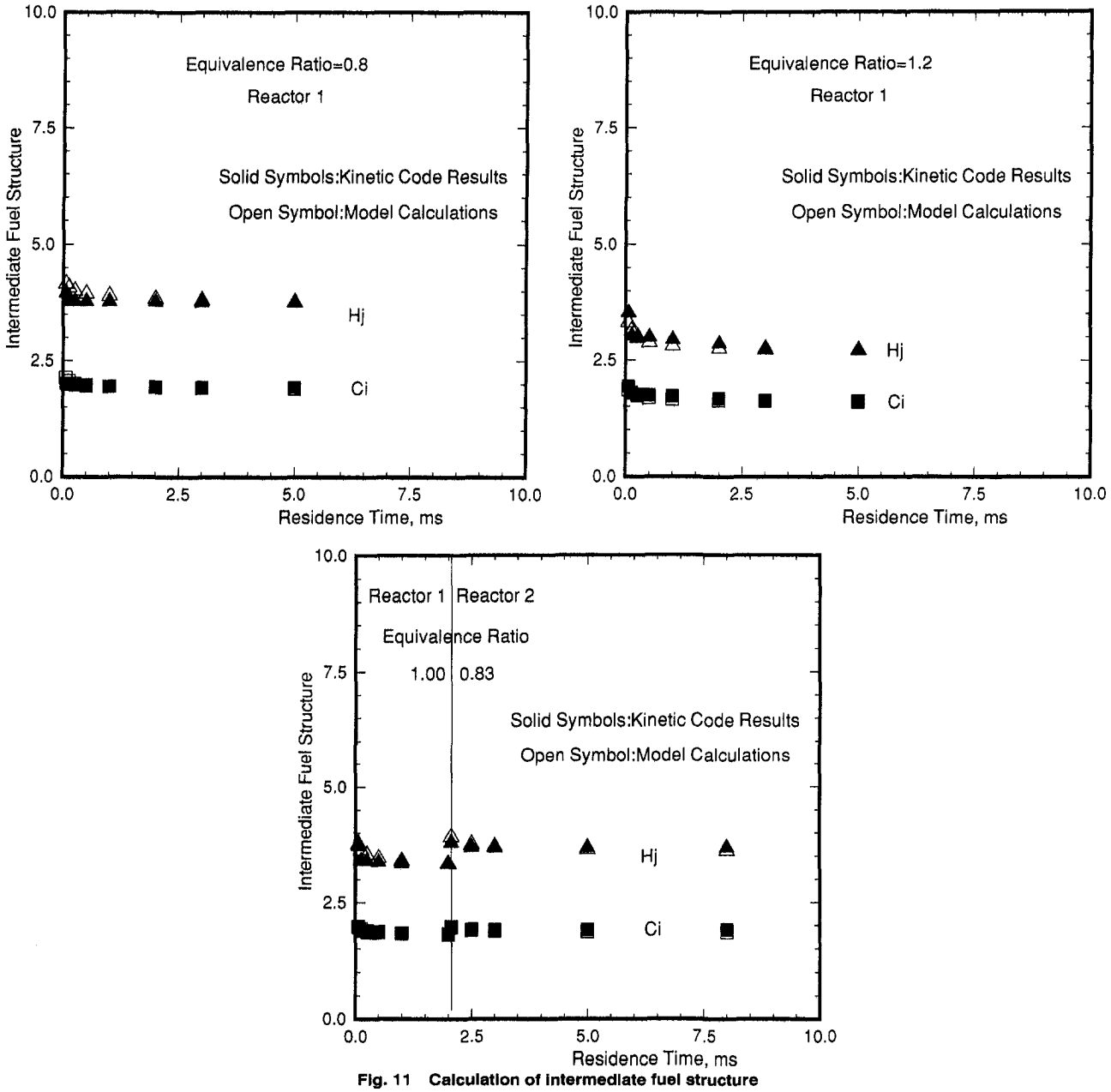

Fig. 11 Calculation of intermediate fuel structure

admittance of the radial jets may slow down the reaction causing the presence of hydrocarbons in the combustor exhaust. The level of agreement with the kinetic code results is quite satisfactory. In the second part of Fig. 3, the results of the calculation of the reaction rate of the intermediate fuel are plotted against the kinetic code data. The high reaction rates shown in this figure indicate that under full combustion conditions, most of the intermediate fuel reacts within a very short time.

Examples of the results obtained in the second stage of the validation effort are illustrated in Figs. 4–11. The developed reaction model was used to calculate the species concentrations and the carbon and hydrogen contents of the intermediate fuel for single-reactor and multiple-reactor arrangements. They represent various situations occurring within the combustor. The operating conditions selected for these calculations simulated those of various concepts of combustors. Also, conditions that caused partial reaction of the fuel, as given by the detailed kinetic scheme, were used to duplicate the reaction under these critical conditions. The calculations were performed for an initial time step of the order of 0.06 ms that increased gradually to a value of 6 ms at the end of the calculations.

To illustrate the different reaction rates that may occur within the combustor, the results obtained for the two-reactor arrangement of Fig. 2 are plotted in Fig. 4. It is shown in the figure that almost all of the fuel introduced into Reactor 1 is consumed within this reactor. However, due to the conditions prevailing in the second reactor, only limited reaction is observed in the initial part of the reactor. When sufficient intermediate fuel concentration becomes available, a rapid reaction may proceed causing complete combustion.

Figure 5 shows the concentrations of CO, H_2, and the intermediate fuel produced under the lean side of the stoichiometric fuel/air mixture. The figure shows the rapid reaction of the intermediate fuel and hydrogen and the continuous decrease of CO with time toward its equilibrium value. Figure 6 illustrates that the concentrations of H_2O and O_2 remain relatively constant throughout the Reactor 1 residence time, while CO_2 concentration shows a rapid increase,

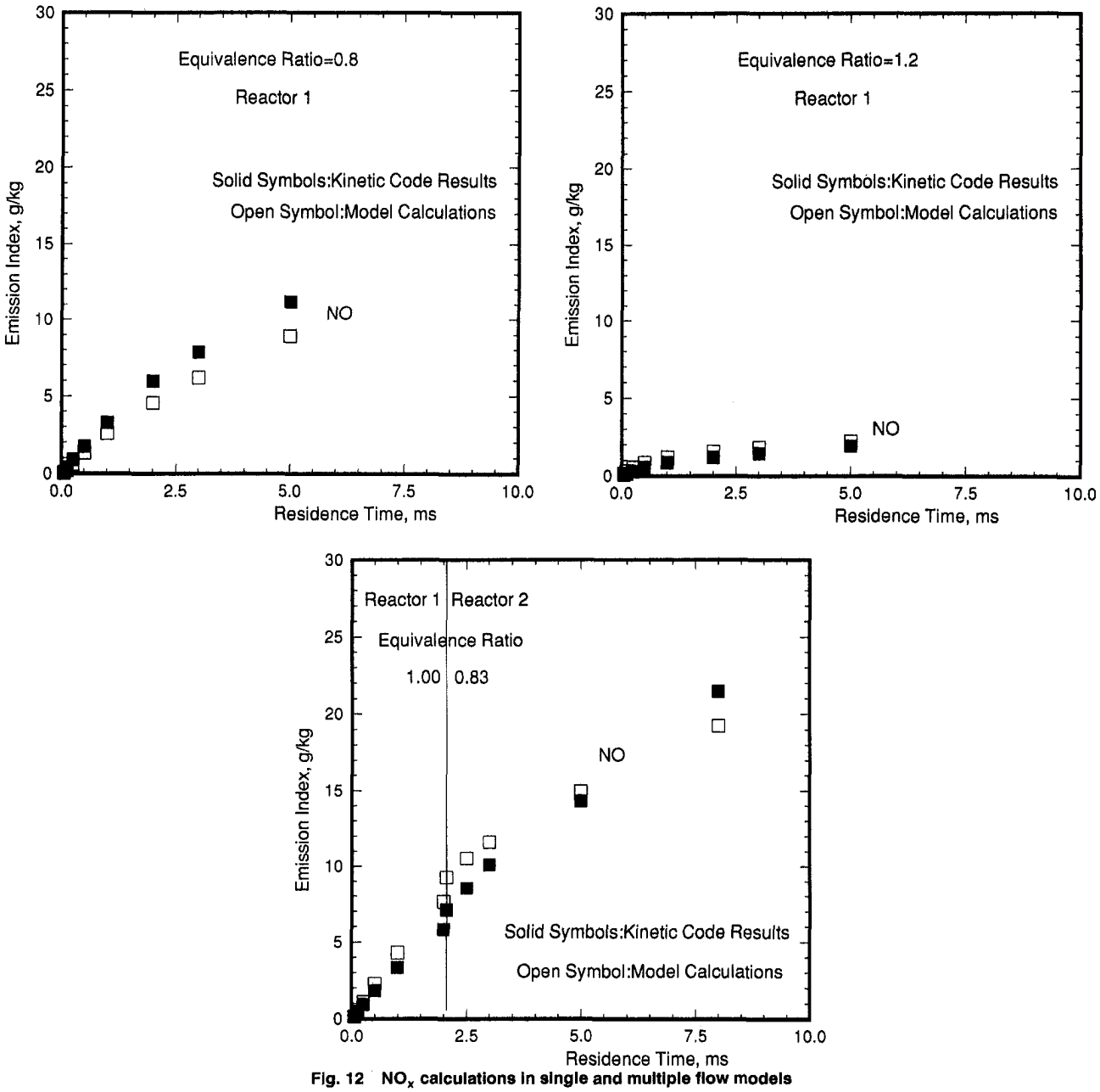

Fig. 12 NO_x calculations in single and multiple flow models

especially at the start of the reaction. Similar results for combustion under fuel rich conditions are plotted in Figs. 7 and 8.

Examples of the specie concentrations in the multiple-reactor flow model are given in Figs. 9 and 10. The increase in concentrations of O_2 and CO at the entrance to the second reactor are due to the admittance of fresh fuel and air into Reactor 2. The carbon/hydrogen structures of the intermediate fuel under different operating conditions are plotted in Fig. 11. It is seen that the intermediate fuel moves to a lower hydrocarbon structure as the fuel/air ratio increases and/or toward the end of the reaction.

The results of NO reaction are given in Fig. 12 for three different cases. The plots show the variation of NO emission index (g/kg fuel) with the residence time in the reactors. The results confirm the finding that, by operating under fuel-rich conditions, a limited amount of NO is formed. In fact, by the proper selection of the fuel/air mixture in the rich zone, the NO formed under more favorable conditions may be even reduced in quantity.

The important conclusion drawn from these results is the satisfactory duplication of the kinetic code outcome using the developed reaction model. This indicates the potential of using the limited number of steps of the developed model to simulate the far more sophisticated kinetic scheme in predicting the emissions produced in the combustor. It can be also seen that by incorporating such a reaction model in two-dimensional and three-dimensional combustor performance codes, enhanced combustion process simulation could be obtained. Regions in the combustor that may be responsible for excessive presence of CO and hydrocarbons in the combustor exhaust could be easily defined.

It is planned to incorporate the developed reaction model into the hybrid three-dimensional combustor performance model developed in recent years and described by Rizk and Mongia (1993a). The model combines the analytical capabilities of the three-dimensional model with proven semi-analytical expressions. The modeled combustor sector is usually divided into a large number of subvolumes, in the order of 1000, in this approach. Each subvolume is treated as a

separate reactor with average values of gas flow rate, flow-averaged temperature, fuel/air ratio, in addition to turbulence characteristics. By this means, sophisticated analytical models are brought closer in, representing actual combustor hardware with significantly less computation.

VI Summary and Conclusions

In order to meet the future demands of improved gas turbine combustor and reduced emissions, better design tools need to be developed. Enhanced combustion models require the inclusion of detailed chemical kinetic mechanisms that account for every possible elementary reaction. It is, however, recognized that the computation cost and time involved in using such a detailed scheme can be a limiting factor, especially if the calculations are performed for multidimensional flow domains. The objective of the present effort was, therefore, to develop a reaction rate model that involves a limited number of steps yet accurately simulates the detailed kinetic scheme for use with various combustor concepts.

The developed reaction model addresses the reaction of a parent fuel into an intermediate hydrocarbon compound, whose carbon and hydrogen contents vary with operating parameters, and hydrogen. The oxygen content of the intermediate fuel is assumed to disappear rapidly from the intermediate fuel. The intermediate compound reacts to CO and H_2 with a mass balance governed by the carbon/hydrogen content of the compound. CO_2 and H_2O are formed from the CO and H_2 reactions. The data used to develop various reaction rate expressions were based on the calculations provided by a detailed chemical code over a wide range of conditions that simulated the actual operation of rich/lean, diffusion flame, and lean combustors. The developed expressions addressed the reaction rates when the available residence time allows for rapid reaction, and also when the residence time dictates a limited reaction rate.

In addition to calculating the reaction rates for the parent fuel, intermediate hydrocarbons, CO, and CO_2, equations to determine NO formation and consumption rates were developed. Procedure to calculate the carbon and hydrogen contents of the intermediate fuel, reaction temperature, and fuel oxygen content was also defined in the developed approach. The model validation included the application of the developed reaction model to a multiple-reactor flow model that simulated the various regions of the combustor. The concentration history of various species was calculated using the developed model and the results were compared with the calculations offered by the detailed chemical kinetic code. The good agreement obtained over wide operating conditions indicates the potential of using the developed model to predict the details of the combustion process and emission formation in various combustor concepts. The validation effort with the experimental data obtained for a large number of conventional and advanced combustors will be reported elsewhere.

The near future plan involves the incorporation of the developed reaction model in a hybrid three-dimensional combustor model that utilizes the capabilities of the analytical tool and the proven semi-analytical expressions to bring the analysis closer to simulating actual combustor hardware.

References

Fletcher, R. S., and Heywood, J. B., 1971, "A Model for Nitric Oxide Emissions From Aircraft Gas Turbine Engines," AIAA Paper No. 71-123.

Glassman, I., 1977, *Combustion*, Academic Press, New York.

Hammond, D. C., Jr., and Mellor, A. M., 1973, "Analytical Predictions of Emission From and Within an Allison J-33 Combustor," *Combustion Science and Technology*, Vol. 6, pp. 279–86.

Hautman, D. J., Dryer, F. L., Schug, K. P., and Glassman, I., 1981, "A Multiple-Step Overall Kinetic Mechanism for the Oxidation of Hydrocarbons," *Combustion Science and Technology*, Vol. 25, pp. 219–235.

Jones, W. P., and Lindstedt, R. P., 1988, "Global Reaction Schemes for Hydrocarbon Combustion," *Combustion and Flame*, Vol. 73, pp. 233–249.

Lefebvre, A. H., 1984, "Fuel Effects on Gas Turbine Combustion-Liner Temperature, Pattern Factor, and Pollutant Emissions," *AIAA Journal of Aircraft*, Vol. 21, No. 11, pp. 887–898.

Lefebvre, A. H., 1985, "Fuel Effects on Gas Turbine Combustion-Ignition, Stability, and Combustion Efficiency," ASME JOURNAL OF ENGINEERING FOR GAS TURBINES AND POWER, Vol. 107, pp. 24–37.

Mellor, A. M., 1976, "Gas Turbine Engine Pollution," *Prog. Energy Combust. Sci.*, Pergamon Press, Vol. 1, pp. 111–133.

Plee, S. L., and Mellor, A. M., 1978, "Flame Stabilization in Simplified Prevaporizing Partially Vaporizing and Conventional Gas Turbine Combustors," *Journal of Energy*, Vol. 2, No. 6, pp. 346–353.

Plee, S. L., and Mellor, A. M., 1979, "Characteristic Time Correlation for Lean Blowoff of Bluff-Body-Stabilized Flames," *Comb. and Flame*, pp. 61–80.

Rizk, N. K., and Mongia, H. C., 1991, "Low NO_x Rich-Lean Combustion Concept Application," AIAA Paper No. 91-1962.

Rizk, N. K., and Mongia, H. C., 1993a, "Three-Dimensional Gas Turbine Combustor Emissions Modeling," ASME JOURNAL OF ENGINEERING FOR GAS TURBINES AND POWER, Vol. 115, pp. 603–611.

Rizk, N. K., and Mongia, H. C., 1993b, "Semianalytical Correlations for NO_x, CO, and UHC Emissions," ASME JOURNAL OF ENGINEERING FOR GAS TURBINES AND POWER, Vol. 115, pp. 612–619.

Rizk, N. K., and Mongia, H. C., 1995, "NO_x Model for Lean Combustion Concept," *AIAA Journal of Propulsion and Power*, Vol. 11, No. 1, pp. 161–169.

Westbrook, C. K., and Dryer, F. L., 1981, "Simplified Reaction Mechanism for the Oxidation of Hydrocarbon Fuels in Flames," *Combustion Science and Technology*, Vol. 27, pp. 31–43.

Westbrook, C. K., and Pitz, W. J., 1984, "A Comprehensive Chemical Kinetic Reaction Mechanism for Oxidation and Pyrolysis of Propane and Propane," *Combustion Science and Technology*, Vol. 37, pp. 117–152.

APPENDIX

This appendix includes all the necessary equations and constants needed to perform the reaction rate calculations of the developed emission model reported in Section IV. As mentioned earlier, it has been observed from the chemical kinetic calculations that the reaction rate could proceed at a completely different rate depending on whether the residence time is smaller or larger than a critical time τ_ℓ. Also it is noticed that the reaction rates are significantly higher at the initial time step of the reactor compared to those at the remaining residence time in the reactor. Thus, a different set of parameters is proposed for each case, as illustrated in the following subsections.

A.1 Fuel Reaction Rate

The proposed equation for a fraction of the fuel reacted in g/kg fuel when reaction time is larger than τ_ℓ is given by:

$$-d(C_xH_y) = C_1 e^{-E/T}(P_3/345)^m(\tau/0.25)^\ell \quad (5)$$

The parameter E varies with pressure P_3 and equivalence ratio ϕ according to the following equation:

$$E = (322.6 - 1127\phi + 1550.3\phi^2 - 1030.4\phi^3 + 319.3\phi^4 - 33.3\phi^5)(P_3/345)^n \quad (6)$$

and

$$n = 5.61 \times 10^4 \phi^{9.2} \exp(-11.42\phi^{0.9}) \quad (7)$$

The exponent m also varies with ϕ according to the following expression:

$$m = 0.034 - 0.104\phi + 0.125\phi^2 - 0.071\phi^3 + 0.018\phi^4 - 0.0013\phi^5 \quad (8)$$

The constant $C1$ is given by:

$$C1 = 207.6 - 561.7\phi + 509.0\phi^2 - 153.45\phi^3 \quad (9)$$

for $\phi \leq 1.2$ and

$$C1 = -161.4 + 407.5\phi - 344.7\phi^2 + 98.5\phi^3 \quad (10)$$

for $\phi > 1.2$.

The residence time exponent ℓ is given by

$$\ell = (\ell p + C2)(400/T_3)^{1.243} - C2 \quad (11)$$

where

$$\ell p = (0.0074 - 0.022\phi + 0.022\phi^2 - 0.007\phi^3) \exp(C3(1/P_3 - 0.0029)) \quad (12)$$

and

$$C2 = 0.004 - 0.011\phi + 0.01\phi^2 - 0.003\phi^3 \quad (13)$$

for $\phi \leq 1.1$ or

$$\ell p = (0.014 - 0.045\phi + 0.054\phi^2 - 0.029\phi^3 + 0.00057) \exp(C3/(1/P_3 - 0.0029)) \quad (14)$$

and

$$C2 = 0.011 - 0.034\phi + 0.04\phi^2 - 0.02\phi^3 + 0.004\phi^4 \quad (15)$$

for $\phi > 1.1$

The constant $C3$ is either given by

$$C3 = 170.2(\phi/0.6)^{0.67} \quad \text{for } \phi \leq 1.0 \quad (16)$$

$$\text{or } C3 = 240.2\phi - 3.43 \quad \text{for } \phi > 1.0 \quad (17)$$

For ϕ equal to or below 0.4, τ_ℓ is given by:

$$\tau_\ell = 0.98 \times 10^{-4}\phi^{-10}\exp(0.2\phi^{-1.3})C4R \quad (18)$$

and for $\phi > 0.4$.

$$\tau_\ell = 0.025\phi^{-3}\exp(0.004\phi^{-6.5})C4R \quad (19)$$

where

$$C4 = (T3/500)^{-m}\exp -96.6(P_3^{-0.75} - 345^{-0.75}) \quad (20)$$

The exponent m is given by

$$m = -4.89(\phi/0.4)^{-1.66} \quad (21)$$

and

$$R = 1.348\left(\frac{[C_xH_y] + [CO]/2.5 + [C_lH_J]/3.0}{FAR/(1 + FAR)}\right) \exp(0.464 - 2[O_2]) - 0.348 \quad (22)$$

For a time step less than τ_ℓ the fuel reaction proceeds gradually as given by:

$$-\frac{d(C_xH_y)}{dt} = C5.\exp(-E1/T)[C_xH_y]^b[O_2]^c [C_lH_J]^d\phi^{-1} \quad (23)$$

The terms within square brackets are mass concentration and the left side term represents rate of fuel reaction in (g/kg fuel/s), and the exponents are given by:

$$b = 1.5\exp(-2.84 \times 10^{-5}P_3^{1.5}) \quad (24)$$

$$c = 0.53 - 0.0023P_3 + 0.33 \times 10^{-5}P_3^2 - 0.95 \times 10^{-9}P_3^3 \quad (25)$$

$$d = 0.607\exp(95.45/P_3) \quad (26)$$

$E1$ is 15,000 and constant $C5$ is given by

$$C5 = 0.333 \times 10^{13}(P_3/345)^{-5.5} \exp 0.24(P_3^{0.5} - 345^{0.5}) \quad (27)$$

To initiate reaction when intermediate fuel concentration is very small (below 0.0005), a time step of 0.1 ms is used to determine the fuel reaction rate from Eq. (23) with the following constants:

$$C5 = 0.84 \times 10^6\exp(210.47/P_3) \quad (28)$$

The constants $E1$, b, c, d, are 9500, 0.6, 0.7, and 0.0, respectively.

A.2 Intermediate Reaction Rate

The intermediate fuel reacts at the following rate:

$$-\frac{d(C_lH_J)}{dt} = C6\exp(-E2/T)[C_xH_y]^b [O_2]^c[C_lH_J]^d f(\phi)[CO]^e \quad (29)$$

For the initial time step in reactor, if less than τ_ℓ, the various parameters are given by:

$$C6 = 0.66 \times 10^8(P_3/345)^{-1.045} \quad (30)$$

$f(\phi) = (\phi/0.4)^{0.8}$, and $E2$, b, c, d, and e are 20,000, 0.5, -0.5, -0.6, and 0.0, respectively. For a time step larger than τ_ℓ the constants for the initial rate of reaction are given by:

$$C6 = 0.38 \times 10^7(P_3/345)^{0.3} \quad (31)$$

$$E2 = 4000(P_3/345)^{0.614}$$

$$f(\phi) = (0.4/\phi)^{1.3}\exp(-0.4/\phi^{1.4}) \quad (32)$$

and the corresponding values of b, c, d, and e are 0.5, 0,4, 0.0, and 0.0.

After the initial time step, the intermediate fuel reacts at a much slower rate. The constants of Eq. (29) for smaller residence time than τ_ℓ are given by:

$$C6 = 0.212 \times 10^{13}(P_3/345)^{0.208} \quad (33)$$

$f(\phi) = (0.4/\phi)^{1.5}$, and the parameters E, b, c, d, and e are 19,500, 0.3, -1.30, 1.35, and 0.0. For larger residence time, the constants are:

$$C6 = 2.13 \times 10^{13}\exp(-538.2/P_3) \quad (34)$$

$$f(\phi) = (0.4/\phi)^a \quad (35)$$

and

$$a = 3.0(P_3/345)^{0.15} \quad (36)$$

The parameters b, c, d, and e are 0.8, 0.1, 0.4, and 0.8.

A.3 CO Reaction Rate

For a time step less than τ_ℓ, the rate of CO reaction is given by:

$$-\frac{d(CO)}{dt} = C7\exp(-14{,}500/T)([C_xH_y] + [CO])^{-2}[O_2]^{7.4}(0.4/\phi)^{-4.0} \quad (37)$$

where

$$C7 = 1.86(P_3/345)^{-0.17} \quad (38)$$

For reaction time above τ_ℓ, the CO reaction during initial time step is given by:

$$-\frac{d(CO)}{dt} = C7\exp(-E3/T)[C_xH_y]^b[O_2]^c [C_lH_j]^d[CO]^e f1(\phi)[H_2O]^f - C8\exp(-E4/T)[O_2]^{cr}[C_lH_J]^{dr} [CO]^{er}[CO_2]^{fr} f2(\phi) \quad (39)$$

The various parameters involved in this equation are given by:

$$C7 = 0.172 \times 10^8 (P_3/345)^{-0.1} \quad (40)$$

$$C8 = 0.9 \times 10^9 (P_3/345)^{-0.2} \quad (41)$$

$$f1(\phi) = (0.4/\phi)^{1.9} \exp(-0.5/\phi^{2.3}) \quad (42)$$

$f2(\phi) = \phi^{0.7}$, and the values of remaining constants are given by:

b	c	d	e	f	cr	dr	er	fr
−0.5	1.5	0.0	0.0	0.0	0.25	0.0	0.0	2.3

$E3$ and $E4$ are 7500 and 4000.

The CO reaction proceeds at a much slower rate, following the initial time step, as given by Eq. (39) but with the following constants:

$$C7 = 0.643 \times 10^{15} (P_3/345)^{0.735} \quad (43)$$

$$C8 = 0.179 \times 10^{16} \exp(0.0253 P_3^{0.5}) \quad (44)$$

$$f1(\phi) = (0.4/\phi)^{3.0} \exp(-1.0\phi^{0.7}) \quad (45)$$

$$f2(\phi) = \phi \exp(-0.3/\phi^{0.3}) \quad (46)$$

The remaining constants are:

b	c	d	e	f	cr	dr	er	fr
0.0	1.7	−	2.3	0.6	1.5	0.6	0.9	1.0

$E3$ and $E4$ are 18,500 and 30,000.

The intermediate fuel concentration parameter in the first term of Eq. (39) is replaced here by the term exp (3.35 $[C_I H_J]^{0.2}$).

A.4 Hydrogen Reaction Rate

The reaction of H_2 if initial time step in reactor is below τ_ℓ is given by:

$$-\frac{d(H2)}{dt} = C9 \exp(-E5/T)[C_x H_y]^b [O_2]^c [C_I H_J]^d [H_2]^g f3(\phi) \quad (47)$$

The equation constants are:

$$C9 = 0.35 \times 10^5 (P_3/345)^{-0.62} \quad (48)$$

$$f3(\phi) = (\phi/0.4)^{0.5} \quad (49)$$

$E5$, b, c, d, and g are 10,500, 0.8, −0.9, −0.5, and 0.0. The reaction proceeds after initial time step at the rate given by Eq. (47) but with these modified constants:

$$C9 = 0.244 \times 10^{14} (P_3/345)^{-0.385} \quad (50)$$

$$f3(\phi) = (\phi/0.4)^{0.6} \exp(-0.1/\phi^{1.4}) \quad (51)$$

$E5$, b, c, d, and g are 18,500, 0.5, 4.5, 1.9, and −1.0. For residence time above τ_ℓ, the H_2 reaction during initial time step is given by Eq. (47) with the following constants:

$$C9 = 0.162 \times 10^8 (P_3/345)^{-0.8} \quad (52)$$

$$f3(\phi) = (0.4/\phi)^{4.2} \exp(-2.5/\phi^{1.4}) \quad (53)$$

$E5$, b, c, d, and g are 1000, 0.2, 0.8, 0.0, and 0.0.

The reaction proceeds after initial step at the rate given by Eq. (47) with the following modifications to the constants:

$$f3(\phi) = (\phi/0.4)^{2.07} \quad (54)$$

A second term Rd is subtracted from the right-hand term of Eq. (47) and is given by:

$$Rd = C10 \exp(7500/T)[O_2]^{-0.5} [C_I H_J]^{0.5} [H_2]^{-0.1} \phi^{-1.0} \quad (55)$$

The constants $C9$ and $C10$ are 0.375 $E8$ and 0.0108. $E5$, b, c, d, and g are 15,125, 0.0, 2.15, 0.5, and 0.0.

A.5 NO_x Reaction Rate

Based on the concentrations of various species, the following NO_x reaction rate equation is proposed:

$$\frac{d(NO_x)}{dt} = C11 \exp(-29{,}000/T)[O_2]^{0.9} [CO]^{0.8} f4(\phi) - C12 \cdot \exp(-60{,}000/T) \{O_2\}^{0.8} (C_I H_J]^{0.7} [NO]^{0.3} [CO]^{2.5} f5(\phi) \quad (56)$$

where

$$C11 = 5.7 \times 10^9 \exp(-13.85/P_3^{0.25}) \quad (57)$$

$$C12 = 1.322 \times 10^{20} \cdot \exp(-340/P_3) \quad (58)$$

$$f4(\phi) = (\phi/0.4)^{4.4} \exp(-2\phi^{3.4}) \quad (59)$$

$f5(\phi) = \phi^{-1}$, and the second term on the right-hand side of Eq. (56) represents the reduction in NO concentration at rich fuel mixtures.

A.6 Intermediate Fuel Structure

The expressions developed for the two elements for the initial time step with time step above τ_ℓ are as follows:

$$I \text{ or } J = C13 \exp(E6/T)[C_x H_y]^b [O_2]^c \left(\frac{0.4}{\phi}\right)^h [C_I H_J]^d \quad (60)$$

where

$$C13 = 2.13(P_3/345)^{0.01674} \quad (61)$$

$$E6 = 230(P_3/345)^{0.3992} \quad (62)$$

and b, c, d, and h are −0.065, 0.11, 0.0, and −0.02.

The expression for the hydrogen content is given by Eq. (60) with the values of $E6$, b, c, d, and h of −220, −0.09, 0.185, 0.0, and −0.02. The constant $C13$ is 5.25.

In the reaction following the initial time step the constants for Eq. (60) are given as follows:

	$E6$	b	c	d	h	$C13$
Carbon	290	0.0	0.04	0.0	0.005	1.91
Hydrogen	−310	0.0	0.045	0.005	0.325	–

$C13$ for the hydrogen expression is given by

$$C13 = 6.61(P_3/345)^{0.03456} \quad (63)$$

For reaction proceeding with a time step below τ_ℓ, the constants for carbon and hydrogen contents at initial time step are given by:

	$E6$	b	c	d	h
Carbon	130	0.035	0.14	0.0	−0.055
Hydrogen	−240	−0.05	0.55	0.0	−0.245

$C13$ for the carbon and hydrogen expressions are given by:

$$C13 = 2.13(P_3/345)^{0.01674} \quad \text{for carbon} \quad (64)$$

$$C13 = 6.63(P_3/345)^{0.00758} \quad \text{for hydrogen} \quad (65)$$

Similarly, the constants for Eq. (60) for the reaction following the initial step are given by:

	$E6$	b	c	d	h	$C13$
Carbon	40	0.0	0.045	0.0	−0.01	2.3
Hydrogen	−630	0.0	0.47	−0.075	−0.215	−

$C13$ for the hydrogen equation is given by:

$$C13 = 11.9(P_3/345)^{-0.01842} \tag{66}$$

A.7 Fuel Oxygen

The expressions for the oxygen given in (g/kg fuel) is as follows:

$$(fO_2) = C14 \exp(E7/T)[C_xH_y]^b[O_2]^c$$
$$[C_lH_J]^d[CO]^f f7(\phi) \tag{67}$$

For reaction with a time step above τ_ℓ the constant $C14$ for initial time step is given by:

$$C14 = 1.9(P_3/345)^{0.21225} \tag{68}$$

The constants $E7$, b, c, d, and f are 12,000, −0.4, 0.3, 0.0, and 0.0. Also:

$$f7(\phi) = (0.4/\phi)^{2.3} \exp(-3.8/\phi^{0.9}) \tag{69}$$

Similarly, the constants for reaction proceeding after the initial time step are as follows:

$$C14 = 0.133 \times 10^{-3}(P_3/345)^{1.2854} \tag{70}$$

$$f7(\phi) = (\phi/0.4)^{2.2} \tag{71}$$

The constants $E7$, b, c, d, and f are 22,100, 1.6, −0.42, 0.2, and −2.3.

For reactions with a time step below τ_ℓ, the constants of Eq. (67) for initial time step are:

$$C14 = 0.338 \times 10^{8}(P_3/345)^{-0.1755} \tag{72}$$

$$f7(\phi) = (0.4/\phi)^{-0.1} \tag{73}$$

The constants $E7$, b, c, d, and f are −5000, −0.2, 2.2, 0.0, and 0.0.

For the reaction following the initial step, the constants are given by:

$$C14 = 0.22 \times 10^{4}(P_3/345)^{-0.2039} \tag{74}$$

$$f7(\phi) = (0.4/\phi)^{-2.2} \tag{75}$$

The remaining constants $E7$, b, c, d, and f are −5000, −1.2, 4.8, 0.0, and −0.4.

A.8 Reaction Temperature

The developed reaction temperature expression, in terms of the equilibrium temperature T_{eq}, is given as follows:

$$T/T_{eq} = C15 \exp(E8/T3) \exp\left(b[C_xH_y]\right)$$
$$\exp(c[O_2]) \cdot \exp(d[C_lH_J])$$
$$\exp(f[CO]) f8(\phi) \tag{76}$$

The constants for reactions with a time step above τ_ℓ for the initial step are:

$$C15 = 0.848(P_3/345)^{0.020} \tag{77}$$

$$f8(\phi) = (0.4/\phi)^{0.125} \exp(0.1\phi^{0.96}) \tag{78}$$

$E8$, b, c, d, and f are 60, 0.277, −0.26, 20.574, and −0.5.

The equation for the reaction following the initial step is given by:

$$T/T_{eq} = 0.463 \exp\left(-2.087[C_xH_y]^{0.5}\right)$$
$$\cdot \exp\left(-0.25[O_2]^{1.1}\right) \exp\left(-3.649\{C_lH_J\}^{2.6}\right)$$
$$\cdot \exp(-0.5[CO]) f8(\phi) \tag{79}$$

and

$$f8(\phi) = (0.4/\phi)^{-0.4} \exp(0.4/\phi^{0.8}) \tag{80}$$

The constants for Eq. (76) used for a time step below τ_ℓ for initial step are given as follows: $E8$, b, c, d, and f are 30, 28.855, 0.38, −23.6, and 0.0. The constant $C15$ is 0.869 and $f8\,(\phi)$ is 1.0.

Similarly, the constants for the reaction following the initial step are given by:

$$C15 = 0.852(P_3/345)^{0.00842} \tag{81}$$

$E8$, b, c, d, and f are 30, −28.855, 0.335, −23.105, and 0.0. The constant $f8\,(\phi)$ is 1.0.

T. Vaskopulos

C. E. Polymeropoulos

V. Sernas

Department of Mechanical and Aerospace Engineering, Rutgers University, Piscataway, NJ 08855

Temperatures in a Gas Turbine Vaporizer at Near Idle Engine Conditions

The work is a laboratory investigation of the effect of different liquids and liquid flow rates on the metal temperature of a gas turbine T vaporizer. Most of the experimentation was carried out using JP5. A limited number of runs using Diesel Fuel Marine and calibration runs using water provided additional data for different fluids. Conditions that approach local liquid depletion inside the vaporizer were identified by monitoring local overheating of the vaporizer metal. Because of apparatus limitations, testing was carried out only at vaporizer pressure and liquid flow rates approaching idle engine operation. An experimental correlation was developed allowing estimation of the mean vaporizer temperature as a function of input conditions and fluid properties.

Introduction

A vaporizer fuel injector consists of a single tube, or set of tubes, projecting into a gas turbine combustion chamber and introducing a mixture of compressor air and fuel into the primary zone. Liquid is supplied at the vaporizing tube entrance at practically combustion chamber pressure, and liquid breakup into particles occurs inside the vaporizer by shear interaction with the air stream and impaction with the tube walls. Since the vaporizer tube is exposed to the hot environment of the primary zone, it reaches a fairly high temperature through convective and radiative heating. This results in significant fuel vaporization inside the vaporizer so that the exiting mixture consists of liquid, air, and fuel vapor. The cooling process due to liquid vaporization serves in keeping the metal temperature at sufficiently low level to prevent failure. Complete vaporization of the liquid is therefore not desirable if the vaporizer tube is to survive the high combustor temperatures.

Previous published work has presented descriptions of different vaporizer types (Lindsey, 1949; Vezhba, 1959; Alperi and Hoffman, 1971; Parnell and Williams, 1971; Sotheran, 1984). The extent of vaporization for different operating conditions has been qualitatively assessed by Low (1987) and Jasuja and Low (1988) using high-speed photography of the exit mixture. Particle size distributions from a vaporizer in cold flow are also presented in Jasuja and Low (1988). The temperature of an engine-mounted vaporizer was measured using temperature-sensitive paints (Sotheran, 1984). Two of the present authors have presented experimental data from laboratory testing at near idle engine operating conditions of an F402 type-L vaporizer fuel injector (Polymeropoulos et al., 1990). Part of the data, which consisted of vaporizer metal temperatures and photographs of the mixture exit, indicated partial vaporization, for local vaporizer metal much in excess of the distillation end points for the fuels tested.

The present work is an experimental investigation of the effect of different liquids and liquid flow rates on the vaporizer temperature. Specifically, conditions that approach local liquid depletion inside the vaporizer were identified by monitoring local overheating of the vaporizer metal. Experimentation was carried out by reducing the liquid flow rate while maintaining all other experimental variables constant, and essentially identified conditions of incipient burnout as defined in Hewitt (1982).[1] The practical importance of the results is that they identify operating conditions to be avoided for prolonging vaporizer lifetime. The vaporizer employed was a T vaporizer, which consists of one inlet tube and two outlet spouts. As in Polymeropoulos et al. (1990), the experimental apparatus allowed heating of the vaporizer in a laboratory noncombusting environment, and permitted accurate control of the rate of heat input to the vaporizer. Because of apparatus limitations, testing was carried out only at vaporizer pressure conditions corresponding to near idle engine operation for the Rolls-Royce Pegasus engine using T vaporizer fuel injectors. Details of the work can be found in Vaskopulos (1990).

Experimental Apparatus

The general experimental setup was similar to that used in the previous work (Polymeropoulos et al., 1990). Provision was also made for heating the liquid fuel before the vaporizer in order to expand the range of mixture inlet conditions.

Contributed by the International Gas Turbine Institute and presented at the 38th International Gas Turbine and Aeroengine Congress and Exposition, Cincinnati, Ohio, May 24–27, 1993. Manuscript received at ASME Headquarters March 17, 1993. Paper No. 93-GT-312. Associate Technical Editor: H. Lukas.

[1]The term burnout, used instead of other possible terms like boiling crisis, dryout, etc., does not imply failure of the vaporizer material.

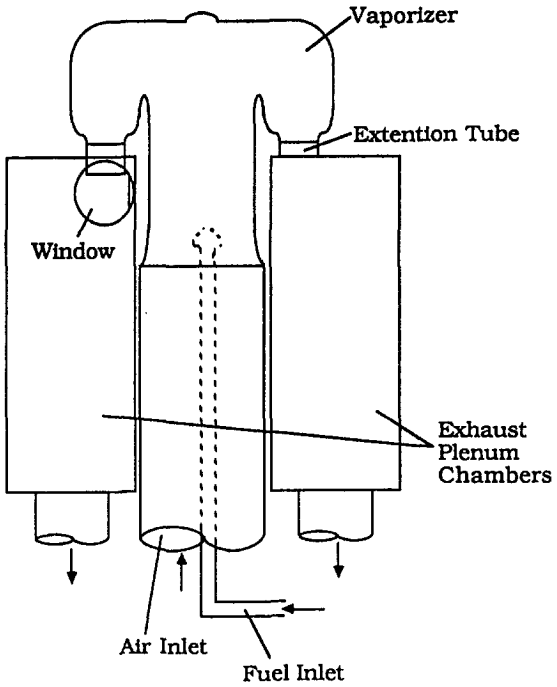

Fig. 1 Schematic diagram of the vaporizer showing fluid inlets and outlets

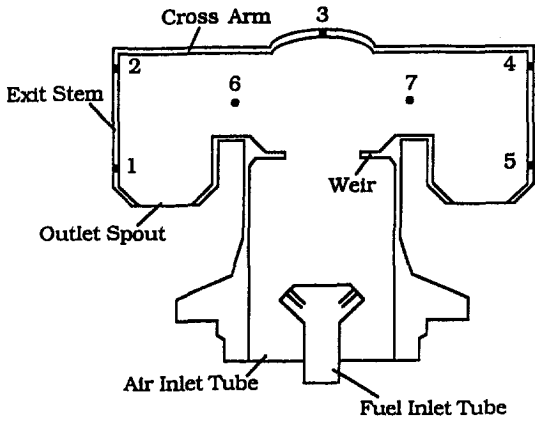

Fig. 2 Schematic cross section of the vaporizer showing thermocouple locations

Figure 1 is a schematic diagram showing the vaporizer connected to the air inlet and to the concentric fuel inlet. The exit mixture was discharged into two separate water-cooled exhaust plenum chambers through 2.0 cm extension tubes welded to the exit spouts. A downstream manifold (not shown) joined the two exit streams and discharged them into a cooling section and a liquid separator. As indicated in Fig. 1, one of the plenum chambers was fitted with windows for photographic observation of the exit mixture using a collimated light beam from a pulsed ruby laser.

As with the previous work, the assembly shown in Fig. 1 was placed in a heater cavity consisting of a series of radiant heaters arranged around the vaporizer. A bare type-B thermocouple placed at the center of the heater cavity monitored the mean heater temperature. A rectangular brass enclosure around the heater cavity was used to isolate the heaters and to contain the nitrogen gas flow needed for maintaining an oxygen-free atmosphere around the graphite heaters.

Figure 2 shows a schematic cross section of the vaporizer. For the vaporizer used the inlet air tube was 2.5 cm ID and the outlet spout was 1.6 cm ID. The center-to-center distance between outlet spouts was 6.0 cm and the distance between the vaporizer outlet spout and the top of the cross arms was 3.5 cm. The fuel was introduced through two 1 mm holes at an angle of about 45 deg to the inlet air stream. The purpose of the two weirs shown was to break up the liquid film that may form on the inlet wall. The exit stems and the cross arm were on the same plane of symmetry, which was offset by approximately 2 mm from the plane of symmetry of the inlet tube. This resulted in a swirling motion within the cross arms and the exit stems, which is intended to enhance liquid contact with the wall (Jasuja and Low, 1988).

The vaporizer was instrumented with K-type grounded thermocouples at the positions shown in Fig. 2.[2] Thermocouples 6 and 7 were located on the downstream portion of the vortex generated by the offset between the air inlet and the cross arms. The thermocouple wire was inconel sheathed, it was placed inside grooves machined along the vaporizer surface, and the grooves were then filled with parent metal and machined to a smooth finish. The temperatures registered were therefore at the midpoint of the 1.7-mm-thick vaporizer wall. The temperatures of the inlet air and liquid streams were monitored by bare junction thermocouples within the air and liquid inlets.

Experimental Procedure

The experimental procedure consisted of two parts. The first involved steady-state operation using different water–air mixtures at different inlet air temperatures and radiant heat inputs to the vaporizer. Using the previously described optical system, conditions that resulted in almost complete vaporization were identified as in Polymeropoulos et al. (1990) by the absence of liquid droplets at the vaporizer exit. An energy balance for the water–air mixtures was then used for constructing a calibration curve of rate of energy input to the vaporizer as a function of heater cavity temperature.

The second part of the experimentation employed mostly JP5-air mixtures and a limited number of DFM[3]–air mixtures for comparison. In all cases the vaporizer was operated at steady-state conditions and at constant radiant input heat flux. Identification of incipient liquid deficiency on the vaporizer surface was accomplished by decreasing the liquid flow rate from a maximum value, consistent with idle operation, to a minimum flow rate for which local temperatures in the vaporizer became excessively sensitive to small adjustments in liquid flow rate. The arbitrary quantitative criterion was that a maximum decrease of approximately 10 percent in liquid flow was followed by a large (and potentially unsafe) excursion in vaporizer temperature, at which point the experimental run was interrupted before the establishment of thermal equilibrium. Empirical observation showed that for the conditions of the present experimentation such sensitivity to changes in liquid fuel flow rate occurred when the local vaporizer temperature approached 700°C. Approaching 700°C at any point of temperature measurement in the vaporizer metal was therefore taken as an alternate way of identifying the minimum JP5 flow rate. The minimum liquid flow rate condition identified using this procedure, was taken to imply liquid phase depletion due to boiling and vapor generation on the wall, thus requiring a relatively large increase in metal temperature to accommodate the constant heat flux. This will be referred to as a local burnout condition consistent with

[2]The thermocouple at position 4, Fig. 2, failed during experimentation, and no results will be shown for that position.

[3]The fuels used were provided by the Naval Air Propulsion Center, Lakewood, New Jersey. The JP5 specification was that of NAPC fuel No. 33 (IBP: 459 K, FBP: 533 K), and the Diesel Fuel Marine was NAPC fuel No. 31 (IBP: 453 K, FBP: 606 K).

Table 1 Range of experimental variables

All Tests	
Test section pressure:	192 kPa
Air mass flow rate:	0.0439 kg/s
Radiant heat input	2.6–2.8 kW
JP5	
Inlet air temperature:	373–453 K
Flow rate:	0.0073–0.0034 kg/s
Inlet fuel temperature:	298–377 K
DFM	
Inlet air temperature:	423 K
Fuel flow rate:	0.0050–0.0041 kg/s
Inlet fuel temperature:	363 K

the definition of Hewitt (1982). The matrix of experimental conditions used is shown in Table 1.

Results and Discussion

Rate of Energy Input to the Vaporizer. As in Polymeropoulos et al. (1990) the energy input to the vaporizer was obtained from experimental data using water as liquid. Convective heat transfer was negligible, and the data were correlated using the following relationship:

$$q = 2.764 \times 10^{-10}\left(T_h^4 - T_{vm}^4\right) \qquad (1)$$

where q (kW) is the rate of energy input, T_h (K) is the radiant heater cavity temperature, and T_{vm} (K) is the arithmetic mean vaporizer temperature. Since $T_h \gg T_{vm}$ the contribution of vaporizer temperature in Eq. (1) was small, and enabled setting and maintaining the desired energy input to the vaporizer using the radiant heater cavity temperature T_h. The use of Eq. (1) implies radiation heat transfer from an enclosure to a small body that does not see itself. An approximate enclosure analysis similar to that presented in the same reference can be carried out for verification and also to show that the vaporizer was uniformly irradiated. For the tests with JP5 and DFM the rate of radiant heat input to the vaporizer was constant at 2.7 ± 0.1 kW (353 ± 13 kW/m^2) corresponding to a radiant heater temperature of approximately 1780 K.

Vaporizer Temperatures. Visualization of the flow pattern inside the vaporizer (Sotheran, 1984; Jasuja and Low, 1988) has shown that it is dominated by a swirling flow within the cross arms and exit stems whose purpose is to enhance the distribution of the liquid on the inside walls. This results in "washing" of the cross-arm and stem walls with a liquid layer formed from particles deposited by the vortical flow pattern. Maintaining an average heat flux requires vaporizer metal temperatures that depend on the convective heat transfer coefficient resulting from the two-phase flow inside the vaporizer. The recorded temperature level and the temperature differences between different portions of the vaporizer can therefore be used to infer the liquid–wall heat transfer interaction.

Figures 3(*a–d*) are examples of vaporizer temperatures from the JP5–air tests showing the effect of reducing JP5 flow rate, all other conditions remaining constant. Figures 4(*a, b*) show the effect of reducing the liquid flow rate using water. The temperatures shown are those recorded by the thermocouples imbedded in the metal. Actual surface temperatures differed by 10–15°C and can be estimated by accounting for conduction heat transfer through the wall and using the mean radiant flux and the mean metal thermal conductivity. Data collected (not shown) using air only through the vaporizer showed temperature symmetry, within 5 percent, among the cross arms and stems and with the highest readings occurring in the stems. This was a confirmation of the uniformity of the imposed radiant heating within the vaporizer. It enables using the temperature data to postulate on the heat transfer between the internal two-phase flow and the vaporizer metal. The results in Figs. 3 and 4 show a consistent temperature nonuniformity between the two exit spouts. In view of the symmetry in the pure air results, this nonuniformity reflects a difference in the liquid supply rate caused by small, but unavoidable, misalignment of the liquid supply tube within the air inlet.

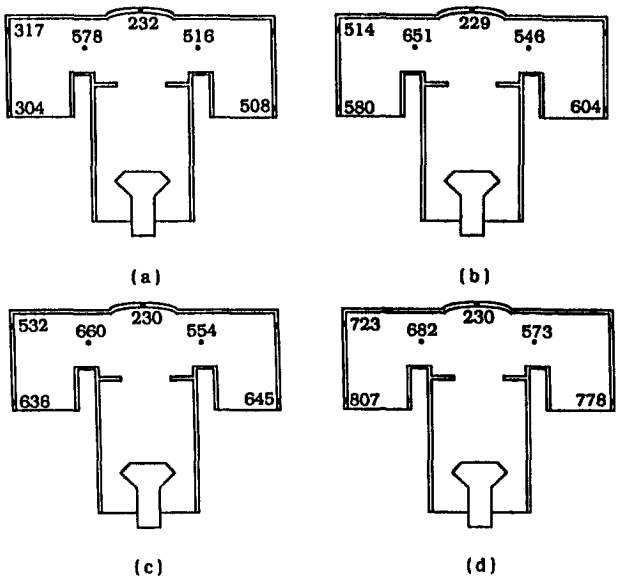

Fig. 3 Effect of JP5 flow rate on vaporizer temperature. T_a = 423 K, T_l = 374-376 K. Radiant heat input = 2.7 kW. Temperatures shown in °C. (*a*) m_l = 0.0073 kg / s, (*b*) m_l = 0.0048 kg / s, (*c*) m_l = 0.0046 kg / s, (*d*) m_l = 0.0045 kg / s.

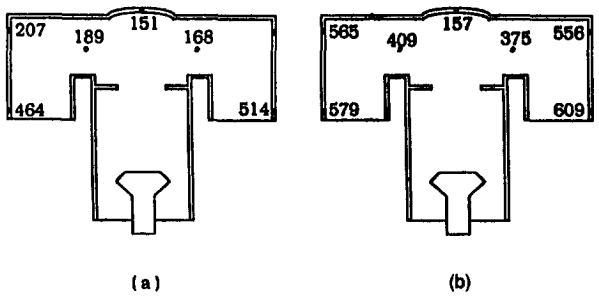

Fig. 4 Effect of water flow rate on vaporizer temperature. T_a = 423 K, T_l = 296-297 K. Radiant heat input = 2.3 kW. Temperatures shown are in °C. (*a*) m_l = 0.00120 kg / s, (*b*) m_l = 0.00099 kg / s.

Figure 3(*a*) is for idle engine liquid flow rate, and Fig. 3(*d*) is one set of measurements recorded during the unsteady temperature excursion induced by reducing the flow rate slightly below that of the steady-state conditions shown in Fig. 3(*c*). Examination of the results in Fig. 3 shows that, as expected, the vaporizer temperatures increased as the liquid flow rate was reduced. An exception was the thermocouple at position 3 located in the middle of the cross arm and above the weirs built into the vaporizer (Fig. 2). The temperatures recorded at this position were substantially lower than those in the remaining vaporizer metal and were also relatively insensitive to changes in liquid flow rate. It appears, therefore, that position 3 was cooled by a liquid layer formed by a portion of the liquid that was not distributed by the weirs into the gas flow, and which effectively cooled the surface around thermocouple 3 by building a substantial liquid film in that region. The maximum temperatures were near the exit spouts reflecting heating of the liquid film, or liquid depletion, in the downstream direction.

It is interesting to compare the maximum temperatures with previously reported Liedenfrost temperatures by Tamura and Tanasawa (1959) for kerosene fuels. Although these data were obtained in the absence of forced convective flow and using single droplets on a hot surface, it can nevertheless provide some qualitative insight on the present results. For kerosene fuels at one atmosphere, Tamura and Tanasawa reported that the unstable region before the Liedenfrost temperature began at approximately 250°C, and that vapor film boiling occurred above approximately 475°C. The present JP5 data in Fig. 3 show that at least for the lowest liquid flow rates the exit spout temperatures were above 700°C. This was considerably larger than the reported Liedenfrost temperature for JP5 and supports the previously postulated liquid deficiency at local metal conditions exceeding 700°C. Similar conclusions can be drawn using the measured exit spout temperatures from the present data for air–water mixtures, which is shown in Fig. 4. The use of DFM resulted in lower measured temperatures compared to those obtained with JP5. This is consistent with previously similar results with a J-type vaporizer (Polymeropoulos et al., 1990).

Thermocouple locations 6 and 7 were downstream from the two weirs and near the entrance to vortex region within the cross arms. For the two hydrocarbon fuels tested the temperatures registered at these two locations were unexpectedly high compared to the remaining vaporizer temperatures as is indicated in Fig. 3 for JP5. However, using water the temperatures at these two locations were consistent with those in the cross arm (Fig. 4). This observed temperature behavior at locations 6 and 7 was probably due to differences in liquid fuel distribution and vaporization among the liquids tested. An adequate explanation based on the mechanisms within the vaporizer and on the effect of the physical properties of the liquids is not yet available. In that respect the use of water resulted in vaporizer temperatures that were considerably lower than those obtained with JP5 or DFM for the same liquid flow and rate of heat input.

Correlation of Experimental Data. The present experimental measurements of vaporizer temperature (including the constant radiant heat input rate results using JP5 and DFM, and the variable input heat rate results using water for calibration), were correlated using the following relationship for which the correlation coefficient, R^2, was 0.97:

$$\frac{q(T_{vm}-T_l)^{0.636}}{(T_{vm}-T_a)} = \frac{62193\, m_l^{0.8}(\rho_l\sigma)^{1.408}\rho_g^{0.145}\mathrm{Pr}^{0.106}}{L^{0.674}[(T_b-T_l)m_l c_l]^{0.353}} \quad (2)$$

where T_a is the inlet air temperature, m_l is the liquid flow rate, T_l is the inlet liquid temperature, c_l is the liquid heat capacity at the inlet liquid temperature, ρ_g and ρ_l are the densities of inlet air and liquid, respectively, L, is the latent heat of vaporization at the boiling point, Pr is the liquid Prandtl number, T_b is the liquid boiling point at the vaporizer pressure, and s is the liquid surface tension computed at the inlet conditions. The term $(T_b - T_l)m_l c_l$ is a liquid subcooling parameter, which includes the influence of the liquid mass flow rate. Fuel properties were obtained from *Aviation Fuel Properties* (1983) and Lefebvre (1983). Equation (2) can be used to compute the mean vaporizer temperature, and Fig. 5 shows predicted and measured values of T_{vm} for all the experimental runs including those with water. The agreement is overall better than 10 percent, which is satisfactory in view of the large range of two-phase flow conditions covered.

Equation (2) can be used to compute mean vaporizer temperatures for experimental conditions different than those used in the present tests, but within a reasonable range of the variables employed for its derivation. Figure 6 shows the

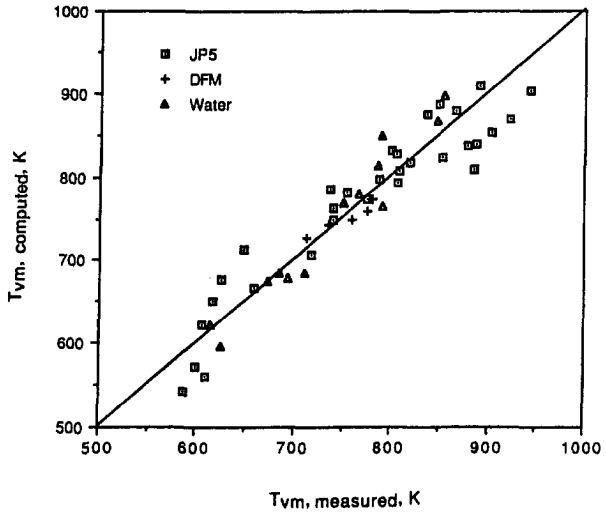

Fig. 5 Computed and mean vaporizer temperatures

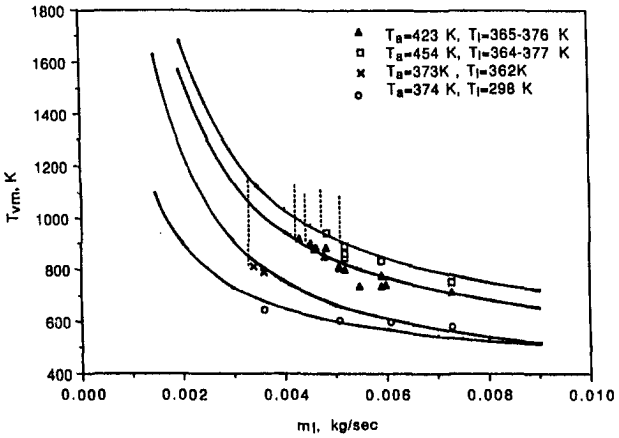

Fig. 6 Variation of mean vaporizer temperature with JP5 flow rate

variation of calculated mean vaporizer temperatures (using Eq. (2)) with JP5 flow rate, and for a variety of inlet air temperatures. For each air temperature the inlet liquid temperature was constant and was chosen within ±5 K of those used during experimentation. This enables comparison with relevant experimental data that are also in the figure. As expected, the agreement between predicted and measured results was satisfactory. As can be seen in Fig. 6, the mean vaporizer temperature increased slowly with decreasing liquid flow rate for relatively large liquid flow rate values. For low liquid flow rates, depending on the initial air temperature, there was rapid and accelerating increase in vaporizer temperature with decreasing liquid flow rate. This behavior reflects the previously noted increased sensitivity of vaporizer temperature to liquid flow rate changes as the liquid flow rate decreases. It is attributed to liquid depletion at the wall and was used experimentally to define critical burnout conditions. The dashed lines in Fig. 6 identify such experimentally determined critical mass flow rates, which are located near the region of rapid vaporizer temperature increase with decreasing liquid flow rate.

The inlet air temperature had a strong influence on the mean temperature of the vaporizer, since it affected the overall temperature level of the device. Increasing the air temperature also enhances heating of the liquid within the air stream. As a result, as is shown in Fig. 6, the mean vaporizer temperature increased at constant liquid flow rate

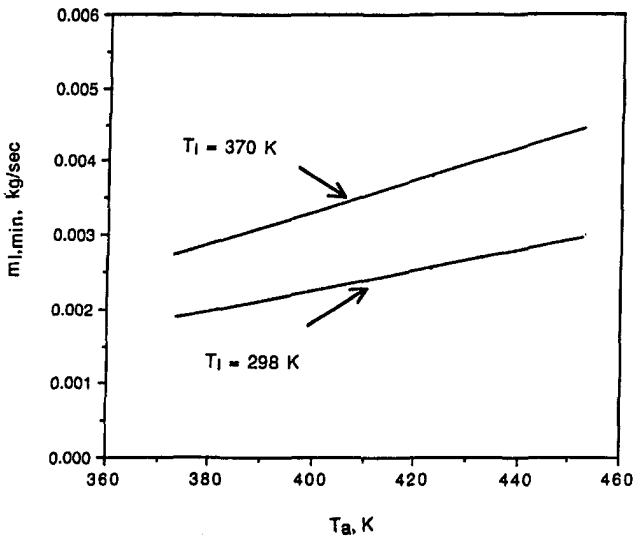

Fig. 7 Minimum JP5 flow rate for a mean vaporizer temperature of 970 K for two inlet liquid temperatures

as the inlet air temperature was increased. The effect of inlet liquid temperature was important only for large changes in liquid temperature.

The results of Fig. 6 can be used to identify minimum liquid flow rates for maintaining steady-state vaporizer temperatures at different inlet conditions. This is shown in Fig. 7 where the minimum JP5 mass flow rate is plotted against inlet air temperature for a mean vaporizer temperature of 970 K and two inlet liquid temperatures, 370 K and 298 K. The results in Fig. 7 reflect the fact that less liquid is needed to cool the vaporizer if the inlet air or liquid temperatures are decreased. Since approaching 970 K was the condition used to identify local incipient burnout conditions on the vaporizer wall, the results in Fig. 7 also identify minimum liquid flow rates for avoiding burnout. Curves similar to those shown in Fig. 7 can be drawn for higher vaporizer temperatures. However, care should be exercised in extrapolating the results from Eq. (2) to very high vaporizer temperatures for which the flow regime progresses to that of postdryout conditions for which the present experimental correlation may not be applicable.

The effect of conditions other than those of idle engine operations should also be considered. Off-idle engine conditions lead to competing effects on vaporizer metal temperature. Increasing compressor exit pressure and temperature is expected to result in increasing liquid vaporization within the vaporizer, accelerating liquid depletion, and thus to contribute to increasing metal temperature. On the other hand the increase in evaporating temperature, which is a consequence of increasing pressure, will act to suppress vapor formation between the liquid and the vaporizer metal, thus increasing the heat transfer rate and acting to depress the metal temperature. The higher liquid flow rate required at off-idle conditions will result in lowering the vaporizer temperature. Finally, increased radiative and convective heat transfer from the combustion primary zone to the vaporizer may increase the vaporizer temperature. The interaction of these competing effects and a quantitative assessment on their influence must await additional experimentation.

Conclusions

Experimental measurements of the metal temperature of a gas turbine T-type vaporizing fuel injector were performed to assess the effect of decreasing the liquid flow rate near idle operating conditions of the Pegasus engine. The test apparatus employed a T vaporizer instrumented with a number of thermocouples embedded into the wall. External heating was provided by placing the test section within a furnace cavity equipped with a set of radiant heaters.

The experimental measurements were used to identify inlet flow conditions corresponding to rapid vaporizer temperature increase with decreasing inlet liquid flow rate. Such rapid temperature change was found when local vaporizer temperatures approached 700°C and was used to identify incipient burnout conditions caused by liquid deficiency due to vapor generation at the wall.

Examination of the measured vaporizer temperatures showed that:

- The highest local vaporizer temperatures were at the two exit spouts.
- A region at the center of the cross arms was well cooled with liquid and always registered a low temperature, which was insensitive to liquid flow rate.
- Vaporizer temperatures using JP5 were higher than those obtained with DFM and considerably higher than those obtained using water.
- There were small temperature nonuniformities between the two arms of the T vaporizer that were probably caused by misalignment of the inlet tube.

An empirical relationship was used to correlate the vaporizer temperature data in terms of the input variables and the properties of the fluids used. This was then used to predict the variation of vaporizer temperature with liquid flow rate and also the minimum required liquid flow rates for maintaining a given vaporizer temperature as the inlet air temperatures are changed. Application and extension of the empirical relationship to operating conditions considerably different from those used in the present experimentation should be undertaken only after additional experimental verification.

Acknowledgments

This work was supported by the Rolls-Royce, Inc., Atlanta, Georgia.

References

Alperi, R. W., and Hoffman, J. S., 1971, "Liquid Distribution of Low Pressure Drop Injection System-Gas Turbine Vaporizer Design," ASME Paper 71-GT-38.

CRC Inc., 1983, *Aviation Fuel Properties*, 3rd ed., Atlanta, GA.

Hewitt, G. F., 1982, "Burnout," *Handbook of Multiphase Systems*, G. Hestroni. ed., Hemisphere, Washington, DC, pp. 6–66.

Jasuja, A. K., and Low, H. C., 1988, "Spray Performance of a Vaporizing Fuel Injector," AGARD Conference on Combustion and Fuels in Gas Turbine Engines, CP 422.

Lefebvre, A., 1983, *Gas Turbine Combustion*, McGraw-Hill, Washington, DC.

Lindsey, W. H., 1949, "The Development of the Armstrong Siddley Mamba Engine," *J. R. Aeronautical Society*, Vol. 53, p. 137.

Low, H. C., 1987, "Recent Research on the Efflux of the Rolls Royce Vaporizer Fuel Injector," AGARD Conference on Combustor Problems in Gas Turbines, Paper No. 353.

Parnell, E. C., and Williams, M. R., 1971, "A Survey of Annular Vaporizing Combustion Chambers," *Comb. and Ht. Tr. in Gas Turbine Systems*, Cranfield International Symposium Series, Vol. 11, Pergamon, London, p. 91.

Polymeropoulos, C. E., Sernas, V., and Sabadics, S., 1990, "Laboratory Testing of a Gas Turbine Vaporizer," *AIAA J. Prop. and Power*, Vol. 6, p. 673.

Sotheran, A., 1984, "The Rolls Royce Annular Vaporizer Combustor," ASME *Journal of Engineering for Power*, Vol. 88, p. 106.

Tamura, Z., and Tanasawa, Y., 1959, "Evaporation and Combustion of a Drop Contacting With a Hot Surface," *Seventh Symposium (International) on Combustion*, Butterworths, London, United Kingdom.

Vaskopulos, T., 1990, "Investigation of Dryout Conditions in a T Type Vaporizer," MS. Thesis, Rutgers University, Piscataway, NJ.

Vezhba, I., 1959, "Experimental Investigation of Fuel Evaporation in the Vaporizing Elements of Combustion Chambers," NASA TM-75383.

Damage-Mitigating Control of Power Systems for Structural Durability and High Performance

M.-K. Wu

A. Ray
Fellow ASME

Mechanical Engineering Department,
The Pennsylvania State University,
University Park, PA 16802

A major goal in the control of complex power systems such as advanced aircraft, spacecraft, and electric power plants is to achieve high performance with increased reliability, availability, component durability, and maintainability. The state of the art in the synthesis of control systems for complex mechanical processes focuses on improving performance and diagnostic capabilities under constraints that do not often adequately represent the dynamic properties of the materials. The reason is that the traditional design is based upon the assumption of conventional materials with invariant characteristics. In view of high performance requirements and availability of improved materials, the lack of appropriate knowledge about the properties of these materials will lead to either less than achievable performance due to overly conservative design, or overstraining of the structure leading to unexpected failures and drastic reduction of the service life. The key idea of the research work reported in this paper is that a significant improvement in service life can be achieved by a small reduction in the system dynamic performance. The concept of damage mitigation is introduced and, to this effect, a continuous-time model of fatigue damage dynamics is formulated. Finally, the results of simulation experiments are presented for transient operations of a reusable rocket engine.

1 Introduction

A major goal in the control of complex mechanical systems such as advanced aircraft, spacecraft, and electric power plants is to achieve high performance with increased reliability, availability, component durability, and maintainability (Lorenzo and Merrill, 1991; Ray et al., 1994a, 1994b). The specific requirements are:

- Extension of the service life of the controlled plant;
- Increase of the mean time between major maintenance actions;
- Reduction of risk in the design of integrated control-structure-materials systems.

Therefore, control systems need to be synthesized by taking performance, mission objectives, service life, and maintenance and operational costs into consideration. The state of the art in the synthesis of decision and control systems for complex power systems focuses on improving dynamic performance and diagnostic capabilities under the constraints that often do not adequately represent the material properties of the critical plant components. The reason is that the traditional design is based upon the assumption of conventional materials with invariant characteristics. In view of high performance requirements and availability of improved materials that may have significantly different damage characteristics relative to conventional materials, the lack of appropriate knowledge about the properties of these materials will lead to either of the following:

- Less than achievable performance due to overly conservative design; or
- Overstraining of the structure leading to unexpected failures and drastic reduction of the useful life span.

As the science and technology of materials continue to evolve, the design methodologies for damage-mitigating control must have the capability of easily incorporating an appropriate representation of material properties. This requires augmentation of the system-theoretic techniques for synthesis of decision and control laws with governing equations and inequality constraints that would model the mechanical properties of the materials for the purpose of damage representation and failure prognosis. The major challenge in this research is to characterize the damage generation process, and then utilize this information in a mathematical form for synthesizing algorithms of robust control, diagnostics, and risk assessment in complex mechanical systems.

2 The Damage-Mitigating Control System

The goal of the damage-mitigating control system (DCS) is to optimize the plant dynamic performance while simultane-

Contributed by the International Gas Turbine Institute for publication in the JOURNAL OF ENGINEERING FOR GAS TURBINES AND POWER. Manuscript received by the International Gas Turbine Institute May 12, 1993; revision received May 26, 1994. Associate Technical Editor: H. L. Julien.

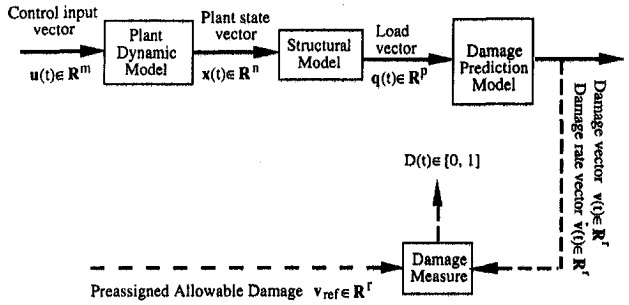

Fig. 1 A conceptual view of the damage-mitigating control system

ously maintaining the accumulated damage and the damage rate of the critical plant component(s) within prescribed limits. Figure 1 shows a conceptual view of the DCS, in which the plant model is a finite-dimensional state-space representation of the power system dynamics. The plant states are inputs to the structural model, which, in turn, generates the necessary information for the damage model. The output of the structural model is the *load vector*, which may consist of (time-dependent) stress, strain, temperature, wear, level of corrosion in gaseous and aqueous environments, and other physicochemical process variables at the critical point(s) of the structure. The damage model is a continuous-time (instead of being a cycle-based) representation of life prediction such that it can be incorporated within the DCS model. The objective is to mitigate the damage rate and accumulated damage at the critical point(s) of the structure, which may be subjected to time-dependent load. The damage state vector $v(t)$ could indicate the level of microcracking, macroscopic crack length, wear, creep, density of slip bands, etc., at one or more critical points, and its time derivative $\dot{v}(t)$ indicates how the instantaneous load is affecting the structural components. The overall damage $D(t)$ is a scalar measure of the combined damage at the critical point(s) resulting from (possibly) different sources (e.g., fatigue, creep, corrosion, or wear) relative to the preassigned allowable level v_{ref} of the damage vector. Although $D(t)$ may not directly enter the feedback or feedforward control of the plant, it can provide useful information for decision-making such as damage prognosis and risk analysis (Ray and Wu, 1994a).

The governing equations of plant dynamic and damage prediction models in Fig. 1 are constituted by nonlinear (and possibly time-varying) differential equations which must satisfy the local Lipschitz condition (Vidyasagar, 1992) within the domain of the plant operating range. The structural model in Fig. 1 consists of solutions of structural dynamic (typically finite element) equations representing the (mechanical and thermal) load conditions. A general structure of the plant and damage dynamics and their constraints is represented in the deterministic setting as follows:

Task period: Starting time t_0 to final time t_f

Plant dynamics:

$$\frac{dx}{dt} = f(x(t), u(t), t); \quad x(t_0) = x_0 \tag{1}$$

Damage dynamics:

$$\frac{dv}{dt} = h(v(t), q(x, t)): \quad v(t_0) = v_0; \quad h > 0 \quad \forall t \tag{2}$$

Damage measure:

$$D(t) = \xi(v(t), v_{\text{ref}}) \text{ and } D(t) \in [0, 1] \tag{3}$$

Damage rate tolerance:

$$0 \le h(v(t), q(x, t)) < \beta(t) \quad \forall t \in [t_0, t_f] \tag{4}$$

Accumulated damage tolerance:

$$[v(t_f) - v(t_0)] < \Gamma \tag{5}$$

where

$x \in \mathbf{R}^n$ is the plant state vector;
$u \in \mathbf{R}^m$ is the control input vector;
$v \in \mathbf{R}^r$ is the damage state vector;
$v_{\text{ref}} \in \mathbf{R}^r$ is the preassigned limit for the damage state vector;
$\beta(t) \in \mathbf{R}^r$ and $\Gamma \in \mathbf{R}^r$ are specified tolerances for the damage rate and accumulated damage, respectively;
$q \in \mathbf{R}^p$ is the load vector; and
$D \in [0, 1]$ is a scalar measure of the accumulated damage.

The vector differential Eqs. (1) and (2) become stochastic if the initial plant and damage states, namely, x_0 and v_0, are random vectors, or if uncertainties in the plant and material characteristics are included in the models as random parameters, or if the plant is excited by discrete events occurring at random instants of time (Sobczyk and Spencer, 1992). The stochastic aspect of damage-mitigating control is a subject of future research, and is not addressed in this paper.

Given an initial condition, the open-loop control policy is obtained via nonlinear programming (Luenburger, 1984) by minimizing a specified cost functional under the prescribed constraints of damage rate and accumulated damage. The objective is to minimize a specified cost functional J (which includes plant state, damage rate, and control input vectors) without violating the prescribed upper bounds of the damage rate and the accumulated damage. The cost functional J is to be chosen in an appropriate form representing a trade-off between the system performance and the damage. The optimization problem is then formulated as follows:

$$\text{Minimize:} \quad J = \sum_{k=0}^{N-1} J_k(\tilde{x}_k, \dot{v}_k, \tilde{u}_k) \tag{6}$$

$$\text{Subject to:} \quad 0 \le h(v_k, q(x_k), k) < \beta(k) \text{ and}$$
$$(v_N - v_0) < \Gamma \text{ for } k = 1, 2, 3, \ldots, N \tag{7}$$

where $\tilde{x}_k = x_k - x_{ss}$ and $\tilde{u}_k = u_k - u_{ss}$ are deviations of the plant state vector and the control input vector from the respective final steady-state values of x_{ss} and u_{ss}; and $\beta(t) \in \mathbf{R}^r$ and $\Gamma \in \mathbf{R}^r$ are specified tolerances for the damage rate and accumulated damage, respectively.

The open-loop control law was synthesized by minimizing the cost functional in Eq. (6) under: (*i*) the inequality constraints in Eq. (7); and (*ii*) the condition that, starting from the initial conditions $x(t_0)$ and $v(t_0)$, the state trajectory must satisfy the plant dynamic model in Eq. (1). The design variables to be identified are the control inputs, u_k, $k = 0, 1, 2, \ldots, N-1$, and the goal is to search for an optimal control sequence $\{u_k\}$.

3 Modeling of Damage Dynamics

Damage of mechanical structures is usually a result of fatigue, creep, corrosion, and their combinations (Suresh, 1991). The prime focus in this research is representation of fatigue damage in the continuous-time setting. As discussed earlier, a time-dependent model of damage dynamics, having the structure of Eq. (2), is necessary for analysis and synthesis of DCS. From this perspective, a dynamic model of fatigue damage has been formulated in the continuous-time setting. Although this damage model has a deterministic structure, it can be recast in the stochastic setting to include the effects of both unmodeled dynamics and parametric uncertainties.

Because of the wide ranges in mechanical properties of materials, extensive varieties of experiments have been conducted for fatigue analysis, and many models have been

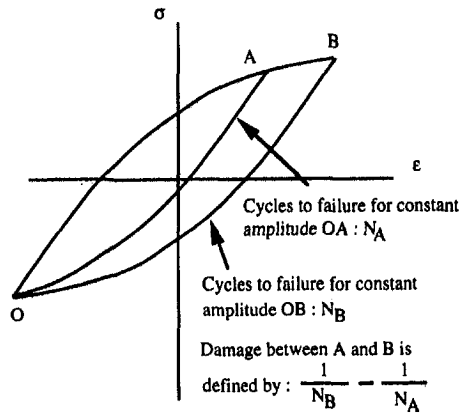

Fig. 2 Damage between two points on the same reversal

proposed for fatigue life prediction in aerospace and ground vehicles (Newman, 1981; Tucker and Bussa, 1977). Each of these models expresses the damage dynamics by an equation with the number of cycles N as the independent variable. In contrast, the damage dynamics in Eq. (2) are expressed as a vector differential equation with respect to time, t, as the independent variable. The advantages of this approach are that it allows the damage model to be incorporated within the constrained optimization problem and that the damage accumulated between any two instants of time can be derived even if the stress–strain hysteresis loop is not closed. This concept is applicable to different models of damage dynamics such as those resulting from cyclic strain or crack propagation. To this end, we propose to model the continuous-time dynamics of fatigue damage based on the following two approaches:

- *Cyclic Strain Life*: In this approach, the local stress–strain behavior is analyzed at certain critical points where failure is likely to occur. The local strain may be directly measured from a strain gage, or computed via finite element analysis. The local stress is estimated from the cyclic stress–strain curve. A cycle-based approach is then used to estimate the fatigue damage from the strain-life curves at different levels of stress and strain in the load history. We propose to determine the damage accumulation within a cycle using the classical Palmgren-Miner rule and subsequently modify it via the damage curve approach of Bolotin (1989).
- *Linear Elastic Failure Mechanics (LEFM)*: The LEFM approach is built upon the concept of a physical measure of damage in terms of the crack length and the size of the plastic zone at the crack tip (Wheeler, 1972). The accumulated damage is computed by integrating the crack growth rate over the number of cycles. This is based on the crack growth rate equation being approximated by an exponential function of stress intensity factor range of the component (Bannantine et al., 1990). The component is assumed to fail when the crack reaches the critical length, which, in turn, is determined from the fracture toughness of the component on the basis of experimental data.

3.1 Damage Modeling via Cyclic Strain Life. The cyclic strain–life approach recognizes that the fatigue life is primarily controlled by the local strain at the critical point(s) of the component. The first goal is to model linear damage accumulation in the continuous-time setting. Referring to Fig. 2, let point O be the starting (reference) point of a reversal, let A and B be two consecutive points on the same rising reversal, and let N_A and N_B represent the total number of cycles to failure with constant load amplitudes, $OA/2$ and $OB/2$, respectively. Then, the half-cycle increment of linear damage δ between points A and B is defined as:

$$\Delta\delta_{A,B} = \frac{1}{N_B} - \frac{1}{N_A} \tag{8}$$

In Eq. (8), it is assumed that the damage occurs only on the rising reversal, i.e., if the stress is monotonically increasing, and no damage occurs during unloading, i.e., if the stress is monotonically decreasing. This assumption is consistent with the physical phenomena observed in the fatigue crack propagation process. Given that $\Delta\sigma$ is the stress increment between point A and point B, the average damage rate with respect to this stress change is equal to $\Delta\delta/\Delta\sigma$. Let Δt be the time interval from A to B, the average rate of linear damage δ in terms of the stress σ can be transformed into the time domain by $\Delta\delta/\Delta t = (\Delta\delta/\Delta\sigma) \times (\Delta\sigma/\Delta t)$. Making Δt infinitesimally small, the instantaneous damage rate becomes $d\delta/dt = (d\delta/d\sigma) \times (d\sigma/dt)$ where the instantaneous stress rate $d\sigma/dt$ can be generated from direct measurements of strain rate or the finite element analysis, and $d\delta/d\sigma$ is derived from the existing cycle-based formulae (Bannantine et al., 1990). The strain-life and the cyclic stress–strain curves are used to evaluate $d\delta/d\sigma$. Replacing the number of cycles to failure, N_f, by $1/\Delta\delta$ where $\Delta\delta$ is the increment in linear damage during one cycle, the strain life relationship (Dowling, 1983) in terms of the elastic damage and plastic damage modes is written as:

$$\frac{|\epsilon - \epsilon_r|}{2} = \frac{\sigma_f' - \sigma_m}{E}\left(\frac{\delta}{2}\right)^{-b} + \epsilon_f'\left(1 - \frac{\sigma_m}{\sigma_f'}\right)^{\frac{c}{b}}\left(\frac{\delta}{2}\right)^{-c} \tag{9}$$

where b, c, σ_f', and ϵ_f' are material constants; σ_m is the mean stress; ϵ_r is the total strain corresponding to the reference stress σ_r at the starting point of a given reversal as determined from the rainflow cycle counting method; and $|\epsilon - \epsilon_r|/2$ is the strain amplitude between the current point and the reference point. This equation does not provide a closed-form solution for the predicted damage δ. The general approach to solve this problem is to separate Eq. (9) into two different modes. The first term on the right side is a modification of the Basquin equation and corresponds to the so-called elastic damage δ_e. The second term on the right side of Eq. (9) is a modification of the Coffin–Manson equation and corresponds to the so-called plastic damage δ_p. These two damages, δ_e and δ_p, can be derived separately in an explicit form.

$$\frac{\Delta\epsilon_e}{2} = \frac{\sigma_f' - \sigma_m}{E}\left(\frac{\Delta\delta_e}{2}\right)^{-b} \quad \text{(modified Basquin equation)} \tag{10a}$$

$$\frac{\Delta\epsilon_p}{2} = \epsilon_f'\left(1 - \frac{\sigma_m}{\sigma_f'}\right)^{\frac{c}{b}}\left(\frac{\Delta\delta_p}{2}\right)^{-c}$$

(modified Coffin-Manson equation) (10b)

where the elastic and plastic strain amplitudes, $\Delta\epsilon_e/2$ and $\Delta\epsilon_p/2$, are related to the state of stress following the cyclic stress–strain characteristics:

$$\frac{\Delta\epsilon_e}{2} = \frac{|\sigma - \sigma_r|}{2E} \tag{11a}$$

$$\frac{\Delta\epsilon_p}{2} = \left(\frac{|\sigma - \sigma_r|}{2K'}\right)^{\frac{1}{n'}} \tag{11b}$$

where n' is the cyclic strain hardening exponent, K' is the cyclic strength coefficient, and σ_r is the reference stress obtained from the cycle counting under spectral loading. From Eqs. (10a), (10b), (11a), and (11b), the closed-form solutions for $\Delta\delta_e$ and $\Delta\delta_p$ can be obtained in terms of stress

instead of strain as given below:

$$\Delta\delta_e = 2 \times \left(\frac{|\sigma - \sigma_r|}{2(\sigma_f' - \sigma_m)} \right)^{-\frac{1}{b}} \tag{12a}$$

$$\Delta\delta_p = 2 \times \left(\frac{1}{\epsilon_f'} \times \left(\frac{|\sigma - \sigma_r|}{2K'} \right)^{\frac{1}{n'}} \times \left(1 - \frac{\sigma_m}{\sigma_f'} \right)^{-\frac{c}{b}} \right)^{-\frac{1}{c}} \tag{12b}$$

Step changes in the reference stress σ_r can occur only at isolated points in the load spectrum. Since the damage increment is zero at any isolated point, the damage accumulation can be evaluated at all points, excluding these isolated points, which constitute a set of zero Lebesgue measure (Royden, 1988). Exclusion of the points of step changes in σ_r does not cause any error in the computation of damage, and $d\sigma_r/dt$ can be set to zero because σ_r is piecewise constant. Further, since it is assumed that no damage occurs during unloading, the damage rate can be made equal to zero if $\sigma < \sigma_r$. When the stress is increasing, i.e., $\sigma > \sigma_r$, the elastic damage rate $d\delta_e/dt$ and the plastic damage rate $d\delta_p/dt$ are computed from Eqs. (12*a*) and (12*b*) in terms of the instantaneous stress rate $d\sigma/dt$ as:

If $\sigma \geq \sigma_r$, then

$$\frac{d\delta_e}{dt} = 2 \times \frac{d}{d\sigma} \left(\left(\frac{\sigma - \sigma_r}{2(\sigma_f' - \sigma_m)} \right)^{-\frac{1}{b}} \right) \times \frac{d\sigma}{dt}, \text{ and} \tag{13a}$$

$$\frac{d\delta_p}{dt} = 2 \times \frac{d}{d\sigma} \left(\left(\frac{1}{\epsilon_f'} \times \left(\frac{\sigma - \sigma_r}{2K'} \right)^{\frac{1}{n'}} \times \left(1 - \frac{\sigma_m}{\sigma_f'} \right)^{-\frac{c}{b}} \right)^{-\frac{1}{c}} \right) \times \frac{d\sigma}{dt}; \tag{13b}$$

else $d\delta_e/dt = 0$ and $d\delta_p/dt = 0$.

The damage rate $d\delta/dt$ is then obtained as the weighted average of the elastic and plastic damage rates as:

$$\frac{d\delta}{dt} = w\frac{d\delta_e}{dt} + (1 - w)\frac{d\delta_p}{dt} \tag{14}$$

where the weighting function, w, is selected on the basis of the elastic and plastic strain amplitudes in Eqs. (11*a*) and (11*b*) as:

$$w = \frac{\Delta\epsilon_e}{\Delta\epsilon_e + \Delta\epsilon_p} \text{ and } 1 - w = \frac{\Delta\epsilon_p}{\Delta\epsilon_e + \Delta\epsilon_p} \tag{15}$$

Equations (13) to (15) are then used to obtain the damage rate at any instant of time. The damage increment between two consecutive points t_k and t_{k+1} on the same reversal can be calculated by integrating the damage differential $d\delta$. This continuous-time damage model has been verified using the experimental data generated in the SAE cumulative fatigue test program (Newman, 1981) for Man-Ten steel. A comparison of the model results and experimental data is reported by Ray and Wu (1994b) and Wu (1993).

The continuous-time damage model in Eqs. (13) to (15) is derived on the basis of linear damage accumulation following the Palmgren–Miner rule. Although this concept of linear damage accumulation has been widely used due to its simplicity in computation, the cumulative damage behavior is actually nonlinear (Bolotin, 1989; Suresh, 1991). Experimental results show that, for variable amplitude loading, the accumulated damage is dependent on the order in which the load cycles are applied. This phenomenon is known as the sequence effect, which is further explained in the next section. Since the structural components of complex mechanical systems are subjected to loads of varying amplitude, the linear rule of damage accumulation, which is commonly used for fatigue life assessment, could lead to erroneous results due to this sequence effect. Therefore, a nonlinear damage rule needs to be established for accurate prediction of the damage rate and damage accumulation in the critical components.

3.2 Modeling of Nonlinear Cumulative Damage Using the Damage Curve Approach. The concept of a nonlinear damage curve to represent the damage was first conceived by Marco and Starkey (1954). No mathematical representation of damage curve was proposed at that time because the physical process of damage accumulation was not adequately understood. Manson and Halford (1981) proposed the double linear rule primarily based on the damage curve approach for treating cumulative fatigue damage. In their paper, an effort was made to represent the damage curve mathematically and approximate it by two piecewise line segments. The total fatigue life was then divided into two phases so that the linear damage rule can be applied in each phase of the life. A concept similar to the damage curve approach was proposed by Bolotin (1989) with a mathematical representation, which does not necessarily assess the damage on the basis of cycles and is more appropriate for modeling in the continuous-time setting. Bolotin used the following analytical relationship between D and δ:

$$D = (\delta)^{\gamma} \tag{16}$$

In Eq. (12), the γ parameter describes the nonlinearity of the damage curve and is usually assumed to be dependent solely on the stress amplitude level (Manson and Halford, 1981). High-strength materials usually yield very large values of γ especially under high-cycle fatigue. At the initial stage of the fatigue life, a large γ creates a very small damage, which could lead to numerical and computational problems. This necessitates formulation of a computationally practical method of damage prediction. It follows from a crack propagation model such as the Paris model (Paris and Erdogan, 1963) that the crack growth rate is dependent not only on the stress amplitude but also on the current crack length. Recognizing the fact that the crack itself is an index of accumulated damage, it is reasonable to assume the γ parameter to be dependent on both stress amplitude and the current level of damage accumulation, i.e., $\gamma = \gamma(\sigma_a, D)$. Therefore, we propose the following modification of Eq. (16):

$$D = (\delta)^{\gamma(\sigma_a, D)} \tag{17}$$

where D and δ are the current states of nonlinear and linear damage accumulation, respectively. Although Eq. (13) has an implicit structure, it can be solved via a recursive relationship.

Ray and Wu (1994a) have developed a nonlinear damage model in the continuous-time setting. In this model, the accumulated damage at any point within a reversal can be obtained by solving the following nonlinear equations:

$$\gamma = \gamma(\sigma_a, D) \text{ and } D = (\delta + \Delta\delta)^{\gamma} \tag{18}$$

where δ is the linear damage at the reference point of a reversal and $\Delta\delta$ is the linear damage increment for the stress amplitude σ_a relative to the reference point. A noniterative numerical approach that operates on a set of discrete points in the load history has been developed for solving the set of implicit Eqs. (18).

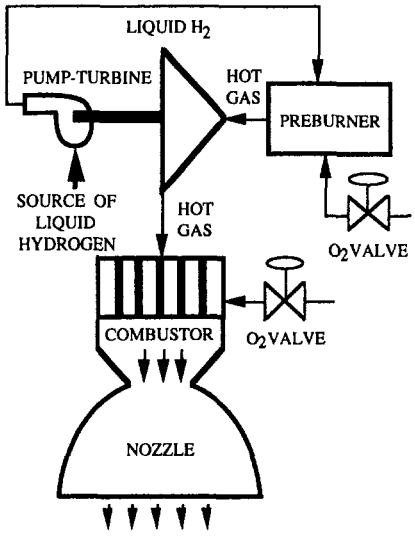

Fig. 3 Schematic diagram of a bipropellant rocket engine

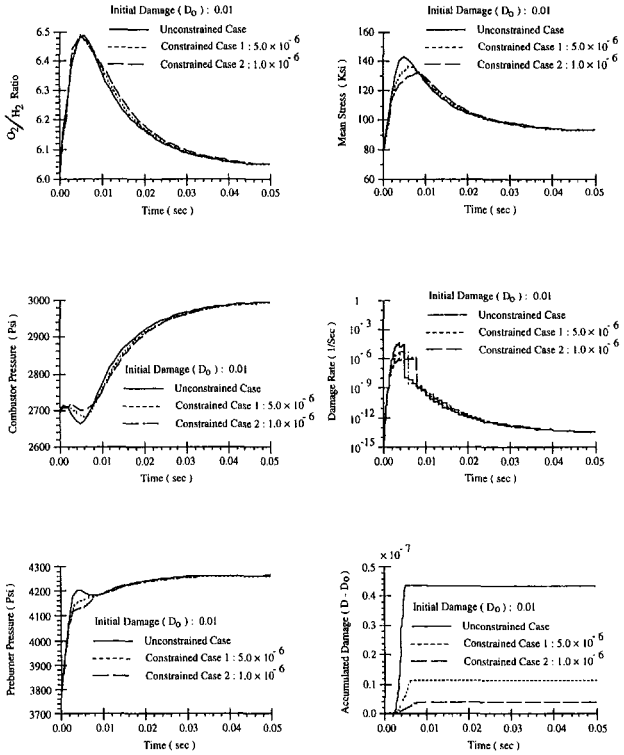

Fig. 4 Upthrust transients of a bipropellant rocket engine

3.3 The γ Parameter Fitting for the Nonlinear Cumulative Damage Model. One major task in this approach is to identify a mathematical representation for the γ parameter as a function of the stress amplitude and the current damage state. It requires knowledge of the physical process of damage accumulation, which may be obtained from either experimental data or a combination of experimental data and analysis, and an appropriate definition of damage. The γ parameters are different, in general, for different materials and follow different structures of the governing equations. Furthermore, because the mechanisms attributed to the damage accumulation at various stages of fatigue life are different, no single approach apparently provides a sufficiently accurate prediction of damage throughout the fatigue life of a component. It is difficult, if not impossible, to construct a single structure for representation of γ. An alternative approach is to evaluate γ by interpolation. Once the damage is appropriately defined, and an analytical method for damage prediction is selected, the information needed for the nonlinear damage model can be generated via experimentation or analysis for a set of constant stress amplitudes. The values of γ are then computed by Eq. (17) for a given stress amplitude and the damage data ranging from the initial damage state D_0 to the failure condition at $D = 1$. The generated data, γ versus D, are then plotted for various amplitudes of stresses. These curves can be either fitted by nonlinear equations, if possible, or as linear piecewise representations. Since it is not practical to perform experiments at infinitesimally small increments of stress amplitude, γ can be only experimentally evaluated at selected discrete levels of stress amplitude. The values of γ for other stress amplitudes can then be interpolated. Since the characteristics of γ may strongly depend on the type of the material, availability of pertinent experimental data for the correct material is essential for the damage-mitigating control synthesis. The γ parameter has been fitted based on the experimental data (Swain et al., 1990) for AISI 4340 steel. Details are reported by Ray and Wu (1994b).

4 Simulation Results and Discussion

The damage mitigation concept is verified by simulation experiments for open loop control of a reusable rocket propulsion engine such as one described by Sutton (1992) and Duyar et al. (1991). The plant model under control is a simplified representation of the dynamic characteristics of a bipropellant rocket engine as shown in Fig. 3. The preburner serves as a gas generator for driving the liquid hydrogen (LH_2)-fuel turbopump. In this model, oxidant is separately supplied to the preburner and the main combustor chamber. Standard lumped parameter methods have been used to model the nonlinear plant dynamics in state-space form where the plant state vector consists of eight state variables, namely turbine shaft speed, pump (LH_2-fuel) mass flow rate, preburner gas pressure, preburner gas density, combustor gas pressure, combustor gas density, and the positions of the two oxidant flow valves.

The critical plant output variables are combustor gas pressure and the oxidant/fuel (O_2/H_2) ratio, and the control inputs are commands for manipulation of the two oxidant valves. The structural model (Ray and Wu, 1994b) represents the cyclic mechanical stresses at the root of a typical turbine blade that is presumed to be a critical component. The blade is represented by a three-node beam model with six degrees of freedom at each node while the first node is kept fixed. The load on the blade is assumed to consist of two components. The first component is due to the (time-dependent) drive torque, which is derived as an output of the plant model. The second component is a dynamic term, which represents the oscillatory load on the blade as it passes each stator. It is the second component that causes high cycle fatigue at the root of the blade while the first component is largely responsible for the mean stress. The fatigue damage model formulated in Sections 2 and 3 was used to generate the results in Fig. 4.

The purpose of this simulation study is to examine the dynamic performance and damage of the nominal plant when the oxidant valves are manipulated to vary the engine thrust according to the open loop control policy described in Section 2. To demonstrate the broad concepts of fatigue damage mitigation, the nominal plant model was used in these simulation experiments with exact initial conditions and no disturbances and noise. However, if these conditions are not met, additional feedback control will be necessary because the open loop control alone would be inadequate. Following the

Table 1 The constraints for the simulation experiment

Time	Contrained case 1	Constrained case 2
0 ms to 2 ms	$\beta = 1.0 \times 10^{-6}\text{s}^{-1}$	$\beta = 0.2 \times 10^{-6}\text{s}^{-1}$
2 ms to 3 ms	$\beta = 2.5 \times 10^{-6}\text{s}^{-1}$	$\beta = 0.5 \times 10^{-6}\text{s}^{-1}$
3 ms to 50 ms	$\beta = 5.0 \times 10^{-6}\text{s}^{-1}$	$\beta = 1.0 \times 10^{-6}\text{s}^{-1}$

structure in Eq. (6), the cost functional J for nonlinear programming was selected as:

$$J = \sum_{k=0}^{N-1} \left[\tilde{x}_k^T Q \tilde{x}_k + \dot{v}_k^T S \dot{v}_k + \tilde{u}_k^T R \tilde{u}_k + W(\text{O}_2/\text{H}_2)_k^2 \right] \quad (15)$$

where the deviations, $\tilde{x}_k$ and $\tilde{u}_k$, in the plant state vector and the control input vector are defined in Eq. (6); and the diagonal matrices Q, R, and W, and the scalar S serve as relative weights on the individual variables. Since the rocket engine performance is very sensitive to the oxidant/fuel (O_2/H_2) ratio, it was brought into the cost functional in Eq. (15) to prevent any large deviations from the desired value of 6.02 through the transients. In the future research, if the main combustion chamber is considered as one of the critical components for damage mitigation, then the explicit dependence of the cost functional on the O_2/H_2 ratio may not be necessary. The simulation results in the plates of Fig. 4 were obtained under the following conditions:

Chamber pressure weight $Q_{55} = 12$;
and all other weights $Q_{ii} = 1$, $i \neq 5$,
Control input weight $R = I$ where I is the identity matrix,
Damage rate weight $S = 0$; and O_2/H_2 ratio weight $W = 10$.

The rocket engine model is initiated from an initial equilibrium condition at 2700 psi chamber pressure and O_2/H_2 ratio of 6.02. From this condition the optimization procedure steers the plant to a new equilibrium position at 3000 psi and the same O_2/H_2 ratio of 6.02 in 50 milliseconds. The control commands to the two oxidant valves are updated at every one millisecond. That is, N is equal to 50 in Eq. (15). The performance cost to be minimized is based on the deviations from the final equilibrium condition at 3000 psi. Simulation experiments were conducted with no constraints on the accumulated damage. Assuming that the blade is already used or minor manufacturing defects are present, the initial damage of the turbine blade is set to $D_0 = 0.01$. Two constrained cases along with the unconstrained case are simulated to examine the effects of damage rate constraints on the dynamic responses of the system. These constraints are listed in Table 1.

The plates on the left side of Fig. 4 exhibit the effects of the varying oxygen inlet flow into the preburner and the main combustor on the resulting transients of the process variables, namely, O_2/H_2 ratio, and the pressure in the preburner and main combustion chamber, for the given simulation condition. For a given level of initial damage, pressure dynamics tend to be slower as the constraint is made more severe. The combustor pressure is seen to rise monotonically in all cases after a small dip at about 2.5 ms while the preburner pressure keeps on increasing. These plots are largely similar except for the transients from 1 ms to 10 ms. Virtually all fatigue damage accumulation in this transient operation takes place during this short interval, and this results in a peak overshoot in the mean stress. This sharp increase in stress, displayed in the top plate on the right side of Fig. 4, is the cause of enhanced damage in the turbine blades. Since the turbine blades are the critical components for damage analysis in this study, the pressure ratio across the turbine that directly influences the torque is very important. For a given preburner pressure, a reduction in the combustor pressure causes an increase in the turbine torque. It is the turbine torque and speed that set the cyclic stress and fatigue damage on the turbine blades. Therefore, the dip in the combustor pressure at about 2.5 ms is largely responsible for the peak mean stress. Both the mean stress and stress amplitude are the basic inputs to the damage model.

The two plates on the bottom right side of Fig. 4 compare the damage rate and the accumulated damage for the given simulation condition. For the unconstrained case, the peak stress causes the largest overshoot in the damage rate, which is plotted on a logarithmic scale. The accumulated damage, plotted on a linear scale, is seen to be significantly influenced by the constraints. This suggests that, for reusable rocket engines, the constraints need to be appropriately specified. The damage rate is dependent on the two sequences of control commands, and the oxidant flows into the preburner and combustor are changed in response.

The important observation in these simulation experiments is the substantial reduction in the accumulated damage, which will extend the service life of the turbopump. The accumulated damage in the unconstrained case is seen to be about four to twelve times that of the constrained case. This is a clear message that the consideration of damage in the control of transients to which a rocket engine is exposed can have a considerable impact on the life of critical components (in this case, the turbine blades). It is noted that there is practically insignificant penalty in the response times of the chamber pressure, i.e., the engine thrust, between the unconstrained and the constrained cases. If one is willing to pay a small price in response time, much larger gains on damage accumulation can be achieved. Additional simulation results, not presented in this paper but reported by Wu (1993) and Ray et al. (1994b), show the effects of nonlinear damage accumulation, which are generated under three different initial values of the accumulated damage, namely, $D_0 = 0.001$, 0.01, and 0.1 while the damage rate constraint is set identical to that of the constrained Case 1 in Table 1. The damage rate and damage accumulation are found to be strongly dependent on the initial damage D_0. This suggests that, for reusable rocket engines, the constraints must be specified based on the knowledge of the initial damage D_0, which must be accurately assessed during the previous flight. However, if D_0 cannot be accurately assessed, then it might be safe to generate the control command sequences on the assumption of a conservative, i.e., larger, value of the initial damage at the expense of the engine performance.

The graphs in Fig. 4 exemplify the effects of upthrust transients for a short period of 50 ms. Complete operations of a rocket engine during a single flight include many such upthrust transients, and the steady-state operation may last for several hundreds of seconds. Although the damage rate during steady state is much smaller than that during a transient operation, the total damage accumulation during steady state may not be relatively insignificant. Therefore, during one flight of a (reusable) rocket engine, the cumulative effects of the transient and steady-state operations need to be considered for estimation of total accumulated damage.

The simulation experiments, described above, only consider a single point of critical stress, namely, the turbine blades. In this case, the damage vector is one dimensional. Simultaneous control of damage at several other critical areas in the rocket engine, such as the nozzle lining, shall render the damage vector to be multidimensional. The optimization problem is then to generate control sequences that will not only make a trade-off between the performance and damage but also strike a balance between potentially conflicting requirements of damage mitigation at these critical points.

5 Summary and Conclusions

The theme of the research in damage-mitigating control of

power systems as reported in this paper is summarized as follows:

- For control of complex power systems, on-line damage prediction and damage mitigation are carried out based on the available sensory and operational information such that the plant can be inexpensively maintained, and safely and efficiently steered under diverse operating conditions.
- High performance is achieved without overstraining the mechanical structures such that the functional life of critical components is increased resulting in enhanced safety, operational reliability, and availability.

Extended life coupled with enhanced safety and high performance will have a significant economic impact in diverse industrial applications. Furthermore, as the science and technology of materials evolve, the damage characteristics of the structural components can be incorporated within the framework of the proposed damage-mitigating control system.

This ongoing research in damage-mitigating control addresses interdisciplinary work in the fields of active control technology and structural integrity, as applied to fatigue life in particular. Efficacy of the proposed damage mitigation concept is evaluated for life extension of the turbine blades of a bipropellant rocket engine via simulation experiments.

Applications of damage-mitigating control of power systems include a wide range of engineering applications such as reusable rocket engines for space propulsion, rotating and fixed wing aircraft, electric power generation plants, automotive and truck engine/transmission systems, and large rolling mills. In each of these systems, damage-mitigating control can enhance safety and productivity accompanied by reduced life cycle cost. A continuous-time damage model will allow timely warnings of these failures, and the resulting decision and control actions will not only avoid an early shutdown but also improve maintainability. Such incidents could be alleviated by a relatively small reduction in plant performance if the control system is structured with the capability of predicting these impending failures and thereby exercising authority over the lower level control modules. A more complex application of the damage mitigation concept is the startup and scheduled shutdown of rocket engines and power plants, and take-off and landing of aircraft, in which the damage information can be utilized for real-time plant control either in the fully automated mode or with human operator(s) in the loop. Another example is the control of automotive engine and transmission systems to reduce stresses in the drive-train components without comprising driving performance and comfort. The result will be a combination of extended life and reduced drive-train mass with associated savings in the fuel consumption.

Acknowledgments

The authors acknowledge benefits of discussion with Mr. C. F. Lorenzo of NASA Lewis Research Center, and Professors M. Carpino and D. A. Koss of Penn State University.

The research work reported in this paper is supported in part by: NASA Lewis Research Center under Grant No. NAG 3-1240; National Science Foundation under Research Grant No. ECS-9216386; Electric Power Research Institute Contract No. EPRI RP8030-05.

References

Bannantine, J. A., Comer, J. J., and Handrock, J. L., 1990, *Fundamentals of Metal Fatigue Analysis*, Prentice Hall, Englewood Cliffs, NJ.

Bolotin, V. V., 1989, *Prediction of Service Life for Machines and Structures*, ASME, New York.

Dowling, N. E., 1983, "Fatigue Life Prediction for Complex Load Versus Time Histories," ASME *Journal of Engineering Materials and Technology*, Vol. 105, pp. 206–214.

Duyar, A., Eldem, V., Merrill, W. C., and Guo, T-H., 1991, "State Space Representation of the Open-Loop Dynamics of the Space Shuttle Main Engine," ASME *Journal of Dynamic Systems, Measurement, and Control*, Vol. 113, pp. 684–690.

Lorenzo, C. F., and Merrill, W. C., 1991, "Life Extending Control: A Concept Paper," *Proc. American Control Conference*, Boston, MA, June, pp. 1080–1095.

Luenberger, D. G., 1984, *Linear and Nonlinear Programming*, Addison-Wesley, Menlo Park, CA.

Manson, S. S., and Halford, G. R., 1981, "Practical Implementation of the Double Linear Damage Rule and Damage Curve Approach for Treating Cumulative Fatigue Damage," *Int. Journal of Fracture*, Vol. 17, No. 2, pp. 169–192.

Marco, S. M., and Starkey, W. L., 1954, "A Concept of Fatigue Damage," *Trans. ASME*, Vol. 76, No. 4, pp. 627–632.

Newman, J. C., Jr., 1981, "A Crack Closure Model for Predicting Fatigue Crack Growth Under Aircraft Spectrum Loading," *Methods and Models for Predicting Fatigue Crack Growth Under Random Loading*, ASTM STP 748, pp. 53–84.

Paris, P. C., and Erdogan, F., 1963, "A Critical Analysis of Crack Propagation Laws," ASME *Journal of Basic Engineering*, Vol. D85, pp. 528–534.

Ray, A., Wu, M-K., Carpino, M., and Lorenzo, C. F., 1994a, "Damage-Mitigating Control of Mechanical Systems: Part I—Conceptual Development and Model Formulation," ASME *Journal of Dynamic Systems, Measurement, and Control*, Vol. 116, No. 3, pp. 437–447.

Ray, A., Wu, M-K., Carpino, M., and Lorenzo, C. F., 1994b, "Damage-Mitigating Control of Mechanical Systems: Part II—Formulation of an Optimal Policy and Simulation," ASME *Journal of Dynamic Systems, Measurement, and Control*, Vol. 116, No. 3, pp. 448–456.

Ray, A., and Wu, M-K., 1994a, "Fatigue Damage Control of Mechanical Systems," *SMART Materials and Structures*, Vol. 3, No. 1, pp 47–58.

Ray, A., and Wu, M-K., 1994b, "Damage-Mitigating Control of Space Propulsion Systems for High Performance and Extended Life," NASA Contractor Report 194470.

Royden, H. L., 1988, *Real Analysis*, 3rd ed., Macmillan Publishing Company, New York.

Sobczyk, K., and Spencer, B. F., Jr., 1992, *Random Fatigue: Data to Theory*, Academic Press, Boston, MA.

Suresh, S., 1991, *Fatigue of Materials*, Cambridge University Press, Cambridge, United Kingdom.

Sutton, G. P., 1992, *Rocket Propulsion Elements*, Wiley Interscience, New York.

Swain, M. H., Everett, R. A., Newman, J. C., Jr., and Phillips, E. P., 1990, "The Growth of Short Cracks in 4340 Steel and Aluminum–Lithium 2090," AGARD Report, No. 767, pp. 7.1–7.30.

Tucker, L., and Bussa, S., 1977, "The SAE Cumulative Fatigue Damage Test Program," *Fatigue Under Complex Loading: Analyses and Experiments*, Vol. AE-6, pp. 1–54.

Vidyasagar, M., 1992, *Nonlinear Systems Analysis*, 2nd ed., Prentice-Hall, Englewood Cliffs, NJ.

Wheeler, O. E., 1972, "Spectrum Loading and Crack Growth," ASME *Journal of Basic Engineering*, Vol. 94, pp. 181–186.

Wu, M-K., 1993, "Damage-Mitigating Control of Mechanical Systems," Ph.D. Dissertation in Mechanical Engineering, The Pennsylvania State University, University Park, PA.

Multivariable Adaptive Control Using Only Input and Output Measurements for Turbojet Engines

Jin-Quan Huang

Jian-Guo Sun

Department of Power Engineering,
Nanjing University of Aeronautics
and Astronautics,
Nanjing, People's Republic of China

Current and future aircraft engines are increasingly relying upon the use of multivariable control approach for meeting advanced performance requirements. A multivariable model reference adaptive control (MRAC) scheme is proposed in this paper. The adaptation law is derived using only input and output (I/O) measurements. Simulation studies are performed for a two-spool turbojet engine. The satisfactory transient responses are obtained at different operating points from idle to maximum dry power within the flight envelope. These show insensitivity of the design to engine power level and flight condition. Simulation results also show high effectiveness of reducing interaction in multivariable systems with significant coupling. Using the multivariable MRAC controller, the engine acceleration time is reduced by about 19 percent in comparison with the conventional engine controller.

Introduction

Integrated flight and propulsion control systems for the next generation of fighter aircraft will require that the propulsion control system vary the engine inlet and exhaust nozzle variables simultaneously. The benefits to the engine will include improved acceleration performance, thrust response, and engine efficiency while maintaining compressor stall protection (Burcham and Haering, 1984; Yonke et al., 1987; Shaw et al., 1985).

The integrated flight and propulsion systems dictate advanced requirements for propulsion systems over wider operational envelopes. To satisfy these performance requirements, variable geometry components have become an integral part of advanced aircraft engines. Future variable-cycle engines may incorporate variable fan, compressor, turbine, and exhaust nozzle geometries to improve overall performance. As a result, modern turbojet engines become multi-input multi-output, nonlinear, time-varying systems with significant coupling. As a result, it is difficult to design controllers for these advanced engines.

Classical control synthesis techniques, which involve the analysis and design of single-output, single-output control loops, have worked quite well for the older, simpler engines. Unfortunately, such techniques yield poor transient and static performance when they are applied to the more complex, multivariable engines.

In recent years, several multivariable control design techniques have been used to design control systems for aircraft engines (Sain et al., 1977; Athans et al., 1986; Peil et al., 1986). The MRAC has made promising advances (Lindorff and Monopoli, 1966; Monopoli, 1981). The design of MRAC schemes using the Lyapunov direct method has been more appealing, because of its inherent assurance of stability. However, there have been a limited number of multivariable control designs for full flight envelope operation (Polley et al., 1989).

Huang and Sun (1993) have proposed an MRAC scheme using the full state vector for a multivariable two-spool turbojet engine control system within the full flight envelope. However, one difficulty in applying the MRAC approach is the need for the knowledge of the full state vector. The use of a state observer is, of course, a natural step toward the relaxation of this condition. However, no substantial results on this subject have yet been obtained.

In this paper, using an accelerated gradient method, a PI adaptation law of MRAC using only input and output measurements of the plant is proposed. The proposed adaptive scheme is applied to the design of the multivariable control system of turbojet engines. The proposed scheme ensures good transient responses at different flight conditions and satisfactory acceleration responses through large ranges in the flight envelope. It also shows high effectiveness of reducing interaction in multivariable systems with significant coupling. Simulations of the multivariable engine control system

Contributed by the International Gas Turbine Institute and presented at the 39th International Gas Turbine and Aeroengine Congress and Exposition, The Hague, The Netherlands, June 13–16, 1994. Manuscript received by the International Gas Turbine Institute March 30, 1994. Paper No. 94-GT-422. Associate Technical Editor: E. M. Greitzer.

show significant reductions of engine acceleration time and increases in engine thrust.

MRAC Using Only *I/O* Measurements

Consider an unknown linear single input/single output plant described by the differential equations

$$\dot{x}_p = A_p x_p + b_p u(t), \quad y_p = h_p^T x_p \tag{1}$$

where u is the input, y_p is the output, x_p is the nth state vector, A_p is an $n \times n$ matrix, and h_p and b_p are n vectors. The transfer function of the plant $W_p(s)$ may be represented as

$$W_p(s) = h_P^T(sI - A_p)^{-1} b_p \triangleq \frac{K_p Z_p(s)}{R_p(s)} \tag{2}$$

where $R_p(s)$ and $Z_p(s)$ are monic polynomials of order n and m ($\leq n - 1$), respectively, and K_p is a constant gain parameter.

A model represents the behavior desired from the plant when it is augmented with a suitable controller. The model has a reference input $r(t)$ and an output $y_m(t)$. The transfer function of the model, denoted by $W_m(s)$, may be represented as

$$W_m(s) = \frac{K_m Z_m(s)}{R_m(s)} \tag{3}$$

where $R_m(s)$ and $Z_m(s)$ are monic polynomials of order n and m, respectively, and K_m is a constant. The purpose is to find u such that the output error

$$e_1 = y_p - y_m \tag{4}$$

tends to zero asymptotically for arbitrary initial conditions and arbitrary piecewise continuous and uniformly bounded reference signals $r(t)$.

The following usual assumptions are made: (a1) the plant is strictly proper with relative degree $n^*(= n - m) = 1$ and $W_m(s)$ has the same relative degree; (a2) only the plant input and output are used to generate u; (a3) the sign of K_p, the "high-frequency gain," is known, and we assume it positive without loss of generality; (a4) $W_m(s)$ is strictly positive real (SPR); (a5) the plant is supposed to be completely observable and controllable; (a6) $W_p(s)$ is minimum phase.

As given by Narendra and Valavani (1978), the following input and output filters, F1 and F2, respectively, are used

$$\dot{v}_1 = \Lambda v_1 + g u, \quad w_1 = c^T v_1 \qquad (F1)$$

$$\dot{v}_2 = \Lambda v_2 + g y_p, \quad w_2 = d_0 y_p + d^T v_2 \qquad (F2) \tag{5}$$

with $c^T = [c_1(t), \ldots, c_{n-1}(t)]$, $d^T = [d_1(t), \ldots, d_{n-1}(t)]$, $g^T = [0, \ldots, 0, 1]$, $v_1, v_2 \in R^{n-1}$ and Λ such that $Z_m(s) = \det(sI - \Lambda)$.

We define the "regressor" vector as $\omega^T = [v_1, y_p, v_2, r]$ and the $2n$ adjustable parameters denoted by a vector $\theta^T = [c^T, d_0, d^T, K_0] \triangleq [\theta_1, \theta_2, \ldots, \theta_{2n}]$. In the usual adaptive control scheme, the control u is structured as

$$u = \theta^T(t)\omega(t) \tag{6}$$

It is well known that under these assumptions there exists a unique constant vector $\theta^* = [c^{*T}, d_0^*, d^{*T}, K_0^*]^T = [\theta_1^*, \theta_2^*, \ldots, \theta_{2n}^*]^T$ such that the plant matches $W_m(s)$ exactly, i.e., the transfer function of the closed-loop plant, from r to y_p, is $W_m(s)$. Of course, θ^* can only be known if $W_p(s)$ is known. When this is not the case, θ is adapted so that $e_1(t) \to 0$ as $t \to \infty$ and eventually (under some signal richness condition) $\theta \to \theta^*$.

The plant (1) plus the filters (5) can be rewritten as

$$\dot{x} = Ax + \bar{b}(u - \theta^{*T}\omega) + br, \quad y_p = h^T x \tag{7}$$

where

$$x^T = \left[x_p^T, v_1^T, v_2^T\right], \bar{b}^T = \left[b_p^T, g^T, 0\right],$$

$$b = \bar{b}\theta_{2n}^*, h^T = [1, 0, \ldots, 0],$$

$$A = \begin{pmatrix} A_p + d_0^* b_p h_p^T & b_p c^{*T} & b_p d^{*T} \\ g d_0^* h_p^T & \Lambda + g c^{*T} & g d^{*T} \\ g h_p^T & 0 & \Lambda \end{pmatrix} \tag{8}$$

$\{A, b, h\}$ is a nonminimal realization of $W_m(s)$ (Narendra and Valavani, 1978). The representation of the reference model can be written in the form

$$\dot{x}_m = Ax_m + br, \quad y_m = h^T x_m \tag{9}$$

Defining the state error vector as $e = x - x_m$, denoting $\phi = \theta(t) - \theta^*$, and subtracting Eq. (9) from Eq. (7), the error equations between the model and the plant can be expressed as

$$\dot{e} = Ae + \bar{b}\phi^T\omega, \quad e_1 = h^T e \tag{10}$$

A typical adaptation law is the gradient law in the form of an integral as

$$\theta = -\Gamma_1 \int e_1 \omega dt, \quad \Gamma_1 = \Gamma_1^T > 0 \tag{11}$$

which can be shown to yield a globally stable adaptive system. Here, we introduce a "proportional + integral "adaptation law (Huang et al., 1993) as

$$\theta = -\Delta e_1 \omega - \Gamma \int e_1 \omega dt, \quad \Delta = \Delta^T > 0, \quad \Gamma = \Gamma^T > 0 \tag{12}$$

Nomenclature

A_8 = exhaust nozzle area, cm^2
e = error vector
e_1 = output error
H = altitude, km
I/O = input and output
M = Mach number
MRAC = model reference adaptive control
n^* = relative degree
N_L = low rotor speed, rpm
PCN_L = percent of low rotor speed
PI = proportional + integral
r = demand for closed-loop control
s = Laplace transform operator
SM_h = high-pressure compressor stall margin
SPR = strictly positive real
t = time, s
u = control variable of closed-loop control
v = output of filter
V = Lyapunov function
W = transfer function
W_f = main fuel flow, kg/s
x = state space vector
y = output variable
γ, δ = adaptive gain
θ = adjustable control gain (vector)

Subscripts

m = model
p = plant

Superscripts

T = transpose of a matrix or vector
$*$ = desired value of a vector or scalar

Since $W_m(s)$ is SPR, there exists $P = P^T > 0$ and $Q = Q^T > 0$ such that

$$A^TP + PA = -2Q, \quad Pb = h \tag{13}$$

The global asymptotic stability of the adaptive system using u given by Eqs. (6) and (12) can be proved with the Lyapunov function

$$V(e, \phi) = \frac{1}{2}\left[e^TPe + \frac{1}{\theta_{2n}^*}(\phi + \Delta e_1\omega)^T\Gamma^{-1}(\phi + \Delta e_1\omega)\right] \tag{14}$$

Calculating the time derivative of V with respect to Eqs. (10) and (11), one has (recall $\dot{\phi} = \dot{\theta}$)

$$\dot{V} = -e^TQe + \omega^T\phi\bar{b}^TPe + \frac{1}{\theta_{2n}^*}\left(\dot{\phi} + \Delta\frac{d(e_1\omega)}{dt}\right)^T\Gamma^{-1}(\phi + \Delta e_1\omega)$$

$$= -e^TQe + \omega^T\phi\bar{b}Pe - \frac{1}{\theta_{2n}^*}e_1^2\omega^T\Delta\omega - \frac{1}{\theta_{2n}^*}e_1\omega^T\phi \tag{15}$$

Noting that $\bar{b} = b/\theta_{2n}^*$, $Pb = h$, $he = e_1$, we obtain

$$\dot{V} = -e^TQe - \frac{1}{\theta_{2n}^*}e_1^2\omega^T\Delta\omega \tag{16}$$

The V in Eq. (14) is positive definite and $\dot{V}$ in Eq. (16) is negative semi-definite in the (e,ϕ) space. Global stability of the origin is implied and moreover $e(t) \to 0$ as $t \to \infty$.

Multivariable Control System for Turbojet Engines

In a conventional engine control system, a certain engine stall margin is required based on the consideration of stability. However, the engine stall margin varies with different operating conditions. For example, the stall margin is small during certain flight maneuvers, engine acceleration or deceleration, and firing. In the current engines, the engine stall margin is determined to avoid stall based on the worst case. Operation with this large stall margin requires the engine thrust to be reduced over what would be obtained if a smaller stall margin could be used. Thus, the performance of the propulsion system is limited.

Additional thrust is obtained by uptrimming the engine pressure ratio in some operating conditions and in parts of the flight envelope where excess stall margin and trubine temperature margin exist (Huang and Sun, 1993).

In this paper, the objective of a nonlinear multivariable controller for a two-spool turbojet engine is to control low rotor speed (N_L) and high-pressure compressor stall margin (SM_h) during accelerations and decelerations while ensuring that predetermined limits on stall margins, speeds, and temperatures are not exceeded. The multivariable controller design developed uses low rotor speed and high-pressure compressor stall margin as the sensed variables, and fuel flow (W_f) and exhaust nozzle area (A_8) as the control variables.

The high-pressure compressor stall margin is defined as

$$SM_h = \left(\frac{\pi_s}{\pi}\right)\left(\frac{G}{G_s}\right) - 1 \tag{17}$$

where π_s and G_s are critical pressure ratio and critical gas weight flow rate, respectively, and π and G are pressure ratio and gas weight flow rate, respectively. Since the high-pressure compressor stall margin defined in Eq. (17) is not measurable directly, we removed the ratio G/G_s from Eq. (17) to get the approximation of SM_h, i.e., $SM_h = (\pi_s/\pi) - 1$.

In order to derive the adaptive law, the engine model and reference model must be chosen. The multivariable adaptive control would be impractical to develop and implement with the nonlinear equations. Therefore, it has been customary to utilize the linearized model of the engine to simplify the mathematic expressions of the adaptive law. By using the decentralized control concept, the multivariable engine control system can be implemented as two subsystems—the rotor speed control subsystem and the stall margin control subsystem. Since the engine has second-order dynamics, each of the subsystems can be served as a linear second order differential equation and the reference model of each subsystem is chosen as

$$W_{mi}(s) = \frac{c_i(s + d_i)}{s^2 + a_is + b_i}, \quad i = 1,2 \tag{18}$$

The input and output filters of two subsystems from Eq. (5) are given by

$$\dot{v}_{11} = -d_1v_{11} + W_f, \dot{v}_{12} = -d_1v_{12} + N_L$$

$$\dot{v}_{21} = -d_2v_{21} + A_8, \quad \dot{v}_{22} = -d_2v_{22} + SM_h \tag{19}$$

The adaptive control scheme is chosen as

$$W_f = \theta_{11}v_{11} + \theta_{12}N_L + \theta_{13}v_{12} + \theta_{14}N_{Lr}$$

$$A_8 = \theta_{21}v_{21} + \theta_{22}SM_h + \theta_{23}v_{22} + \theta_{24}SM_{hr} \tag{20}$$

where $\theta_{ij}(i = 1,2, j = 1, \ldots, 4)$ are eight adjustable control gains.

From Eq. (12), we can obtain the adaptive law in the form of a "*PI*" law as follows:

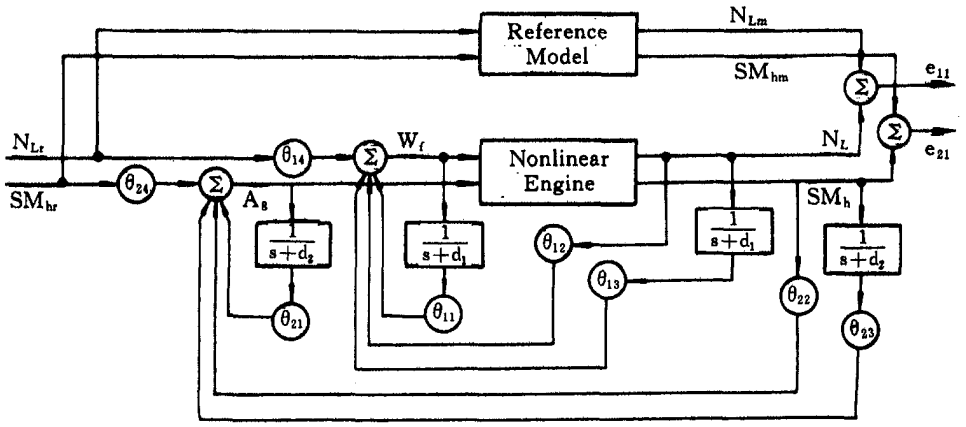

Fig. 1 Multivariable adaptive control system for turbojet engines

$$\theta_{11} = -\delta_{11}e_{11}v_{11} - \gamma_{11}\int e_{11}v_{11}dt$$
$$\theta_{12} = -\delta_{12}e_{11}N_L - \gamma_{12}\int e_{11}N_L dt$$
$$\theta_{13} = -\delta_{13}e_{11}v_{12} - \gamma_{13}\int e_{11}v_{12}dt$$
$$\theta_{14} = -\delta_{14}e_{11}N_{Lr} - \gamma_{14}\int e_{11}N_{Lr}dt$$
$$\theta_{21} = -\delta_{21}e_{21}v_{21} - \gamma_{21}\int e_{21}v_{21}dt$$
$$\theta_{22} = -\delta_{22}e_{21}SM_h - \gamma_{22}\int e_{21}SM_h dt$$
$$\theta_{23} = -\delta_{23}e_{21}v_{22} - \gamma_{23}\int e_{21}v_{22}dt$$
$$\theta_{24} = -\delta_{24}e_{21}SM_{hr} - \gamma_{24}\int e_{21}SM_{hr}dt \qquad (21)$$

where $e_{11} = N_L - N_{Lm}$, $e_{21} = SM_h - SM_{hm}$, δ_{ij}, γ_{ij} ($i = 1, 2$, $j = 1, \ldots, 4$) are positive constant parameters.

The block diagram of multivariable adaptive system is shown in Fig. 1.

Compared to the integral adaptation law, the *PI* law has new properties of fast adaptation and perfect model following. It is important to note that in the adaptation law (21) the integral term provides the memory of the adaptation, and the proportional term is introduced in order to accelerate the reduction of the output error at the beginning of the adaptation process. Therefore, the new adaptation law is also called "accelerated gradient law."

The ratio between the values of the proportional gain δ_{ij} and the values of the integral gain γ_{ij} in the *PI* law (21) has an important influence on the speed of reduction of the output error. It has been shown that a high-speed reduction of the error between model and plant is obtained for large value of δ_{ij} and γ_{ij}, but in counterpart, the control energy is higher. The simultaneous augmentation of proportional and integral gains improves the speed of adaptation, but the gains are limited by the saturations existing in the adaptation loop and by the imperfect characterization of the plant (Huang et al., 1993).

Simulation Results

A nonlinear time-varying and coupling model of a two-spool turbojet engine for full flight envelope operation is used in the simulation. The engine consists of low-pressure compressor, high-pressure compressor, combustor, high-pressure turbine, low-pressure turbine, augmentor, and exhaust nozzle. All these are represented by equations or table lookup. A Newton–Raphson iterative solution is used to ensure flow continuity between components and energy balance so that calculated pressure and temperature changes are consistent with enthalpy and entropy changes of real gases throughout the engine. The nonlinear model is a simplified model in which the volume dynamics in the engine are not included in this study. The dynamics of the engine are significantly different at different operating conditions. For example, response time ranged from 1 to 6 seconds at sea level from idle to maximum dry power.

The reference models of the two subsystems are chosen with $a_i = 10$, $b_i = 25$, $c_i = 2.5$, $d_i = 10$, $i = 1, 2$. The choice of positive constant parameters δ_{ij} and γ_{ij} plays a crucial role in the MRAC developed. The parameters are selected to obtain the best tracking property and are given as $\delta_{11} = 10^{-7}$, $\delta_{12} = 10^{-2}$, $\delta_{13} = 10^{-6}$, $\delta_{14} = 10^{-7}$, $\gamma_{11} = 5 \times 10^4$, $\gamma_{12} = 50$, $\gamma_{13} = 5 \times 10^5$, $\gamma_{14} = 5 \times 10^4$, $\delta_{21} = \delta_{22} = \delta_{23} = \delta_{24} = 10^{-7}$, $\gamma_{21} = 10^{-7}$, $\gamma_{22} = 10^{-2}$, $\gamma_{23} = 10^{-6}$, $\gamma_{24} = 10^{-7}$.

Satisfactory response properties were obtained at various operating points within the full flight envelope. Figure 2 shows step responses of N_L with MRAC at different operating points within the full flight envelope, i.e., at different altitudes and different Mach numbers. Figure 3 shows the time responses of SM_h using the MRAC scheme in the full flight envelope. The demand of SM_h is a slope signal from the initial SM_h to the desired value of 0.09 within 0.5 second.

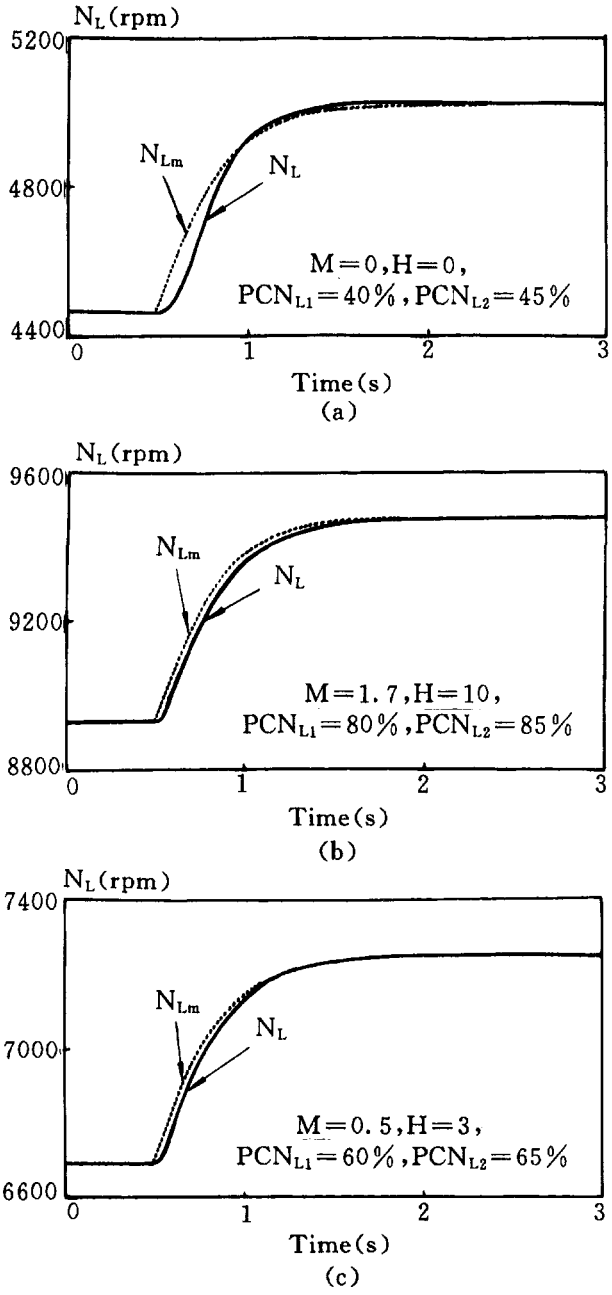

Fig. 2 Step responses of N_L with MRAC in full flight evelope

Figure 3(*b*) shows that the exhaust nozzle area arrives at its minimum value of the geometry limit. The simulation results show that the control scheme can compensate very well for unknown and nonlinear time-varying engine dynamics.

Acceleration simulations with conventional control and with the multivariable MRAC proposed are performed (Fig. 4) to compare their acceleration performances. Both accelerations are run at sea level from $PCN_{L1} = 60$ percent to $PCN_{L2} = 100.5$ percent. The desired value of high-pressure compressor stall margin SM_{hr} is 0.09. The adaptive controller controls SM_h as close as possible to the desired value by manipulating exhaust nozzle A_8. Meanwhile, it keeps the turbine temperature within its limit. Using the multivariable MRAC controller, the engine acceleration time is reduced by about 19 percent (Fig. 4(*a*)), the engine thrust is significantly increased during acceleration, and is increased by about 8 percent at maximum dry power (Fig. 4(*b*)) as compared to the conventional engine controller. The improved thrust is achieved by decreased exhaust nozzle area to uptrim engine

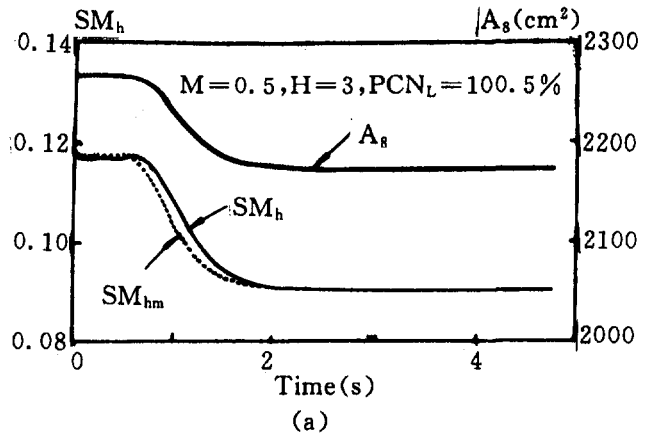

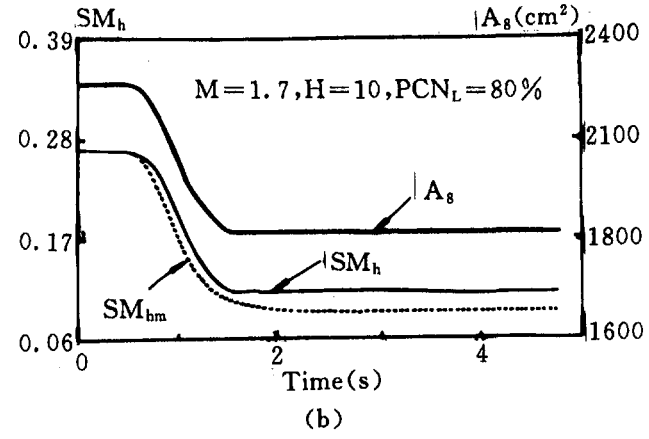

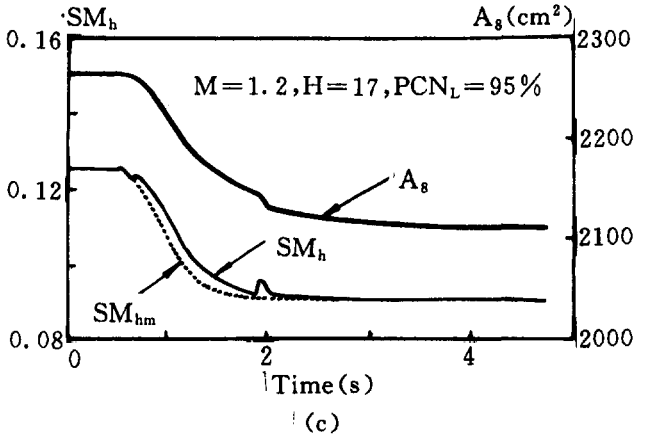

Fig. 3 Time responses of SM_h with MRAC in full flight envelope

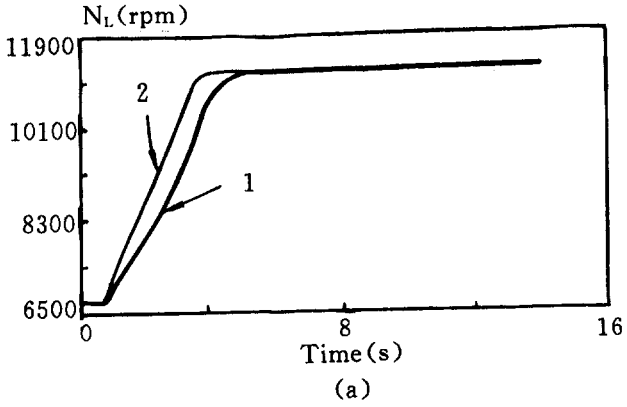

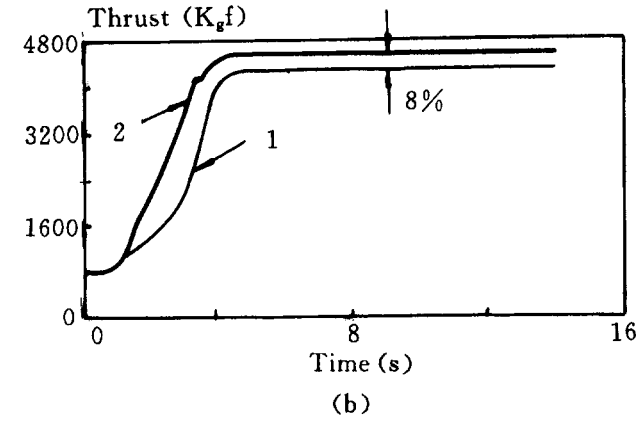

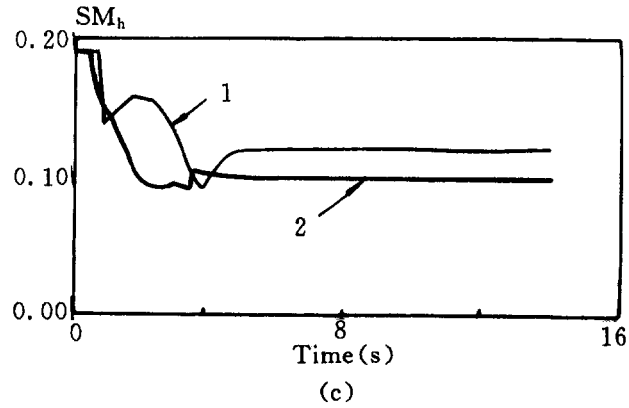

Fig. 4 Acceleration responses with conventional controller and multivariable adaptive controller. (1—conventional controller, 2—multivariable adaptive controller)

pressure ratio. The stall margin decreases with uptrim. However, the minimum stall margin is not reduced during acceleration when acceleration performance is achieved using the adaptive controller in comparison with the conventional controller (Fig 4 (*c*)). Figure 4 also shows satisfactory effectiveness of reducing the interactions in the multivariable control system with significant coupling and the insensitivity of the design to engine power level and flight condition.

Conclusions

This paper has summarized an approach for designing a multivariable nonlinear controller of MRAC for turbojet engines. The MRAC scheme is designed using only input and output measurements. The multivariable control system ensures good transient responses at different flight conditions and satisfactory acceleration and deceleration responses through large ranges in the flight envelope. Using the multivariable adaptive controller, the engine acceleration time is reduced by about 19 percent in comparison with the conventional engine controller.

Compared the MRAC law proposed by Huang and Sun (1993), the multivariable adaptive scheme developed in this paper offers advantages as follows:

1 only the input and output measurements are used to generate the control signals;
2 satisfactory performance and the insensitivity of the design to engine power level and flight condition;
3 eliminating or substantially reducing interaction in multivariable system with significant coupling;
4 using the proposed MRAC controller, the engine accel-

eration time is reduced and the thrust is increased significantly in comparison with the conventional engine controller.

References

Athans, M., Kapassouris, P., Kappos, E., and Spang, H. A., III, 1986, "Linear-Quadratic-Gaussian With Loop-Transfer-Recovery Methodology for the F-100 Engine," *AIAA Journal of Guidance, Control, and Dynamics*, Vol. 9, pp. 45–52.

Burcham, F. W., Jr., and Haering, E. A., Jr., 1984, "Highly Integrated Digital Engine Control System on an F-15 Airplane," AIAA Paper No. 84-1259.

Huang Jin-Quan, and Sun Jian-Guo, 1993, "Multivariable Adaptive Control for Turbojet Engines," ASME Paper No. 93-GT-44.

Huang Jin-Quan, Sun Jian-Guo, and Liu Xiao, 1993, "An Accelerated Gradient Method for Adaptive Control Using Only Input and Output Measurements," *Proceedings of Asia–Pacific Conference on Control and Measurements*, Kunming, China; *Trans. of Nanjing University of Aeronautics & Astronautics*, Vol. 10, No. 1, pp. 47–51.

Lindorff, D. P., and Monopoli, R. V., 1966, "Control of Time Variable Nonlinear Multivariable System Using Lyapunov's Direct Method," *Proceedings, 8th JACC*, pp. 394–403.

Monopoli, R. V., 1981, "Model Following Control of Gas Turbine Engines," ASME *Journal of Dynamic Systems, Measurement, and Control*, Vol. 103, pp. 285–289.

Narendra, K. S., and Valavani, L., 1978, "Stable Adaptive Controller Design—Direct Control," *IEEE Trans. on AC-23*, pp. 570.

Peil, W. H., Athans, M., and Spang, H. A., III, 1986, "Multivariable Control of the GET700 Engine Using the LQG/LTR Design Methodology," *Proceedings, ACC*, Seattle, WA.

Polley, J. A., Adibhatla, S., and Hoffman, P. J., 1989, "Multivariable Turbofan Engine Control for Full Flight Envelope Operation," ASME JOURNAL OF ENGINEERING FOR GAS TURBINES AND POWER, Vol. 111, pp. 130–137.

Sain, M. K., Peczkowski, J. L., and Melsa, J. L., eds., 1977, "Alternatives for Linear Multivariable Control," National Engineering Consortium.

Sastry, S. S., 1984, "Model-Reference Adaptive Control—Stability, Parameter Convergence, and Robustness," *IMA J. Mathematical Control and Information*, Vol. 1, pp. 27–66.

Shaw, P. D., Blumberg, K. R., Joshi, D. S., Anes, R., Vincent, J. H., and Skira, C., 1985, "Development and Evaluation of an Integrated Flight and Propulsion Control System," AIAA Paper No. 85–1423.

Yonke, W. A., Landy, R. J., and Stewart, J. F., 1987, "HIDEC Adaptive Engine Control System Flight Evaluation Results," ASME Paper No. 87-GT-257.

A New Approach to the Challenge of Machinery Prognostics

R. J. Hansen

D. L. Hall

Applied Research Laboratory,
Pennsylvania State University,
State College, PA 16804

S. K. Kurtz

Materials Research Institute,
Pennsylvania State University,
University Park, PA 16802

Current generation mechanical diagnostic equipment is designed to identify individual events or trends in the output of sensors mounted on a mechanical component, subsystem, or system. Such equipment can provide a useful indication that a failure condition may be developing, but it cannot provide reliable predictions of the remaining safe or operational life. Typically, these diagnostic systems simply compare the output of individual sensors against a priori thresholds to establish a measure of the system's health. Two problems result from this approach: (1) There is no advantage taken of possible synergy among the sensors, i.e., the determination of health is one dimensional; and (2) the diagnosis provides only a statement regarding the current equipment health, but does not provide a prediction of the time remaining to failure. This often leads to an operational environment in which diagnostic equipment outputs are either ignored because of frequent false alarms or frequent (and costly) time-based preventive maintenance is performed to avoid hazardous failures. This paper describes a new approach to the development of a more robust diagnosis and prognostic capability. It is based on the fusion of sensor-based and model-based information. Sensor-based information is the essence of current diagnostic systems. Model-based information combines dynamic models of individual mechanical components with micromechanical models of relevant failure mechanisms, such as fracture and crack propagation. These micromechanical models must account for initial flaw size distribution and other microstructural parameters describing initial component condition. A specific application of this approach is addressed, the diagnosis of mechanical failure in meshing gears. Four specific issues are considered: (a) how to couple a validated numerical simulation of gear transmission error (due to tooth spacing irregularity, contour irregularity, or material inhomogeneity) with physically and empirically based descriptions of fatigue crack growth to predict a failure precursor signature at the component level; (b) how to predict the manifestation of this signature at the subsystem or system level where sensors are located; (c) how to fuse this model-based information with the corresponding sensor-based information to predict remaining safe or operational life of a gear; and (d) issues associated with extending this methodology to bearings and other rotating machinery components.

Introduction

In the nearly one-half century since the end of World War II, extensive work has been done on the characterization of failure modes in electronic, mechanical, and most recently software systems. A combination of in-service testing and testing to failure (reliability life testing) has served to highlight fundamental, underlying differences in failure mechanisms among these three types of system and significant limitations in the application of existing probabilistic distributions of failure rate for mechanical systems.

This paper first examines the characteristics of mechanical system failure that restrict the utility of probabilistic methods of failure prediction. The current status of an alternative for mechanical systems, condition-based maintenance, is then examined. Finally, a new approach to prognostics for mechanical systems is described in terms of its applicability to gear systems where fatigue crack growth is assumed to be the dominant failure mechanism.

Probabilistic Description of Failure

A quantity commonly used to describe the instantaneous probability of failure in the time interval between t and $t + \Delta t$ is the hazard rate, $h(t)$. It is related to $R(t)$, the reliability function or probability of survival for total time interval of zero to t, through the relationship

$$h(t) = -\frac{d \ln R(t)}{dt}. \quad (1)$$

Typical hazard signatures for electrical, software, and mechanical systems are shown in Fig. 1 (Lewis, 1987). In the

Contributed by the International Gas Turbine Institute and presented at the 39th International Gas Turbine and Aeroengine Congress and Exposition, The Hague, The Netherlands, June 13–16, 1994. Manuscript received by the International Gas Turbine Institute January 28, 1994. Paper No. 94-GT-3. Associate Technical Editor: E. M. Greitzer.

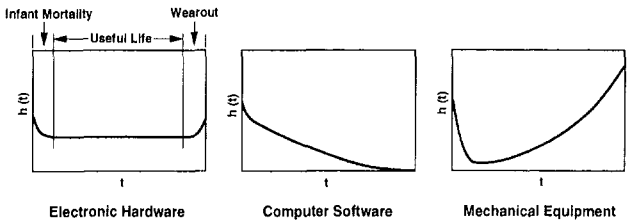

Fig. 1 Mechanical failure distinctives

case of the electronic system, the initial rapid decrease in $h(t)$ over a few thousand operating hours defines a region of "infant mortality" related to manufacturing defects. The essentially constant region of $h(t)$ defines the useful lifetime with random external causes of failure, and the subsequent increase in $h(t)$ the onset of intrinsic, gradual wear out or failure mechanisms. After the "infant mortality" region, software systems become progressively less prone to failure with the passing of time (assuming corrections in the software are made as they are identified). Mechanical systems have the undesirable feature that wear out mechanisms and the attendant increase in failure rate become evident immediately after the "infant mortality" region. Microcracks and other imperfections are present in a mechanical system at the outset and grow to critical size (above a critical stress level) with increasing frequency. Thus, it is much more difficult to define a useful life in the same sense as in electronic systems. Instead, mechanical systems progressively deteriorate with use until failure occurs or until the performance becomes unacceptable. This fact makes the development of a maintenance strategy inherently more difficult for mechanical components or systems where even a single failure is unacceptable because of safety or cost considerations. An example of the former is a helicopter main gearbox and of the latter any machine that causes a whole production line to shut down when it fails. A tradeoff must be made between the cost of frequent preventive maintenance and the risk of unanticipated failure.

Until recently, the only available tools for predicting the hazard rate of a mechanical system were experimentally determined or assumed reliability distribution functions. For example, if the assumption is made that the dominant failure mechanism is fatigue and that this phenomenon can be modeled as a single event, weak link fracture process, the resulting distribution of $R(t)$ is given by

$$R(t) = \exp -(t/\eta)^{\beta}. \tag{2}$$

Here η, the characteristic life, is the value of t at which 63 percent of the devices have failed. β is the independent shape parameter that determines the qualitative behavior of the hazard rate function, i.e.,

$$h(t) = \frac{\beta t^{\beta-1}}{\eta^{\beta}}. \tag{3}$$

This distribution, known as the Weibull distribution, can be used to model all three types of hazard rate behavior shown in Fig. 1. For $\beta = 1$, the hazard rate is constant as in electronic systems, $\beta < 1$ gives a decreasing hazard rate with time as in software systems, and $\beta > 1$ a hazard rate increasing with time characteristic of wear out in mechanical systems.

While the majority of earlier mechanical reliability studies have employed the Weibull distribution (Haugen, 1980; Kapur and Lamberson, 1977), more recent work has made clear the importance of lognormal random process models of fatigue crack propagation (e.g., Sobczyk and Spencer, 1992; Harris, 1992; Hudak et al., 1990). Unfortunately, no experimental study or micromechanical theoretical analysis provides definitive guidance in which distribution to employ in a given circumstance, even though the resulting hazard rates can differ significantly (orders of magnitude difference at early times, with the Weibull being the more conservative of the two).

Condition-Based Maintenance

While probabilistic methods of failure prediction have been useful in many circumstances, their shortcomings for critical components and systems have prompted research and development along two complimentary lines. One is to incorporate microstructural material parameters into a more physically motivated distribution of failure as a function of time. The second is to monitor the condition of the critical component or system on a continuous or periodic basis and perform maintenance when a precursor to failure is identified. The precursor may take the form of an individual identifiable event, the change in the spectrum of a measured quantity, or the development of a trend in a measured quantity. Theoretical work conducted on the dynamics of meshing gears (Mark, 1992), for example, suggests that changes in spectral quantities may be indicative of a change in the state of one of the gears.

The benefits of employing condition-based maintenance have now been documented by a number of private corporations. At the 1992 International Gas Turbine and Aeroengine Congress, for example, KLM outlined the benefits realized through the measurement of selected engine parameters (Lanser, 1992). More recently, companies in other industrial sectors have reported maintenance cost benefits realized by implementing condition-based maintenance. Within the electric power utility sector, for example, the costs of developing and operating a condition-based maintenance system may be recovered through reduced maintenance costs in as little as three months, with a maximum cost recovery time of two to three years. This variability in cost recovery time is attributable at least in part to the manner in which development and other one-time costs are amortized. As would be expected intuitively, the installation cost of a given condition monitoring system is generally highest for the first unit and decreases as experience in installation is gained (Colsher et al., 1992).

While condition-based maintenance represents a significant improvement over probability-based descriptions of failure for critical components and systems, it is still inherently diagnostic in character. The improvements to date have resulted in sensing technology and from the application of multisensor data fusion techniques, which improve the probability of correctly identifying a failure (see for example Hall, 1992; Hall and Nauda, 1989 and Kumara et al., 1989). However, the detection of a failure precursor only indicates that a failure will eventually occur, but it does not predict the remaining safe or operational life of the system. The predictive, or prognostic, capability identified at the 1992 International Gas Turbine Institute Symposium as the essential improvement in condition-based maintenance systems of the future is not and cannot be realized in presently used approaches. This perspective has subsequently been confirmed to the present authors by a broad range of present and potential condition-based maintenance system users.

Prognostics for Mechanical Systems

Conceptually, the ability to predict the remaining safe or operational life of a system, based on observation of a failure precursor requires the combination of the following: (*a*) models for the growth or development of critical failure mechanisms (e.g., fatigue crack growth); (*b*) models for the dynamic interaction of interacting components (e.g., trans-

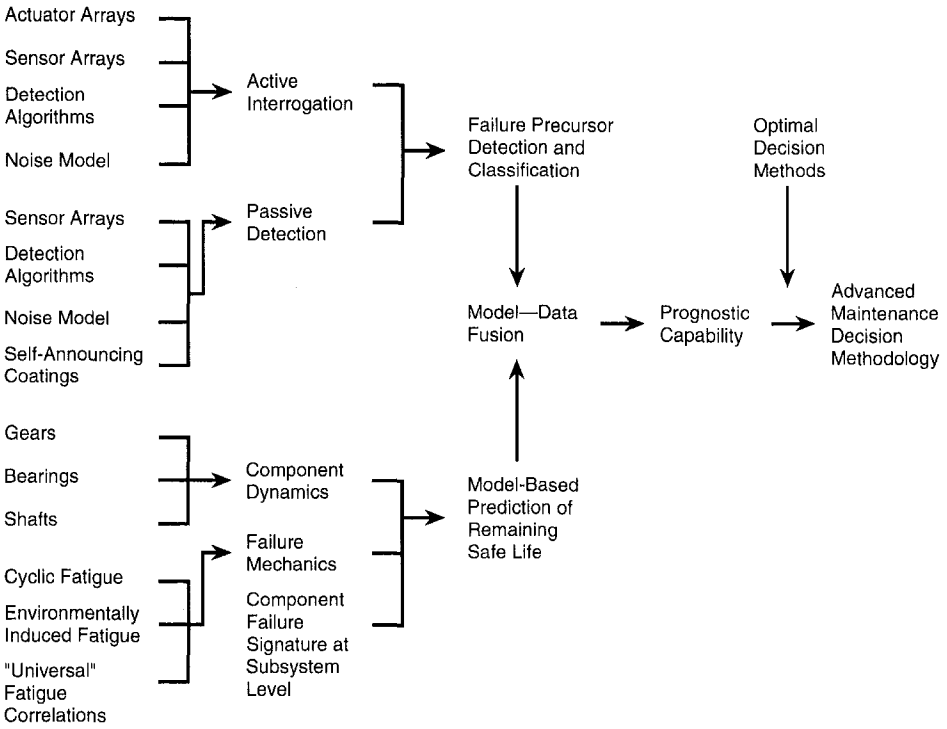

Fig. 2 Prognostics development road

mission error in meshing gears); (*c*) models for propagation of a failure precursor signature from its point of origin to the positions of the sensors used in monitoring the system state; and (*d*) fusion of model and sensor-based information to classify the fault characteristics. (As explained subsequently, characterization of the initial state of components may also be required.) A schematic representation of this concept is shown in Fig. 2. Additional information on the components of this approach is given below.

Modeling of Critical Failure Mechanics. Virtually all components of gear systems are subject to cyclic loading and the attendant fatigue crack growth. Prior to use, such components may only have stress concentrations or microcracks. Under the loads imposed in operation, however, these nucleation sites can spawn a crack that grows to the point that a gear tooth or other component actually fails. A prognostic capability requires a reliable empirical or analytic description of crack growth as a function of load.

Very recent work by Vasudevan et al. (1993) establishes the threshold conditions for fatigue crack growth. By re-examining experimental evidence for a broad range of materials, they show that two threshold stress intensity criteria must be simultaneously met for fatigue cracks to grow. They are the critical cyclic stress intensity, ΔK^*_{th}, and the critical maximum stress intensity, $K^*_{\max}$. The requirement on ΔK^*_{th} ensures that the threshold cyclic load imparts cyclic damage. That on $K^*_{\max}$ allows the peak load to break open bonds in a damaged region. The values of these two critical parameters depend upon material type and environment (e.g., moist air versus vacuum). They are intrinsic to a given material and environment rather than dependent on extrinsic factors such as crack closure, however. Moreover, the value of ΔK^*_{th} measured near a load ratio of unity varies linearly with that of $K^*_{\max}$ measured near a load ratio of zero. The constant of proportionality is independent of material type and dependent only upon the environment (e.g., vacuum versus air).

Above the critical condition for crack growth, deterministic fracture mechanics models and associated experiments indicate that the fatigue crack growth (da/dN, where a is the crack length and N is the number of cycles) is related to stress intensity through the Forman crack growth relationship or a simplification thereof. In reality, the initial distribution of crack lengths and depths together with local variations in material properties will provide a distribution of crack lengths after any number of cycles of loading, N. This probabilistic extension of deterministic fracture mechanics has been reviewed by Provan (1987) and Harris (1992).

An empirical formulation for the latter stages of material failure has been advanced by Voight (1989). It is of the form

$$(\dot{\epsilon}^{-\alpha}) \times \ddot{\epsilon} - A = 0 \tag{4}$$

where ϵ is the strain, $\dot{\epsilon}$ and $\ddot{\epsilon}$ the creep rate and acceleration, respectively; and $\times$ denotes multiplication. The parameters α and A are constants characteristic of the specific material and its configuration. Solution of Eq. (4) shows that the remaining time before failure is given by

$$t_f - t_* = \frac{\dot{\epsilon}^{1-\alpha}}{A(\alpha - 1)} \tag{5}$$

where $t_* < t_f$ is the time at which the strain rate is measured as $\dot{\epsilon}_*$. For steels and other high-strength alloys, α is close to 2, in which case

$$t_f - t_* = \frac{1}{A\dot{\epsilon}_*}. \tag{6}$$

Thus, if one can continuously monitor the strain rate $\dot{\epsilon}$, and one has previously determined A from a log-log plot $\ddot{\epsilon}$ versus $\dot{\epsilon}$, one has a measure of how much time is left before failure.

While such empirically based relationships appear to have significant potential for use with dynamic gear models, significant progress is being made as well in the development of three-dimensional numerical simulation at the microstructure level. For example, one of the present authors and his co-workers (Kumar et al., 1992) can now visualize and compute effects of loading on the microstructure of a material represented by a random subdivision of space using the Voronoi tessellation. Such a fundamental representation of a material at the microstructural level will in the future provide

a basis for testing existing empirical crack initiation and growth models and where necessary developing new relationships that can be used with a dynamic model of a gear train to predict remaining safe or operational life. In the longer term, such simulations may replace empirical relationships and will certainly improve them when combined with experiments.

Dynamic Gear Models. The seminal work of W. D. Mark, now of the Applied Research Laboratory of The Pennsylvania State University, provides an exact description of gear tooth-induced vibrations. This work provides both the basis for specifying the time-varying load fields in which crack initiation and growth occur and the change in vibration spectrum (transmission error) that results from the presence of cracks. An excellent overview of this work and its implications is provided in the most recent edition of *Noise and Vibration Control Engineering—Principles and Applications* (see Mark, 1992). Additional detail on predicting manufacturing errors in gears is provided by Mark (1992). Most modern spur and helical gears utilize gear tooth geometries that are involute curves or modifications thereof, which ideally transmit an exactly constant angular velocity ratio between meshing gears. In reality, deviations from the ideal tooth contour result in vibratory excitation originating at the meshing teeth of each gear pair. These deviations can arise from such causes as elastic deformation of the gear teeth, machining errors in the contours of individual teeth, tooth spacing errors, and tooth wear. The detailed harmonic analysis methodology that has been developed as a part of Mark's works allows a priori prediction of the spectral content associated with these and other deviations in gear configurations from the ideal, or alternatively, a time history of the same quantities.

The various components of transmission error, predicted by the model, are shown in power spectrum form for one gear pair in Fig. 3. The contribution due to a tooth spacing error appears at the rotational fundamental and multiples thereof. Tooth-to-tooth random errors, tooth elastic deformations, and mean tooth surface deviations create spectral peaks at the tooth mesh fundamental and multiples thereof. Note that the tooth mesh fundamental is n times the rotational fundamental where n is the number of teeth on the gear. The side band spacing, associated with tooth-to-tooth random errors, is spaced at integer values of the rotational fundamental from the tooth mesh fundamental. These are shown to scale in Fig. 3. Undulation errors are attributable to an irregularity in the machining process used to fabricate an individual gear, and the spectral peak introduced has no particular relationship to either the rotational fundamental or the tooth mesh fundamental. Careful comparisons of the predicted spectra associated with all of these errors and

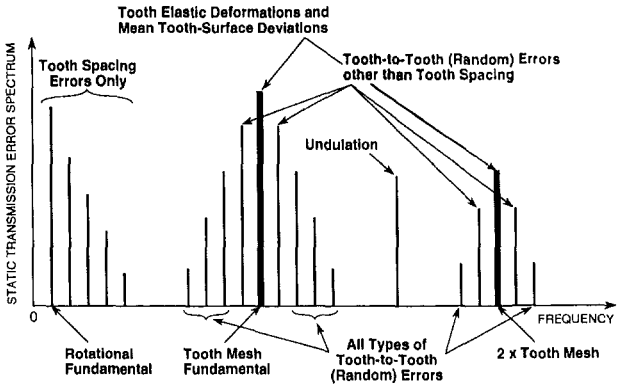

Fig. 3 Contributions to static transmission error spectrum from various types of tooth errors on a single gear or pinion

deviations have been made with the corresponding experimental results. The agreement is excellent.

The existence of a crack causes the effective local modulus of elasticity of the nearest tooth to be reduced. Consequently, the effect will be manifested at the rotational fundamental and multiples thereof rather than at the tooth mesh fundamental. That is, it is an effect associated with that single tooth rather than with the gear as a whole. In order to identify the presence of the crack at an early stage, it will be necessary to remove the competing effect of tooth spacing errors. This is accomplished by measuring these errors a priori and subtracting out their predicted contribution to the transmission error. It has already been established that the accuracy and fidelity of Mark's model permits such an operation.

Failure Signatures at the Subsystem Level. In many applications of prognostics, sensors will be somewhat removed from the individual components at which the failure precursor signatures of interest originate. Therefore, methods to predict the subsystem level manifestations of these local signatures are required. Existing finite element methods are employed to make these predictions of failure precursors as seen at actual sensor locations.

It should be noted that a combination of fatigue crack models (or other failure mechanism models) with the transmission error model and prediction of failure signature at the component level is important in its own right. It offers a method of doing seeded fault testing in the simulation environment. Such numerical seeded fault testing can be carried out at a small fraction of the cost of fault testing on a test stand. As a result, the examination of the effects of a wide range of faults is practical.

Fusion of Model and Sensor-Based Information to Characterize the Fault. In principle, the measured transmission error for a gear system will be continuously or periodically compared with that predicted for this system in the absence of faults. When a deviation is identified, the model for the system with faults will be exercised to predict the fault characteristics. Using this fault characteristic as an initial condition, the remaining safe or operational life for the gear set under any user-specified loading conditions will be predicted. This process is inherently the solution of an inverse problem (i.e., given the fault signature determine the fault). As such it is much more difficult than numerical seeded fault testing in which the fault is prescribed and the associated signature is to be predicted.

The integration of model predictions and sensor readings may be addressed as a problem in multisensor data fusion. In particular, a rich source of technology can be adapted from data fusion techniques developed for Department of Defense situation assessment and threat assessment applications (viz., the concept of monitoring sensor data and using predictive models to assess equipment failure and prescribing maintenance is highly analogous to monitoring a battlefield situation, assessing/predicting enemy threats, and identifying countermeasures). Numerous algorithms and techniques are available to address this problem. A survey and discussion of techniques can be found from Hall (1992) and Waltz and Llinas (1990).

A conceptual model for this model/sensor fusion is illustrated in Fig. 4. The figure shows multiple (active and passive) sensors observing the operation of gear equipment and the associated environment. These sensor data are individually processed via filtering and signal processing algorithms. Subsequently, four levels of fusion processing are identified. Level 1 processing combines parametric information from sensors to achieve accurate estimates of the attributes of equipment components and the surrounding environment. Level 1 processing aligns the data (in time, space, and units

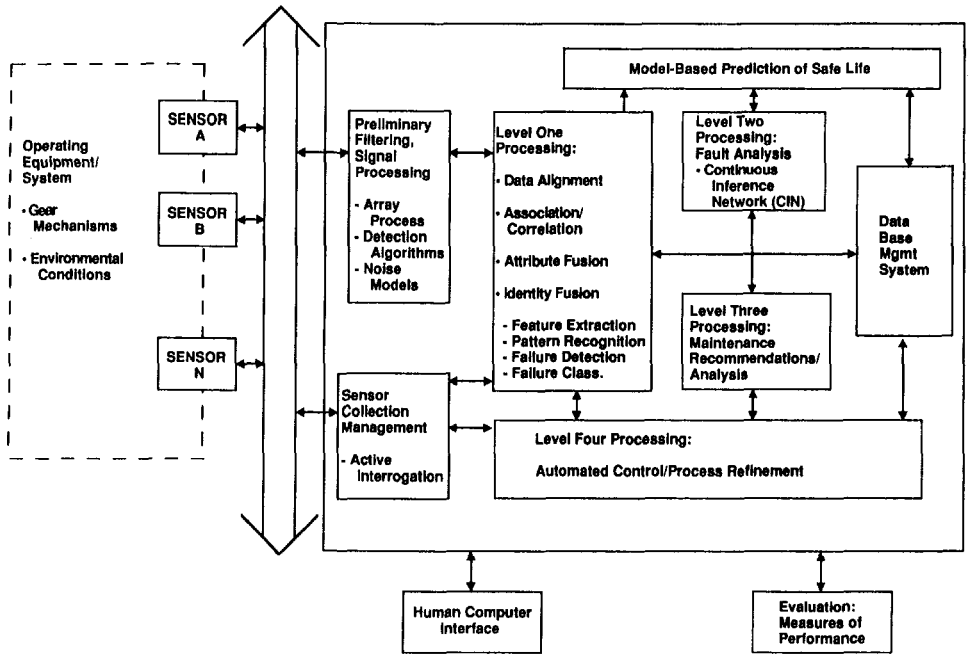

Fig. 4 A process model for condition-based maintenance

of measurement), associates and correlates data from diverse sensors, and applies statistical techniques to estimate attribute parameters. Feature extraction and pattern recognition techniques (e.g., templates, neural networks, or cluster analysis) are applied to detect and initially classify potential faults or failures. A second process (Level 2 processing) is performed to analyze and characterize the potential faults. This Level 2 processing uses reasoning techniques and input from predictive models to characterize the current state of the operating equipment and the potential remaining life. Level 2 processing considers not only individual equipment components, but also groups of components as well as considering the effects of the environment (i.e., applied stress, external temperatures, etc.). Higher level reasoning techniques must be applied such as expert systems, logical templates, fuzzy reasoning, or adaptive neural systems. Finally, Level 3 processing uses predictive models and heuristic reasoning to provide recommendations for system maintenance. A fourth process (Level 4 processing) monitors the operation of the condition-based maintenance diagnostic system for automated control and process refinement. A detailed taxonomy of algorithms and techniques for Levels 1, 2, 3, and 4 processing is provided by Kessler et al. (1992).

A particularly applicable method for Level 2 (fault analysis) processing is a generalization of fuzzy reasoning developed by the Applied Research Laboratory. J. A. Stover and R. E. Gibson (1993) have developed and implemented the concept of a continuous inference network (CIN).

Stover and Gibson have defined continuous functions (analogous to fuzzy set membership functions, e.g., Zadeh, 1968), which allow quantification of imprecise concepts. These continuous functions are defined on the interval [0, 1] and provide a representation of inferences about a system (e.g., a gear assembly may be "faulty" if the specified acoustic spectral features are present). These functions provide a mapping between parametric sensor data (such as temperature, acoustic spectra, etc.) and assertions or inferences concerning a system's state. Stover and Gibson have defined a calculus of representation and propagation, which allows representation of uncertainty in sensor data, representation of uncertainty or imprecision in inferences (given the sensor data), logical connectives (Boolean equivalent AND/OR operations) and propagation of these inferences and uncertainties to effectively reason about imprecise concepts. In particular, they define a BLEND function based on sigmoid functions that allows precise specification of these fuzzy representations and combinations of these functions for logical reasoning. These are a generalization of the ad hoc figure of merit (FOM) functions originally developed by Wright (1980).

The definition of fuzzy membership relations to represent imprecise information and fuzzy logical operators as continuous, discriminatory functions provides a robust mechanism for reasoning about imprecise concepts in system diagnosis and maintenance. Stover and Gibson's continuous inference network (CIN) provides a means of developing complex chains of reasoning to transform from sensor data to conclusions about the state of a system. Thus, the CIN performs an intelligent perception function transforming hierarchically from sensor data to inferred properties of the monitored gear system. The concept is illustrated in Fig. 5. Moreover, unlike the more traditional expert system techniques or templating methods, the CIN inference process is effective for adaptive control systems. This reasoning technique represents a significant breakthrough in application of fuzzy logic concepts to dynamic systems.

Extension to Other Failure Modes and Subsystem Types. The methodology described for predicting the remaining safe or operational life of gears with fatigue as the dominant failure mechanism is readily extendable to other failure types and geometries. The essential requirements are models for the dominant failure mechanism on the local level and of the dynamic behavior of the components or subsystems. The methodology developed for fatigue failure of gears is, for example, equally applicable to failure modes such as pitting and components such as shafts and bearings. The applicability extends beyond rotating machinery components as well. For any mechanical system that can be instrumented and dynamically modeled, subject to any failure mode that can be modeled, a capability to predict remaining safe or operational life can be developed with the methodology developed herein.

Summary

The essential capability of next-generation mechanical diagnostic systems identified by potential users is the predic-

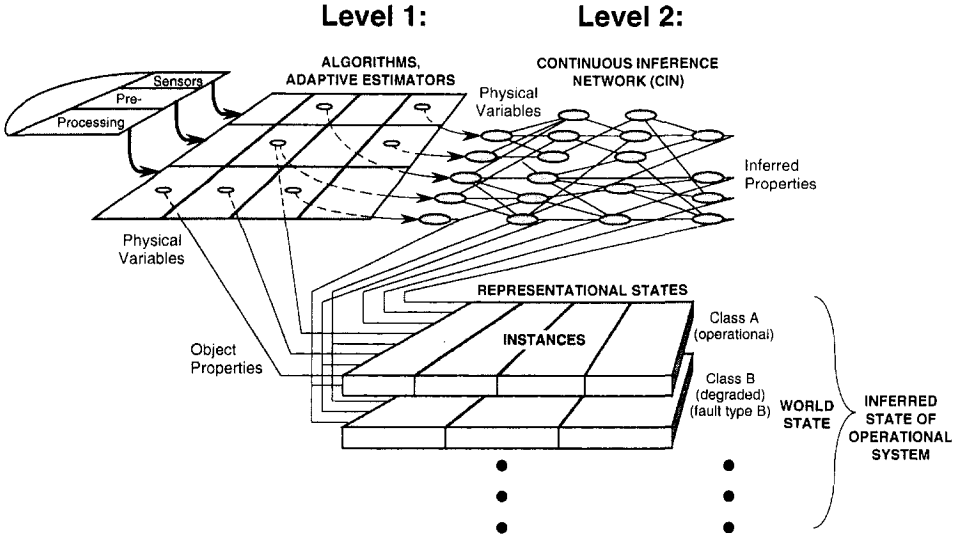

Fig. 5 Automated inference process for equipment diagnosis

tion of remaining safe or operational life. A methodology has been developed for realizing this goal that involves the fusion of sensor-based with model-based information. The methodology draws upon recent advances in both data fusion and material failure models. The applicability of the methodology has been discussed primarily in terms of fatigue crack growth of gears, but its broader applicability is apparent as well. It is anticipated that the methodology will have a major impact on the safety and life cycle cost of critical mechanical systems and components.

References

Colsher, R., Frank, R., Matusheski, R., McElroy, J., and Leonard, W., 1992, "The Benefits of an Integrated Predictive Maintenance Program in a Power Plant Environment," PDM Conference, Knoxville, Sept. 21–23.

Hall, D. L., and Nauda, A., 1989, "Embedded AI-Based Diagnostic System for Signal Collection and Processing System," *Journal of Wave-Material Interaction*, Vol. 4, pp. 1–14.

Hall, D. L., 1992, *Mathematical Techniques in Multisensor Data Fusion*, Artech House, Inc., Norwood, MA.

Harris, D. O., 1992, "Probabilistic Fracture Mechanics With Applications to Inspection Planning and Design," *Reliability Technology*, T. A. Cruse, ed., Vol. AD-28, pp. 57–76.

Haugen, E. B., 1980, *Probabilistic Mechanical Design*, Wiley, New York.

Hudak, S. J., et al., 1990, "Comparison of Single Cycle vs Multiple Cycle Proof Testing Strategies," NASA Contractor Report No. 4318.

Kapur, K. C., and Lamberson, L. R., 1977, *Reliability in Engineering Design*, Wiley, New York, Chap. 11.

Kessler, O., Askin, K., Beck, N., Lynch, J., White, F., Buede, D., Hall, D., and Llinas, J., 1991, "Functional Description of the Data Fusion Process," report prepared for the Office of Naval Technology, published by NAWC, Warminster, PA.

Kumar, S., Kurtz, S. K., Banavar, J. R., and Sharma, M. G., 1992, "Properties of a Three-Dimensional Poisson-Voronoi Tesselation: A Monte Carlo Study," *Journal of Statistical Physics*, Vol. 67, pp. 523–551.

Kumara, S. T., Kashyap, R. L., and Soyster, A. L., 1989, *AI in Manufacturing: Theory and Practice*, Institute of Industrial Engineering.

Lanser, H., 1992, "Engine Condition Monitoring as a Tool for Lifetime Extension of HPT Rotor Blades," panel discussion at the 37th ASME International Gas Turbine & Aeroengine Congress and Exhibition, Cologne, Germany, June 1–4.

Lewis, E. E., 1987, *Introduction to Reliability Engineering*, Wiley, New York, Fig. 4.2.

Mark, W. D., 1992, "Contribution to the Vibratory Excitation of Gear Systems From Periodic Undulations on Tooth Running Surfaces," *Journal of the Acoustical Society of America*, Vol. 91, pp. 166–186.

Mark, W. D., 1992, "Elements of Gear Noise Prediction," *Noise and Vibration Control Engineering—Principles and Applications*, L. L. Beranek and I. L. Ver, eds., Wiley, New York, Chap. 21.

Provan, J. W., 1987, *Probabilistic Fracture Mechanics and Reliability*, Martinus Nijhoff Publishers, Dordrecht, pp. 176–183.

Sobcyzk, K., and Spencer, B. F., 1992, *Random Fatigue: From Data to Theory*, Academic Press, New York, pp. 174–176, 234–235.

Stover, J. A., and Gibson, R. E., 1993, "A Processing Architecture for Autonomous Systems," submitted for publication in *Artificial Intelligence Journal*.

Vasudevan, A. K., Sadananda, K., and Louat, N., 1993, "Two Critical Stress Intensities for Threshold Fatigue Crack Propagation," *Scripta Metallurgica et Materialia*, Vol. 28, pp. 65–70.

Voight, B., 1989, "A Relation to Describe Role Dependent Material Failure," *Science*, Vol. 243, pp. 200–203.

Waltz, E., and Llinas, J., 1990, *Multisensor Data Fusion*, Artech House, Inc., Norwood, MA.

Wright, F. L., 1980, "The Fusion of Multisensor Data," *Signal*, pp. 39–43.

Zadeh, L. A., 1968, "Fuzzy Algorithms," *Information and Control*, Vol. 12, pp. 94–102.

A Blade-by-Blade Tip Clearance Measurement System for Gas Turbine Applications

A. G. Sheard

B. Killeen

Rotadata Limited,
Derby, United Kingdom

It is difficult to make a reliable measurement of running clearance in the hostile environment over the blading of a modern gas turbine. When engine manufacturers require the measurement to be made over every blade during live engine tests, system reliability, ruggedness, and ease of operation are of primary importance. This paper describes a tip clearance measurement system that can measure clearance over every blade around a rotor. The measurement system concept is presented, and the system design described in detail. Commissioning of the measurement system on a compressor test facility, and the results obtained are discussed. An analysis of system performance during the commissioning trials concludes the paper.

1 Introduction

In this paper a program of work is described that was undertaken by the authors to develop and test a clearance measurement system that could be used to measure the clearance over individual blades around a rotor. The objective of the work was to reduce the practical problems associated with system operation, providing a "plug in and play" measurement system that relatively unskilled operators could use. In principle this enables a routine measurement of the clearance on a blade-by-blade basis during those rig and engine tests that constitute a new gas turbine's development.

The tip clearance measurement system described is a third-generation electromechanical device. The first two generations were reported by Davidson et al. (1983) and Sheard and Turner (1992), respectively. The clearance measurement system utilizes a Stepper Motor-driven Probe (SMP) and a spark/discharge technique to ascertain the proximity of an electrically grounded target, typically a rotating compressor or turbine blade. This proximity measurement is to the longest blade around a rotor. A Frequency Modulated (FM) capacitance probe, described by Chivers (1989), is incorporated into the "blade-by-blade" SMP, which provides a measure of the difference in blade length of each blade relative to the longest blade.

In the current program of work, the authors focused on minimizing complexity of operation, while providing a system that was completely self-calibrating over a wide range of temperatures over a 6 mm range.

The decision to undertake this development program was taken after a thorough review of the gas turbine community's current and future clearance measurement requirements. This review is presented by Sheard and Killeen (1993), who went on to consider the available techniques for blade-by-blade tip clearance measurement before proposing a third-generation blade-by-blade SMP.

2 Clearance Measurement System Concept

The blade-by-blade SMP integrates an FM capacitance probe and electrode into a single probe. The probe is driven from its rear datum to the blading over which it is mounted by an electromechanical actuator. When the probe comes within a few microns of the longest blade a spark discharge occurs. Each time a spark discharge occurs the controller retracts the probe by 0.1 mm, thus eliminating the possibility of the probe touching the blades during transient engine operation. While within range of the blading, blade-by-blade tip clearance information may be logged at up to 30 kHz.

The FM capacitance probe is recessed approximately 0.1 mm from the electrode, so is close to the longest blade around the rotor when the spark/discharge occurs. The probe is retracted from the blading in 0.05 mm steps, with capacitance probe output for each blade at each step being recorded as described by Killeen et al. (1991). The algorithms developed by Sheard et al. (1992a) are used to generate a calibration from the FM capacitance probe output at each step.

Two factors are used in the calculation of tip clearance over the longest blade (as shown in Fig. 1). The first is distance, R, from the blade-by-blade SMP electrode to the inner casing when the probe is against its rear datum. The second is stroke, S, of the probe when a spark/discharge occurs. Clearance over the longest blade may be defined as:

$$Cl = S - R$$

Cl = the clearance over the longest blade around the rotor.

On-line calibration of the capacitance probe enables the distance, cn, between FM capacitance probe and each blade

Contributed by the International Gas Turbine Institute and presented at the 39th International Gas Turbine and Aeroengine Congress and Exposition, The Hague, The Netherlands, June 13–16, 1994. Manuscript received by the International Gas Turbine Institute February 4, 1994. Paper No. 94-GT-40. Associate Technical Editor: E. M. Greitzer.

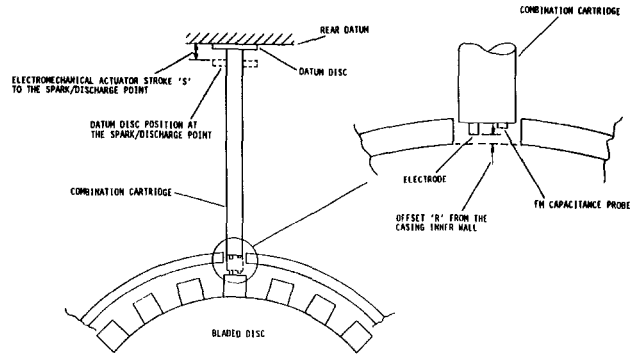

Fig. 1 A schematic view of the probe installation illustrating the factors used to calculate tip clearance over the longest blade

to be calculated. The blade with the minimum clearance, cl, between the FM capacitance probe and blade tip must be the longest blade, to which the electrode spark/discharge occurred. The difference in clearance, Δcn, between the longest blade and every other may be calculated:

$$\Delta cn = cn - cl$$

n = the blade number.

The clearance for each blade, Cn, may be calculated from the clearance over the longest blade, Cl, and the difference in clearance between the longest blade and every other blade:

$$Cn = Cl + \Delta cn$$

The technique above enables the capacitance probe to be calibrated after every spark/discharge, therefore ensuring that geometry effects and drift are eliminated.

The FM capacitance probe is physically transported to the rotor blading. Capacitance probe range, therefore, only has to be large enough to measure from the electrode spark discharge point to the shortest blade around the rotor. As the distance from the capacitance probe tip to the longest blade to which the spark discharge occurred is typically only 0.1 mm, the capacitance probe is effectively only required to resolve the difference in clearance between different blades. The capacitance probe, therefore, requires only a short range. This permits the use of a capacitance probe of smaller diameter than the blade thickness, and so is insensitive to variations in blade thickness from blade to blade.

2.1 The Probe. The blade-by-blade SMP contains a probe that combines an electrode and an FM capacitance probe into a single unit. The probe is described in detail by Sheard and Killeen (1993), and therefore will be described only briefly.

The probe, Fig. 2, incorporates a datum disk that consists of a metal ring electrically charged to 400 V. This is mounted on an insulated disk to isolate it electrically from the probe body. During normal operation the probe is driven in until the 400 V on the electrode has shorted to ground.

Once the electrode has shorted to ground it is retracted, following the method of Sheard et al. (1992) to allow the FM capacitance probe in the tip, Fig. 3, to be calibrated. The distance traveled from spark/discharge on the rear datum to the spark discharge to the longest blade and the capacitance probe output may be related to tip clearance over each blade as described in Section 2.

2.2 The Electromechanical Actuator. The major design criterion when designing the electromechanical actuator was minimum overall size. The design, Fig. 4, incorporates two principal components: the stepper motor drive assembly and electronics module. The design specifications are summarized in Table 1.

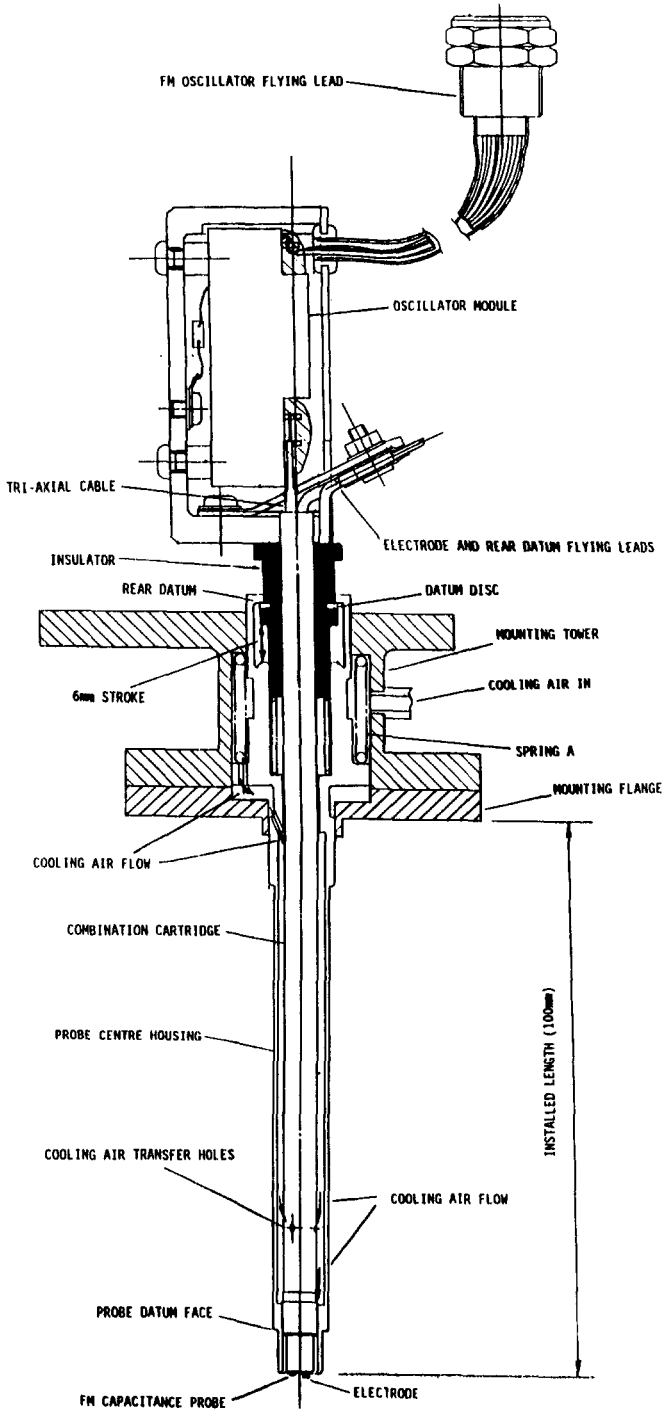

Fig. 2 A 100 mm installed length, 6 mm stroke blade-by-blade SMP probe

The actuator is described in detail by Sheard and Killeen (1993), and therefore will be described only briefly. The stepper motor drive assembly moves the probe to and from the blading in 2.5 μm steps. The electronics module generates the 400 V that is applied to the datum disk and the electrode. The electronics module also senses the sparking of the electrode or datum disk, latches the event, and cuts off the current with less than 2 pJ of energy being transferred.

2.3 Cooling Requirements. The electromechanical actuator and probe are designed for use in modern gas turbines where Turbine Entry Temperature can exceed 1800 K and therefore cooling techniques must be employed.

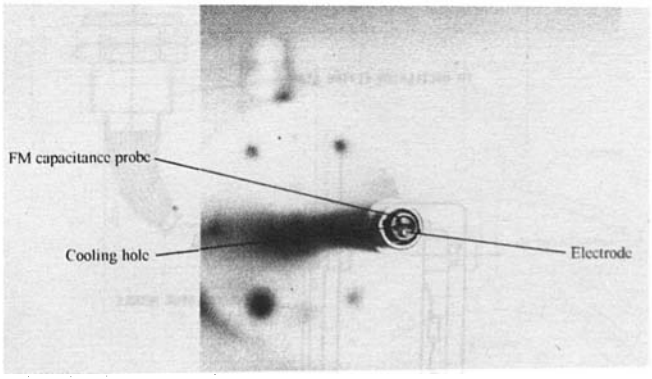

Fig. 3 A close-up view of a probe tip, with electrode (bottom), FM capacitance probe (top), and cooling holes (left and right)

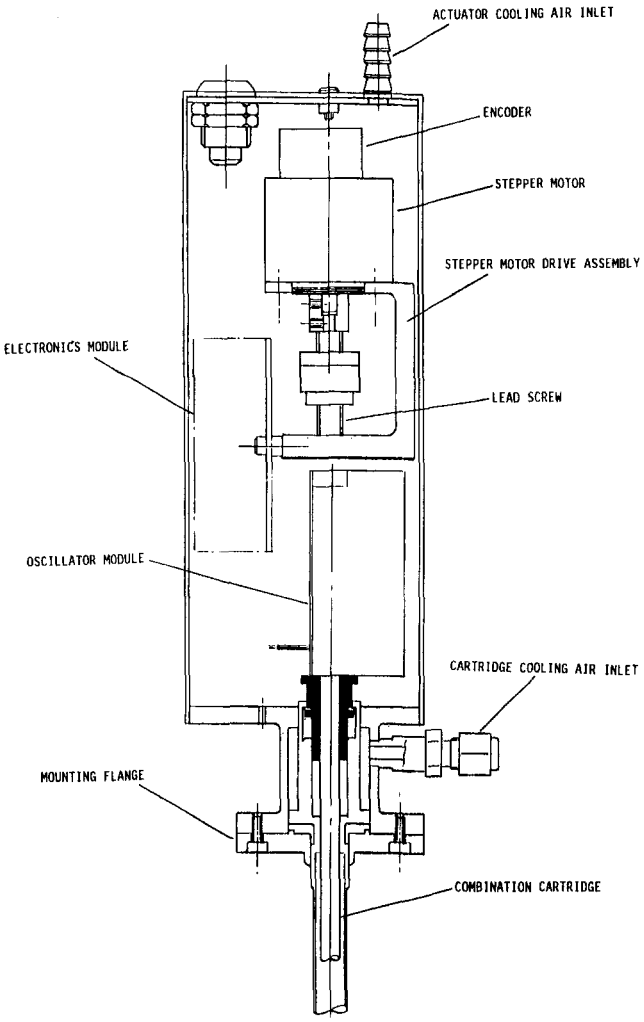

Fig. 4 The blade-by-blade SMP probe and electromechanical actuator

The probe and actuator are cooled by a dry purge air supply. During the initial commissioning trials oxygen-free bottled nitrogen was used as the air supply. Later standard "shop" compressed air was used. In both cases the purge air was filtered through a 0.3 μm filter immediately prior to entry into the probe. The purge air is fed into the mounting tower, Fig. 4, and exits from the probe tip. The purge air also prevents contaminants from entering the probe from the gas path and causing false short circuits from the electrode to ground.

Table 1 Blade-by-blade tip clearance measurement system specification

Range	6.0 mm
Resolution	2.5 microns
Repeatability	+/- 6 microns
Accuracy (Ambient)	+/- 10 microns
Accuracy (900 K)	+/- 25 microns
Sample Rate	30 KHz
Minimum target presentation time	2 micro seconds
Probe diameter at the tip	4.8 mm
Maximum uncooled probe temperature	900 K
Maximum gas temperature	1800 K
Actuator dimensions	215 x 72 x 60 mm
Actuator weight	1.7 Kg
Actuator environmental temperature limits	50 C
Output from the controller	RS232

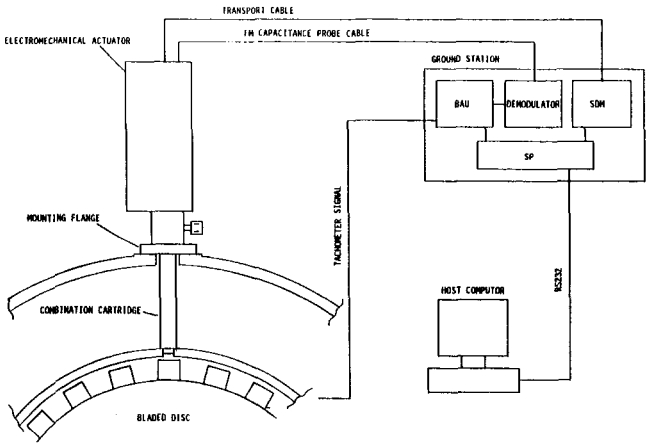

Fig. 5 The interrelationship between ground station modules, electromechanical actuator, and host computer

2.4 The Electronic Controller. The probe and actuator are driven by a ground station, Fig. 5, that performs all functions necessary to generate data sets of clearance over each blade versus blade number. The ground station consists of four separate modules. A stepper motor drive module (SDM) generates all stepper motor drive signals, interrogates encoder output to verify correct motion of the drive, and checks for a front or rear spark/discharge. The second module, an FM capacitance probe demodulator, converts the oscillator FM signal from the probe into a voltage pulse train. The third module is a Blade Analyzer Unit (BAU), which latches the height of each blade passing pulse and converts it from an analogue voltage peak to a digital number. A tachometer signal triggers the BAU's analogue-to-digital converter. The next tachometer signal triggers the data set of pulse heights to be closed and passed to the BAU's output stage.

The SDM and BAU communicate with the fourth module, the system processor (SP), via RS232 links. The SP is the ground station's interface between an external data acquisition system and the first three modules. The SP firmware contains the algorithms developed by Sheard et al. (1992) to calibrate the capacitance probe on line and calculate clearance over each blade. The output of the SP is a stream of data sets, where each data set comprises a list of blade number versus tip clearance in engineering units.

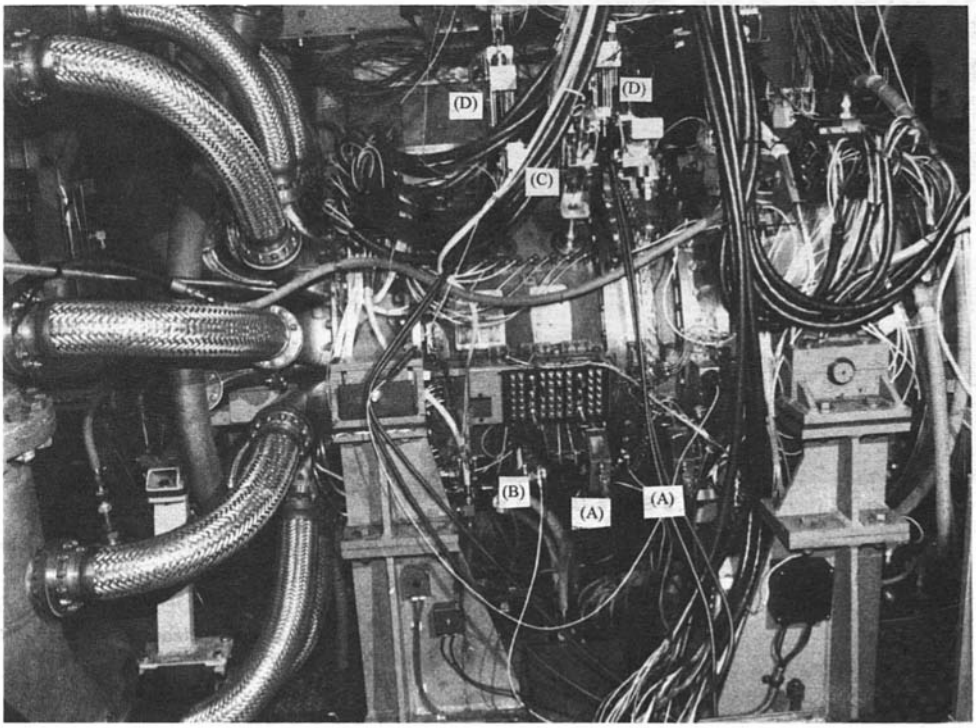

Fig. 6 The C147 compressor at DRA Pyestock fitted with two of Davidson et al.'s SMPs (A), a blade-by-blade SMP (B), a radial traverse (C), and two area traverses (D). Courtesy British Crown (1993).

Table 2 The C147 overall design parameters

Pressure Ratio	6.4
Mass Flow (at 288K & 1 Atm. inlet)	49.5 Kg/s
Rotational Speed (at 288K inlet)	6894 rpm
Exit Hub/Tip Ratio	0.912
Exit Blade Height	38.1 mm
Inlet Tip Diameter	917 mm

Table 3 Commissioning test vehicle conditions

Stage Number	Last of 5
Number of Blades	91
Rotational Speed	6894 rpm
Gas Path Total Temperature	234 C
Approximate Ambient Air Temperature Local to the SMP	20 C
Gas Path Total Pressure	400 KPa abs.
Vibration	4 mm/s

2.5 PC Software. In order to acquire data from the ground station, an IBM-compatible computer was used as a host computer. A program was written to enable setup information to be downloaded to the SP. As the SP performed all conversion of raw data to engineering units it was not necessary for the program to perform any further calculations. In essence the software provided only a preset setup facility, a test control facility, and a data logging facility. The software was also able to display clearance versus blade number as it was acquired; this facility made the interpretation of tip clearance data as it was acquired possible.

3 Test Facility

Commissioning of the blade-by-blade SMP was conducted on the C147 large-scale, high-speed, high-pressure research compressor at the Defence Research Agency (DRA), Pyestock, Fig. 6. The C147 overall design parameters are given in Table 2 and are described by Calvert (1989). The rig conditions local to the SMP are given in Table 3.

The facility is extensively instrumented, Fig. 6, with up to two area traverse mechanisms, five radial traverse mechanisms, and five spark/discharge clearance measurement systems for measuring clearance to the longest blade around each rotor. Two radial traverse mechanisms may be seen in Fig. 6 on top of the rig, but are partially obscured by the facility cabling. The radial traverse system is described by Sheard and Palmer (1993); the spark/discharge clearance measurement systems are described by Davidson et al. (1983). The blade-by-blade SMP was designed to be interchangeable with Davidson et al.'s system, allowing it to be fitted into the same mounting tower, Fig. 7. The blade-by-blade SMP was installed without any modification to the facility, the only addition being a second cable from the actuator to carry the FM capacitance probe signal.

4 Commissioning

Commissioning on the final stage of C147 was undertaken to demonstrate system ability to withstand the environment found around running turbomachinery. The ability of any system to operate in an ambient environment is no guide as to its likely performance when installed on a live compressor or turbine.

The compressor was driven to 100 percent design speed and held at that speed for five hours. The blade-by-blade SMP was used to measure clearance over each blade around the rotor every 15 minutes during the time spent at condi-

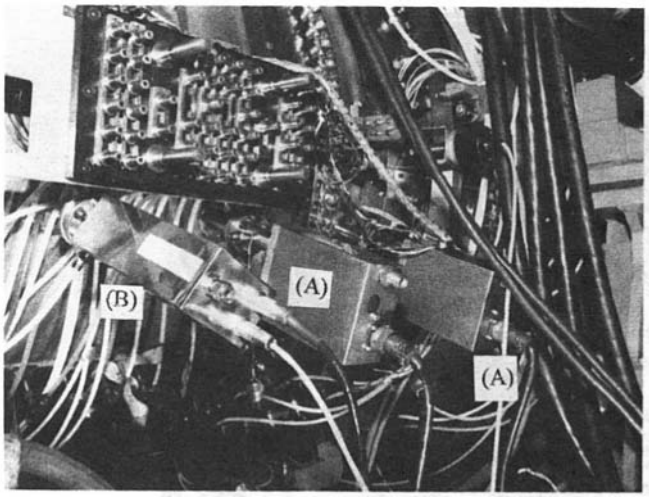

Fig. 7 C147 fitted with two of Davidson et al.'s SMP's (A) and a blade-by-blade SMP (B). Courtesy British Crown (1993).

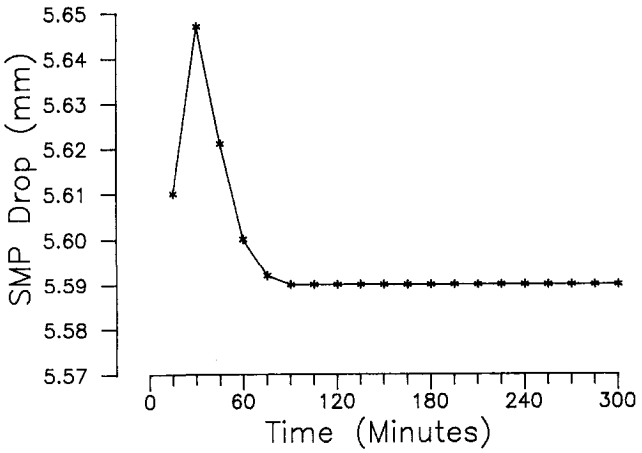

Fig. 8 Measured distance from the blade-by-blade SMP datum to the Stage 4 longest blade during commissioning

tion, to ascertain measurement system reliability and repeatability. No operational problems were encountered with the radial transport and spark discharge electronics, with the actuator and probe cooling system keeping both at near ambient temperature. System reliability was, therefore, concluded to be as good on C147 as had been reported by Sheard and Killeen (1993) in the laboratory.

The drop from probe internal datum to the spark discharge point on the longest blade increased by 0.04 mm over the first 15 minutes at design condition, then over the next 75 minutes decreased by 0.06 mm, Fig. 8. The drop then remained constant for the remainder of the test. The authors drew two conclusions from the drop measurements at design condition. Firstly, the facility took one and a half hours to stabilize thermally after reaching the design point. Secondly, transport repeatability during the last four hours at design condition was excellent, with no evidence of probe tip erosion.

The commissioning trial was conducted at the conclusion of a 400 hour test program, during which Davidson et al.'s tip clearance measurement system had been utilized extensively to measure clearance over the longest blade on the compressor's final stage. The clearance over the longest blade measured using the blade-by-blade SMP was compared with that measured using Davidson et al.'s measurement system, Fig. 9. The minimum and maximum clearances measured with the blade-by-blade SMP were within the scatter of the previous

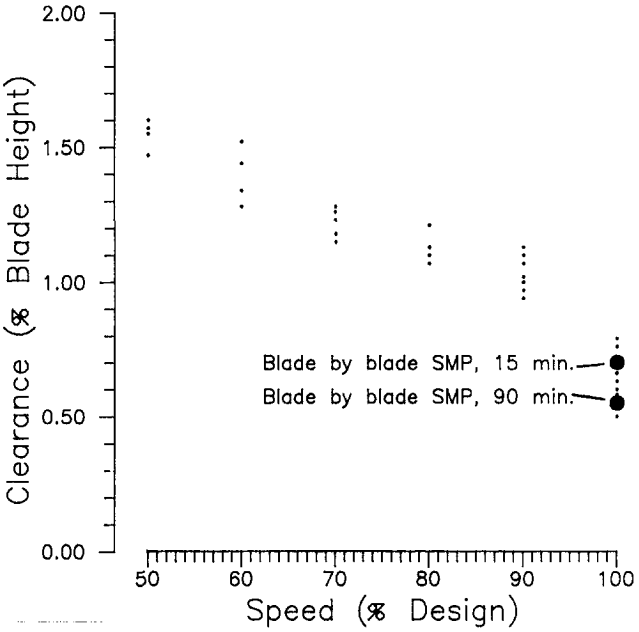

Fig. 9 Measured Stage 4 clearance, from Davidson et al.'s SMP and results from the blade-by-blade SMP

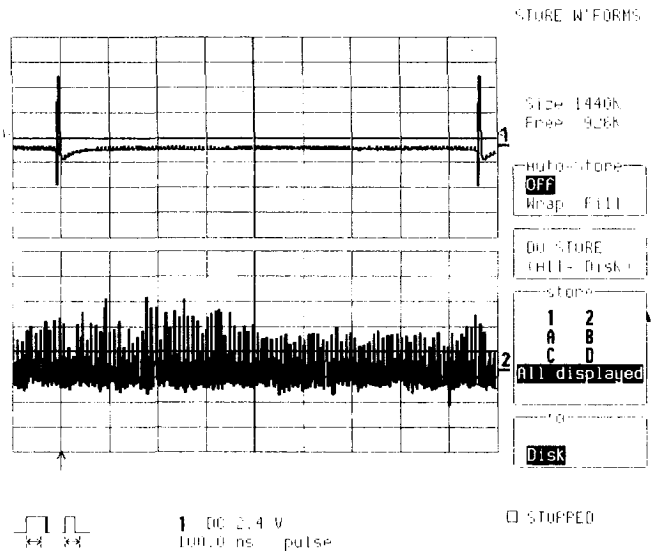

Fig. 10 A typical FM capacitance probe output voltage signal after a spark discharge to the longest blade (bottom) and tachometer signal (top)

results. The authors concluded first that the blade-by-blade SMP results were in excellent agreement with the earlier data, and second a significant contributor to the scatter of the earlier results was due to results being taken during the thermal stabilizing time of the compressor.

The primary aspect of the commissioning program was to measure clearance over individual blades. The FM capacitance probe was used to measure blade-by-blade clearance over the 91 blades around the final stage. A typical example of the capacitance probe raw output voltage, Fig. 10, illustrates the voltage peak associated with each blade passing event. The raw output is reduced to a data set of clearance over each blade versus blade number, where Blade 1 is defined as the first blade to follow the falling edge of the once per revolution tachometer signal.

The data sets acquired during the last four hours at design condition showed a high degree of repeatability, with the

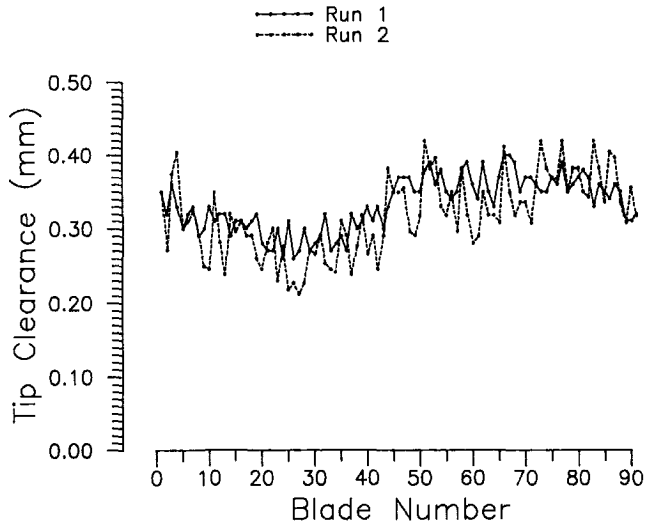

Fig. 11 Two data sets of tip clearance versus blade number acquired after one and three hours at the compressor design point

clearance over individual blades varying randomly by approximately 0.025 mm. Two data sets acquired after one hour at design condition (Run 1) and three hours at design condition (Run 2), Fig. 11, illustrate this point clearly.

The blading around a rotor is a loose fit in its root fixing, with Sheard et al. (1992) measuring a 0.050 mm variation in blade radius from one cycle of a rotor to the next. The authors speculated that the blading might move in its root fixing over a period of time due to unsteady aerodynamic forces on the blading and the mechanical vibration of the rig. This phenomenon might explain the variation in clearance of 0.025 mm over individual blades from one data set to the next.

It appears that the C147 rotor assembly was running eccentric, a phenomenon that can be more clearly seen by replotting the data in Fig. 11 after subtracting the mean clearance, and expanding the clearance axis, Fig. 12. The once per revolution eccentricity of the rotor is clearly seen as a ± 0.050 mm sinusoidal variation in tip clearance around the rotor. This level of eccentricity was self-consistent with the 0.075 mm design clearance in the bearings, plus a small allowance on the rear bearing squeeze film. There were insufficient vibration data available to confirm that the once per revolution eccentricity was the synchronous unbalance response of the rotor; however, this was considered most likely.

5 Summary and Conclusions

1 A blade-by-blade tip clearance measurement system has been successfully used on a compressor under test to measure clearance over every blade around a rotor.
2 The blade-by-blade SMP has a similar geometry to Davidson et al.'s SMP, facilitating the free exchange of the two clearance measurement systems in an engine installation.
3 The blade-by-blade SMP survived the commissioning trial, with no operational problems of the transport mechanism, the spark/discharge electronics or the cooling system. On completion of the trial the actuator and probe were inspected and showed no signs of distress.

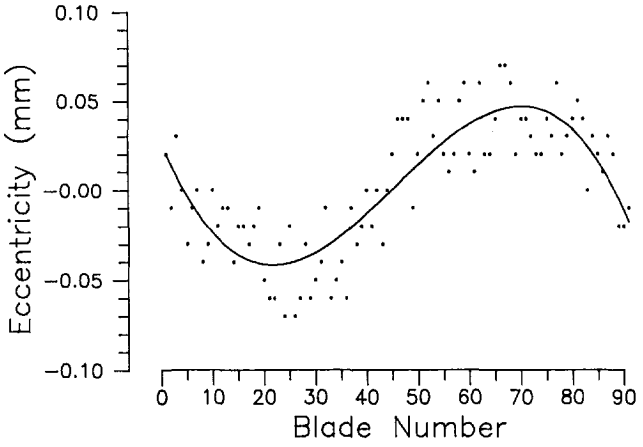

Fig. 12 A data set of tip clearance versus blade number, after subtracting the mean clearance

4 Clearance over the longest blade around the compressor final stage rotor measured using the blade-by-blade SMP and Davidson et al.'s SMP were in close agreement, giving confidence in the new system.
5 The blade-by-blade SMP revealed a ± 0.050 mm eccentricity of the rotor.

Acknowledgments

The authors gratefully acknowledge the assistance of Ian McKenzie of DRA Pyestock who organized the commissioning trials on the C147 compressor. The authors acknowledge the assistance of D. Allen, G. Brock, A. Brown, B. H. Edmundson, A. H. Lock, D. J. Taylor, A. Wooler, and others of Rotadata Ltd. Finally the authors would like to thank Rotadata Ltd. for permission to publish the work in this paper.

References

Calvert, W. J., Ginder, R. B., McKenzie, I. R. I., and Way, S., 1989, "Performance of a Highly-Loaded HP Compressor," ASME Paper No. 89-GT-24.

Chivers, J. W. H., 1989, "A Technique for the Measurement of Blade Tip Clearance in a Gas Turbine," AIAA Paper No. 89-2916.

Davidson, D. P., DeRose, R. D., and Wennerstrom, A. J., 1983, "The Measurement of Turbomachinery Stator to Drum Running Clearance," ASME Paper No. 83-GT-204.

Killeen, B., Sheard, A. G., and Westerman, G. C., 1991, "Blade by Blade Tip Clearance Measurement in Aero and Industrial Turbomachinery," *Proceedings of the 37th ISA International Symposium of Measurement Technique*, pp. 429–447.

Sheard, A. G., and Turner, S. R., 1992, "Electromechanical Measurement of Turbomachinery Blade Tip-to-Casing Running Clearance," ASME Paper No. 92-GT-50.

Sheard, A. G., Westerman, G. C., and Killeen, B., 1992, "An On-Line Calibration Technique for Improved Blade by Blade Tip Clearance Measurement," *Proceedings of the 38th ISA International Instrumentation Symposium*, pp. 32–51.

Sheard, A. G., and Killeen, B., 1993, "A Hybrid System for High Temperature Tip Clearance Measurement," *Proceedings of the 39th ISA International Instrumentation Symposium*, pp. 379–394.

Sheard, A. G., and Palmer, A. A., 1993, "Miniature Traverse Actuator for Mapping the Flow Field Between Gas Turbine Blade Rows," *Proceedings of the 3rd I.Mech.E Machine Actuators and Controls*, pp. 1–11.

Sheard, A. G., Westerman, G. C., Killeen, B., and Fitzpatrick, M., 1994, "A High-Speed Capacitance-Based System for Gaging Turbomachinery Blading Radius During the Tip Grind Process," ASME JOURNAL OF ENGINEERING FOR GAS TURBINES AND POWER, Vol. 116, pp. 243–249.

R. J. Roby[1]

A. J. Hamer[1]

E. L. Johnsson[2]

Department of Mechanical Engineering,
Virginia Polytechnic Institute
and State University,
Blacksburg, VA 24061

S. A. Tilstra[3]

T. J. Burt

Rosemount Aerospace, Inc.,
Eagan, MN 55121

Improved Method for Flame Detection in Combustion Turbines

A fast response chemiluminescent flame detection approach is presented along with field test results from a fiber optic based flame detector device. Chemiluminescence, the light given off by molecules formed in their excited states, has long been recognized as a diagnostics method for use in combustion. The recent advent of higher quality optical fibers with improved transmission properties in the UV, as well as UV optical detectors, has made the use of chemiluminescence for gas turbine diagnostics and monitoring practical. Advances in combustor designs on new low-emissions machines as well as reliability issues with some existing machines are creating the need for improved flame dynamics measurements as well as improvements in reliability for existing measurements such as combustor flame detection. This paper discusses the technology, principle of operation, and detectors that operate on the chemiluminescence principle.

Introduction

There is an increasing need for accurate flame detection in both the annular and multiple combustor configurations of stationary gas turbines. Combustor flame detection is necessary to prevent catastrophic failure of the gas turbine by assuring that all of the multiple combustor flames are lit when activated and remain lit throughout the operation of the gas turbine.

New demands presently being imposed on combustion devices to meet increasingly stringent air pollution standards require tighter control of the parameters at which combustors operate. While emissions levels, especially of nitrogen oxides (NO_x) and unburned hydrocarbons, continue to be limited, the same or better power and performance are expected from combustors. These requirements have resulted in the development of "Dry, Low NO_x" gas turbine combustors, which operate near the lean limit. This operation results in increased chances for flashback or blowout. In order to monitor flame stability and other parameters, the need for a real-time combustion diagnostics system capable of determining light-off or blow-off of flames with minimal delay and in specific locations within the combustor has developed.

Currently, the most commonly used flame detection sensor for gas turbine combustors is the Geiger-Mueller Phototube. Each tube contains a gas that is easily ionized. When ultraviolet radiation in the 180 to 260 nanometer (nm) range from the combustor flame impinges on the gas in the tube, a current is produced. The current charges a capacitor to its operating voltage, causing it to discharge. The discharge frequency is monitored and analyzed. A frequency greater than a pre-established point is considered a stable flame signal. The response time of the Geiger-Mueller phototube, including signal processing, is about 100 to 200 milliseconds (ms) (Walsh, 1984). For modern gas turbines this is a relatively slow response time.

An alternative flame detector, which uses the chemiluminescent signals from the combustor flame and detects states of burner ignition, blowoff, and instability, is described in this paper. Such a detector is capable of providing faster, more reliable and, if necessary, localized flame detection for a variety of gas turbines.

Chemiluminescence is the light released by excited molecules when the excited electron drops down to its equilibrium ground state. The phenomenon is induced by combustion and the magnitude of the signals is on a much larger scale than that of thermal emissions. The strongest chemiluminescent signals in a turbine engine combustor are generated by the return of the excited state free radicals, CH*, OH*, C_2^*, CN*, and NH* to their ground states. These radicals exhibit strong signals and are commonly found because the resonance transition from the ground state to the lowest excited state requires relatively low energy. This energy level is available in the limited temperature of flames effectively to excite these transitions and create bands in the visible and near-ultraviolet wavelengths.

Chemiluminescence has been used before to study flame characteristics. Schott (1960) used the technique to study OH concentration maxima in a hydrogen-oxygen reaction in 1960. Lyon and Kydd (1961) studied C_2, CH, and OH absorption a a function of time in acetylene flames by observing chemiluminescent signals. More recently in the 1980s, Beyler (1981)

[1]Current address: Hughes Associates, Inc., Columbia, MD.
[2]Current address: NIST, Gaithersburg, MD.
[3]Current address: U.S. Horizon Inc., Grand Rapids, MI.

Contributed by the International Gas Turbine Institute and presented at ASME Cogen Turbo Power '94, Portland, Oregon, October 25–27, 1994. Manuscript received by the International Gas Turbine Institute July 23, 1994. Associate Technical Editor: E. M. Greitzer.

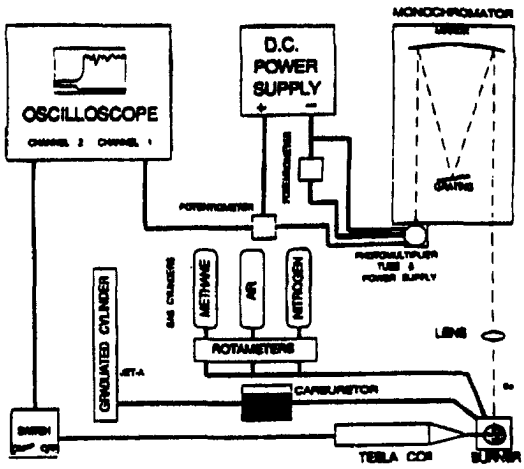

Fig. 1 Schematic diagram of light-off experimental setup, original configuration

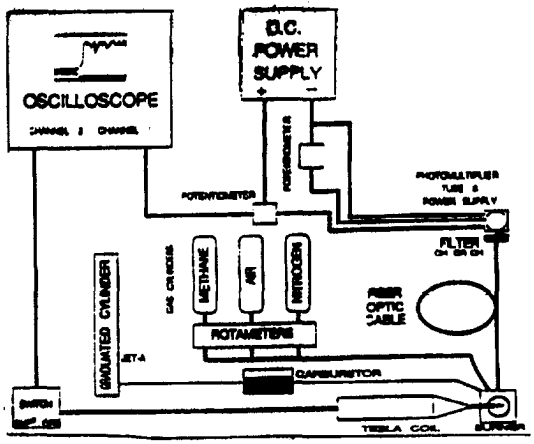

Fig. 2 Schematic diagram of light-off experimental setup, final configuration

used chemiluminescent measurements of OH, CH, and CO_2 to examine flame structure in a premixed swirl-stabilized combustor.

Experiments aimed at developing a fast response light-off detector based on chemiluminescence are described below. Included are the determination of the best chemiluminescence signals for flame detection, determination of response time, development of a simple fiber optic-based sensor, and results of field tests.

Experimental Apparatus/Procedure

Two different experimental setups were used for the laboratory tests in this study. Both systems consisted of the same basic apparatus: a burner, an optical system to detect the light signals, and a data acquisition system.

A schematic of the apparatus used for the initial flame detector tests is shown in Fig. 1. For this setup, the flame image was projected through a fused silica lens (38 mm diameter, 150 mm focal length) onto the entrance slit of a monochromator. The monochromator used was a 0.5 m scanning monochromator (Jarrel-Ash Model 82-020) with a grating of 1180 lines/mm capable of scanning at speeds from 0.2 to 50 nm/min. The monochromator resolution was better than 0.1 nm. In order to capture the most light and achieve the greatest signal, the entrance slit was adjusted to its maxima of 2 mm wide and 15 mm high.

The second set of ignition experiments used fiber optics and filters in place of the lens and monochromator (Fig. 2). The two band pass interference filters used for transmitting only the light surrounding the OH and CH bands were Oriel #53375 and #53815. The transmittance of these filters peaks is at 308 nm and 430 nm, respectively. The fiber optic cable used was Oriel #77562 with a 3 ft (91.4 cm) long, 1.6 mm diameter bundle of 200 fibers of 200 μm diameter each. The fibers could transmit wavelengths of light from 280 nm to 2200 nm. Each beam probe (Oriel #77644) had a fused silica lens with a 19 mm focal length. An additional set of experiments were run where the Photo Multiplier Tube (PMT) was replaced with a photo diode to simplify the detection system further.

The photomultiplier tube was an RCA model #1P28B. It featured a nine-stage electron cascade and a side window. The PMT was sensitive to light ranging from 200 nm to 660 nm, and its response time was 1.8 ns. A high-voltage power supply, RCA model PF 1042, was necessary to operate the PMT. The PMT power supply required an input voltage of 13.5 volts DC. A potentiometer was used to control the PMT power supply output voltage. The potentiometer was set at a resistance of 340 Ω which generated approximately 1000 volts as input to the PMT.

Gaseous fuel was burned in a standard half-inch methane Bunsen burner. A laminar premixed methane/air flame was investigated. Flow rates were controlled using calibrated Matheson rotameters in the 602 to 604 tube sizes.

The liquid fuel investigated was Jet-A aircraft fuel. The spray flame nozzle used to burn liquid fuel was a Siphon Type SNA air atomizer (Delavan P/N Nozzle 30609-2 and adaptor P/N 17147). This nozzle provided a vertical solid cone of finely atomized liquid fuel spray. A graduated cylinder was used as a reservoir to enable fuel consumption rates to be calculated. The graduated cylinder fed an automobile carburetor, which maintained the active lift height and, therefore, the fuel supply pressure of the nozzle constant. Compressed air or nitrogen at 6 psig was used as the atomizing gas.

An ignition system was required for the light-off and intermittent ignition tests. It consisted of a Tesla coil (Black & Decker #10) with a nichrome wire attached to the tip to transfer the high voltage to the burner. Nichrome was selected due to its durability at high temperatures. The system was operated with a switch that simultaneously supplied power to the Tesla coil and supplied a -1.5 volt DC signal to channel 2 of the oscilloscope. This signal would trigger channel 1 to start recording. Turning off the switch returned both voltages to zero. For intermittent flame tests, the Tesla coil was kept on and the triggering was performed manually.

The size of the flame image that was projected onto the front of the detector, i.e., the entrance slit of the monochromator, was controlled by three variables: (1) the focal length of the lens, (2) the distance between the lens and the object (flame), and (3) the distance between the lens and the image projection location (the entrance slit of the monochromator). By varying these parameters, different flame image magnifications were investigated.

Experimental Procedure

Light-Off Ignition Test. A number of light-off ignition tests were performed. In the gaseous fuel test, methane flowed through the Bunsen burner unignited until the tesla coil was activated. The nichrome wire of the tesla coil was positioned 3 mm above the top of the burner on the edge of the gas stream. As the tesla coil was turned on, the oscilloscope was triggered on Channel 1 to start recording the waveforms. With the high voltage being applied to the fuel by the tesla coil, the methane ignited and the PMT's transient response was recorded on Channel 2. Bunsen burner tests were run at a magnification of 0.67, flow rate of 12.8 cc/s,

methane pressure of 40 psig, and an oscilloscope sampling speed of 10 μs per point.

In the liquid fuel test, atomized fuel (Jet-A) flowed through the nozzle unignited until the tesla coil was activated. Nozzle tests were performed at a magnification of 1.0, atomizing gas flow rate of 115 cc/s, and pressure of 6 psig. To provide a constant pressure, a lift height of 18.3 cm was used. The oscilloscope sampling speed was 10 μs per point.

Intermittent Light-Off Ignition Test. A number of intermittent light-off ignition tests were performed. In the gaseous fuel test, the methane flow rate was increased to 0.067 L/s. This caused the velocity of the fuel to become higher than the local turbulent flame speed, which resulted in the flame blowing off. When the tesla coil was turned on, the high voltage caused the flame to ignite only intermittently.

In the liquid fuel test, the atomizing gas flow rate was decreased to 100 cc/s, which prevented the fuel from becoming completely atomized or entrained. In addition, the nichrome wire of the tesla coil was positioned so the high voltage was initially applied to the partially atomized mixture further downstream than in the light-off ignition test. Therefore, the flame did not always ignite, and if it did ignite, the flame was not sustained. With the high voltage being applied by the tesla coil, the fuel sporadically ignited, and the PMT's transient response was recorded on Channel 2.

Experimental Results

In order to develop a sensor based upon a chemiluminescent signal of combustion, the first step was to determine what signals were available in a steady flame, and what chemical radicals corresponded to those signals. The quantity, proportion, and wavelength corresponding to each species were needed in order to determine which one would provide the fastest, strongest, and most reliable signal for light-off. Initial tests, burning methane, were performed with a monochromator for wavelength selection and a photomultiplier tube for light detection. Full spectra scans were run from 280 nm to 610 nm to identify the possible signatures of flame presence (see Fig. 1). The chemiluminescent signals of interest were determined to be produced by the OH and CH radicals in the flame.

The main process by which OH* is formed is the reaction:

$$CH + O_2 = CO_2 + OH^* \quad (1)$$

The main process by which CH* is formed is the reaction:

$$C_2 + OH = CO + CH^* \quad (2)$$

Some CH* may also be formed by the reaction:

$$CH + OH + H = CH^* + H_2O \quad (3)$$

The asterisks imply that the radicals are in their excited state.

Light-Off Ignition Test Results. Many aspects of the light-off ignition tests were similar for all three fuels tested. OH and CH concentrations, represented as voltages, were recorded versus time. In the figures, the bottom curve indicated power being supplied to the tesla coil. The top curves were the transient responses of the OH or CH radicals. The figures also show that the tesla coil was not needed to maintain each flame, i.e., when the tesla coil was turned off the flames continued to burn. For both fuels, the OH and CH light-off ignition test results agreed with the visual observation of the fuel igniting and then burning in a steady-state mode.

Methane Test Results. Figure 4 shows the results of a typical light-off ignition test while burning a premixed methane/air fuel and recording the transient history of the

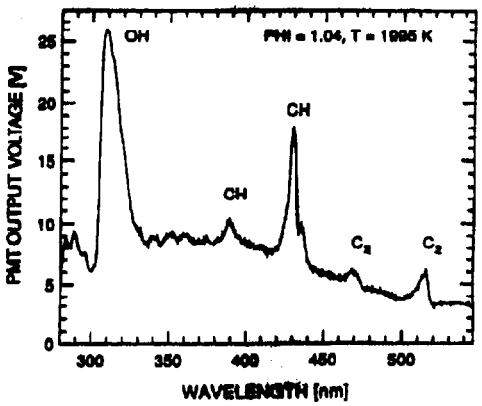

Fig. 3 Methane and air flame spectra scan

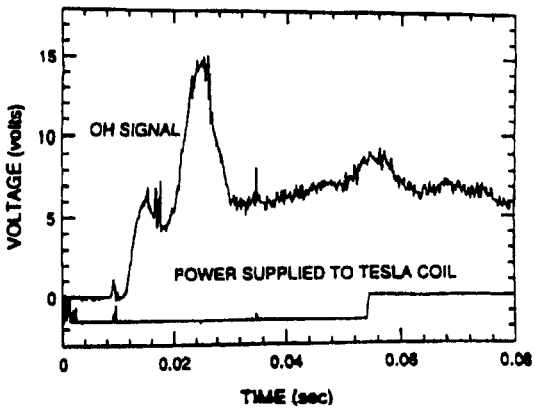

Fig. 4 OH measurements in a methane-fueled light-off ignition test

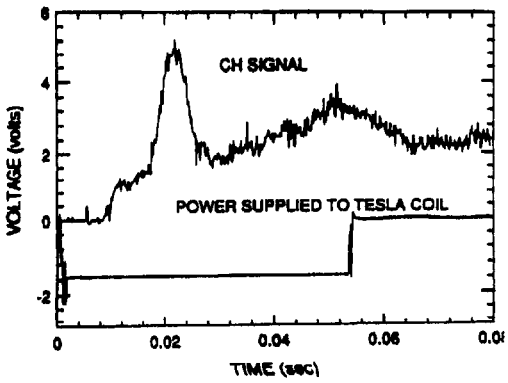

Fig. 5 CH measurements in a methane-fueled light-off ignition test

OH radical. The presence of OH, indicative of the flame, is initially detected at about 12 ms. The large presence of OH radicals at about 25 ms is due to the large volume of gas that is suddenly ignited. The tesla coil is turned off at about 54 ms.

Figure 5 shows the results for the same test procedure, but with the CH concentration being recorded. The presence of CH, indicative of the flame, is initially detected at about 10 ms. The steady-state level of CH radicals occurs at about 28 ms. As before, the large volume of gas that suddenly ignites produces a strong CH signal at about 25 ms. The tesla coil is turned off at about 54 ms. In agreement with the full methane scan, Figs. 4 and 5 show that the OH signal is significantly stronger than the CH signal.

Jet-A Test Results. Jet-A, an aircraft fuel containing complex hydrocarbons, burned with a very bright yellow flame

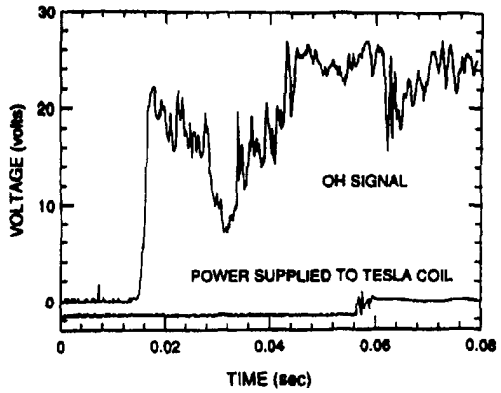

Fig. 6 OH measurements in a Jet-A-fueled light-off ignition test

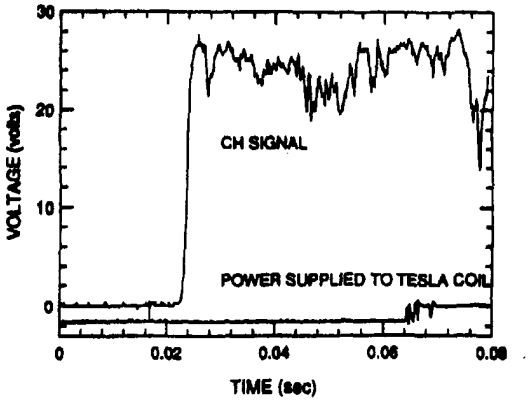

Fig. 7 CH measurements in a Jet-A-fueled light-off ignition test

that lit up the darkened room. The coloring was due to a more sooty flame—the complex hydrocarbons did not burn completely, but left residual carbon particles (soot) that were heated to incandescence. The Jet-A flame structure had sharp tongues and little smoothness. It also created much acoustic noise.

Figure 6 shows the OH signal history for a Jet-A light-off test performed on the initial monochromator setup. The flame continued to burn after the spark was shut off, showing the flame's stability. This test also had turbulent signal fluctuations over half of the steady-state average in amplitude.

Figure 7 shows the corresponding results of a test recording the CH signal history of a Jet-A flame. The amplitude of the signal was slightly higher, and the signal fluctuations only reached 50 percent of the steady-state average once. The OH signal results in Fig. 8 were recorded from a Jet-A flame with the fiber optic probe setup. The overall signal strength was slightly stronger than that in the original experiment due to imaging effects, but the fluctuations are half the magnitude. Similar results from the CH peak during Jet-A light-off are shown in Fig. 9. The CH signal was nearly 10 V stronger than the OH signal and the fluctuations are almost negligible.

Intermittent Ignition Test Results. Many aspects of the intermittent flame light-off ignition tests were similar for both flames tested. OH and CH concentrations, represented as voltages, were recorded versus time. In the figures, the bottom curve indicated power being supplied to the tesla coil. The top curves were the transient responses of the OH and CH radicals. For both fuels, the OH and CH light-off ignition test results agreed with the visual observation of a brief initial flash of a flame that is not sustained.

Methane Test Results. Figure 10 shows the results of a typical intermittent light-off ignition test using the monochromator setup while burning a premixed methane/air fuel. The presence of OH, indicative of the flame, is initially detected at about 110 ms. The tesla coil is turned off at about 180 ms, the flame continues to burn briefly, but then extinguishes at 220 ms as it cannot sustain itself.

In Fig. 11 the Bunsen burner intermittent light-off ignition test is also performed with the monochromator set on the CH head (430 nm). The presence of CH, indicative of the flame, is initially detected at about 100 ms. The flame burns briefly and then is extinguished at about 240 ms even though

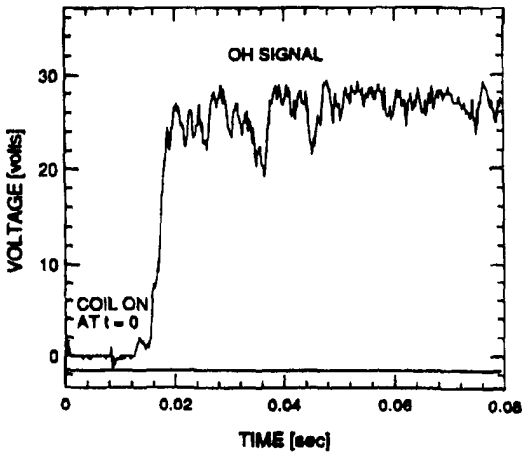

Fig. 8 OH measurements in a Jet-A-fueled light-off ignition test, final configuration

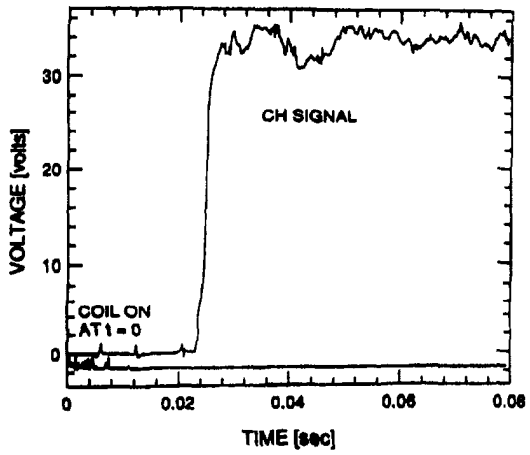

Fig. 9 CH measurements in a Jet-A-fueled light-off ignition test, final configuration

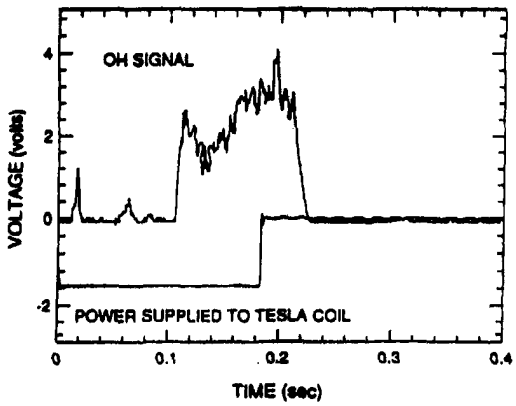

Fig. 10 OH measurements in a methane-fueled intermittent light-off ignition test

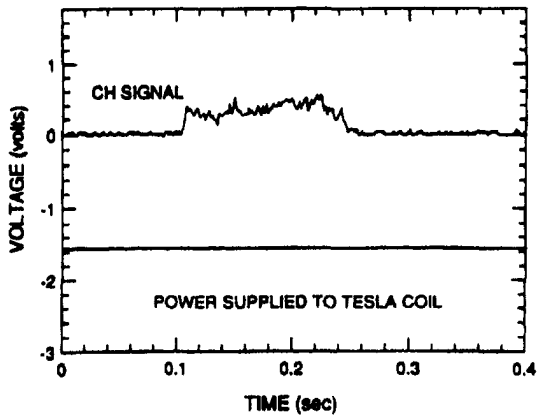

Fig. 11 CH measurements in a methane-fueled intermittent light-off ignition test

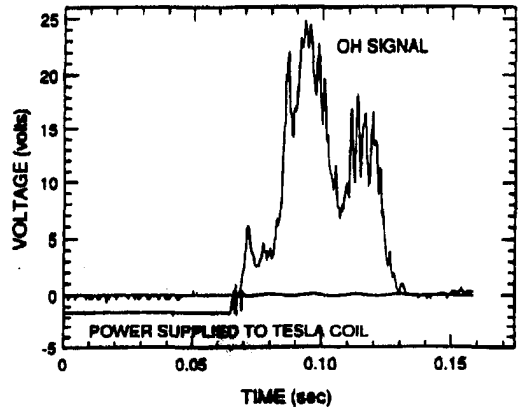

Fig. 12 OH measurements in a Jet-A-fueled intermittent light-off ignition test

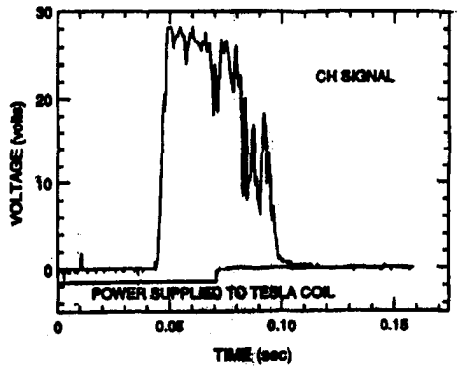

Fig. 13 CH measurements in a Jet-A-fueled intermittent light-off ignition test

the tesla coil is still applying a high voltage to the methane/air mixture.

These figures also show that the OH signal is considerably stronger than the CH signal. This is in agreement with the methane full scan test and the light-off ignition tests.

Jet-A Test Results. Figure 12 shows the transient OH signal of an unstable, intermittent Jet-A flame recorded from a test performed using the monochromator setup. The intermittent OH signal average was only about two-thirds as high as the steady-state average for the light-off ignition test. The unstable fluctuations were of similar amplitude to those of the stable flame, but were a much higher percentage of the unstable signal average than those of the stable flame compared to the stable average. The voltage history of Fig. 13

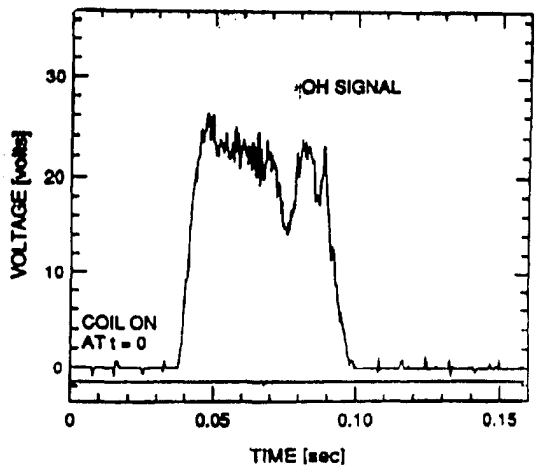

Fig. 14 OH measurements in a Jet-A-fueled intermittent ignition test, final configuration

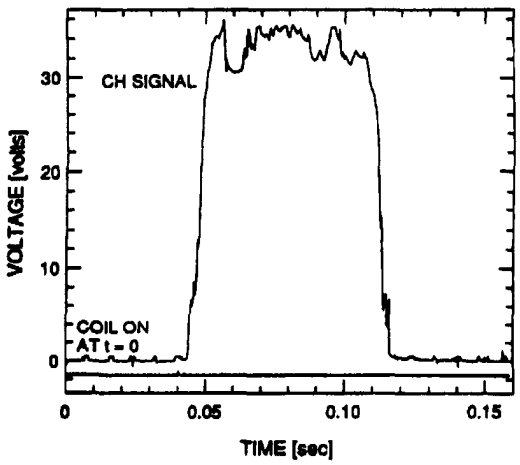

Fig. 15 CH measurements in a Jet-A-fueled intermittent ignition test, final configuration

shows the CH signal had large fluctuations of over 75 percent of the average. The unstable average was about two-thirds of the stable average. The amplitude of the voltage fluctuations was a little larger for the unstable tests.

Figure 14 shows the OH signal using the fiber optic probe setup for the intermittent Jet-A flame. The average OH voltage was a little less than the light-off average. The signal fluctuations reached up to about half of the average, which is slightly larger than those of the stable flame. The overall OH signal had fewer fluctuations than the one recorded with the monochromator. In Fig. 15, the CH signal of the intermittent flame recorded with the fiber optic probe setup quickly reached the stable flame average and had similar levels of fluctuation. When compared to the corresponding test with the original setup, this CH signal was much stronger and more consistent.

Magnification Test Results

Methane Results. Figure 16 shows the OH and CH radical concentration plotted as the PMT output voltage versus the Z position across the base of a flame. This figure was for a 30 mm premixed methane and air flame of magnification 2.0. This magnification means the size of the flame imaged onto the entrance slit of the monochromator was twice the actual flame size. Therefore, a 30 mm flame height was projected as 60 mm. The entrance slit was set at its maximum height of 15 mm. Therefore, only the bottom 25 percent of the flame image was allowed into the monochromator through the

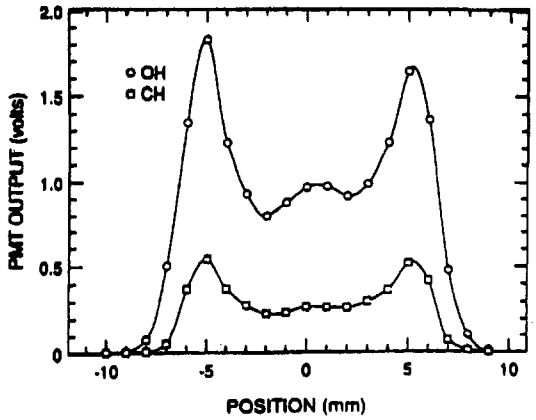

Fig. 16 Radical measurements for the methane flame, magnification = 2.0

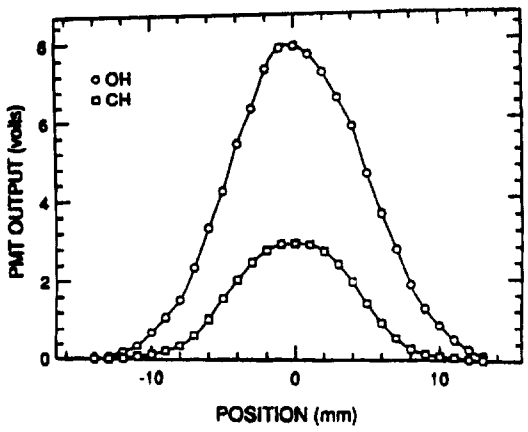

Fig. 17 Radical measurements for the methane flame, magnification = 0.33

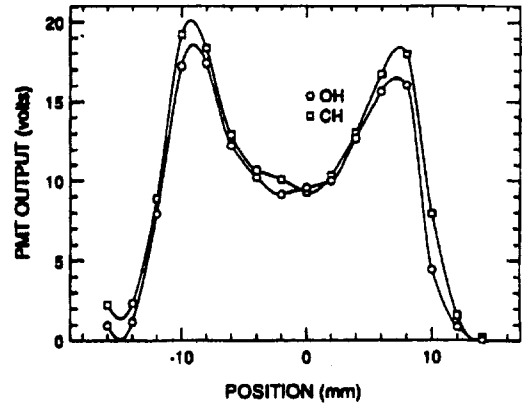

Fig. 18 Radical measurements for the air atomized Jet-A, magnification = 2.0

entrance slit. The OH signal intensity was approximately 3.5 times the CH signal intensity.

Additional tests were conducted at magnifications of 1.5, 1.0, 0.66, and 0.33 (Fig. 17). The OH and CH intensities remained relatively similar, but as the magnification was reduced the two outside peaks merged together, eliminating the center trough.

Jet-A Results. Three magnifications were investigated using the air-atomized Jet-A fuel. In the methane experiment the minimum voltage was obtained for the 2.0 magnification. This was also the case in the Jet-A tests (Fig. 18). The 0.33 magnification, seen in Fig. 19, produced the highest voltage.

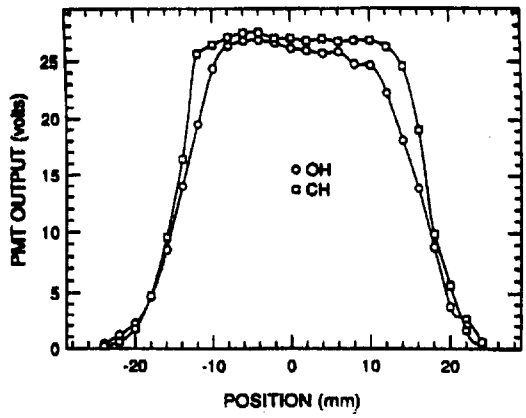

Fig. 19 Radical measurements for the air atomized Jet-A, magnification = 0.33

The merging of the two outside peaks again occurred at lower magnifications.

In all three Jet-A magnification tests the CH signal intensity was slightly higher than the OH signal intensity. This is in agreement with the full spectral scan test, the light-off ignition tests, and the intermittent light-off ignition tests.

Discussion

Determination of Rise Times. The purpose of this work was to develop a fast response light-off detector for flame sensing. It was assumed that the initial combustion reactions that form OH and CH radicals occur on the time scale of a few hundred microseconds to a few milliseconds. Therefore, by monitoring the chemiluminescent emissions from these excited species, light-off and blowout of a flame could be detected in a matter of milliseconds.

To calculate a rise time, a reference voltage is needed. For the liquid fuel tests this value was calculated by averaging the steady-state values from the light-off ignition tests. Once the voltages became nonzero (and stayed nonzero) all voltages after that time were used to calculate the average voltage. Compared to the light-off ignition test, a steady-state OH or CH level is never obtained in the intermittent light-off ignition tests. This confirms that a steady-state level of OH or CH radical is a signature of a stable flame.

Rise times for the light-off ignition tests were calculated by determining how long it took for the PMT voltage to exceed certain percentages (10, 50, 90, and 100 percent) of the calculated average value.

It is obvious from the figures that a 100 or 90 percent level would not be ideal, due to the turbulent nature of the flames. Standard deviations were calculated to examine these turbulent effects. The standard deviations of the tests were 20 to 33 percent of the average voltage level. By using 100 or 90 percent of the average voltage, a signal indicating "No Flame" could be sent to the controller, even though a flame is present. The 50 percent level would be a better choice, as it does a better job of compensating for the large fluctuations. It may be possible to use a smaller percentage to obtain a faster response, but this may not be necessary as the 50 percent level provides an adequate response time. The 10 percent level may be too low because of possible signal noise.

Table 1 compares the 100, 90, and 50 percent rise times obtained from the monochromator system to those of the fiber optic probe system. For practical purposes, 50 percent of the steady-state average was chosen as the threshold value to signify if a flame was on or off. The OH and CH 50 percent rise times for the initial tests ranged from 0.8 ms to 4.5 ms for individual tests with the averages for two signals of

Table 1 Comparison of rise times; rise time units are milliseconds

Configuration	JET-A OH		JET-A CH	
	Initial	Final	Initial	Final
Ave of 4 tests each				
100% rise time	2.75	4.42	4.38	5.14
Stand. dev.	1.33	1.81	2.24	0.28
Ave of 4 tests each				
90% rise time	2.63	4.01	4.03	2.97
Stand. dev	1.30	1.60	2.31	0.35
Ave of 4 tests each				
50% rise time	1.44	2.37	2.61	1.96
Stand. dev	0.48	1.21	1.10	0.59

Table 2 Comparison of voltage levels and fluctuations. The AVE column represents the average nonzero PMT output voltage of four separate tests. The S.D. AVE column represents the standard deviation of the average of the four tests. The S.D. column represents the standard deviation of all nonzero voltages from one ignition test.

SIGNAL	ORIGINAL CONFIGURATION			FINAL CONFIGURATION		
	AVE (V)	S.D. AVE	S.D.	AVE (V)	S.D. AVE	S.D.
JET-A OH	17.15	2.67	4.98	23.57	1.04	2.21
JET-A CH	23.2	0.23	8.00	32.50	0.28	1.30

1.44 to 2.61 ms, respectively. The 50 percent rise times for the tests using the fiber optic probe configuration averaged 2.37 and 1.96 ms. The use of the fiber optic probe system resulted in 90 and 100 percent rise times that were 1–2 ms greater than those found with the monochromator apparatus. This is still significantly less than the current technology time response, which is on the order of 100 ms.

The ignition tests were very repeatable. Each test showed similar characteristics to others of the same type. In general, OH and CH rise times were within standard deviations of each other.

Light-Off Ignition Tests. There were some important differences in the results from the fiber optic probe setup compared to the monochromator system. Table 2 contains some of the results by which the two methods may be compared. It lists the average voltages, standard deviations of the average voltages, and typical overall standard deviations for each type of test. The test-to-test variations were lower for the fiber optic probe system. The typical overall standard deviations show that the fiber optic probe system had a significantly diminished level of fluctuations as compared to the monochromator system. It would be much easier to set a threshold voltage level for ignition because the signal would not decrease to nearly "off" levels during the history of a stable flame. The flame signals for both CH and OH were much cleaner and provided a well-defined step input for light-off or pulse for an intermittent flame.

The fiber optic probe setup provided this signal quality for at least two reasons. The first is that the band pass interference filters allowed a wider range of wavelengths to reach the PMT than the monochromator did. The light from other vibrational and rotational transitions within a band was added to that of the peak wavelengths transition so the signal did not solely rely on one limited phenomenon within the band, but resulted from all of the variety of transitions possible within the main electronic transition.

The fact that a wider range of wavelengths input to the PMT provided greater signal consistency does not lead to the conclusion that a continued increase of the range of input wavelengths would further enhance the performance of the detector. The ultimate result of such a conclusion would be a detector sensitive to all ultraviolet radiation. The negative effect of such a detector would be the possibility of false signals arising from stray sources such as the ignition spark. The limitation of the range of light that could generate a flame ignition signal to one or two electronic transitions prevents such false detection. Since the chemiluminescence wavelengths are characteristic of combustion and are of a magnitude much greater than could be produced by another source, they are the best signals to rely upon for ignition detection.

The other source of signal clarity was the larger flame volume viewed by the fiber optic system than the lens system. The fiber optic system probe gathered light from approximately four times the projected area the lens did. The greater amount of flame activity viewed smoothed out the turbulence that would have been seen more locally.

Another difference with the fiber optic probe system was that the unstable flame signals reached the steady-state values of the stable flames. With the monochromator setup, the intermittent flame signal often remained below 50 percent of the stable, steady-state level. This clear signal of the flashes of an unstable flame would allow operators of a stationary gas turbine to observe in real time the unstable behavior of a combustor rather than just the decrease in discharge frequency of a Geiger-Mueller tube.

With the fiber optic probe system, the steady-state voltages for CH were higher than those recorded with the monochromator setup when compared to the relative strength of the OH voltages. This difference could be explained by considering the band pass interference filters and the fiber optic cable. The peak transmittances of the filters were approximately located at the peak spectral signals and the transmittance dropped-off to zero 20 nm on each side of the OH filter peak and 15 nm on each side of the peak of the CH filter.

Since the peak transmittance of the CH filter was 40 percent as compared to 20 percent for the OH filter, and because the wavelengths surrounding the peak were also the strongest signals from the flame the CH filter allowed a larger percentage of the flame's emitted signal to be detected than the OH filter. While the filters did not transmit the full intensity of the incoming light, light integrated over a range of wavelengths passed through. This made the fiber optic probe signals for CH much higher than the signals from the monochromator system, which received the full intensity of light in a very narrow wavelength range.

The fiber optic cable also had an effect on the relative signal strength of the OH and CH signals. The attenuation curve of the fiber optic has a negative slope in the range of interest. Therefore the OH signal was attenuated by a larger percentage than the CH signal.

Magnification and Position Effects. As expected, the output signal voltages were found to be sensitive to the flame image magnification and the position of the flame under observation. The maximum voltages were found to occur at the position which corresponded to the "sides" of the flame. This is because a greater volume of the annular flame was being scanned.

The smaller magnifications (0.33 and 0.67) were found to be broader than the larger magnifications (1.5 and 2.0). This means it took more Z positions to scan completely across the flame, because those changes in position (1 mm increments) had a smaller effect on moving the flame image at the monochromator entrance slit. For example, the Jet-A magni-

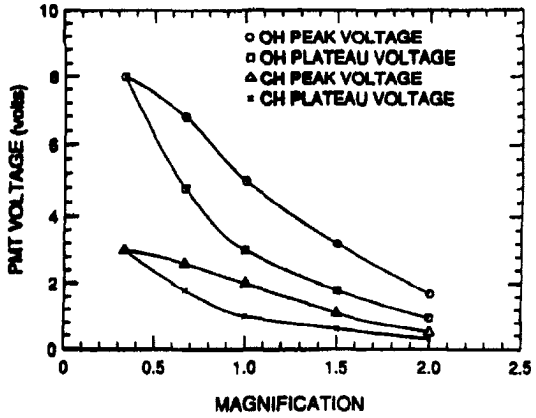

Fig. 20 PMT output voltage versus magnification

fication of 2.0 took 28 increments to completely scan across the flame, while the 0.33 magnification took 48 increments.

Figure 20 shows how the PMT voltages for the methane magnification tests varied with magnification. The peak voltages correspond to the average voltage at the two luminous cones. The plateau voltage is the average of the points between the peaks. As the magnifications decreased from 2.0, the two luminous cone peaks grew closer together until at the 0.33 magnification, they disappeared completely. This is because the flame image resolution has been reduced.

The figure shows that the 0.33 magnification, compared to the 2.0 magnification, produced voltages about four times greater for the OH peak voltage and about eight times greater for the OH plateau voltage. The CH peak and plateau voltages were about three times greater when comparing the two magnifications. The smaller magnifications have these greater PMT outputs because a greater amount of light is being imaged into the same input slit area. However, it is not believed that as the magnification is decreased the voltage will continue to increase indefinitely. Once the magnification is so small that the whole flame fits into the input slit, further flame image reductions will have little effect.

These results show the importance of observing the correct flame location and magnification to obtain the maximum signal possible. To obtain the maximum voltage possible, observations should be on the peak location of a small flame image magnification.

Effect of Hydrogen to Carbon (H/C) Ratio. The results of the methane full spectral scan showed that the CH signal was about 40 percent the intensity of the OH signal intensity. This led to an initial belief that the OH radical should be used as the signal to detect light-off as it was the stronger signal. However, it should be noted that the hydrogen to carbon ratio (H/C) of methane is 4:1. As liquid fuels are more realistic to those used in jet engines, they were investigated next. The results of the Jet-A full spectral scan showed that the CH signal had increased to about 13 percent stronger than the intensity of the OH signal. The H/C ratio of Jet-A is about 1.8:1.

It appeared that as the H/C ratio of the fuel tested was decreased, the CH signal intensity (as a percentage of the OH signal intensity) increased. Therefore, for liquid fuels used in aircraft turbine engines, the CH radical may be just as valuable, if not more so, than the OH radical in detecting light-off.

After the next two tests were performed (light-off ignition, intermittent light-off ignition and magnification), the same pattern was evident. Burning methane produced average CH signals that were 36 percent of the intensity of the OH signals. Burning Jet-A produced average CH signals that were 110 percent the intensity of the OH signals.

Further tests must be performed to determine which signal, or both, should be monitored for light-off detection. However, OH has the advantage over CH in that its radiation is emitted from deeper in the UV spectrum where background radiation will not be a problem.

Field Testing

The flame detection approach explored in this paper was next applied to develop a fiber optic based flame detection sensor. The sensor utilized a nonintrusive probe that viewed the combustion zone of a ground turbine engine. Attached to the probe was a ground turbine engine. Attached to the probe was a high-temperature fiber optic cable that transmitted the chemiluminescent combustion signals to a remote electronics box. The remoteness of the electronics box eliminated the need for special cooling of the electronics that has been required in many of the Geiger-Mueller tube flame detection installations. The electronics box then transmitted the "flame" and "no flame" signals to the engine control system and/or other monitoring devices, such as strip chart recorders.

These flame detectors were tested in two key situations. First, they were tested on ground turbine engines under development. These engines utilized unique combustion designs that required detection and monitoring of flame in multiple combustion zones within the combustor. Second, they were evaluated on a long-term test on an existing ground turbine engine at Southern California Edison's CoolWater Station in Daggett, CA.

The development engine testing provided the flame detectors with multiple scenarios. Individual flame detectors were used to monitor individual combustion zones within a combustor. Therefore, they were required to distinguish among the possible scenarios of combustion in the different zones. In addition, both oil and natural gas fuels were monitored. After minor adjustments were made to correct for various background signals related to different mounting locations of the probe, the flame detectors successfully monitored the combustion process as it was transitioned through each of the scenarios. In particular, the detectors were able successfully to monitor the use and transition of oil combustion, which the existing sensors could not do. This testing initially took place on test stands at GE Power Generation in Schenectady, NY. After modifications the testing was transitioned to field tests in Alaska, New Jersey, Massachusetts, and Inchon, Korea with excellent results.

The long-term test assisted in determining what modifications to the initial design would be required to ensure ease of use and long-term reliability during exposure to the extreme environment of a ground turbine engine installation. This test was started in July of 1993 and is ongoing. It is being conducted on a Westinghouse 501B peaking engine at Southern California Edison's CoolWater Station. Two of the four existing flame detectors were replaced with fiber optic based chemiluminscent flame detectors and have accumulated over 3500 hours of operating time and over 120 engine starts.

Attenuation of the fiber optic cable in the wavelengths of interest created a desire to minimize its length in order to maximize the chemiluminescent signal received at the detector. A determination of the most appropriate location for minimizing the cable length while also minimizing the temperature exposure of the electronics box had to be made. The ideal location to mount the electronics box is near the ground in a cool area of the engine hush house or outside.

Field test results to date have shown that the signal from the new flame detectors is faster in response to flame while providing a steadier reliable signal than the existing sensors. The sensors also have the ability to monitor flame stability, which existing Geiger-Mueller phototubes are incapable of doing. An additional key advantage of these devices is that

cooling, which is required for many existing Geiger-Mueller phototube installations, is not necessary.

Conclusions

An improved method for detection of light-off in gaseous and liquid spray flames has been developed. The method uses chemiluminescent signals from OH and CH radicals to indicate the presence of a flame. The method was successfully tested on methane and Jet-A in the laboratory and has been tested on combustion turbines in both natural gas and fuel oil. Light-off ignition tests and intermittent light-off tests showed that both signals (OH and CH) were good indicators of flame presence, showing a response time of less than 2 ms.

Signal intensity was found to be sensitive to flame image magnification and flame position under observation. Small magnifications and the luminous cone peaks provided the highest output signal voltages.

The strength of the CH signal (as a percentage of the OH signal) was found to be a function of the H/C ratio of the fuel tested. As the H/C ratio of the fuel decreased, the CH signal intensity increased.

Results of laboratory and field tests show that a flame detector based on chemiluminescence is ready for application to turbine engine combustors.

Acknowledgments

The authors would like to thank GE Power Generation for their willingness to support this effort by providing combustor test time both on test stands and in the field at various engine installations. This test time was invaluable for the research and ongoing development of this technology.

The authors would also like to thank Southern California Edison for the support they provided out of their Rosemead research group and, in particular, for the support that has been provided by the staff at CoolWater. The lessons learned through their assistance have been critical to optimizing this research and development effort.

References

Beyler, C. L., 1981, "Flame Structure and Stabilization in Premixed Swirl-Stabilized Combustion," M.S. Thesis, Cornell University, Ithaca, NY.

Lyon, R. K., and Kydd, P. H., 1961, *Journal of Chemical Physics*, Vol. 34, p. 1069.

Schott, G. L., 1960, *Journal of Chemical Physics*, Vol. 32, p. 710.

Walsh, E. J., 1984, "Gas Turbine Multiple-Combustion System," GER-3435A, Gas Turbine Division, General Electric Company, Schenectady, NY.

A Scanning Radiation Thermometry Technique for Determining Temperature Distribution in Gas Turbines

M. De Lucia

G. Masotti
Research Fellow.

Department of Energy Engineering,
Università di Firenze,
Florence, Italy

A scanning radiation thermometry technique for determining temperature distributions in gas turbines is presented. The system, an enhancement of an earlier work, can be used by operators even without special training, since the temperature distribution is measured and corrected in terms of the error due to the reflected radiation only on the basis of the turbine's known geometry and the physical properties of the materials. In the proposed model, the surface-exitent radiances are directly acquired via 360-deg scans. Experimental testing was performed on a static turbine-blading model. Since the angle factors emerged as a notable influence on the accuracy of the model, two angle factor calculation methods, selected for suitability from a literature survey, are exhaustively investigated, and their selection criteria defined.

Introduction

In gas turbines, temperature distribution must be known throughout the life of the machine if performance is to be properly monitored. Yet, owing to the inherent difficulties and expense involved in determining it, this information is not always readily available, even to machine operators. With noncontact radiation thermometers, temperatures can be measured in the harshest environments, especially when moving components are involved. In an earlier paper, De Lucia and Lanfranchi (1994) proposed a radiation thermometry model based on the use of theoretical temperature distributions to correct target temperature. This work presents an enhanced version of the earlier system that enables the determination of temperature distribution on the basis of multiple radiation thermometer measurements.

In a radiation thermometry system, the radiation emitted by each turbine component is measured and its temperature determined with the aid of calculation assumptions (Beynon, 1981, 1982; Scotto and Eismeier, 1980). Provided there is optical access, temperatures may be rapidly and accurately measured at any point or profile of the rotating component (Douglas, 1980; Kirby et al., 1986). However, in nonisothermal systems such as gas turbine cooled stages, the total sensed (exitent) radiation comprises two major components (DeWitt and Incropera, 1988):

1 Radiation produced as the result of the target surface temperature (emittent radiation)
2 Radiation reflected due to interreflection between the target surface and its surroundings.

Consequently, we must first estimate and subtract from the exitent radiations (L_{ex}) the reflected radiation (L_r), which is related to the surface temperature distribution and geometry, before proceeding to invert Planck's law. Hence, since the radiation thermometer reads the global target radiation, the reflected component represents a bothersome source of error. In the earlier model, the temperature distribution and geometry are separate, thereby allowing correction of the measured value with good approximation. However, the earlier model requires input of the theoretical temperature distribution, which, in many cases, is unknown to those actually carrying out the measurements. As a result, despite its simplicity and ease of use, it is not always suitably accurate, especially when the machine behavior deviates from theoretical predictions. This limitation has been overcome in the present model, which has the advantage of not requiring prior knowledge of the theoretical temperature distribution to determine gas turbine temperatures accurately.

Description of the Model

Like its predecessor, the present model considers surface-exitent thermal radiations in calculating the temperature distribution, with the difference that the radiations are measured by a scanning radiation thermometry technique solely on the basis of the known geometry and the physical properties of the materials. In the scanning radiation thermometry

Contributed by the International Gas Turbine Institute and presented at the 39th International Gas Turbine and Aeroengine Congress and Exposition, The Hague, The Netherlands, June 13–16, 1994. Manuscript received by the International Gas Turbine Institute February 4, 1994. Paper No. 94-GT-39. Associate Technical Editor: E. M. Greitzer.

technique, all the radiations exiting the surfaces that can be optically accessed by a 360-deg radiation thermometer scan are acquired and used in calculating the radiations exchanged by the surfaces through their angle factors.

The following assumptions were made:

- Radiative heat transfer was assumed at steady-state conditions.
- All radiances, powers, energies, and emissivities were assumed spectral, allowing evaluation at the radiant thermometer's constant wavelength.
- The surfaces were assumed isothermal and gray, that is, as emitting and reflecting diffusely.
- The considered surfaces were assumed to form an insulated system, that is, without radiative heat transfer to the environment.

The radiation thermometer measures the target exitent radiance L_{ex}. (In our case, the system supplies a signal related to temperature in converting to radiance with Planck's law.) In our description of the model, radiance is used instead of radiant power for convenience, since they are simply related as $P_{ex_i} = A_i \cdot L_{ex_i}$. However, the measured radiance includes the term L_{em}, due to target temperature, and the term L_r, from the reflection on the target surface of the radiances exitent from other bodies, since we are dealing with nonideal bodies. This yields

$$L_{ex_i} = L_{em_i} + L_{r_i} = L_{b_i} \cdot \epsilon_{m_i} + L_{r_i} \tag{1}$$

The earlier model uses an $(n \times n)$ system, with n representing the number of modeling surfaces, to calculate the L_{ex_i} exiting the surfaces, and thus assuming a given temperature distribution, L_b. By contrast, the proposed model envisages direct measurement of the surface-exitent radiances with a 360-deg scan. Having determined the L_{ex_i} of all the surfaces, except top and bottom (whose calculation assumptions will be detailed in the section dealing with the angle factor calculation), we can compute the corresponding reflected radiances for each surface, since

$$L_{r_i} = \frac{(1 - \epsilon_{m_i})}{A_i} \cdot \sum_{J=1}^{n} A_j L_{ex_j} F_{ij} \tag{2}$$

where F_{ij} is the ratio between the power ($P_{ex_{ij}}$) exitent from the jth surface reaching the ith surface and the total power (P_{ex_i}) exitent from the ith surface

$$F_{ij} = \frac{P_{ex_{ij}}}{P_{ex_i}} \tag{3}$$

Combining Eqs. (1) and (2), we get

$$L_{b_i} = \frac{1}{\epsilon_{m_i}} \left[L_{ex_i} - \frac{(1 - \epsilon_{m_i})}{A_i} \cdot \sum_{J=1}^{n} A_j L_{ex_j} F_{ij} \right] \tag{4}$$

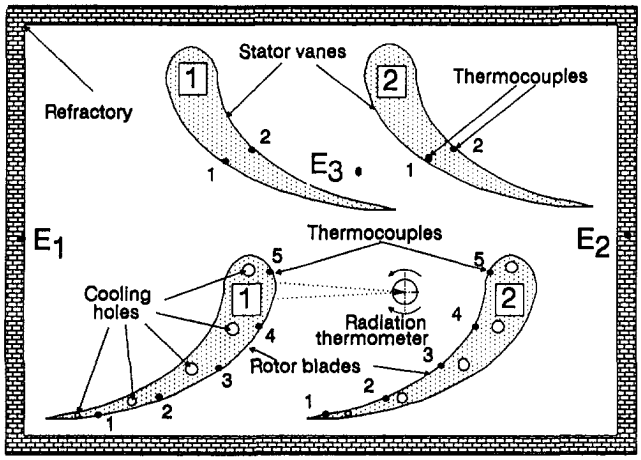

Fig. 1 Experimental setup

Thus, having determined the radiance of black body L_{b_i} we can obtain the classical form of Planck's law to determine T_i by finding the apparent value of the emissivity ϵ_{a_i} of the ith element of the surfaces considered. Applying the analytical definition (Ono, 1988)

$$\epsilon_{a_i} = \frac{L_{ex_i}}{L_{b_i}} \tag{5}$$

we obtain an inverted Planck's law

$$T_i = \frac{c_2}{\lambda \cdot \ln\left(1 + \dfrac{c_1 \epsilon_{a_i}}{\lambda^5 L_{ex_i}}\right)} \tag{6}$$

We can thus determine the correct temperature of all the isotherm surfaces used in modeling the geometry, taking into account the reflected radiation term, since electromagnetic radiations are always present in gas turbines: With heat flowing only from the higher to the lower-temperature body, the electromagnetic waves, in this case infrared, emitted through the body's heat radiation, reach all the other optically accessible bodies without being affected by their temperature. Therefore, having reached the real body surface, the electromagnetic radiations reflect only in relation to the material properties, i.e., wholly independently of body temperature. Evidently, all the radiation thermometer readings are diversely affected by this value, which, if disregarded, produces an incorrect temperature evaluation.

Experimental Model

The static model used in experimental testing is schematically illustrated in Fig. 1. Like the earlier version (De Lucia

Nomenclature

A = surface area, m^2
a = distance, m
c_1 = first radiation constant, $W\ \mu m^4 m^{-2}\ sr^{-1}$
c_2 = second radiation constant, $\mu m\ K$
F = angle factor
h = height, m
L = radiance, $W\ m^{-2}\ sr^{-1}$
l = length, m
n = number of surfaces per side (simplified geometry)
P = radiant power, W
r = distance between surfaces, m
s = width, m
T = temperature, K
x = spatial coordinate, m
α = angle between target and surface (Figs. 3 and 4)
γ = angle between perpendicular and y axis, rad
ϵ = emissivity
λ = wavelength, μm
φ = angular width, rad

Subscripts

a = apparent
b = black-body conditions
em = emittent
ex = exitent
i, j = ith and jth elements
m = material
r = reflected

and Lanfranchi, 1994), it is composed of two stator vanes and two rotor blades instrumented with K-type thermocouples (precision: 0.4–0.7 percent) simulating a 10 MW heavy-duty gas turbine. The model has been redesigned for displacement capabilities and with optimized cooling and radiation thermometer-positioning systems.

The blades and the vanes were of completely oxidized inconel with an emissivity of 0.83. The static model was lined in a refractory material with an emissivity of 0.3. We assumed that these values were constant in our working temperature range of 650–950°C. The silicon photodiode used in the radiation thermometer probe detects 1 μm wavelength radiances with a very narrow bandwidth to reduce negative effects that would have otherwise been produced.

The position of the radiation thermometer in our experimental setup, which is evidently impossible in an operating turbine, was selected solely to facilitate the construction of the experimental setup and to provide an optimum viewing angle (delimited by the perpendicular to the surface midpoints and the radiation thermometer viewing line) with respect to our area of interest (primary zone). In the operating turbine, however, the same optimum viewing angle can be attained from a different position. This is achieved by exploiting the motion of the moving blades when the relationship between the blade rotating and sampling frequencies is known, since, in gas turbine geometry, the radiation thermometer is far more sensitive to the viewing angle than the target surface distance.

The development of a more sophisticated experimental model requires the use of a larger number of complex devices. In the experimental setup, the radiation thermometer probe is housed inside a viewing tube (optional in standard applications where the sensor is preferably tilted at a preset angle; Kirby et al., 1986). At one end of the radiation thermometer viewing tube is a rhodium–platinum mirror with a 45-deg inclination that deviates the radiation by 90 deg. This provides a 360-deg scan by simple rotation of the viewing tube, while the rest of the system remains immobile.

However, in addition to representing an added expense, the mirror obviously introduces a potential source of additional noise in the measuring chain. To counter the effects of the mirror's high degradability index due to the turbine environment, which indicates reduced reflectivity, it is necessary to incorporate an effective cooling system. We selected nitrogen gas as a coolant and also to clean the mirror surface. In addition, the use of the mirror calls for special care in the angular calibration of the radiation thermometer (angular calibration being necessary in view of the fact that the measured signal is related to the angle at which the surface is viewed). It is thus possible to interpret the data measured during the 360-deg scan properly and evaluate the radiances coming from the surfaces at several different viewing angles. Lastly, a computerized radiation thermometer displacement system permits scanning via a law of motion that allows the data to be acquired and correlated to the relative geometric surface used in discretizing the system.

The experimental setup is wholly computerized. Among the required inputs are furnace temperature (in our experimental case) or operating conditions such as delivered power or reference temperature (in the case of operating machines). Decisions regarding whether or not to conduct update scans of the reciprocal radiances for calculating the target temperature are based on the changes in conditions indicated by the inputs. However, owing to the low sensitivity of the system (De Lucia and Lanfranchi, 1994), frequent updates are unnecessary. In addition, the higher the number of discretization surfaces, the lesser the system sensitivity to temperature variations.

Testing was carried out at steady-state condition at furnace temperatures ranging from 650°C to 950°C. The blade cooling loop relative pressures were varied between 0–2 bar, thereby creating a blade-furnace temperature difference ranging from 0°C to 200°C and blade-to-blade temperature difference ranging from 0°C to 100°C. The nitrogen flow in the pneumatic loop was regulated on the basis of indications from thermocouples positioned by the lens and the nitrogen exiting the viewing tube. A vacuum pump connected to a duct coaxial to the viewing tube was used to remove the incoming nitrogen, thereby preventing leakage of cold gas that could cause uncontrolled blading and system temperature fluctuations at steady-state condition.

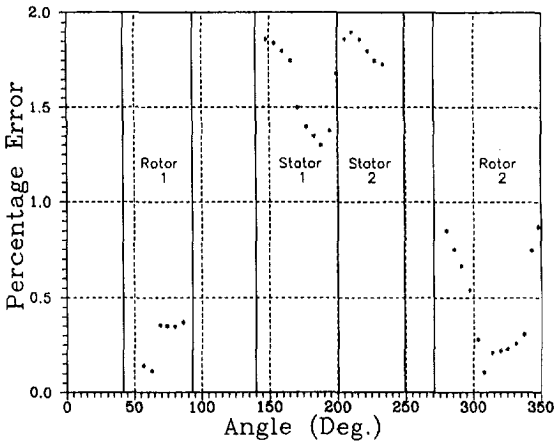

Fig. 2 Experimental results in terms of temperature error

In comparison to the earlier model, which only corrects target temperature, the enhanced model has the advantage of furnishing a global description of the temperature distribution over the scanning plane surfaces without necessitating solution of a linear equation system and without requiring information on the theoretical temperature distribution. In addition, by moving the radiation thermometer radially with respect to the machine or vertically as in the experimental model, we obtain a complete mapping of the hub-to-tip blading temperature.

Test Results

The curve in Fig. 2 represents the percentage difference between the model-processed temperature and the actual temperature measured by the thermocouples positioned as in Fig. 1. Test temperatures were 800°C for the furnace, 670°C for blade 1, 720°C for blade 2, and 780°C for the two stator vanes. The positioning system for the 360-deg scan acts on the radiation thermometer viewing tube with a step-by-step rotation of 4–5 deg gradients to provide a slight overlap between successive positions so that no surface radiance data are missed.

Since the errors for blades 1 and 2 are comparable to the thermocouple errors, we can infer that the model worked without error in the primary zone, which, in our case, was the rotor blades. Generally, the error is primarily a result of two factors: (1) the error in the angular calibration, which, however, is necessary to account for the steep surface-view line inclination (to facilitate use of the technique by operators without special training, the angular calibration has not been fully considered herein) and (2) the glare from the furnace's background refractory surface. Since the law of motion does not account for the change from the blade to the refractory surface, measurements on the steeply inclined blading edges are inevitably affected by radiations from the refractory surface.

The error is analogous for the points relative to the stator vanes, reaching almost 2 percent with the radiation thermometer positioned for maximum accuracy in the primary

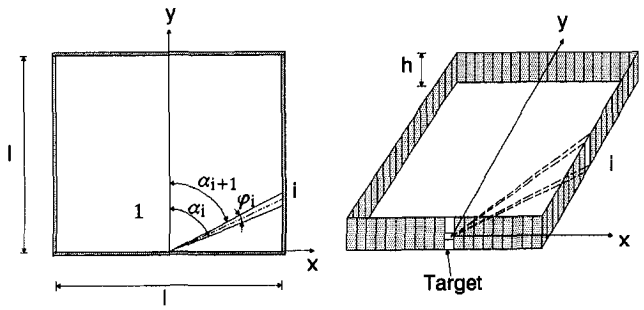

Fig. 3 Simplified geometry

measuring zone, in this case the rotor blades, to the disadvantage of the other surfaces. In other words, the vane surfaces view the radiation thermometer at a considerable angle, thereby mandating correct angular calibration. Unfortunately, the vanes being stationary, the position of the radiation thermometer must be optimized in relation to the investigation zone. As validated by the experimental results, system optimization is not normally necessary—however, when optimization is required, a high level of detailed information is necessary, which might be unavailable. However, the aim of this work was simply to validate the reliability of the model for use by operators without specific training. We wanted to avoid having to overly refine the hardware and/or management systems, since, having obtained satisfactory results, focusing on error reduction at this stage rather than during the application of the system to the actual turbine would have represented a considerable waste of effort.

The test results revealed an appreciable sensitivity of the method to the angle factors. As a result, we decided to investigate the parameters affecting the accuracy of the angle factor calculation.

Considerations Concerning the Angle Factors

The method is extremely sensitive to the angle factor calculation, with slight variations amplifying the temperature error due to the six- to ninefold difference in magnitude between the angle factor and L_{ex} in the reflected radiance calculation [Eq. (2)]. Hence, measuring accuracy is closely related to proper evaluation of the angle factors and thus to the system's geometric discretization. Having completed the discretization, we can then assign a given weight to the isothermal areas through the angle factors. Hence, even a tiny error at this stage can notably affect the final temperature calculation in relation to the surface area's absolute temperature during operation. To this end, we shall present some calculations for a simple geometry to highlight the parameters affecting accuracy and to what degree they do so.

The simplified geometry represented in Fig. 3 is composed of a closed box of fixed length l and variable height h. By varying the n number of surfaces used in modeling the sides, we can reproduce the typical decision situations presented to the operator when deciding how the gas turbine geometry should be discretized (Douglas, 1980).

Angle factor calculations are based on the general definition in Eq. (7) (Sparrow and Cess, 1978)

$$F_{ij} = \frac{1}{A_i}\int_{A_i}\int_{A_j} \frac{\cos \Phi_i \cos \Phi_j}{\pi r^2} dA_i dA_j \qquad (7)$$

The literature provides several integrated formulas for calculating angle factors for elementary known geometries with appropriate approximations (Bejan, 1993; De Lucia and Lanfranchi, 1994; Kreith, 1973; Sparrow and Cess, 1978). The two most promising solutions were examined: the model

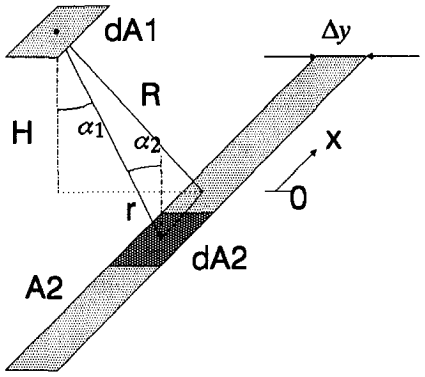

Fig. 4 Model A geometry

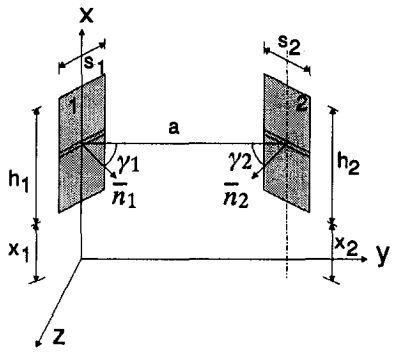

Fig. 5 Model B geometry

proposed by Bejan (1993) hereinafter designated model A, which was adapted and implemented to account for the finite dimensions and the top and bottom surfaces, and the model proposed by De Lucia and Lanfranchi (1994), hereinafter designated model B.

Referring to Figs. 3 and 4, Bejan's formula for two thin, facing-plane, isothermal surfaces integrated between $-h/2$ and $h/2$ is

$$F_{1,2} = \frac{1}{\pi}(\sin \alpha_{i+1} - \sin \alpha_i) \cdot \left[\tan^{-1}\left(\frac{h}{2r}\right) + 2 \cdot \frac{h \cdot r}{4r^2 + h^2}\right] \qquad (8)$$

By contrast, De Lucia and Lanfranchi's general formula referring to two planar surfaces positioned as in Fig. 5 is

$$F_{1,2} = \frac{s_1 s_2 \cos \gamma_1 \cos \gamma_2}{2\pi A a} \cdot \Bigg[(x_1 + h_1 - x_2) \cdot \tan^{-1}\left(\frac{x_1 + h_1 - x_2}{a}\right) + (x_1 - h_2 - x_2) \cdot \tan^{-1}\left(\frac{x_1 - h_2 - x_2}{a}\right) - (x_1 - x_2) \cdot \tan^{-1}\left(\frac{x_1 - x_2}{a}\right) - (x_1 + h_1 - x_2 - h_2) \cdot \tan^{-1}\left(\frac{x_1 + h_1 - x_2 - h_2}{a}\right)\Bigg] \qquad (9)$$

which, in the simplified geometry, reduces to

$$F_{1,2} = \frac{s_1 s_2 \cos \gamma_1 \cos \gamma_2}{\pi A a} \cdot \left[h \cdot \tan^{-1}\left(\frac{h}{a}\right)\right] \qquad (9a)$$

To account for the top and bottom edges, we used (De Lucia and Lanfranchi, 1994)

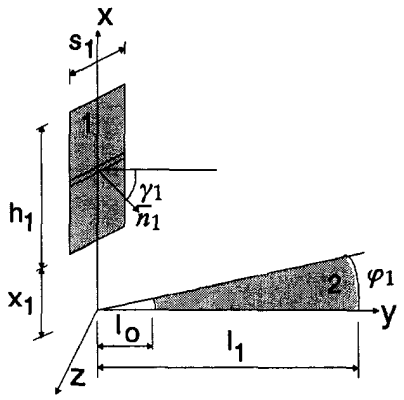

Fig. 6 Common geometry

$$F = \frac{s_1}{2\pi A}[\sin(\gamma_1 + \varphi_1) - \sin(\gamma_1)] \cdot \left[x_1 \tan^{-1}\left(\frac{l_0}{x_1}\right) - x_1 \tan^{-1}\left(\frac{l_1}{x_1}\right) - (x_1 + h_1) \cdot \tan^{-1}\left(\frac{l_0}{x_1 + h_1}\right) + (x_1 + h_1) \cdot \tan^{-1}\left(\frac{l_1}{x_1 + h_1}\right)\right] \quad (10)$$

which, in the simplified geometry (Fig. 6), becomes

$$F = \frac{s_1}{2\pi A}[\sin(\gamma_1 + \varphi_1) - \sin(\gamma_1)] \cdot \left[h \cdot \tan^{-1}\left(\frac{l_1}{h}\right)\right] \quad (10a)$$

The experimental model does not allow measurement of the radiances exiting the circular sectors of the top and bottom surfaces, since mirror displacement would necessitate an additional degree of freedom, thereby complicating the modeling procedure. Hence, for lack of more precise information, by assigning the same temperatures to the circular sectors previously measured for the correspondent rectangular thin strip, we can reduce error to approaching zero for large-size machines, i.e., those with high h/l ratios.

The main parameters to be defined for discretizing the geometry and thus calculating the angle factors are:

1 The number of plane surfaces n for approximating the blade profiles.
2 The geometry's h/l ratio.

Since l is a characteristic geometric parameter of gas turbines, we can divide h into several parts. Note that h can be the total blade height or only a part of blade height, in which case it is necessary to conduct the calculation by circular rows. The h/l parameter varies from 0.3 to 5.5 for typical heavy-duty gas turbine geometries.

To allow for examination of a suitable number of situations, the simplified geometry was nondimensionalized assuming side l of unitary length and varying the number of surfaces n by which each side is discretized, with h constant (which modifies the h/s ratio), and then varying h at n constant. The results, given in percentage of error, refer to one (since the summation of all the angle factors for a well-discretized closed geometry should be unitary), thereby showing the relation of the error as a function of the variations in the parameters.

With model A (Fig. 7), as h/l varies, there is a maximum around 2.5 where the system loses accuracy and shows poor sensitivity as n varies. However, even with n variable between 5 and 20, the improvement is only 0.8 percent of the value, with the curves overlapping between 20 and 100, while, if h/l is varied from 0.1 to 6, the error increases by one magnitude. By contrast, model B (Fig. 8) markedly improves

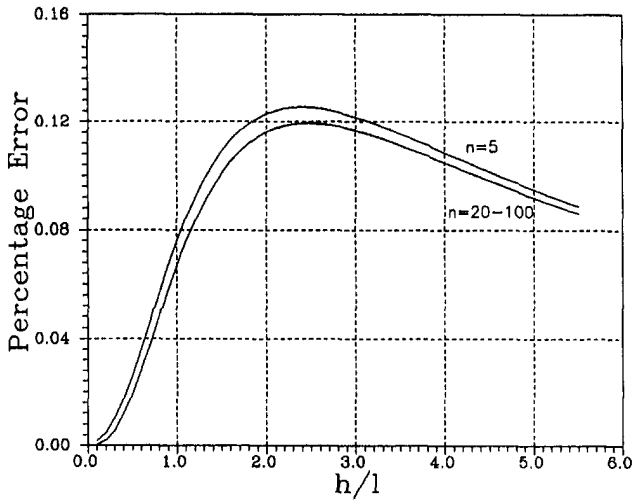

Fig. 7 Angle factor error (model A)

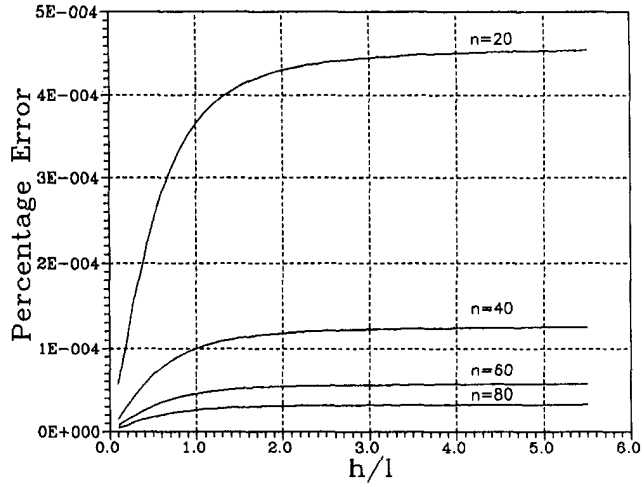

Fig. 8 Angle factor error (model B)

when n is increased and loses sensitivity to h/l at values in excess of 2. The advantages to be gained from increasing the discretization surface are evident (improved accuracy of around two to three orders of magnitude), since the curves do not overlap as in the previous case.

In both cases, with $h/l < 2.5$, the error decreases as h/l decreases. While, with geometric conditions being equal, we can reduce h/l by repeating the calculation for different circular rows, this notably increases complexity and, in addition, since the two models were developed for thin-strip isothermal surfaces, an excessive decrease could create problems in the h/s parameter, and thus negatively affect accuracy. To be able to assume isothermal thin strips for the surface discretization, we must necessarily consider the h/l ratios in relation to the actual machine geometric conditions such as swirl and, in addition, to the radial temperature distributions. With appropriate geometric conditions and radial temperature distribution, model B allows performing a sole angle factor calculation without resorting to circular rows.

Model A, while simpler, is more than two orders of magnitude less accurate than model B. Further, model A is exceedingly sensitive to the h/l ratio, whereas model B is affected primarily by n for h/l values above 2. Hence, model A should be used when it is not possible or convenient to increase n, while model B should be used in all other cases for accuracy.

From the above, it is evident that the angle factor calculation is more complex than the radiation thermometer measurements—albeit with the advantage of not having to be repeated unless the machine geometry is changed. Hence, the procedure can be carried out by two different operators: one without special training to carry out the measurements and the other with the requisite mathematical skills to calculate the angle factors. This means that, once the latter are calculated, the turbine manufacturer can then furnish the angle factors without having to divulge proprietary information regarding machine geometry.

Conclusions

- The scanning radiation thermometry technique described requires no prior knowledge of theoretical gas turbine temperature distribution and, in addition, does not require specially trained operators.
- The angle factors, calculated by personnel possessing the requisite mathematical skills, can be furnished by the manufacturer in lieu of proprietary information about machine geometry.
- The model furnishes the steady-state and near-steady-state temperature distribution with an error comparable to that of the measuring chain in the primary measuring zone.
- Error can be further reduced, especially in the vanes, by refining the model in terms of angular calibration, positioning the radiation thermometer with respect to the vanes, and optimizing the law of motion.
- The model furnishes not only target temperatures, and thus the distribution of the temperatures obtained from the blade movements, but also, without further complicating the calculation, a 360-deg distribution.
- In the experimental testing, as the model was found to be sensitive to the angle factors and thus to parameter discretization, two angle factor calculation methods were examined: The simpler one proved useful when it is not possible or convenient to increase n, while the more complex one is recommended in all other cases for accuracy.

Acknowledgments

The authors are grateful to Pierluigi Nava and Valter Quercioli of NuovoPignone and Umberto Lucia for their valuable technical contribution and to Professor Ennio Carnevale for his unfailing support. The support of NuovoPignone S.p.A. is also gratefully acknowledged.

References

Bejan, A., 1993, *Heat Transfer*, Wiley, New York.

Beynon, T. G. R., 1981, "Turbine Pyrometry—An Equipment Manufacturer's Viewpoint," ASME Paper No. 81-GT-136.

Beynon, T. G. R., 1982, "Infrared Radiation Thermometry Applied to the Development and Control of Gas Turbine Engines," *Proceedings, International Conference on Infrared Technology*, Butterworth Scientific Ltd., Sevenoaks, United Kingdom, pp. 3–16.

De Lucia, M., and Lanfranchi, C., 1994, "An Infrared Pyrometry System for Monitoring Gas Turbine Blades: Development of a Computer Model and Experimental Results," ASME JOURNAL OF ENGINEERING FOR GAS TURBINES AND POWER, Vol. 116, pp. 172–177.

DeWitt, P. D., and Incropera, F. P., 1988, "Physics of Thermal Radiation," *Theory and Practice of Radiation Thermometry*, P. D. DeWitt and G. Nutter, eds., Wiley, New York, pp. 21–89.

Douglas, J., 1980, "High-Speed Turbine Pyrometry in Extreme Environments," *Proceedings, New Orleans Gas Turbine Conference*, ASME, New York, pp. 335–343.

Kirby, P. J., Zachary, R. E., and Ruiz, F., 1986, "Infrared Thermometry for Control and Monitoring of Industrial Gas Turbines," ASME Paper No. 86-GT-267.

Kreith, F., 1973, *Principles of Heat Transfer*, Dun-Donnelley Publishing Corporation, New York, pp. 217–304.

Love, T. J., 1988, "Environmental Effects on Radiation Thermometry," *Theory and Practice of Radiation Thermometry*, P. D. DeWitt and G. Nutter, eds., Wiley, New York, pp. 189–229.

Ono, A., 1988, "Methods for Reducing Emissivity Effects," *Theory and Practice of Radiation Thermometry*, P. D. DeWitt and G. Nutter, eds., Wiley, New York, pp. 565–623.

Schulemberg, T., and Bals, H., 1987, "Blade Temperature Measurements of Model V84.2 100 MW/60 Hz Gas Turbine," ASME Paper No. 87-GT-135.

Scotto, M. J., and Eismeier, M. E., 1980, "High-Speed Noncontacting Instrumentation for Jet Engine Testing," ASME JOURNAL OF ENGINEERING FOR GAS TURBINES AND POWER, Vol. 102, pp. 912–917.

Sparrow, E. M., and Cess, R. D., 1978, *Radiation Heat Transfer*, Hemisphere Publishing, Washington, DC, pp. 81–143.

Steam-Injected Gas Turbine Analysis: Steam Rates

I. G. Rice
Consulting Engineer,
Spring, TX 77383

This paper presents an analysis of steam rates in steam-injected gas turbines (simple and reheat). In considering a gas turbine of this type, the steam-injection flow is separated from the main gas stream for analysis. Dalton's and Avogadro's laws of partial pressure and gas mixtures are applied. Results obtained provide for the accurate determination of heat input, gas expansion based on partial pressures, and heat-rejection steam-enthalpy points.

Introduction

Gas turbine scholars, users, and manufacturers are all becoming more interested in steam injection. Steam injection can take one or more forms. Water can be injected directly into the combustor to control NO_x and therein produce steam. Steam can be alternatively injected for both NO_x control and power augmentation. Water can be evaporated by the compressor-discharge hot air, an example being the Humid Air Turbine (HAT) cycle as reported by Day and Rao (1992). Steam can be mixed with compressor air either at the discharge (GE LM2500 and LM5000) or at extraction (W/MHI 501F and 701F) to improve cooling. Another example of steam injection is the proposed Chemically Recuperated Gas Turbine (CRGT) cycle where a mixture of steam and reformed natural gas becomes the gas turbine fuel (Janes, 1989).

Humidified nitrogen return and/or coal-gas fuel provides a form of steam injection for the integrated coal-gas combined cycle (ICGCC) as reported by Shell Oil Co. (Bayens and Cremer, 1991). The Department of Energy (DOE) Morgantown is proposing a water-injected regenerative indirect-fired coal-fuel cycle with some of the features of the HAT cycle as suggested by Parsons et al. (1991). A further example of steam injection is the Compressed-Air Storage Cycle with Air Humidification (CASH) with or without integrated coal-gas fuel (IGCASH) as projected by Cohn and Nakhamkin (1992).

The injected steam produces more power for a given turbine (rotor) inlet temperature (TIT) in all cases, but additional heat input is required to heat the steam to full TIT. There is a need to evaluate steam injection in terms of incremental power output and heat input. Up to now, the task evaluating limited steam injection for a given turbine design has been left to the manufacturers. This paper provides analysis and insight for the individual turbine engineer because in the future we can expect the manufacturers to make greater design changes to optimize for steam injection for both power augmentation and cooling.

The steam-injected Allison 501-K, GE LM2500, and LM5000 turbines have been in operation for several years. Reliability, capital, and operating costs and maintenance considerations have been field-evaluated and the results are positive. The door is now open to future applications and optimization.

Steam rates are presented to evaluate potential power augmentation for a given amount of steam injection. Incremental output can be determined by dividing the particular injection steam flow (lb/hr) by the steam rate (lb/kW hr) to obtain kW incremental power output as is commonly done for steam turbines—but with the understanding of certain gas turbine limitations. These limitations will be explained near the end of the paper.

Existing Steam-Injection Systems

The first steam-injected gas turbines in the mid-1950s piped steam directly to the inside of the combustor liners. Steam was injected into the compressor discharge (CD) air through ports in the casing during the 60s. More recently steam has been injected with the fuel (or around the fuel-nozzle tips) to control NO_x.

As an example of present designs, a schematic diagram of the high-pressure section of the steam-injected General Electric STIG LM5000 is shown in Fig. 1 (Smith, 1989). Seven percent steam by weight of the core air flow is injected in this particular high-pressure design. Turbine modifications are minimal so that a nearly standard gas turbine can be used. Half of the steam is injected around the fuel tips and the top part of the compressor discharge. This latter portion flows around the outer part of the annular liner. The other half is injected into the compressor discharge to mix with the CD air and then to flow around the inside ID of the annular liner with a small amount being fed to the shaft sealing area and therefrom to the first-stage rotating blades for improved cooling. The mixture of steam and air on both sides of the combustor liner provides better first-stage nozzle-vane cooling.

Contributed by the International Gas Turbine Institute and presented at the 38th International Gas Turbine and Aeroengine Congress and Exposition, Cincinnati, Ohio, May 24–27, 1993. Manuscript received at ASME Headquarters March 1, 1993. Paper No. 93-GT-132. Associate Technical Editor: H. Lukas.

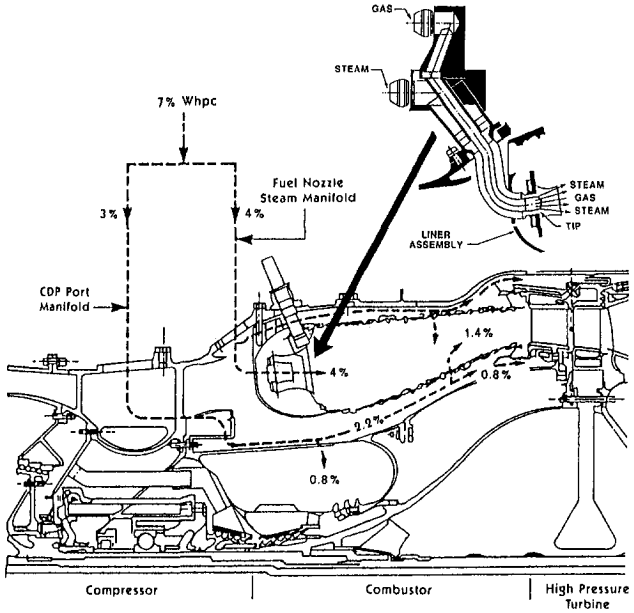

Fig. 1 Steam-injection arrangement of the gas generator high-pressure section of the GE LM5000 full STIG

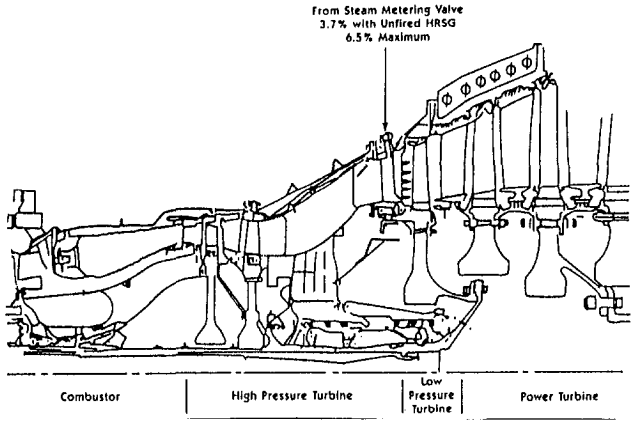

Fig. 2 Steam-injection arrangement of the gas generator low-pressure turbine of the GE LM5000 full STIG

Additional steam is injected in front of the low-pressure gas-generator nozzle ring (up to 6.5 percent of weight air flow) as noted in Fig. 2. This steam is passed through the interior of the nozzle vanes and is then exited at high velocity through nozzle holes at the vanes' trailing edges.

The vanes (high pressure and low pressure) provide the means for injecting the steam evenly to the gas stream at a high velocity so work can be extracted from the steam by the downstream rotating blades. The leading-edge stream exiting the high-pressure vanes expands with the air from full pressure as it helps film cool the vanes.

The power output of the gas turbine is increased from 34 MW to 52 MW as a result of the steam injection, yet the air flow remains about constant. The turbine-nozzle areas are increased to accommodate the addition of the steam flow. Also, the power turbine, located downstream of the gas generator (not shown), is designed to accept the increased mass flow and expansion ratio and thus produce the 52 MW.

Other arrangements of steam injection/blade cooling have been suggested in ASME papers by Rice in 1979 and 1984.

Intercooling

A schematic diagram of a steam-injected-intercooled reheat gas turbine is given in Fig. 3. Intercooling reduces the

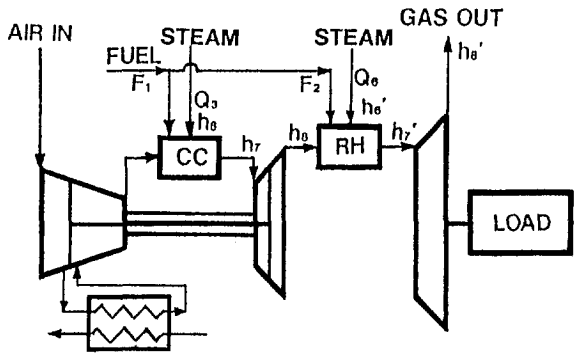

Fig. 3 Schematic diagram of the steam-injected intercooled reheat gas turbine

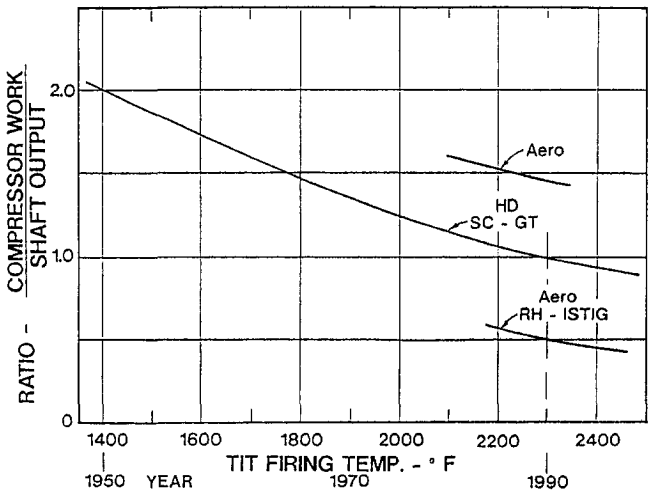

Fig. 4 Ratio of compression work divided by shaft output versus TIT

work of air compression, leaving more work for power output. Intercooling also reduces the high-pressure compressor (HPC) discharge temperature for improved NO_x control and better blade cooling.

Intercooling does one thing: It makes it possible to pass significantly more air mass through the gas generator core by utilizing an oversized low-pressure compressor (LPC). The HPC is essentially a constant inlet-volume flow device and pumps the same volume air rate, but the mass is increased indirectly as the ratio of the absolute LPC outlet temperature divided by the intercooled discharge absolute temperature according to both Charles' and Boyles' Laws ($PV = WRT$). The increase in mass flow for a given core is thus increased by a significant amount.

Intercooling is receiving more attention by manufacturers (Leonard, 1992) and is being mentioned for future cycle consideration. Intercooling, however, has no effect on steam-injection power augmentation or heat input to the steam as can be determined by Fig. 3.

In all proposed cases cited earlier in this paper, steam is injected downstream of the compressor discharge. In the case of the HAT and CASH cycles, part of the heat of compression of the LPC (intercooler heat) is used to evaporate water at a low partial pressure and low temperature for a very efficient heat-exchange arrangement (second law of thermodynamics).

In the early 50s industrial gas turbines firing at about 1400°F TIT (760°C) required twice as much work to compress the air as was left over to drive the load; refer to Fig. 4. Over the years the firing temperatures have been increased to produce more net power. By the year 1990, the new "F"

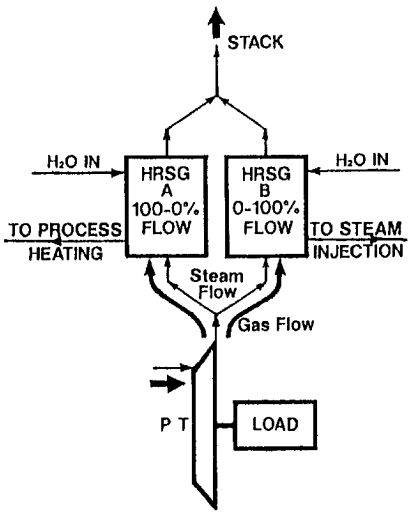

Fig. 5 Stream separation schematic diagram

technology gas turbines had reached TIT levels of 2300°F (1260°C). As a result, the ratio of compressor work to shaft output was reduced to a ratio of about one. The aero engines have dropped to a level of only about 1.5 because of their high-cycle pressure ratios (CPRs) of 30 to 35 and the extra compression work required.

The introduction of intercooling, steam injection, and reheat reduces the compressor/output ratio to about 0.5. Reference is made to both Figs. 3 and 4. The significance of this low ratio is important. The air compressor now becomes far less dominant. Compressor efficiency and fouling degradation becomes less significant. The tail (compressor) no longer wags the dog (power output). Steam injection becomes far more significant because power output is increased without the required work of air compression. Water is pumped as a liquid at very low power input and not compressed as a gas at very high power input. The air then becomes a means to heat the steam directly before expansion and stoichiometric conditions are approached for full steam injection.

Stream Separation

Reference is made to Fig. 5 showing a schematic flow diagram of a steam-injected expander turbine. Both gas (heavy arrow) and steam (light arrow) enters the power turbine (PT) at a given TIT. TIT is defined by U.S. heavy duty and aero manufacturers as the average total temperature of the gas and nozzle coolant mixture striking the first-stage rotating blades. The coolant (air and/or steam) and the combustor-outlet gas–steam mixture condition is projected back to the first-stage nozzle inlet at essentially constant entropy to obtain this value. The combustor outlet temperature is therefore some 150 to 175°F (83 to 97°C) higher than the TIT.

The steam part of the working fluid, at its own partial pressure, expands through the PT at a given isentropic efficiency and exits at its own specific temperature and partial pressure enthalpy. The steam, with its sensible heat component, then passes through a heat-recovery steam generator (HRSG). Schematically all or zero steam flow can pass through the portion of the HRSG (A) that produces steam for process use. The other part passes through the part of the HRSG (B) to produce incremental steam for the steam injection. The two streams then meet again schematically to form the stack gas.

Figure 5 is helpful in visualizing stream separation and recovery separation for analytical purposes knowing that in reality there is no such separation or division of flow. There is no change in total enthalpy of the stream.

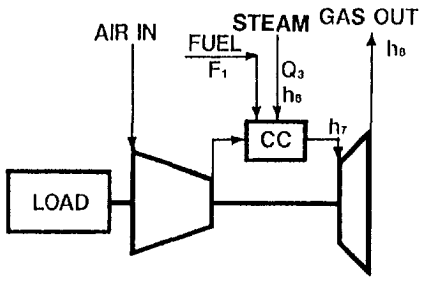

Fig. 6 Schematic diagram of a steam-injected simple-cycle gas turbine

Steam Rates

The steam-rate calculating procedure can now be presented using the previous background of stream separation and TIT definition. A computer program called "Steam 92" (Strong, 1992) has been used to obtain accurate steam enthalpy and temperature numbers for each point. The ASME steam tables are limited to 1500°F (816°C) and do not give partial pressure data whereas the software provides very accurate answers up to and beyond the TITs encountered by present-day gas turbines.

Partial pressures have been used in the calculations. However, full throttle pressure expansion introduces only a small error of 0.87 Btu/lb (2.02 kJ/kg) when expanding steam at constant entropy from 450 psia (approximately 30 atmospheres) at 2400°F TIT (1316°C) to 15 psia (one atmosphere) when comparing full pressure to 1 percent partial pressure (4.5 psia to 0.15 psia). The expansion-exit temperature variation is only 1.89°F (1.05°C). A computer printout is included in the appendix showing the entering and exiting data. Partial pressure expansion provides more accurate answers, but full pressures can be used without introducing a significant error.

Simple-Cycle Gas Turbine. A schematic diagram of the steam-injected simple-cycle gas turbine is presented as Fig. 6. Steam or water flow Q_3 enters combustion chamber (CC) at enthalpy h_6. The flow is heated to h_7 and is expanded to h_8. (The particular numbered enthalpy subscripts are used to be consistent with the rest of the paper.) The steam exhausts in most cases to a HRSG. Feedwater is heated from an assumed temperature of 100°F (38°C) ($h = 68$). In the case of steam, the enthalpy rise of the water and steam inside the HRSG plus the enthalpy rise across the CC gives the total enthalpy of h_7. The work output is the enthalpy drop across the turbine (h_7–h_8) taking into consideration expansion efficiency.

In the case of water injection, water is heated by incremental fuel from 100°F (38°C) all the way to the CC outlet (h_7). The work output remains the same, that is, (h_7–h_8).

Steam rates are calculated using the following formula:

$$SR = \frac{3412.1416}{(h_7 - h_8)} = \text{lb/kW hr} \qquad (1)$$

It is important to note that if steam is injected directly inside the combustor liner—or such that it enters the CC—the steam is heated to the combustor outlet temperature. If the steam is injected into the compressor-discharge outlet, the steam is mixed with the CD air and a portion of the steam is used with the air to cool the blades and rotor. In this latter case, the TIT lower temperature takes into account a cooling penalty for the first-stage nozzle vanes. A cooling penalty for the downstream blading and rotor is not taken into account.

Figures 7 and 8 are graphs of steam rate (lb/kW hr) versus expansion ratio (P_2/P_1) for TIT inlet temperatures of 2000 to 2600°F (1093 to 1427°C).

Referring to Fig. 8 and considering a 15 expansion ratio

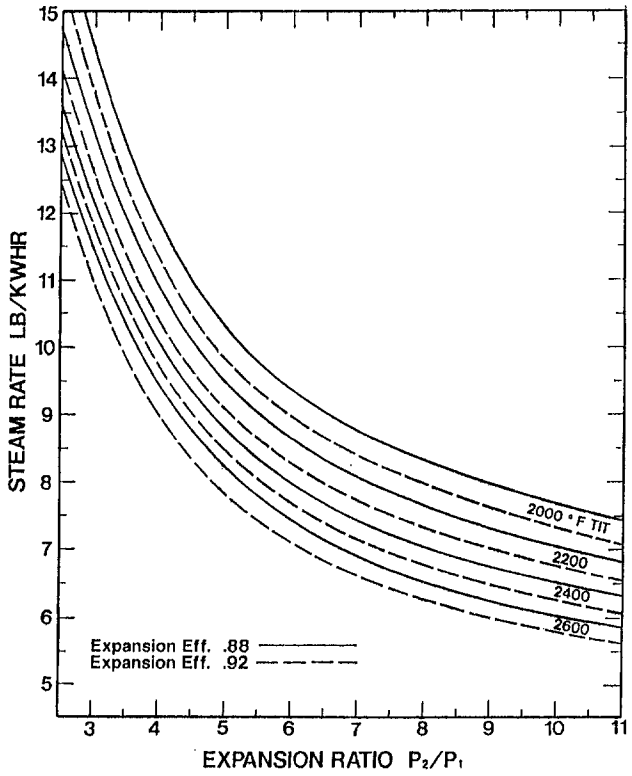

Fig. 7 Steam rate versus gas turbine expansion ratios (low)

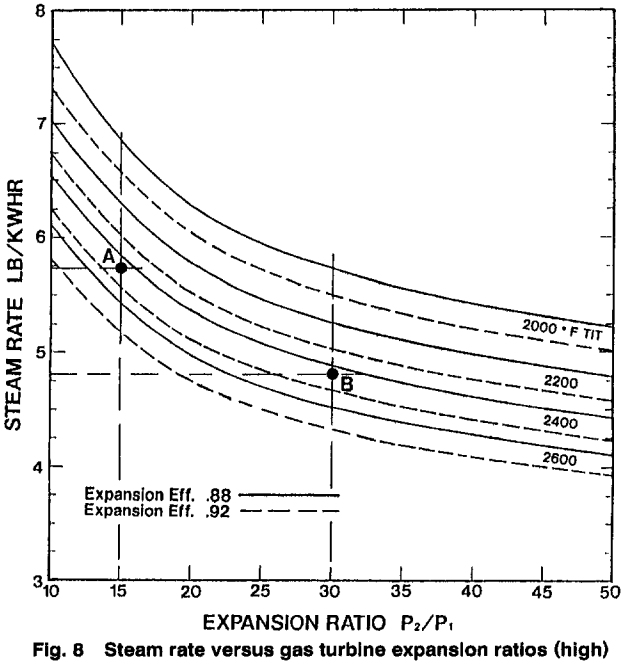

Fig. 8 Steam rate versus gas turbine expansion ratios (high)

for 2400°F TIT (1316°C) and 90 percent efficiency, point A is read off the graph to be 5.7 lb/kW hr (26 kg/kW h). Considering a 30 expansion ratio for these conditions, the steam rate drops to 4.8 lb/kW hr (2.2 kg/kW h) (point B). The shaft power output is simply the steam injection flow in lb/hr divided by the steam rate. If the injection flow is 200,000 lb/hr (90, 718 kg/h) for point B, the shaft power developed would be 41.7 MW.

There are some practical considerations such as fixed nozzle area, extra cooling required, and reduction in TIT, which can reduce this potential output. These considerations will be reviewed at the end of the paper.

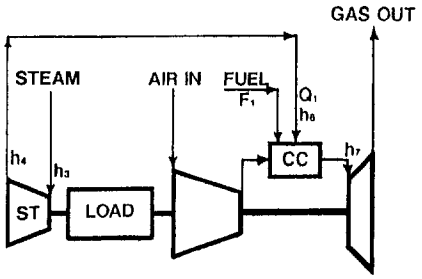

Fig. 9 Schematic diagram of a steam-injected simple-cycle gas turbine with a topping steam turbine

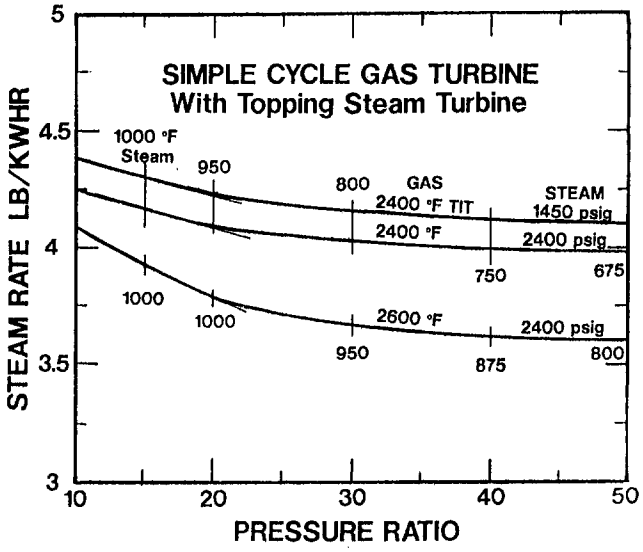

Fig. 10 Steam-rate curves versus expansion ratio of a steam-injected simple-cycle gas turbine with a topping steam turbine

Simple-Cycle Gas Turbine With Topping Steam Turbine. Let us now consider the case where steam is first run through a topping (noncondensing) steam turbine before it is injected into the gas turbine. The steam turbine can be connected in tandem to the outer end of the electric generator, or alternately it can be in the form of a large separately-positioned steam turbine. Reference is made to Fig. 9.

The total enthalpy rise is the HRSG enthalpy rise to the steam turbine throttle plus the enthalpy rise from the steam-turbine exit point to the gas turbine TIT. The work output is the enthalpy drop across the steam turbine plus the enthalpy drop across the gas turbine.

The topping steam turbine increases output per unit weight of steam flow and thereby decreases the steam rate. Figure 10 is a graph showing steam rates for various pressure ratios, throttle pressure, and TITs. Note that the exhaust temperature of the gas turbine limits the steam temperature as the CPR increases; and therefore the steam rates flatten out above a pressure ratio of about 20. Even so, very low steam rates of 4 lb/kW hr (1.8 kg/kW h) are possible for a TIT of 2400°F (1316°C) coupled to a 2400 psig (166.5 bar) throttle pressure. This steam rate is far better than can be achieved with a 2400 psig 1000/1000°F (166.5 bar 538/538°C reheat condensing steam turbine.

When considering a topping steam turbine, the steam rates of the topping steam turbine can be determined from the ASME *Theoretical Steam Rate Tables* by applying an appropriate expansion efficiency. Alternately steam-table software can be used as was done for Figs. 7 and 8. The overall combined steam rate can be readily calculated using the following formula:

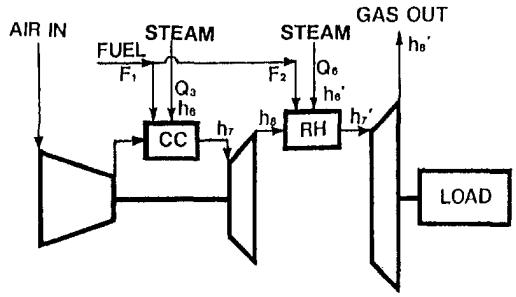

Fig. 11 Schematic diagram of a steam-injected reheat gas turbine

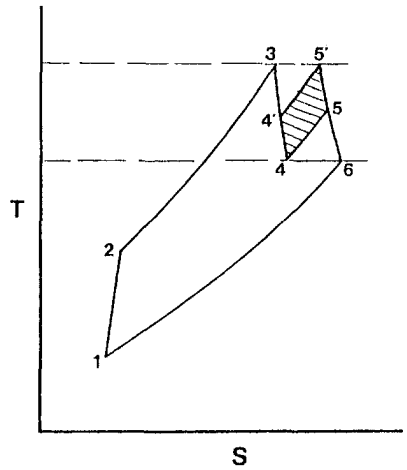

Fig. 12 *T–S* diagram showing effect of steam injection

$$SR = \frac{1}{\frac{1}{SR_{st}} + \frac{1}{SR_{gt}}} = \text{lb/kW hr} \qquad (2)$$

where SR = overall steam rate
SR_{st} = steam rate of topping steam turbine
SR_{gt} = steam rate of gas turbine.

It can be noted that the reciprocal of the steam rate is actually work per unit mass of steam (kW hr/lb steam). These work units can be added together and then converted back to steam rates.

Reheat Gas Turbine. Steam-injection steam rates are lower for reheat (RH) gas turbines. The steam is reheated in the reheat combustor after partial expansion and more power is produced for a given injection rate. Figure 11 presents a schematic flow diagram of a steam-injected reheat gas turbine. Steam can be injected into both the gas generator combustor (CC) and the reheat combustor (RH).

The steam or water that is injected in the gas generator combustor (CC) is heated to TIT level and is then expanded to produce driving power for the air compressor. Considering appropriate nozzle-area changes and rotating-blade modifications, the gas-generator exit pressure will rise. Additional work is produced by the steam and less by the hot gas, and the expansion ratio is reduced for the fixed power requirements of the air compressor. Reference is made to Fig. 12, which presents a *T–S* diagram illustrating the rise in pressure. Without steam injection the gas is expanded from TIT point 3 to point 4. When steam is injected the gas is only expanded to point 4′ and the steam work makes up the difference as the steam also expands from point 3 to point 4′. The shaded area 4′–4–5–5′ represents the additional work provided by the air side for a given pre-selected exit temperature, point 6. Incremental power is thus produced by both the air side and the steam side of the two stream system.

As an indication of the pressure rise, reference is made to

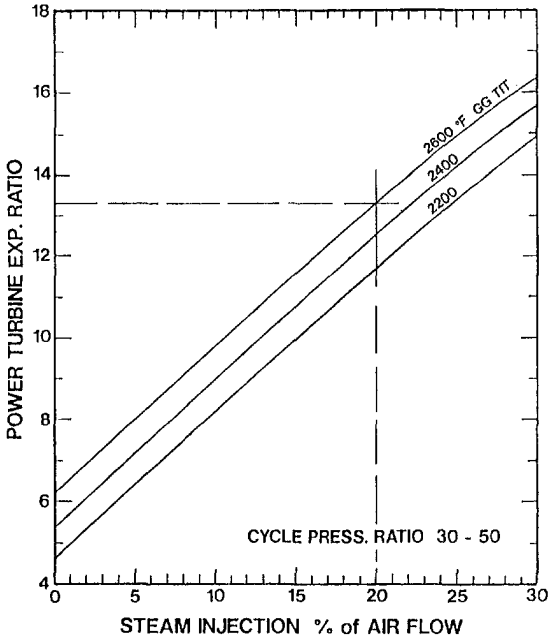

Fig. 13 Power-turbine expansion ratio versus steam-injection rate

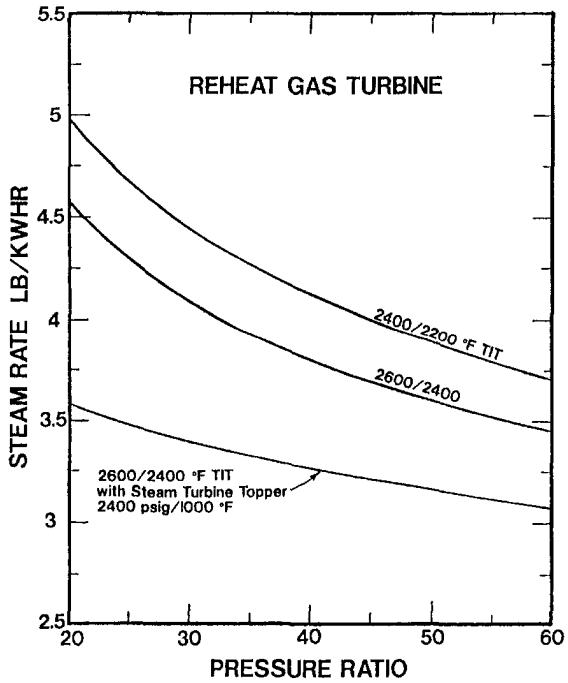

Fig. 14 Steam-rate curves versus expansion ratio of a reheat gas turbine—with and without a topping steam turbine

Fig. 13, which is a plot of power-turbine expansion ratio versus steam-injection rate. Considering zero steam injection, the power-turbine expansion ratios of different gas generator (GG) TITs are rather low, ranging from 4.6 to 6.25 (Rice, 1982). A steam injection rate of 15 percent increases the power-turbine expansion ratios to a range of 9.5 to 11 as can be noted. Data taken from various studies and those contained in the GE ISTIG study for the California Energy Commission (Janes, 1989) have been used to prepare this graph. These higher expansion ratios are ideally suited for a three-stage power turbine.

The steam-rate graph of Fig. 14 is a plot of steam rate versus overall cycle pressure ratio both with and without a topping steam turbine for various TIT levels. The bottom line, which represents a topping steam turbine, shows steam

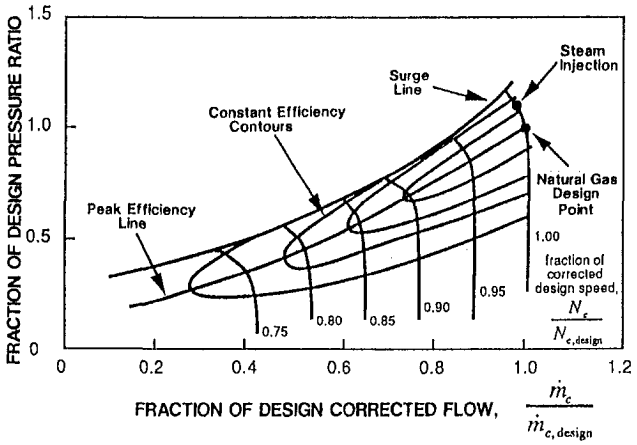

Fig. 15 Typical normalized compressor map showing effect of steam injection

rates ranging from 3.1 to 3.5 lb/kW hr (1.4 to 1.6 kg/kW h), which are about half the steam rates of a 2400 psig 1000/1000°F (166.5 bar 538/538°C) reheat condensing steam turbine. In other words, twice as much power is produced for a given steam flow.

Practical Considerations

There are several practical points to consider when dealing with steam-injection for existing gas turbines. New gas turbines being designed from a clean sheet of paper should also take into consideration practical limitations. The steam rates given in this paper do not take into consideration such things as nozzle-area requirements, compressor pressure-ratio and flow changes, changes in compressor efficiency, increases in rotating-blade loading, additional blade-cooling requirements and changes in expansion efficiency. The power turbine of a reheat gas turbine requires more rotor, blade, and casing cooling, which necessitates different steam-cooling methods. Some of these points will be discussed in the following paragraphs.

When a gas turbine is steam injected by moderate rates of 2 to 4 percent weight of air flow, no nozzle-area changes are generally needed. Reference is made to Fig. 15, a typical compressor map taken from an EPRI Report (Eustis and Johnson, 1990). When steam is injected, the compressor discharge pressure will rise, the compressor efficiency will be reduced, and the air flow will also fall off. The net results will tend to increase the steam rates given in Figs. 7 and 8. At high-ambient inlet-air temperatures, however, the operating points are lower, and compressor efficiency can be improved for a given nozzle area at very little reduction in air flow.

Another limitation example in using Figs. 7 and 8 is cited in the case of the new LM6000 gas turbine. This gas turbine, adapted from the GE CF6 dash 80 aero engine (without turbine flow-path modifications) has an exit flow limitation. The power-turbine exit velocity is about Mach 0.8, and if any steam or water is injected, the TIT has to be lowered to maintain the flow volume. The parametric graph of Fig. 16 illustrates this point. The top family of curves represent aeroderivative engines and the bottom curves the heavy-duty machines.

Published data are plotted for the LM6000 as points *A*, *B*, and *C* as reported by deBiasi (1990) and Johnson (1992). Point *A* is for the LM6000 without any steam injection. Point *B* is for this engine for 25 ppm NO_x utilizing steam injection where the TIT is reduced from 2275 to 2180°F (1246 to 1193°C). When water is injected for a NO_x level of 42 ppm, point *C*, the TIT is lowered from 2275 to only 2240°F (1246 to only 1227°C).

As a note of interest, the GE Frame 7F and 7FA gas

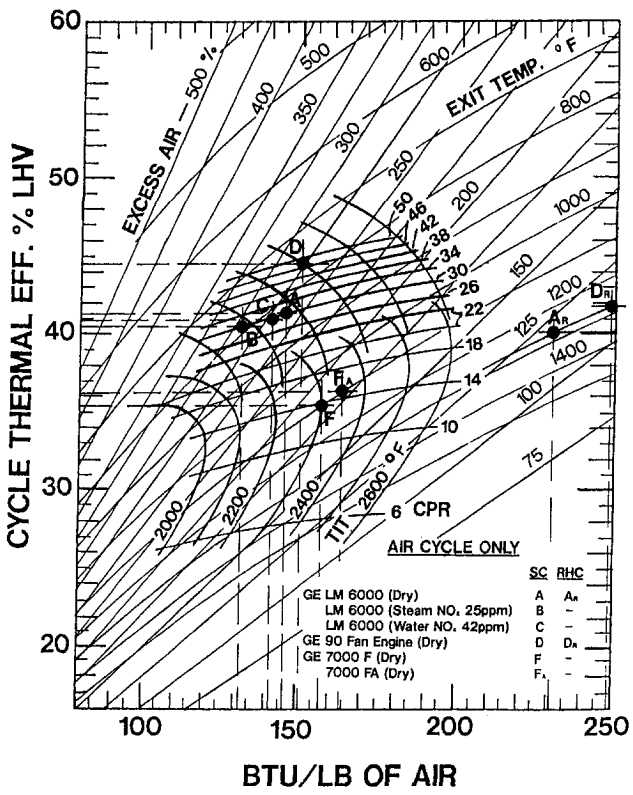

Fig. 16 Parametric thermodynamic map giving operating points of various gas turbines

turbines are spotted in Fig. 16 as points *F* and F_A. Also point *D* represents the new GE-90AD engine when adapted as an industrial prime mover (Leonard, 1992). Note points A_r and D_r for reheat gas turbines.

If a gas turbine were designed specifically for steam injection and steam cooling, then all the above considerations could be taken into account to capture the full potential of steam injection in terms of the lowest possible steam rate.

Conclusion

This paper presents steam rates for various gas turbines with and without a topping steam turbine function. The steam rates for high cycle-pressure ratio and high TIT gas turbines are appreciably lower than steam rates for condensing steam turbines. The steam rate is about 4 lb/kW hr (1.8 kg/kW h) when considering a CPR of 20, a TIT of 2450°F (1343°C), and when a 2400 psig 1000/1000°F (166.5 bar 538/538°C) *RH* topping steam turbine is utilized. The graphs presented can be used to obtain estimated steam rates for any given cycle pressure ratio and TIT. Both simple and reheat-gas-turbine cycles are included.

The lowest steam rate is obtained for the reheat gas turbine utilizing a topping steam turbine, for example using extracted steam from a steam turbine. Steam rates as low as 3.1 lb/kW hr (1.4 kg/kW h) are projected for the reheat gas turbine with a 2400 psig, 1000/1000°F (166.5 bar 538/538°C) *RH* topping steam turbine.

This paper provides a procedure for calculating steam-injection incremental power. Useful steam-rate curves are given. Various methods of steam injection have been presented, and practical limitations have been discussed.

Acknowledgments

Appreciation is expressed to my loyal wife and business manager, Carolyn Keyes Rice, for her continued assistance with my papers. Without her diligent support, encourage-

ment, patience, and toil the work could not have been accomplished.

Appreciation is also extended to Egon Doering and Dennis Salzman of the Shell Oil Co. who have supported my work in the area of steam injection (fuel and return nitrogen heating and humidification) for the Shell coal-gas integrated combined cycle.

References

Bayens, C. A., and Cremer, G. A., 1991, "Cost Improvements in Shell CGCC: 1991 Design," presented at the Tenth EPRI Conference on Coal Gasification Power Plants, San Francisco, CA.

Cohn, A., and Nakhamkin, M., 1992, "Performance and Economic Characteristics of Compressed-Air Storage With Air Humidification (CASH) Power Plant With Integrated Gasification and Natural Gas Firing," presented at Power-Gen '92, Orlando, FL.

Day, W. H., and Rao, A. D., 1992, "FT4000 Hat With Natural Gas Fuel," ASME *CogenTurbo*, IGTI-Vol. 7.

de Biasi, V., 1990, "LM6000 Dubbed the 40/40 Machine Due for Full-Load Tests in Late 1991," *Gas Turbine World*.

Eusti, F. H., and Johnson, M. S., 1990, "Gas Turbine Effects on Integrated-Gasification Combined-Cycle Power Plant Operations," EPRI Report GS/ER-6770.

Janes, J., 1989, "Chemically Recuperated Gas Turbines," California Energy Commission Draft Report.

Johnson, P., 1992, "First Test Results Reported for GE's LM6000 Gas Turbine," *Diesel & Gas Turbine Worldwide*.

Leonard, G., 1992, "Advanced Gas Turbines, Looking Past the 90's," *The Energy Daily*, handout material, Advanced Combustion Turbine Conference, Washington, DC.

Parsons, E. L., Jr., et al., 1991, "Performance Gains Derived From Water Injection in Regenerative, Indirect-Fired, Coal-Fueled Gas Turbines," ASME Paper No. 91-GT-288.

Rice, I. G., 1979a, "Steam-Cooled Blading in a Combined Reheat Gas Turbine/Reheat Steam Turbine Cycle, Part I—Performance Evaluation," ASME Paper No. 79-JPGC-GT-2.

Rice, I. G., 1979b, "Steam-Cooled Blading in a Combined Reheat Gas Turbine/Reheat Steam Turbine Cycle, Part II—Design Considerations," ASME Paper No. 79-JPGC-GT-3.

Rice, I. G., 1982, "The Reheat Gas Turbine With Steam-Blade Cooling—A Means of Increasing Reheat Pressure, Output and Combined-Cycle Efficiency," ASME JOURNAL OF ENGINEERING FOR POWER, Vol. 104, pp. 9–22.

Rice, I. G., 1984a, "The Integrated Gas/Steam Nozzle With Steam Cooling, Part I—Application," ASME Paper No. 84-GT-134.

Rice, I. G., 1984b, "The Integrated Gas/Steam Nozzle With Steam Cooling, Part II—Design Considerations," ASME Paper No. 84-GT-135.

Rice, I. G., 1993a, "Steam-Injected Gas Turbine Analysis: Part I—Steam Rates," ASME Paper No. 93-GT-132.

Rice, I. G., 1993b, "Steam-Injected Gas Turbine Analysis: Part II—Steam Cycle Efficiency," ASME Paper No. 93-GT-420.

Rice, I. G., 1993c, "Steam-Injected Gas Turbine Analysis: Part III—Steam Regenerated Heat," ASME Paper No. 93-GT-421.

Smith, S. S., 1989, "Aeroderivative Gas Turbine Performance, Emissions, and STIG," General Electric publication GER 3572A.

Smith, S. S., et al., 1989, "GE LM5000 Aircraft-Derivative Gas Turbine System," General Electric publication GER 3425B.

Strong, R., 1992, "Steam 92," Interactive Steam Tables Computer Program.

APPENDIX

```
STEAM'92(8,P)= .15000000E+00Properties Operations  Inactive   any Key 13:42:47
                          S T A T E   P O I N T S   ( Water )
PROPERTY UNITS\ Pt 1     Pt 2     Pt 3     Pt 4     Pt 5     Pt 6     Pt 7     Pt 8
Press: psia     450.000  15.0000  45.0000  1.50000  4.50000  .150000  1.50000[.150000]
Temp:  °F       2400.00  1025.52  2400.00  1027.06  2400.00  1027.22  1208.53  1208.74
Enthal:Btu/lbm  2342.72  1547.71  2344.68  1548.87  2344.87  1548.99  1644.36  1644.50
Qualty:         1.00000  1.00000  1.00000  1.00000  1.00000  1.00000  1.00000  1.00000
SpcVol:ft^3/lb  3.78694  58.9456  37.8565  590.389  378.554  5904.83  662.466  6625.72
Avail: Btu/lbm  1290.68  495.669  1167.48  371.676  1042.85  246.961  437.380  312.685
Entrop:Bt/lb°R  2.13974  2.13974  2.39427  2.39427  2.64817  2.64817  2.45486  2.70876
IntEng:Btu/lbm  2027.38  1384.10  2029.44  1384.99  2029.64  1385.08  1460.48  1460.59
Nozzle: p/v     1449.45  3.10397  14.4994  .030991  .144998  .000310  .027619  .000276
PROPERTY UNITS\ Pt 1     Pt 2     Pt 3     Pt 4     Pt 5     Pt 6     Pt 7     Pt 8
 Cp:    Bt/lb°R .637906  .518248  .635898  .517757  .635698  .517709  .534731  .534710
 Cv:    Bt/lb°R .526073  .407612  .525505  .407484  .525450  .407472  .424471  .424475
DynVis:lbm/f-H  .141087  .074270  .141004  .074348  .140997  .074356  .084077  .084087
HtTran:Bt/HrfF  .105828  .042528  .106337  .042559  .106394  .042563  .050270  .050277
SndSpd:ft/sec   3094.78  2281.48  3090.45  2283.19  3090.04  2283.36  2408.22  2408.39
Bulk|T:psia     450.191  14.9909  45.0015  1.49991  4.50001  .149999  1.49994  .149999
Hemhlz:Btu/lbm  -4091.6  -1793.8  -4817.4  -2174.7  -5543.2  -2552.4  -2634.7  -3058.7
Gibbs: Btu/lbm  -3776.2  -1630.2  -4502.2  -2010.8  -5228.0  -2388.5  -2450.8  -2874.8
PROPERTY UNITS\ Pt 1     Pt 2     Pt 3     Pt 4     Pt 5     Pt 6     Pt 7     Pt 8
KEYS      Soln:  Analy.   Analy.   Analy.   Analy.   Analy.   Analy.   Analy.   Analy.
AT        Regn:  Vp:SC     Vp:SC    Vp:SC    Vp:SC    Vp:SC    Vp:SC    Vp:SC    Vp:SC
F10=Help!,→↑↓Cursor,F3=Calc.,F5=SAVE,F1/F2=Copy,Esc=OPPS!,...     12/16/1992

STEAM'92(8,P)= .89381388E+00Transports Reference              any Key 13:43:35


PROPERTY UNITS\ Pt 1     Pt 2     Pt 3     Pt 4     Pt 5     Pt 6     Pt 7     Pt 8
Prandl:         .849977  .904553  .842748  .903990  .841990  .903934  .893847[.893814]
Wc/A:  lb/in2s  3.35470  .157828  .335231  .015770  .033521  .001577  .014842  .001484
Exp|s:          1.21309  1.27065  1.21011  1.27054  1.20982  1.27053  1.25971  1.25969
KinVis:ft^2/Hr  .533998  4.37548  5.33499  43.8704  53.3458  438.820  55.6677  556.836
Comp|P:1/°R     .000352  .000675  .000350  .000673  .000350  .000673  .000600  .000599
Comp|S:1/psia   .001832  .052467  .018364  .524711  .183682  5.24715  .529222  5.29229
Bulk|S:psia     545.892  19.0598  54.4549  1.90581  5.44420  .190580  1.88957  .188954
NatCon:e+9/f3F  .005405  .000154  .000054  .000002   .5E-06   .2E-07   .8E-06   .8E-08
ThrDif:ft^2/Hr  .628250  4.83718  6.33047  48.5297  63.3568  485.456  62.2788  622.988
SurfTn:lbm/s^2   .0E+00   .0E+00   .0E+00   .0E+00   .0E+00   .0E+00   .0E+00   .0E+00
Dielec:         1.00700  1.00075  1.00062  1.00007  1.00006  1.00001  1.00006  1.00001
Comp|T:1/psia   .002221  .066707  .022221  .666707  .222222  6.66671  .666692  6.66669
   Z:           1.00038   .99940  1.00004   .99994  1.00001  1.00000   .99997  1.00000
PROPERTY UNITS\ Pt 1     Pt 2     Pt 3     Pt 4     Pt 5     Pt 6     Pt 7     Pt 8

                          IMPULSE Engineering
                  STEAM'92/PC v3.2 (C) 1991 B.R.Strong,Jr.,PE.

 PgUp to return to properties.
```

A New Constitutive Model for Several Metals Under Arbitrary Temperature and Loading Conditions

P. W. Whaley
Department of Mechanical Engineering,
Oklahoma Christian University
of Science and Arts,
Oklahoma City, OK 73136

A new theory of viscoplasticity is described that models yielding as a random phenomenon. A circle on the deviatoric stress plane represents the intensity of yielding with the radius equal to the random yielding microstress. This random model does not utilize a yield surface; yielding intensity is quantified by expected values defined in the deviatoric stress plane. The circle in the deviatoric stress plane with a random radius is a simple way to model multi-axial loading. Approximations for stress, strain energy density, and plastic strain energy density are used to improve the computational efficiency of parameter selection and to quantify the flow criterion. The exact state equations are derived, which can be manipulated to describe a wide variety of loading conditions for a broad temperature range. Reversed loading, stress relaxation, creep, and nonproportional loading are all natural properties of the model, which require little additional elaboration. Material properties were specified for five metals, three at room temperature and two over a wide temperature range.

Introduction

Unified constitutive theories of viscoplasticity attempt to model all inelastic deformation by a single mechanism. This approach leads to a set of state variables that have physical meaning in the microstructure and are not totally phenomenological. While a curve fit is usually necessary in order to determine required parameter values, unified theories of viscoplasticity typically include portions that have been derived from basic principles. For a discussion of various theories of viscoplasticity, the interested reader should consult Lindholm et al. (1984) or Freed et al. (1991).

The constitutive theory described in this paper models yielding as a random process in the deviatoric stress plane. This approach was introduced by Whiteman (1959), and a random model for molecular bond breakage has also been used to model fatigue damage by Altus (1991). When the process of yielding is assumed to be random, there will be no yield surface and yielding is quantified using expected values. Yielding intensity is modeled by the radius of a circle on the deviatoric stress plane. The radius of the circle is equal to the random yielding microstress. Instead of applying traditional differential concepts as in continuum mechanics, expected value concepts are used to transform equations in the microdomain to the mesodomain.

Contributed by the International Gas Turbine Institute and presented at the 38th International Gas Turbine and Aeroengine Congress and Exposition, Cincinnati, Ohio, May 24–27, 1993. Manuscript received at ASME Headquarters March 17, 1993. Paper No. 93-GT-317. Associate Technical Editor: H. Lukas.

The properties of the random yielding microstress are described by a probability distribution function, and yielding intensity gradually increases with increasing load. Using a random model for yielding implies some theoretical scatter in stress–strain data. There is a theoretical yield stress, which is the expected value of the random yielding microstress. This approach is intuitively pleasing since nonzero yielding intensity at low stress levels is consistent with fatigue failure, which can result from loading well below the 0.2 percent yield stress of the material.

Overview of Random Yielding

Three domains of material response are used to relate continuum mechanics to the dynamic response of the microstructure, as illustrated in Fig. 1. The macrodomain is the familiar scale of continuum mechanics. The microdomain is the scale of the material microstructure. It is a fundamental goal of constitutive modeling to develop a reliable relationship between the macrodomain and the microdomain. The mesodomain is an intermediate scale and provides the relationship between the microdomain of material science and the macrodomain of continuum mechanics (Haritos et al., 1988).

A population of micro-elements in the mesodomain is used to develop constitutive equations for mechanical response in the macrodomain. State equations are derived in the microdomain for the micro-element of Fig. 1(*c*), and expected value concepts are used to transform the equations

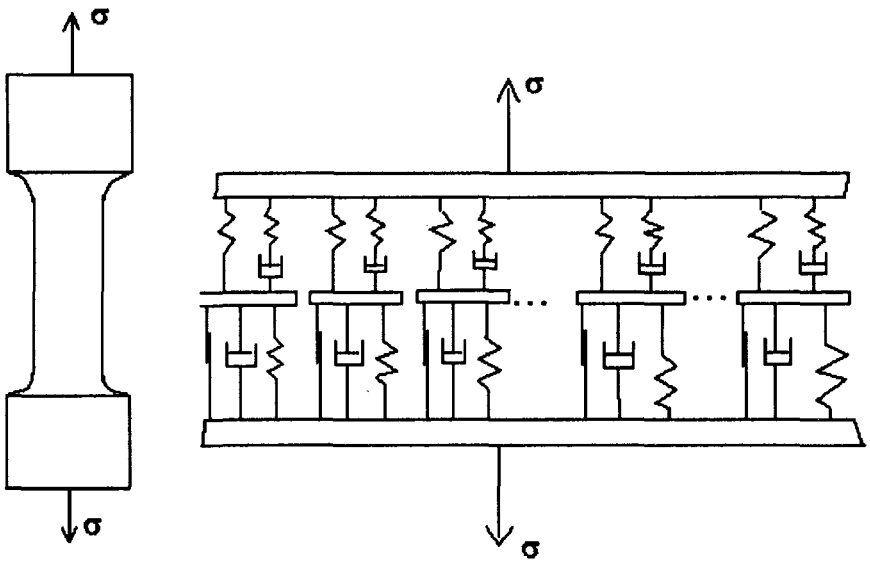

(a) Macrodomain of Materials Testing (b) Population of Microelements in the Mesodomain

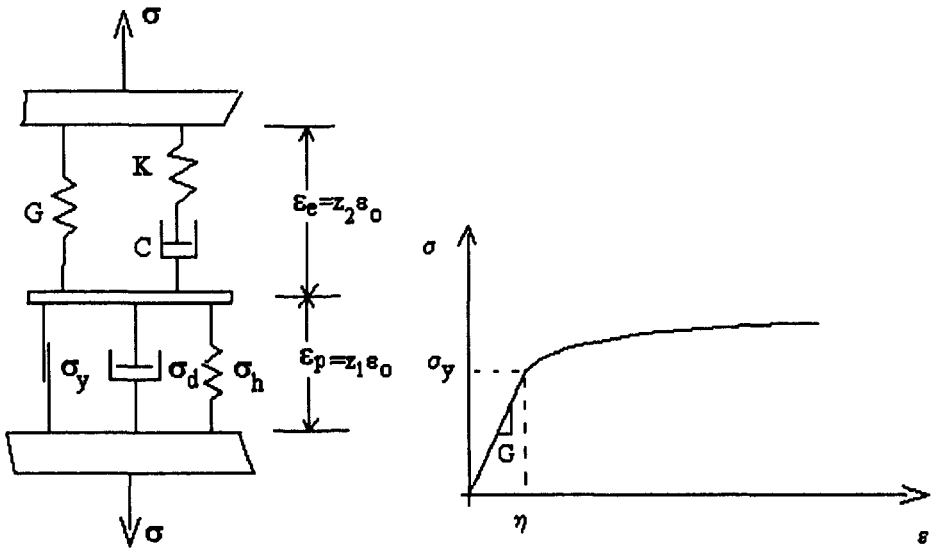

(c) Microdomain Model for one Microelement (d) Microstress Response of one Microelement

Fig. 1 Schematic diagram illustrating the three scale domains used in the constitutive model for metals based on random yielding in the deviatoric stress plane

Nomenclature

A = strain hardening function used in Eq. 2(b)
E = elastic modulus
G = shear modulus
P = probability distribution function of random yielding defined by Eq. (1)
W = deviatoric strain energy density
W_p = deviatoric plastic strain energy density
W_c = critical deviatoric plastic strain energy density
Y_h = strain hardening parameter used in Eq. (2)
z_1 = state variable that models normalized plastic strain = ϵ_p/ϵ_0
z_2 = state variable that models elastic portion of post-yielded normalized strain = ϵ_e/ϵ_0
z_3 = state variable that models normalized stress contribution of yielded elements
z_4 = state variable that models normalized stress contribution of unyielded micro-elements
ϵ_0 = log mean of normalized random yielding microstress
η = normalized random yielding microstress used in Eq. (1)
θ = absolute temperature
μ = normalized strain
μ_p = normalized plastic strain
ν = Poisson ratio
σ_d = strain-rate sensitivity microstress function given in Eq. (3)
σ_h = strain hardening microstress function given in Eq. (2a)
σ_y = random yielding microstress as illustrated in Fig. 1(d)
ψ = standard deviation of random yielding microstress

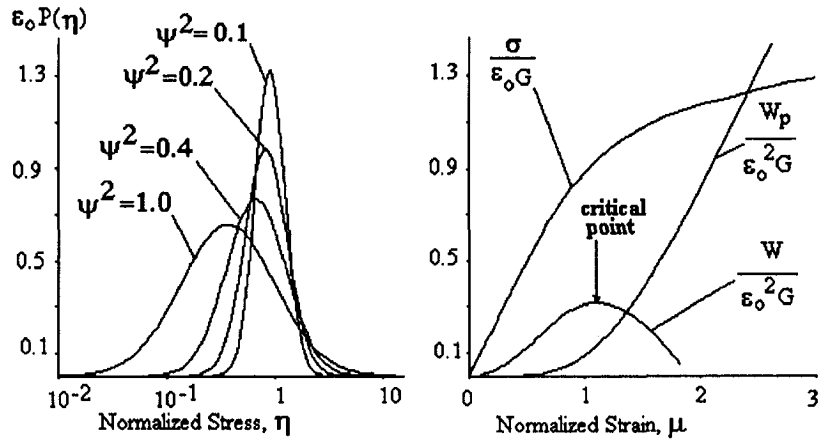

(a) Probability Distribution of Yielding

(b) Expected Values for Stress and Strain energy Densities

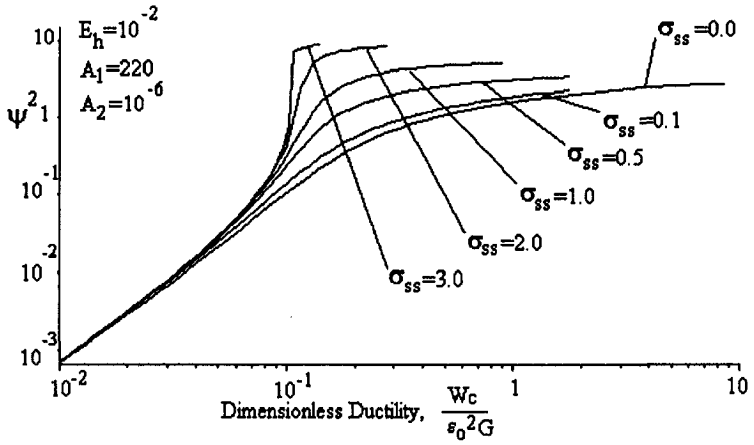

(c) Relationship Between Yielding Variance and Critical Plastic Deviatoric Strain Energy Density, Including the Influence of Loading Rate in the Variable σ_{SS} Given in Equation (6)

Fig. 2 Analysis of the variance of random yielding based on the assumption that plastic strain energy dissipation at the critical point is a material property

to the mesodomain. Figure 1 suggests that the mesodomain includes a statistically significant number of micro-elements, giving the mesodomain a mathematical meaning rather than a physical one.

The inelastic mechanisms described by this model can be conveniently organized into three areas: random plastic deformation, strain hardening, and strain-rate sensitivity. Each micro-element in Fig. 1 is composed of the nonlinear strain hardening function, σ_h, the viscoplastic strain-rate function, σ_d, and the random yielding microstress, σ_y, in addition to the elastic constants.

The probability distribution function for the random yield stress is assumed to be log normal (Whiteman, 1959). Two parameters are required: the variance of the random yielding, ψ^2, and the log mean of the dimensionless random yielding microstress, ϵ_0. It is convenient to normalize the analysis using ϵ_0, where the normalized random yielding microstress is defined as $\eta = \sigma_y/(\epsilon_0 G)$. The normalized log-normal probability distribution function used in this research is:

$$\epsilon_0 P(\eta) = \frac{\exp\left[-\log(\eta)^2/2\psi^2\right]}{\psi\eta\sqrt{2\pi}} \qquad (1)$$

This equation can be used to model a broad range of material behavior, as illustrated in Fig. 2(*a*). When the variance is small, yielding is concentrated around ϵ_0 and the response is very brittle. This means that yielding would occur very suddenly and the ultimate stress is indistinguishable from the yield stress. As ψ increases, yielding becomes more distributed and the material is ductile. This implies that the variance is a material property and also a function of temperature.

The random model for plastic deformation provides a gradually decreasing slope of the stress–strain curve for ductile materials, as described by Whiteman (1959). This means that strain hardening is a natural part of the random model for yielding in ductile materials. However, for brittle materials, the random approach is more like the elastic–perfectly plastic case of classical plasticity theory. Therefore a strain hardening function is needed to model the slope of the stress–strain curve when yielding is fully developed. The function used for σ_h is:

$$\sigma_h = Y_h A\left[1 - \exp\left(-\frac{|\mu_p|}{A}\right)\right]\text{sign}(\mu_p) \qquad (2a)$$

$$A = A_1 \exp(-A_2 W_p) \qquad (2b)$$

The deviatoric plastic strain energy density is W_p, and the normalized plastic strain is $\mu_p = \epsilon_p/\epsilon_0$, where the plastic strain is ϵ_p. Equation (2*a*) is quite versatile using just two

parameters. Y_h is the slope of the stress–strain curve in the fully yielded condition, when the plastic strain is small or when A is large. For those materials with approximately constant slope of the stress–plastic strain curve, A should therefore be large. Equation (2*b*) is a model for changes in strain hardening as plastic strain energy density accumulates. This permit substantial modeling flexibility using just three parameters: Y_h, A_1, and A_2.

The response of most metals is a function of the rate of the applied loading. This is the plastic strain rate sensitivity function, σ_d. The function used for σ_d is the inverse hyperbolic sine function after Sherby and Miller (1979):

$$\sigma_d = C_1 \sinh^{-1}\left(C_2 \mid \dot{\mu}_p \mid^{\beta}\right)^{\gamma} \operatorname{sign}\left(\dot{\mu}_p\right) \tag{3}$$

Four parameters provide enough flexibility for most situations; C_1, C_2, β, and γ. When the argument of the inverse hyperbolic sine function is small, Eq. (3) reduces to a power law.

These are the nine parameters that must be determined: three parameters for the strain-hardening stress function; four parameters for the strain-rate sensitivity stress function; and two parameters for random yielding. All of these parameters may be functions of temperature. The strain hardening and strain-rate sensitivity parameters can be estimated from stress–strain data at various strain rates and temperatures. As a first approximation, 0.2 percent yield stress data can be used to estimate the mean of random yielding. The variance can be determined by curve fitting to the shape of the stress–strain curve at moderate strain rates. First, however, it is necessary to decide how the variance should be modeled.

The variance of random yielding quantifies the degree of ductility in the response as shown in Fig. 1(*a*), and is related to the flow criterion of classical plasticity theory as well as to the strain energy release rate from classical fracture mechanics. Of course, the variance could be approximated by a phenomenological function of temperature. However, in the context of a flow criterion a more basic definition is desired. The amount of plastic deformation a material is able to withstand before fully developed yielding occurs would be a better flow criterion. The onset of plastic deformation is assumed to occur when the deviatoric strain energy density function reaches a maximum value. This analysis is described in the next section.

Analysis of the Variance of Yielding

Since the micro-element in Fig. 1 is composed of mechanical springs and dampers, equations for stress, strain energy density, and plastic strain energy density can be derived in a straight-forward manner. The derivation follows the approach used by Whiteman (1959), with the addition of strain hardening and strain-rate sensitivity as described in the previous section. Since the strain-rate sensitivity makes the response a function of strain rate as well as strain, the dynamic microstress will be approximated as a function of the micro plastic strain. First, σ_d and σ_h are linearized at a particular operating point:

$$C_\ell = C_1 C_2 \beta\gamma \frac{\sinh^{-1}\left(C_2 \dot{\mu}_p^{\beta}\right)^{\gamma-1}}{\sqrt{1 + \left(C_2 \dot{\mu}_p^{\beta}\right)^2}} \dot{\mu}_p^{\beta-1} \tag{4}$$

$$K_\ell = Y_h \exp\left(-\frac{\mu}{A}\right)\int_0^{\mu} \exp\left(\frac{\eta}{A}\right) P(\eta)d\eta \tag{5}$$

Then the dynamic microstress is approximated by solving for the response in the nonlinear part of the yielded micro-elements. The equivalent dynamic microstress as a function of normalized strain is σ_{ss}:

$$\sigma_{ss} = C_1 \sinh^{-1}\left(C_2 \dot{\mu}^{\beta}\right)^{\gamma}\left[1 - \exp\left(-\frac{\mu - \eta}{B}\right)\right] \tag{6}$$

$$B = \frac{C_\ell}{Y + K_\ell}$$

The normalized strain is $\mu = \epsilon/\epsilon_0$, where ϵ is the local deviatoric strain.

For most metals the Zener thermoelastic damping is much smaller than the energy dissipated by plastic deformation, so it is reasonable to neglect the linear dashpot constant, C, in the linear part of the micro-element of Fig. 1(*c*). The elastic part of the fully yielded strain is also neglected. The dynamic stress response is the sum of the response of those micro-elements that have yielded and those micro-elements that have not yielded. The total deviatoric stress in the macrodomain is:

$$\begin{aligned}\frac{\sigma}{\epsilon_o G} = {} & \mu\left[1 - \int_0^{\mu} P(\eta)d\eta\right] + \int_0^{\mu} \eta P(\eta)d\eta \\ & - Y_h A \exp\left(-\frac{\mu}{A}\right)\int_0^{\mu} \exp\left(\frac{\eta}{A}\right) P(\eta)d\eta \\ & + Y_h A \int_0^{\mu} P(\eta)d\eta + \sigma_{ss}\int_0^{\mu} P(\eta)d\eta \\ & - \sigma_{ss} \exp\left(-\frac{\mu}{B}\right)\int_0^{\mu} \exp\left(\frac{\eta}{B}\right) P(\eta)d\eta\end{aligned} \tag{7}$$

The first two terms of Eq. (7) are identical to the stress equation derived by Whiteman. That is as expected since Whiteman neglected strain hardening and strain rate sensitivity. Figure 2(*b*) shows a plot of Eq. (7) for a variance of 0.2. Gaussian quadrature was used to calculate the expected value integrals.

The deviatoric strain energy density function can be easily calculated based on the micro-elements of Fig. 1. The contributions from the yielded and unyielded micro-elements are added together to give the total deviatoric strain energy density:

$$\begin{aligned}\frac{W}{e_o^2 G} = {} & \frac{1}{2}\mu^2\left[1 - \int_0^{\mu} P(\eta)d\eta\right] + \frac{3}{2}\int_0^{\mu} \eta^2 P(\eta)d\eta \\ & - \mu\int_0^{\mu} \eta P(\eta)d\eta - Y_h A\int_0^{\mu} \eta P(\eta)d\eta \\ & + Y_h A^2 \exp\left(-\frac{\mu}{A}\right)\int_0^{\mu} \exp\left(\frac{\eta}{A}\right) P(\eta)d\eta \\ & + Y_h A(\mu - A)\int_0^{\mu} P(\eta)d\eta \\ & + \sigma_{ss}\int_0^{\mu} \eta P(\eta)d\eta - \sigma_{ss}(\mu - B)\int_0^{\mu} P(\eta)d\eta \\ & - \sigma_{ss} B \exp\left(-\frac{\mu}{B}\right)\int_0^{\mu} \exp\left(\frac{\eta}{B}\right) P(\eta)d\eta\end{aligned} \tag{8}$$

Equation (8) is also plotted in Fig. 2(*b*), showing the critical point where the deviatoric strain energy density function reaches a maximum value. Since loading past this critical point results in a decrease in strain energy density, the strain begins to increase rapidly without substantial corresponding increase in stress. This is a good definition of fully developed plastic flow. The critical point can be determined by taking the derivative of the deviatoric strain energy density:

$$\frac{dW/d\mu}{\epsilon_0^2 G} = \mu\left[1 - \int_0^\mu P(\eta)d\eta\right] - \int_0^\mu \eta P(\eta)d\eta$$
$$- Y_h A \exp\left(-\frac{\mu}{A}\right)\int_0^\mu \exp\left(\frac{\eta}{A}\right)P(\eta)d\eta$$
$$+ (Y_h A - \sigma_{ss})\int_0^\mu P(\eta)d\eta$$
$$+ \sigma_{ss} \exp\left(-\frac{\mu}{B}\right)\int_0^\mu \exp\left(\frac{\eta}{B}\right)P(\eta)d\eta \quad (9)$$

The critical point can be determined using this equation, but does not directly quantify the amount of plastic dissipation in the material at yielding.

The amount of plastic strain energy dissipated at the onset of yielding is assumed to be a constant. The deviatoric plastic strain energy density is:

$$\frac{W_p}{\epsilon_0^2 G} = \mu\phi\eta P(\eta)d\eta - \phi\eta^2 P(\eta)d\eta \quad (10)$$

Since plastic deformation is path dependent, contour integrals are required in Eq. (10). Equation (10) is also plotted in Fig. 2(*b*). The critical plastic strain energy density can be determined by combining Eqs. (9) and (10):

$$\frac{W_c}{\epsilon_0^2 G} = \mu_c\int_0^{\mu_c} \eta P(\eta)d\eta - \int_0^{\mu_c} \eta^2 P(\eta)d\eta \quad (11)$$

The critical plastic strain energy density, W_c, is a function of temperature, and depends on the variance of random yielding. Figure 2(*c*) is a plot of the yielding variance versus the dimensionless critical plastic strain energy density given in Eq. (11). Equations (7)–(11) are in dimensionless form to generalize the effect of ductility on the variance of random yielding. Equation (11) combines all sources of ductility in one dimensionless variable and Fig. 2(*c*) shows how the variance can be determined from that one ductility variable. Figure 2(*c*) also shows the influence of loading rate on the variance, which gives the response a strain-rate history sensitivity.

With W_c, ϵ_0, and G specified as functions of temperature, ψ^2 can be calculated from temperature dependent material properties. This method for modeling the variance is superior to a phenomenological equation for ψ^2, since a dimensionless quantity is used to combine all sources of ductility into one variable. The dimensionless number on the left side of Eq. (11) is called the dimensionless ductility.

To summarize, the nine parameters that must be determined as functions of temperature are: the mean of random yielding, the critical plastic strain energy density used to model the variance as illustrated in Fig. 2(*c*), the three strain hardening parameters, and the four strain-rate sensitivity parameters. Once these parameters are known, the response due to arbitrary loading and temperature history can be calculated. This requires the exact state equations, developed in the next section.

State Equations

The equations used in the previous section to define the dimensionless ductility function are usually sufficiently accurate for calculating the stress at fully developed plastic flow. Those equations are exact when the strain rate sensitivity is negligible, and are very important for efficient curve-fitting procedures. However, the exact state equations are needed for more accurate predictions. All of the calculations in the previous section were in the normalized deviatoric stress plane, but general multi-axial loading is required for response predictions. Transformations from the normalized deviatoric stress plane are routine. The component of loading normal to the yielding intensity circle in the deviatoric stress plane gives rise to plastic deformation, independent of the tangential loading direction. The component of loading in the tangential loading direction does not influence plastic deformation.

Four state equations are necessary to describe the response. The total strain is $\mu = z_1 + z_2 + \eta$, where η is the random normalized microslip stress as illustrated in Fig. 1(*d*). Referring to Fig. 1(*c*), the first state equation comes from applying a stress balance in the yielded micro-elements and solving for the plastic strain rate, dz_1/dt:

$$\frac{dz_1}{dt} = \left[\frac{1}{C_2}\sinh\left(\frac{|\sigma_d|}{C_1}\right)^{1/\gamma}\right]^{1/\beta} \text{sign}(\sigma_d) \quad (12)$$

Equation (12) is just the inverse relationship for the strain-rate-dependent microstress, which is:

$$\sigma_d = z_3 - \int_0^{z4} \eta P(\eta)d\eta - Y_h A\int_0^{z4} P(\eta)d\eta$$
$$- Y_h A \exp\left(-\frac{\mu - z_2}{A}\right)\int_0^{z4} \exp(\eta/A)P(\eta)d\eta$$

The second state equation is the strain rate balance:

$$\frac{dz_2}{dt} = \frac{d\mu}{dt} - \frac{dz_1}{dt} \quad (13)$$

The third state equation comes from the linear differential equation in the elastic portion of the yielded micro-elements:

$$\frac{dz_3}{dt} = \left[-z_3 + z_2\int_0^{z4} P(\eta)d\eta + \int_0^{z4} \eta P(\eta)d\eta\right]\frac{K}{C}$$
$$+ \left(1 + \frac{K}{Y}\right)\int_0^{z4} P(\eta)d\eta \frac{dz_2}{dt} \quad (14)$$

The fourth state equation comes from the linear differential equation in the elastic portion of the unyielded micro-elements:

$$\frac{dz_4}{dt} = [-z_4 + \mu]\frac{K}{C} + \left[1 + \frac{K}{Y}\right]\frac{d\mu}{dt} \quad (15)$$

The normalized stress in the macrodomain consists of the contributions of the unyielded and yielded micro-elements:

$$\frac{\sigma}{\epsilon_0 G} = z_3 + z_4\left[1 - \int_0^{z4} P(\eta)d\eta\right] \quad (16)$$

These four state equations can be integrated to calculate stress and strain as a function of strain rate. Since the Zener thermoelastic damping is much smaller than the energy dissipated by plastic deformation, C is assumed to be much smaller than K as before. This gives the following simplification:

$$z_4 = \mu \quad (17)$$

$$z_3 = z_2\int_0^\mu P(\eta)d\eta + \int_0^\mu \eta P(\eta)d\eta \quad (18)$$

These state equations are not dependent on assumptions about loading history. Needed elaborations for cyclic loading and creep are described next.

Cylic Loading. The cyclic loading condition without strain hardening or strain-rate sensitivity has already been derived by Whiteman (1959), who described a change in the probability structure. When the loading is reversed, the elastic strain portion is released so that the initial portion of the unloading

is elastic. At the fully reversed loading condition, all the micro-elements will have yielded in the opposite direction. This requires a transformation of variables used in describing the expected values. The following defintions are used:

σ_i = stress at which ith strain rate reversal occurs
η_i = normalized random yielding microstress at the ith strain-rate reversal
μ_i = normalized strain at which ith strain-rate reversal occurs
z_{1i} = normalized plastic strain at which ith strain-rate reversal occurs
z_{2i} = elastic portion of post-yielded normalized strain at which ith strain-rate reversal occurs

The change in the probability structure of random yielding is modeled by introducing the following transformations for the ith strain rate reversal:

$$\eta_m = \frac{[\eta_i - \text{sign}(\eta_i)\eta]}{2} \tag{19}$$

$$\mu_m = \frac{[\mu_i - \text{sign}(\mu_i)\mu]}{2} \tag{20}$$

$$z_{1m} = \frac{[z_{1i} - \text{sign}(z_{1i})z_1]}{2} \tag{21}$$

$$z_{2m} = \frac{[z_{2i} - \text{sign}(z_{2i})z_2]}{2} \tag{22}$$

$$z_{3m} = \frac{[z_{3i} - \text{sign}(z_{3i})z_3]}{2} \tag{23}$$

$$z_{4m} = \frac{[z_{4i} - \text{sign}(z_{4i})z_4]}{2} \tag{24}$$

The state equations are modified to reflect these definitions by substituting η_m for η, μ_m for μ, z_{1m} for z_1, z_{2m} for z_2, z_{3m} for z_3 and z_{4m} for z_4. The stress is calculated by introducing the ith amplitude weighting constant, α_i:

$$\sigma_i = \alpha_i\left\{z_3 + z_4\left[1 - \int_0^{z_4} P(\eta_m)d\eta_m\right]\right\} \tag{25}$$

In Eq. (25) the weighting constant is:

$$\alpha_1 = 2$$

$$\alpha_i = 1 + \frac{|\sigma_{i-1}|}{|\sigma_i|}, \quad i \geq 2$$

The expected value integrals must be re-initialized at each strain-rate reversal. For symmetric hysteresis loops, $\alpha_i = 2$ for all i, in agreement with Whiteman's analysis.

Gaussian quadrature was used for the expected value integrals and the fourth-order Runge–Kutta algorithm was used for the state equations. The following variable step size was used as a guideline to improve numerical integration efficiency and stability:

$$\Delta t = B_0 \frac{C_\ell}{K_\ell}, \quad 10^{-2} \leq B_0 \leq 10^{-1}$$

These equations describe strain-controlled loading. Uniaxial loading is modeled by specifying a strain rate. Stress relaxation can be modeled by loading to some strain, then setting strain rate to zero.

Creep Response. The creep response can be calculated by solving for the response of the state equations when stress is specified. This condition can be determined by taking the derivative of Eq. (16):

$$\frac{1}{\epsilon_0 G}\frac{d\sigma}{dt} = \frac{dz_3}{dt} + \frac{dz_4}{dt}\left[1 - \int_0^{z_4} P(\eta)d\eta - z_4 P(\mu)\right] \tag{26}$$

Defining creep as a stress-controlled process, the applied stress rate is to be specified. During the initial loading phase of creep, a stress rate, $d\sigma/dt$, is specified. When the stress reaches the desired level, the stress rate is specified as zero and the resulting strain is calculated. Using Eqs. (17) and (18), the strain rate equation is:

$$\frac{d\mu}{dt} = \frac{\left[\frac{1}{\epsilon_0 G}\frac{d\sigma}{dt} + \frac{dz_1}{dt}\int_0^{\mu} P(\eta)d\eta\right]}{[1 + z_2 P(\mu)]} \tag{27}$$

Equations (12) and (13) can be combined with Eq. (27) to determine the strain response to constant stress. In the next section temperature dependence of the parameters is examined.

Temperature Dependence of Parameters

Nine parameters, in addition to elastic constants, have been identified in the previous sections, and all of them could be functions of temperature. The temperature dependence of the elastic modulus is described by the following equation:

$$E = Y_1 - \frac{Y_2}{\exp(Y_3/\theta) - 1} \tag{28}$$

This equation is a theoretical relationship as described by Varshni (1970) and used by many other researchers (Ledbetter, 1982). The parameters Y_1, Y_2, and Y_3 can be easily determined by least-square curve fitting, since the logarithm of E gives a linear relation for Y_1, Y_2, and Y_3. Temperature-dependent modulus data are available for aluminum (Sutton, 1953), for steel (Everett and Miklowitz, 1944), for titanium (Follansbee and Gray, 1989), and for B1900 + HF (Lindholm et al., 1985), as well as many other metals (Ledbetter, 1982). For this paper, the Poisson ratio was assumed to be constant.

The remaining parameters were modeled by the following phenomenological equations:

$$Y_{ft} = Y_4 \exp\left[Y_5(\theta/273)^{Y_6}\right] \tag{29}$$

$$A_1 = Y_7 \exp\left[Y_8(\theta/273)^{Y_9}\right] \tag{30}$$

$$\epsilon_0 = Y_{10} \exp\left[Y_{11}(\theta/273)^{Y_{12}}\right] \tag{31}$$

$$W_c = Y_{13} \exp\left[Y_{14}(\theta/273)^{Y_{15}}\right] \tag{32}$$

$$C_1 = Q_1 \exp\left[Q_2(\theta/273)^{Q_3}\right] \tag{33}$$

$$C_2 = Q_4 \exp\left[Q_5(\theta/273)^{Q_6}\right] \tag{34}$$

$$\beta = Q_7 \exp\left[Q_8(\theta/273)^{Q_9}\right] \tag{35}$$

$$\gamma = Q_{10} \exp\left[Q_{11}(\theta/273)^{Q_{12}}\right] \tag{36}$$

The strain-hardening parameter, A_2, was assumed to be constant for this study.

Twenty-eight parameters must be determined for each material, in order to model temperature dependence. The parameter selection procedure consists of five parts, four of which are iterative, as outlined in Fig 3. First, the temperature dependence of the elastic modulus is determined by least-squared error curve fitting. The second part is the selection of the strain hardening parameters and it is usually routine, although some alloys require iterations on the strain-hardening constant since random yielding also con-

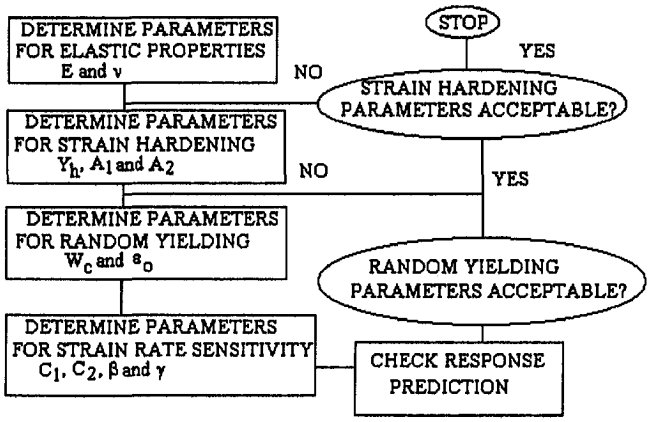

Fig. 3 Flow chart for selecting parameters at a single temperature

Table 1 Parameter selections for five metals

Parameter	1100-O Aluminum	1020 Steel	Pure Titanium	B1900+Hf	Titanium Aluminide
ν	0.33	0.33	0.33	0.335	0.3
Y_1	$80.1x10^9$	$199.0x10^9$	$131.4x10^9$	$199.0x10^9$	$100.4x10^9$
Y_2	$10.7x10^9$	$2.14x10^4$	$11.7x10^9$	$686.6x10^9$	$189.4x10^9$
Y_3	$2.53x10^2$	$6.51x10^3$	$1.98x10^2$	$2.94x10^3$	$1.45x10^3$
Y_4	$2.2x10^{-2}$	$2.8x10^{-1}$	$9.0x10^{-3}$	$7.38x10^{-3}$	$3.88x10^{-2}$
Y_5	---	---	---	$-3.34x10^{-5}$	$6.06x10^{-3}$
Y_6	---	---	---	6.83	3.82
Y_7	$2.20x10^2$	$2.2x10^2$	$1.0x10^2$	$3.06x10^{-2}$	$1.0x10^2$
Y_8	---	---	---	-0.865	---
Y_9	---	---	---	-2.65	---
Y_{10}	$2.98x10^{-4}$	$1.25x10^{-3}$	$3.47x10^{-3}$	$4.65x10^5$	$1.02x10^{-2}$
Y_{11}	---	---	---	$-1.58x10^{-4}$	$-1.71x10^{-6}$
Y_{12}	---	---	---	6.38	7.13
Y_{13}	$1.08x10^3$	$1.17x10^4$	$5.91x10^4$	$1.33x10^2$	$2.47x10^5$
Y_{14}	---	---	---	$-1.24x10^{-5}$	$-1.01x10^{-2}$
Y_{15}	---	---	---	7.41	3.42
A_2	10^{-6}	1.6	10^{-4}	10^{-4}	10^{-4}
Q_1	$4.66x10^{-2}$	0.674	0.713	0.394	$7.31x10^{-2}$
Q_2	---	---	---	$-1.09x10^4$	$7.58x10^{-3}$
Q_3	---	---	---	-7.96	3.18
Q_4	$8.22x10^{-2}$	$2.18x10^{-2}$	$1.53x10^{-2}$	$1.50x10^5$	$1.02x10^2$
Q_5	---	---	---	$-2.10x10^{-6}$	$-3.39x10^{-6}$
Q_6	---	---	---	9.16	6.63
Q_7	0.471	0.302	0.104	0.673	0.116
Q_8	---	---	---	$-3.54x10^4$	$6.74x10^{-4}$
Q_9	---	---	---	-7.82	5.30
Q_{10}	1.0	1.0	1.0	2.16	1.0
Q_{11}	---	---	---	$-1.92x10^{-6}$	---
Q_{12}	---	---	---	7.52	---

tributes to strain hardening. Random yielding parameters require the most trial and error, while the strain-rate sensitivity parameters are determined by least-squared error curve fitting. These parameters must be determined for at least three temperatures, and then a final least-square error curve fit is required to determine the temperature dependence.

The initial estimate for ϵ_0 is a least-squared error curve fit using yield stress data for the zero strain-rate loading case. Both W_c and ϵ_0 require iterations since they control strain rate history effects. Figure 3 outlines the procedure required to determine parameters at a particular temperature.

When an estimate for all the other parameters is available, C_1, C_2, β and γ are determined at a particular temperature by least-squared error curve fitting. The procedure begins by setting β to unity and selecting C_2 such that the argument of the hyperbolic sine function is unity at a very high strain rate. Then C_1 and γ are determined by a least-square curve fit to the two or three lowest strain rates. If the strain-rate sensitivity follows a power law pattern, then this set of parameters is very close to the final values. In order to control the parameter searching pattern, C_2 is adjusted by changing the value of strain rate where the argument of the hyperbolic sine function becomes unity using the relationship:

$$\left(C_2 \dot{\mu}_u^{\beta}\right)^{\gamma} = 1$$

Using the lowest strain-rate data when power law behavior is more likely, $\beta\gamma$ will be a constant; β is therefore adjusted such that $\beta\gamma$ is constant. Once a suitable estimate of the four parameters has been completed, the least-squared error curve fit is made using the following steps:

1 Curve fit C_1 and γ using the lowest two or three strain-rate data points while holding C_2 and β constant.
2 Curve fit β while holding $\beta\gamma$ and $d\mu_u/dt$ constant, using all of the available strain-rate data.
3 Curve fit $d\mu_u/dt$ while holding $\beta\gamma$ constant, using all of the available strain-rate data.
4 Return to step 1 with the updated parameter values if the error has not yet reached the minimum.

These steps outline an iterative procedure, which must be repeated for each trial value of W_c and ϵ_0. The resulting parameter values for several metals are listed in Table 1.

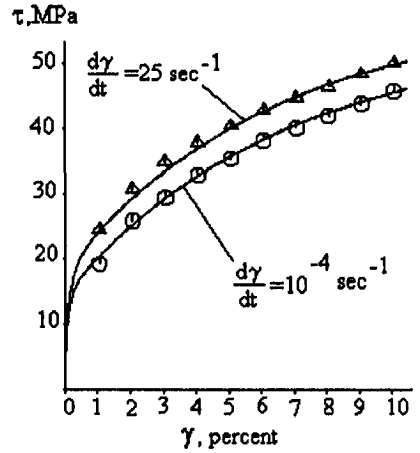

Fig. 4 Shear stress versus shear strain in 1100-O aluminum at room temperature; symbols indicate data from Nicholas (1971) used in the curve fitting

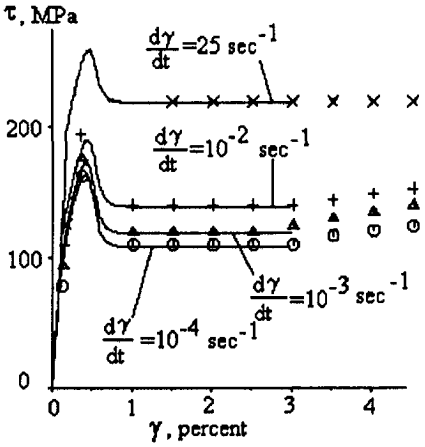

Fig. 5 Shear stress versus shear strain in 1020 steel at room temperature; symbols indicate data from Nicholas (1971) used in the curve fitting

Results

In Figs. 4–9, solid lines are response predictions of the model and symbols are data from the literature. Figure 4 shows shear strain versus shear strain in 1100-O aluminum, where the strain-rate dependence is weak. The variance of random yielding is high in Fig. 4, as evident by the gradually

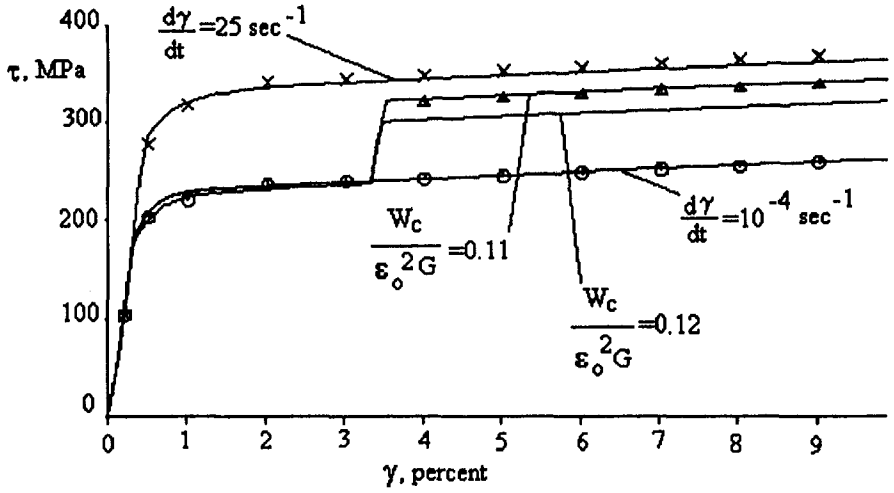

(a) Shear Stress versus Shear Strain for 50-A Titanium Showing Influence of Strain Rate History; Symbols Indicate Data From Nicholas (1971) Used in the Curve Fitting Procedure

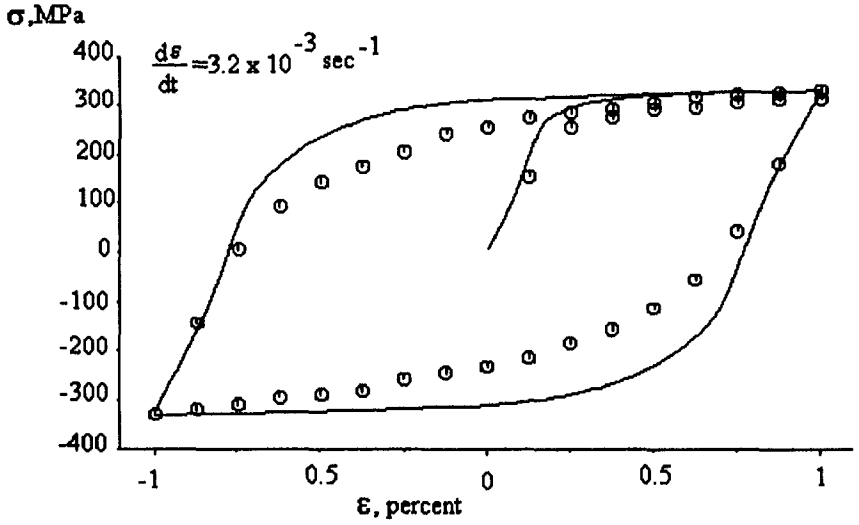

(b) Predicted Hysteresis Loop for Uniaxial Cyclic Strain Controlled Loading Based on Parameters Determined from Torsion Tests by Nicholas (1971); Symbols Indicate Data From Bodner and Partom(1979)

Fig. 6 Response calculations for 50-A titanium at room temperature showing the strain-rate history effect and hysteresis loop predictions

decreasing slope of the stress–strain curve in the fully yielded region. Figure 5 shows shear stress versus shear strain in 1020 steel where the strain rate dependence is stronger, and where strain hardening is more complicated Figures 4 and 5 show model predictions along with the data used to determine the parameters. However, Fig. 6 shows response prediction capability in 50-A titanium; part (*a*) illustrates the strain-rate history sensitivity compared with some of the data used to determine the parameters, and part (*b*) is the hysteresis loop for uniaxial strain-controlled cyclic loading. Figure 6(*a*) illustrates strain-rate history dependent response prediction, and shows why identifying W_c is subject to trial and error. Dimensionless ductilities of 0.11 and 0.12 have an insignificant effect on the stress–strain curve, while the difference in the strain rate history prediction is notable. Figure 6(*b*) is significant because it is a favorable prediction of the hysteresis loop in uniaxial tension using parameters selected by monotonic shear tests.

Figure 7 illustrates still another predictive capability for 50-A titanium. Figure 7(*a*) shows a favorable prediction of stress relaxation in commercially pure titanium, and Fig. 7(*b*) shows a prediction of the creep response. Figure 7 illustrates how the same set of state equations can be subjected to different loading conditions to predict different response patterns.

The results illustrated by Figs. 4–7 are encouraging because they illustrate the ability to model several important mechanical response patterns with parameters determined during monotonic testing. However, all of those tests were at room temperature. The model is also capable of predicting the mechanical response at various temperatures.

Figure 8 shows a typical nonproportional loading response case for B1900 + Hf. Parameters for B1900 + Hf were determined from uniaxial tension tests reported by Chan et al. (1986). Some of the strain-rate sensitive data were estimated based on strain rate jump tests. Prediction of the hysteresis loop for B1900 + Hf is also possible, although not reported here.

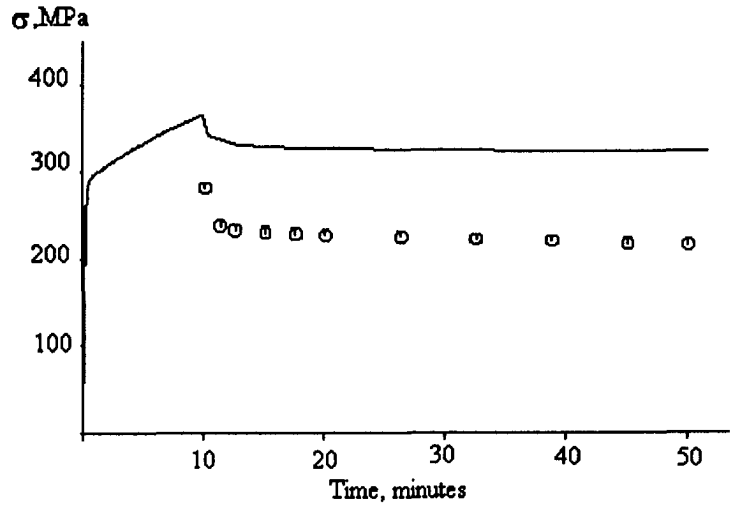

(a) Stress Relaxation Prediction in 50-A Titanium After Loading at a Uniaxial Strain Rate of 1.6×10^{-4} sec^{-1} Until Strain of 9.6 percent is Reached; Symbols Indicate Data From Bodner and Partom (1975)

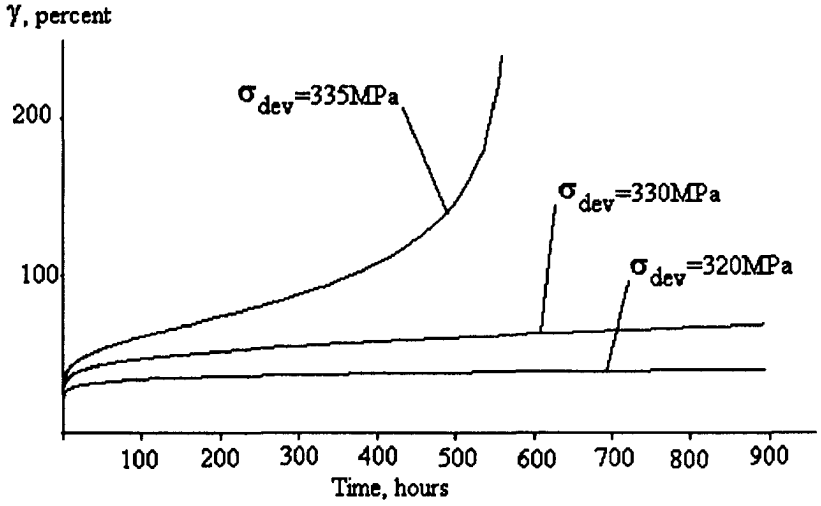

(b) Creep Predictions in 50-A Titanium for Three Deviatoric Stress Levels

Fig. 7 Stress relaxation and creep response predictions in 50-A titanium using parameters determined from the torsion data by Nicholas (1971)

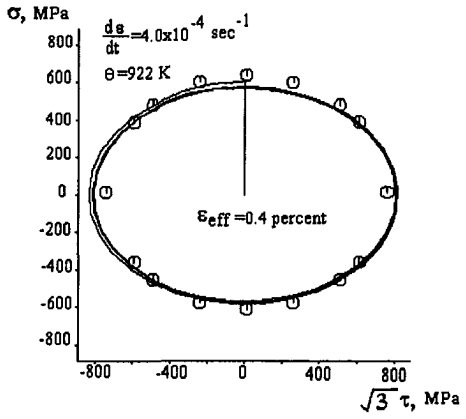

Fig. 8 Nonproportional loading for B1900 + Hf at $\theta = 922$ K, $d\epsilon/dt = 4.0 \times 10^{-4}$ s^{-1} for effective strain amplitude of 0.4 percent; symbols are data from Lindholm et al. (1985); uniaxial data from Chan et al. (1986) used to determine parameters

Figure 9 shows stress–strain curves for titanium aluminide at negligible strain rate and various temperatures. The data given in Fig. 9 were used in determining the parameters, so the agreement between the model and data is misleading.

Conclusions

A new theory of viscoplasticity has been described that models yielding as a random process. A circle on the deviatoric stress plane represents the intensity of yielding, with the radius equal to the random yield stress. Multi-axial loading is treated by the transformation of the expected values from the deviatoric stress plane to ordinary stress space.

The state equations model the response of the material to a wide variety of loading conditions. Parameter selection is typically based on uniaxial loading at constant strain rate and temperature. Once parameters are known, reversed loading, stress relaxation, creep, and nonproportional loading are all natural properties of the model, which require only minor modifications. The theory should also describe combined thermomechanical loading, but that is left to a future effort.

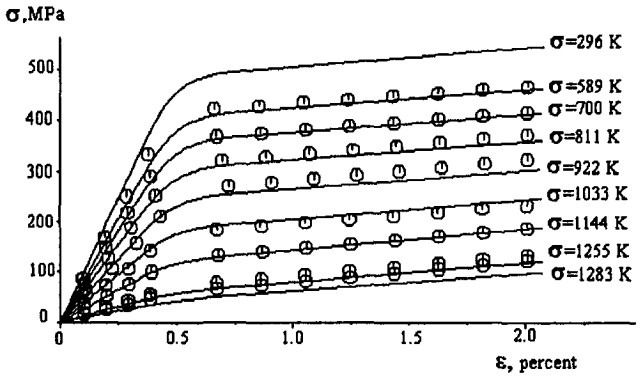

Fig. 9 Stress strain curves for titanium aluminide (Ti-24Al-11Nb) at negligible strain rate and several temperatures

Acknowledgments

Portions of this work were completed while the author was on Air Force reserve duty at the Metals and Ceramics Division, Materials and Manufacturing technology Directorate, Wright-Patterson AFB, Ohio. Data for Ti-24Al-11Nb are from published work performed at the Materials Behavior Branch.

References

Altus, E., 1991, "A Cohesive Micromechanic Fatigue Model. Part I: Basic Mechanisms," *Mechanics of Materials*, Vol. 4, No. 1, pp. 10–19.

Bodner, S. R., and Partom Y., 1975, "Constitutive Equations for Elastic-Viscoplastic Strain-Hardening Materials," ASME *Journal of Applied Mechanics*, Vol. 42, pp. 385–389.

Bodner, S. R., Partom, I., and Partom, Y., 1979, "Uniaxial Cyclic Loading of Elastic-Viscoplastic Materials," ASME *Journal of Applied Mechanics*, Vol. 46, pp. 805–810.

Chan, K. S., Lindholm, U. S., Bodner, S. R., Hill, J. T., Weber, R. M., and Meyer, T. C., 1986, "Constitutive Modeling for Isotropic Materials," NASA CR 179522.

Everett, F. L., and Miklowitz, J., 1944, "Poisson's Ratio at High Temperatures," *Journal of Applied Physics*, Vol. 15, pp. 592–598.

Follansbee, P. S., and Gray, G. T., 1989, "An Analysis of the Low Temperature, Low and High Strain-Rate Deformation of Ti-6Al-4V," *Metallurgical Transactions A*, Vol. 20a, pp. 863–874.

Freed, A. D., Chaboche, J.-L., and Walker, K. P., 1991, "A Viscoplastic Theory With Thermodynamic Considerations," *Acta Mechanica*, Vol. 90, pp. 155–174.

Haritos, G. K., Hager, J. W., Amos, A. K., Salkind, M. J., and Wang, A. S. D., 1988, "Mesomechanics: The Microstructure-Mechanics Connection," *International Journal of Solids and Structures*, Vol. 24, No. 11, pp. 1081–1096.

Ledbetter, H. M., 1982, "Temperature Behavior of Young's Moduli of Forty Engineering Alloys," *Cryogenics*, Vol. 12, pp. 653–656.

Lindholm, U. S., Chan, K. S., Bodner, S. R., Weber, R. M., Walker, K. P., and Cassenti, B. N., 1984, "Constitutive Modeling for Isotropic Materials," NASA CR 174718.

Lindholm, U. S., Chan, K. S., Bodner, S. R., Weber, R. M., Walker, K. P., and Cassenti, B. N., 1985, "Constitutive Modeling for Isotropic Materials," NASA CR 174980.

Nicholas, T., 1971, "Strain-Rate and Strain-Rate-History Effects in Several Metals in Torsion," *Experimental Mechanics*, Vol. 11, pp. 370–374.

Sherby, O. D., and Miller, A. K., "Combining Phenomenology and Physics in Describing the High Temperature Mechanical Behavior of Crystalline Solids," ASME *Journal of Engineering Materials and Technology*, Vol. 101, pp. 387–395.

Sutton, P. M., 1953, "The Variation of the Elastic Constants of Crystalline Aluminum With Temperature Between 63 K and 773 K," *Physical Review*, Vol. 91, No. 4, pp. 816–821.

Varshni, Y. P., 1970, "Temperature Dependence of the Elastic Constants," *Physical Review B*, Vol. 2, No. 10, pp. 3952–3958.

Whiteman, I. R., 1959, "A Mathematical Model Depicting the Stress–Strain Diagram and the Hysteresis Loop," ASME *Journal of Applied Mechanics*, Vol. 21, pp. 95–100.

Load Control–Strain Control Isochronous Stress–Strain Curves for High Temperature Nonlinear Analysis

G. S. Bechtel

T. S. Cook

GE Aircraft Engines,
Cincinnati, OH 45215

Aircraft gas turbine components are subjected to severe operating conditions. High temperatures, large thermal strains, and mechanical loads combine to cause the material to undergo significant nonlinear behavior. In order to assure safe, durable components, it is necessary that analysis methods be available to predict the nonlinear deformation. General purpose finite element codes are available to perform elastic and viscoplastic analyses, but the analyses are expensive. Both large plastic and creep strain analyses can require significant computer resources, but typically a plastic solution is more economical to run than a time-stepping creep or viscoplastic model solution. For those applications where the deformation is principally time dependent, it is advantageous to include time-dependent creep effects in a "constant time" or "isochronous" analysis. Although this approach has been used in the past to estimate rupture life, this paper will present several significant new techniques for doing an isochronous analysis to analyze time-dependent deformation.

Introduction

In order to assure that aircraft gas turbine components can safely undergo the loads placed on them, considerable analysis must take place. The primary approach for this analysis is the finite element method (FEM). While other methodologies are equally adept at geometric modeling, the advantage of the FEM lies in its ability to incorporate a variety of constitutive models.

The constitutive models for use in these codes are based on two different approaches. In the classical approach inelastic strains are separated into time-independent (plastic) strains and time-dependent (creep) strains. In the unified approach all inelastic strains are considered together. While there are many potential advantages of unified models, they are generally less economical in run times for structural applications. This can be particularly true for analyses that might otherwise be handled with a plasticity solution alone.

The approach to nonlinear deformation presented in this paper is based on the classical constitutive models. The technique is to include time-dependent creep effects in a "constant time" or "isochronous" analysis. Although the use of isochronous stress–strain is not new, it has principally been used to estimate long-term rupture behavior. This is because the creep–rupture stress is given by the maximum value of the isochronous stress–strain curve for that time interval (Shanely, 1957). This paper will use the isochronous curves in a general analysis context, and present several new techniques for using isochronous curves.

The deformation behavior of a material undergoing time-dependent inelastic strain (creep) may be represented in a variety of ways. The most common approach is to represent creep strain as a function of time for different levels of stress, as shown schematically in Fig. 1. Since stress is the control parameter, most models of creep deformation use this format with time as the independent variable. An alternative viewpoint is to plot the creep data as stress–strain curves with time as the control parameter. When the elastic and time-independent inelastic (plastic) strain is added to this curve, the result is a constant time or "isochronous" stress–strain curve. This is shown in Fig. 2. Isochronous stress–strain curves can be used to replace a creep problem with a plasticity problem. It should be noted that isochronous stress–strain curves are not generally applicable to transient loading conditions.

By modifying the stress–strain curve used for plasticity analysis, isochronous stress–strain curves can be used to include creep effects in finite element analyses using programs with limited creep capability. This approach can be significantly more economical than traditional time stepping approaches, and may also avoid numerical problems associated with very high creep rates. This approach has also been useful for the analysis of creep buckling problems (Kraus, 1980). A similar approach has also been used by Kim et al. (1988) to capture creep and strain rate effects in thermomechanical fatigue. In that work, the hysteresis loops produced

Contributed by the International Gas Turbine Institute and presented at the 38th International Gas Turbine and Aeroengine Congress and Exposition, Cincinnati, Ohio, May 24–27, 1993. Manuscript received at ASME Headquarters March 1993. Paper No. 93-GT-411. Associate Technical Editor: H. Lukas.

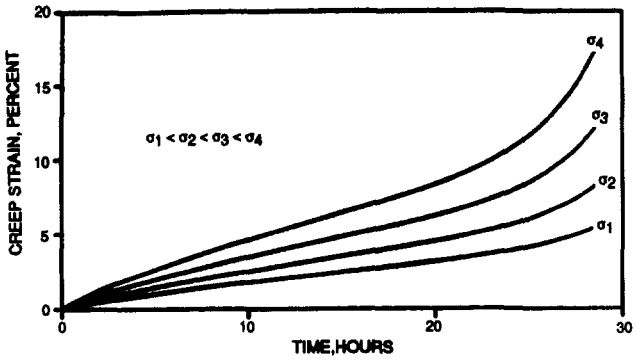

Fig. 1 Creep strain versus time for multiple stress levels

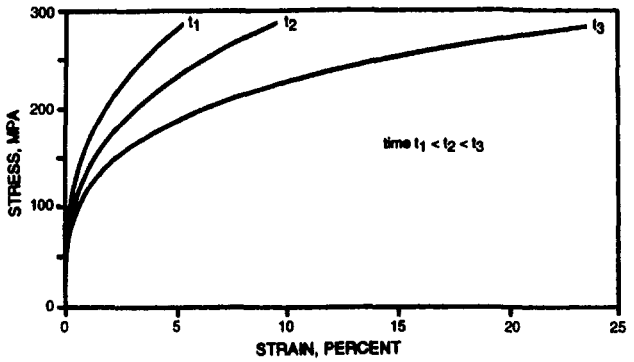

Fig. 2 Stress versus total strain for different time values (isochronous stress–strain curves)

by time stepping and by elastic–plastic analysis using the correct strain rate were compared and found to be identical.

All the finite element analyses described in this work used the nonlinear finite element program CYANIDE (CYclic ANalysis of Inelastic DEformations) (McKnight, 1975). The CYANIDE program has been used for material nonlinear finite element analysis at GE Aircraft Engines for nearly 20 years. The CYANIDE program performs incremental plasticity analysis using the Prandtl–Reuss flow rule, and the Von Mises yield criteria. CYANIDE uses Besseling's subvolume method to depict kinematic hardening. Numerous features have been built into the CYANIDE program to facilitate creep analysis. These features include several creep hardening options, dynamic time incrementing, and options for different creep formulations. All material properties are input at several temperatures, and the program interpolates the data to the temperatures specified for the model.

All the examples described in the investigation are either one dimensional or axisymmetric in geometry. The CYANIDE program is fully three dimensional so the isochronous curve approach can be used in general structural applications. Without loss of generality, the stresses and strains in the equations in this paper can be related to a multiaxial state by using effective quantities and the Prandtl–Reuss flow rule.

New Approach

Goldhoff (1972) presented a number of ways to estimate isochronous stress–strain curves. In addition to crossplotting the data of Fig. 1, techniques based on time–temperature parametric plots of creep data are also presented. For most of these methods, the creep strain is determined for a constant stress (really load) over a fixed time interval. This creep strain is then added to the strain from the high strain rate or time-independent curve at the applied stress level.

This load control approach to generating isochronous stress–strain curves assumes that the stresses do not change significantly as a result of the creep strains. The validity of this assumption is problem dependent. For load control problems, such as the deflection of a hook under constant load, the structure may be modeled accurately. Other problems, such as the creep relaxation of a bolt, may not be modeled with sufficient accuracy.

This paper presents a new approach to doing an isochronous analysis. This technique involves doing an iterative relaxation solution using a displacement control assumption. In this approach the stress–strain curve is formed by holding the total strain constant and calculating the stress value reached by the material as it relaxes over a specified period of time. Automatic time step adjustment is used during the relaxation simulation to obtain an accurate solution efficiently. This new stress–strain combination forms a point on the displacement control isochronous stress–strain curve.

In order to obtain the displacement controlled curves, an iteration procedure is required. The curves of Fig. 1 are generally represented by a creep function, e.g., power law creep. The load control curves can be easily generated by simply inserting the stress, time, and temperature into the formulation and evaluating the creep strain. On the other hand, for the displacement control curve the stress is not constant. Therefore the formulation must be applied incrementally using a creep hardening rule. Strain hardening is generally accepted to give reasonable results, so this is incorporated into the iterative relaxation calculations.

In addition to the iterative procedure required to determine the displacement-controlled curves, the program includes options to produce load-controlled curves or a combined load–displacement control curve. The latter is necessary as there are numerous locations that are not totally load or displacement control. The combination control curve is composed of stress–strain pairs that are calculated as weighted averages of the stress–strain pairs on the load and displacement control curves. A number of other features are incorporated in the program such as graphics, and the ability to generate "zero creep" curves for temperatures below the creep cutoff temperatures.

A simplified flowchart of the program used to automate the generation of isochronous stress-strain curves is shown in Fig. 3. The data input for this program consists of the stress–strain pairs that describe the time-independent material response, and the creep constants used with the creep formulation. The current program uses a five term model of creep deformation:

$$\epsilon_c = k\sigma^n t^m + q\sigma^r t \tag{1}$$

where t is time, and k, n, m, q, and r are material constants. These constants are functions of temperature; the program contains appropriate temperature interpolation routines. Other creep models can be added as needed to fit material requirements. The output for this program consists of stress–strain pairs, which describe the material response after a specified period of time.

Simple Verification Test Case

Creep relaxation of a bolted connection at a constant temperature is a simple example of a displacement control problem. Timoshenko (1956) gives a solution for bolt relaxation for a problem where the creep is modeled as a constant rate power function of stress:

$$\dot{\epsilon}_c = q\sigma^r \tag{2}$$

The initial strain in the bolt is all elastic and is equal to the elastic plus creep strain at subsequent times:

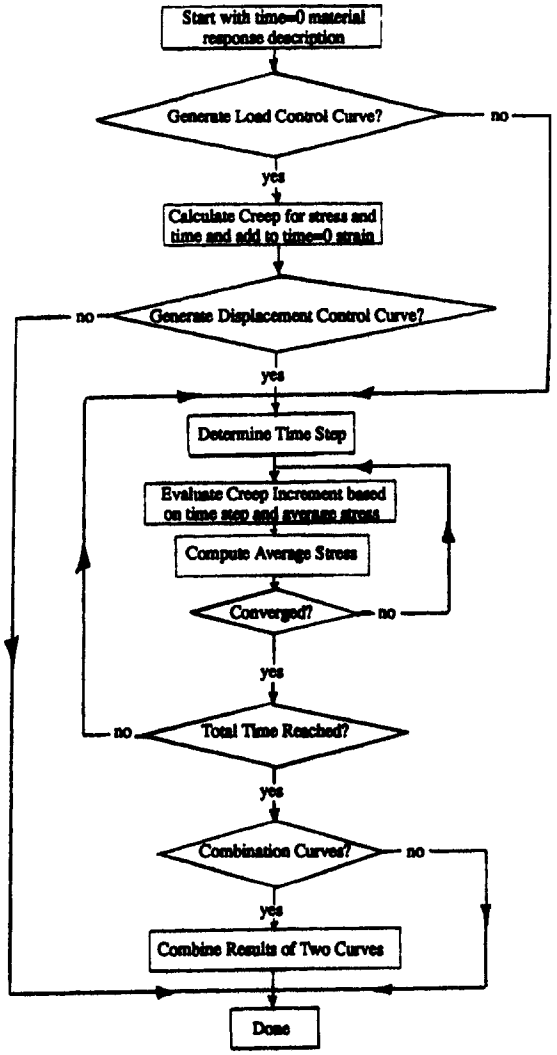

Fig. 3 Flow chart for isochronous stress–strain curve generation

$$\epsilon_c + \frac{\sigma}{E} = \frac{\sigma_0}{E} \tag{3}$$

Combining these two equations and differentiating with respect to time gives

$$\frac{d\epsilon_c}{dt} = q\sigma^r = -\frac{1}{E}\frac{d\sigma}{dt} \tag{4}$$

Rearrangement and integration of this equation gives

$$t = \frac{1}{(r-1)qE}\frac{1}{\sigma^{r-1}}\left[1 - \left(\frac{\sigma}{\sigma_0}\right)^{r-1}\right] \tag{5}$$

Typical values for the material parameters are q = 4.8E-30/hour, r = 7, and E = 207 GPa (30E6 psi) (Imgrund and Ostergaard, 1990). Using these values with an initial stress of 6900 kPa (1000 psi) the stress reduces to 6244.5 kPa (905.0 psi) after 950 hours.

A simple finite element analysis of this problem was conducted using the isochronous curve approach. The isochronous curves were calculated using the program just described. Figure 4 shows the resulting three isochronous curves at a time of 950 hours and compares them to the initial elastic stress–strain path. The curves are not widely separated, but note that the scale of the curves is very small. At a given strain, the curves are only separated by values on the order of 69 kPa. However, this is a 10 percent variation in stress and is consistent with the stress relaxation determined by Timoshenko.

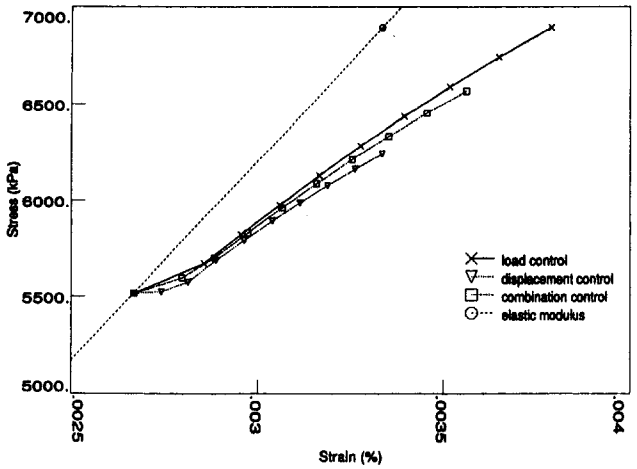

Fig. 4 Isochronous stress–strain curves at time = 950 hours

The boundary condition in this problem is that the bolt is subject to a fixed end displacement. While this simple example is isothermal, the method can handle nonuniform temperature distributions. The displacement control isochronous curve was used as the constitutive model in the finite element analysis. With this curve, the results of the finite element analysis agree exactly with the theoretical solution. If the traditional load control isochronous stress–strain curve is used, the predicted final stress is 6364 kPa(922.3 psi). If all creep strain calculations are made using the initial stress value, the predicted final stress is 5956 kPa (863.2 psi).

This simple test problem demonstrates that accurate values of time-dependent quantities can be obtained using the isochronous curve approach. The next question to be addressed is whether the technique provides any savings in computer time. A series of simple test cases were run to provide this comparison. A simple geometric model consisting of four constant strain triangles was subjected to a constant displacement and the stress relaxation determined.

The problem was analyzed using both traditional time-stepping creep analysis and a plasticity analysis using the displacement control isochronous curves. For a problem in which the initial applied strain is elastic, the typical iteration time for the isochronous curve approach is less than one tenth that required by the time stepping method.

When the initial applied strain contains a plastic component, the potential savings can be even greater. For this case the isochronous stress–strain curve would be constructed using the regular stress–strain curve (time = 0) as the starting point. The isochronous analysis would still involve an iterative "plastic" solution. On the other hand, the classical analysis would involve both an iterative plastic solution, and a time-stepping creep solution. Even when the time required to construct the isochronous curves is included, a time savings can still be achieved. The program developed to generate the isochronous curves takes relatively little time to run when compared to the time spent setting up and running a large creep model.

Isochronous stress–strain curves may be useful as a way of including time-dependent material response in a finite element problem that does not have creep capability. There are also cases when isochronous curves can be used to avoid the numerical problems associated with very high creep rates. For example, the time step size for a large model may be limited by the high creep rate around a relatively small stress concentration. In this case a considerable amount of computation may be done calculating near zero creep increments for the bulk of the model. There are a number of features that can be included to make the creep increment calculation logic more robust, but the features are not generally available

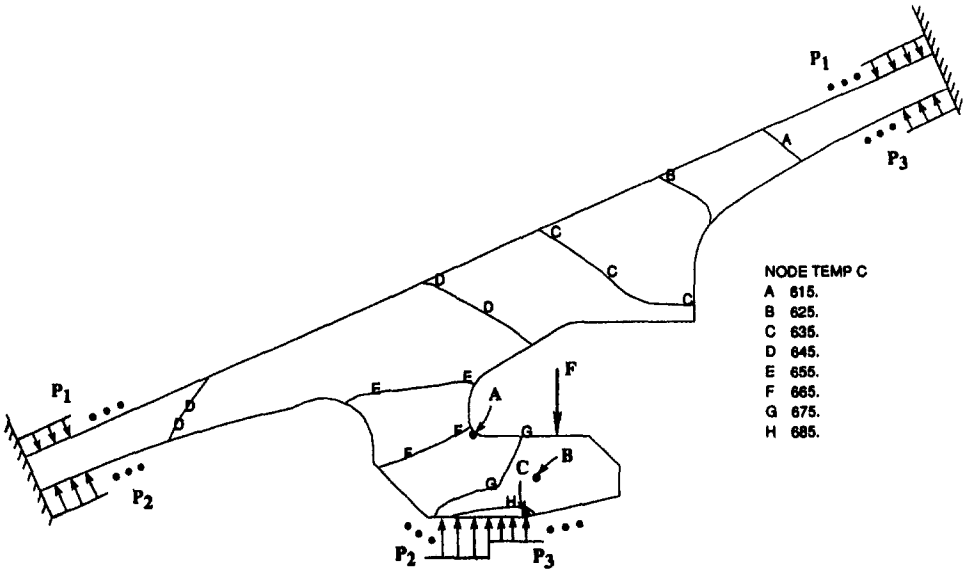

Fig. 5 Axisymmetric case submodel

(at the present time) in commercially available finite element programs.

The isochronous curve approach may also be viewed as a simple engineering substitute for the unified constitutive model approach. While a unified model is capable of handling the creep problems discussed in this work, unified models are not yet generally available in finite element packages. This is the main reason for not including a unified model in the current investigation. A second reason is that, depending on the choice of unified model, determination of the model constants can require a significant data base. This is particularly the case in hot structure analyses since the nonuniform temperatures require extensive interpolation of temperature-dependent quantities. Determination of the various unified model parameters will therefore require greater data than the usual creep database available for many engineering applications.

Application of Combination Control Stress–Strain Curves

Most structural analyses are neither purely load control nor displacement control. In fact, the control mode may even vary with location in a given component. It is possible to bound the structural response by performing the analysis with both load control and displacement control isochronous curves. With experience it is possible to select an appropriate combination of the load and displacement control curves that approximate the actual control state for a particular geometry and load. For problems that should be intermediate to the load control and displacement control curves, it may be reasonable to estimate the response using a 50/50 control curve. The "combination control" isochronous stress–strain curves are useful in correlating analytical results with observed behavior.

As an example, a typical component with potential creep limitations would be the section from the axisymmetric case shown in Fig. 5. This static support structure has a variety of force, displacement, and pressure boundary conditions acting on it. A finite element model of this casing structure was created consisting of over 1800 constant strain triangles and over 1000 nodes. The model included an external pressure acting on the case, as well as two different internal pressure levels (forward and aft of the hook attachment). The ends of the case section are assumed to be held in place by the remainder of the structure. The section in Fig. 5 is a submodel of a larger structure; the ends of the submodel are set by the displacement results of the overall structure. The component that attaches to the hook was simulated by a force acting radially inward on the hook. As given in the figure, the temperature distribution is nonuniform and is high enough, particularly in the hook, for creep to be significant. A detailed creep analysis was carried out to determine the deflection of the tip of the hook over time, and to determine the relaxed stress state in the hook.

Figure 5 highlights three locations on the hook. The peak stress occurs at location "A," which is at the notch root of the hook. Location "B" is in the interior part of the hook. Location "C" is on the inner diameter of the hook, and is near the peak temperature point. Note that this structure is a mixed boundary value problem, i.e., neither load control nor displacement control. It is expected that some locations near the hook would be essentially in load control while other locations would be controlled by the displacement of the component. One of the objectives of this analysis was to ascertain what isochronous curve should be used for the constitutive model and how well a single isochronous curve modeled the behavior of the entire structure.

Table 1 gives a summary of results obtained for the hook using an elastic analysis, a time-stepping creep analysis, and three different isochronous stress–strain curve solutions. The first isochronous solution used the traditional load control curves, the second used the displacement control curves, and the third used a 50/50 combination of displacement and load control.

Figure 6 compares the effective stress contours at 10,000 hours for the four inelastic models. From the figures, it is clear that the general features of the stress distribution are the same for all of the models. Concentrating on the distribution through the hook, the stress at the critical location A is best described by either the load or 50/50 control curves. However, all the isochronous curves give values that are less than 10 percent different than the time stepping solution. The load control value is more conservative away from the stress concentration. The displacement control curve gives stresses that are in better agreement with the creep values.

At location A, the difference in effective stress between the elastic and creep solution is about 30 percent. This relaxation is sizable but small compared to the 70 percent at the other two locations in Table 1. This variation is another indication of the amount of displacement control existing at the various locations.

Table 1 Summary results for axisymmetric case with hook (stress in MPa, strain in percent, displacement in mm)

Output Quantity (location)	Elastic Solution	Creep (time stepping)	Load Control	Displacement Control	50/50 Control
eff. stress – (A)	206.	143.	151.	130.	145.
eff. stress – (B)	161.	47.6	68.3	47.6	62.7
eff. stress – (C)	168	42.1	66.9	42.7	60.0
eff. inelastic strain – (A)	–	.1708	.1679	.4200	.2098
eff. inelastic strain – (B)	–	.0853	.0717	.1262	.0809
eff. inelastic strain – (C)	–	.0893	.0738	.1190	.0821
tip radial displacement	4.979	4.938	4.936	4.888	4.927
run time CPU sec.	85.	1396.	249.	906.	430.

When the effective inelastic strains are compared in the same area, a different pattern emerges. As shown in Table 1, the displacement control curves predict inelastic strains that are over 100 percent in error, while the 50/50 curve is about 20 percent conservative. The load control curve accurately predicts the strains, but the values are now nonconservative. As the distance from the stress concentration at the base of the hook increases, the full and partial displacement curves improve in accuracy while the load control values increases in error. The displacement control curve continues to yield the worst results for the local strain, however.

Two factors are responsible for the trend of the strain values. First, this area of the structure is not well represented by a displacement control model. Second, the very steep stress gradient at the notch root and the flat displacement control stress–strain curve combine to overestimate the plastic strains. Because the displacement control stress–strain curve is flat, the small increment in the stress predicts a very large increase in plastic strain. As the stress gradient drops off away from the hook root, the accuracy improves. Also as the distance increases the elastic loading of the hook becomes more and more like a displacement control problem, thus shifting the situation toward the 50/50 control problem.

In a structure undergoing creep, it is vital to examine the displacements as well as the stress field. Frequently, excessive deformation rather than material separation will limit the structural performance. Table 1 shows that all of the isochronous curves produce radial displacements at the hook tip that are in good agreement with the time-stepping solution. A comparison of the displacement contours for the entire structure as produced by the time stepping solution and the combined load–displacement control solution shows the results are in very good agreement for both the axial and radial displacements. The displacement components calculated using the load control curve are generally in agreement with the creep solution, particularly in the hook area. However, the load control displacement contours are in less agreement with the time stepping solution throughout the rest of the structure. The displacement control components are in better agreement with the creep solution away from the load bearing hook.

The final entry in the table compares the problem run time on a Hewlett Packard 700 series workstation. The loads acting on the casing produce stresses that are below the yield so all strains are either elastic or creep. For this simple loading, the isochronous approach gives a factor of between 1.5 and 5.6 on solution time. The time savings is greater for the load control solution than the displacement control solution. This is because the load control curve lies above the displacement control curve. The additional "strain hardening" of the load control curve results in less inelastic deformation, and thus less iteration time. For either case the savings in computer time is very significant. If the loading were high enough to produce plastic strains, then it is expected that the advantage would be even greater.

This sample problem points out the necessity for careful examination of numerical results. If the only goal is to predict creep life, then the load control values will allow a reasonable, conservative estimate of the stress and the resulting creep life. Note, however, that moving away from the stress concentration gives stress values that are 50 percent in error and would probably be overly conservative in the long life creep regime. The displacement control curves show a crossover, with the 50/50 curve being better at the notch root while the pure displacement control is better away from the hook. This undoubtedly recognizes the transition of the boundary conditions from close to load control at the tip of the hook to a higher percentage of displacement control in the interior of the structure. Similar observations apply to the strain distribution, but the situation is aggravated by the flatness of the stress–strain curves.

This problem demonstrates that the entire structure can be analyzed using any of the stress–strain curves. However, at a load-controlled stress concentration, the maximum stress or strain should not be based on the displacement control curves if the stress–strain curve is very flat. The 50/50 curves should be used for these purposes. As the point of interest moves away from the maximum stress location, the pure displacement curves are better able to simulate the creep solution. Of course, all this depends on the structure and requires that the engineer apply some judgment as to the type of boundary conditions the structure is actually subjected to.

Summary

Isochronous stress–strain curves have historically been used to predict rupture life at a critical location. The isochronous curve technique has a much broader application and can be used economically to predict the overall creep deformation of a structure as well. The savings are achieved by replacing the creep analysis by the less expensive plasticity analysis. The example of a case subject to a variety of loading conditions, operating in the creep regime, demonstrates the

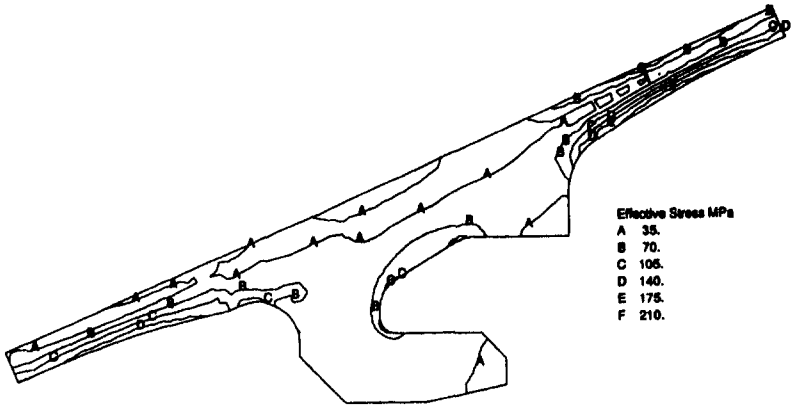

Fig. 6(*a*) Effective stress after 10,000 hour time-stepping creep solution

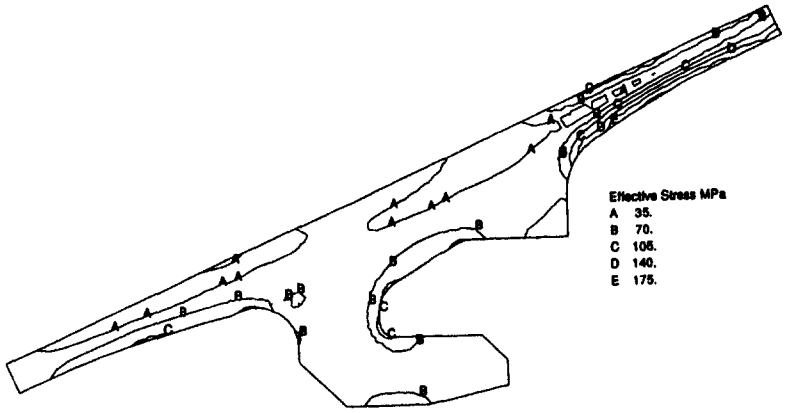

Fig. 6(*b*) Effective stress using 10,000 hour load control isochronous curves

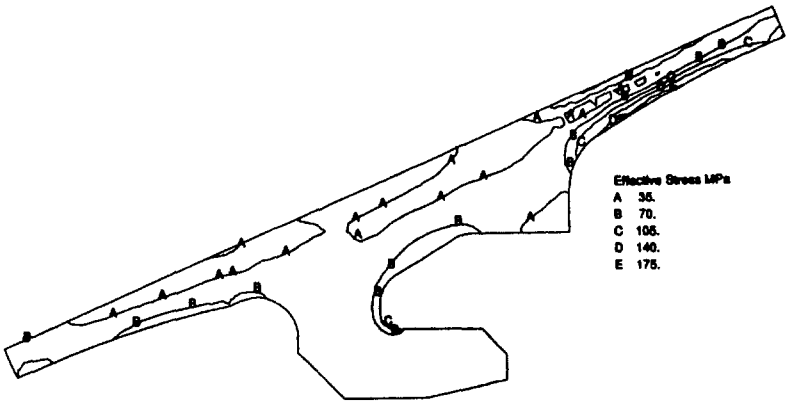

Fig. 6(c) Effective stress using 10,000 hour displacement control isochronous curves

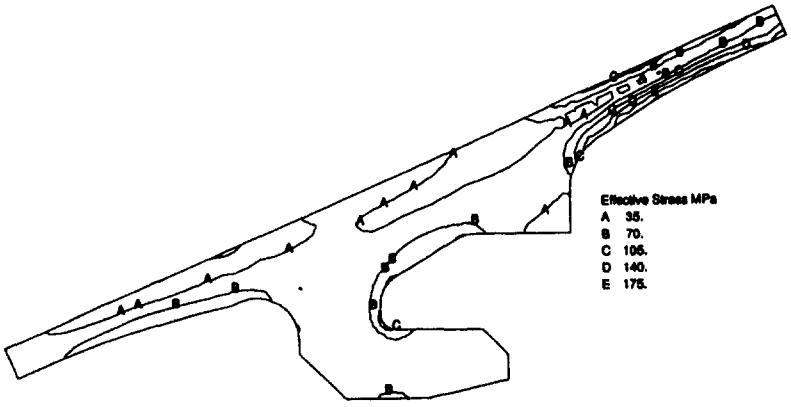

Fig. 6(d) Effective stress using 10,000 hour 50 / 50 control isochronous curves

validity of this concept. The overall deformation and the effective stress at the attachment were accurately described by using the combination control stress–strain curve in the finite element analysis. At the attachment root, the stress computed using the load control curve was not quite as accurate as the value obtained using the combined control curve. Presumably it would be conservative as operating structures would possess some degree of displacement control and allow some local stress relaxation. The degree to which this takes place can always be checked by comparing an elastic solution to the isochronous analysis. The greater the amount of load drop, the greater the degree of displacement control.

The analysis discussed in this paper concentrated on the numerical results, but the primary motivation is the sizable savings in computer time that can be obtained with the isochronous curve approach. Time-stepping solutions can have considerable run times. This becomes even more significant as the size of the structural model increases. Although the time-dependent deformation may be confined to a small area, the entire structure must undergo the time-stepping procedure. Even when the preliminary efforts are included, the total analysis savings can be considerable. For the relatively simple structural problem investigated in detail, the computer run times were found to be between 1.5 and 5.6 times less than for a traditional time-stepping creep analysis.

The isochronous curve approach provides a tool to develop an appropriate stress–strain curve and then conduct a time-independent analysis. Isochronous stress–strain curves can be used to simulate creep behavior in a finite element code, which would otherwise be limited to time independent analysis. The computed stresses and deformations are then available for life determinations and the structural displacement calculations. Of course, if the structure is undergoing rapid transient conditions, then a time-dependent analysis will be necessary. Isochronous curves could conceivably be used, but the analysis procedure would probably require more effort than a traditional time-stepping analysis.

References

Goldhoff, R. M., 1972, "Methods for Constructing Isochronous Creep Curves," *The Generation of Isochronous Stress–Strain Curves*, A. Schaeffer, ed., ASME, New York.

Imgrund, M. C., and Ostergaard, D. F., eds., 1990, "Stress Relaxation of a Tightened Bolt Due to Creep," *ANSYS Engineering Analysis System Verification Manual for ANSYS Revision* 4.4, Swanson Analysis Systems, Inc., Houston, PA, verification problem 132.

Kim, K., Cook, T. S., and McKnight, R. L., 1988, "Constitutive Response of René 80 Under Thermal Mechanical Loads," *Third Symposium on Nonlinear Constitutive Relations for High Temperature Applications*, NASA conference publication 10010, pp. 395–418.

Kraus, H., 1980, *Creep Analysis*, Wiley, New York, pp. 132–141.

McKnight, R. L., 1975, "Finite Element Cyclic Thermoplasticity Analysis by the Method of Subvolumes," Ph.D. dissertation, Department of Aerospace Engineering, University of Cincinnati, OH.

Shanely, F. R., 1957, *Strength of Materials*, McGraw-Hill, New York.

Timoshenko, S., 1956, *Strength of Materials, Part II. Advanced Theory and Problems*, 3rd ed., D. Van Nostrand Co., Inc., New York, pp. 530–533.

Experimental Investigation of Thermoelastic Deformation in Turbojet-Engine Bearings Under Maintenance Inspection

A. J. Kochevar
Engineer,
Commodities, Engineering and Planning Branch,
Oklahoma City Air Logistics Center,
Tinker Air Force Base, OK 73145

C. W. Bert
Director and Perkinson Chair,
School of Aerospace and Mechanical Engineering,
The University of Oklahoma,
Norman, OK 73019
Fellow ASME

The present investigation examined the vertical and horizontal thermoelastic changes in the outside diameter of a turbojet-engine roller bearing. Thermal loads were imparted to the bearing by the hands of a bearing technician during a rework operation. A worst-case analysis was examined by assuming a three-minute dwell time and diametrically symmetric thermal loading. Contact temperature was experimentally determined and used in conjunction with a numerical model to simulate thermal propagation throughout the bearing outer ring. Diametric deflection data, obtained using the contact temperature in conjunction with analytic and finite elements, have been shown for comparative purposes. Experimental diametric expansions of the bearing outer ring were determined and compared with the predicted results. Assuming a worst-case scenario, this investigation yielded vertical expansions in the bearing outer ring's diameter, which would be problematic for some bearings during the rework operation; appropriate corrective action was discussed.

1 Introduction

An aircraft gas turbine engine has a limited service life, after which it must be completely dismantled and each component must be inspected for damage, repaired, and/or replaced if necessary. The engine is then reassembled, tested, and returned to service. It is necessary for the engine components to be maintained with strict adherence to governing regulations set forth by federal agencies, engine and engine component manufacturers. With respect to the overhaul facility, rebuilt components, as well as the final engine assembly, must pass the same performance standards, including tolerances, required of newly manufactured counterparts.

Bearings are widely used components throughout an aircraft gas turbine engine. The present work focused on the No. 5 position, main shaft engine roller bearing for a large turbojet engine.

Although the repair of precision aircraft bearings is a very complicated and time-consuming process, large monetary savings, in many cases, may be gained by avoiding the cost of purchasing new bearings. Whereas a new jet engine main shaft bearing may cost as much as $2500, refurbishment of the same used bearing may only cost $300, yielding a cost avoidance of $2200. Therefore, the remanufacture of aerospace bearings can amount to a sizable savings to the aircraft customer.

Contributed by the International Gas Turbine Institute for publication in the JOURNAL OF ENGINEERING FOR GAS TURBINES AND POWER. Manuscript received by the International Gas Turbine Institute November 12, 1993; revision received June 7, 1994. Associate Technical Editor: R. E. Kielb.

Engineering challenges that must be addressed often arise within the refurbishment process. This investigation was devoted to one such challenge: determining the deformation of a bearing due to thermal loading (handling) by the bearing reconditioner (i.e., operator, technician, etc.) during the outside diameter (O.D.) measurement procedure.

2 Problem Significance and Background

The O.D. measurement procedure was one of several dimensional verifications used to determine the serviceability of the bearing. This bearing consisted of a removable inner ring and an outer ring containing a nonremovable retainer with rolling elements. However, during the O.D. measurement process, the bearing inner ring was removed; thus, it was not a factor in this problem.

The measurement procedure required the measurement of the maximum O.D. of the bearing outer ring using a vertical height gage calibrated to ± 0.0003 cm using precision gage blocks. The bearing outer ring, containing both retainer and rolling elements, was placed vertically between the baseplate and dial gage indicator of the vertical height gage (see Fig. 1). For stability purposes, the bearing reconditioner was required to hold the bearing outer ring with both hands while it was rotated and/or positioned on the vertical height gage. Typically, the required measurement could be performed within three minutes; therefore, this was the process time defined for this analysis.

The bearing O.D. was required to be within the manufac-

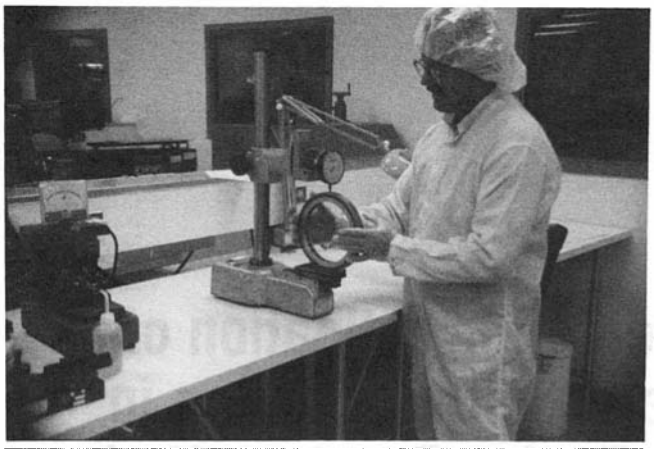

Fig. 1 O.D. measurement of the No. 5 bearing (inner ring removed) as performed by a bearing technician. The bearing was positioned on a vertical height gage which was calibrated to measure within ±0.0003 cm. O.D. measurement procedure was performed within a class 100,000 clean room (see Chap. I, Kochevar, 1993).

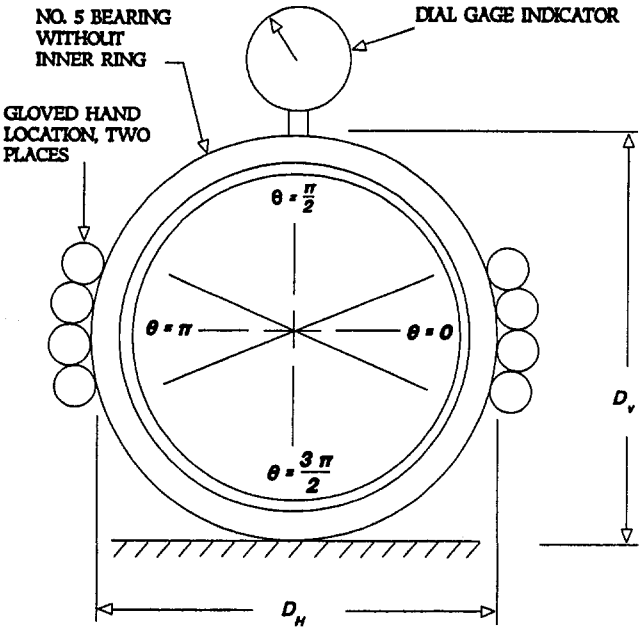

Fig. 2 Observed gloved hand placement of operator during the O.D. measurement procedure. (Note: D_V and D_H denote the orientations of respective vertical and horizontal diametric changes exhibited by the bearing.)

turer's specified tolerances of ±0.0025 cm at 22 ± 3°C for the O.D. to have met serviceable requirements. As a result, it was of importance to know what dimensional effect on the O.D., if any, resulted from the operator handling the bearing during the measurement process. Furthermore, it was possible for the operator performing the measurement to condemn the entire bearing if the maximum O.D. was measured outside of the serviceable limits. On the other hand, a bearing with a measured O.D. within the serviceable limits did not necessarily guarantee that the entire bearing was in serviceable condition. Additional serviceability requirements (e.g., internal radial clearance, visual inspection, etc.) must also have been successfully passed before the entire bearing was returned to service.

The O.D. measurement procedure, as well as all other precision-bearing gaging, was, by regulation, performed in a Class 100,000 Clean Room, a carefully controlled environment with the following requirements: a maximum of 100,000 airborne particles of 0.5 μm diameter or larger per cubic foot, 0.13 cm of H_2O positive pressure between the clean room and immediately outside of the clean room, 40 ± 10 percent relative humidity, and 22 ± 3°C temperature. Strict adherence to the above-mentioned requirements minimized the effects of thermal deformation, contamination, corrosion, etc., on bearings being precision gaged.

3 Goals and General Assumptions

The general goal of this investigation was to determine solutions that described the vertical and horizontal dimensional influence on the O.D. of the bearing (D_V and D_H, respectively, see Fig. 2) as a result of being measured by the bearing reconditioner; solutions were to be simple to use and to predict deflections which may be exhibited accurately. The specific goal was to determine by experimental analysis what magnitudes of both vertical and horizontal O.D. dimensional changes occurred after the three-minute measurement procedure.

Change in the bearing O.D. vertical diameter (D_V, see Fig. 2) was most important to this analysis since its expansion (or contraction) would ultimately alter the bearing's condition status as perceived by the bearing technician. However, change in horizontal diameter, D_H, was also significant to this analysis for comparison purposes. Depending on the magnitude and direction of the vertical deflection, if shown to be significant, corrective actions would then be recommended such as the implementation of a measurement correction factor, modification of the measurement equipment and/or process, etc.

The problem defined herein was that of a time-dependent thermomechanical nature: Transient heat conduction imparted to the bearing from temperature loading (operator handling the bearing) for a short period of time caused the bearing steel to expand thermally, thereby deforming the O.D. and increasing internal stress. Due to the complexity involved with solving heat transfer and deformation equations simultaneously, a simplifying yet accurate engineering approximation was made. That is, initially the heat transfer segment of the problem was solved using an O.D. measurement time of three minutes to yield bearing temperature distributions; subsequently, bearing deformations were determined. Division of the problem analysis into the two aforementioned steps yielded the needed solutions for this problem, which might have otherwise been very difficult, if not impossible to solve. Additional assumptions were used to simplify this problem's analysis and/or model the problem as a worst-case scenario. The worst-case approach was chosen to obtain the maximum possible bearing O.D. deformations, or upper displacement limits, resulting from the O.D. measurement process. The following are general assumptions that impacted the entire problem; additional assumptions are discussed in their respective sections:

(*a*) The bearing steel was assumed to be homogeneous and exhibit linear isotropic thermoelastic behavior. Additionally, the steel was assumed to have material and thermal properties that were independent of temperature.
(*b*) The effect of gravity on the bearing during the O.D. measurement process was assumed to be negligible.
(*c*) The operator was primarily concerned with holding the bearing upright and steady while using the vertical height gage; therefore, hand pressure applied to this bearing during the O.D. measurement process was assumed to be negligible.
(*d*) Although slight variances in the clean room ambient temperature occurred on a day-to-day basis, it remained at approximately 20°C, the constant value assumed here.

4 Outline of Methodology

An overview of the procedure used to determine the deflections is summarized below:

(*a*) First, the bearing outer ring was found to be the most temperature-critical component; thus, the average contact temperature imparted to this component was determined (see Sec. 5).

(*b*) Next, the average contact temperature from above was used together with a heat transfer model to simulate temperature distributions exhibited by the bearing outer ring after an O.D. measurement procedure time of three minutes (see Chap. III of Kochevar, 1993).

(*c*) Direct measurements of the horizontal and vertical displacements of the bearing outer ring were made (see Sec. 6).

5 Experimental Analysis of Contact Temperature

Preliminary Considerations. Analysis of the bearing under thermal load required knowledge of the final temperatures exhibited throughout the bearing after the three-minute O.D. measurement process. An experimental procedure was employed that duplicated this process; temperatures were measured at various locations on the bearing, particularly areas of hand-to-bearing contact, between thermal loading times of $t = 0$ and $t = 180$ s. Contact temperature (T_c) was defined as the temperature at the points of contact between the vinyl-gloved hands of the operator and the outside surface of the bearing outer ring.

To examine the bearing's worst-case thermal loading, it was assumed that the bearing reconditioner's hand positions remained stationary throughout the O.D. measurement procedure. In addition, through observation, it was determined that the bearing reconditioner consistently placed gloved hands approximately 180 deg symmetric about the bearing outer ring with each hand about 90 deg from the top of the vertical height gage (see Fig. 2). In summary, the thermal loading from the operator was assumed to be statically applied and symmetric about the vertical diameter of the bearing outer ring throughout the measurement procedure.

Measurement Procedure. Temperature measurements were made using an Inframetrics, Model 600, Scanning Infrared Camera (SIC) with color video monitor. The SIC measured apparent temperature of the surface on which it was focused to within ± 0.3°C. All temperature measurements were made in a room with an ambient temperature and humidity approximately the same as that of the clean room where the bearing was reworked.

A bearing specimen was cleaned free from lubricating oil, dirt, etc., using standard paint thinner, then allowed to air-dry completely. Next, one face of the bearing was painted completely using off-the-shelf, flat black spray paint to reduce the reflectance (contributed by other heat sources in the room). The emissivity of the bearing was assumed to be negligibly affected by the aforementioned procedure, since removal of the preservation film and subsequent application of paint resulted essentially in the replacement of one coating with another.

The experimental measurement procedure was as follows:

(*a*) A gloved participant, using the same vinyl gloves as those used to rework the bearing, placed both hands on the bearing as they would be placed during the O.D. measurement process (see Figs. 1 and 2).

(*b*) Using the "Point Mode," the SIC cross hairs were focused on various locations of the bearing's painted side, especially in the immediate vicinity of hand-to-bearing contact. Temperatures at each of these points were measured and recorded directly from the color video monitor between $t = 0$ and $t = 180$ s.

Results. The contact temperatures varied between 27.9°C and 29.4°C shortly after the initiation of thermal contact. Thus, it was not possible to correlate a specific T_c with its corresponding diametric displacement. Furthermore, this temperature range remained approximately the same even after three minutes of static handling; therefore, it was concluded that the temperatures throughout the O.D. measurement process remained approximately constant. For further simplification, it was assumed that the constant contact temperature was the average of those temperatures recorded, or 28.7°C with a tolerance of ± 0.3°C (i.e., the uncertainty of the SIC).

It was observed, via the SIC, that the majority of temperature increases experienced by the bearing during the experiment were exhibited by the outer ring. Thus, the deformation analysis was limited to only that of the bearing outer ring, and it was assumed that during the O.D. measurement process, negligible heat transfer occurred between the bearing outer ring and the following: bearing retainer and rolling elements, baseplate and the dial gage indicator of vertical height gage.

The average contact temperature, 28.7°C $\pm$ 0.3°C, was used in conjunction with a heat transfer model formulated using finite difference equations (see Chap. III of Kochevar, 1993). The numerical model yielded three-dimensional temperature fields throughout the bearing outer ring at $t = 180$ s. These distributions were then used to obtain analytic and finite element deflection solutions (see Chap. III of Kochevar, 1993, and Kochevar and Bert, 1995), which were compared in Sec. 7 with those displacements determined experimentally.

6 Experimental Analysis of Deformations

Preliminary Considerations. Experimental deformation measurements were made on two bearings having dimensions approximately equal to those of an average No. 5 bearing. The problem assumptions and simplifications discussed in Sec. 3 of the present paper and in Chapter III of Kochevar (1993) required the retainers with rolling elements to be cut from each of the two bearing outer rings prior to experimentation.

Ring deformations were measured using a Pratt & Whitney Electrolimit Supermicrometer Model B, used as a comparator, as shown in Fig. 3. The supermicrometer had a calibrated meter scale with divisions of 0.00005 cm each; however, experimental measurements were read to the nearest one-half division. The manufacturer's instruction book specified the instrument to have a measurement accuracy of 1 percent (Pratt & Whitney Co., 1963).

It was assumed that the transfer of heat was negligible between the supermicrometer's measurement probes and the

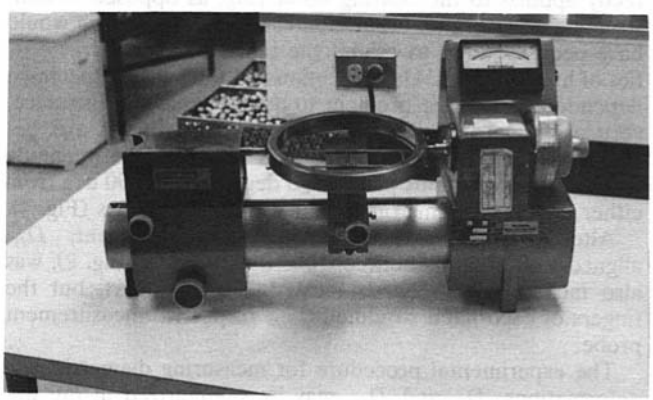

Fig. 3 Experimental setup: Pratt & Whitney Electrolimit Supermicrometer (model B), support fixture (positioned to measure a vertical diametric deflection), and the bearing outer ring

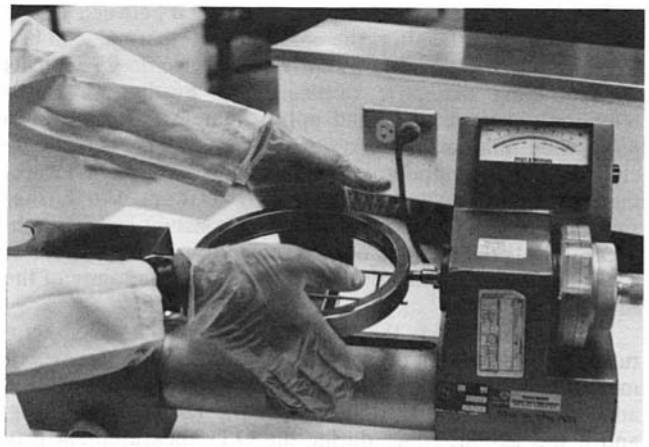

Fig. 4 Gloved hand locations for the experimental measurement of the bearing outer ring vertical deflection, D_V

following: gloved hands of the experimenter and points of contact with the bearing outer ring surfaces.

Measurement Procedure. Each specimen was given permanent alignment marks that denoted the maximum O.D. and the O.D. offset by 90 deg from the maximum to position the two bearing outer rings on the supermicrometer accurately for deflection measurements. The maximum O.D.'s of the two outer rings were measured with a Sheffield Cordax Digital Readout Gage (I.D./O.D. machine). The contact points between the I.D./O.D. machine and one of the bearing outer rings made during the measurement, located 180 deg apart, were marked on one face of the outer ring using a permanent ink, felt tip pen. The same bearing outer ring was then rotated approximately 90 deg and the new contact points made with the I.D./O.D. machine were marked on the same face as that used for the previous marks.

To facilitate measurement of the diametric changes exhibited by the large bearing outer rings, a support fixture, made of stainless steel welding rods tack-welded together, was used (see Fig. 3).

The support fixture had the following characteristics:

(*a*) The small-diameter welding rods used to construct the fixture minimally affected the heat transfer behavior of the bearing outer ring.

(*b*) The relatively small areas of contact between the support fixture and bearing outer ring yielded minimal frictional resistance between the two surfaces; thus, the bearing outer ring was allowed to expand relatively unobstructed.

(*c*) The fixture did not interfere with the supermicrometer's measuring apparatus.

To simplify the experiment, vinyl gloved hands were directly applied to the bearing outer ring, as opposed to constructing an elaborate experimental heat source, which would have been required to exhibit the same thermal characteristics of human hands. Hand locations on the bearing specimen depended on the displacement to be measured. For instance, vertical diametric deflection, D_V, aligned with the axis between $\theta = \pi/2$ and $3\pi/2$ (see Fig. 2), was experimentally determined with hands placed 180 deg apart and 90 deg from either of the supermicrometer measurement probes (Fig. 4).

Alternatively, horizontal diametric displacement, D_H, aligned with the axis between $\theta = 0$ and π (see Fig. 2), was also measured with hands located 180 deg apart, but the fingers of each hand straddled their respective measurement probe.

The experimental procedure for measuring diametric ring deformations, D_V and D_H, may be summarized in the following steps:

(*a*) The bearing outer rings were allowed to stabilize in the clean room environment ($T_\infty = 20°C$) for approximately 24 hours prior to any experimentation.

(*b*) One of the bearing outer ring specimens was approximately centered on the supporting fixture with one set of its alignment marks (180 deg symmetric about the ring) in-line with the supermicrometer's measurement probes.

(*c*) The experimenter then placed vinyl gloved hands (the same gloves as those used in the O.D. measurement process) in the positions corresponding to the desired diametric deflection measurement. The applied hand pressure did not cause the calibrated meter scale to fluctuate from 0.00000 cm at time $t = 0$ s; therefore, the pressure through which the thermal load was being applied was below the sensitivity threshold of the supermicrometer. The hand pressure remained at an approximately insignificant level throughout the experiment.

(*d*) The experimenter's hand positions were then held stationary on the bearing outer ring for a three-minute period, thus applying an approximate constant thermal load until $t = 180$ s.

(*e*) These steps were repeated until five vertical and five horizontal deflections were recorded using an alternating sequence of the two specimens (see Tables 1 and 2).

Table 1 Vertical diametric elongations, D_V, measured on two bearing outer rings under thermal load

Measurement No.	Specimen No.	Experimental Displacement $\bar{D}_{V_1}$ (cm.)	Experimental Displacement with Correction Factor[1] D_{V_1} (cm.)
1	-2	-0.00097	-0.00105
2	-1	-0.00091	-0.00099
3	-2	-0.00091	-0.00099
4	-1	-0.00076	-0.00084
5	-2	-0.00076	-0.00084

Notes:

[1] $D_H = \bar{D}_{H_1} + D_W$ ($D_W = -0.00008$ cm, as determined in Appendix F of Kochevar, 1993

[2] A negative displacement denotes an expansion as defined by the coordinate system in Fig. 2.

The gage force (2.78 N) imparted by the two opposing measurement probes of the P & W Supermicrometer slightly impeded the bearing outer ring from free thermal expansion during the experimental analysis. The equivalent displacement, or "correction factor," provided by the force of the measurement probes, calculated in Appendix F of Kochevar (1993), has been added to the experimental displacements shown in Tables 1 and 2.

7 Comparison of Results

Discussion. The results of this investigation, as well as analytic and finite elements (FE) results (Kochevar, 1993; Kochevar and Bert, 1995), may be seen in Table 3. Changes to both the vertical and horizontal diameters of the bearing outer ring are shown as well as average contact temperatures. To reiterate from Sec. 3, deflection of the bearing outer ring vertical diameter was of primary importance to this investigation; the contribution made by D_V may have affected the perceived condition status of the entire bearing.

Each analysis method in Table 3 is accompanied by three average contact temperatures, which, when used as a set, define the range of contact temperature (i.e., 28.4°C–29.0°C) valid for that method. Similarly, each analysis method corresponds to three diametric deflections beneath each of columns three and five, which define the respective solution ranges for D_V and D_H pertaining to that method.

For Methods 1–3 in Table 3, each average contact temperature respectively yielded two corresponding diametric de-

flections located on the same row. However, Method 4 simply produced two ranges of experimental deflections, which correspond to the range of average contact temperature. That is, Method 4 does not imply a direct correlation between a particular average contact temperature and the two diametric displacements on the same row.

In general, Methods 1–3 consistently predicted both vertical and horizontal diametric displacements, which were larger than those found using Method 4. Although the experimental vertical expansions (Method 4) were the most conservative values yielded by any method (-0.00084 cm to -0.00104 cm), they were still significant when compared with an O.D. dimensional tolerance of the same magnitude as that of the Sec. 2 example: 21.5900 ± 0.0025 cm.

Experimental Uncertainty. The predominant source of experimental uncertainty encountered in this investigation stemmed from the statistical analysis of the experimental displacement data; accuracy of the deflection measurement apparatus (1 percent) was negligible in comparison. The experimental horizontal and vertical displacement ranges shown in Table 3 may be alternately viewed as the average horizontal and average vertical displacements, respectively, plus or minus their corresponding mean standard deviation, or: -0.00056 ± 0.00010 cm and -0.00094 ± 0.00010 cm, respectively.

Note 6 in Table 3 refers to a commonly used approximation for statistical uncertainty using fewer than 20 experimental measurements. First, the average horizontal and average vertical displacements were calculated using the five experimental measurements (corrected) obtained for each orientation. Next, sample standard deviations were determined for both the horizontal and vertical displacements; each deviation was then divided by the square root of the number of measurements (five in each case), thus producing the standard deviation of the mean displacement for both directions. Finally, each of the two mean displacement deviations were multiplied by a statistical constant (2), which approximated 21 to 1 odds of measurement repeatability. Therefore, this procedure yielded two diametric average displacements, each with its tolerance range defined by its respective sample standard deviation. Holman (1984) discussed this entire procedure and Note 6 in Table 3 references his work.

The discrepancies among the experimental data and those results found using the analytic and FEA techniques may possibly be attributed to several sources including: unaccounted experimental uncertainty, equipment limitations, etc. The following are some examples of these sources:

1 Although temperature equipment uncertainty was included in the data analysis of this investigation, some experimental uncertainty was difficult to determine, such as that contributed by the application of gloved hands directly to the bearing outer ring.
2 The tolerance of the P & W supermicrometer was somewhat large for the small deflections measured experimen-

Table 2 Horizontal diametric elongations, D_H, measured on two bearing outer rings under thermal load

Measurement No.	Specimen No.	Experimental Displacement D_{H_1} (cm.)	Experimental Displacement with Correction Factor[1] D_{H_1} (cm.)
1	-1	-0.00046	-0.00054
2	-2	-0.00051	-0.00059
3	-1	-0.00041	-0.00049
4	-2	-0.00041	-0.00049
5	-1	-0.00066	-0.00074

Notes: Same as those for Fig. 1.

Table 3 Comparison of analytic, FEA, and experimental results

Method	Average Contact Temperature, $T_c(^\circ C)$	Change in Vertical Diameter, $D_V(cm.)$	% Difference of Corresponding D_V Range from Experimental D_V Range	Change in Horizontal Diameter, $D_H(cm.)$	% Difference of Corresponding D_H Range from Experimental D_H Range
1.Analytic: Linear Temperature Variation	28.4 28.7 29.0	-0.00109 -0.00114 -0.00117	4.81 to 39.29 (21.28)	-0.00066 -0.00069 -0.00071	0.00 to 54.35 (23.21)
2.Analytic: Cosine Temperature Variation	28.4 28.7 29.0	-0.00107 -0.00109 -0.00114	2.89 to 35.71 (15.96)	-0.00071 -0.00074 -0.00076	7.58 to 65.22 (31.14)
3. FEA	28.4 28.7 29.0	-0.00114 -0.00117 -0.00122	9.62 to 45.24 (24.47)	-0.00071 -0.00074 -0.00076	7.58 to 65.22 (31.14)
4. Experimental	[28.4 28.7 29.0]	[-0.00084 -0.00094 -0.00104]	--	[-0.00046 -0.00056 -0.00066]	--

NOTES:
1. A negative change in diameter denotes an expansion as defined by the coordinate system in Fig. 2.
2. } - denotes the respective method's solution range.
3. [ ] - denotes that no direct relation exists between a particular average contact temperature and change in vertical diameter on the same row.
4. ( ) - denotes the % difference between the corresponding Method's average deflection from the average experimental deflection in the same direction.
$$\left[\frac{D_n - D_n(\text{exp.})}{D_n(\text{exp.})} \times 100;\ n = \text{vertical or horizontal direction}\right]$$
5. Solution ranges in Methods 1-3 were produced using contact temperature uncertainty of $\pm$ 0.3 $^\circ$ C.
6. Experimental deflection ranges in Method 4 reflect statistical uncertainty assuming (21 to 1) odds of measurement repeatability; see Holman (1984).
7. Assuming three minutes of contact.

tally. A measurement apparatus of lower tolerance may have yielded experimental data that would have more closely emulated those results obtained analytically and numerically.

8 Concluding Remarks

The vertical expansions, D_V, of the bearing outer ring determined in this investigation indicated that the condition status of some bearings would be adversely perceived by the operator performing the O.D. measurement process assuming a worst-case scenario. The problem solution adopted as a result of this analysis was to incorporate the use of a Sheffield I.D./O.D. gage, which did not require the bearing to be held by the bearing technicians during the O.D. measurement process.

The vertical deflections of the bearing outer rings, which were determined experimentally, were duplicated with reasonable accuracy by the analytic solution method with cosine temperature variation. On the other hand, the horizontal deflections, which were exhibited experimentally by the bearing outer ring, were found to be most accurately replicated by the analytic method with linear thermal load.

The thermoelastic ring analysis performed in this investigation may be extended for use in structural applications such as a circular stiffening member in an aerospace vehicle, or overhead walkway subjected to diametrically symmetric heating, e.g., solar, etc. Moreover, the present investigators have found no previously published experimental data corresponding to the diametrically symmetric thermoelastic circular ring cases evaluated herein.

Acknowledgments

The authors acknowledge helpful discussions with Professor W. H. Sutton on the thermal contact investigation. This paper is based upon a thesis submitted by the first author in partial fulfillment of the requirements for the degree of Master of Science in Mechanical Engineering at the University of Oklahoma, Norman, May 1993.

References

Holman, J. P., 1984, *Experimental Methods for Engineers*, 4th. ed., McGraw-Hill, New York.

Kochevar, A. J., 1993, "Thermoelastic Deformation Analysis of a Turbojet Bearing Undergoing Maintenance Inspection," M.S. thesis, The University of Oklahoma, Norman, OK.

Kochevar, A. J., and Bert, C. W., 1995, "Thermal Deformations in Thin Circular Rings Subjected to Localized Heating," *Journal of Thermal Stresses*, to appear.

Pratt & Whitney Co., 1963, "Pratt & Whitney Electrolimit Supermicrometer (Model B) Instruction Book," West Hartford, CT.

Finite Element Analysis of Structural Engineering Problems Using a Viscoplastic Model Incorporating Two Back Stresses

V. K. Arya
Visiting Associate Professor,
Department of Mathematical Sciences,
The University of Akron,
Akron, OH;
NASA-Lewis Research Center,
Cleveland, OH 44135

G. R. Halford
NASA-Lewis Research Center,
Cleveland, OH 44135

The feasibility of a viscoplastic model incorporating two back stresses and a drag strength is investigated for performing nonlinear finite element analyses of structural engineering problems. The model has recently been put forth by Freed and Walker. The feasibility of the viscoplastic model is demonstrated for nonlinear structural analyses by implementing the model into a finite element program and performing nonlinear finite element analyses for several uniaxial and multiaxial problems. Good agreement is shown to exist between the results obtained using the finite element implementation and those obtained experimentally. The advantages of using advanced viscoplastic models for performing nonlinear finite element analyses of structural components are indicated.

Introduction

Classical creep-plasticity constitutive models treat creep and plastic strains as independent noninteracting entities. These models are, therefore, incapable of accounting for the observed interactions between creep and plastic strains at high temperatures. Viscoplastic models, on the other hand, consider all the inelastic strain (including plasticity, creep, relaxation, etc.) as a single unified time-dependent quantity and thus automatically include interactions among them. Viscoplastic models, therefore, provide more realistic descriptions of time-dependent inelastic behavior of materials at high temperatures.

The endeavor to make viscoplastic models more realistic leads to inclusion of as much material physics as possible into them. This results in complex mathematical frameworks for viscoplastic models. The constitutive differential equations of viscoplastic models that govern the flow and evolution laws are generally highly nonlinear and mathematically "stiff." The closed-form solutions for structural engineering problems are virtually intractable when viscoplastic models are employed to define the stress–strain relationship. To assess the advantages offered by more realistic viscoplastic models it becomes mandatory, therefore, to employ numerical solution methodology involving, for example, the finite element method or the boundary element method.

The present paper is directed toward this aim. It presents a finite element solution methodology developed at NASA (National Aeronautics and Space Administration)-Lewis Research Center for use in conjunction with the general purpose finite element program MARC [1]. The methodology is designed for use with viscoplastic models. The methodology is demonstrated in this paper for a viscoplastic model recently developed by Freed and Walker [2] that incorporates *two* back stresses. However, the methodology is general in nature and can easily be adapted for use with other viscoplastic models.

For completeness, the paper includes brief descriptions of the viscoplastic model by Freed and Walker [2] and the finite element solution methodology. The methodology is illustrated by applying it to several uniaxial and multiaxial problems.

Viscoplastic Model

The viscoplastic model used in this paper is a recent viscoplastic model put forth by Freed and Walker [2]. The model contains one scalar internal state variable D, called the drag strength, and a tensorial internal variable B_{ij}, called the back stress. The back stress B_{ij} is assumed to be composed of two back stresses that are denoted by B^s_{ij} and B^l_{ij}, respectively. A small displacement and a small strain formulation is employed.

The stress σ_{ij} is taken to be related to elastic strain by Hooke's law:

$$\epsilon^e_{ij} = \frac{1+\nu}{E}\sigma_{ij} - \frac{\nu}{E}\sigma_{kk}\delta_{ij} \qquad (i,j = 1,2,3) \qquad (1)$$

where E is Young's modulus, ν is Poisson's ratio, and δ_{ij} is the Kronecker delta. The symbol ϵ denotes the strain and the superscript e denotes the elastic component of strain. Following Einstein's summation convention, the repeated

Contributed by the International Gas Turbine Institute for publication in the JOURNAL OF ENGINEERING FOR GAS TURBINES AND POWER. Manuscript received by the International Gas Turbine Institute November 20, 1993. Associate Technical Editor: H. L. Julien.

subscripts in Eq. (1) and elsewhere imply summation over the range of symbol.

The total strain rate $\dot{\epsilon}_{ij}$ is written as the sum of elastic $\dot{\epsilon}^e_{ij}$, inelastic (including plasticity, creep, relaxation, etc.) $\dot{\epsilon}^v_{ij}$, and thermal $\dot{\epsilon}^t_{ij}$ strain rate components. In symbols

$$\dot{\epsilon}_{ij} = \dot{\epsilon}^e_{ij} + \dot{\epsilon}^v_{ij} + \dot{\epsilon}^t_{ij} \qquad (1, j = 1, 2, 3) \tag{2}$$

In this equation the superscripts v and t denote the viscoplastic and thermal components of strain rate, respectively. A dot over a symbol indicates its derivative with respect to time t.

The deviatoric stress S_{ij} and the deviatoric total strain rate $\dot{E}_{ij}$ have the following expressions:

$$S_{ij} = \sigma_{ij} - \frac{1}{3}\sigma_{kk}\delta_{ij} \tag{3}$$

and

$$\dot{E}_{ij} = \dot{\epsilon}_{ij} - \frac{1}{3}\dot{\epsilon}_{kk}\delta_{ij} \tag{4}$$

The back stress B_{ij} is defined as the sum of two back stress components B^s_{ij} and B^l_{ij}, that is

$$B_{ij} = B^s_{ij} + B^l_{ij} \tag{5}$$

The effective stress Σ_{ij} is defined as

$$\Sigma_{ij} = S_{ij} - B_{ij} \tag{6}$$

The temperature dependence of the model is mainly contained in the thermal diffusivity function Θ, which is defined as

$$\Theta = \begin{cases} \exp(-Q/kT) & T_t \le T \le T_m \\ \exp\left[-\dfrac{Q}{kT_t}\left\{\ln\left(\dfrac{T_t}{T}\right) + 1\right\}\right] & 0 \le T \le T_t \end{cases} \tag{7}$$

In Eq. (7), Q is the activation energy, k is the Boltzmann constant, T is absolute temperature, T_t is transition temperature, and T_m is the melting temperature of the material.

The function Z, the Zener–Hollomon parameter, is defined by

$$Z = A \sinh^n\left(\sqrt{J_2/D}\right) \tag{8}$$

where

$$J_2 = \Sigma_{ij}\Sigma_{ij}/2$$

Here A and n are inelastic material constants.

The evolution equations for the internal state variables are

$$\dot{B}^\alpha_{ij} = 2H_\alpha\left(\dot{\epsilon}^v_{ij} - \frac{B^\alpha_{ij}}{2L_\alpha} I_2\right) \tag{9}$$

where $\alpha = s, l$. The strain invariant I_2 is defined by

$$I_2 = \begin{cases} \Theta Z & \text{if } J_2 < K^2 \\ P_{ij}\dot{E}_{ij}/P^M & \text{otherwise} \end{cases} \tag{10}$$

In Eq. (10)

$$P_{ij} = \frac{E}{2(1+\nu)}\frac{\Sigma_{ij}}{\sqrt{J_2}} \tag{11}$$

and $\dot{E}_{ij}$ is defined by Eq. (4). Also

$$P^M = \frac{E}{2(1+\nu)} + \Sigma_\alpha \frac{H_\alpha}{L_\alpha}\left(L_\alpha - \frac{1}{2}B^\alpha_{ij}\frac{\Sigma_{ij}}{\sqrt{J_2}}\right) \tag{12}$$

The functions K, H_α, and L_α in these equations are given by

$$K = (C - D_0)(C + D_0)/4\delta C \tag{13}$$

$$H_s = \frac{E}{2(1+\nu)} \quad ; \quad H_l = \frac{E}{2(1+\nu)H_0} \tag{14}$$

and

$$L_s = f\frac{(C - D)(D - D_0)}{\delta C}$$

$$L_l = (1 - f)\frac{(C - D)(D - D_0)}{\delta C} \tag{15}$$

Here C, δ, H_0, and f are material constants and D_0 denotes the minimum value that the drag strength D can take for a given material.

The drag strength D evolves according to the following equation:

$$\dot{D} = h(I_2 - \Theta r); \qquad D_0 \le D \le D_{\max} \tag{16}$$

where

$$D_{\max} = (C + D_0)/2$$

and

$$r = A \sinh\left\{(D - D_0)/\delta C\right\}^n$$

The function h is defined as

$$h = h_D\left[\frac{(D - D_0)/\delta C}{\sinh\left\{(D - D_0)/\delta C\right\}}\right]^m \tag{17}$$

where

$$h_D = \begin{cases} h_1 & T_t \le T \le T_m \\ h_0 - \dfrac{h_0 - h_1}{T_t} T & 0 < T \le T_t \end{cases} \tag{18}$$

In Eq. (18), h_0 and h_1 are material constants.

In addition to elastic material constants, the shear modulus μ, Poisson's ratio ν, and the coefficient of thermal expansion α, the above-mentioned viscoplastic model has thirteen inelastic material constants, viz., A, C, δ, D_0, f, H_0, h_0, h_1, m, n, Q, T_m, and T_t. The values of these constants taken from Freed and Walker [2] are listed in Table 1.

Description of MARC Program

A viscoplastic model is most advantageous if it can be used on a practical scale for the solution of structural engineering problems faced by, for example, the aerospace and nuclear industries. To demonstrate the feasibility of the present viscoplastic model for performing complex nonlinear structural analyses, the same was implemented into the general purpose finite element program MARC [1]. Any other finite element program that possesses a capability for performing nonlinear viscoplastic structural analyses may equally well be used. The MARC program employs sophisticated integration algorithms and advanced finite element formulations. It is specially tailored to fit the requirements of a nonlinear structural analysis.

The MARC program provides the user a convenient way of implementing and integrating the constitutive differential equations of Freed and Walker's model [2]. This is accomplished through the user subroutine HYPELA provided in MARC. The details of subroutine HYPELA are given in [1]. The subroutine HYPELA developed for Freed and Walker's model and the self-adaptive time integration strategy used in

Table 1 Material constants for copper (source Freed and Walker [12])

Constant	Unit	Value
α	K^{-1}	18×10^{-6}
μ_0	MPa	43,000
μ_1	MPa/K	-17
ν	-	0.36
A	s^{-1}	2×10^{7}
C	MPa	13
f	-	0.75
H_0	-	20
h_0	MPa	50
h_1	MPa	15
m	-	0.5
n	-	4.5
Q	J/mol.	200,000
T_m	K	1356
$\mu = \mu_0 + \mu_1 T$; T is in degrees Kelvin $D_0 = C/100$; $\delta = 0.035$; $T_t = 0.5\ T_m$		

it, follow essentially the same structure as given in Arya and Kaufman [3] and Cassenti [4].

In the MARC program all the material nonlinearities are incorporated into an initial load vector that is treated as a pseudo-body force in finite element equilibrium equations. The constitutive equations of viscoplastic models are known to be mathematically "stiff." A subincrement technique is employed to form the incremental constitutive equations corresponding to a given finite load increment.

In subincrement technique a given finite load increment is split into a number of equal subincrements. The constitutive equations of the viscoplastic models are then integrated over these small subincrements to obtain an accurate representation of the incremental constitutive equations over the finite load increment. Structural engineering problems encountered in aerospace and nuclear industries usually involve large degrees of freedom. Since the use of an explicit integration method does not require the assembly and inversion of Jacobian matrices, it is more suitable for problems involving large degrees of freedom. The explicit forward Euler method with a self-adaptive time step was employed to integrate the constitutive equations over the subincrements. The integration strategy is found to work efficiently and accurately, even for large finite element load increments, provided the subincrements are suitably small to ensure the stability of the forward Euler method (see, for example, Arya [5] and Arya and Arnold [6]). However, it is difficult for the user to select efficient subincremental steps and there is a considerable incentive to use as few subincrements as possible without affecting the stability of the constitutive equations associated with the viscoplastic model. For an experienced user, however, it is relatively easy to optimize the number of subincrements.

It is appropriate here to provide a brief introduction to the MARC program. The intent is to familiarize the user with the operation of MARC (for complete details of the MARC program, see volumes A through D of [1]). This introduction, taken from [3, 4], is presented in the following paragraphs.

"The principle of virtual work may be used to generate the MARC nonlinear equilibrium equations governing the incremental response of the structure to an increment of load. In evaluating the nonlinear structural response of a component, the program assumes that the load history is divided into incrementally applied loads. Each load step is sequentially analyzed as a linear matrix problem using an appropriate stiffness matrix and load vector. Although each load step uses linear matrix methods to solve the incremental equations, the incremental equations themselves are nonlinear since the load vector will depend on the displacement increment obtained in the solution of incremental equilibrium equations.

"The principle of virtual work may be written, for applied external point loads P_i, or displacement u_i, in the form:

$$\Sigma \int_V \delta \epsilon_i^T \sigma_i dV = \delta u_i^T P_i \tag{19}$$

where the integral extends over the volume, V, of each finite element and the summation sign extends to all the elements in structure.

"In Eq. (19) the virtual displacement vector δu_i is related to the virtual strain vector $\delta \epsilon_i$ through the relationship:

$$\delta \epsilon_i = B_{ij} \delta_{uj} \quad \text{so that} \quad \delta \epsilon_i^T = \delta_{uj}^T B_{ij}^T \tag{20}$$

where B_{ij} is the strain displacement matrix and the superscript T denotes transposition. Since δu_i is an arbitrary virtual displacement vector, Eqs. (19) and (20) may be written in the form:

$$\Sigma \int_V B_{ij}^T \sigma_j dV = P_i \tag{21}$$

"This relation expresses the equilibrium of structure when the applied load vector is P_i and the stress vector is σ_i. If an incremental load ΔP_i is applied to the structure and the stress vector changes to $\sigma_i + \Delta \sigma_i$, the relation expressing the equilibrium of the structure at the end of the incremental load application may be written as:

$$\Sigma \int_V B_{ij}^T (\sigma_j + \Delta \sigma_j) dV + P_i + \Delta P_i \tag{22}$$

"Hence, the relation expressing the equilibrium of the structure during the application of the incremental load vector ΔP_i is obtained from Eqs. (21) and (22) by subtraction in the form:

$$\Sigma \int_V B_{ij}^T \Delta \sigma_j dV = \Delta P_i \tag{23}$$

"The MARC code allows the user to implement very general constitutive relationships into the program by means of the user subroutine HYPELA. Within this subroutine, the user must specify the values of elasticity matrix D_{ij} and the inelastic stress vector $\Delta \zeta_i$ in the incremental vector constitutive relationship:

$$\Delta \sigma_i = D_{ij} (\Delta \epsilon_j - \delta_j \alpha \Delta \theta) - \Delta \zeta_i \tag{24}$$

The inelastic stress increment vector $\Delta \zeta_i$ is computed in HYPELA using the constitutive relationships of the viscoplastic model.

"In Eq. (24), α denotes the coefficient of thermal expansion and δ_j is the vector Kronecker delta symbol,

$$\delta_j = \begin{cases} 1 & \text{if } 0 \le j \le 3 \\ 0 & \text{if } 3 \le j \le 6 \end{cases} \tag{25}$$

"For the viscoplastic models, the incremental inelastic stress vector $\Delta \zeta_i$ depends in a highly nonlinear manner on the incremental strain vector $\Delta \epsilon_j$. Since $\Delta \epsilon_j = B_{ij} \Delta_{uj}$, the incremental stress vector $\Delta \zeta_i$ depends in a highly nonlinear manner on the nodal displacement vector Δ_{uj}, so that $\Delta \zeta_i = \Delta \zeta(\Delta_{uj})$.

"Substitution of Eq. (24) into Eq. (23) produces the incremental equilibrium equations for MARC program in the form:

$$\Sigma K_{ij}\Delta u_j = \Delta P_i + \Delta R_i + \Sigma\int_V B_{ij}^T \Delta\zeta_j dV + \Sigma\int_V B_{ij}^T \delta_j \alpha \Delta\theta DV \tag{26}$$

where K_{ij} is the elemental elastic stiffness matrix defined by the relation:

$$K_{ij} = \int_V B_{ik}^T D_{kl} B_{ij} dV \tag{27}$$

The vector ΔR_i is the residual load correction vector or out-of-equilibrium force vector from the preceding load increment:

$$\Delta R_i = P_i - \Sigma\int_V B_{ij}\sigma_j dV \tag{28}$$

which is added to the current increment in order to restore the structure to equilibrium. The nonlinearity in the incremental equilibrium relationship, defined in Eq. (26), arises because the inelastic stress increment vector $\Delta\zeta_j$ depends nonlinearly on the displacement increment vector Δu_j. Values of D_{ij} and $\Delta\zeta_j$ appropriate to the current incremental load step are returned to the main program by subroutine HYPELA and the incremental equilibrium relations in Eq. (26) are solved by successive iteration.

The solution of the incremental equilibrium relations in Eq. (26) is accomplished within the MARC code by the following algorithm. At the start of the increment the user subroutine HYPELA is entered to determine the elasticity matrix D_{ij} and the incremental inelastic stress vector $\Delta\zeta_i$. On entry to the subroutine, the input consists of the strain increment vector $\Delta\epsilon_j$, the temperature increment $\Delta\Theta$, the time increment Δt over which the incremental external load vector ΔP_i is applied to the structure, and the values of stress, strain, temperature, and viscoplastic state variables at the beginning of the increment. Since the incremental strain vector, $\Delta\epsilon_i = B_{ij}\Delta_{uj}$, can only be accurately determined after the solution to the incremental equilibrium relationship in Eq. (26) has yielded the correct solution vector Δ_{uj}, the strain increment vector $\Delta\epsilon_i$ initially used to generate the inelastic stress vector $\Delta\zeta_i$ must be estimated. The initial estimate for $\Delta\epsilon_i$ is assumed to be the value obtained for $\Delta\epsilon_i$ in the preceding increment. On exit from subroutine HYPELA the elasticity matrix D_{ij} and the estimated inelastic stress increment vector $\Delta\zeta_i$ are passed into the main program. After the values of D_{ij} and $\Delta\zeta_i$ are obtained for each integration point in the structure, the incremental equilibrium relationship in Eq. (26) is assembled and solved for the incremental node displacement vector Δ_{uj}. The incremental strain vector, $\delta\epsilon_i = B_{ij}\Delta_{uj}$, is then computed and compared with the initial guess for $\Delta\epsilon_i$ used to generate the inelastic incremental stress vector $\Delta\zeta_j$. If this incremental strain vector is equal, within a user-specified tolerance, to the incremental strain vector used to compute $\Delta\zeta_j$ in the assembly phase, the solution is assumed to have converged. Otherwise the updated strain increment vector, obtained from the solution of the equilibrium relations in Eq. (26), is passed into subroutine HYPELA, a new vector, $\Delta\zeta_j$, is computed and the equilibrium equations resolved to yield an improved value of Δ_{uj} and $\Delta\epsilon_i$. The process is repeated until the value of vector $\Delta\epsilon_i$ on the assembly phase is equal, within a user-specified tolerance, to the value of vector $\Delta\epsilon_i$ on the solution phase. After convergence is achieved, the temperature, stress vector, strain vector and viscoplastic state variables are updated by adding the incremental values generated during the current increment to the values of these variables at the beginning of the increment. The program then passes on to the next load increment where the process is repeated."

Application to Problems

Uniaxial Problems. Some uniaxial problems were solved first to demonstrate and validate the implementation of Freed and Walker's model into MARC program. These included calculations of tensile stress–strain response at different temperatures and cyclic response under isothermal and nonisothermal loadings. The constitutive equations (including the flow and evolution laws) of the viscoplastic model were implemented in MARC in their generalized three-dimensional form. The implementation was carried out through the user subroutine HYPELA. This generalized finite element implementation was used to perform the uniaxial computations that are presented in this paper. The values of constants for copper listed in Table 1 and taken from [2] were utilized in these computations. Figures 1 through 4 show the results for uniaxial problems.

Multiaxial Problem. *The Cowl Lip Problem.* To demonstrate the feasibility of performing complex structural analyses using viscoplastic model, the validated finite element implementation of Freed and Walker's viscoplastic model was applied to a sample structural component used in the aerospace industry. The component, called a *cowl lip*, is part of the leading edge of a hypersonic aircraft engine inlet. To achieve high inlet aerodynamic performance for proposed hypersonic flight between Mach 3 and 25, not only must the high heat flux and high heating rates be tolerated, but also distortions caused by thermal warping of the structure must be minimized. Consequently, the need arises for the development of actively cooled leading edges fabricated from specialized materials with innovative cooling concepts to enable the structure to withstand the severe thermal loading conditions. The details of different cooling concepts proposed under a NASA-Lewis-sponsored program, called COLT (Cowl Lip Technology Program) were presented by Melis and Gladden [7]. In the present paper a cooling concept, called the parallel flow concept, is investigated. In this concept the coolant channels are laid parallel to the leading edge of the cowl lip (see Fig. 5) and the coolant is flowed through them to contain the temperature of the component. The viability of the parallel flow concept is investigated by performing the structural analysis with the finite element implementation of Freed and Walker's viscoplastic model.

The cowl lip geometry is shown in Fig. 5. The dimensions of the cowl lip are 15.2 cm × 3.8 cm × 0.64 cm. However, for the finite element analysis only the 5 cm central portion of the cowl lip was modeled to avoid end effects that would be difficult to quantify. The finite element mesh for this central portion was constructed by Melis and Gladden [7]. The model was made up of 3294 solid eight-noded hexagonal elements and has 4760 nodes. A large number of finite elements was required to deal with the severity of thermal loadings and gradients. The severity of thermal loading illustrated in Fig. 6 can be judged by noticing that the temperature at a critical location of the component rises from 21 to 758°C in only 0.75 seconds (see Fig. 7). However, the geometric symmetry of component facilitates only half of it necessary to be considered in the finite element analysis. This results in a considerable saving in CPU time.

Figure 6 depicts the thermal loading cycle used in finite element analysis. The steady-state temperature distribution in the component was obtained from [7]. This reference includes the details and results of a steady-state heat transfer analysis that was performed to obtain the steady-state temperature distribution in the cowl lip. This temperature distribution in the cowl lip is shown in Fig. 7. The transient temperature distribution was obtained by employing a linear interpolation technique. It is observed that the highest temperatures in the component occur along the leading edge of the cowl lip. The temperature values thus obtained for the

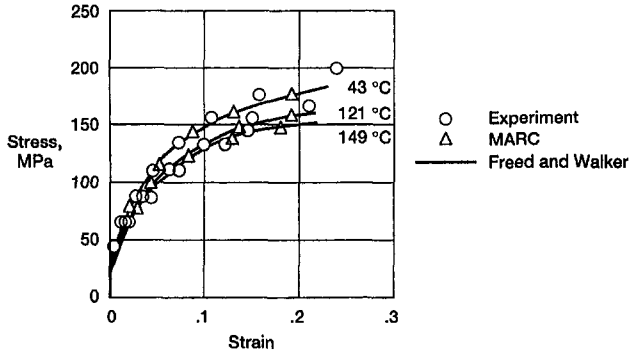

Fig. 1 Tensile stress–strain curves at different temperatures; stress rate is 0.0061 MPa / s

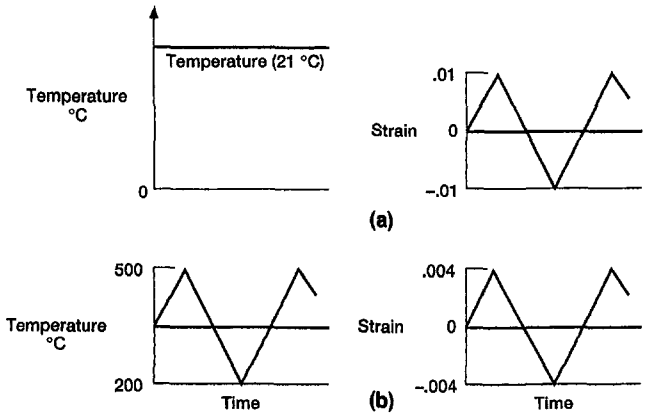

Fig. 2 Thermal and mechanical loadings used for generating hysteresis loops using the finite element implementation: (*a*) isothermal and (*b*) nonisothermal

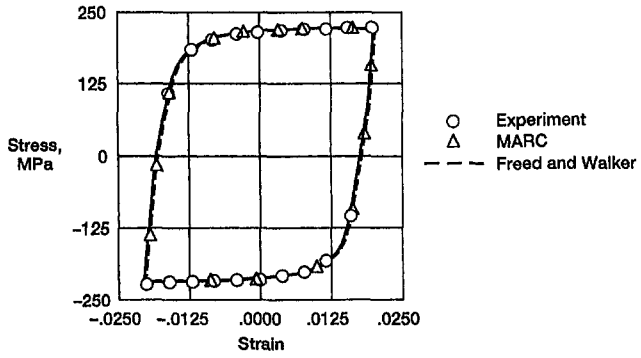

Fig. 3 Isothermal hysteresis loops at 21°C: strain rate 0.02 / s; strain range 4 percent

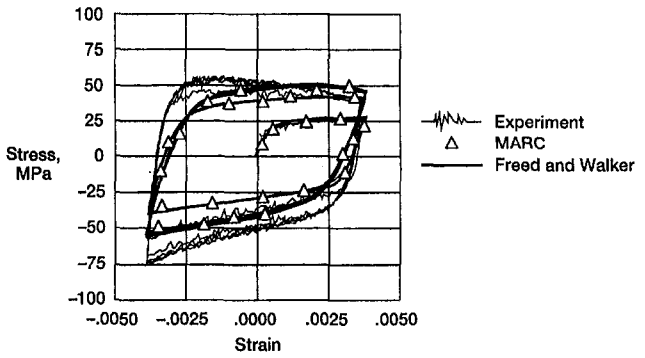

Fig. 4 Nonisothermal (in phase) hysteresis loops. Temperature range: 200–500°C; strain range: 0.0075. Strain rate is 1.5×10^{-5} / s.

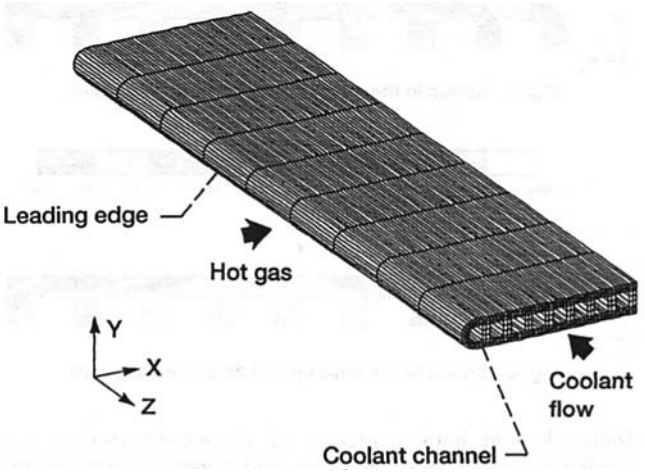

Fig. 5 Cowl lip finite element model; elements: 3294; nodes: 4760

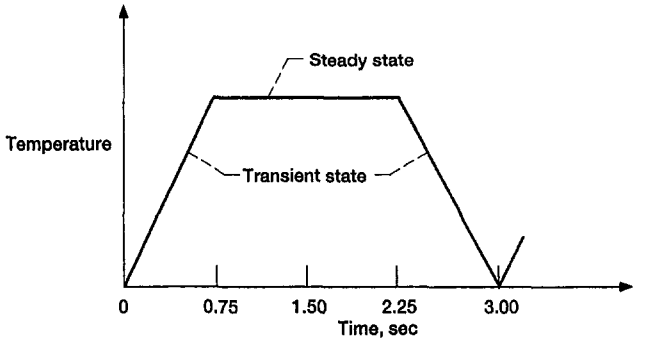

Fig. 6 Thermal loading cycle

complete thermal loading cycle were used to perform the cyclic finite element analysis of the cowl lip.

Results and Discussion

Uniaxial Problems. Figure 1 shows isothermal tensile stress–strain curves at different temperatures obtained using the finite element implementation of Freed and Walker's viscoplastic model. The stress rate used in these computations is 0.0061 MPa s^{-1}. Curves obtained by Freed and Walker and those obtained experimentally are also drawn in this figure to facilitate comparison. It is seen from this figure that there is good agreement among the curves obtained by Freed and Walker, by experiments and by using the present implementation of the viscoplastic model.

The thermal and mechanical loadings used to generate the isothermal and nonisothermal hysteresis loops are shown in Fig. 2. These hysteresis loops for isothermal and nonisothermal loadings are shown in Figs. 3 and 4, respectively. The strain rates used in generating these isothermal and nonisothermal hysteresis loops are 0.001 s^{-1} and 1.5×10^{-5} s^{-1}, respectively. These figures also exhibit the hysteresis loops obtained in experiments. Again good agreement is seen to exist between the curves obtained experimentally and by using the finite element implementation. The difference in the values of stress obtained by using the finite element implementation and those predicted by experiments and shown in Fig. 4, is inherent in the viscoplastic model and is also seen in the results of Freed and Walker [2]. It does not imply an error in the finite element implementation.

The good agreement between the calculated values from the finite element implementation and those obtained from experiments for the tensile curves and isothermal and nonisothermal hysteresis loops validates the finite element implementation of Freed and Walker's model. Such validation of

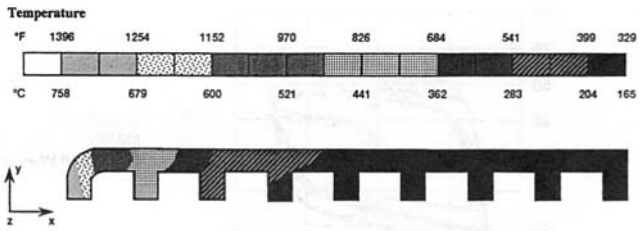

Fig. 7 Steady-state temperature distribution in the cowl lip

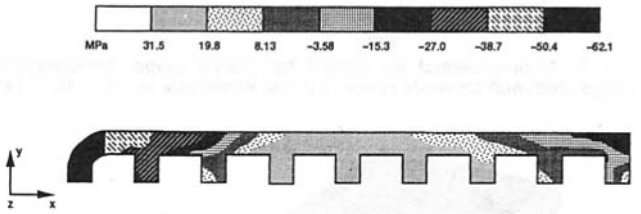

Fig. 8 Stress in the cowl lip at 0.75 s; z component

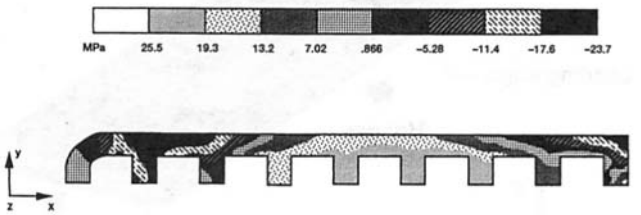

Fig. 9 Stress in the cowl lip at 2.25 s; z component

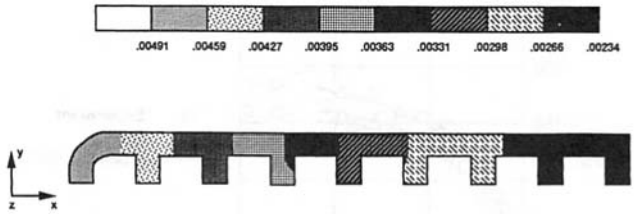

Fig. 10 Strain in the cowl lip at 0.75 s; z component

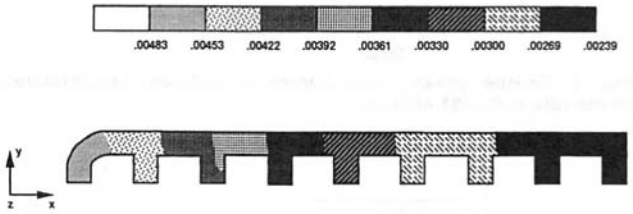

Fig. 11 Strain in the cowl lip at 2.25 s; z component

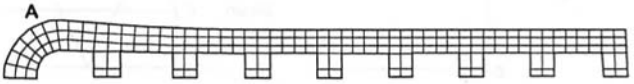

Fig. 12 Deformed shape of the segment at 0.75 s (the deformations are magnified by a factor of 1000 to facilitate visual interpretation)

finite element implementation of viscoplastic models is a worthwhile investment of effort and computer time before applying the same to industrial structural engineering problems. These problems, in general, involve complex thermal/mechanical loadings besides their complex geometries and are, therefore, computationally intensive and time consuming.

Cowl Lip Problem. The most significant results of the cowl tip problem are obtained by plotting the stresses and strains along the leading edge, that is, the z direction in Figs. 8–11. The stress distribution in the z direction at 0.75 s is exhibited in Fig. 8. It is seen that the maximum (compressive) stress occurs at the leading edge of cowl lip. Figure 9 displays the stress distribution in the z direction of the cowl lip at 2.25 s. A comparison of these figures reveals significant redistribution of stress in the component due to inelastic deformation. The stress along the leading edge is now seen to be tensile. This shows that viscoplastic models are capable of picking the redistribution of stress due to inelastic deformation even for a short duration of 1.5 s. It is interesting to note that a nonunified elastic-plastic-creep analysis of this component performed by Arya et al. [8] was unable to capture this redistribution of stress.

The strain distributions in z direction in the cowl lip at 0.75 s and 2.25 s are shown in Figs. 10 and 11, respectively. These figures show the values of total strain at different locations of cowl lip. The compressive inelastic strain along the leading edge is found to accumulate (increase) with time. This makes the total (tensile) strain along the leading edge to reduce with time. This fact can be observed by comparing Figs. 10 and 11. For example, the total strain along the edge of cowl lip reduces from a value of 0.00491 at 0.75 s to a value of 0.00483 at 2.25 s.

The deformed shape of the segment at 0.75 s is plotted in Fig. 12. The displacements in this figure are magnified by a factor of 1000 to facilitate visual interpretation of the results. It is seen from this figure that the maximum deformation of the segment occurs in the vicinity of point A. The component is seen to thicken in this neighborhood. The thickening of component in this region will lead to distortion of coolant channel configuration. This thickening of leading edge will also result in a greater time for cooling down of leading edge. This will lead to an early failure of the component implying that the parallel flow concept to cool the cowl lip down is not a particularly viable concept.

Conclusions

A numerical solution methodology based on the finite element method is described for a viscoplastic model recently developed by Freed and Walker. It is illustrated for the finite element program MARC. However, the generality of methodology makes it adaptable with any other finite program relatively easily. The viability of methodology is demonstrated by applying it to several uniaxial and a multiaxial cowl lip problem. The results for uniaxial tensile and cyclic loadings obtained using the finite element implementation show good agreement with the experimental results and also the results reported in the literature. The advantages of using an advanced viscoplastic model for nonlinear structural analyses are established by applying it to a multiaxial cowl lip problem and investigating the proposed parallel flow design concept. The results from the viscoplastic finite element analysis indicate that the parallel flow concept for the design of cowl lip is not a particularly viable concept as it will lead to an early failure of the component.

References

1 MARC *General Purpose Finite Element Program*, MARC Analysis Research Corporation, Palo Alto, CA, Vols. A–D, 1992.

2 Freed, A. D., and Walker, K. P., "Viscoplasticity With Creep and Plasticity Bounds," *International Journal of Plasticity*, Vol. 9, No. 2, 1993, pp. 213–242.

3 Arya, V. K., and Kaufman, A., "Finite Element Implementation of Robinson's Viscoplastic Model and Its Application to Some Uniaxial and Multiaxial Problems," *Journal of Engineering Computations*, Vol. 6, No. 3, 1989, pp. 237–247.

4 Cassenti, B. N., "Research and Development Program for the Development of Advanced Time–Temperature Dependent Constitutive Rela-

tionships," R83-956011-1,-2, United Technologies Research Center; NASA Contract NAS3-23273, NASA CR-168191, 1983.

5 Arya, V. K., "Nonlinear Structural Analysis of Cylindrical Thrust Chambers Using Viscoplastic Models," *Journal of Propulsion and Power*, Vol. 8, No. 3, 1992, pp. 598–604.

6 Arya, V. K., and Arnold, S. M., "Viscoplastic Analysis of an Experimental Cylindrical Thrust Chamber Liner," *AIAA Journal*, Vol. 30, No. 3, 1992, pp. 781–789.

7 Melis, M. E., and Gladden, H. J., "Thermostructural Analysis With Experimental Verification in a High Heat Flux Facility of a Simulated Cowl Lip," in: *29th Structures, Structural Dynamics and Material Conference*, Part 1, AIAA, New York, 1988, pp. 106–115.

8 Arya, V. K., Melis, M. E., and Halford, G. R., "Finite Element Elastic-Plastic-Creep and Cyclic Life Analysis of a Cowl Lip," *International Journal of Fatigue and Fracture of Engineering Materials and Structures*, Vol. 14, No. 10, 1991, pp. 967–977.

G. E. Weber
Commonwealth Edison Co.,
Fossil Technical Services Dept.,
1411 Opus Pl., Suite 250,
Downers Grove, IL 60515

W. M. Worek
Department of Mechanical Engineering
(M/C 251),
University of Illinois at Chicago,
842 West Taylor Street,
Chicago, IL 60607-7022

The Application of a Method to Evaluate the Design Performance of a Feedwater Heater With a Short Drain Cooler

The application of the Modified Delaware Method, which was developed by Weber and Worek (1994) to evaluate the design performance of a feedwater heater with a short drain cooler, is illustrated. All calculations used in obtaining the heat transfer coefficients and pressure drops in the desuperheating, condensing, and drain cooling zones are shown by applying the method to an actual heater design.

1 Introduction

As explained in Part I (Weber and Worek, 1994), feedwater heaters are a costly necessity. Therefore, utilities need a method to evaluate the heater manufacturer performance specifications and understand the theory behind the design of a heater. Further, if the manufacturer's design data are not verified before the heater is installed, it may be too late to correct a design problem after installation.

This paper utilizes the Modified Delaware Method to evaluate a typical feedwater heater design. The method used is a revision of the original Delaware Method (Bell, 1986) to enable it to produce acceptable results when applied to a feedwater heater. To apply the Modified Delaware Method to a three-zone (i.e., desuperheating, condensing, and drain cooling) feedwater heater, the heater must be divided into three separate heat exchangers, each representing one of the three zones (Weber, 1992). Note that the method cannot be applied in the condensing zone because of the shell-side fluid change of state. The reference by Clemmer et al. (1965) is used in this zone.

The following example applies and illustrates the theory developed by Weber and Worek (1994) to an actual feedwater heater design. The feedwater heater design is courtesy of Marley Heat Transfer Corporation (Biar, 1991).

2 Application

A 570 MW coal-fired steam generating unit requires a new feedwater heater. The existing heater, which has copper–nickel tubes, is beyond its useful life. The utility has specified that the new heater be designed with Type 304 stainless steel tubes. The thermal performance requirements for this heater are a terminal temperature difference of $-1.67°$ ($-3.00°$F) and a drain cooler approach temperature of 5.56°C (10.00°F). Heater design data available from the manufacturer are listed in Table 1, and detailed baffle information is shown in Figs. 1 and 2.

2.1 Desuperheating Zone Heat Transfer

2.1.1 Shell-Side Heat Transfer Coefficient. The steam properties at the inlet to the shell side of the feedwater heater are:

$$k_s = 5.23 \times 10^{-2} \text{ W/mK } (3.024 \times 10^{-2} \text{ Btu/hrft}^2\,°\text{F})$$

$$C_s = 2622.0 \text{ J/kgK } (0.627 \text{ Btu/lb}\,°\text{F})$$

$$\mu_s = 2.156 \times 10^{-5} \text{ kg/ms } (1.446 \times 10^{-5} \text{ lb}_\text{m}/\text{secft})$$

$$\rho_s = 15.065 \text{ kg/m}^3 \ (0.9405 \text{ lb}_\text{m}/\text{ft}^3)$$

The crossflow area is calculated using the method developed by Bell (1986) and modified by Weber and Worek (1994). That is:

$$S_m = (CM)(A)(S)/(0.866\, D_{\text{otl}})$$
$$= (0.125)(\pi/2)(0.762)^2\, 0.2334/[0.866(1.524)]$$
$$= 0.020162 \text{ m}^2 \ (0.2170 \text{ ft}^2).$$

The Reynolds number may then be calculated using Bell (1986):

$$\text{Re} = D_0 \dot{m}_s/\mu_s S_m$$
$$= (1.588 \times 10^{-2})(42.791)/$$
$$(2.156 \times 10^{-5}\,(2.016 \times 10^{-2}))$$
$$= 1.563 \times 10^6$$

Using data from Fig. 4 of Weber and Worek (1994) we obtain: $j_f = 1.61 \times 10^{-3}$.

The base heat transfer coefficient is calculated next using Bell (1986). It is calculated assuming that the entire shell-side stream flows across the ideal tube bank formed by the tube

Contributed by the Power Division for publication in the JOURNAL OF ENGINEERING FOR GAS TURBINES AND POWER. Manuscript received by the Power Division April 26, 1993. Associate Technical Editor: R. W. Porter.

Table 1 Feedwater heater design specifications

	Shell side		Tube side
Fluid circulated	Steam	Drains	Feedwater
Fluid entering, kg/s (lb/hr)	42.791(338907.30)		455.6239(3,616,063)
Inlet enthalpy, kJ/kg (Btu/lb)	3054.26(1314.00)		883.78(380.22)
Outlet enthalpy, kJ/kg (Btu/lb)		900.96(387.61)	1085.59(467.04)
Inlet temperature, °C (°F)	333.16(631.69)		205.11(401.20)
Saturation temperature, °C (°F)	247.93(478.27)		
Outlet temperature, °C (°F)		210.67(411.20)	249.61(481.30)
Operating pressure, kPa (psia)	3840.40(557.00)		22752.8(3300.0)
Pressure drop, kPa (psia)	DSH 10.41(1.51)	DC 26.34(3.82)	68.95(10.0)
Number of passes	Desuperhtg., condensing and drain cooling zones		2

Zone	Heat exchanged MW (MMBtu/hr)	Effective area, m^2 (ft^2)	LMTD, °C (°F)	Heat transfer coefficient, $W/m^2 \cdot C$ ($Btu/hrft^2 \cdot F$)	Baffle spacing, cm (in.)	Baffle Type
Desup.	9.0694(30.9664)	402.92(4337.0)	39.48(71.06)	570.11(100.47)	23.338(9.188)	Multi
Cond.	75.4672(257.6728)	1824.89(19643)	13.09(23.57)	3157.92(556.51)	92.87(36.563)	N/A
D. C.	7.4165(25.3228)	208.16(2240.0)	16.56(29.80)	2151.77(379.20)	28.100(11.063)	Single

Tube material: Stainless steel		Overall performance
Number of tubes: 2325	D_{otl}, m (ft) 1.524(5.000)	TTD °C (°F) −1.67 (−3.00)
Tube outer diameter, cm (in.) 1.588(0.625)		DCA °C (°F) 5.56(10.00)
Tube wall thickness cm (in.) 0.1829(0.072)		
Tubing pitch, cm (in.) 2.1432(0.8438)		

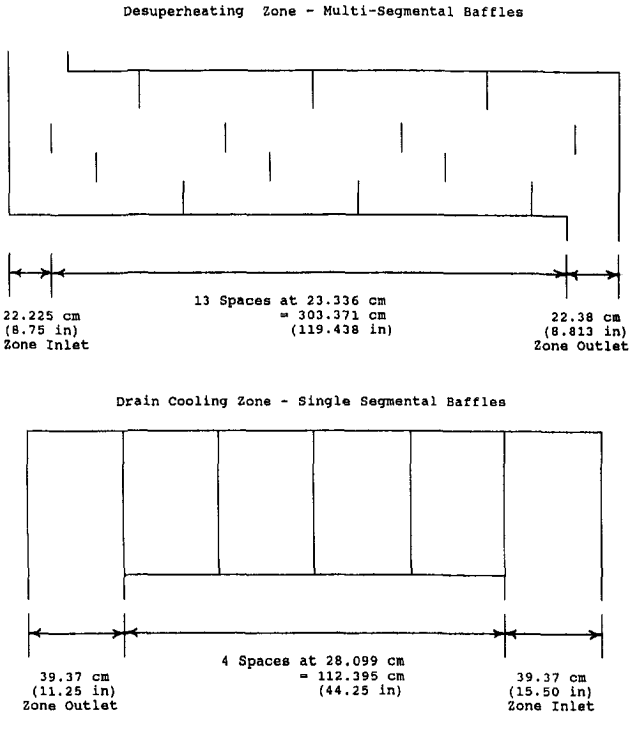

Fig. 1 Baffle dimensions

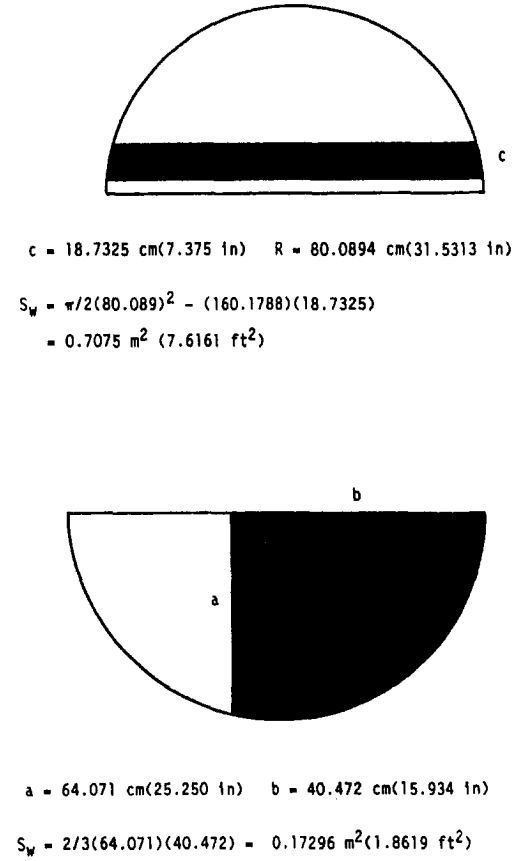

Fig. 2 Baffle windows in the drain cooling and desuperheating zones

array at the centerline of the zone. This is the greatest amount of heat transfer attainable. That is:

$$h_{base} = \left(j_f\, C_s\, \dot{m}_s/S_m\right)\left(k_s/C_s\, \mu_s\right)^{0.667}$$

$$= \left[1.61 \times 10^{-3}\,(2622)\,42.791/2.016 \times 10^{-2}\right] \times \left[5.230 \times 10^{-2}/\,(2622)(2.150 \times 10^{-5})\right]^{0.667}$$

$$= 8.523 \times 10^3\ \mathrm{W/m^2k}\ \left(1.502 \times 10^3\ \mathrm{Btu/hrft^2\ F}\right)$$

This value is multiplied by a series of correction factors for crossflow (J_c), leakage (J_l), bundle bypass (J_b) and baffle spacing (J_s). Using Figs. 5, 7, and 8 from Weber and Worek (1994) $J_c = 0.194$, $J_l = 0.515$, and $J_s = 1.0$, respectively. The bundle bypass correction factor, J_b, is very difficult to obtain because it involves heater design data that may be confidential. Therefore it is assumed to be equal to 0.9, which is representative of a well-designed heater (Bell, 1986). The adjusted shell-side heat transfer coefficient, given by Bell (1986), is:

$$h_0 = h_{\text{base}}\,(J_c)\,(J_l)\,(J_s)\,(J_b)$$
$$= 8.523 \times 10^3\,(0.194)\,(0.515)\,(1.0)\,(0.9)$$
$$= 766.4\ \text{W/m}^2\text{K}\ (135.1\ \text{Btu/hrft}^2\,^\circ\text{F})$$

2.1.2 Tube Side Heat Transfer Coefficient. The tube side heat transfer coefficient is calculated using the Dittus–Boelter relation given by Clemmer et al. (1965), where:

$$h_i = (k_f/D_i)\ 0.023\ \text{Re}^{0.8}\ \text{Pr}^{0.4}$$
$$T_{\text{avg}} = 228^\circ\text{C}\ (442.4^\circ\text{F}),$$
$$P_{\text{avg}} = 22.75\ \text{MPa}\ (3300\ \text{psia}).$$

The feedwater properties are:

$$\rho_f = 964.3\ \text{kg/m}^3\ (60.2\ \text{lb}_\text{m}/\text{ft}^3)$$
$$\mu_f = 1.255 \times 10^{-4}\ \text{kg/ms}\ (8.433 \times 10^{-5}\ \text{lb}_\text{m}/\text{ft sec})$$
$$k_f = 0.663\ \text{W/mk}\ (0.383\ \text{Btu/hr ft}^2\,^\circ\text{F})$$
$$C_f = 4525\ \text{J/kgk}\ (1.082\ \text{Btu/lb}_\text{m}\,^\circ\text{F})$$
$$\text{Pr} = C_f\,\mu_f/k_f = (4525)\,(1.255 \times 10^{-4})/0.663 = 0.8565$$

and

$$V_f = \dot{m}_f/(\rho_f\,A_i N)$$
$$= 456.57/\left[964.3\pi\,(0.25)\,(1.221 \times 10^{-2})^2\,2325\right]$$
$$= 1.739\ \text{m/s}\ (5.71\ \text{ft/sec})$$

The Reynolds number, given by John and Haberman (1980), is

$$\text{Re} = \rho_f\,V_f\,D_i/\mu_f = 1.631 \times 10^5$$

Using the values obtained above the tube-side heat transfer coefficient is:

$$h_i = (0.663/1.220 \times 10^{-2})\,(0.023)\,(1.631 \times 10^5)^{0.8}\,(0.8565)^{0.4}$$
$$= 1.738 \times 10^4\ \text{W/m}^2\text{K}\ (3.062 \times 10^3\ \text{Btu/hrft}^2\,^\circ\text{F})$$

2.1.3 Overall Heat Transfer Coefficient. The total zone thermal resistance is a sum of the shell-side convection shell-side fouling, conduction, and tube-side convection resistances (Bell, 1986). That is:

$$R_t = 1/h_0 + R_{f0} + (\Delta x_w/k_w)\,(A_0/A_m) + (1/h_i)\,(A_0/A_i)$$

The thermal conductivity of stainless steel at 250°C is:

$$k_w = 17.815\ \text{W/mK}$$

Substituting the values obtained previously and calculating the area ratio we obtain:

$$R_t = (1/766.4) + 5.283 \times 10^{-5}$$
$$+ (1.835 \times 10^{-3}/17.815)\,(1.588 \times 10^{-2}/1.404 \times 10^{-2})$$
$$+ (1/1.738 \times 10^4)\,(1.588 \times 10^{-2}/1.221 \times 10^{-2})$$
$$= 1.550 \times 10^{-3}\ \text{m}^2\text{K/W}$$

The overall zone heat transfer coefficient may then be calculated:

$$U = 1/Rt = 645.2\ \text{W/m}^2\text{K}\ (113.7\ \text{Btu/hrft}^2\,^\circ\text{F})$$

2.2 Condensing Zone Heat Transfer. The overall heat transfer coefficient in the condensing zone is calculated using Clemmer et al., (1965). The heat transfer coefficient is obtained by inverting the sum of the heat transfer resistances. There are four resistances to calculate: condensing heat transfer, and shell-side fouling (R_c), tube side convective heat transfer (R_h), tube-wall conduction heat transfer (R_w), and tube-side fouling (R_{ts}). The thermal resistance is given as:

$$R_t = R_c + R_h + R_w + R_{ts}$$

Condensing heat transfer and shell-side fouling are both included in R_c and given by:

$$R_c = 7.046 \times 10^{-2}\ \text{m}^2\,^\circ\text{C/kW}\ (4.000 \times 10^{-4}\ \text{hrft}^2\,^\circ\text{F/Btu})$$
$$\text{if } T_{\text{sat}} > 160^\circ\text{C}\ (320^\circ\text{F})$$
$$R_c = 12.0434(1.8\,T_{\text{sat}} + 32)^{-0.8912}\ \text{m}^2\,^\circ\text{C/kW}\left(6.834 \times 10^{-2}\right.$$
$$\left.\times (T_{\text{sat}})^{-0.8912}\ \text{hrft}^2\,^\circ\text{F/Btu}\right)\ \text{if } T_{\text{sat}} < 160^\circ\text{C}(320^\circ\text{F})$$

Therefore, for $T_{\text{sat,ext}} = 247.9^\circ\text{C}\,(478.3^\circ\text{F})$, $R_c = 7.046 \times 10^{-5}\ \text{m}^2\text{K/W}\ (4.00 \times 10^{-4}\ \text{hrft}^2\,^\circ\text{F/Btu})$. The tube-side convective heat transfer utilizes the same values of h_i used in the desuperheating and drain cooling zones. It is given by:

$$1/R_h = h_i\,D_i/D_0 = 1.336 \times 10^4\ \text{W/m}^2\text{K}$$
$$R_h = 7.485 \times 10^{-5}\ \text{m}^2\text{K/W}\ (4.247 \times 10^{-4}\ \text{hrft}^2\,^\circ\text{F/Btu})$$

The tube wall conduction resistance is given by:

$$R_w = tD_0/(kD_m)$$
$$= 1.165 \times 10^{-4}\ \text{m}^2\text{K/W}\ (6.6107 \times 10^{-4}\ \text{hrft}^2\,^\circ\text{F/Btu})$$

Tube side fouling is given by:

$$R_{ts} = 3.522 \times 10^{-5}\ D_0/D_i$$
$$= 4.581 \times 10^{-5}\ \text{m}^2\text{K/W}\ (2.5994 \times 10^{-4}\ \text{hrft}^2\,^\circ\text{F/Btu})$$

The thermal resistance is:

$$R_t = 7.046 \times 10^{-5} + 7.485 \times 10^{-5} + 1.165 \times 10^{-4}$$
$$+ 4.581 \times 10^{-5}$$
$$= 3.076 \times 10^{-4}\ \text{m}^2\text{K/W}$$

The condensing zone heat transfer coefficient is obtained by inverting R_t:

$$h = 1/R_t = 3251\ \text{W/m}^2\text{K}\ (573.0\ \text{Btu/hrft}^2\,^\circ\text{F})$$

2.3 Drain Cooling Zone Heat Transfer. The heat transfer coefficient in the drain cooling zone is calculated the same as in the desuperheating zone except where specified.

2.3.1 Shell-Side Heat Transfer Coefficient. Using the following data:

$$k_s = 0.614\ \text{w/mK}\ (0.3550\ \text{Btu/hrft}^2\,^\circ\text{F})$$
$$C_s = 3847\ \text{J/kgk}\ (0.9195\ \text{Btu/lb}_\text{m} \times \text{F})$$
$$\mu_s = 1.060 \times 10^{-4}\ \text{kg/ms}\ (7.123 \times 10^{-5}\ \text{lb}_\text{m}/\text{ftsec})$$
$$\rho_s = 809.4\ \text{kg/m}^2\ (50.53\ \text{lb}_\text{m}/\text{ft}^3)$$

we obtain:

$$S_m = (CM)\,(A)\,S/(0.866\ D_{\text{otl}})$$
$$= (0.5)\,(\pi\,(.762)^2/2)\,(0.2809)/(0.866(1.524))$$
$$= 9.706 \times 10^{-2}\ \text{m}^2\ (1.045\ \text{ft}^2)$$

and

$$\text{Re} = (1.588 \times 10^{-2})\,(42.79)/$$
$$\left[(1.060 \times 10^{-4})\,9.706 \times 10^{-2}\right]$$
$$= 6.605 \times 10^4$$

Using Fig. 4 given by Weber and Worek (1994), $j_f = 5.00 \times 10^{-3}$. Substituting these values into the same equation we utilized for h_{base} in the desuperheating zone, we obtain:

$$h_{base} = j_f C_s \dot{m}_s / S_m (k_s / C_s \mu_s)^{0.667}$$
$$= 1.114 \times 10^4 \text{ W/m}^2\text{K} (1963 \text{ Btu/hrft}^2 \cdot ^\circ\text{F})$$

This value is then multiplied by crossflow (J_c), leakage (J_l), baffle spacing (J_s), and bundle bypass (J_b) correction factors as it is in the desuperheating zone. However, a different figure is used to calculate the crossflow correction factor in this zone because the baffle design and hence the cross flow is different. Using Figs. 7, 6, and 8 from Weber and Worek (1994), $J_c = 0.900$ and $J_l = 0.654$. Using Bell (1986), we find $J_s = 0.95$. The adjusted shell-side heat transfer coefficient is:

$$h_0 = h_{base} (J_c) (J_l) (J_s) (J_b)$$
$$= 1.114 \times 10^{-4} (0.90) (0.654) (0.95) (0.90)$$
$$= 5.606 \times 10^3 \text{ W/m}^2\text{K} (987.9 \text{ Btu/hrft}^2 \cdot ^\circ\text{F})$$

2.3.2 Tube-Side Heat Transfer Coefficient. The tube side heat transfer coefficient in the drain cooling zone is the same value calculated for the desuperheating zone. That is:

$$h_i = 1.738 \times 10^4 \text{ W/m}^2\text{K} (3.063 \times 10^3 \text{ Btu/hrft}^2 \cdot ^\circ\text{F})$$

2.3.3 Overall Heat Transfer Coefficient. The overall heat transfer coefficient is then calculated by substituting the values obtained above into the same equation utilized in the desuperheating zone:

$$1/h = (1/5.606 \times 10^3) + 5.283 \times 10^{-5}$$
$$+ (1.8358 \times 10^{-3}/17.815) (1.588 \times 10^{-2}/1.404 \times 10^{-2})$$
$$+ 1/1.738 \times 10^4 (1.588 \times 10^{-2}/1.221 \times 10^{-2})$$
$$= 4.226 \times 10^{-4} \text{ m}^2\text{K/W}$$
$$h = 2.366 \times 10^3 \text{ W/m}^2\text{K} (417.0 \text{ Btu/hrft}^2 \cdot ^\circ\text{F})$$

2.4 Shell-Side Pressure Drop. The shell-side pressure drop is calculated by summing the losses through the baffle windows (ΔP_w) and across the tubes (ΔP_b).

2.4.1 Desuperheating Zone. The crossflow pressure drop is given by:

$$\Delta P_b = 2 f_i (\dot{m}_s)^2 N_c / (\rho_s g_c S_m^2)$$

Using Fig. 9 given in Weber and Worek (1994), we find: $f_i = 4.66 \times 10^{-4}$. The number of tubes in crossflow is given by Bell (1986):

$$N_c = S_m/(S(P)) = 2.016 \times 10^{-2}/$$
$$(2.334 \times 10^{-1}(2.143 \times 10^{-2})) = 4.03 \text{ tubes}$$

Substituting, the crossflow pressure drop for one baffle is:

$$\Delta P_b = 2(4.66 \times 10^{-4})(42.791)^2(4.03)/$$
$$(15.065(2.016 \times 10^{-2})^2)$$
$$= 1123 \text{ Pa}$$

The baffle window pressure drop is given by:

$$\Delta P_w = \dot{m}_s^2 / (S_w^2 \rho_s)$$

where S_w is the baffle window area calculated using Fig. 3 from Weber and Worek (1994).

For the desuperheating zone, the window area is given by:

$$S_w = \pi/2 (R)^2 - 2C(R)$$
$$= \pi/2 (80.089)^2 - (160.179) (18.7325)$$
$$= 7.075 \times 10^{-1} \text{ m}^2$$

Substituting the pressure drop through one window we find:

$$\Delta P_w = (42.791)^2/(7.075 \times 10^{-1})^2(15.065) = 242.82 \text{ Pa}$$

The crossflow and window pressure drops calculated above are then summed over the entire heater and corrected for leakage, bundle bypass, and baffle spacing using the method developed by Bell (1986) and modified by Weber and Worek (1994). That is:

$$\Delta P_s = ((N_b - 1) (\Delta P_b) J_b + N_b \Delta Pw) J_l + 2 \Delta P_b J_b J_s$$

The number of baffles is given by:

$$N_b = (L - L_{si} - L_{so})/L_s + 1$$
$$= (347.976 - 22.225 - 22.380)/23.336 + 1 + 14$$

The total zone pressure drop is then:

$$\Delta P_s = [13(1123.03)(0.9) + 14(242.82)](0.515)$$
$$+ 2(1123.03) (0.9) (1.0)$$
$$= 10.539 \text{ kPa} (1.53 \text{ psia})$$

2.4.2 Condensing Zone. The condensing zone pressure drop is negligible. There is no crossflow in this zone; the steam condenses and falls to the bottom of the heater as condensate before entering the drain cooling zone.

2.4.3 Drain Cooling Zone. The pressure drop calculation in the drain cooling zone is similar to the desuperheating zone except where specified. The crossflow pressure drop between two baffles in this zone is given by (Bell, 1986):

$$\Delta P_b = 2 f_i \dot{m}_s^2 N_c / (\rho_s g_c S_m^2)$$

From Fig. 9 of Weber and Worek (1994), we find $f_i = 0.85$. The number of tubes in crossflow is given by:

$$N_c = S_m/S (P) = 0.0971/(0.2809(0.02143)) = 16.13$$

Substituting the crossflow pressure drop for one baffle we find:

$$\Delta P_b = [2(0.85) (42.791)^2 16.13] / [(809.4) (9.710 \times 10^{-2})^2]$$
$$= 6579 \text{ Pa}.$$

The baffle window pressure drop equation in the drain cooling zone is not the same formula utilized in the desuperheating zone. This zone uses the original Delaware Method (Bell, 1986); whereas we have:

$$\Delta P_w = \dot{m}_s^2 / (\rho_s S_m S_w)$$
$$= (42.791)^2 / ((809.4) (9.710 \times 10^{-2}) (0.1730))$$
$$= 134.7 \text{ Pa}.$$

The number of baffles is:

$$N_b = (L - L_{si} - L_{so})/L_s + 1$$
$$= (191.135 - 39.37 - 39.37)/28.099 + 1 = 5$$

The total zone pressure drop is:

$$\Delta P_s = [4(6579)(0.9) + 5(134.7)](0.654)$$
$$+ 2(6579.4)(0.9)(0.95)$$
$$= 27.181 \text{ kPa} (3.94 \text{ psia})$$

2.5 Calculation of Feedwater Outlet Temperature. Once the heat transfer coefficients and the zone pressure drops have been calculated, the feedwater outlet temperature is calculated next. The calculation begins in the drain cooling zone because both the shell and feedwater side conditions are known. The zone boundary conditions are obtained from the heater specifications supplied by the manufacturer. The shell-side inlet conditions are saturated liquid ($x = 0.0$) at heater operating pressure. As explained in detail by Weber and Worek (1994), after an energy balance is obtained in the drain cooling zone the condensing zone is analyzed next. After an energy balance is obtained in the condensing zone, the desuperheating zone is analyzed. If an energy balance is not obtained in the desuperheating zone using the feedwater outlet conditions from the condensing zone and extraction steam inlet conditions supplied by the manufacturer, the extraction steam mass flow rate must be adjusted and the entire heater must be re-evaluated until an energy balance is obtained. Iterations resulted in a steam mass flow rate of 42.886 kg/s (340, 365 lb/hr) and the following data for each zone:

Drain Cooling Zone

$h_{si} = 1074.3$ kJ/kg (462.2 Btu/lbm)

$T_{si} = 247.8\,°C\ (478.0\,°F)$

$h_{so} = 897.9$ kJ/kg (386.3 Btu/lbm)

$T_{so} = 210.1°C\ (410.1°F)$

$h_{fwi} = 883.8$ kJ/kg (380.22 Btu/lbm)

$T_{fwi} = 205.1°C\ (401.2°F)$

$h_{fwo} = 900.5$ kJ/kg (387.4 Btu/lbm)

$T_{fwo} = 208.9°C\ (408.1°F)$

$\Delta T_{im} = 16.37°C\ (29.47°F) \qquad F = 0.936$

$R = 10.04 \quad P = 0.0882 \quad CF = 0.8763$

$Q_{dc} = 7.565 \times 10^3$ kW $(25.830 \times 10^6$ Btu/hr)

Condensing Zone

$h_{si} = 2833.9$ kJ/kg (1219.2 Btu/lbm)

$T_{si} = 257.5°C\ (495.5°F)$

$h_{so} = 1074.3$ kJ/kg (462.2 Btu/lbm)

$T_{so} = 247.8°C\ (478.0°F)$

$h_{fwi} = 900.5$ kJ/kg (387.4 Btu/lbm)

$T_{fwi} = 208.9°C\ (408.1°F)$

$h_{fwo} = 1066.0$ kJ/kg (458.6 Btu/lbm)

$T_{fwo} = 245.6°C\ (474.1°F)$

$\Delta T_{im} = 12.72°C\ (22.89°F)$

$Q_{dsc} = 1.498 \times 10^3$ kW $(5.115 \times 10^6$ Btu/hr)

$Q_{cd} = 7.3971 \times 10^4$ kW $(252.566 \times 10^6$ Btu/hr)

$Q_{\text{cond}} = 7.5469 \times 10^4$ kW $(257.681 \times 10^6$ Btu/hr)

Desuperheating Zone

$h_{si} = 3054.3$ kJ/kg (1314.0 Btu/lbm)

$T_{si} = 333.2\ (631.7°F)$

$h_{so} = 2833.9$ kJ/kg (1219.2 Btu/lbm)

$T_{so} = 257.5\ (495.5°F)$

$h_{fwi} = 1066.0$ kJ/kg (458.6 Btu/lbm)

$T_{fwi} = 245.6°C\ (474.1°F)$

$h_{fwo} = 1086.7$ kJ/kg (467.5 Btu/lbm)

$T_{fwo} = 250.1°C\ (482.2°F)$

$\Delta T_{im} = 36.59°C\ (65.87°F) \qquad F = 0.9933$

$R = 16.92 \quad P = 0.0511 \quad CF = 0.9466$

$Q_{DS} = 9.452 \times 10^3$ kW $(32.273 \times 10^6$ Btu/hr)

After all the heat transfer coefficients and zone temperatures have been calculated, the TTD and DCA can be easily obtained. Using Eq. (33) from Weber and Worek (1994) the TTD for this heater is:

$$\text{TTD} = T_{\text{sat,ext}} - T_{\text{fwo},ds}$$
$$= 247.93 - 250.1 = -2.17°C\ (-3.91°F)$$

Using Eq. (34) from Weber and Worek (1994) the DCA is:

$$\text{DCA} = T_{so,dc} - T_{fwi,dc} = 210.1 - 205.1 = 5.0\ (9.0°F)$$

These values are better than the guaranteed values of −1.67°C and 5.56°C, respectively. Therefore, this heater design meets the guaranteed specifications and is acceptable.

The authors wish to note a correction to the development of this method published in Weber and Worek (1994). The title of Fig. 7 is incorrect. The title currently is: Crossflow correction factor for the desuperheating and drain cooling zones. The title should be: Crossflow correction factor for the drain cooling zone.

3 Conclusion

This paper illustrates a practical method of validating feedwater heater performance using the Modified Delaware Method. The method enables a utility to verify that a feedwater heater meets specifications before it is purchased. Although there was no drain inlet to the heater given in the example, a heater with a drain inlet could easily be incorporated into the method. The method could also be easily implemented into a computer design program. The authors wish to acknowledge Dr. G. Minner of Haliburton NUS Corporation for his assistance with this paper.

References

ASME Steam Tables, 1967, ASME, New York.

Bell, K. J., 1986, *Delaware Method for Shell Side Design*, pp. 129–166.

Biar, M., 1991, "Feedwater Heater Design Data," Marley Heat Transfer Corp., Houston, TX.

Clemmer, A. B., and Lemezis, S., 1965, "Selection and Design of Closed Feedwater Heaters," presented at the ASME 1965 Winter Annual Meeting, Chicago, IL.

John, J. E. A., and Haberman, W. L., 1980, *Introduction to Fluid Mechanics*, Prentice Hall, Englewood Cliffs, NJ.

Palen, J. W., 1986, *Heat Exchanger Sourcebook*, Hemisphere Publishing Corp., New York.

Reynolds and Perkins, 1977, *Engineering Thermodynamics*, McGraw-Hill, New York.

Weber, G., 1992, Masters Thesis, University of Illinois at Chicago.

Weber, G. E., and Worek, W. M., 1994, "Evaluating the Design Performance of a Feedwater Heater With a Short Drain Cooler, Part I—Method Development," ASME JOURNAL OF ENGINEERING FOR GAS TURBINES AND POWER, Vol. 116, No. 2, pp. 434–441.